

Retinal Image Analysis using Sub-Riemannian Geometry in $\text{SE}(2)$

Colophon

The cover illustrates the gradual lifting (from left to right) of vessel curves in the plane \mathbb{R}^2 to the Lie group $SE(2)$, the space in which most geometrical analysis in this thesis takes place. The lifted curves in this higher dimensional domain $SE(2)$ have their tangent vectors contained in a *sub*-space (illustrated with rectangles) of the full 3D tangent space. The retinal image is taken with an EasyScan (EasyScan B.V.).

The work described in this thesis was part of the Sino-Dutch research consortium *RetinaCheck*, and was performed at the Technische Universiteit Eindhoven and EasyScan B.V. in the Hague.

The work described in this thesis has received funding from EasyScan B.V. and the Netherlands Organization for Scientific Research (NWO) as part of the Hé Programme of Innovation Cooperation (Dossier no. 629.001.003). Funding is also received from the European Foundation for the Study of Diabetes (EFSD), the Chinese Diabetes Society, and the Lilly Programme for Collaborative Diabetes Research between China and Europe (2012).



This thesis was typeset by the author using L^AT_EX 2 _{ε}

Printed by Gildeprint, Enschede

A catalogue record is available from the Eindhoven University of Technology Library.

ISBN: 978-94-6233-511-0

Cover design and layout by Erik Bekkers. Cover background by www.DinPattern.com.

Copyright © 2016 E.J. Bekkers, Eindhoven, The Netherlands.

All rights are reserved. No part of this publication may be reproduced by print, photocopy or any other means without the permission of the copyright owner.

Retinal Image Analysis using Sub-Riemannian Geometry in SE(2)

PROEFSCHRIFT

ter verkrijging van de graad van doctor aan de
Technische Universiteit Eindhoven, op gezag van de
rector magnificus, prof.dr.ir. F.P.T. Baaijens, voor een
commissie aangewezen door het College voor
Promoties in het openbaar te verdedigen
op maandag 23 januari 2017 om 16.00 uur

door

Erik Johannes Bekkers

geboren te Woerden

Dit proefschrift is goedgekeurd door de promotoren en de samenstelling van de promotiecommissie is als volgt:

voorzitter: prof.dr. J.P.W. Pluim

promotor: prof.dr.ir. B.M. ter Haar Romeny

copromotor: dr.ir. R. Duits

leden: prof.dr. B. van Ginneken (Radboud Universiteit Nijmegen)

prof.dr. J. Weickert (Universität des Saarlandes)

prof.dr.ir. B. Koren

dr. L. Cohen (Centre National de la Recherche Scientifique, Paris)

adviseur: Th. van Elzakker (i-Optics)

Het onderzoek dat in dit proefschrift wordt beschreven is uitgevoerd in overeenstemming met de TU/e Gedragscode Wetenschapsbeoefening.

Contents

Preface	ix
I Introduction	1
1 Clinical Background	3
1.1 Retinal Imaging	4
1.2 Motivations for Retinal Vessel Analysis	7
1.3 Research on the Retinal Microvasculature	9
1.3.1 Age and Gender	12
1.3.2 Hypertension	12
1.3.3 Diabetes Mellitus	13
1.4 Retinal Image Analysis Algorithms	13
1.4.1 Anatomical Landmark Detection (Ch. 5)	14
1.4.2 Retinal Vessel Segmentation (Ch. 6)	14
1.4.3 Retinal Vessel Modeling (Ch. 7, 8 & 9)	16
1.4.4 Lesion Segmentation	16
1.4.5 Feature/Biomarker Extraction (Ch. 10, 11 & 12)	17
2 Technical Background: Orientation Scores and Lie Groups	19
2.1 Invertible Orientation Scores	20
2.1.1 What are Orientation Scores?	20
2.1.2 What is the Motivation for Using Orientation Scores?	20
2.1.3 Why Call Them Orientation Scores?	24
2.1.4 How is an Orientation Score Constructed?	25
2.1.5 What Kind of Wavelets Can Be Used?	27
2.1.6 Why Do We Need Group Theory and Sub-Riemannian Geometry?	31
2.2 Group Theoretical Prerequisites	38

CONTENTS

2.2.1	Groups, Lie Groups, and Representations	38
2.2.2	Tangent Spaces and Left-Invariant Vector Fields	41
2.2.3	Matrix Groups and the Exponential Map	43
2.2.4	The Lie Algebra	45
2.3	The Roto-Translation Group and Left-Invariant Processing via Invertible Orientations Scores	46
2.3.1	The Lie group $SE(2)$	46
2.3.2	Left-Invariance	47
2.3.3	Left-Invariant Vector Fields	48
3	The Developed Retinal Image Processing Applications	51
3.1	Anatomical Landmark Detection (Ch. 5)	53
3.2	Vessel Enhancement (Ch. 6)	56
3.3	Vessel Tracking Part I (Ch. 7)	60
3.4	Vessel Tracking Part II & III (Ch. 8 & 9)	62
3.5	Artery-Vein Classification (Ch. 10)	68
3.6	Vessel Feature Analysis (Ch. 11 & 12)	69
II	Differential Geometrical Tools	75
4	Sub-Riemannian Geometry in the Orientation Score Domain	77
4.1	Riemannian Geometry	78
4.2	The Lie Group $SE(2)$ and its Tangent Bundle $T(SE(2))$	79
4.2.1	The Lie Group $SE(2)$	79
4.2.2	The Tangent Bundle $T(SE(2))$	80
4.2.3	Horizontal Curves and the Sub-Bundle Δ	80
4.3	The Left-Invariant Metric Tensor of Interest	81
4.3.1	The sub-Riemannian Manifold	81
4.3.2	A Riemannian Approximation of the Sub-Riemannian Manifold .	82
4.4	The Co-Tangent Bundle $T^*(SE(2))$ and Differential Forms	84
4.5	Short \neq Straight: the Left Cartan Connection	86
4.5.1	Connections	86
4.5.2	The Levi-Civita Connection	87
4.5.3	The Left Cartan Connection on $SE(2)$	88
4.5.4	Why Do We Use the Left Cartan Connection?	90

III Applications	93
5 Retinal Landmark Detection	95
5.1 Introduction	96
5.2 Template Matching & Regression on \mathbb{R}^2	100
5.2.1 Object Detection via Cross-Correlation	100
5.2.2 Optimizing t Using Linear Regression	101
5.2.3 Optimizing t Using Logistic Regression	102
5.2.4 Template Optimization in a B-Spline Basis	103
5.3 Template Matching & Regression on $SE(2)$	105
5.3.1 Orientation Scores on $SE(2)$	105
5.3.2 Object Detection via Cross-Correlation	105
5.3.3 Optimizing T Using Linear Regression	106
5.3.4 Optimizing T Using Logistic Regression	106
5.3.5 Template Optimization in a B-Spline Basis	107
5.4 Probabilistic Interpretation of the Smoothing Prior in $SE(2)$	108
5.4.1 Resolvent Diffusion Processes	108
5.4.2 The Fundamental Single Patch Problem	109
5.4.3 Expansion in B-splines	111
5.4.4 The Drunkman’s Pencil	113
5.5 Applications	114
5.5.1 The Experimental Set-Up	115
5.5.2 Optic Nerve Head Detection in Retinal Images	117
5.5.3 Fovea Detection in Retinal Images	125
5.5.4 Pupil Detection	130
5.5.5 General Observations	137
5.6 Conclusion	137
6 Vessel Enhancement	139
6.1 Introduction	140
6.2 Methods	141
6.2.1 Orientation Scores	141
6.2.2 Gaussian Derivatives in Orientation Scores	141
6.2.3 Gauge Derivatives and Exponential Curve Fits in $SE(2)$	142
6.2.4 Scale–Orientation Scores	144
6.2.5 Vesselness Filtering on Scale–Orientation Scores	146
6.3 Experiments	148

CONTENTS

6.4	A Fast Alternative $SE(2)$ Gauge Frame Method	150
6.5	Conclusion	151
7	Vessel Tracking Part I: Iterative Tracking via Local Optimization	153
7.1	Introduction	154
7.2	Tools From Orientation Score Theory	155
7.2.1	Double-Sided vs Single-Sided Wavelets, Orientation vs Direction	157
7.3	Vessel Tracking in Orientation Scores via Optimization in Transversal Tangent Planes \mathcal{V}	159
7.3.1	Methods	159
7.3.2	Validation	165
7.4	Vasculature Tracking	172
7.4.1	Methods	173
7.4.2	Validation	178
7.5	Conclusion	180
8	Vessel Tracking Part II: Sub-Riemannian Geodesics in $SE(2)$	183
8.1	Introduction	184
8.1.1	Structure of the Chapter	186
8.2	Problem Formulation	187
8.3	Solutions via Data-driven Wavefront Propagation	188
8.4	An Iterative IVP-procedure to Solve the SR-Eikonal BVP	193
8.5	Construction of the Non-Uniform Cost	196
8.6	Implementation	197
8.7	Experiments and Results	198
8.7.1	Verification for the Uniform Cost Case	198
8.7.2	Feasibility Study for Application in Retinal Imaging	202
8.7.3	Sub-Riemannian Fast Marching	206
8.8	Conclusion	207
9	Vessel Tracking Part III: Sub-Riemannian Geodesics in $SO(3)$	209
9.1	Introduction	210
9.1.1	Chapter Outline	213
9.2	Prerequisites	214
9.2.1	Spherical Images	214
9.2.2	The Lie Group $SO(3)$	218
9.3	The Problems $\mathbf{P}_{\text{curve}}$ on S^2 and \mathbf{P}_{mec} on $SO(3)$	219

CONTENTS

9.3.1	Statement of the Problem $\mathbf{P}_{\text{curve}}$	219
9.3.2	Statement of the Problem \mathbf{P}_{mec} on $SO(3)$	219
9.3.3	Relation Between the Problems $\mathbf{P}_{\text{curve}}$ and \mathbf{P}_{mec}	220
9.4	Analytic Formulas Obtained via the Left-Cartan Connection	223
9.4.1	Cartan Connection	223
9.4.2	Parallel Momentum	224
9.4.3	The Hamiltonian System in Sub-Riemannian Arc-Length Parameterization	224
9.4.4	Exact Solutions	225
9.4.5	Alternative Derivation of the Analytic Solution via the Left Cartan Connection	227
9.5	PDE Approach for Data-Driven Sub-Riemannian Geodesics on $SO(3)$.	228
9.5.1	Sub-Riemannian Fast Marching in $SO(3)$	229
9.6	Experiments	230
9.6.1	Verification of the Fast Marching Method in the Case of Uniform External Cost	231
9.6.2	Comparison of Sub-Riemannian Geodesics in $SO(3)$ and $SE(2)$ for $C = 1$	232
9.6.3	Vessel Analysis via Sub-Riemannian Geometry on $SO(3)$ and $SE(2)$.	233
9.7	Conclusion	236
10	Artery-Vein Classification	239
10.1	Introduction	240
10.2	Methods	241
10.2.1	Energy Function Definition	241
10.2.2	Feature Extraction and Training	242
10.2.3	Energy Minimization	244
10.3	Experiments	246
10.3.1	Ground Truth Data	246
10.3.2	Method Parameterization and Validation	246
10.4	Conclusion	248
11	Vessel Geometry In Orientation Scores Part I: Pixel-wise Curvature Measurements and Curvature-Based Biomarkers	249
11.1	Introduction	250
11.2	Theory	251
11.2.1	Exponential Curves in $SE(2)$	251

CONTENTS

11.2.2 Exponential Curve Fits	252
11.3 Global Tortuosity Measures From Pixel-Wise Curvature Voting	254
11.3.1 Global Tortuosity Measures	254
11.3.2 Orientation Confidence	255
11.3.3 Iterative Stabilization of Orientation Confidence	256
11.3.4 Extensions and a Conventional Processing Pipeline	256
11.4 Validation	257
11.4.1 Validation on Local Curvature Measurements	257
11.4.2 Repeatability/Reproducibility	258
11.5 Application to Clinical Data	259
11.5.1 Response to Diabetic Retinopathy Images	259
11.5.2 Curvature Biomarker in Association with Diabetes Mellitus Type 2	259
11.5.3 Curvature Biomarker in Association with Hypertension	262
11.6 Conclusion	265
12 Vessel Geometry In Orientation Scores Part II: A New Tubularity Measure	267
12.1 Introduction	268
12.2 A Tubularity Measure Obtained From the Right-Regular Representation	269
12.2.1 A Tubularity Measure Obtained from the Right-Regular Representation	269
12.2.2 Relation to the Optimally Oriented Flux Filter and the Chen-Cohen Tubularity Measure	273
12.2.3 Some Properties of the New Tubularity Measure	274
12.3 Applications of the Tubularity Measure	275
12.3.1 New Biomarkers	275
12.3.2 Vessel Tracking and Connectivity Analysis	278
12.4 Conclusion	279
IV Appendices	281
A Retinal Landmark Detection	283
A.1 The Smoothing Regularization Matrix R	283
A.2 Normalized Cross Correlation	286
A.2.1 Normalized Cross-Correlation in \mathbb{R}^2	286
A.2.2 Normalized Cross-Correlation in $SE(2)$	287

CONTENTS

A.2.3	Efficient Local Normalization of \hat{f}_x and $\hat{U}_{f,g}$	288
A.2.4	Including a Region of Interest Mask	288
A.3	Additional Details on the Detection Problems	289
A.3.1	Processing Pipeline, Settings and Timings	289
B	Vessel Tracking Part I: Iterative Tracking via Local Optimization	293
B.1	A Mathematical Underpinning of Optimization in the Tangent Planes \mathcal{V}	293
B.1.1	Geometrical Principle Behind the ETOS-algorithm	293
B.1.2	Application of the Geometrical Principle to Completion Fields	295
B.1.3	In the Heisenberg Approximation of Completion Fields our Approach Produces B-splines	297
B.1.4	Concluding Remarks	298
C	Vessel Tracking Part II: Sub-Riemannian Geodesics in $SE(2)$	301
C.1	Application of Pontryagin's Maximum Principle	301
C.2	Lemmas Applied in the Proof of Theorem 2	302
C.3	Viscosity Solutions for HJB-systems in $SE(2)$	305
C.4	Proof of Theorem 3	306
C.5	The Limiting Procedure (8.15) for the Sub-Riemannian Eikonal Equation	308
C.6	Embedding into Geometric Control Theory	311
References		338
Summary		339
About the Author		341
List of Publications		343

Preface

Can we use retinal images to recognize and identify the development of (systemic) diseases in such an *early stage* that treatment is most effective (before pathologies occur), and perhaps, that further disease progression can be prevented all together? I believe that the answer to this question is a "definite maybe". Computer aided diagnosis and automatic disease screening in retinal imaging are already becoming common practice due to state-of-the-art approaches in which quantitative image analysis algorithms and machine learning methods are ingeniously combined to effectively determine the presence of retinal pathologies. With respect to *early* diagnosis the following developments are promising: (1) the growing body of evidence found in literature that shows that alterations in the vascular system (induced by systemic diseases) can be quantified using retinal images; and (2) the ever advancing field of machine intelligence. With the purpose of supporting *large-scale* clinical studies, which are necessary to learn more about the vascular components of disease progression, and supporting large-scale screening programs, I describe in this thesis a comprehensive retinal image processing toolset. As such, I hope to contribute to the realization of early diagnosis screening programs and getting one step closer to a "definite yes".

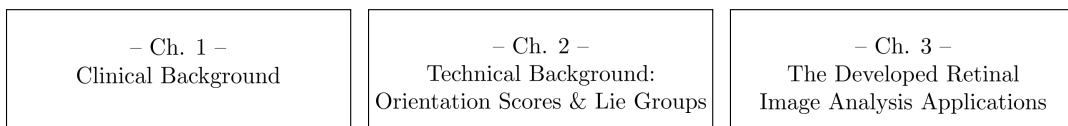
In each specialized retinal image analysis task one has to deal with fundamental problems: large variations in appearance of anatomical landmarks; short-cuts and over/under-segmentation in vessel tracking and segmentation due to complex patterns; the presence of pathologies; low image quality; and the involved quantification of geometrical vessel properties. As described in this thesis, all of the aforementioned problems can be effectively addressed in a unified approach in which curves and image data are analyzed in a higher dimensional space $SE(2)$ of positions (x, y) and orientations θ . This approach is inspired by the finding of multi-orientation columns in our visual cortex. In this new representation, 2D curves become 3D curves (illustrated on the cover of this thesis) that have their tangent vectors restricted to *sub-spaces* (illustrated with rectangles) of the full 3D tangent spaces, and 2D images are analyzed as functions

0. PREFACE

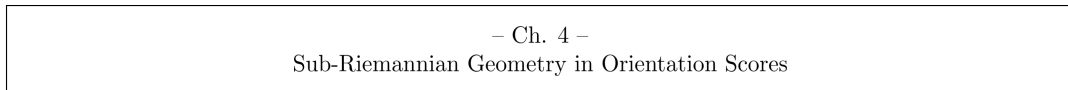
on the 3D space $SE(2)$. In the analysis we have to deal with the curved geometry of $SE(2)$, and together with the imposed restrictions on the 3D curves, this has the consequence that we have to consider a sub-Riemannian geometry on $SE(2)$.

In order to solve problems encountered in conventional image processing, I applied and designed fundamental differential geometrical methods. In this process I had to expand my knowledge on abstract formal concepts, which was both interesting and challenging coming from an engineering background. I have put effort in explaining the basics of sub-Riemannian geometry on position and orientation space as intuitively as possible, and with many illustrations. As such, I hope to have delivered a thesis which is also accessible to other engineers in medical image processing.

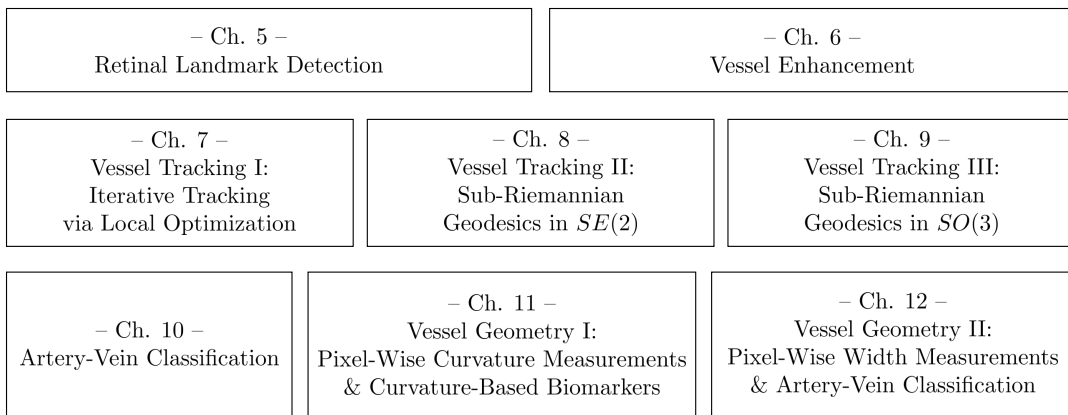
Part I: Introduction



Part II: Differential Geometrical Tools



Part III: Applications



The contents of this thesis are illustrated in the diagram above, and are organized in three parts as follows:

I: Introduction: This part is split into three chapters. A clinical motivation of this research is given in Ch. 1, a technical background of the used theory is given in Ch. 2, and an overview of all the applications developed in this thesis is provided

in Ch. 3. In particular Ch. 3 can be read as a sequence of (extended) abstracts which can guide the reader through the main content of this thesis (Part III).

II: Differential Geometrical Tools: In Ch. 4 the differential geometrical tools used in the processing and analysis of orientation scores (image data represented as densities on $SE(2)$) are explained. Together with Ch. 2 it defines the basis on which all the subsequent applications of Part III are based.

III: Applications: The chapters 6 to 12 each describe a different application in retinal imaging based on the theory of Part II. These chapters can be read separately, in no specific order.

I wrote the thesis in such a way that the reader

- who is primarily interested in the (results of the) addressed applications can concentrate on the comprehensive overview in Ch. 3.
- who first wants to get acquainted with the basic mathematical tools can find them in Ch. 2 and Ch. 4.

I would like to acknowledge that this thesis could not have obtained its final form without the contributions of others involved in this project. This includes all the co-authors that have contributed to the publications of the contents of this thesis. In specific I would like to acknowledge the first authors of the publications on which chapters 6, 9 and 10 are based, which are respectively Julius Hannink, Alexey Mashtakov and Koen Eppenhof. I am very grateful to use this joint work in my thesis, as it gives a more complete picture of the topic of this thesis and my contributions therein, which for these chapters are as follows. In Ch. 6 I supported the implementation of adaptive frame techniques, the implementation of scale-orientation scores, and the validation of the developed enhancement methods. In Ch. 9 I prepared the implementation and the experimental validation of data-adaptive sub-Riemannian geodesics for non-uniform cost. In Ch. 10 I provided the vessel models which were generated by the tracking method of Ch. 7, and supported only in the theoretical development of the method. Contributions by Gonzalo Sanguinetti on the sub-Riemannian geodesic chapter Ch. 8 are also gratefully acknowledged. Last but certainly not least, I would like to thank my copromotor Remco Duits for all the discussions about the contents of this thesis; these fruitful interactions strengthened both theory and algorithm development. In particular he is gratefully acknowledged for his support on the theoretical underpinning of the ideas and methods discussed in this thesis, and for his contributions in Ch. 8, App. B and App. C.

0. PREFACE

Finally, I would like to acknowledge the funding parties in this project, which are EasyScan B.V. and the Netherlands Organization for Scientific Research (NWO) as part of the Hé Programme of Innovation Cooperation (Dossier no. 629.001.003). In particular I would like to thank EasyScan B.V. for hosting me in their inspiring offices in the Hague. Above all, I gratefully acknowledge my promotor Bart ter Haar Romeny on his feedback on this research and for his great efforts that lead to the realization of this thesis and the encompassing *RetinaCheck.org* project.

Erik Bekkers
Eindhoven, 30 September, 2016

Part I

Introduction

Chapter 1

Clinical Background

1. CLINICAL BACKGROUND

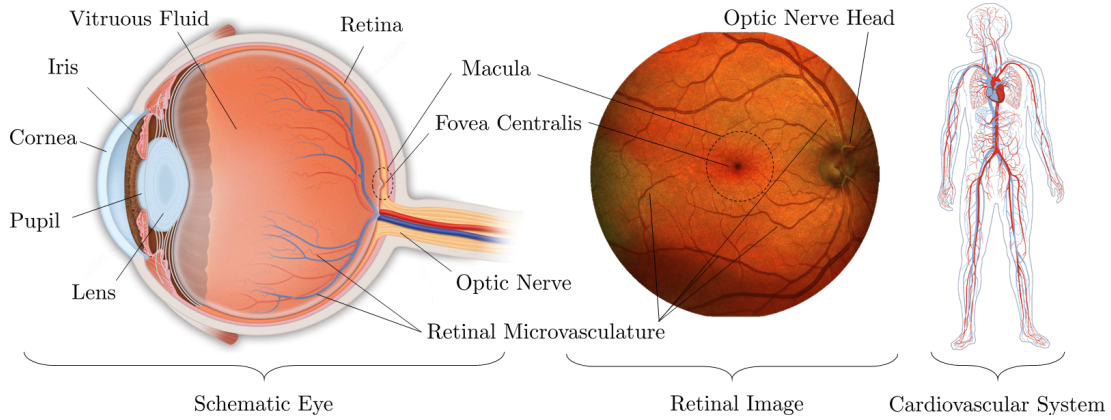


Figure 1.1: From left to right the anatomy of the eye, an image obtained with a retinal imaging device, an illustration of the human vascular system. A special property of the retina is that it is one of the only places in the human body where the vascular system can be directly observed.

1.1 Retinal Imaging

The eyes are our window to the outside world, and like many other windows, it works two ways. It allows the outside world to take a look inside the human body as well. The fact that our vision is based on an optical path that maps light (from the outside world) to the retina allows for the imaging of the inside of the eye. This is the main principle on which most retinal imaging devices are based: they make use of an optical system consisting of a light source and a system of lenses that corrects for the refraction of light caused by the cornea, lens and vitreous fluid (see Fig. 1.1 for the anatomy of the eye). As such, these devices allow for the direct and non-invasive optical imaging of the living tissue that covers the inside of the eye.

The interior of the eye is called the fundus and its most complex structure is the retina: a thin layer of tissue responsible for converting light into neuronal signals that are forward (via the optic nerve) to the brain for processing. Optical imaging devices for photography of the fundus are usually called fundus cameras, and they are more generally referred to as retinal imaging devices. Retinal imaging devices allow us to observe the retina in great detail, and are proven to be of great diagnostic value. They can be used to diagnose a wide variety of eye diseases, even before visual symptoms appear.

There are many different types of optical retinal imaging devices, each allowing to image different aspects of the retina. In this thesis we however limit ourselves to work

1.1 Retinal Imaging



Figure 1.2: A scanning laser ophthalmoscopy camera (EasyScan, EasyScan B.V.).

with the 2D retinal images coming from the most used cameras in retinal imaging, which are the color fundus (CF) camera and the scanning laser ophthalmic (SLO) camera. An example of a SLO camera is given in Fig. 1.2. The main difference between CF and SLO cameras is the light source used to image the retina; CF uses a white light flash and SLO uses a coherent (laser) light source of which the wavelength is typically tuned for optimal contrast between blood (vessels) and background pigmentation, see for example Fig. 1.3. Also in large scale clinical studies and screening programs the CF and SLO camera is the best choice due to its low cost and non-invasive nature. An interesting recent development is that such cameras are also more frequently used outside clinical environments: they are also used in the optical retail market/optician stores, serving as a convenient access point for screening and tele-diagnosis.

Retinal imaging devices have one specific property which makes them very special. They are one of the very few tools available for direct and non-invasive imaging of the humans circulatory system¹ in vivo. This property makes that the clinical application

¹Apart from the eyes, the only other place in the human body where the microvasculature can be directly observed is at the base of the nails. Here the capillaries can be imaged via a microscope and this imaging process is called nailfold capillaroscopy.

1. CLINICAL BACKGROUND

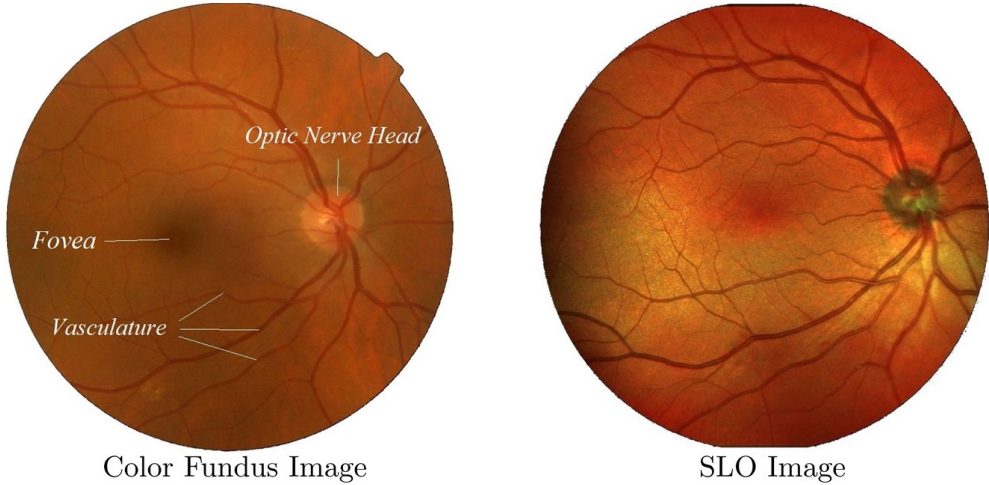


Figure 1.3: The left image is obtained with a CF camera (Topcon NW200, Topcon corp., Japan) by flashing a white light into the eye and measuring its reflectance, a process much like normal photography. The right image is a pseudo color image obtained with an SLO camera (Easyscan, EasyScan B.V., the Netherlands), obtained using two laser light sources with wavelengths of 785nm (near infra red) and 532nm (green). Although both camera-types image the same retinal structures, there are subtle differences in the way the images look (e.g. appearance of the optic nerve head, contrast, and noise characteristics), which have to be taken into account when analyzing the images.

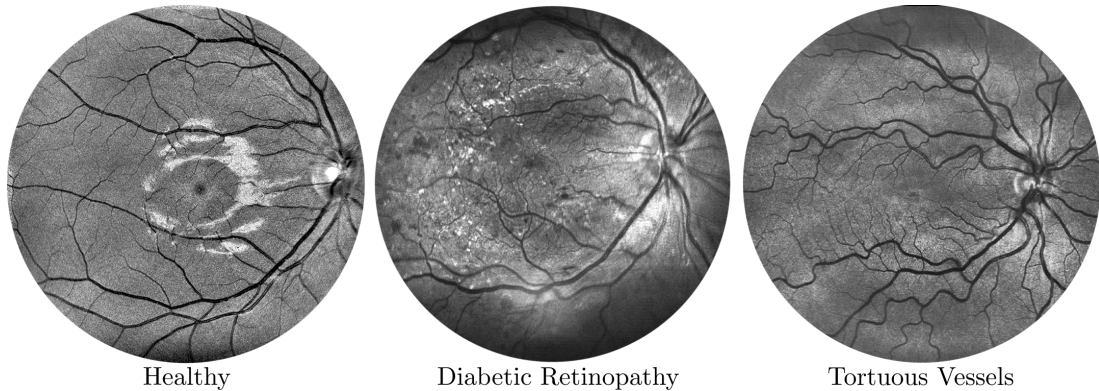


Figure 1.4: From left to right a retina of healthy subject, a retina with diabetic retinopathy, and a retina with increased vessel tortuosity of a patient with hypertension. The images are obtained with an SLO camera (EasyScan, EasyScan B.V., the Netherlands) and show the green channel (532nm).

1.2 Motivations for Retinal Vessel Analysis

area of retinal imaging is not only restricted to investigate and diagnose ocular diseases, but more generally to the research of any (systemic) disease that has a vascular component (see also Fig. 1.1). This property makes that retinal imaging is used in a wide range of clinical studies that are aimed at finding associations with vessel parameters (such as vessel caliber, tortuosity and bifurcation geometry) and systemic diseases. The objective of such clinical research is typically twofold:

1. To obtain insight in how the micro-vasculature changes with progression towards certain diseases.
2. To investigate the potential of screening and diagnosis of certain diseases via the analysis of retinal blood vessels.

In this thesis we develop (semi-) automatic quantitative retinal image analysis algorithms that can be used in large-scale clinical research programs and potentially for use in (early diagnosis) screening programs. A summary of such clinical research programs and their findings is given in Section 1.3. The kind of retinal image analysis algorithms that are typically used in such studies are described in Section 1.4. But before we continue, let us first summarize the main motivations for *this* thesis from a clinical perspective.

1.2 Motivations for Retinal Vessel Analysis

While the retinal image analysis tools developed in this thesis are useful in a wide range of (automated) retinal image analysis applications, the main focus of this work is on the analysis of the retinal vasculature. As described in the previous section (and in more detail in the upcoming Section 1.3), there are many diseases with a vascular component that can be studied in the retina. Some diseases, e.g. diabetes mellitus type 2 (DM2), might for example damage the vasculature to such an extent that the vessels start to leak and cause bleedings. In the eye this is particularly troublesome as this could eventually lead to blindness. Patients diagnosed with DM2 therefore have a regular examination of their retinas in order to check if the disease has not yet lead to diabetic retinopathy (damage to the retina due to DM2, see Fig. 1.4). If it has, the patient needs to be referred for additional treatment. To reduce the workload of clinical graders, and in order to perform large scale screening of DR for the prevention of blindness, a branch of computerized retinal image analysis therefore focuses specifically on the automatic detection of diabetic retinopathy.

1. CLINICAL BACKGROUND

As with many diseases early diagnosis is crucial: the earlier a disease is detected, the cheaper and more effective treatment typically is. Early detection and treatment of diabetic retinopathy can for example reduce the risk of blindness by 95% NIH-National Eye Institute (2015). Since leakage and bleeding of the blood vessels start with changes and damage to the blood vessels Stewart (2010), it is relevant to investigate whether or not (geometrical properties of) the retinal blood vessels can be used as biomarkers for *early* diagnosis of diabetic retinopathy. Furthermore, if retinal vessel analysis gains new insight in the diagnosis of prediabetes (a condition of elevated glucose levels that could develop into DM2), the development into DM2 can even be prevented all together due to timely treatment Tuomilehto *et al.* (2001). Currently, prediabetes can be diagnosed using a fasting plasma glucose test and an oral glucose tolerance test, which are both invasive (requires blood samples) and which both require the patient to be in a fasting state. If the *non-invasive* analysis of retinal blood vessels, through retinal imaging, provides new insight into the process of progression towards DM2 and diabetic retinopathy, this could be of great importance for cost-effective screening, diagnosis, treatment monitoring and prevention of the disease.

Examples such as the previous motivate research groups to study the retinal vasculature:

1. *Retinal vessel analysis allows for studying a wide range of diseases and medical conditions.* Retinal imaging allows to observe living tissue, including the circulatory system. As there are many (systemic) diseases and conditions that affect the vascular network, research using retinal imaging is not limited to the study of ocular diseases alone, but includes more generally the study of diseases with a vascular component, see for example studies on the retinal vasculature in association with diabetes mellitus Cheung *et al.* (2012), hypertension Ikram *et al.* (2006b), Alzheimer's disease Williams *et al.* (2015) and stroke Wong *et al.* (2001).
2. *Retinal vessel analysis could provide means for non-invasive early diagnosis of diseases.* Many severe complications, like for example diabetic retinopathy, start with damage to the vascular network Stewart (2010). If early alterations of the vascular network could be recognized in the retina, diseases might be detected in an early stage before severe complications take place. In particular the use of *invasive* screening methods, such as the fasting plasma glucose (FPG) test, which requires overnight fasting and a blood draw (e.g. taking blood samples), seems unnecessarily uncomfortable to (possibly healthy) subjects. Research in retinal vascular analysis could lead to reliable *non-invasive* screening methodologies.

1.3 Research on the Retinal Microvasculature

3. *Retinal imaging is a non-invasive method with presence in both clinical and commercial environments.* In addition to the non-invasive nature of retinal imaging (item 2), the presence in both clinical and commercial environments (e.g. optical retail shops) seems to make retinal imaging devices ubiquitous. As such, retinal imaging is a convenient access point for disease screening and health monitoring.
4. *Both clinical research and screening programs need to deal with large quantities of images.* Computerized algorithms can assist researchers and clinical graders to deal with large amounts of data via the (semi-) automatic analysis of retinal images. Other studies have shown that such computer assistance can reduce costs while maintaining similar grading performance to that of manual labor Bojke *et al.* (2008); Fleming *et al.* (2007); Olson *et al.* (2003); Scotland *et al.* (2007).
5. *Both clinical research and screening programs need to deal with quantification of observations.* Properties of the retinal vasculature (e.g. the size of arteries or the tortuosity/curvature of veins) need to be quantified in order to have *objective* observations, human experts are not good at this. Such quantification can be done reliably, efficiently and objectively using computerized retinal image analysis algorithms.

1.3 Research on the Retinal Microvasculature

There is growing evidence that variations in retinal vessel geometry (e.g., vessel caliber and tortuosity) are associated with a range of systemic conditions and diseases. Research that studies such associations is typically done using cross-sectional studies, i.e., studies that involve the analysis of data collected from a population (usually consisting of certain patient groups and a control group) at a certain point in time. Cross-sectional studies are a category of epidemiological studies, i.e., the study and analysis of patterns, causes, and effects of health and disease conditions in defined populations. A good introduction to different types of epidemiological studies is given in Mann (2003).

Cross-sectional studies involving the analysis of the retinal vasculature have so far primarily focused on studying retinal vessel caliber in association with systemic diseases like hypertension Hubbard *et al.* (1999); Ikram *et al.* (2006b); Leung *et al.* (2003); Mitchell *et al.* (2007); Sun *et al.* (2009); Taarnhøj *et al.* (2006); Wang & Wong (2006); Wong *et al.* (2003) and diabetes mellitus Cheung *et al.* (2015); Nguyen *et al.* (2007); Sabanayagam *et al.* (2015); Wong *et al.* (2002, 2005). More recently, studies

1. CLINICAL BACKGROUND

have also focused on geometrical properties of the vasculature that are more complex to quantify, such as vessel tortuosity Cheung *et al.* (2011b); Han (2012); Hughes *et al.* (2006); Owen *et al.* (2008); Sasongko *et al.* (2015); Wu *et al.* (2013); Zhu *et al.* (2014) and fractal dimension Aliahmad *et al.* (2014); Broe *et al.* (2014); Cheung *et al.* (2011a); Grauslund *et al.* (2010); Huang *et al.* (2015); Yau *et al.* (2010).

In the upcoming subsections we provide a condensed overview of the current knowledge on how retinal vessel properties are associated with certain diseases and medical conditions. Here we restrict our summary to the most studied diseases (hypertension and diabetes), and the most studied vessel features (vessel caliber and tortuosity) in the context of retinal vessel research.

In this thesis we developed a novel method for direct analysis of vessel tortuosity (Subsec. 3.6 and Chapter 11), see e.g. Fig. 1.5. The method relies on analysis of so-called orientation scores (explained in Chapter 2) rather than the 2D images, allowing us to directly compute tortuosity related features without the need of prior vessel segmentation. We used this tool in two populations studies to investigate how our developed tortuosity measure is associated with respectively diabetes mellitus and hypertension. In the first study healthy subjects are compared against patients with different types of diabetes. In this dataset 1,574 subjects were included. In the second study healthy subjects are compared to patients with hypertension. In this dataset 421 subjects are included. In the following subsections we will indicate how our findings relate and contribute to the literature, full details will be provided in Chapter 11.

Remark 1. *When studying the association of geometrical retinal vessel properties with certain diseases or health conditions, one has to take confounding variables into account. A confounding variable is a variable which correlates with both the dependent parameter of interest (e.g. vessel caliber) and the independent parameter (e.g. blood pressure). Such confounding variables need to be corrected for in order not to draw incorrect conclusions. For example, vessel caliber is known to change with age, and if one finds that patients with high blood pressure have smaller blood vessels, one wants to make sure that this is not due to the fact that this patient group contains more elderly people. I.e., one wants to correct for the confounding effect of age. The conclusions summarized in Subsec. 1.3.2 and 1.3.3 include such corrections. In Subsec. 1.3.1 we briefly discuss the two most encountered confounding parameters in retinal vessel research.*

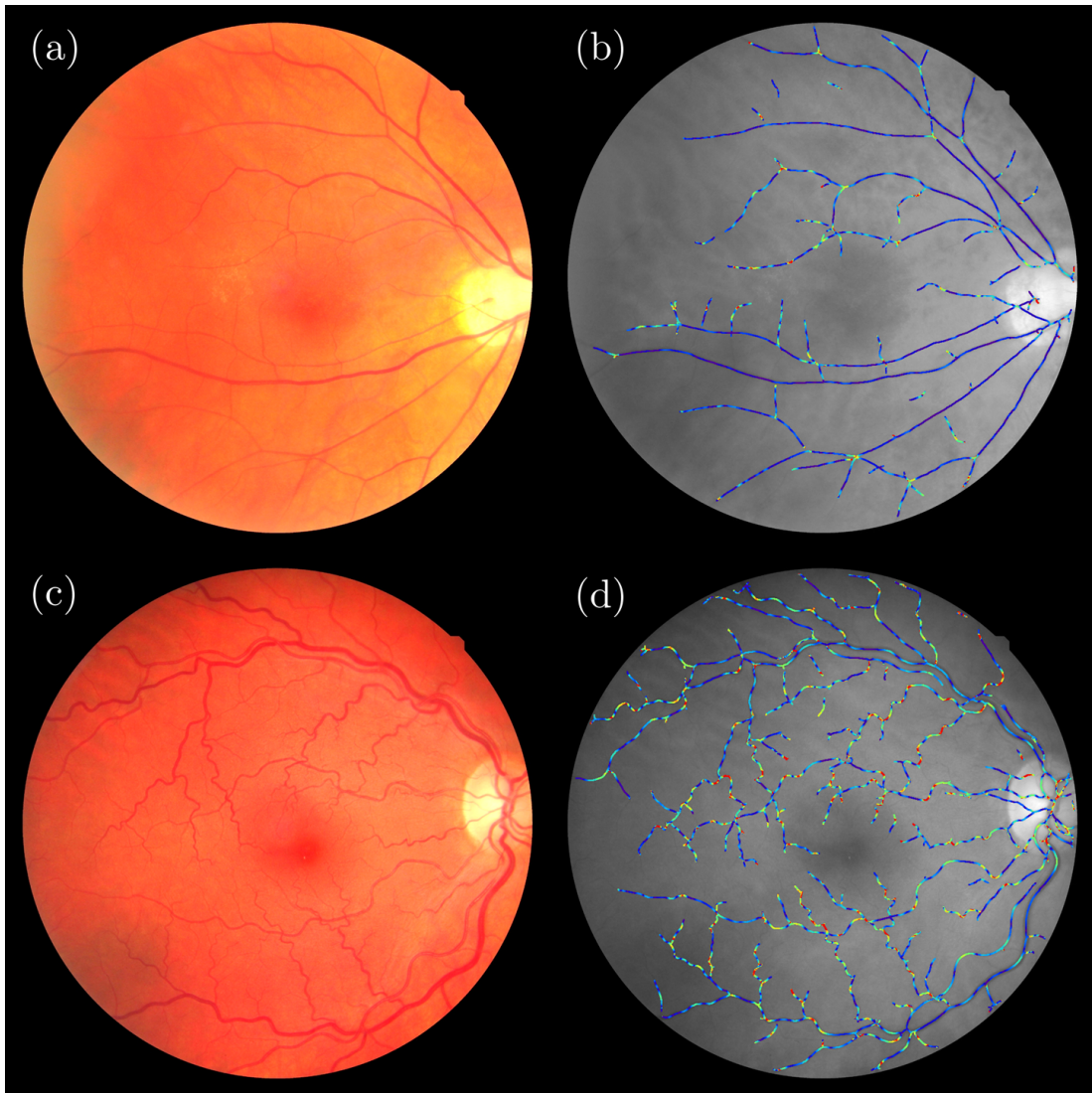


Figure 1.5: A fundus image with low vessel tortuosity from a healthy volunteer (a), and an image with high vessel tortuosity from a diabetic patient (c). Figures (b) and (d) show the responses of the curvature filter developed in Chapter 11. The filter assigns to every pixel a curvature value, here color coded (blue/purple is low curvature, red is high curvature), and a vessel confidence. The confidence value at each pixel is used to weigh the corresponding curvature value when computing global tortuosity measures (for details see Chapter 11).

1. CLINICAL BACKGROUND

1.3.1 Age and Gender

The human circulatory system changes with age, and this can be observed in the retina. A large amount of cross-sectional studies uniformly demonstrates that the retinal blood vessel's cross-sections decrease in size with increasing age, see Sun *et al.* (2009) and references therein. In a lesser number of publications, and with less agreement among them, vessel tortuosity is also associated with older age. In contrast to Cheung *et al.* (2011b); Wu *et al.* (2013) where a decrease in tortuosity is reported to be associated with older age, Han (2012) reports an increase of tortuosity with age.

Literature also reports anatomical differences between males and females: the retinal blood vessels of females are generally more tortuous than those of males Cheung *et al.* (2011b); Wu *et al.* (2013); Zhu *et al.* (2014). Generally the arteriolar vessel caliber in females is found to be larger than those in males, see Sun *et al.* (2009) and references therein.

Our findings. In our two studies on retinal tortuosity we generally found that lower vessel tortuosity is associated with increasing age. Our results also indicates a higher tortuosity in females compared to males. For full details see Subsec. 11.5.2 and 11.5.3.

1.3.2 Hypertension

Hypertension is a long term medical condition in which the arterial blood pressure is persistently elevated. It is generally found that a decrease in retinal vessel caliber is associated with an increase in blood pressure, see Sun *et al.* (2009); Zhu *et al.* (2014) and references therein. While not all studies find a significant decrease in venular diameter, the arteries are in all studies found to decrease in size. Regardless of whether or not the veins decrease in size, the arteriolar to venular width ratio (AVR) is consistently found to be smaller in patients with hypertension. Interestingly, these findings seem also to be the case for both current hypertension and past hypertension. This suggest that retinal arteriolar caliber changes reflect persistent damage from long-term hypertension.

An increase in tortuosity is also found to be associated with increased blood pressure Cheung *et al.* (2011b); Han (2012); Hughes *et al.* (2006); Owen *et al.* (2008). In Han (2012) a comprehensive overview is provided of a wide range of medical conditions that lead to an increase of tortuosity in blood vessels in each part of the body. It is generally found that hypertension increases the tortuosity specifically of the arteries, and to a lesser extent of the veins Han (2012); Owen *et al.* (2008). In Cheung *et al.* (2011b); Hughes *et al.* (2006) it is however the venular tortuosity that is found to be increased

in hypertensive patients.

Our findings. In our clinical study (which will be presented in Ch. 11) we found that higher vessel tortuosity is significantly associated with the status of hypertension. We also show that this association is mainly caused by an increase in arteriolar tortuosity. For full details see Subsec. 11.5.2 and 11.5.3.

1.3.3 Diabetes Mellitus

Also in diabetes research vessel caliber is the most studied geometric retinal vessel parameters. Here a decrease in AVR is found to be associated with several types of diabetes Ikram *et al.* (2006a); Klein *et al.* (2003); Sun *et al.* (2009); Wong *et al.* (2004, 2006). However, in contrast to hypertension, this decrease in AVR is not explained by a relative decrease in arteriolar caliber, but rather by an increase in venular caliber. Both an increase in arteriolar and venular caliber is associated with diabetes, and the increase in venular caliber is bigger than that of the arteries.

Although there is increasing evidence that an increase in vessel tortuosity is associated with diabetes mellitus type 2 and progression towards diabetic retinopathy, in literature there seems to be no consensus on the topic yet. Cheung *et al.* Cheung *et al.* (2012) for example have found a negative association of tortuosity (straighter vessels) with diabetes, whereas Sasongko *et al.* Sasongko *et al.* (2015) have found a positive association (more curved vessels) with diabetes. In Sasongko *et al.* (2015) it is suggested that this inconsistency could be due to the duration of diabetes of the patients involved: it could be that an increase in tortuosity only occurs after long exposure (over 10 years) to diabetes. In another recent study Weiler *et al.* (2015) the authors found a positive association of arterial tortuosity with diabetic retinopathy. In a smaller study (30 subjects) it was found that average tortuosity was 26% higher in patients with diabetes type 2, compared to healthy controls Tam *et al.* (2011).

Our findings. In our clinical study we found higher vessel tortuosity in DM2 patients in comparison to healthy subjects, increasing with the development stages of the disease. Here the difference between arteries and veins was not investigated. For full details see Subsec. 11.5.2 and 11.5.3.

1.4 Retinal Image Analysis Algorithms

Retinal image analysis involves a wide variety of algorithms (Fig. 1.6), and can roughly be categorized in the following: anatomical landmark detection, vessel segmentation,

1. CLINICAL BACKGROUND

vessel tracking, lesion segmentation, junction detection and biomarker extraction. In this thesis we have developed algorithms in all of the aforementioned categories except for lesion segmentation. The developed algorithms are summarized in Chapter 3 and are all based on a shared image processing framework (Chapter 2): image analysis via invertible orientation scores. For a condensed overview of the methods developed in this thesis *and* other methods developed within the *RetinaCheck* project, of which the work described in this thesis is part of, see ter Haar Romeny *et al.* (2016). In the following subsections we briefly describe the different categories of retinal image analysis algorithms.

1.4.1 Anatomical Landmark Detection (Ch. 5)

At the core of any retinal image analysis system is the detection of the anatomical landmarks. In the retina, the main anatomical structures are the optic nerve head, the fovea and the blood vessels (cf. Fig. 1.3). Of these, the optic nerve head and the fovea (Fig. 1.6(a)) are considered the key anatomical landmarks. Clinical studies typically make use of standardized measurement protocols in which the measurements (e.g. microaneurysm count, or vessel width analysis) are performed in fixed regions of interest that are specified relative to the landmark locations (see e.g. Fig. 1.6(h)). Also in other retinal image processing modules these landmarks play a crucial role. E.g., vessel tracking algorithms, such as the one developed in this thesis (Chapter 7), are typically initialized in the region around the optic nerve head (Fig. 1.6(d)).

1.4.2 Retinal Vessel Segmentation (Ch. 6)

Retinal vessel segmentation is the process of producing binary maps that label each pixel as either vessel or background (Fig. 1.6(b)). Vessel segmentations are mostly used as a starting point for the construction of models of the retinal vasculature, as a reference structure relative to which other processes are performed (such as lesion segmentation), or as a direct format for the analysis of retinal vascular properties (e.g. fractal analysis).

Vessel segmentation algorithms are typically divided into supervised, non-supervised and tracking methods. Both supervised and non-supervised methods perform pixel-wise labeling of the pixel into the vessel or background category. Supervised methods require training data (manual segmentations of blood vessels) to train a system to recognize a pixel as belonging to a blood vessel. Non-supervised methods do not require training data and typically rely on differentio-geometrical processing. Vessel tracking methods

1.4 Retinal Image Analysis Algorithms

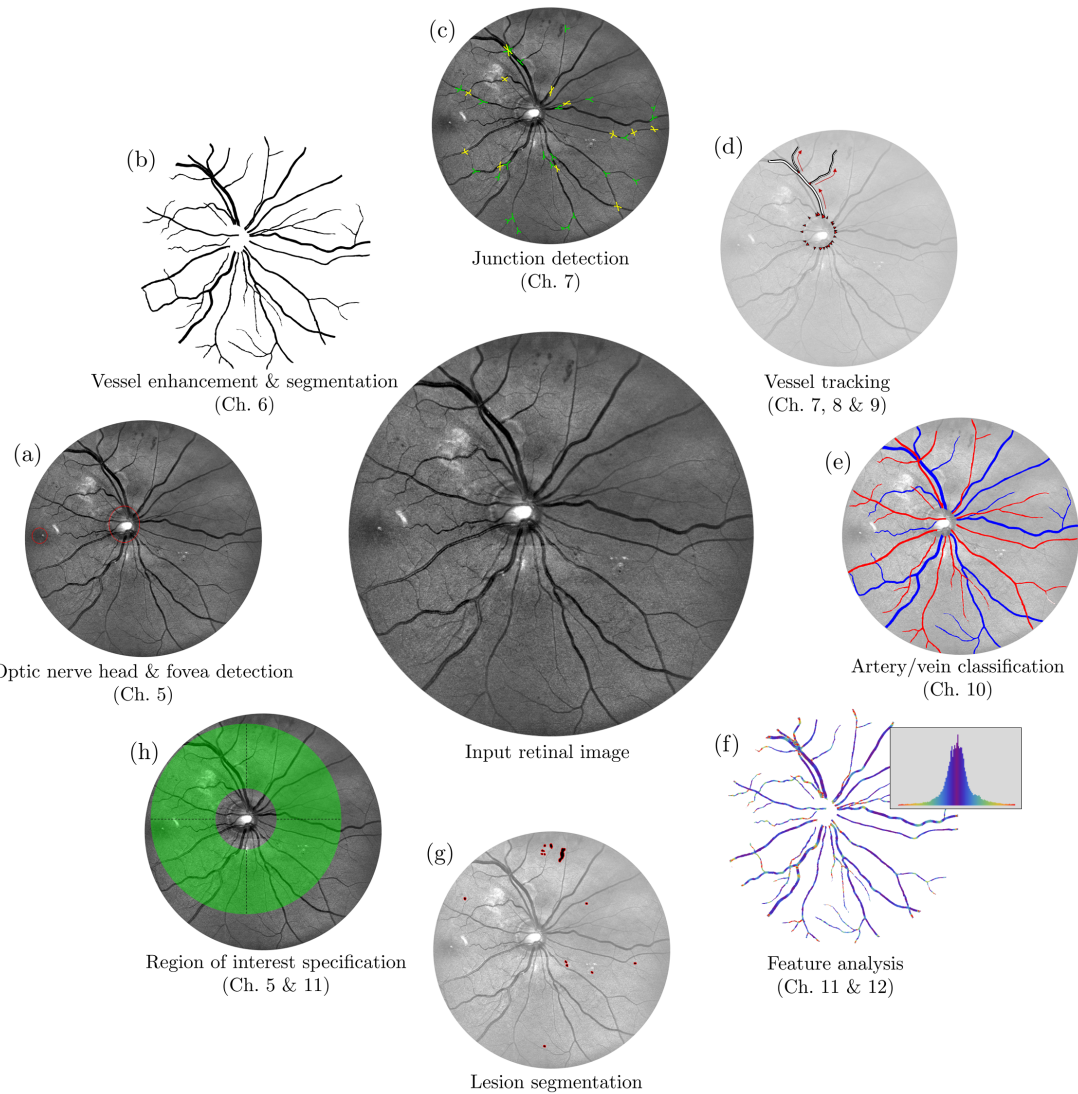


Figure 1.6: An overview of different types of retinal image analysis algorithms and their connection to the chapters of this thesis.

1. CLINICAL BACKGROUND

iteratively expand a connected model of the vasculature, starting from detected seed points (typically around the optic nerve head).

1.4.3 Retinal Vessel Modeling (Ch. 7, 8 & 9)

Iterative Tracking Vessel tracking is the process of constructing (parametric) models of the vasculature (Fig. 1.6(d)). Here we make a distinction between single vessel models, and full vasculature models. A single vessel model consists of parameterization of a single blood vessel, e.g., an ordered sequence of centerline coordinates or a sequence of paired vessel edge coordinates, possibly accompanied with a labeling of the vessel being artery or vein (Fig. 1.6(e)). A full vasculature model is a collection of such single blood vessel models together with a structure that describes the relations between those blood vessels, e.g., parent-child relations between bifurcating blood vessels.

From Segmentation to Model An alternative approach to the construction of models of the retinal vasculature is by taking pixel-wise vessel segmentation as a starting point. A set of single vessel models is then typically constructed by computing a skeleton from the binary segmentation, and splitting the skeleton at junction points (locations where multiple vessel segments meet). The construction of a full model of the vasculature (including parent-child relations) is then more difficult. This requires first the identification of junction points, and then establishing relations between the segments (junction resolving). Establishing the relations between vessel segments is typically done by either resolving each junction separately or simultaneously in a graph optimization approach.

1.4.4 Lesion Segmentation

Lesion segmentation is the process of recognizing pathological regions in the retina and labeling them as such (Fig. 1.6(g)). The automatic and robust detection of lesions (such as micro-aneurysms and drusen) is of great importance since lesions directly threaten vision by damaging the retina. Diabetic retinopathy (DR) and age related macula degeneration (AMD) are two of the most occurring sight threatening pathologies, and are heavily characterized by the presence of respectively red lesions (such as micro-aneurysms and hemorrhages) and white lesions (such as drusen).

1.4.5 Feature/Biomarker Extraction (Ch. 10, 11 & 12)

The main goal of almost any retinal image analysis system is the extraction of retinal biomarkers, i.e., the computation of objective measurements (such as the quantification of vessel curvature, see Fig. 1.6(f)) from retinal image data which can be used to quantify the health condition of a person. In the case of DR and AMD a count of the number of lesions inside certain regions of interest quite directly describes the state of these diseases International Council of Ophthalmology (2014); Klein *et al.* (1991); Wilkinson *et al.* (2003). Measurements of the retinal vasculature have a less straightforward relation with disease progression, but can be regarded as biomarkers nevertheless. E.g., as described in the previous Subsec. 1.3 venular widening relative to the arteries is an indicator of diabetes and diabetic retinopathy.

The computation of retinal biomarkers typically involves a pipeline composed of a large set of (interdependent) processing modules, such as the ones described in the previous subsections. One particularly important component of a vessel based biomarker extraction pipeline is that of artery/vein classification (Fig. 1.6(f)). Arteries and veins behave differently under pathological conditions. As such, it is important to define and study biomarkers separately for arteries and veins.

Chapter 2

Technical Background: Orientation Scores and Lie Groups

2. TECHNICAL BACKGROUND

Retinal image analysis via orientation scores is a major theme in this thesis. In this section we aim to familiarize the reader with the concept of an orientation score, and we motivate why it is important (and convenient) to resort to group theory in the processing of orientation scores.

2.1 Invertible Orientation Scores

2.1.1 What are Orientation Scores?

An **orientation score** U_f is a function on the space of positions and orientations $\mathbb{R}^2 \times S^1$, and can be obtained from an image f via a wavelet type transform Kalitzin *et al.* (1999); Duits (2005); Duits *et al.* (2007a,b); Franken & Duits (2009). In this transformation, orientation sensitive filters ψ_θ are used that filter the image at different orientations. These anisotropic filters, which we will discuss soon in Subsec. 2.1.5, respond well in the presence of structures that match the filter's orientation, and do not or hardly respond to structures perpendicular to it. In this sense, the filters "score" the local presence of oriented structures, and it is indeed the full stack of filter responses that we call an orientation score. Consider to this end the top row of figures in Fig. 2.1. In Subsec. 2.1.4 we provide details on the construction of orientation scores. First, we provide a motivation for using orientation scores in image analysis.

2.1.2 What is the Motivation for Using Orientation Scores?

In an orientation score a full range of orientations are represented at each location, and it is precisely this property that makes the use of orientation scores in image processing attractive. In image processing one often encounters crossing structures. These crossings either disturb the processing pipeline, e.g., in the 2D vesselness filter Frangi *et al.* (1998) or in anisotropic diffusions (e.g., with adaptive scalar diffusivity Perona & Malik (1990), adaptive matrix-valued diffusion tensors Weickert (1999); Scharr (2006)), or adaptive metric diffusivity Sochen *et al.* (1998)), or require special attention to be dealt with appropriately. In an orientation score however, crossings no longer exist as they are manifestly disentangled on the basis of their local orientations. In the score, due to the extra dimension we can now accommodate multiple orientations in one spatial position. See Fig. 2.1 and Fig. 2.2C for an illustration. As shown in this thesis with multiple applications in retinal image analysis, this neat organization of image data in orientation scores allows for the construction of both effective and fast algorithms.

Interestingly, such an organization of visual data based on position and orientations

2.1 Invertible Orientation Scores

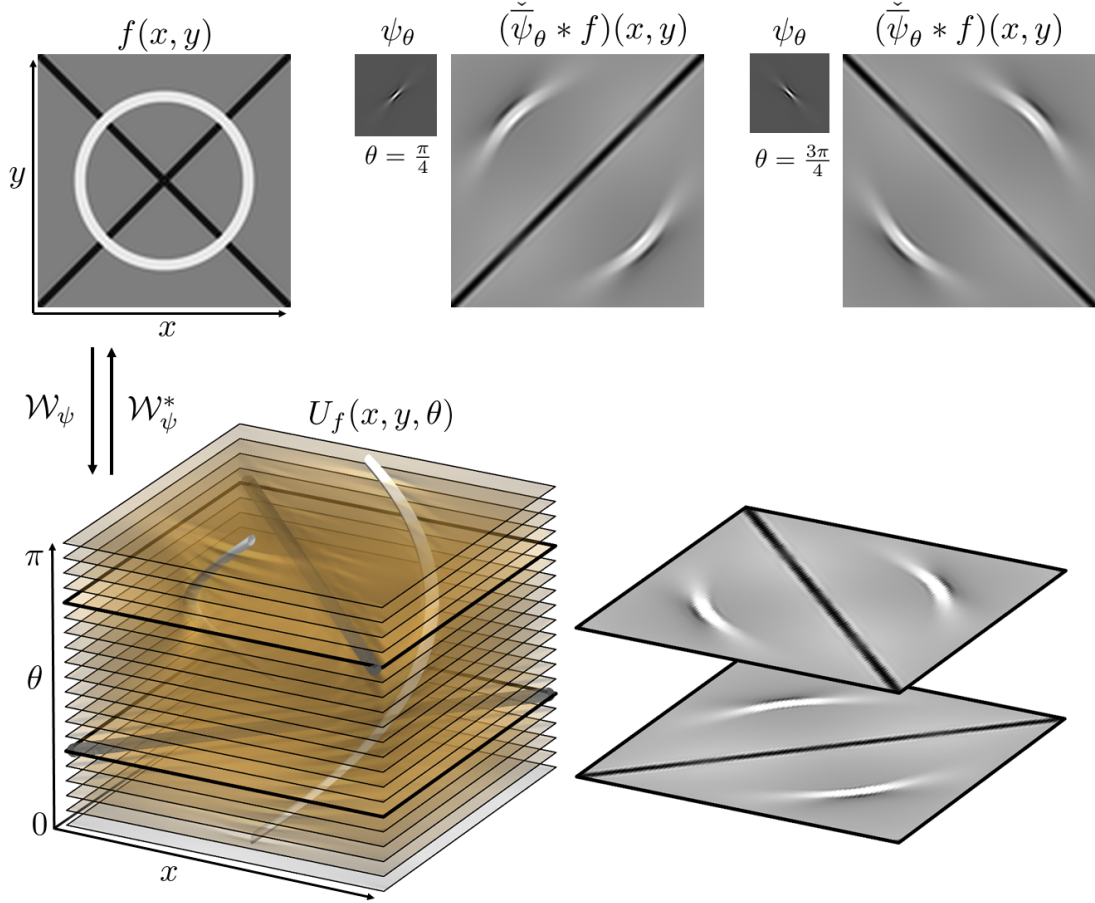


Figure 2.1: An orientation score can be constructed by filtering an image with a set of rotated anisotropic filters ψ_θ . The top row shows two of such rotated filters ψ_θ and their responses on the input image. In an orientation score U_f , obtained via the orientation score transform \mathcal{W}_ψ , such responses are “stacked” on top of each other. Using so-called cake-wavelets (to be explained in Sec. 2.1.5) for ψ one obtains an invertible orientation score transformation \mathcal{W}_ψ , for which a stable inverse transformation \mathcal{W}_ψ^* exists: one can reconstruct the image from the orientation score without loss of information.

2. TECHNICAL BACKGROUND

also seems to take place in the visual system of higher mammals. Hubel & Wiesel (1959) showed that the visual cortex in the mammalian brain contains so-called simple cells, whose receptive fields are tuned to various locations and orientations (Fig. 2.2A). They showed by tangential electrode tracking that the orientation preference of simple cells gradually varies across the surface of the primary visual cortex. The use of optical imaging techniques later showed that assemblies of oriented receptive fields are grouped together in pinwheel-like structures Bonhoeffer *et al.* (1991), known as the orientation preference structure, see Fig. 2.2B. The orientation preference structure is a mapping of the 3D space of positions and orientations $\mathbb{R}^2 \times S^1$ onto the 2D surface of the primary visual cortex. Due to the difference in dimensionality the orientation preference structure is formed by a tessellation of pinwheels, of which the centers form singularities Ohki *et al.* (2006). In an orientation score we also obtain a decomposition of visual data into localized oriented responses, and similar to a pinwheel region on the visual cortex a single column of orientations in the score (see Fig. 2.2C) encodes for all possible orientations at that location.

While the previous paragraph only motivates the use of a data representation on the space of positions and orientations, the neurophysiology of vision also motivates the use of a sub-Riemannian geometry on this domain. Synaptic physiological studies of the horizontal pathway (neuronal connections parallel to the cortical surface) in the visual cortex of tree shrews show that neurons with aligned receptive fields excite each other Bosking *et al.* (1997). Apparently the visual system not only constructs a score of local orientations, it also accounts for context and alignment by excitation and inhibition. Petitot showed that the horizontal connections of primary visual cortex implement the (sub-Riemannian) contact structure of a continuous fibration with base space the retinal area (i.e. the space \mathbb{R}^2) and a projective line of orientations (i.e. the space S^1) Petitot (2003). A refinement of this model on the roto-translation group was proposed by Citti & Sarti Citti & Sarti (2006). Subsequently, Boscain & Duits & Sachkov derived its optimal solutions in Boscain *et al.* (2014); Duits *et al.* (2013a) and related it to a mechanical problem for which optimal synthesis was obtained by Sachkov Sachkov (2010).

We take inspiration by the superior pattern recognition capabilities of the human brain and recent insights on how this is accomplished Fregnac & Shulz (1999); Petitot (2003), and rely on a novel operator design aiming at better results than would be obtained by conventional 2D image processing. This novel operator design combines (partial) differential equations on Lie groups (induced by stochastic processes and sub-Riemannian geometric control) with continuous wavelet transforms. More precisely, in

2.1 Invertible Orientation Scores

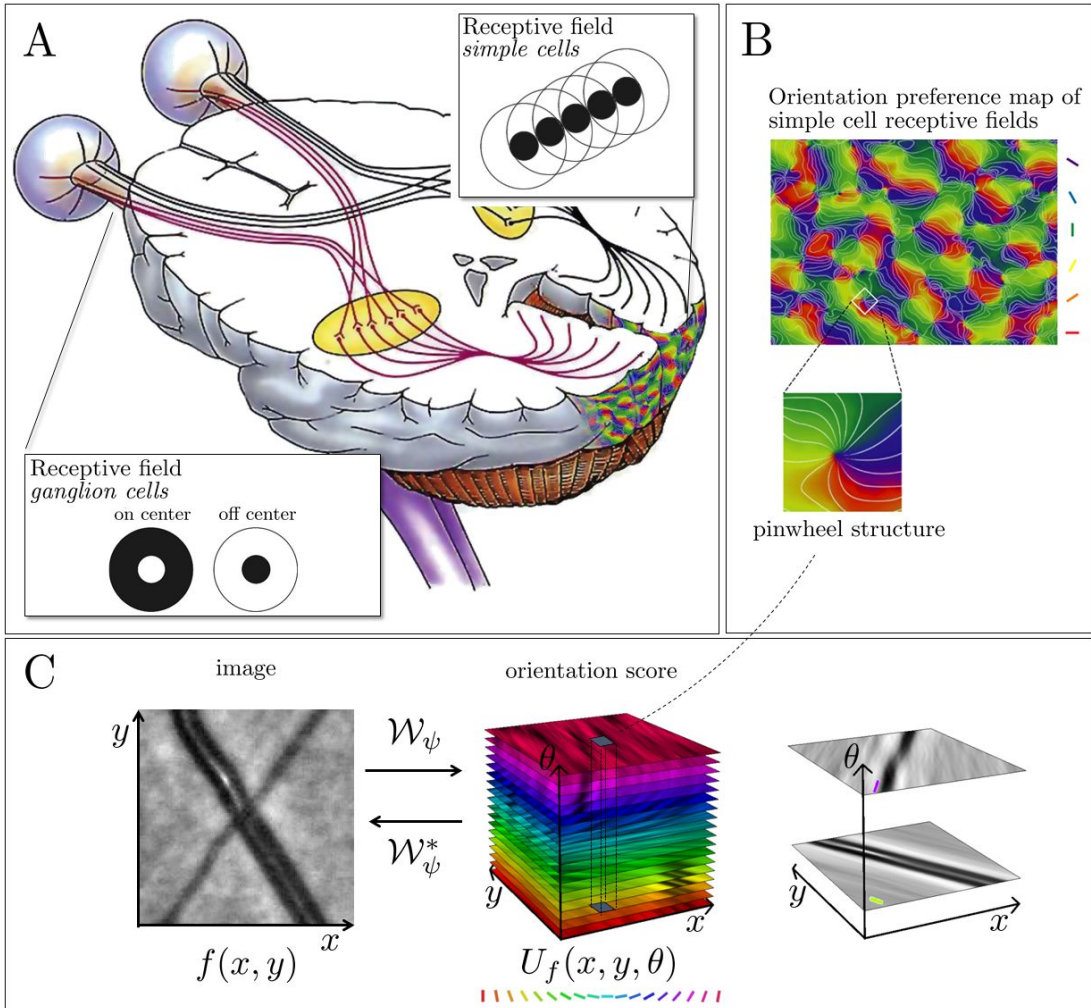


Figure 2.2: **A:** A receptive field of a sensory neuron describes the pattern of input stimuli that activates a response of that neuron. At a very low level in the visual pathway, the output of photo-receptors in the retina is combined into isotropic center-surround receptive fields of ganglion cells. As such, the ganglion cells encode locally for contrast (analog to the pixels a 2D image). The outputs of ganglion cells are combined to form the receptive fields of simple cells, which respond to oriented line stimuli and encode for both position and orientation (similar to the voxels in an orientation score).

B: The simple cells are neatly organized on the surface of the primary visual cortex and the orientation preference map of simple cells contains pinwheel structures. These pinwheel regions encode all orientations at a certain spatially localized area (and have singularities at the very center). [Illustration adapted from O'Reilly et al. (2012)]

C: In an orientation score we obtain a similar organization of visual data, however now as a 3D object instead of a 2D surface.

2. TECHNICAL BACKGROUND

in this PhD thesis we focus on new mathematical, computational, sub-Riemannian techniques with applications to retinal imaging. Although we do take great inspiration from visual cortex modeling, we do not claim to model the rather complex visual system of mammals, as this would require verification by neurophysiological and neuropsychological experiments which is clearly outside our general research scope.

2.1.3 Why Call Them Orientation Scores?

With respect to the naming of orientation scores as such, one might also appreciate the analogy to musical scores: In a musical score a certain melody is represented along a time axis, and the axis perpendicular to it encodes pitch (the axis along which notes can be placed). Such musical notation allows for multiple pitches at a certain point in time (e.g., as is the case with harmonies and chords). In fact, this kind of time-frequency decomposition is reflected in a Gabor transform Gabor (1946); Helstrom (1966). In the analysis of Gabor transforms one can employ the Heisenberg group structure by left-invariant processing Duits *et al.* (2013b); Gröchenig (2001). In this case one must take into account an extra phase factor in the short time Fourier transform Allen (1977) in order to obtain a transform of the type $g \mapsto (\mathcal{U}_g \psi, f)_{\mathbb{L}_2(\mathbb{R}^2)}$ with \mathcal{U} the Schrödinger representation on the Heisenberg group.

In general we call $G \ni g \mapsto (\mathcal{U}_g \psi, f)_{\mathbb{L}_2(\mathbb{R}^2)}$ the score of image f with respect to the Lie group G , and \mathcal{U} a certain representation of the group. A special case arises when \mathcal{U} is the Schrödinger representation, in which case the score is a Gabor transform. If \mathcal{U} is the left-regular representation (cf. Subsec. 2.3) of the roto-translation group $SE(2)$ (i.e. rotation and translation) the score is an orientation score. If \mathcal{U} is the left-regular representation of the similitude group $SIM(2)$ (i.e. rotation, translation and scaling) the score is a continuous wavelet transform. In all of these cases we want to employ the geometry and the intrinsic structure that lives in the domain of the scores, which is reflected by the group structure. It is therefore inevitable that we resort to Lie group theory in the analysis of orientation scores. The very basics of group theory will be introduced in Subsec. 2.2, and what it means to rely on Lie group theory in our analysis of orientation scores will be discussed in Subsec. 2.3. In Chapter 3 we then go through the applications developed in this thesis and briefly discuss how Lie group analysis contributes to state-of-the-art performance of the methods. However, before we go there, let us first focus on some practical aspects and address the following questions in the upcoming subsections:

- How do we construct an orientation score? (Subsec. 2.1.4)

2.1 Invertible Orientation Scores

- What kind of wavelets can we use to construct an orientation score? (Subsec. 2.1.5)
- Why do we need group theory in the processing and analysis of orientation scores? (Subsec. 2.1.6)

2.1.4 How is an Orientation Score Constructed?

Consider a 2D image f as a function $f : \mathbb{R}^2 \rightarrow \mathbb{R}$, with compact support on the image domain $\Omega = [0, X] \times [0, Y]$, with image dimensions $X, Y \in \mathbb{R}^+$, and which we assume to be square integrable, i.e. $f \in \mathbb{L}_2(\mathbb{R}^2)$. An orientation score, constructed from image f , is defined as a function $U_f : \mathbb{R}^2 \times S^1 \rightarrow \mathbb{C}$ and depends on two variables (\mathbf{x}, θ) , where $\mathbf{x} = (x_1, x_2) \in \mathbb{R}^2$ denotes position and $\theta \in [0, 2\pi]$ denotes the orientation variable.

An orientation score U_f of a function f can be constructed by means of convolution with some anisotropic filter ψ via

$$U_f(\mathbf{x}, \theta) := \mathcal{W}_\psi f = (\check{\psi}_\theta * f)(\mathbf{x}) = \int_{\mathbb{R}^2} \overline{\psi(\mathbf{R}_\theta^{-1}(\mathbf{y} - \mathbf{x}))} f(\mathbf{y}) d\mathbf{y}, \quad (2.1)$$

where $\psi \in \mathbb{L}_1(\mathbb{R}^2) \cap \mathbb{L}_2(\mathbb{R}^2)$ is the anisotropic convolution kernel oriented along the x -axis which we identify with $\theta = 0$, and where \mathcal{W}_ψ denotes the transformation between image f and orientation score U_f . The overline denotes complex conjugation, $\check{\psi}_\theta(\mathbf{x}) := \psi_\theta(-\mathbf{x})$, and the rotation matrix \mathbf{R}_θ is given by

$$\mathbf{R}_\theta = \begin{pmatrix} \cos \theta & -\sin \theta \\ \sin \theta & \cos \theta \end{pmatrix}, \quad (2.2)$$

see Fig. 2.1.

Exact reconstruction¹ from the orientation scores constructed by (2.1) is given by

$$\begin{aligned} f &= \mathcal{W}_\psi^* \mathcal{W}_\psi f \\ &= \mathcal{F}^{-1} \left[M_\psi^{-1} \mathcal{F} \left[\mathbf{x} \mapsto \frac{1}{2\pi} \int_0^{2\pi} (\psi_\theta * U_f(\cdot, \theta))(\mathbf{x}) d\theta \right] \right], \end{aligned} \quad (2.3)$$

where \mathcal{F} is the unitary Fourier transform on \mathbb{R}^2 , where \mathcal{W}_ψ^* denotes the adjoint wavelet transformation (see Duits (2005) for details), and $M_\psi : \mathbb{R}^2 \rightarrow \mathbb{R}^+$ is calculated by

$$M_\psi = 2\pi \int_0^{2\pi} \overline{\mathcal{F}[\psi_\theta]} \mathcal{F}[\psi_\theta] d\theta = 2\pi \int_0^{2\pi} |\mathcal{F}[\psi_\theta]|^2 d\theta. \quad (2.4)$$

¹The reconstruction formula can easily be verified using the convolution theorem, $\mathcal{F}[f * g] = 2\pi \mathcal{F}[f] \mathcal{F}[g]$, and the fact that $\mathcal{F}[\check{\psi}_\theta] = \overline{\mathcal{F}[\psi_\theta]}$.

2. TECHNICAL BACKGROUND

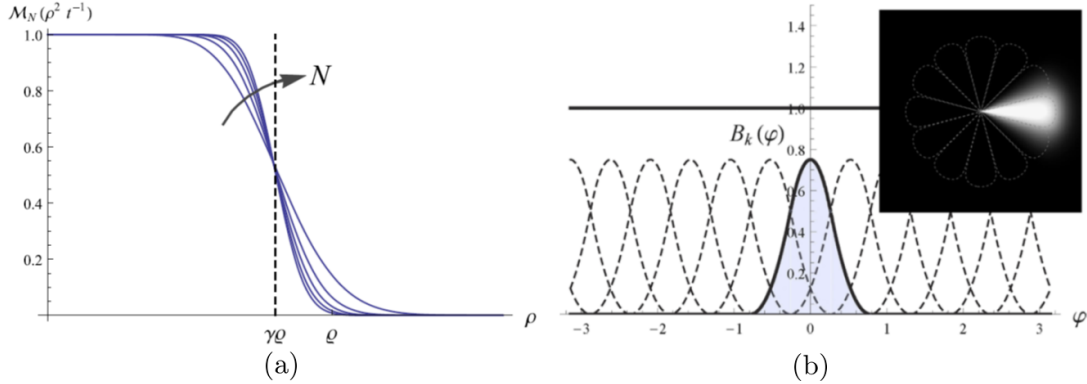


Figure 2.3: (a) Plots of $\mathcal{M}_N(\rho^2/t)$ (cf. Eq. (2.6)), with $t = \frac{2(\gamma\rho)^2}{1+2N}$ for $N = 5, 10, 15, 20, 25$. (b) The use of B-splines in the construction of cake wavelets. The plot shows quadratic B-splines ($k = 2$); the sum of all shifted B-splines adds up to 1. The image in the upper right corner illustrates a Fourier cake wavelet $\tilde{\psi}^{\text{cake}}$ constructed using quadratic B-splines and \mathcal{M}_N with $N = 60$, according to Eq. (2.8).

The function M_ψ provides a stability measure of the inverse transformation. Theoretically, reconstruction is well-posed, as long as

$$0 < \delta < M_\psi(\omega) < M < \infty, \quad (2.5)$$

where δ is arbitrarily small, since then the condition number of W_ψ is bounded by $M\delta^{-1}$, see (Duits, 2005, Thm. 20).

Remark 2. If we do not restrict ourselves to band-limited/disk-limited functions, this requirement (Eq. (2.5)) bites the assumption $\psi \in \mathbb{L}_1(\mathbb{R}^2) \cap \mathbb{L}_2(\mathbb{R}^2)$ since it implies $\mathcal{F}[\psi]$ is a continuous function vanishing at infinity (see e.g. Rudin (1973)) and so is M_ψ . In that case we have to resort to distributional wavelet transforms¹ whose closure is again a well-defined unitary map from $\mathbb{L}^2(\mathbb{R}^2)$ into a reproducing kernel subspace of $\mathbb{L}_2(\mathbb{R}^2 \times S^1)$, for details see (Bekkers et al., 2014a, App. B). So in principle our restriction to band-limited images is convenient, but not necessary.

In practice, to prevent numerical problems, it is best to aim at $M_\psi(\omega) \approx 1$ for $\|\omega\| < \varrho$, where ϱ is the Nyquist frequency of the discretely sampled image, meaning that all relevant frequency components within a ball of radius ϱ are preserved in the

¹This is comparable to the construction of the unitary Fourier transform $\mathcal{F} : \mathbb{L}_2(\mathbb{R}^2) \rightarrow \mathbb{L}_2(\mathbb{R}^2)$ whose kernel $k(\omega, \mathbf{x}) = e^{-i\omega \cdot \mathbf{x}}$ is also not square integrable.

2.1 Invertible Orientation Scores

same way. Because of the discontinuity at $\|\boldsymbol{\omega}\| = \varrho$, which causes practical problems with the discrete inverse Fourier transform, we will use wavelets ψ , with $M_\psi(\boldsymbol{\omega}) = \mathcal{M}_N(\rho^2 t^{-1})$, $N \in \mathbb{N}$, $t > 0$ and $\rho = \|\boldsymbol{\omega}\|$ where

$$\mathcal{M}_N(\rho^2 t^{-1}) = e^{-\frac{\rho^2}{t}} \sum_{k=0}^N \frac{(\rho^2 t^{-1})^k}{k!} \leq 1, \quad (2.6)$$

where t denotes a scale parameter. To fix the inflection point close to the Nyquist frequency, say at $\rho = \gamma \varrho$ with $0 \ll \gamma < 1$, we set $t = \frac{2(\gamma \varrho)^2}{1 + 2N}$ (to fix the bending point: $\frac{d^2}{d\rho^2} \mathcal{M}_N(\rho^2 t^{-1})|_{\rho=\gamma \varrho} = 0$, see Fig. 2.3a). The function \mathcal{M}_N basically is a Gaussian function at scale t , multiplied with the Taylor series of its inverse up to a finite order $2N$ to ensure a slower decay. The function \mathcal{M}_N smoothly approximates 1 on the domain $\rho \in [0, \varrho]$, see Fig. 2.3a. A wavelet $\psi : \mathbb{R}^2 \rightarrow \mathbb{C}$ with such a M_ψ will be called a **proper wavelet**.

2.1.5 What Kind of Wavelets Can Be Used?

As explained in the previous section, orientation scores are constructed using anisotropic filters. In this thesis we consider two types of such anisotropic filters: cake wavelets¹ and Gabor wavelets.

Cake Wavelets Cake wavelets are constructed from the Fourier domain. By using polar coordinates, the Fourier domain can be uniformly divided into N_o equally wide samples ("pieces of cake") in the angular direction, see Fig. 2.3b. The spatial wavelet is given by

$$\psi^{cake}(\mathbf{x}) = \mathcal{F}^{-1}[\tilde{\psi}^{cake}](\mathbf{x})G_{\sigma_s}(\mathbf{x}), \quad (2.7)$$

where G_{σ_s} is a Gaussian window, with $1 \ll \sigma_s$, that is used to avoid long tails in the spatial domain. Note that multiplication with a large window in the spatial domain corresponds to a convolution with a small window in the Fourier domain, such that M_ψ is hardly affected with σ_s sufficiently large. Function $\tilde{\psi}^{cake}$ is given by

$$\tilde{\psi}^{cake}(\boldsymbol{\omega}) = \left(B^k \left(\frac{(\varphi \bmod 2\pi) - \pi/2}{s_\theta} \right) \right)^\nu (\mathcal{M}_N(\rho))^{\frac{1}{2}}, \quad (2.8)$$

¹The cake wavelets ψ are not continuous mother wavelets (for the similitude group $SIM(2)$) in the classical sense, instead they carry all scales simultaneously. Nevertheless, they can still be called wavelets (for the group $SE(2)$).

2. TECHNICAL BACKGROUND

with $\boldsymbol{\omega} = (\rho \cos \varphi, \rho \sin \varphi)$, where $s_\theta = 2\pi N_o^{-1}$ is the angular resolution in radians, and with $\nu \in \{\frac{1}{2}, 1\}$ a design parameter. Default we set $\nu = \frac{1}{2}$ such that $\sum_{i=0}^{N_o-1} |\tilde{\psi}^{cake}(\mathbf{R}(is_\theta)\boldsymbol{\omega})|^2 = \mathcal{M}_N(\rho)$. The function \mathcal{M}_n specifies the radial function in the Fourier domain given by (2.6). B^k denotes the k th order B-spline given by

$$B^k(x) = (B^{k-1} * B^0)(x), \\ B^0(x) = \begin{cases} 1 & \text{if } -1/2 < x < +1/2 \\ 0 & \text{otherwise} \end{cases}. \quad (2.9)$$

Orientation scores constructed from an image f using cake wavelets are denoted by U_f^{cake} .

The approach of constructing wavelets directly from the Fourier domain allows indirect control over the spatial shape of the filter, and it can easily be adapted. For example, the number of orientations N_o specifies the angular resolution s_θ : If N_o is large, the resolution in the orientation dimension is large and the filters become very narrow. This is illustrated in Fig. 2.4. The cut-off frequency (at the inflection point) of the function \mathcal{M}_n , which is usually set as the Nyquist-frequency, could be lowered to filter out high-frequency noise components.

Moreover, because B-splines and the function \mathcal{M}_n are used to sample the Fourier domain, the sum of all cake wavelets is approximately 1 over the entire Fourier domain (within a ball of radius $\gamma\varrho$), see Fig. 2.3 and 2.4. Thus the cake wavelets indeed are proper wavelets, allowing a stable reconstruction via Eq. (2.3). Furthermore, because the cake wavelets uniformly cover the Fourier domain ($\mathcal{M}_N \approx 1$), when setting $\nu = 1$ one can omit the extra convolution with ψ_θ in (2.3) and omit division by $M_\psi^{-1} \approx 1$ in order to obtain a fast approximate reconstruction, which is given by integration of the orientation scores over the angles only:

$$f(\mathbf{x}) \approx \frac{1}{2\pi} \int_0^{2\pi} U_f^{cake}(\mathbf{x}, \theta) d\theta, \quad (2.10)$$

for details see Duits (2005). I.e., for low order B-splines $|\psi_\theta(\boldsymbol{\omega})|^2 \approx |\psi_\theta(\boldsymbol{\omega})|$ and the choice of ν is not crucial.

Cake wavelets are quadrature filters, meaning that the real part contains information about the locally even (symmetric) structures, e.g. ridges, and the imaginary part contains information about the locally odd (antisymmetric) structures, e.g. edges. That is, the real and imaginary part of the filter ψ_θ are related to each other by the Hilbert transform in the direction perpendicular to the wavelets orientation, which is defined by

$$\mathcal{H}^\eta(\psi_\theta)(\mathbf{x}) = \mathcal{F}^{-1}[\boldsymbol{\omega} \mapsto i \operatorname{sign}(\boldsymbol{\omega}^T \cdot \mathbf{e}_\eta(\theta)) \mathcal{F}[\psi_\theta](\boldsymbol{\omega})](\mathbf{x}), \quad (2.11)$$

2.1 Invertible Orientation Scores

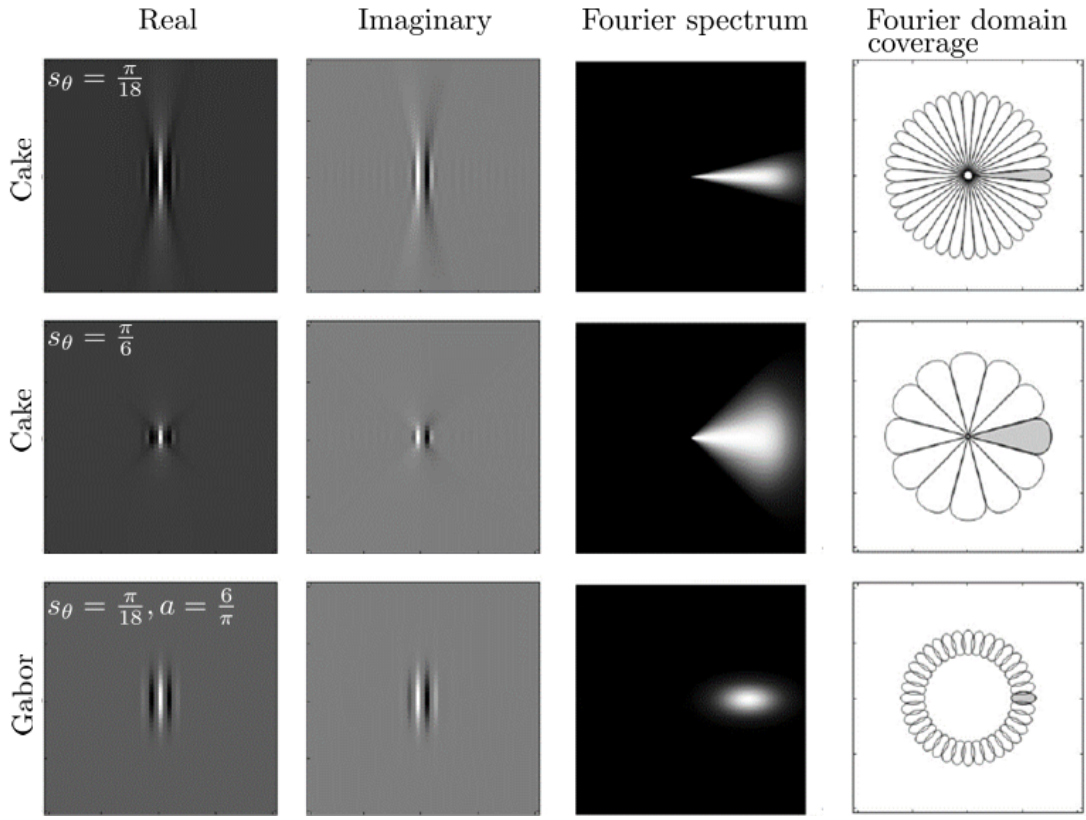


Figure 2.4: Overview of the wavelets used in this thesis. From left to right: the real and imaginary parts of the wavelet in the spatial domain (zoomed by a factor of 8 for the sake of visualization), the wavelet in the Fourier domain and an illustration of the Fourier domain coverage by the filters where contours are drawn at 80% of the filter maximum. Note that this last figure also gives an impression of M_ψ . The top row shows the cake wavelet constructed using $N_o = 36$, middle row with $N_o = 12$ and the bottom row shows the Gabor wavelet at scale $a = 6/\pi$ and $N_o = 36$.

2. TECHNICAL BACKGROUND

where $\mathbf{e}_\eta(\theta) = (-\sin \theta, \cos \theta)^T$ specifies the direction in which the Hilbert transform is performed. In Chapter 7 we make use of this quadrature property for vessel tracking in orientation scores; the quadrature property allows us to directly detect vessel edges from the imaginary part of the orientation scores, without having to calculate first-order derivatives perpendicular to the vessel orientation.

Remark 3. If $N_o \rightarrow \infty$ then $\tilde{\psi}^{cake} \rightarrow \delta_0^y$ in the distributional sense. In this case the wavelet transform converges to the localized Radon transform, which has been proposed for effective retinal vessel detection in Krause et al. (2013). The advantage however of taking $N_o \ll \infty$ is that we obtain non-singular kernels in the spatial domain while allowing a stable reconstruction for all a-priori set $N_o \in \mathbb{N}$.

Gabor Wavelets are directional wavelets, and can be tuned to specific spatial frequencies (and inherently scales). In the field of retinal image processing they are used for vessel detection in various studies Li et al. (2006); Soares et al. (2006). We can exploit the tuning of the wavelet to specific spatial frequencies to match differently sized blood vessels. The 2D Gabor wavelet is a Gaussian, modulated by a complex exponential, and is defined as:

$$\begin{aligned}\psi^{Gabor}(\mathbf{x}) &= \frac{1}{C_\psi} e^{i\mathbf{k}_0 \mathbf{x}} e^{-\frac{1}{2}|\mathbf{Ax}|^2}, \\ C_\psi &= 2\pi\sqrt{\epsilon} e^{-\frac{1}{2}|\mathbf{A}^{-1}\mathbf{k}_0|^2},\end{aligned}\tag{2.12}$$

where $\mathbf{A} = \text{diag}[\epsilon^{-1/2}, 1]$ with $\epsilon \geq 1$ is a 2×2 diagonal matrix that defines the anisotropy of the wavelet. The vector \mathbf{k}_0 defines the spatial frequency of the complex exponential and C_ψ normalizes the wavelet to unity. In our method we use $\epsilon = 4$, which makes the filter elongated in the x-direction and we choose $\mathbf{k}_0 = (0, 3)^T$, which causes oscillations perpendicular to the orientation of the wavelet. We can dilate the filter by a scaling parameter $a > 0$:

$$\psi_a^{Gabor}(\mathbf{x}) := a^{-1} \psi^{Gabor}(a^{-1}\mathbf{x}).\tag{2.13}$$

Orientation scores constructed from an image f using Gabor wavelets at scale a are denoted by $U_{f,a}^{Gabor}$.

The real and imaginary part of the wavelet in the spatial domain, as well as the coverage of the wavelet in the Fourier domain are shown in Fig. 2.4. Similar to the cake wavelets, Gabor wavelets also have the quadrature property orthogonal to their orientation.

In the Fourier domain, the Gabor filters are represented as Gaussian functions shifted from the origin by \mathbf{k}_0 . The set of all rotated Gabor functions at a certain scale a covers therefore a certain annulus in the Fourier domain, and a single Gabor wavelet can thus be regarded as an oriented band-pass filter. This is also clearly depicted by the outlines of the frequency responses as shown in Fig. 2.4.

Remark 4. *In our applications we remove the DC-component to avoid responses for the real part of the wavelets on locally constant images. In order to remove this smoothly, and in order to remove low-frequency fluctuations, we apply the transform $f \mapsto f - G_{\sigma_s} * f$, with G_{σ_s} a 2D Gaussian and with $\sigma_s \gg 0$ sufficiently large (typically we set $2\sigma_s = \frac{N}{2}$ on $N \times N$ images). I.e., in the Fourier domain we apply $\tilde{f} \mapsto (1 - e^{-\frac{1}{2}\sigma_s^2|\omega|^2})\tilde{f}$ before applying \mathcal{W}_ψ . This is also commonly done in continuous wavelet transforms Mallat (1999).*

2.1.6 Why Do We Need Group Theory and Sub-Riemannian Geometry?

In this section we first motivate whey we need group theory in the processing and analysis of orientation scores. Then, we explain the basics of group theory in Subsec. 2.2, after which in Subsec. 2.3 we will finally introduce the Lie group of interest: the roto-translation group $SE(2)$.

The fact that orientation scores are constructed via translations and rotations of oriented wavelets actually quite naturally brings us the notion of a group structure on the domain of an orientation score, namely that of the roto-translation group $SE(2)$. Indeed, every location (\mathbf{x}, θ) in the domain of an orientation score $(\mathbf{x}, \theta) \mapsto U_f(\mathbf{x}, \theta)$ is associated with a rotation (by θ) and translation (by \mathbf{x}) of an anisotropic wavelet ψ . But we also recognize a curved geometry in orientation scores: notions of alignment and distance seem to change depending on location and orientations (see for example Fig. 2.1 where we see that a planar circle becomes a spiral in the orientation score). The group $SE(2)$ is responsible for this curved geometry, and allows us to quantify this notion of alignment in terms of sub-Riemannian distances on the group $SE(2)$. What is exactly meant by sub-Riemannian distances will become clear in Ch. 4. For now let us stick with intuition and first make some observations on orientation scores and their domain. Below we list these observations and we will identify the relevant relations to group theory without going into full details. Full details will follow later in the subsequent Subsections 2.2 and 2.3 and Part II of this thesis.

2. TECHNICAL BACKGROUND

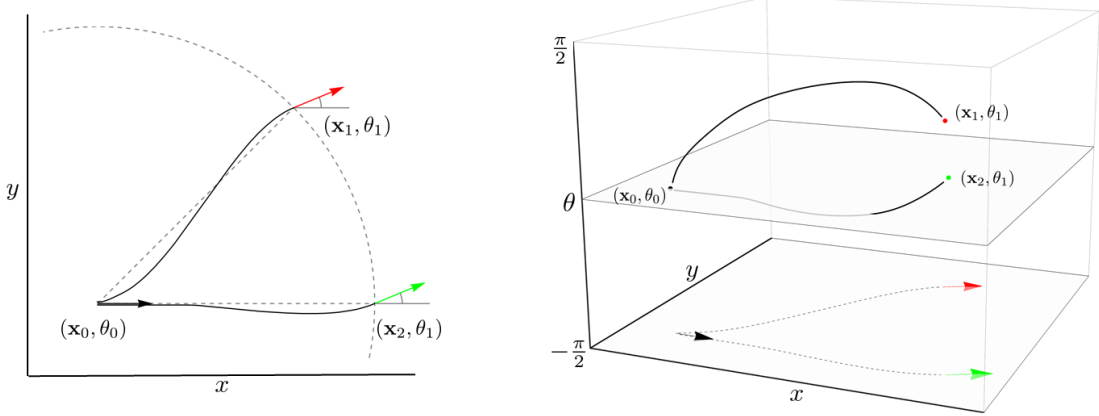


Figure 2.5: Even though the spatial and angular distances between (\mathbf{x}_1, θ_1) and (\mathbf{x}_0, θ_0) are the same as the spatial and angular distances of (\mathbf{x}_2, θ_1) with (\mathbf{x}_0, θ_0) , our perception is that the green arrow (\mathbf{x}_2, θ_1) is more aligned with (\mathbf{x}_0, θ_0) . The left-invariant sub-Riemannian structure on the Lie group $SE(2)$ takes this alignment into account. The connecting curves in the left image are spatial projections of sub-Riemannian geodesics in $SE(2)$, which are shown in the right figure.

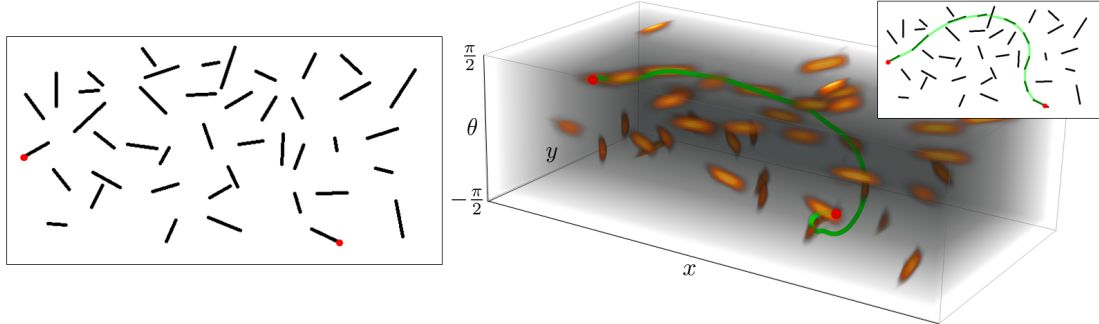


Figure 2.6: In the perception of contours the human mind couples positions and orientations, and groups line segments in accordance with the Gestalt law of good continuation Koffka (1935). The left image shows a collection of line segments in which one can imagine a continuous curve from one red point to the other. In the right figure this curve is shown in green in a rendering of the orientation score of the left image, and superimposed in the 2D image (top right). The shown curve is in fact the data-adaptive sub-Riemannian geodesic in $SE(2)$ that connects the two red dots, and is computed using our tracking method presented in Ch. 8.

2.1 Invertible Orientation Scores

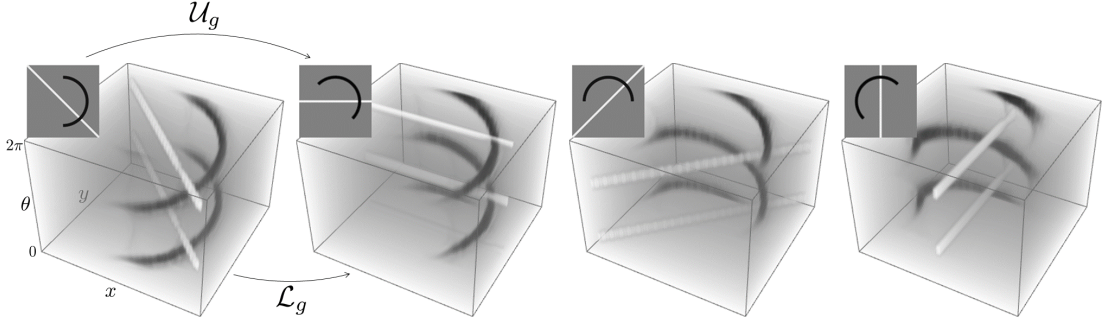


Figure 2.7: A roto-translation of the image corresponds to a shift-twist of the orientation score, both defined via a group representations of $SE(2)$ on the image and the orientation score. Shift-twist of images and orientation scores are denoted respectively by the left-regular representations \mathcal{U}_g and \mathcal{L}_g , cf. Eq. (2.38) and Eq. (2.37). In this illustration of crucial Eq. (2.41) we have set $g = (\mathbf{0}, \theta)$, with θ increasing θ from left to right.

1. Positions and Orientations are Coupled There is a coupling between positions and orientations as alignment of local orientations is done via translations and orientations. This coupling of positions and orientations is reflected by the *group product* $g \cdot g'$ of elements of $g, g' \in SE(2)$, which is given by

$$g \cdot g' = (\mathbf{x}, \theta) \cdot (\mathbf{x}', \theta') = (\mathbf{R}_\theta \mathbf{x}' + \mathbf{x}, \theta + \theta'), \quad (2.14)$$

with $g = (\mathbf{x}, \theta)$ and $g' = (\mathbf{x}', \theta')$, in which we see θ showing up in the spatial part. In fact, in our perception of contours and lines in images we also seem to (unconsciously) couple positions and orientations when determining alignment of local orientations via Gestalt principles Koffka (1935);Kanizsa (1955);Petitot (1999). Consider for example Fig. 2.5 and Fig. 2.6.

2. Roto-translations of Images Correspond to Shift-Twists of Orientation Scores A rotation and translation of the image corresponds to a shift-twist of the orientation score. Both roto-translations and the shift-twist operator are defined by a *group representation* of $SE(2)$ on respectively the image and the orientation score. Consider for example Fig. 2.7.

3. One Should Work with a Rotating Derivative Frame In order to define operators that commute with rotations and translations of the image we need to work with rotating derivative frames in orientation scores. Such a derivative frame is

2. TECHNICAL BACKGROUND

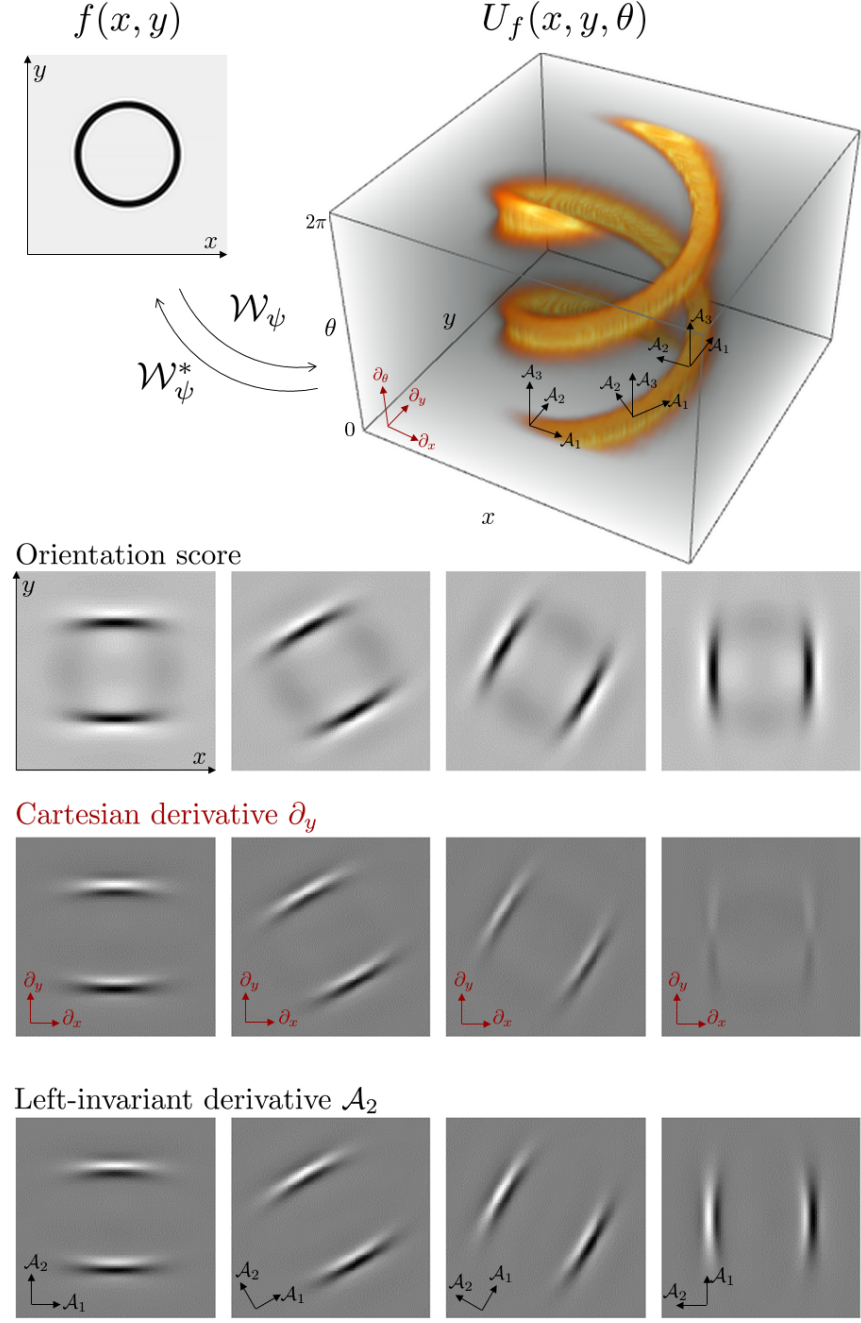


Figure 2.8: In orientation scores a left-invariant derivative frame $\{\mathcal{A}_1, \mathcal{A}_2, \mathcal{A}_3\}$ should be used instead of the axes-aligned frame $\{\partial_x, \partial_y, \partial_\theta\}$ (illustrated in the top figure). The bottom three rows of figures compare different orientation layers of the orientation score with the Cartesian derivative ∂_y and left-invariant derivative \mathcal{A}_2 . Here we see that \mathcal{A}_2 is invariant under the orientation, i.e., its interpretation does not change.

2.1 Invertible Orientation Scores

invariant under shift-twists of the orientation scores, and in a group theoretical setting such derivative frame is called *left-invariant* and is obtained via *push-forward* of the left-multiplication from the axis aligned derivative frame $\{\partial_x, \partial_y, \partial_\theta\}|_e$ at the origin $e = \{0, 0, 0\}$. Consider for example Fig. 2.8. As we can see it is instead better to work with the moving frame of derivatives $\{\mathcal{A}_1, \mathcal{A}_2, \mathcal{A}_3\}|_g$ at each g given by

$$\boxed{\begin{aligned}\mathcal{A}_1|_g &:= \cos \theta \partial_x + \sin \theta \partial_y \\ \mathcal{A}_2|_g &:= -\sin \theta \partial_x + \sin \theta \partial_y \\ \mathcal{A}_3|_g &:= \partial_\theta,\end{aligned}} \quad (2.15)$$

rather than the fixed frame of derivatives $\{\partial_x, \partial_y, \partial_\theta\}|_g$.

4. We Recognize a Curved Geometry on the Domain We recognize a curved geometry in which curves with constant tangent vector components expressed in the rotating derivative frame (Eq. (2.15)) become circular spirals. Consider for example Fig. 2.8 and Fig. 2.9(a). Such curves are called *exponential curves* on the group $SE(2)$, and are in fact the “straight” lines with respect to the curved geometry. Moreover, that we deal with a curved geometry becomes clear when we see that we have non-zero *commutators* of the *Lie algebra* of $SE(2)$.

The fact that the Lie algebra is not commutative is due to the fact that the group is not commutative. I.e., rotations and translations often do not commute. For a first intuition of how this non-commutative structure imposes a curved geometry on the domain of orientation scores, consider for example Fig. 2.11. Here we see that first moving along a preferred spatial direction (i.e. along \mathcal{A}_1), followed by a rotation, yields a different result than first rotating and then translating: rotations and translations generally do not commute.

5. Analysis of Lines in Orientation Scores Requires a Sub-Riemannian Geometry We observe that the data in orientation scores concentrates around naturally lifted curves $\gamma(t)$, so-called horizontal curves with the property $\gamma(t) = (x(t), y(t), \theta(t))$ for which

$$\theta(t) = \arg\{\dot{x}(t) + i\dot{y}(t)\}. \quad (2.16)$$

Such naturally lifted curves (see Fig. 2.9(a)) have their tangent vectors $\dot{\gamma}(t)$ at each location $\gamma(t)$ restricted to a sub-space $\Delta|_{\gamma(t)}$ of the full tangent space $T_{\gamma(t)}(SE(2))$, and live therefore in a *sub-Riemannian* geometry. Consider for example Fig. 2.9(a), in which a lifted curve and its tangent vector at a certain location g is depicted. A parallel can be drawn between these curves and the paths of moving cars: a car can only move

2. TECHNICAL BACKGROUND

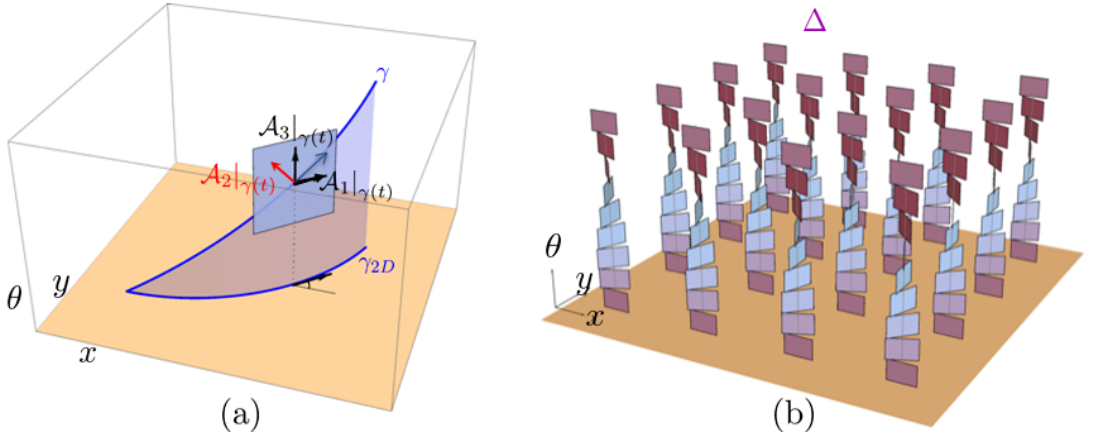


Figure 2.9: (a) A lifted curve $\gamma(t)$ of a planar curve $\gamma_{2D}(t) = (x(t), y(t))$ is called horizontal if it is defined as $\gamma(t) = (x(t), y(t), \theta(t))$, with $\theta(t) = \arg\{\dot{x}(t) + i\dot{y}(t)\}$. A consequence is that horizontal curves always have their tangent vectors $\dot{\gamma}(t)$ contained in a sub-space $\Delta|_{\gamma(t)} = \text{span}\{\mathcal{A}_1|_{\gamma(t)}, \mathcal{A}_3|_{\gamma(t)}\}$ of the full tangent space $T_{\gamma(t)}(SE(2)) = \text{span}\{\mathcal{A}_1|_{\gamma(t)}, \mathcal{A}_2|_{\gamma(t)}, \mathcal{A}_3|_{\gamma(t)}\}$. In this figure we have illustrated a special case: an exponential curve. Exponential curves have constant tangent vector components expressed in the rotating frame $\{\mathcal{A}_1|_{\gamma(t)}, \mathcal{A}_2|_{\gamma(t)}, \mathcal{A}_3|_{\gamma(t)}\}$. Such curves are circular spirals in $SE(2)$ and are regarded as the “straight” lines in the curved geometry of $SE(2)$. (b) An illustration of the distribution Δ , i.e., the sub-bundle of the full tangent bundle $T(SE(2))$.

2.1 Invertible Orientation Scores

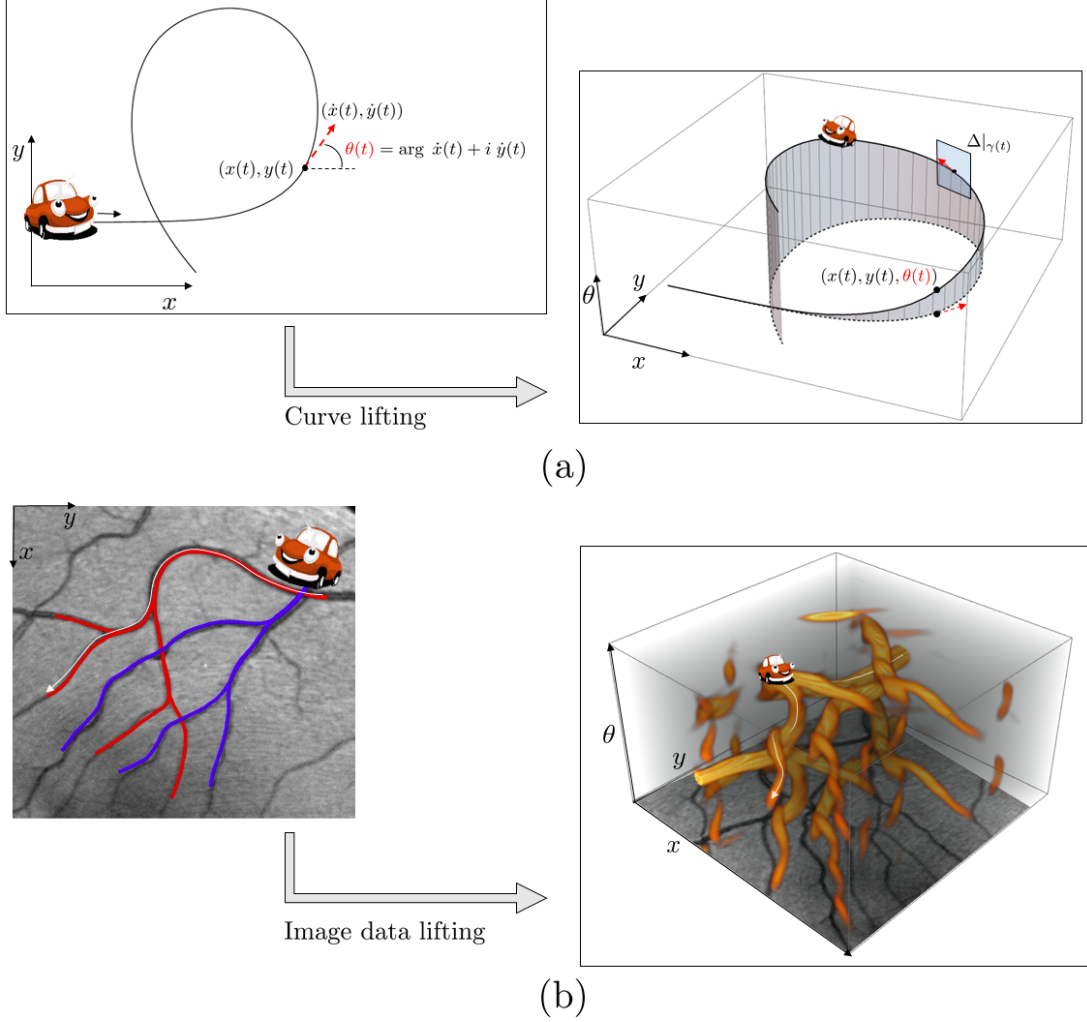


Figure 2.10: (a) A natural way of lifting a smooth planar curve $(x(t), y(t)) \in \mathbb{R}^2$, e.g. the path of a moving car, to the space $SE(2)$ is by considering $\theta(t) = \arg\{\dot{x}(t) + i \dot{y}(t)\}$ as a third coordinate in $\gamma(t) = (x(t), y(t), \theta(t)) \in SE(2)$. Curves lifted in this manner are horizontal curves and they always have their tangent vector components restricted to a sub-space $\Delta|_{\gamma(t)}$ of the full tangent space $T_{\gamma(t)}(SE(2))$, see also Fig. 2.9. In our analogy of driving a car, this restricted tangent space essentially means that a car is not able to move sideways. (b) The mass of data in orientation scores seems to concentrate around horizontal curves. As such, we only consider horizontal curves when analyzing and extracting curves in orientation scores. The vessel paths shown in (b) are the spatial projections of data-adaptive sub-Riemannian geodesics computed using the tracking method presented in Ch. 8. I.e., these curves are shortest paths that are computed under the restriction that they are also horizontal.

2. TECHNICAL BACKGROUND

forward and change direction, but is not able to move sideways, see Fig. 2.10. We then include a metric tensor \mathcal{G}^ξ on the sub-bundle (called ‘distribution’) $\Delta = \{\Delta|_g\}_{g \in SE(2)}$ of the tangent bundle $T(SE(2)) = \{T_g(SE(2))\}_{g \in SE(2)}$, where we include a balancing parameter ξ for spatial forward motion (‘hitting the gas’) and angular motion (‘turning the wheel’). Fig. 2.9(b) illustrates the sub bundle Δ , i.e., the collection of horizontal tangent spaces at all locations g in $SE(2)$.

From the Frobenius theorem it follows that the distribution Δ is non-integrable, meaning that there does not exist a submanifold of $SE(2)$ whose tangent space is given by Δ . This does not even hold locally! In fact we are in the special case of a contact manifold, and we have (complete) non-integrability of Δ around every point g in the sub-Riemannian manifold. The only integrable submanifolds are 1D and they coincide with (the lifted) horizontal curves. All of this can be seen in Fig. 2.9 and Fig. 2.11. The violation of the Frobenius theorem¹ Boothby (2003) is visible in Fig. 2.11, where the order of integrations along horizontal vector fields $\mathcal{A}_1 = \cos \theta \partial_x + \sin \theta \partial_y$ and $\mathcal{A}_3 = \partial_\theta$ matters, and moreover, the infinitesimal displacement between the blue and red corkscrew is not within the distribution. The non-integrability is visible in Fig. 2.9(b), where clearly there exists no submanifold of $SE(2)$ that is tangent to the depicted family of sub-tangent planes.

2.2 Group Theoretical Prerequisites

2.2.1 Groups, Lie Groups, and Representations

A **group** (G, \cdot) is a set of elements G equipped with a **group product**² \cdot , a binary operator, that satisfies the following four axioms:

- *Closure*: Given two elements g and h of G , the product $(g \cdot h)$ is also in G .
- *Associativity*: For $g, h, i \in G$ the product \cdot is associative, i.e., $g \cdot (h \cdot i) = (g \cdot h) \cdot i$.
- *Identity element*: There exists an identity element $e \in G$ such that $e \cdot g = g \cdot e = g$ for any $g \in G$.
- *Inverse element*: For each $g \in G$ there exists an inverse element $g^{-1} \in G$ such that $g^{-1} \cdot g = g \cdot g^{-1} = e$.

¹In words the Frobenius theorem states that a system of vector fields is integrable if it is involutive (i.e., closed under the Lie-brackets)

²We will often omit the group product symbol ‘.’ and simply write gh instead of $g \cdot h$, it should then be clear from context that the group product is used.

2.2 Group Theoretical Prerequisites

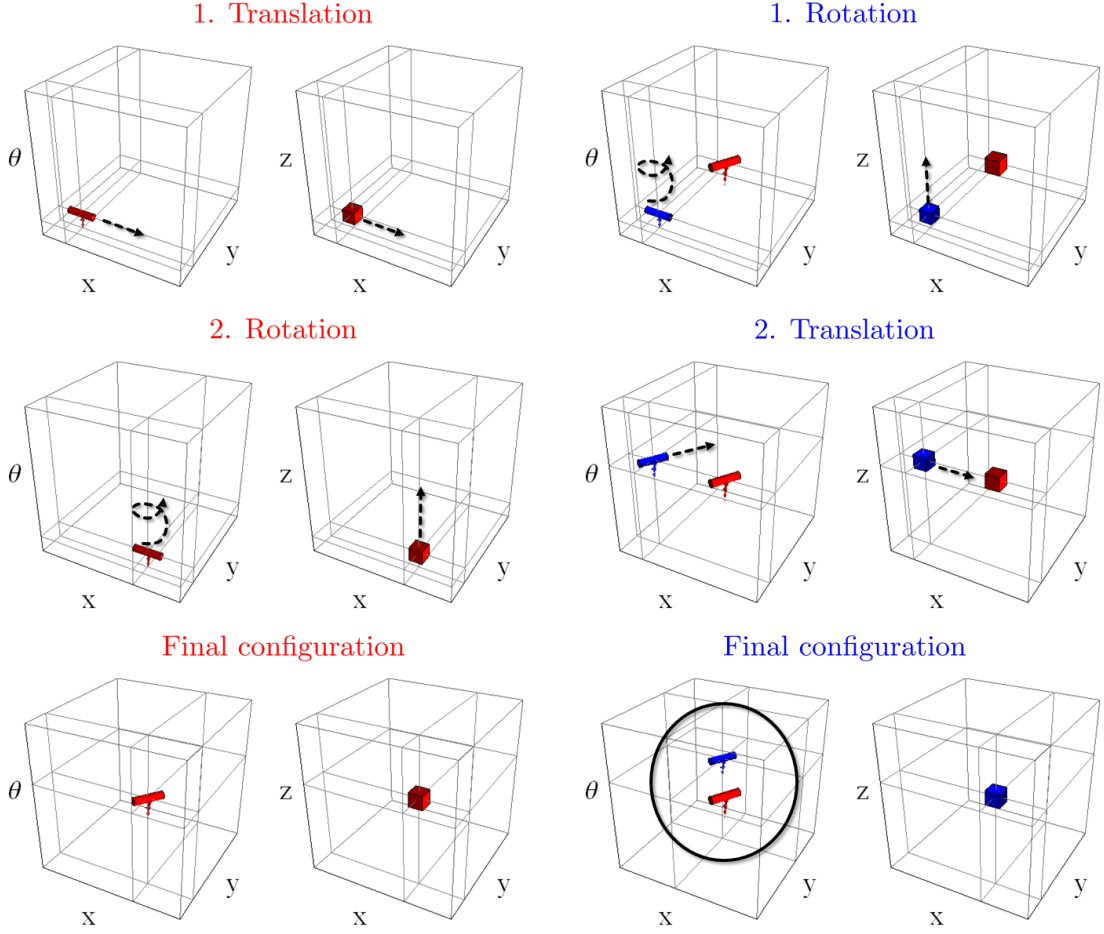


Figure 2.11: The left sub-columns show a concatenation of motions (obtained via group products) in $SE(2)$, the moving object is illustrated as a corkscrew. The right sub-columns illustrate uncoupled motions in the flat Euclidean space \mathbb{R}^3 , the moving object is illustrated as square box. In this illustration two motions are considered: translation along a “forward” direction (the A_1 -direction (cf. Fig. 2.8) in the $SE(2)$ case, the ∂_x -direction in the \mathbb{R}^3 case), and movement in the vertical direction (which corresponds to rotation in the $SE(2)$ case). Note that at the first frame A_1 and ∂_x coincide at the origin. The left column (red) shows the concatenation of first translating and then rotating, and the right column (blue) shows the concatenation of first rotating and then translating of the corkscrew and square box. In the flat Euclidean geometry of \mathbb{R}^3 the end configuration is the same for blue and red box. In the curved geometry of $SE(2)$ the location of the red and blue corkscrew is however not the same. The figure is based on an animation by Erik Franken (2008), which is available at <http://erikbekkers.bitbucket.io/data/thesis/commutationSE2.gif>

2. TECHNICAL BACKGROUND

A basic example of a discrete infinite group is the group $(\mathbb{Z}, +)$ of integers quipped with the addition operator $+$. An example of a continuous infinite group is the the **translation group** $(\mathbb{R}^2, +)$, with group product and inverse given by

$$\begin{aligned} g \cdot h &= (\mathbf{x}) (\mathbf{y}) = \mathbf{x} + \mathbf{y} \\ g^{-1} &= (-\mathbf{x}), \end{aligned} \tag{2.17}$$

with $g = (\mathbf{x}), h = (\mathbf{y}) \in \mathbb{R}^2$.

In fact, the group $(\mathbb{R}^2, +)$ is a **Lie group**. A Lie group is a continuous group whose group elements are parameterized by a finite dimensional differentiable manifold. In essence, this means that a Lie group is a group to which we can apply differential geometry. While such differential geometry is not per se necessary for the group $(\mathbb{R}^2, +)$, it does allow us to introduce (classical) differential geometrical tools in the general setting of a Lie group, in particular for our main group of interest: the **roto-translation group** $SE(2)$.

In order to map the structure of the group to some mathematical object, one requires a **representation**. If we generally say that H is the vector space to which our mathematical object belongs (e.g. $H = \mathbb{L}_2(\mathbb{R}^2)$ in case of 2D images) and \mathcal{B} is the space of bounded linear invertible operators $H \rightarrow H$ (e.g. translation of an image), then a representation is defined as follows. A representation is a mapping of the form $\mathcal{V} : G \rightarrow \mathcal{B}(H)$ that maps a group element to an operator, i.e., $\mathcal{V} = (g \mapsto \mathcal{V}_g)$, such that:

- the identity element maps to the identity operator: $e \mapsto \mathcal{I}$,
- the group product is preserved: $g \cdot h \mapsto \mathcal{V}_{gh} = \mathcal{V}_g \circ \mathcal{V}_h$,
- and consequently the inverse is preserved: $g^{-1} \mapsto (\mathcal{V}_g)^{-1}$.

Here “ \circ ” denotes operator concatenation, so we have $\mathcal{V}_{gh}(f) = \mathcal{V}_g(\mathcal{V}_h(f))$. An example of a representation for the group $G = (\mathbb{R}^2, +)$ is given by

$$(\mathcal{T}_g \circ f)(h) = f(g^{-1}h) = f(\mathbf{y} - \mathbf{x}),$$

with $g = \mathbf{x}, h = \mathbf{y} \in \mathbb{R}^2$, i.e., a translation of an image f . In fact, the translation operator \mathcal{T}_g is the **left-regular representation** of the Lie group $(\mathbb{R}^2, +)$. It is called left-regular, as the (group) multiplication takes place on the left side. Generally we denote left-regular representations by \mathcal{L}_g , and **left-multiplication** of group elements by L_g , e.g.,

$$(\mathcal{L}_g \circ f)(h) = (f \circ L_g^{-1})(h) = f(g^{-1}h),$$

2.2 Group Theoretical Prerequisites

where $L_g(h) = g \cdot h$.

An operator $\Phi : \mathbb{L}_2(G) \rightarrow \mathbb{L}_2(G)$, i.e., an operator acting on \mathbb{L}_2 functions on G , is called **left-invariant** if it commutes with the left-regular representation:

$$\forall g \in G : \Phi \circ \mathcal{L}_g = \mathcal{L}_g \circ \Phi. \quad (2.18)$$

In our 2D example an operator is thus called left-invariant if it does not matter if we apply the operator first and then translate the image, or if we translate the image first and then apply the operator.

2.2.2 Tangent Spaces and Left-Invariant Vector Fields

Associated with each group element $g \in G$ is a **tangent space** $T_g(G)$. The tangent space at g is defined as

$$T_g(G) = \{\dot{\gamma}(0) \mid \gamma : \mathbb{R} \rightarrow G \text{ differentiable, with } \gamma(0) = g\}, \quad (2.19)$$

i.e., the union of all possible tangent vectors $\dot{\gamma}(0)$ of differentiable curves $\gamma(t)$ for which $\gamma(0) = g$. The union of all tangent spaces $T_g(G)$ (at each $g \in G$) is called the **tangent bundle** $T(G)$, i.e.,

$$T(G) = \{T_g(G)\}_{g \in G}.$$

Each tangent space can be spanned by a basis. In this work we will work with a left-invariant frame of basis vectors $\{\mathcal{A}_i|_g\}_{i=1}^N$ for which we have the property that if we express any tangent vector $\dot{\gamma}(t)$ in this basis, i.e. $\dot{\gamma}(t) = \sum_{i=1}^N c^i(t) \mathcal{A}_i|_{\gamma(t)}$, the tangent vector components $c^i(t)$ remain unchanged if the curve $\gamma(t)$ is moved around via left multiplication by an arbitrary group element $g \in G$. This is illustrated in Fig. 2.12 for both $(\mathbb{R}^2, +)$ and $SE(2)$ where in the $(\mathbb{R}^2, +)$ case the left multiplication $g \cdot \gamma(t)$ with $g = (\mathbf{x}) \in \mathbb{R}^2$ corresponds to a translation of the curve $\gamma(t)$, and in the $SE(2)$ case this corresponds to a translation by \mathbf{x} and rotation by θ with group elements $g = (\mathbf{x}, \theta)$. The operation of transporting tangent vectors from $\dot{\gamma}(0) \in T_e(G)$ to $g \cdot \dot{\gamma}(0) \in T_g(G)$ is called the **push-forward** of left-multiplication L_g and is denoted by $(L_g)_*$. We thus associate to each basis vector A_i a **left-invariant vector field** given by

$$\mathcal{A}_i|_g = (L_g)_* A_i, \quad \text{for all } g \in G. \quad (2.20)$$

Such vector fields can be considered as differential operators acting on functions on the group G . This viewpoint will be applied extensively in this thesis, and therefore the reader must keep in mind the following remark:

2. TECHNICAL BACKGROUND

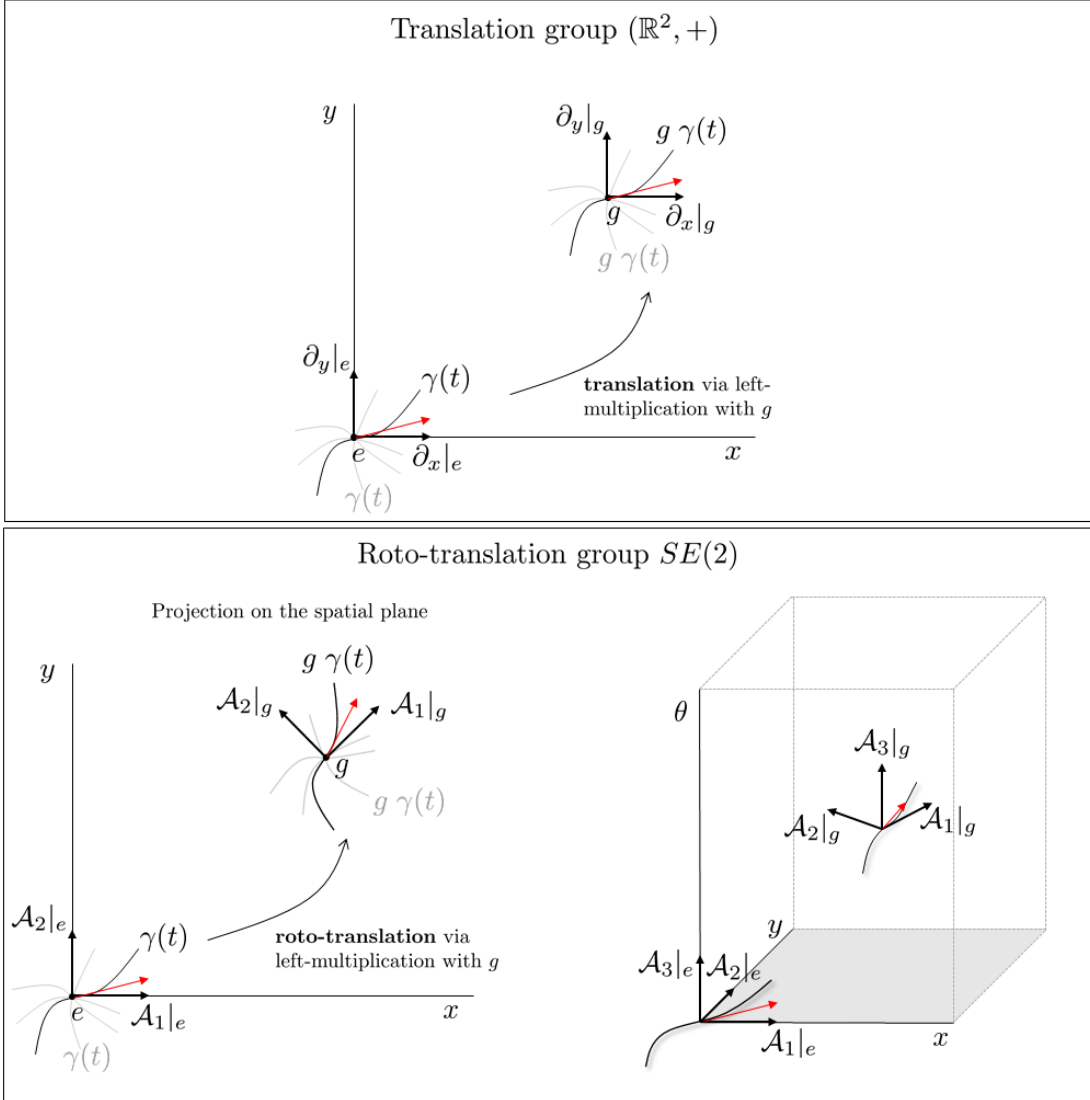


Figure 2.12: The tangent space $T_e(G)$ of the group at the identity e is the union of all possible tangent vectors $\dot{\gamma}(0)$ of curves $\gamma(t)$ with $\gamma(0) = e$. The full tangent space is spanned by some basis defined at e ; in the $(\mathbb{R}^2, +)$ case we define $T_e(\mathbb{R}^2) = \text{span}\{\partial_x|_e, \partial_y|_e\}$, in the $SE(2)$ case we define $T_e(SE(2)) = \text{span}\{\mathcal{A}_1|_e, \mathcal{A}_2|_e, \mathcal{A}_3|_e\}$. In the left-figure of the $SE(2)$ case we only show the spatial projections of curves γ and group elements g , these are however actually three dimensional objects as shown in the right figure. The tangent spaces at arbitrary points on a curve $\gamma(t)$ can be defined in such a way that the components of tangent vectors $\dot{\gamma}(t)$ (indicated in red) expressed in the basis vectors that span $T_{\gamma(t)}(G)$ are invariant to left-multiplication by arbitrary $g \in G$. Such a set of basis vectors forms a left-invariant vector field.

2.2 Group Theoretical Prerequisites

Remark 5. In differential geometry there exist two equivalent viewpoints on tangent vectors $\mathcal{A}_g \in T_g(G)$: either one considers them as tangents to locally defined curves; or one considers them as differential operators on locally defined functions. The connection between these viewpoints is as follows. We identify a tangent vector $\dot{\gamma}(t) \in T_{\gamma(t)}(G)$ with the differential operator

$$\dot{\gamma}(t)f := \frac{d}{dt}f(\gamma(t)) \quad (2.21)$$

for all locally defined, differentiable, real-valued functions $f \in \mathbb{L}_2(G)$.

When considering each $\mathcal{A}_i|_g$ as a differential operator acting on smooth locally defined functions f we can define the push forward as follows

$$\mathcal{A}_i|_g f = (L_g)_* \mathcal{A}_i|_e f := \mathcal{A}_i|_e(f \circ L_{g^{-1}}). \quad (2.22)$$

For the $SE(2)$ case we arrive at the left-invariant derivative frame $\{\mathcal{A}_1|_g, \mathcal{A}_2|_g, \mathcal{A}_3|_g\}$ given in Eq. (2.15) by letting the push-forward of the left-multiplication act on the axis aligned derivative frame $\{\partial_x|_e, \partial_y|_e, \partial_\theta|_e\}$. In the $(\mathbb{R}^2, +)$ case the generated vector field $\{\partial_x|_g, \partial_y|_g\}$ is parallel (w.r.t. a flat connection) for all $g \in (\mathbb{R}^2, +)$.

With respect to the notation of vectors and vector fields we remark the following: The basis vectors at the origin are denoted with $A_i := \mathcal{A}_i|_e$, these are used to construct left-invariant vector fields which we denote with \mathcal{A}_i , and the tangent vector that arises by restricting the vector field to group element g is denoted with $\mathcal{A}_i|_g$.

2.2.3 Matrix Groups and the Exponential Map

Many Lie groups can be expressed as matrix groups. For such a matrix Lie group, both group elements $g \in G$ and tangent vectors $\mathcal{A}|_g \in T_g(G)$ can be expressed as $N \times N$ matrices, denoted by $\mathbf{G}_g \in \mathbb{C}^{N \times N}$ and $\mathbf{A}|_g \in \mathbb{C}^{N \times N}$ respectively. Such matrix representations are convenient as in many cases they will simplify equations and definitions. For example, a group product $g g'$ can be written as the matrix product $\mathbf{G}_g \mathbf{G}_{g'}$, and group inverse g^{-1} as the matrix inverse \mathbf{G}_g^{-1} .

Example 1. In the $(\mathbb{R}^2, +)$ case the group elements can be represented as

$$g = (x, y) \leftrightarrow \mathbf{G}_g = \begin{pmatrix} 1 & 0 & x \\ 0 & 1 & y \\ 0 & 0 & 1 \end{pmatrix}, \quad (2.23)$$

2. TECHNICAL BACKGROUND

and the basis vectors ∂_x and ∂_y

$$\partial_x \leftrightarrow \mathbf{A}_x = \begin{pmatrix} 0 & 0 & 1 \\ 0 & 0 & 0 \\ 0 & 0 & 0 \end{pmatrix}, \quad \text{and} \quad \partial_y \leftrightarrow \mathbf{A}_y = \begin{pmatrix} 0 & 0 & 0 \\ 0 & 0 & 1 \\ 0 & 0 & 0 \end{pmatrix}. \quad (2.24)$$

Indeed we see that the matrices \mathbf{G}_g again form a group, and that $\mathbf{G}_g \mathbf{G}_h = \mathbf{G}_{gh}$, and $\mathbf{G}_g^{-1} \mathbf{G}_g = \mathbf{G}_{g^{-1}} \mathbf{G}_g = \mathbf{G}_{g^{-1}g} = \mathbf{G}_e = \mathbf{I}$, with \mathbf{I} the identity matrix (the matrix representation of the identity element e).

In matrix form the push-forward is simply obtained by matrix multiplication of group elements with tangent vectors:

$$\mathcal{A}_i|_g = (L_g)_* A_i \leftrightarrow \mathbf{A}_i|_g = \mathbf{G}_g \mathbf{A}_i. \quad (2.25)$$

The group elements and tangent vectors relate to each other via the **exponential mapping** $\exp : T_e(G) \rightarrow G$, which in matrix form is obtained as the matrix exponent of tangent vectors \mathbf{A} :

$$\mathbf{G} = \exp(\mathbf{A}) = \mathbf{I} + \sum_{n=1}^{\infty} \frac{\mathbf{A}^n}{n!} = \sum_{n=0}^{\infty} \frac{\mathbf{A}^n}{n!}. \quad (2.26)$$

The exponential map defines the **logarithmic mapping** $\log : G \rightarrow T_e(G)$ which is computed by

$$\mathbf{A} = \log(\mathbf{G}) = \sum_{n=1}^{\infty} \frac{(-1)^{n-1}}{n} (\mathbf{G} - \mathbf{I})^n. \quad (2.27)$$

The exponential map also defines **exponential curves**. These are curves of the form

$$\gamma_g^c(t) := g \exp(tA_c), \quad (2.28)$$

with $A_c = \sum_{i=1}^N c^i A_i$ a tangent vector defined by the tangent vector components $\mathbf{c} = (c^1, c^2, \dots, c^N) \in \mathbb{R}^N$. Such curves are completely defined by A_c and have constant tangent vector components expressed in the left-invariant basis vectors \mathcal{A}_i . Exponential curves are given as solutions of the following ordinary differential equation

$$\begin{cases} \frac{d}{dt} \mathbf{G}_{\gamma(t)} = \mathbf{G}_{\gamma(t)} \mathbf{A}_c \\ \gamma(0) = g \end{cases} \leftrightarrow \begin{cases} \dot{\gamma}(t) = (L_{\gamma(t)})_* A_c \\ \gamma(0) = g \end{cases} \leftrightarrow \begin{cases} \dot{\gamma}(t) = \sum_{i=1}^N c^i \mathcal{A}_i|_{\gamma(t)} \\ \gamma(0) = g \end{cases} \quad (2.29)$$

with $\gamma(t) = \gamma_g^c(t)$ given by (2.28).

2.2 Group Theoretical Prerequisites

Example 2. In the $(\mathbb{R}^2, +)$ case exponential curves are straight lines as they are the solutions of

$$\begin{pmatrix} 0 & 0 & \dot{x} \\ 0 & 0 & \dot{y} \\ 0 & 0 & 0 \end{pmatrix} = \begin{pmatrix} 0 & 0 & c^1 \\ 0 & 0 & c^2 \\ 0 & 0 & 0 \end{pmatrix}. \quad (2.30)$$

2.2.4 The Lie Algebra

The last group theoretical notion that we discuss in this section is that of a **Lie algebra**. A Lie algebra is a vector space (e.g. the tangent space at the identity element $T_e(G)$) that is endowed with a binary operator called the **Lie bracket** or **commutator** $[\cdot, \cdot] : T_e(G) \times T_e(G) \rightarrow T_e(G)$ with the following properties

- *bilinearity*: $[aA + bB, C] = a[A, C] + b[B, C]$ and $[C, aA + bB] = a[C, A] + b[C, B]$ for all $A, B, C \in T_e(G)$ and all $a, b, c \in \mathbb{R}$.
- *anticommutativity*: $[A, B] = -[B, A]$ for all $A, B \in T_e(G)$.
- *Jacobi identity*: $[A, [B, C]] + [B, [C, A]] + [C, [A, B]] = 0$ for all $A, B, C \in T_e(G)$.

In general, for matrix groups the commutator $[A, B]$ of two vector fields A, B is defined as

$$[A, B] = \lim_{t \rightarrow 0} \frac{\gamma(t) - e}{t^2}, \quad (2.31)$$

where the curve γ is defined as

$$\gamma(t) = \exp(-tB) \exp(-tA) \exp(tB) \exp(tA). \quad (2.32)$$

Intuitively seen, this operator describes the infinitesimal displacement obtained by following the path of $\gamma(t)$ as defined in (2.32), which is illustrated in Fig. 2.13. Using the matrix representation of tangent vectors, the commutator is defined as

$$[\mathbf{A}, \mathbf{B}] = \mathbf{AB} - \mathbf{BA}. \quad (2.33)$$

It is readily verified that all the commutators of the basis vectors \mathbf{A}_x and \mathbf{A}_y (cf. Eq. (2.24)) of the tangent space $T_e(\mathbb{R}^2)$ are zero. For the left-invariant vector fields on $SE(2)$ this is not the case, see Fig. 2.11 and Fig. 2.13(b).

2. TECHNICAL BACKGROUND

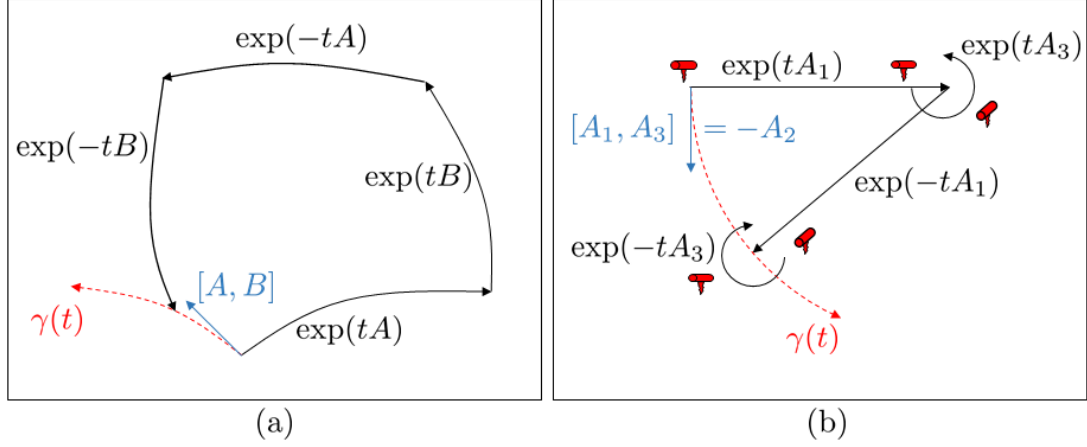


Figure 2.13: The commutator is defined by Eq. (2.31) and describes the direction obtained by infinitesimal displacement along curve $\gamma(t)$ defined in (2.32). Panel (a) illustrates the commutator and the path $\gamma(t)$ for vectors A and B in an arbitrary manifold. Panel (b) illustrates the commutator for the $SE(2)$ group for tangent vectors $A_1, A_3 \in T_e(SE(2))$. Here only the spatial part of the trajectory of $\gamma(t)$ is illustrated, and the same directions of movement A_1 and A_3 (cf. 2.15) of the corkscrew as in Fig. 2.11 are considered.

2.3 The Roto-Translation Group and Left-Invariant Processing via Invertible Orientations Scores

2.3.1 The Lie group $SE(2)$

The Lie group $SE(2)$ is of special interest in this thesis as we identify it as the domain of orientation scores. In this section the previously described group theoretical notions will be repeated here for the group $SE(2)$ specifically.

The group $SE(2)$ is the group of rigid body motions $g = (\mathbf{x}, \mathbf{R}_\theta) \in SE(2)$ which acts on the space of positions and orientations $\mathbb{R}^2 \times S^1$ via

$$g \cdot (\mathbf{x}', \theta') = (\mathbf{R}_\theta \mathbf{x}' + \mathbf{x}, \theta + \theta'). \quad (2.34)$$

Note here that $(\mathbf{x}, \theta) = (\mathbf{x}, \mathbf{R}_\theta) \cdot (\mathbf{0}, 0)$, which allows us to uniquely identify the space of positions and orientations with the rigid body motion group $SE(2) = \mathbb{R}^2 \times SO(2)$, i.e., we identify

$$\mathbb{R}^2 \times S^1 \ni (\mathbf{x}, \theta) \leftrightarrow (\mathbf{x}, \mathbf{R}_\theta) = g \in \mathbb{R}^2 \rtimes SO(2),$$

with $SO(2)$ denoting the group of planer rotations. As the combination of two rigid

2.3 The Roto-Translation Group and Left-Invariant Processing via Invertible Orientations Scores

body motions is again a rigid body motion, $SE(2)$ is equipped with the group product and group inverse:

$$\begin{aligned} g \cdot g' &= (\mathbf{x}, \mathbf{R}_\theta) \cdot (\mathbf{x}', \mathbf{R}_{\theta'}) = (\mathbf{R}_\theta \mathbf{x}' + \mathbf{x}, \mathbf{R}_{\theta+\theta'}) \\ g^{-1} &= (-\mathbf{R}_\theta^{-1} \mathbf{x}, -\theta). \end{aligned} \quad (2.35)$$

Note that because the rotation shows up in the translation part of the group product (also recall our intuition on coupling of positions and orientations from Subsec. 2.1.6 and Fig. 2.5), we cannot just write the Cartesian product \times to denote the group $SE(2)$ as the (uncoupled) combination of translations \mathbb{R}^2 and rotations $SO(2)$. Instead, because we have this coupling, we have to use the **semi-direct product** \rtimes and write $SE(2) = \mathbb{R}^2 \rtimes SO(2)$, or equivalently $SE(2) = \mathbb{R}^2 \rtimes S^1$. The matrix representation \mathbf{G}_g of group elements $g = (\mathbf{x}, \theta) = (x, y, \theta) \in SE(2)$ is given by

$$\mathbf{G}_g = \begin{pmatrix} \mathbf{R}_\theta & \mathbf{x} \\ \mathbf{0} & 1 \end{pmatrix} = \begin{pmatrix} \cos \theta & -\sin \theta & x \\ \sin \theta & \cos \theta & y \\ 0 & 0 & 1 \end{pmatrix}. \quad (2.36)$$

It is readily verified that $\mathbf{G}_{gg'} = \mathbf{G}_g \mathbf{G}_{g'}$ for all $g, g' \in SE(2)$.

2.3.2 Left-Invariance

The left-regular representation of the $SE(2)$ group on orientation scores $U \in \mathbb{L}_2(SE(2))$ is given by

$$(\mathcal{L}_g \circ U)(h) = (U \circ L_g^{-1})(h) = U(g^{-1} \cdot h), \quad (2.37)$$

with left-multiplication $L_g(h) = g \cdot h$. The left-regular representation on images $f \in \mathbb{L}_2(\mathbb{R}^2)$ is given by

$$(\mathcal{U}_g \circ f)(\mathbf{y}) = f(\mathbf{R}_\theta^{-1}(\mathbf{y} - \mathbf{x})), \quad g = (\mathbf{x}, \theta) \in SE(2), \quad \mathbf{x} \in \mathbb{R}^2. \quad (2.38)$$

Alternatively, the right-regular representation is given by

$$(\mathcal{R}_g \circ U)(h) = (U \circ R_g)(h) = U(h \cdot g). \quad (2.39)$$

Recall Subsec. 2.1.1, where we remarked that in general different kind of scores can be obtained via different kind of group representations. Indeed, an orientation score U_f (Eq. 2.1) is constructed from an image $f \in \mathbb{L}_2(\mathbb{R}^2)$ by means of the left-regular representation of $SE(2)$ on wavelets $\psi \in \mathbb{L}_2(\mathbb{R}^2)$ via

$$U_f(\mathbf{x}, \theta) = (\mathcal{U}_{(\mathbf{x}, \theta)} \psi, f)_{\mathbb{L}_2(\mathbb{R}^2)}. \quad (2.40)$$

2. TECHNICAL BACKGROUND

Let $\Phi : \mathbb{L}_2(SE(2)) \rightarrow \mathbb{L}_2(SE(2))$ be an operator acting on orientation scores, then it is said to be left-invariant if it commutes with the left-representation \mathcal{L}_g , recall Eq. 2.18. Let $\Upsilon = \mathcal{W}_\psi^* \circ \Phi \circ \mathcal{W}_\psi$ be the net effect of processing images via orientation scores, i.e., the effect of reconstructing (via \mathcal{W}_ψ^*) an orientation score (obtained via \mathcal{W}_ψ) that is processed via Φ . The net operator Υ on the image f is Euclidean invariant (invariant to roto-translations of the image) if $\Upsilon \circ \mathcal{U}_g = \mathcal{U}_g \circ \Upsilon$ for any $g \in SE(2)$. Generally this is a property that one aims for in the development of operators Φ , and it has the consequence that the operators Φ should be left-invariant Duits (2005). In fact, under the assumption that Φ maps the space of orientation scores onto itself we have

$$\forall_{g \in SE(2)} \Phi \circ \mathcal{L}_g = \mathcal{L}_g \circ \Phi \Leftrightarrow \forall_{g \in SE(2)} \Upsilon \circ \mathcal{U}_g = \mathcal{U}_g \circ \Upsilon.$$

The key idea behind this relation is

$$\mathcal{W}_\psi \mathcal{U}_g = \mathcal{L}_g \mathcal{W}_\psi. \quad (2.41)$$

2.3.3 Left-Invariant Vector Fields

The left-invariant vector fields on $SE(2)$ are obtained via push-forward of the left-multiplication acting on the axis aligned derivative frame $\{\partial_x|_e, \partial_y|_e, \partial_\theta|_e\}$ at the origin. As such we take $A_1 = \partial_x|_e$, $A_2 = \partial_y|_e$ and $A_3 = \partial_\theta|_e$ as the Lie algebra, and obtain the left-invariant vector fields

$$\begin{aligned} \mathcal{A}_1|_{(x,y,\theta)} &:= (L_{(x,y,\theta)})_* A_1 = \cos \theta \partial_x|_{(x,y,\theta)} + \sin \theta \partial_y|_{(x,y,\theta)} \\ \mathcal{A}_2|_{(x,y,\theta)} &:= (L_{(x,y,\theta)})_* A_2 = -\sin \theta \partial_x|_{(x,y,\theta)} + \cos \theta \partial_y|_{(x,y,\theta)} \\ \mathcal{A}_3|_{(x,y,\theta)} &:= (L_{(x,y,\theta)})_* A_3 = \partial_\theta|_{(x,y,\theta)}. \end{aligned} \quad (2.42)$$

The corresponding commutators (recall (2.33)) are given by

$$\begin{aligned} [A_1, A_3] &= -A_2, & [A_2, A_3] &= A_1, & [A_1, A_2] &= 0, & \text{and} \\ [\mathcal{A}_1, \mathcal{A}_3] &= -\mathcal{A}_2, & [\mathcal{A}_2, \mathcal{A}_3] &= \mathcal{A}_1, & [\mathcal{A}_1, \mathcal{A}_2] &= 0, \end{aligned} \quad (2.43)$$

In general we have Lie algebra constants

$$[\mathcal{A}_i, \mathcal{A}_j] = \sum_{k=1}^3 c_{ij}^k \mathcal{A}_k, \quad (2.44)$$

with nonzero structure constants

$$c_{13}^2 = -1, \quad c_{23}^1 = 1, \quad c_{31}^2 = 1, \quad c_{32}^1 = -1. \quad (2.45)$$

2.3 The Roto-Translation Group and Left-Invariant Processing via Invertible Orientations Scores

The matrix representation of the Lie algebra is given by

$$\mathbf{A}_1 = \begin{pmatrix} 0 & 0 & 1 \\ 0 & 0 & 0 \\ 0 & 0 & 0 \end{pmatrix}, \quad \mathbf{A}_2 = \begin{pmatrix} 0 & 0 & 0 \\ 0 & 0 & 1 \\ 0 & 0 & 0 \end{pmatrix}, \quad \mathbf{A}_3 = \begin{pmatrix} 0 & -1 & 0 \\ 1 & 0 & 0 \\ 0 & 0 & 0 \end{pmatrix}. \quad (2.46)$$

Now that the basis vectors \mathbf{A}_i for the Lie algebra are explicitly defined we can also compute the group elements via the exponential mapping defined in Eq. (2.26):

$$\begin{aligned} \mathbf{G}_{(x,y,\theta)} &= \exp(x\mathbf{A}_1)\exp(y\mathbf{A}_2)\exp(\theta\mathbf{A}_3) \\ &= \begin{pmatrix} 1 & 0 & x \\ 0 & 1 & 0 \\ 0 & 0 & 1 \end{pmatrix} \begin{pmatrix} 1 & 0 & 0 \\ 0 & 1 & y \\ 0 & 0 & 1 \end{pmatrix} \begin{pmatrix} \cos\theta & -\sin\theta & 0 \\ \sin\theta & \cos\theta & 0 \\ 0 & 0 & 1 \end{pmatrix} \\ &= \begin{pmatrix} \cos\theta & -\sin\theta & x \\ \sin\theta & \cos\theta & y \\ 0 & 0 & 1 \end{pmatrix}, \end{aligned} \quad (2.47)$$

and see that this indeed corresponds to the matrix representation of the group elements defined in Eq. (2.36). In fact (2.47) shows that (x, y, θ) are exponential coordinates of the second kind (i.e. a product of matrix exponentials). It is also possible to use exponential coordinates (c^1, c^2, c^3) of the first kind:

$$\begin{aligned} \mathbf{G}_g &= \exp(\mathbf{A}_c) = \exp(c^1\mathbf{A}_1 + c^2\mathbf{A}_2 + c^3\mathbf{A}_3) \\ &= \begin{pmatrix} \cos c^3 & -\sin c^3 & \frac{c^1 \sin c^3 - c^2(1 - \cos c^3)}{c^3} \\ \sin c^3 & \cos c^3 & \frac{c^1(1 - \cos c^3) + c^2 \sin c^3}{c^3} \\ 0 & 0 & 1 \end{pmatrix}, \end{aligned} \quad (2.48)$$

from which we directly obtain the expression in our regular group notation

$$g = (x, y, \theta) = \exp(A_c) = \exp(c^1 A_1 + c^2 A_2 + c^3 A_3) \quad (2.49)$$

with

$$\begin{aligned} x &= \frac{c^1 \sin c^3 - c^2(1 - \cos c^3)}{c^3}, & y &= \frac{c^1(1 - \cos c^3) + c^2 \sin c^3}{c^3}, & \theta &= c^3, & \text{if } c^3 \neq 0, \\ x &= c^1, & y &= c^2, & \theta &= 0, & \text{if } c^3 = 0. \end{aligned} \quad (2.50)$$

2. TECHNICAL BACKGROUND

The logarithmic mapping $\log : SE(2) \rightarrow T_e(SE(2))$ is in matrix notation given by

$$\mathbf{A}_c = \log(\mathbf{G}_g) = \begin{pmatrix} 0 & -\theta & \frac{1}{2}\theta(y + x \cot \frac{\theta}{2}) \\ \theta & 0 & \frac{1}{2}\theta(-x + y \cot \frac{\theta}{2}) \\ 0 & 0 & 0 \end{pmatrix} \quad (2.51)$$

Using the regular group notations we write

$$A_c = \log(g), \quad (2.52)$$

with

$$\begin{aligned} c^1 &= \frac{1}{2}\theta(y + x \cot \frac{\theta}{2}), & c^2 &= \frac{1}{2}\theta(-x + y \cot \frac{\theta}{2}), & c^3 &= \theta, & \text{if } \theta \neq 0, \\ c^1 &= x, & c^2 &= y, & c^3 &= 0, & \text{if } \theta = 0. \end{aligned} \quad (2.53)$$

Chapter 3

The Developed Retinal Image Processing Applications

3. THE DEVELOPED APPLICATIONS

In Chapter 1 we introduced retinal imaging as a versatile medium for studying various health parameters. A large amount of research in this field is done on the study of retinal microvasculature and its relation to systemic diseases such as diabetes melitus, or more generally, any other health status (such as blood pressure and body mass index). In order to facilitate this kind of research as to allow for large scale clinical studies, and in order to support large scale screening programs that rely on retinal images, the following applications have been developed in this thesis:

- *Anatomical landmark detection* (Ch. 5): Automatic detection of the key anatomical landmarks (the fovea and the optic nerve head) in retinal images.
- *Vessel enhancement* (Ch. 6): Robust crossing preserving vessel enhancement of blood vessels.
- *Vessel tracking and segmentation*: Construction of models (parameterizations) of the retinal blood vessels. Here we developed three of such techniques:
 - *Part I: Vessel segmentation via locally optimal tracking* (Ch. 7): Fully automated tracking of the vessel edges, and tracking of the complete retinal vasculature.
 - *Part II: Vessel centerline extraction via globally optimal tracking in $SE(2)$* (Ch. 8): Semi-automatic tracking of vessel centerlines using Sub-Riemannian geodesics in $SE(2)$.
 - *Part III: Vessel centerline extraction via globally optimal tracking in $SO(3)$* (Ch. 9): An extension of the tracking method to the tracking in spherical images.
- *Vessel Analysis* (Ch. 10, Ch. 11, Ch. 12): Extraction of clinically relevant (geometrical) vessel features such as artery/vein classification, vessel curvature and vessel caliber.

In each of these applications new algorithms are developed in the framework of left-invariant processing of orientation scores. In the following subsections we go through these applications one by one, and discuss briefly 1) the motivation of the problem, 2) how we solve the problem, and 3) how the developed method compares to the state of the art. In all of these applications we will see that it has indeed been favorable to resort to left-invariant processing of orientation scores, rather than to use conventional 2D image processing techniques. In the Chapters 5 to 12 each of the applications will then be discussed in full detail.

3.1 Anatomical Landmark Detection (Ch. 5)

Motivation In this application we detect the location of the fovea and the optic nerve head (ONH) (cf. Subsec. 1.1 and Fig. 3.1). Both the fovea and the ONH are key anatomical landmarks in the retina as they play an important role in the following:

1. They both are used as reference locations in standardized measurement protocols Group *et al.* (1991); Klein *et al.* (1991); Wilkinson *et al.* (2003). E.g., vessel features are typically analyzed in a region between one optic disk diameter to two diameters away from the ONH center, and the presence of lesions around the fovea heavily determines the severity of pathologies such as diabetic retinopathy and age related macular degeneration. Lesions that are closer to the fovea affect vision more severely, and are an indicator of faster disease progression Wilkinson *et al.* (2003).
2. The optic nerve head is the place from which the vascular tree departs. As such it is a preferred location for the initialization of tracking methods that iteratively grow models of the retinal vasculature Bekkers *et al.* (2014a); Jiang *et al.* (2007); Zhang *et al.* (2014).
3. In other automated retinal image analysis algorithms the (distance to the) fovea and/or the ONH location are used as features in supervised methods for automatic pathology grading Quellec *et al.* (2016), image quality assessment Fleming *et al.* (2006), and artery/vein classification Zamperini *et al.* (2012).

Robust localization of the fovea and ONH is thus essential as many retinal image analysis pipelines rely on the correct localization of these structures.

Method The developed method for the detection of the key anatomical landmarks focuses on two aspects: speed and robustness. Speed is achieved by using a simple and short processing pipeline that relies on template matching via cross-correlation. Robustness is achieved by performing template matching with templates learned from training samples and do the matching in both the image and orientation score domain. Both the fovea and landmarks are characterized by blob-like intensity patterns and vessel patterns, and are addressed by respectively template matching in images and orientation scores. The fovea is recognized as a dark blob lying in an avascular region of the retina. It is surrounded by the main vessel arcades and a pattern of small blood vessels oriented towards the dark blob. The ONH is usually recognized as a bright disk-

3. THE DEVELOPED APPLICATIONS

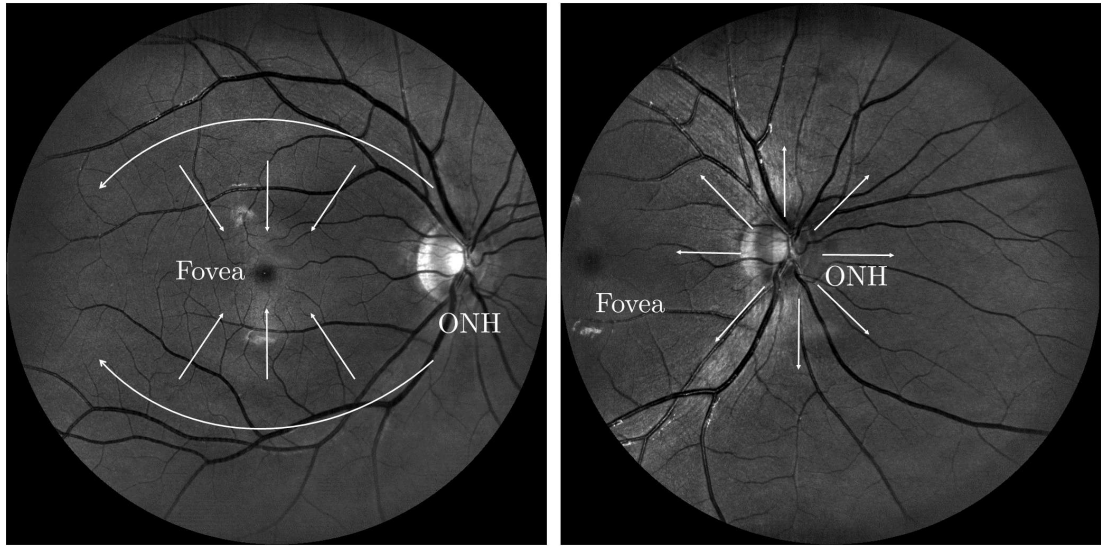


Figure 3.1: Left: the appearance of the fovea is characterized by a dark blob structure, a pattern of bigger blood vessels that arc around it, and a pattern of smaller blood vessels that are oriented towards the center. Right: the optic nerve head (ONH) is characterized by a disk-like shape (better visible on the left image), and a pattern of blood vessels that radiate outwards from the center of the ONH.

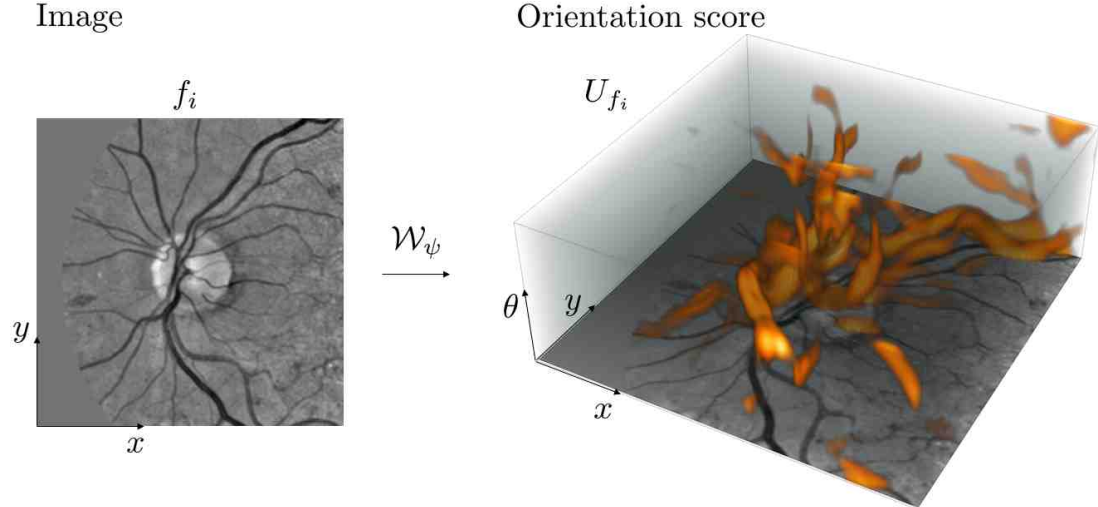


Figure 3.2: An image patch f_i centered around the optic nerve head and a volume rendering of the corresponding orientation score U_{f_i} .

3.1 Anatomical Landmark Detection (Ch. 5)

like structure (or dark/gray on SLO images), with a pattern of blood vessels radiating outwards. See for example Fig. 3.1 in which these patterns are illustrated.

In 2D, template matching via cross-correlation is based on taking inner products of a roto-translated template $t \in \mathbb{L}_2(\mathbb{R}^2)$ with the image $f \in \mathbb{L}_2(\mathbb{R}^2)$, and optimize objective functionals

$$P(\mathbf{x}, \theta) = (\mathcal{U}_{(\mathbf{x}, \theta)} t, f)_{\mathbb{L}_2(\mathbb{R}^2)}, \quad (3.1)$$

with $(\cdot, \cdot)_{\mathbb{L}_2(\mathbb{R}^2)}$ the standard inner product between 2D images, and with \mathcal{U}_g the left-regular representation of $SE(2)$ on images, recall Eq. (2.38). I.e., the most likely object location and orientation is given by

$$(\mathbf{x}^*, \theta^*) = \underset{\mathbf{x} \in \mathbb{R}^2, \theta \in S^1}{\operatorname{argmax}} P(\mathbf{x}, \theta).$$

To get the best out of this approach, we learn templates t in a linear regression based frame work, where we minimize energy functionals of the form

$$E_{lin}(t) = \underbrace{\frac{1}{N} \sum_{i=1}^N ((t, f_i)_{\mathbb{L}_2(\mathbb{R}^2)} - y_i)^2}_{\text{data-term}} + \underbrace{R(t)}_{\text{regularization-term}}, \quad (3.2)$$

with f_i one of N image patches that either contains the object of interest, in which case desired response is $y_i = 1$, or when it does not, in which case the desired response is $y_i = 0$. The term $R(t)$ is an additional penalty functional (prior) that imposes additional constraints on the template such as smoothness. An example of an image patch f_i that contains the ONH and the corresponding orientation score U_{f_i} (used in the extension to $SE(2)$) is given in Fig. 3.2.

In Ch. 5 we describe our approach in full detail and propose extensions for template matching and training of templates using orientation scores. There we also propose an adaptation to learning templates via logistic regression instead of linear regression. In our extension of template matching and linear/logistic regression on $SE(2)$ we include a regularization term that imposes an anisotropic smoothness of the templates along line structures. This regularization term is defined via the left-invariant derivative frame $\{\mathcal{A}_1, \mathcal{A}_2, \mathcal{A}_3\}$, and thereby takes into account the curved geometry of the domain $SE(2)$ (cf. Subsec. 2.1.6).

We will also establish a theoretical connection between our left-invariant smoothing prior and time integrated (with a negatively exponentially distributed traveling time) hypo-elliptic Brownian motions on $SE(2)$. This gives us a stochastic interpretation of the regularization induced by the prior. Furthermore, we show that our linear regression approach can also be used for smoothing of images and orientation scores.

3. THE DEVELOPED APPLICATIONS

Table 3.1: Comparison to state of the art: Optic nerve head detection success rates, the number of fails (in parentheses), and computation times. The MESSIDOR, DRIVE and STARE databases contain respectively 1200, 40 and 81 images.

Method	MESSIDOR	DRIVE	STARE	Time (s)
Lu (2011)	99.8% (3)		98.8% (1)	5.0
Lu & Lim (2011)		97.5% (1)	96.3% (3)	40.0
Yu <i>et al.</i> (2012)	99.1% (11)			4.7
Aquino <i>et al.</i> (2012)	99.8% (14)			1.7
Giachetti <i>et al.</i> (2013)	99.7% (4)			5.0
Ramakanth & Babu (2014)	99.4% (7)	100% (0)	93.83% (5)	0.2
Marin <i>et al.</i> (2015)	99.8% (3)			5.4 [†]
Dashtbozorg <i>et al.</i> (2015)	99.8% (3)			10.6 [†]
Proposed	99.8% (2)	97.8% (1)	98.8% (1)	0.5

[†] Timings include simultaneous disk segmentation.

Results In Ch. 5 we extensively validate the method on five different databases, three of which are publicly available benchmark datasets, and two of which are private databases that contain images from both a traditional fundus camera and an SLO camera. For optic nerve head detection a success rate of 99.83% was achieved on a test set of 1737 images (only 4 failed detections), with the detection taking on average 0.5 seconds per image. In comparison to the state of the art on ONH detection, our method improves both on speed and detection performance, see Table. 3.1. For fovea detection a success rate of 99.32% was achieved on a set of 1616 images. As our fovea detection algorithm is based on the same method as ONH detection, also here the processing times is on average 0.5 seconds per image. With only 3 failed detections and a processing time of 0.5 seconds, compared to 11 fails and a processing time of 5 seconds by the best performing method on a public benchmark set of 1200 images, our method again improves both on speed and detection performance, see Table. 3.2.

3.2 Vessel Enhancement (Ch. 6)

Motivation Proper enhancement of blood vessels is a core ingredient in many retinal image analysis pipelines. Here we use the term vessel enhancement for the construction

Table 3.2: Comparison to state of the art: Fovea detection success rates, the number of fails (in parentheses), and computation times. The MESSIDOR database contains 1200 images.

Method	MESSIDOR		Time (s)
Niemeijer <i>et al.</i> (2009)	97.9%	(25)	7.6 [†]
Yu <i>et al.</i> (2011)	95.0%*	(60)	3.9 [†]
Gegundez-Arias <i>et al.</i> (2013)	96.9%	(37)	0.9
Giachetti <i>et al.</i> (2013)	99.1%	(11)	5.0 [†]
Aquino (2014)	98.2%	(21)	10.9 [†]
Proposed	99.7%	(3)	0.5

*Success-criterion based on half optic radius.

[†]Timing includes ONH detection.

of a function that has high value at vessel locations and low values otherwise. Such functions are also referred to as “soft vessel segmentations” or “vesselness functions”. In particular the performance of vessel segmentation and tracking methods heavily relies on the construction of a reliable vessel enhancement. For example, a typical vessel segmentation algorithm takes a soft-segmentation as input and thresholds it to obtain a hard segmentation. In geodesic tracking methods, such as the one presented in this thesis in Chapter 8, vessel enhancements are necessary to construct cost functions that give low penalty to curves that are aligned with blood vessels. In this thesis we will also use soft-segmentations to weight pixel-wise feature values. For example, using one of the methods described in Chapter 11 we can assign to every pixel a curvature value. A global curvature value for the full image is then defined as the weighted average of the curvature values, weighted by their vesselness value.

One of the most used and well established vessel enhancement methods in literature is Frangi’s vesselness filter Frangi *et al.* (1998). The filter enhances blood vessels whereby it relies on an anisotropy measure derived from the eigenvalues of the Gaussian Hessian matrix. A drawback of Frangi’s vesselness filter is that it does not work on crossings and bifurcations as these structures are not anisotropic. In order to deal also with these structures we derive a vesselness filter via processing of orientation scores (recall from Subsec. 2.1.1 that there are no such things as crossings in orientation scores). The result is a crossing-preserving vessel enhancement method.

3. THE DEVELOPED APPLICATIONS

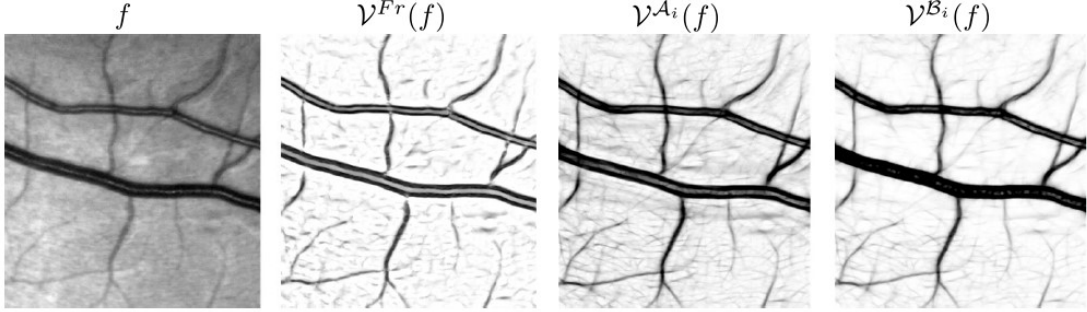


Figure 3.3: An image patch f and the vesselness results obtained by the classical Frangi vesselness filter (denoted by $\mathcal{V}^{Fr}(f)$), vesselness in $SE(2)$ using the left-invariant derivative frame $\{\mathcal{A}_i\}_{i=1}^3$ (denoted with $\mathcal{V}^{\mathcal{A}_i}(f)$), and vesselness in $SE(2)$ using the gauge frame $\{\mathcal{B}_i\}_{i=1}^3$ (denoted with $\mathcal{V}^{\mathcal{B}_i}(f)$).

Method In the 2D Frangi vesselness filter, blood vessels are enhanced on the basis of two vesselness measures which are derived from the Hessian in the image domain. Measure one is an anisotropy measure which we denote by \mathcal{R} , measure two is a structureness measure which we denote by \mathcal{S} . The classical Frangi vesselness filter $\mathcal{V}^{Fr}(f) : \mathbb{R}^2 \rightarrow \mathbb{R}^+$ of image $f \in \mathbb{L}_2(\mathbb{R}^2)$ takes the following form:

$$\mathcal{V}^{Fr}(f) = \begin{cases} 0 & \text{if } \mathcal{Q} \leq 0 \\ \exp(-\frac{\mathcal{R}^2}{2\sigma_1^2}) \left[1 - \exp(-\frac{\mathcal{S}}{2\sigma_2^2}) \right] & \text{if } \mathcal{Q} > 0 \end{cases} \quad (3.3)$$

with $\mathcal{R} = \frac{\lambda_1}{\lambda_2}$ the anisotropy term, $\mathcal{S} = \sqrt{\lambda_1^2 + \lambda_2^2}$ the structureness term, and \mathcal{Q} a convexity measure (in order to enhance either dark or bright line structures), and with λ_1, λ_2 the eigenvalues ($|\lambda_1| \leq |\lambda_2|$) of the Gaussian Hessian matrix

$$\mathcal{H}^{\sigma_s}(f) = \begin{pmatrix} \partial_x^2(G_{\sigma_s} * f) & \partial_x \partial_y(G_{\sigma_s} * f) \\ \partial_x \partial_y(G_{\sigma_s} * f) & \partial_y^2(G_{\sigma_s} * f) \end{pmatrix} \quad (3.4)$$

computed in the image domain at scale s . Parameters σ_1 and σ_2 in Eq. (3.3) scale respectively the anisotropy and structureness measures. In our generalization to $SE(2)$ the general definition stays the same, however now we define the vesselness filter $\mathcal{V}^{\mathcal{A}_i} : \mathbb{L}_2(SE(2)) \rightarrow \mathbb{L}_2(SE(2))$, and redefine measures $\mathcal{R}, \mathcal{S}, \mathcal{Q}$ in terms of second order left-invariant derivatives of orientation scores. The vessel enhanced orientation score $(\mathcal{V}^{\mathcal{A}_i}(U_f))(\mathbf{x}, \theta)$ can then be projected to the plane (e.g. via a maximum intensity projection over orientation θ), resulting in a 2D vesselness image. As we will show in Chapter 6 the results are very similar to those of the standard Frangi vesselness filter, however, now with a preservation of vessel structures at crossings and bifurcations.

3.2 Vessel Enhancement (Ch. 6)

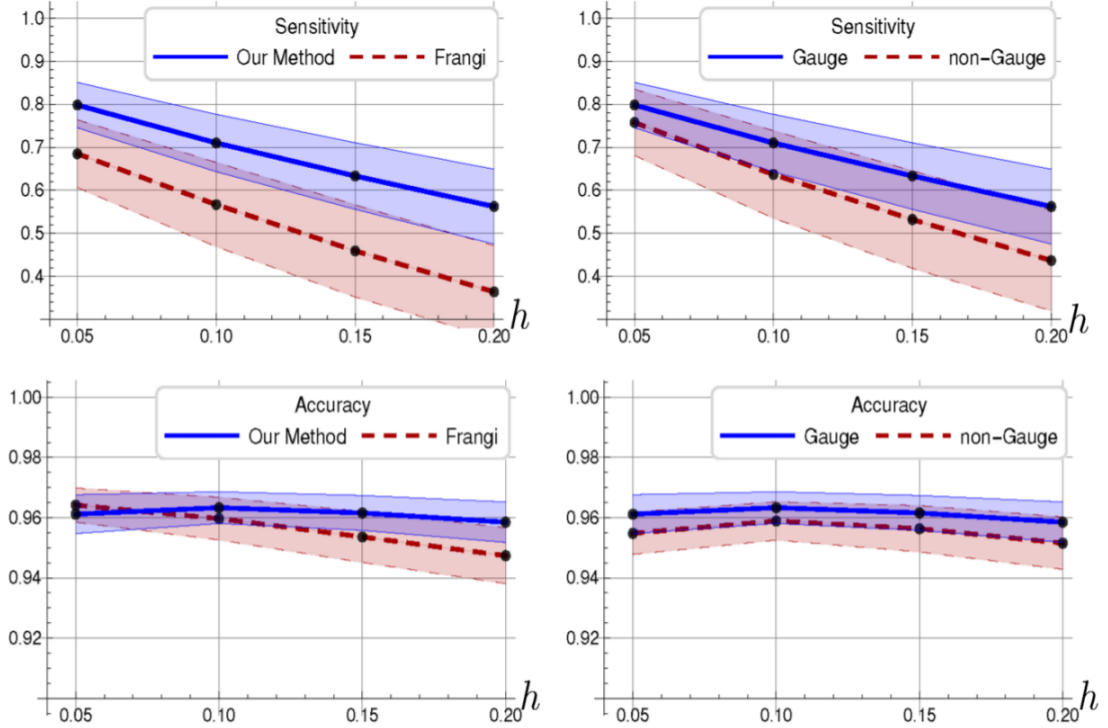


Figure 3.4: Left: comparison of multiple-scale Frangi vesselness and vesselness via gauge frames. Average accuracy and sensitivity on the HRF dataset Odstrcilik et al. (2013) over threshold values h . Shaded regions correspond to $\pm 1\sigma$. Right: comparison of the $SE(2)$ vesselness filter with and without including the gauge frame Duits & Janssen et al. (2016).

In Chapter 6 we then further extended the generalization of Frangi vesselness filtering to $SE(2)$ by replacing the left-invariant derivative frame $\{\mathcal{A}_1, \mathcal{A}_2, \mathcal{A}_3\}$ in the definition $\mathcal{R}, \mathcal{S}, \mathcal{Q}$ with a gauge frame $\{\mathcal{B}_1, \mathcal{B}_2, \mathcal{B}_3\}$. The gauge frame is obtained from the 3D left-invariant Hessian matrix. As such, in this frame the filter is no longer confined to the fixed discrete θ -slices, but is fully aligned with the 3D line structures in the orientation scores. This increase in data-adaptivity gives a further improvement on the results.

Results Computing vesselness via left-invariant processing of the orientation score results in a crossing-preserving vessel enhancement method. Vesselness defined in a left-invariant gauge frame results in a further improvement, mainly observed as additional noise suppression. A preview of the results is given in Fig. 3.3. These conclusions are supported by quantitative evaluation on public benchmark dataset, which will be fully

3. THE DEVELOPED APPLICATIONS

discussed in Chapter 6, and which are summarized in Fig. 3.4.

3.3 Vessel Tracking Part I (Ch. 7)

Motivation Models of the retinal vasculature form the basis for many vessel measurements that are used in clinical research. In the application discussed in this section models of the vasculature are constructed via an iterative vessel tracking method. Reliable vessel measurements demand high accuracy in the construction of vessel models. This means that automated algorithms have to deal with crossings, bifurcations, and other complex configurations that challenge vessel tracking, without compromising vessel model accuracy. In this application we again deal with such challenging situations by performing vessel tracking in the domain of orientation scores, as here such complex vessel structures are neatly disentangled based on their difference in orientation. A basic example is given in the top panel of Fig. 3.5.

Method The developed tracking method grows a full vasculature model starting from an initial set of seed points which are automatically detected around the optic nerve head. For each seed point the method iteratively expands a blood vessel model, and detects new seed points along the way. Each vessel model consists of a sequence of paired vessel edge points. These edge points are simultaneously traced through an orientation score based on the following principle. We consider a curve $t \mapsto \gamma(t) = (\mathbf{x}(t), \theta(t)) \in SE(2)$ to be *locally optimal* if it optimizes an objective function in the transversal 2D tangent plane

$$\mathcal{V}_{\gamma(t)} = \text{span}\{\mathcal{A}_2|_{\gamma(t)}, \mathcal{A}_3|_{\gamma(t)}\}.$$

Since the imaginary part of orientation scores directly encodes for edges (cf. Subsec. 2.1.5), it can be directly used as objective function in our transversal optimization scheme to find the most probable edge paths. This is the fundamental principle on which the developed iterative vessel tracking method is based, and it is illustrated in the bottom panel of Fig. 3.5. Also in view of extracting modes in completion fields this approach indeed leads to *globally optimal* curves, cf. Chapter 7 and (Bekkers *et al.*, 2014a, App. A)Duits & Van Almsick (2008).

Results In Chapter. 7 we validate the reliability of the width measurements provided by the vessel models using ground truth data, and show that the iterative tracking method performs excellently in comparison to other state of the art algorithms.

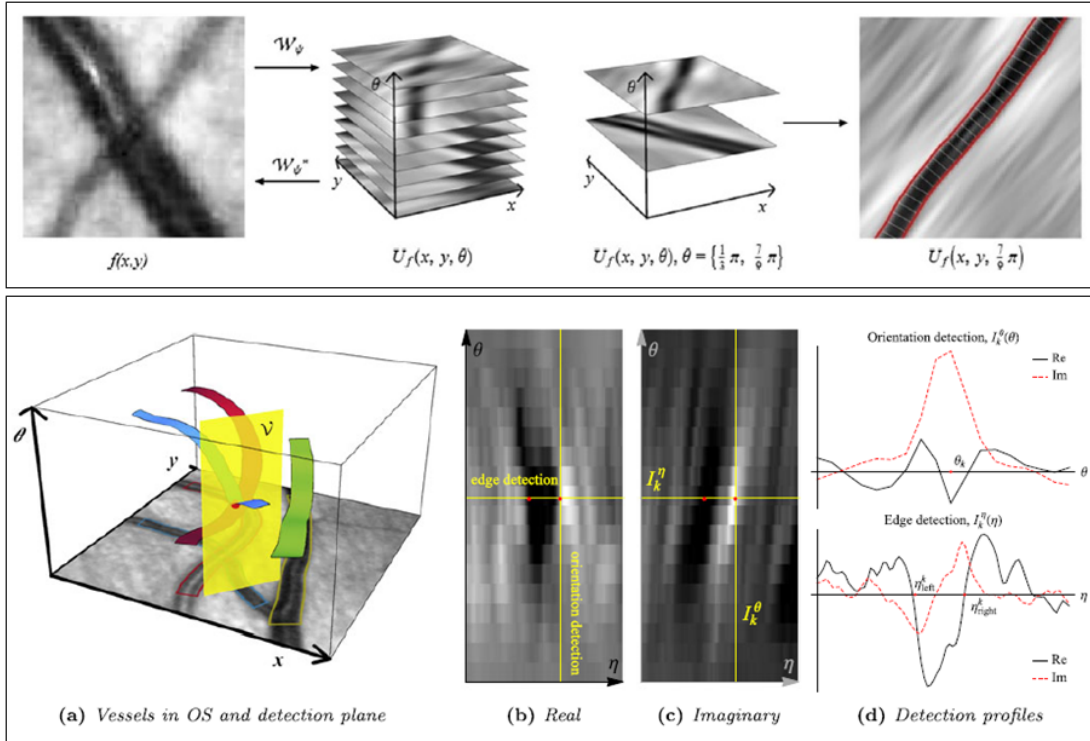


Figure 3.5: Illustration of the iterative vessel tracking method from Chapter 7. **Top panel:** An illustration of the orientation score transform at a crossing in which the two crossing vessels are disentangled, this allows for robust vessel tracking through crossings (right figure). **Bottom panel:** (a) Graphical representation of blood vessels in the orientation score. The real and imaginary part of the orientation score on the yellow plane V (perpendicular to the blood vessel) are represented in (b) and (c) respectively. In (c) the left and right edge of the blood vessel are expressed as black and white blobs respectively. The edge and orientation detection profiles are demonstrated in (d) .

3. THE DEVELOPED APPLICATIONS

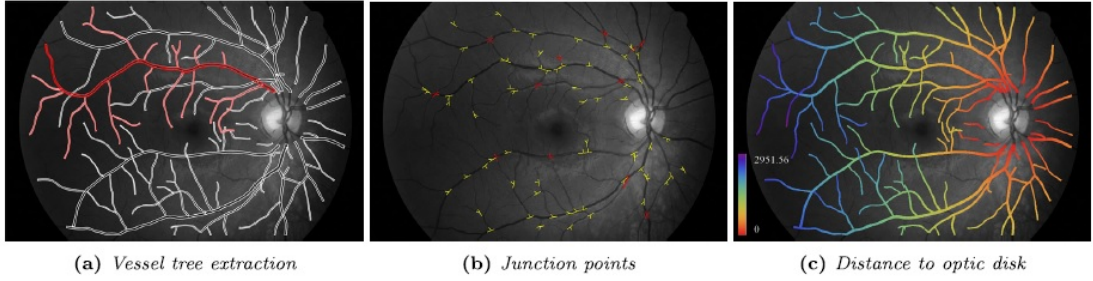


Figure 3.6: (a) The hierarchical structure of the generated vasculature models allow the segmentation and analysis of complete branches. (b) The automatic extraction of branching (yellow) and crossing points (red). (c) The distance to the optic disk; a feature that can easily be extracted because of the guaranteed connectedness of vessel segments in the generated vasculature models.

Validation of the topology of the models showed that our method constructs clean topological models of the vascular tree, i.e. they contain very few false positive vessels. An exemplary result of the tracking method is given in Fig. 3.6, in which we demonstrate some of the key features of the method: The method provides a full vascular tree segmentation including topological information (Fig. 3.6a); bifurcations and crossings can be readily obtained from the vascular model (Fig. 3.6b); and the method guarantees a connectedness of the vessels and allows therefore the computation of features such as the distance to the vessel tree source (Fig. 3.6c).

3.4 Vessel Tracking Part II & III (Ch. 8 & 9)

Motivation In the previous Subsec. 3.3 we discussed a *fully automated* method for the extraction of a full model of the vascular tree, which was based on *local* curve optimization. This method was based on the automatic tracking of a vessel, provided a given seed point. In some applications however one wants not only to compute a curve starting from a certain seed point, but also the guarantee that it ends at a certain location. This guarantee cannot be provided by the local curve optimization method. In this section we describe a novel method for the computation of the most optimal curve connecting a given source- and sink-point. Initially we assume that these points are manually provided and as such we consider the method a *semi-automatic* method for *globally optimal* curve computation.

The method proposed in Ch. 8 solves the variational problem of finding the shortest

3.4 Vessel Tracking Part II & III (Ch. 8 & 9)

horizontal curve $\gamma(t) \in SE(2)$ connecting two given points $g_0 = (\mathbf{x}_0, \theta_0), g_1 = (\mathbf{x}_1, \theta_1) \in SE(2)$ given a sub-Riemannian metric tensor $\mathcal{G}_0^{\xi, \mathcal{C}}|_{\gamma(t)}$ that depends on a smooth external cost function \mathcal{C} . This problem is formulated as follows

$$\gamma^* = \underset{\gamma \in S(g_0, g_1)}{\operatorname{argmin}} \int_0^T \sqrt{\mathcal{G}_0^{\xi, \mathcal{C}}|_{\gamma(t)}(\dot{\gamma}(t), \dot{\gamma}(t))} dt, \quad (3.5)$$

in which $S(g_0, g_1)$ denotes the set of smooth (infinitely differentiable) horizontal curves (c.f. Eq. (2.16)) that connect $g_0 = \gamma(0)$ with $g_1 = \gamma(T)$, and which have their tangent vectors contained in distribution Δ (c.f. Figs. 2.9 and 2.10). Here the metric $\mathcal{G}_0^{\xi, \mathcal{C}} : SE(2) \times \Delta \times \Delta \rightarrow \mathbb{R}^+$ measures the length of tangent vector $\dot{\gamma}(t)$, and the cost $\mathcal{C} : SE(2) \rightarrow \mathbb{R}^+$ (obtained from image data) penalizes the curve to move through areas with low curve saliency. More precisely,

$$\mathcal{G}_0^{\xi, \mathcal{C}}|_{\gamma(t)}(\dot{\gamma}(t), \dot{\gamma}(t)) = \mathcal{C}(\gamma(t))^2 \left(\xi^2 |\dot{x}(t) \cos \theta(t) + \dot{y}(t) \sin \theta(t)|^2 + |\dot{\theta}(t)|^2 \right),$$

in which parameter ξ balances the cost of moving in spatial direction relative to the change in orientation. The cost can for example be constructed by means of vesselness filtering (Subsec. 3.2 and Ch. 6) in order to encourage the curve to follow the vessels. Curves that solve (3.5) are called *sub-Riemannian geodesics*. So far we have already seen examples of sub-Riemannian geodesics in the Figures 2.5, 2.6 and 2.10.

The proposed method for finding shortest (data-adaptive) curves in $SE(2)$ using a sub-Riemannian geometry has two main advantages over conventional 2D methods:

1. *Shortcuts*. By solving the shortest path problem in $SE(2)$ short-cuts are less likely to occur due to the disentanglement of crossing lines in orientation scores. See for example the left part of Fig. 3.7.
2. *Smoothness*. By employing a sub-Riemannian geometry (cf. Subsec. 2.1.6 and Figs. 2.9 and 2.10) we obtain horizontal curves in $SE(2)$ whose projections to the plane are smooth¹. See for example the right part of Fig. 3.7. The amount of flexibility of the extracted curves can be controlled by a parameter μ that weights the amount of change in orientation (curvature) with respect to spatial movement.

¹While the curves are smooth in the lifted domain $SE(2)$, their projections to the plane may contain so-called cusp-points, which are sharp corners with infinite curvature. In the moving car analogy (Fig. 2.10), such points correspond to putting the car in reverse and continue a smooth path in the other direction. Our method provides means to detect and analyze the occurrence of such points and we will discuss this in great detail in Chapter 8.

3. THE DEVELOPED APPLICATIONS

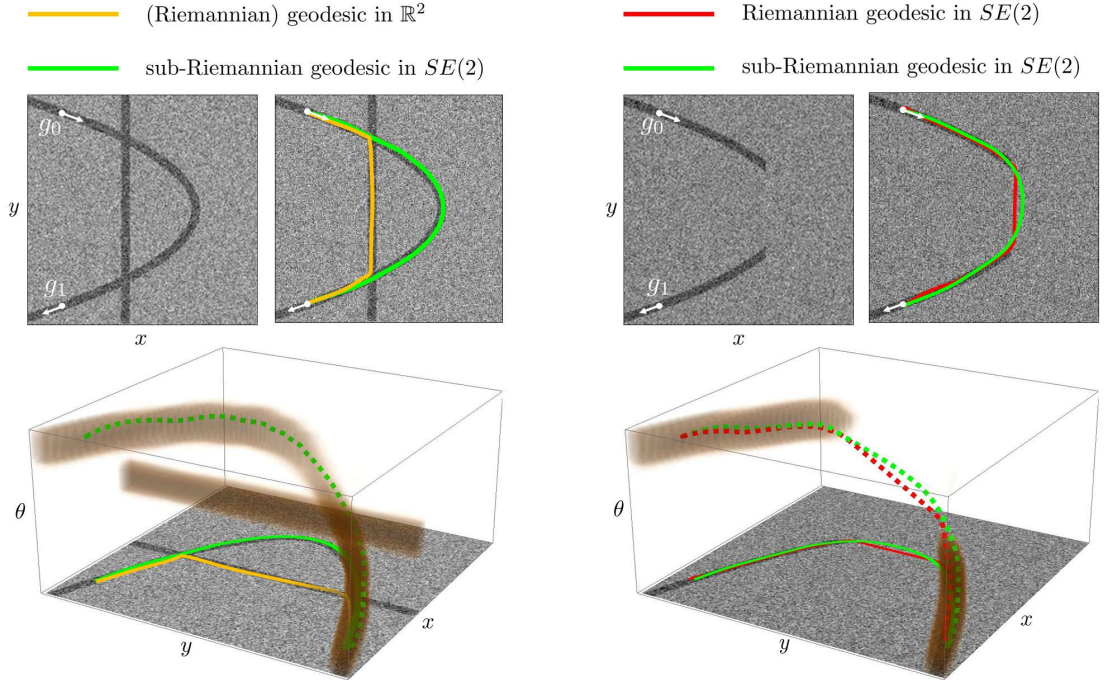


Figure 3.7: A comparison of geodesic curves obtained via (anisotropic) fast marching. **Left:** A comparison of the standard approach using a Riemannian 2D metric with the proposed method using a sub-Riemannian metric in $SE(2)$. The top figures show on the left the source g_0 and sink g_1 which are to be connected, and on the right the (spatial projections) of the computed curves. The bottom figure shows a volume rendering of the $SE(2)$ cost function used, and as a dashed line the obtained geodesic curve in $SE(2)$. This figure illustrates how the problem of short-cuts that occur at crossings are naturally dealt with by computing the geodesics in the extended space of positions and orientations. **Right:** A comparison of our proposed method using an (isotropic) Riemannian metric in $SE(2)$ with our proposed method using a sub-Riemannian metric in $SE(2)$. This figure illustrates how a sub-Riemannian metric in $SE(2)$ results in more natural paths (and completion of missing data) compared to using a (isotropic) Riemannian metric in $SE(2)$. Recall from Subsec. 2.1.6 and Figs. 2.9 and 2.10 that horizontal curves are the natural curves to consider in orientation scores, and that these curves live in a sub-Riemannian space.

3.4 Vessel Tracking Part II & III (Ch. 8 & 9)

While sub-Riemannian geodesics are well studied in literature Ben-Yosef & Ben-Shahar (2012); Boscain *et al.* (2014); Duits *et al.* (2013a); Hladky & Pauls (2009); Mashtakov *et al.* (2013); Moiseev & Sachkov (2010), no solutions have been provided for the case where one wants to compute data-adaptive sub-Riemannian geodesics. In this work we combine the knowledge from sub-Riemannian geodesic literature with numerical approaches for geodesic computation Jbabdi *et al.* (2008); Lin (2003); Mirebeau (2014); Péchaud *et al.* (2009a); Peyré *et al.* (2010); Sethian (1999); Tsitsiklis (1995), and provide two methods for computing data-adaptive sub-Riemannian geodesics: a PDE approach and a fast marching approach.

In Ch. 9 we then extend our method for computing data-adaptive geodesics in $SE(2)$, to data-adaptive geodesics in $SO(3)$: the group of 3D rotations acting transitively on the sphere S^2 . The main and first motivation for this extension comes from the fact that the retina is a spherical object and that it is therefore more natural to consider spherical image data and include the spherical object geometry in the tracking. The group structure of $SO(3)$ allows us to compute smooth (horizontal) curvature penalized shortest paths on the sphere S^2 .

The second motivation comes from models of the visual system of mammals. As mentioned by U. Boscain and F. Rossi Boscain & Rossi (2008) the problem of curvature penalized geodesics on S^2 can be considered an extension of a (flat) cortical based model for perceptual completion, as proposed by G. Citti, A. Sarti Citti & Sarti (2006) and J. Petitot Petitot (2003). Such an extension is of course again motivated by the fact that the retina is not flat.

The third motivation for the study of sub-Riemannian geodesics in $SO(3)$ is that in geometric control theory optimal synthesis for the sub-Riemannian problem on $SO(3)$ has not been achieved in the general case (not even for the case of uniform cost $C = 1$), despite many efforts by Berestovskii (2016, 1994); Beschastnyi & Sachkov (2014); Bonnard & Chyba (2014); Bonnard *et al.* (2014); Boscain & Rossi (2008); Calin *et al.* (2008); Chang *et al.* (2009). In Ch. 9 we will not provide optimal synthesis analytically, but instead we do provide a Hamilton-Jacobi-Bellman theory for computing globally optimal (data-driven) geodesics.

Method In Ch. 8 we develop the numerical tools for computing data-adaptive SR geodesics in $SE(2)$, i.e., solving problem (3.5). Such globally optimal curve optimization problems are typically solved by first constructing a distance map that assigns to every possible end-point the distance to the source. Then, each end-point defines a geodesic curve that can be obtained via steepest descent backtracking (via the Pon-

3. THE DEVELOPED APPLICATIONS

tryagin Maximum Principle) on the distance map. In our problem, the distance map is defined as follows

$$W(g) = \min_{\gamma(t) \in S(e,g)} \int_0^T \sqrt{\mathcal{G}^C|_{\gamma(t)}(\dot{\gamma}(t), \dot{\gamma}(t))} dt. \quad (3.6)$$

Each $W(g)$ gives thus the geodesic distance of point g to the origin e . We provide two numerical methods for computing distance map W :

- *PDE-method.* The sub-Riemannian distance map can be obtained as a viscosity solution of the sub-Riemannian eikonal equation

$$\begin{cases} \|\nabla^{sr} W(g)\|_{sr} = 1, & \text{if } g \neq e \\ W(e) = 0, \end{cases} \quad (3.7)$$

where for now we will write abstractly $\|\cdot\|_{sr}$ for the sub-Riemannian norm, and ∇_{sr} for the (manifold intrinsic) sub-Riemannian gradient, and give full details in Ch. 8. Initially this partial differential equation (PDE) is solved via a left-invariant finite-difference discretization of the PDE together with a suitable iterative upwind scheme, and updating of initial conditions.

- *Fast-marching.* In the second part of Ch. 8 the sub-Riemannian eikonal equation is solved using a fast-marching approach Sethian (1999). Classical fast-marching based eikonal solvers are not able to deal with the extreme (degenerate) anisotropy of our sub-Riemannian metric. We solve this numerical issue by considering a (anisotropic) Riemannian relaxation of the sub-Riemannian problem, and use a recent state-of-the-art fast-marching eikonal solver that is capable of dealing with large anisotropies Mirebeau (2014).

Results Both the iterative upwind scheme and the fast-marching approach to solving the sub-Riemannian eikonal equation (3.6) are compared to the exact solutions for the case $C = 1$ (i.e., for the case without data-adaptivity). We find a remarkable accuracy and convergence toward exact solutions, 1st Maxwell sets (i.e., the location where for the first time two distinct geodesics of equal length meet), and the cusp surface Boscain *et al.* (2014); Duits *et al.* (2013a).

In Chapter 8 we then also demonstrate the advantage of computing data-adaptive sub-Riemannian geodesics in $SE(2)$, in comparison with data-adaptive geodesics in \mathbb{R}^2 , and in comparison with data-adaptive Riemannian geodesics in $SE(2)$ (in which case

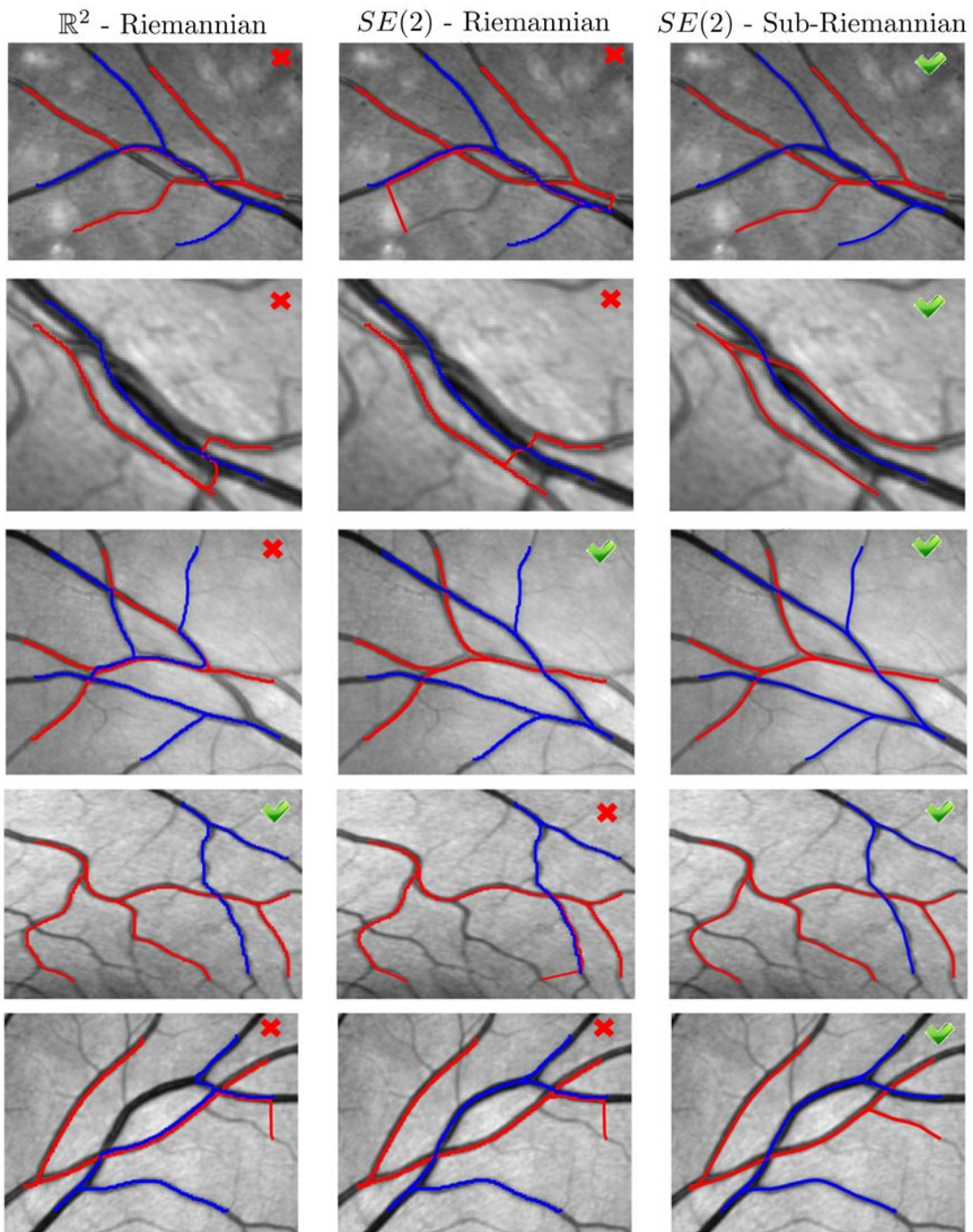


Figure 3.8: A comparison of geodesic tracking methods using (from left to right) an (isotropic) Riemannian metric in \mathbb{R}^2 , an (isotropic) Riemannian metric in $SE(2)$ and a sub-Riemannian metric in $SE(2)$.

3. THE DEVELOPED APPLICATIONS

we treat the domain $SE(2)$ as a flat 3D Euclidean domain), see respectively the left and right sub-figure in Fig. 3.7. On a test dataset consisting of retinal image patches we have annotated in total a challenging set of 184 pairs of begin- and end-points, and qualitatively and (semi-)quantitatively validated the performance of connecting these pairs using the three approaches for data-adaptive geodesic computation. A selection of visual results is given in Fig. 3.8. Out of 184 begin- and end-point pairs the 2D approach successfully connected 71.7%(132/184) pairs, the Riemannian $SE(2)$ approach successfully connected 82.6%(152/184) pairs, and the sub-Riemannian $SE(2)$ method successfully connected 92.4%(170/184). These results confirm the advantage of using geodesic curve computation in $SE(2)$ over \mathbb{R}^2 , and that of using a sub-Riemannian metric over Riemannian metric in $SE(2)$.

3.5 Artery-Vein Classification (Ch. 10)

Motivation We complete our tool set for automatic analysis of the retinal vasculature by providing a method for the automatic classification of blood vessels into arteries and veins. This is an important feature as the arteries and veins are both functionally and geometrically different and this is to be taken into account in the study of microvascular changes in relation to disease progression. For example, it is found that a higher blood pressure is associated with a narrowing of the arteries, whereas the veins remain relatively¹ constant in size Scheie (1953).

Method In Chapter 10 we present a novel method for artery/vein classification which is based on both local and contextual feature analysis of retinal vessels. Here we describe local features of each blood vessel in the form of transverse intensity profiles (see e.g. the lower profile in Fig. 3.5d). A naive Bayes classifier is then used to assign to each classifier a probability of it being an artery or a vein. Contextual information is provided by the crossings and bifurcations, which are obtained from the full (topological) vasculature models (Chapter 7, see e.g., Fig. 3.6). The local and contextual features are integrated into a non-submodular energy function which is optimized exactly using graph cuts, this is illustrated in Fig. 3.9.

Results The method is validated on a ground truth data set of 150 retinal fundus images. On this dataset the method achieves an accuracy of 88.0% for all vessels and 94.0% for the six arteries and six veins with highest caliber in the image. This

¹With very severe hypertension also the veins narrow Akman *et al.* (1998)).

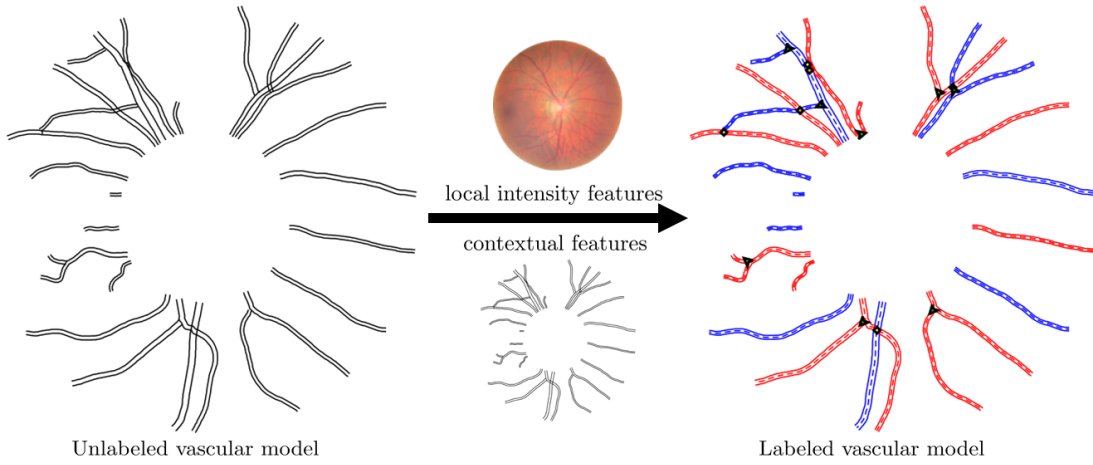


Figure 3.9: The developed artery/vein classification method relies on topological models of the retinal vasculature which are created by the tracking method of Ch. 7. An optimal labeling of the vasculature (based on both intensity features and contextual information) is obtained via a graph-cuts approach (cf. Ch. 10).

compares well to accuracy levels acquired with methods in literature that were validated on different data sets (87.6% Grisan & Ruggeri (2003), 85.5% Li *et al.* (2003), 88.3% Dashtbozorg *et al.* (2014), 88.8% Vazquez *et al.* (2010)).

3.6 Vessel Feature Analysis (Ch. 11 & 12)

Motivation As motivated in the introduction (Sec. 1.2), one of the main objectives of this thesis is to develop retinal image processing tools that can be used to assist large scale clinical research of the retinal microvasculature. I.e., the objective is to be able to define and compute quantitative biomarkers and study its relation to disease progression. In Chapters 5 to 10 we have developed the necessary tools that enable the automatic and semi-automatic analysis of the retinal blood vessels. In the final chapters of this thesis (Ch. 11 and Ch. 12) we develop new methods for the analysis of blood vessels and biomarker computation. In contrast to conventional approaches, however, our aim is to define vessel-based biomarkers by direct analysis of orientation scores instead of analysis of vessel segmentations/models obtained via extensive processing pipelines.

For example, vessel tortuosity descriptors are typically computed via an extensive pipeline (including manual interventions) of image pre-processing, segmentation, thinning and splitting of the vascular network, after which tortuosity values are computed

3. THE DEVELOPED APPLICATIONS

from the extracted vessel centerlines Cheung *et al.* (2012); Hart *et al.* (1999); Kalitzeos *et al.* (2013); Wilson *et al.* (2008). In such pipelines, errors introduced in each processing step may accumulate, and information might get lost along the way. This might eventually result in unreliable biomarkers. As an alternative, we propose a reduced pipeline that does not rely on explicit segmentation of the blood vessels, but instead computes tortuosity features directly from retinal image data.

The approach that we take is via the construction of feature maps $f_{feature} : \mathbb{R}^2 \rightarrow \mathbb{R}$ that assign to each pixel a value of the feature of interest (e.g. curvature) and corresponding feature confidence maps $c_{feature} : \mathbb{R}^2 \rightarrow \mathbb{R}^+$ that assign to each pixel a confidence on how reliably the feature measurement is performed. Both maps can then be used to define global feature measurements, e.g., the weighted average of the feature values is then given by

$$\begin{aligned}\mu_{feature} &= \frac{1}{c_{feature}^{total}} \int f_{feature}(\mathbf{x}) c_{feature}(\mathbf{x}) d\mathbf{x}, \quad \text{with} \\ c_{feature}^{total} &= \int c_{feature}(\mathbf{x}) d\mathbf{x}.\end{aligned}$$

In Chapter 11 we have developed pixel-wise feature measurement methods for the following features: vessel curvature, vessel caliber and vessel artery-vein class, see Fig. 3.10. In the next paragraphs we briefly summarize how this is made possible by direct analysis of orientation scores.

Method *Vessel Curvature.* The curvature extraction method proposed in Chapter 11 is based on theory of best exponential curve fits in orientation scores. Here the 2D image is first lifted to an orientation score. In the extended domain of positions and orientations we then study so-called exponential curves, whose curvature values (of its planar projections) are constant. Such exponential curves are circular spirals in the domain $SE(2)$, see Subsec. 2.1.6 and Fig. 2.9. By locally fitting exponential curves to data in orientation scores, we are able to assign to each location a curvature and measurement-confidence value, which we use to define global tortuosity measures. Additionally, we improve the accuracy of best-exponential curve fits by proposing a novel refinement procedure, resulting in more accurate curvature estimations.

Vessel Caliber A property of blood vessels is that both the left and right edge run parallel to each other, and that (the spatial derivative of) one edge has a different sign than the opposite edge. In this application of pixel-wise vessel caliber measurements we make use of two convenient properties of orientation scores:

1. The imaginary part of the orientation score encodes for (oriented) edges. It allows

3.6 Vessel Feature Analysis (Ch. 11 & 12)

us to detect vessel edges in the orientation score without having to calculate first-order derivatives perpendicular to the vessel orientation.

2. In orientation score we can make use of the group product on $SE(2)$ to shift data around. E.g., we can move every voxel in the score to the right by an amount of r using the right-regular representation (Subsec. 2.3):

$$(\mathcal{R}_{g_\eta(r)} U)(g) = U(g g_\eta(r)) = U((x, y) + \mathbf{R}_\theta(0, r), \theta),$$

with $g = ((x, y), \theta)$ and $g_\eta(r) = ((0, r), 0)$.

For vessel width measurements in orientation scores we can then use the right-regular representation \mathcal{R}_{g_r} to shift the right edge responses to the left (left-shift), and the left-edge responses to the right (right-shift) by a certain value for r until the edge responses overlap. We then define a basic tubularity measure (a likelihood of finding two opposite edges at distance $2r$) as the *product* of the left- and right-shifted edge responses. An example result is given in Fig. 3.10 where at the centerline of the blood vessels we have a maximal response of the tubularity measure for the value of r that corresponds to the actual vessel radius.

Artery Vein Labeling In Chapter 10 we describe a method for the labeling of arteries and veins in vascular models. A key ingredient of this method is the local feature analysis that uses a Bayesian approach to assign to each transversal intensity profile of the blood vessel a likelihood of it being an artery or a vein. In this chapter we will do the same, however, instead of relying on precomputed vessel models to define the transversal intensity profiles we assign to each pixel in the image the most likely orientation and corresponding radius by looking at which combination r and θ gave maximal response in the tubularity measure. This allows us to construct transversal intensity profiles for each pixel in the image, and use the Bayes classifier of Chapter 10 to assign an artery probability to each pixel.

Results In Ch. 11 we show that curvature values can be accurately computed by fitting exponential curves to data in orientation scores. There we also show via repeatability analysis (on repeated patient measurements) that our proposed method for computing global tortuosity scores was more stable than conventional approaches that rely on a segmentation-based pipeline. Finally, we used the curvature based biomarkers obtained via the exponential curve fits in $SE(2)$ in several clinical studies. Our clinical findings are summarized in the *our findings* paragraphs of Sec. 1.3.

3. THE DEVELOPED APPLICATIONS

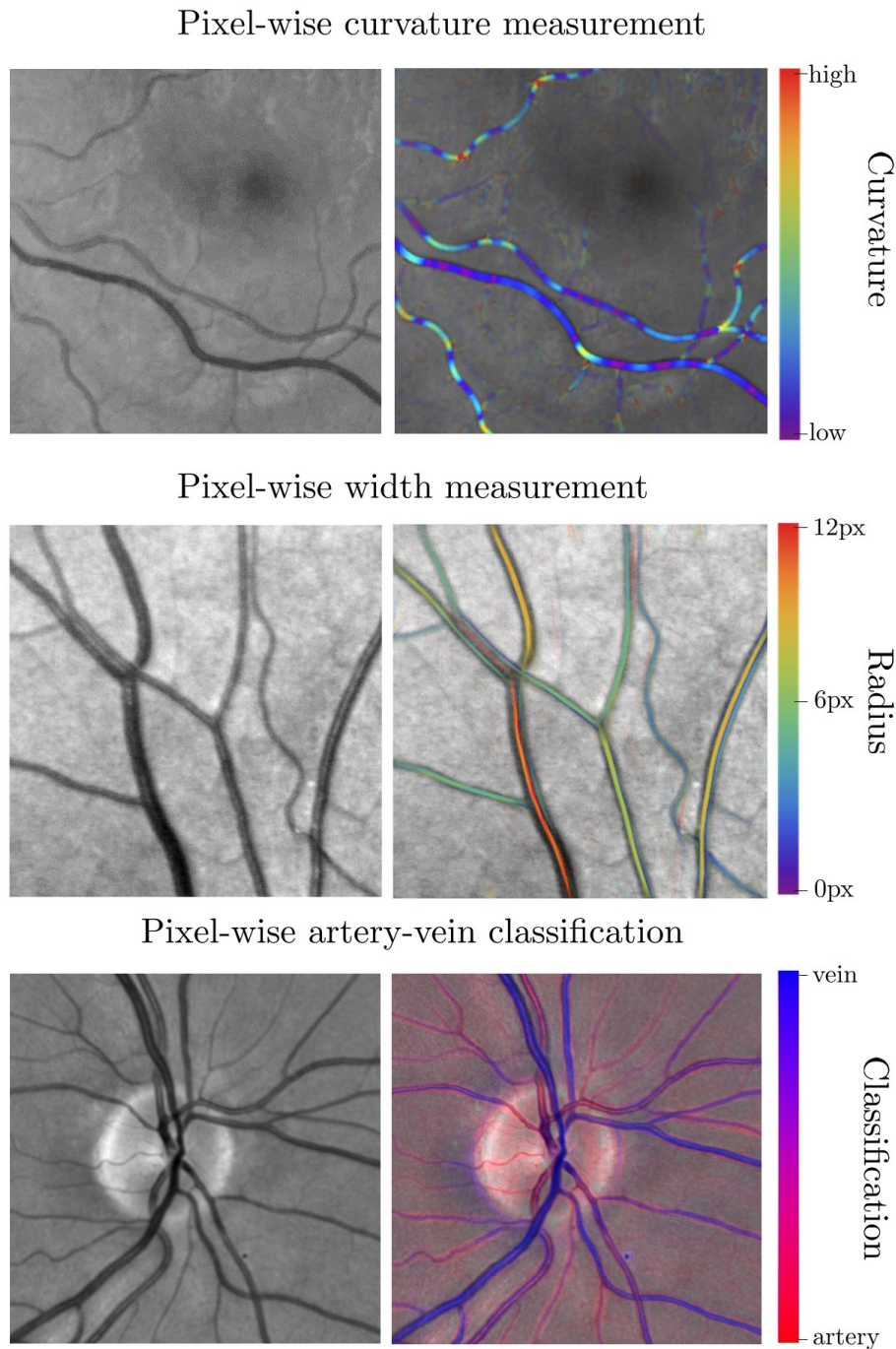


Figure 3.10: Illustration of the developed pixel-wise feature analysis algorithms. From top to bottom: Pixel-wise curvature measurements, pixel-wise vessel width measurements and pixel-wise artery-vein classification. Left: the input image. Right: a color-coded overlay of the computed features.

3.6 Vessel Feature Analysis (Ch. 11 & 12)

In the final chapter of this thesis (Ch. 12) we propose a new tubularity measure (Sec. 12.2) and have shown that it can be used to compute new pixel-wise vessel measurements such as vessel width and artery/vein labeling. There we explore new types of retinal image analyses (and extensions of the methods developed in this thesis) that are made possible by considering the analysis of tubularity measures and the induces feature maps. Both in vessel tracking and in connectivity analyses the tools presented in this chapter can be most helpful. In Ch. 11 the clinical analysis showed that it is relevant to consider the analysis of vessel geometry for arteries and veins separately. Therefore, we conjecture that the proposed pixel-wise artery/vein labeling can be of great interest in further clinical studies, as it allows to compute a wide range of new (artery/vein specific) biomarkers that can now be computed fully automatically.

Part II

Differential Geometrical Tools

Chapter 4

Sub-Riemannian Geometry in the Orientation Score Domain

4. SUB-RIEMANNIAN GEOMETRY IN ORIENTATION SCORES

In the previous chapters we motivated why we focus on retinal vascular research (Chapter 1) and what kind of mathematical tools are used (Chapter 2) in the applications developed in this thesis (Chapter 3). In Chapter 2 the focus was on an intuitive description and explanation of the methodologies used in this thesis, namely that of *sub-Riemannian* geometry in $SE(2)$. In this chapter we aim to give precise definitions of the mathematical tools that are used in the developed retinal image analysis applications (Chapters 5 to 12).

4.1 Riemannian Geometry

A manifold is a (topological) set that is locally diffeomorphic to \mathbb{R}^n . A Riemannian manifold is a smooth manifold M with at each element $m \in M$ an inner product $\mathcal{G}|_m$ on the tangent space $T_m(M)$ defined (see Subsec. 2.2.2 for a definition of a tangent space). Let $\gamma(t)$ be a curve in M , with $\gamma(0) = m$. The length of the tangent vector $\dot{\gamma}(0)$ is then given by $\sqrt{\mathcal{G}|_m(\dot{\gamma}(0), \dot{\gamma}(0))}$. The length of arbitrary tangent vectors $\dot{\gamma}(t)$ is given by $\sqrt{\mathcal{G}|_{\gamma(t)}(\dot{\gamma}(t), \dot{\gamma}(t))}$. The Riemannian distance between any two points $m_1, m_2 \in M$ is given by

$$d(m_1, m_2) = \inf_{\begin{array}{l} \gamma \in C^\infty([0, 1], M), \\ \gamma(0) = m_1, \\ \gamma(1) = m_2 \end{array}} \int_0^1 \sqrt{\mathcal{G}|_{\gamma(\tau)}(\dot{\gamma}(\tau), \dot{\gamma}(\tau))} d\tau. \quad (4.1)$$

Distances between two points on a manifold are thus defined as the length of the shortest possible curve connecting the two points, where the total length is measured using all inner products $\mathcal{G}|_{\gamma(t)}$ along the curve γ . A minimizing **geodesic** is defined as the curve minimizing the total curve length measured by $\mathcal{G}|_{\gamma(t)}$ and has length $d(m_1, m_2)$.

The inner product $\mathcal{G}|_m$ is a (0,2)-tensor (it takes two tangent vectors and returns a scalar) and is generally called the **metric tensor**. In the case of Riemannian geometry, the metric tensor takes the following form:

$$\mathcal{G}|_m(\dot{\gamma}(t), \dot{\alpha}(t)) = \sum_{i,j=1}^{\dim(M)} \dot{\gamma}^i(t) \dot{\alpha}^j(t) g_{ij}(m), \quad (4.2)$$

in which $m = \gamma(t) \in M$ and $\dot{\gamma}(t), \dot{\alpha}(t) \in T_{\gamma(t)}(M)$, with γ^i and α^i the tangent vector components of $\dot{\gamma}$ and $\dot{\alpha}$ expressed in some n -dimensional bases of $T_m(M)$. The elements of the metric tensor $g_{ij}(m)$ form a positive definite symmetric matrix which varies smoothly with $m \in M$. We will refer to a distance function d of the form (4.1) as a

4.2 The Lie Group $SE(2)$ and its Tangent Bundle $T(SE(2))$

metric on manifold M , and the tensor $\mathcal{G}|_m$ used to compute such distances the **metric tensor**.

Example 3. Euclidean geometry is a special case of Riemannian geometry in which case $M = \mathbb{R}^n$, the tangent space at each m is spanned by the basis $\{\partial_{x^i}\}_{i=1}^2$ with $\partial_{x^1} = \partial_x$ and $\partial_{x^2} = \partial_y$, and the metric tensor is given by the identity matrix, i.e.,

$$g_{ij}(m) = \mathcal{G}|_m(\partial_{x^i}, \partial_{x^j}) = \delta_{ij} = \begin{cases} 1 & \text{if } i = j \\ 0 & \text{if } i \neq j \end{cases}.$$

The Euclidean distance between two elements $\mathbf{x}, \mathbf{y} \in \mathbb{R}^n$ is then given by

$$d(\mathbf{x}, \mathbf{y}) = \|\mathbf{x} - \mathbf{y}\|,$$

and its geodesics are straight lines given by $\gamma(t) = \mathbf{x}(t-1) - t\mathbf{y}$, with $0 \leq t \leq 1$.

4.2 The Lie Group $SE(2)$ and its Tangent Bundle $T(SE(2))$

This thesis is primarily concerned with sub-Riemannian geometry on the manifold $M = SE(2)$ (defined in Subsecs. 4.3.1), and a Riemannian approximation hereof (defined in Subsecs. 4.3.2). In Chapter 2 we already introduced the Lie group $SE(2)$, first conceptually in Sec. 2.1, then in more detail in Sec. 2.3. For the sake of convenience, we first briefly repeat some of the fundamental definitions of the Lie group $SE(2)$ and its tangent bundle $T(SE(2))$ in respectively Subsec. 4.2.1 and Subsec. 4.2.2, before introducing the differential geometrical tools that rely on these definitions.

4.2.1 The Lie Group $SE(2)$

Recall that the Lie group $SE(2)$ is the three dimensional manifold consisting of the coupled space $\mathbb{R}^2 \times S^1$ of positions and orientations (cf. Sec. 2.3). Its group elements are given by

$$g = (\mathbf{x}, \theta),$$

with $\mathbf{x} = (x, y) \in \mathbb{R}^2$ and $\theta \in S^1$, with S^1 the space of rotations. The group product is given by

$$g \cdot g' = (\mathbf{x}, \theta) \cdot (\mathbf{x}', \theta') = (\mathbf{R}_\theta \mathbf{x}' + \mathbf{x}, \theta + \theta').$$

Recall Sec. 2.3 for more details on the domain of the Lie group $SE(2)$.

4. SUB-RIEMANNIAN GEOMETRY IN ORIENTATION SCORES

4.2.2 The Tangent Bundle $T(SE(2))$

Recall from Sec. 2.3 that the tangent space $T_g(SE(2))$ at each element $g \in SE(2)$ is spanned by a left-invariant basis

$$T_g(SE(2)) = \text{span}\{\mathcal{A}_1|_g, \mathcal{A}_2|_g, \mathcal{A}_3|_g\},$$

where $\mathcal{A}_i|_g$ denotes the vector field \mathcal{A}_i restricted to group element g . The left-invariant vector fields \mathcal{A}_i are defined by

$$\begin{aligned} \mathcal{A}_1|_{(x,y,\theta)} &:= \cos \theta \partial_x|_{(x,y,\theta)} + \sin \theta \partial_y|_{(x,y,\theta)}, \\ \mathcal{A}_2|_{(x,y,\theta)} &:= -\sin \theta \partial_x|_{(x,y,\theta)} + \cos \theta \partial_y|_{(x,y,\theta)}, \\ \mathcal{A}_3|_{(x,y,\theta)} &:= \partial_\theta|_{(x,y,\theta)}. \end{aligned}$$

For more details on the left-invariant vector fields see Subsecs. 2.2.2 and 2.3.3. Each element in $g \in SE(2)$ is thus associated with a tangent space $T_g(SE(2))$. The collection of all tangent spaces $T_g(SE(2))$ forms a tangent bundle

$$T(SE(2)) = \{T_g(SE(2))\}_{g \in SE(2)}. \quad (4.3)$$

Remark 6. Recall from Subsec. 2.2.2 and Remark 5 that the vector fields described in Eq. (2.42) can be considered as differential operators acting on functions on the group $SE(2)$.

4.2.3 Horizontal Curves and the Sub-Bundle Δ

Since all tangent vectors are spanned by a left-invariant basis, tangents $\dot{\gamma}(t) \in T_{\gamma(t)}(SE(2))$ along smooth curves $t \mapsto \gamma(t) = (x(t), y(t), \theta(t)) \in SE(2)$ can be expressed as

$$\dot{\gamma}(t) = \sum_{i=1}^3 u^i(t) \mathcal{A}_i|_{\gamma(t)}, \quad (4.4)$$

where the contravariant components $u^i(t)$ of the tangents (velocities) can be considered as control variables¹. Note that controls depend on the choice of parametrization. Throughout this thesis we use the following parameters for curves in $SE(2)$

- $t \in [0, T]$, metric induced \mathcal{G} -arclength parameterization, such that $T = d(\gamma(0), \gamma(T))$ (see Eq. (4.1)).

¹In the formulation of optimal control problems one usually speaks of state variables (e.g. $(x(t), y(t), \theta(t))$) and control variables (e.g. $(u^1(t), u^2(t), u^3(t))$).

4.3 The Left-Invariant Metric Tensor of Interest

- $\tau \in [0, 1]$, rescaled \mathcal{G} -arclength parameterization.
- $s \in [0, \ell]$, *spatial* arclength parameterization for curves in $SE(2)$ that can be parameterized by such a parameter (e.g. SR-geodesics whose spatial projections do not have cusps).

The default is \mathcal{G} -arclength parametrization (by t) in $SE(2)$.

In this thesis, however, we will be mainly concerned with horizontal curves, which have their tangent vectors contained within a sub-bundle Δ of the full tangent bundle $T(SE(2))$. As seen in Sec. 2.1.6 we can lift planar curves $\gamma_{2D}(t) = (x(t), y(t))$ in \mathbb{R}^2 to curves $\gamma(t) = (x(t), y(t), \theta(t))$ in $SE(2)$, simply by taking the orientation of the 2D tangent vectors as the third coordinate:

$$\theta(t) = \arg\{\dot{x}(t) + i\dot{y}(t)\}.$$

Such naturally lifted curves γ are horizontal curves, and their tangent vector components are contained within a sub-bundle Δ defined by

$$\Delta := \text{span}\{\mathcal{A}_1, \mathcal{A}_2\}. \quad (4.5)$$

Accordingly, the tangent vectors $\dot{\gamma}(t) \in \Delta$ can be expressed with just two of the three control variables u^i (as $u^2 = 0$):

$$\dot{\gamma}(t) = \sum_{i \in \{1, 3\}} u^i(t) \mathcal{A}_i|_{\gamma(t)}. \quad (4.6)$$

4.3 The Left-Invariant Metric Tensor of Interest

4.3.1 The sub-Riemannian Manifold

The sub-Riemannian manifold is defined by the triplet $(SE(2), \Delta, \mathcal{G}_0^{\xi, \mathcal{C}})$, with domain $SE(2)$, tangent bundle Δ (cf. Eq. (4.5)), and with the sub-Riemannian metric tensor $\mathcal{G}_0^{\xi, \mathcal{C}} : SE(2) \times \Delta \times \Delta \rightarrow \mathbb{R}$ given by

$$\mathcal{G}_0^{\xi, \mathcal{C}}|_{\gamma(t)}(\dot{\gamma}(t), \dot{\gamma}(t)) = \mathcal{C}(\gamma(t))^2 \left(\xi^2 |\dot{x}(t) \cos \theta(t) + \dot{y}(t) \sin \theta(t)|^2 + |\dot{\theta}(t)|^2 \right), \quad (4.7)$$

with $\gamma : \mathbb{R} \rightarrow SE(2)$ a smooth horizontal curve on $\mathbb{R}^2 \rtimes S^1$, with $\mathcal{C} : SE(2) \rightarrow [\delta, 1]$ a given external smooth cost which is bounded from below by $\delta > 0$. Since orientation and spatial direction have different physical units, a conversion factor is needed. This stiffness parameter ξ has unit 1/length. It determines the shape of both *exponential*

4. SUB-RIEMANNIAN GEOMETRY IN ORIENTATION SCORES

curves and the geodesics in $SE(2)$. An increase of ξ makes it cheaper to bend curves, whereas a decrease of ξ makes it cheaper to stretch curves. Mathematically, ξ appears as the only free parameter in the (sub-)Riemannian metric on $SE(2)$.

Remark 7. *Intuitively, a horizontal curve (cf. Fig. 2.9) can be seen as a lifted trajectory of a (Reeds-Shepp) car Montgomery (2006); Sachkov (2011). The stiffness parameter ξ puts a relative costs on hitting the gas (i.e. moving in \mathcal{A}_1 -direction) and turning the wheel (i.e. moving in \mathcal{A}_3 -direction). The external cost included in (4.7) weights the metric tensor, and $\frac{1}{C}$ can be interpreted as the speed of the car. The connectivity property, i.e. any two group elements can be connected by a horizontal curve, reflects the intuitive fact that in an empty plane, a car can be parked in any position and orientation.*

4.3.2 A Riemannian Approximation of the Sub-Riemannian Manifold

The sub-Riemannian metric tensor can be approximated by an anisotropic Riemannian metric tensor $\mathcal{G}_\epsilon^{\xi,C} : SE(2) \times T(SE(2)) \times T(SE(2)) \rightarrow \mathbb{R}$ given by

$$\mathcal{G}_\epsilon^{\xi,C}\Big|_{\gamma(t)}(\dot{\gamma}(t), \dot{\gamma}(t)) = \mathcal{G}_0^{\xi,C}\Big|_{\gamma(t)}(\dot{\gamma}(t), \dot{\gamma}(t)) + C(\gamma(t))^2 \epsilon^{-2} \xi^2 |\dot{x}(t) \sin \theta(t) + \dot{y}(t) \cos \theta(t)|^2, \quad (4.8)$$

in which the additional term penalizes the non-horizontal part of the tangent vectors $\dot{\gamma}(t)$, and ϵ controls the amount of anisotropy between \mathcal{A}_2 and Δ . This definition bridges the sub-Riemannian case, obtained at the limit $\epsilon \downarrow 0$, with the full Riemannian metric tensor when $\epsilon = 1$ (isotropic in the spatial directions \mathcal{A}_1 and \mathcal{A}_2), see for example Fig. 4.1. This is perhaps better seen when we express the tangent vectors $\dot{\gamma}(t)$ in terms of control variables $u^i(t)$ (cf. Eq. (4.4)) the anisotropic Riemannian metric tensor can be expressed as follows:

$$\mathcal{G}_\epsilon^{\xi,C}\Big|_{\gamma(t)}(\dot{\gamma}(t), \dot{\gamma}(t)) = C(\gamma(t))^2 (\xi^2 |u^1(t)|^2 + \epsilon^{-2} \xi^2 |u^2(t)|^2 + |u^3(t)|^2). \quad (4.9)$$

When $\epsilon \downarrow 0$, tangent vector components $u^2(t)$ are infinitely punished, and as a result the minimizing geodesics in

$$d_\epsilon(g_1, g_2) = \inf_{\substack{\gamma \in C^\infty([0, 1], SE(2)), \\ \gamma(0) = g_1, \\ \gamma(1) = g_2}} \int_0^1 \sqrt{\mathcal{G}_\epsilon^{\xi,C}\Big|_{\gamma(\tau)}(\dot{\gamma}(\tau), \dot{\gamma}(\tau))} d\tau, \quad (4.10)$$

4.3 The Left-Invariant Metric Tensor of Interest

will have $u^2(t) = 0$, and they will be the sub-Riemannian geodesics.

While the previous paragraph does not formally prove that the limit $\epsilon \downarrow 0$ is valid, and that it results in sub-Riemannian geodesics, it can be formally shown via a tangential approach to the one in (Chen, 2016, App. A). There Euler elastica curves are approximated using a numerical scheme (fast marching) that relies on a Finsler metric which contains a penalization parameter similar to our ϵ . In Chapter 8 we will go into extensive detail on the computation of sub-Riemannian geodesics using several methods, and show that with the anisotropic Riemannian approximation we can compute near to exact sub-Riemannian geodesics.

4.3.2.1 Matrix Representation in the Cartesian Frame

The anisotropic approximation of the sub-Riemannian metric tensor (Eq. 4.8) can be described in the standard Cartesian frame using a symmetric positive definite matrix \mathbf{M}_ϵ . This matrix \mathbf{M}_ϵ can be obtained by a basis transformation from the left-invariant frame $\{\mathcal{A}_1, \mathcal{A}_2, \mathcal{A}_3\}$ as follows:

$$\mathbf{M}_\epsilon(\gamma(t)) = \begin{pmatrix} \cos \theta(t) & -\sin \theta(t) & 0 \\ \sin \theta(t) & \cos \theta(t) & 0 \\ 0 & 0 & 1 \end{pmatrix} \begin{pmatrix} \xi^2 & 0 & 0 \\ 0 & \xi^2 \epsilon^{-2} & 0 \\ 0 & 0 & 1 \end{pmatrix} \begin{pmatrix} \cos \theta(t) & -\sin \theta(t) & 0 \\ \sin \theta(t) & \cos \theta(t) & 0 \\ 0 & 0 & 1 \end{pmatrix}^T. \quad (4.11)$$

Here the diagonal matrix in the middle encodes the anisotropy between the \mathcal{A}_i directions, while the other 2 rotation matrices are the basis transformation. The metric tensor can then be written as

$$\mathcal{G}_\epsilon^{\xi, \mathcal{C}} \Big|_{\gamma(t)} (\dot{\gamma}(t), \dot{\gamma}(t)) = \mathcal{C}(\gamma(t))^2 \dot{\gamma}(t)^T \mathbf{M}_\epsilon(\gamma(t)) \dot{\gamma}(t),$$

with $\dot{\gamma}(t) = (\dot{x}(t), \dot{y}(t), \dot{\theta}(t))$ expressed in the fixed frame. Each matrix $\mathbf{M}(g)$ is symmetric positive definite, and can be visualized as an ellipsoid (Fig. 4.1). Such matrix representation is a convenient form to use in numerical approaches for computing geodesics. In Ch. 8 for example we use this matrix representation to compute (approximate) sub-Riemannian geodesics using a Fast Marching solver that can deal with large anisotropies ($\epsilon \ll 1$).

4. SUB-RIEMANNIAN GEOMETRY IN ORIENTATION SCORES

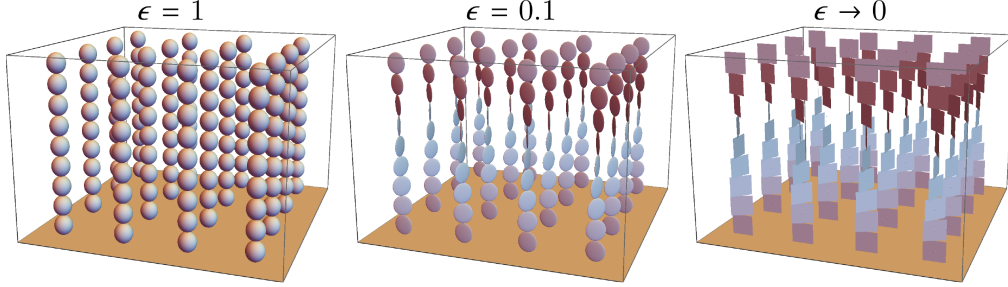


Figure 4.1: Each ellipsoid represents the Tissot's indicatrix of the metric \mathcal{G}_ϵ^ξ at different elements $g \in SE(2)$ (for the case $\xi = 1$). The parameter ϵ in Eqs. (4.8) and (4.9) bridges the Riemannian case with the sub-Riemannian one. When $\epsilon = 1$ each direction has the same cost. At the limit $\epsilon \downarrow 0$, the direction A_2 has infinite cost and the distribution Δ appears.

4.4 The Co-Tangent Bundle $T^*(SE(2))$ and Differential Forms

Co-vectors are elements of the co-tangent spaces $T_g^*(SE(2)) = \text{span}\{\omega^1|_g, \omega^2|_g, \omega^3|_g\}$. They are (continuous) linear functionals on the tangent space. The dual basis $\{\omega^i\}$ is defined via the Kronecker product

$$\langle \omega^i, \mathcal{A}_j \rangle = \delta_j^i, \quad \text{with} \quad \delta_j^i = \begin{cases} 1 & \text{if } i = j \\ 0 & \text{if } i \neq j \end{cases}, \quad (4.12)$$

which gives

$$\begin{aligned} \omega^1 &= \cos \theta dx + \sin \theta dy, \\ \omega^2 &= -\sin \theta dx + \cos \theta dy, \\ \omega^3 &= d\theta, \end{aligned} \quad (4.13)$$

Example 4. In the \mathbb{R}^2 case, where tangent spaces are spanned by the basis $\{\partial_{x^i}\}_{i=1}^2$ with

$$\partial_{x^1} = \partial_x, \quad \partial_{x^2} = \partial_y,$$

the basis of co-tangent spaces is defined via $\langle \omega^i, \partial_{x^j} \rangle = \delta_j^i$ as

$$\omega^1 = dx, \quad \omega^2 = dy. \quad (4.14)$$

In 2D image analysis the most commonly known co-vector is the derivative operator acting on images $f \in \mathbb{L}_2(\mathbb{R}^2)$, given by

$$df = (\partial_x f)dx + (\partial_y f)dy.$$

4.4 The Co-Tangent Bundle $T^*(SE(2))$ and Differential Forms

For a directional derivative at m in the direction $v(m)$ we have

$$\langle df(m), v(m) \rangle := df|_m(v(m))$$

where brackets just denote functional evaluation.

Now given the metric tensor $\mathcal{G}|_m$ at $m \in M$ one defines the gradient $\nabla f(m)$ uniquely by:

$$\langle df(m), v(m) \rangle = \mathcal{G}|_m(\nabla f(m), v(m)) \text{ for all } v(m) \in T_m(M).$$

In view of the famous Riesz representation theorem, we say that the gradient of f at m (which is a tangent vector in $T_m(M)$) equals the Riesz representative of the derivative of f at m (which is a covector in $T_m^*(M)$).

Now it is common to identify the metric tensor with the corresponding linear map from tangent bundle to cotangent bundle, in which case one typically writes

$$\nabla f(m) = G_m^{-1} df(m).$$

This is also referred to as the ‘manifold intrinsic gradient’, as it is the gradient induced by the metric tensor (and not the gradient w.r.t. a flat metric in some flat embedding space).

Our Riemannian metric tensor $\mathcal{G}_\epsilon^{\xi, \mathcal{C}}$ on $SE(2)$, given in (4.8), is expressed in the basis of left-invariant vector fields and an expression of the derivative of U at $g \in SE(2)$ is given by

$$dU(g) = \sum_{i=1}^3 (\mathcal{A}_i|_g U) \omega^i|_g, \quad (4.15)$$

whereas the gradient is defined as

$$\nabla^\epsilon U(g) = \mathcal{G}_\epsilon^{\xi, \mathcal{C}}{}^{-1}|_g dU(g) = \sum_{i=1}^3 \xi_i^{-2} \mathcal{C}(g)^{-2} (\mathcal{A}_i|_g U) \omega^i|_g \quad (4.16)$$

with $\xi_1 = \xi$, $\xi_2 = \xi/\epsilon$ and $\xi_3 = 1$. The sub-Riemannian gradient, based on the sub-Riemannian metric tensor \mathcal{G}_0^ξ given in (4.7), is defined as

$$\nabla^{SR} U(g) := \nabla^0 U(g) = \lim_{\epsilon \rightarrow 0} \nabla^\epsilon U(g) = \sum_{i \in \{1, 3\}} \xi_i^{-2} \mathcal{C}(g)^{-2} (\mathcal{A}_i|_g U) \omega^i|_g. \quad (4.17)$$

Remark 8. When expressing the derivative in the moving dual frame one must keep in mind that the moving dual frame is not an exact frame. An exact differential k -form is a differential form that is the exterior derivative of another differential $(k-1)$ -form. In the \mathbb{R}^2 case the co-vectors ω^i (see Example 4) are exact 1-forms, obtained by taking

4. SUB-RIEMANNIAN GEOMETRY IN ORIENTATION SCORES

the exterior derivative of a 0-form, i.e. a smooth differentiable function on \mathbb{R}^2 . Exact forms, such as the ones in (4.14), are also closed since

$$d\omega^1 = ddx = 0.$$

In $SE(2)$ this is not the case for the local dual frame $\{\omega^i\}_{i=1}^3$ defined in (4.13). For example

$$\begin{aligned} d\omega^1 &= d(\cos \theta dx + \sin \theta dy) \\ &= -\sin \theta d\theta \wedge dx + \cos \theta d\theta \wedge dy \\ &= d\theta \wedge (-\sin \theta dx + \cos \theta dy) \\ &= c_{23}^1 (\omega^2 \wedge \omega^3) \neq 0 \end{aligned}$$

This shows that the left-invariant coframe varies along the Lie group and in general (on Lie groups) we have the structural formulas of Cartan:

$$d\omega^k = \sum_{i,j} \frac{1}{2} c_{ij}^k (\omega^i \wedge \omega^j). \quad (4.18)$$

4.5 Short \neq Straight: the Left Cartan Connection

4.5.1 Connections

With the left-invariant vector fields and covector fields defined, we can now define derivatives on images and orientation scores. For example we have seen (Example 4) that we can use left-invariant derivatives to compute the derivative of an image or an orientation score, and that the result is a covectorfield. If we would like to define second order differential operators (such as the Hessian), we need to know how to take (directional) derivatives of such vector fields. The way this is done is defined in **connections**, which are also often referred to as **covariant derivatives**. To indicate the directional derivative of a vector field Y , along vector field X as defined via the connection ∇ we write $\nabla_X Y$.

Given two vector fields X and Y on a manifold (M, \mathcal{G}) expressed in a basis ∂_{x^i} , i.e.,

$$X|_m = \sum_{i=1}^{\dim(M)} x^i(m) \partial_{x^i}|_m, \quad \text{and} \quad Y|_m = \sum_{i=1}^{\dim(M)} y^i(m) \partial_{x^i}|_m, \quad (4.19)$$

and with corresponding covector basis ω^i , a connection takes the following form

$$\nabla_X Y := \sum_{k=1}^{\dim(M)} \left(\dot{y}^k + \sum_{i,j=1}^{\dim(M)} \Gamma_{ij}^k x^i y^j \right) \partial_{x^k}, \quad (4.20)$$

4.5 Short \neq Straight: the Left Cartan Connection

with \dot{y}^k the directional derivative along direction vector $X|_m$ of the k^{th} component of the vector $Y|_k$ given by

$$\dot{y}^k|_m := dy^k|_m(X|_m),$$

and with the derivative of y^k given by

$$dy^k|_m = \sum_{i=1}^{\dim(M)} (\partial_{x^i}|_m y^k) \omega^i|_m.$$

In (4.20), the first term \dot{y}^k is thus the directional derivative (along X) of the separate components of the vector field Y . The second term compensates for motion of the moving frame of reference and is characterized by the **Christoffel symbols** Γ_{ij}^k . In principle the choice for Christoffel symbols is free, and each choice defines a different connection, i.e., a different way of taking covariant derivatives. In the subsequent subsections we consider two types of connections: the Levi-Civita connection and the left Cartan connection, of which we will see in Subsec. 4.5.4 that the latter is of most interest to us.

4.5.2 The Levi-Civita Connection

Usually in Riemannian geometry people work with the Levi-Civita connection ∇^{LC} , which is the unique torsion free metric compatible¹ connection on the Riemannian manifold (M, \mathcal{G}) . The requirement that the connection should be torsion free means that

$$T(X, Y) = \nabla_X Y - \nabla_Y X - [X, Y] = 0.$$

Under these conditions the Levi-Civita connection is uniquely defined (fundamental theorem of Riemannian geometry), and the Christoffel symbols are then given by

$$(\Gamma^{LC})_{ij}^k = \frac{1}{2} \sum_{m=1}^{\dim M} g^{im} \left(\frac{\partial g_{mk}}{\partial x^l} + \frac{\partial g_{ml}}{\partial x^k} - \frac{\partial g_{kl}}{\partial x^m} \right) \quad (4.21)$$

and with matrix $[g_{ij}] = [\mathcal{G}(\partial_{x^i}, \partial_{x^j})]$ and $[g^{ij}]$ the corresponding inverse matrix.

For the Levi-Civita connection we have that stationary curves of

$$\min_{\substack{\gamma \in C^\infty(\mathbb{R}, M) \\ \gamma(0) = m_0 \\ \gamma(1) = m_1}} \int_0^1 \sqrt{\mathcal{G}|_{\gamma(\tau)}(\dot{\gamma}(\tau), \dot{\gamma}(\tau))} d\tau, \quad (4.22)$$

¹Metric compatible means $\nabla_X \mathcal{G}(Y, Z) = \mathcal{G}(\nabla_X Y, Z) + \mathcal{G}(Y, \nabla_X Z)$

4. SUB-RIEMANNIAN GEOMETRY IN ORIENTATION SCORES

satisfy the following geodesic equations

$$\nabla_{\dot{\gamma}}^{LC} \dot{\gamma} = 0, \quad (4.23)$$

see e.g. (Jost, 2011, Lemma 5.1.1). Expressed in holonomic coordinates $\{x^i\}_{i=1}^{\dim(M)}$ this gives

$$\ddot{\gamma}^k + \sum_{i,j=1}^{\dim(M)} (\Gamma^{LC})_{ij}^k \dot{\gamma}^i \dot{\gamma}^j = 0, \quad \text{with } \dot{\gamma}^k = \langle \omega^k \Big|_{\gamma}, \dot{\gamma}^k = \frac{d}{dt} \dot{\gamma}^k.$$

In general, curves for which $\nabla_{\dot{\gamma}} \dot{\gamma} = 0$ are called **auto parallel** curves with respect to the connection ∇ . The auto parallel curves with respect to the Levi-Civita connection ∇^{LC} are the geodesics, which in the standard Euclidean case are straight lines as we show in the next example.

Example 5. Consider the standard 2D Euclidean setting with $M = \mathbb{R}^2$, with the metric $g_{ij} = \delta_{ij}$, and with the standard basis $\{\partial_{x^i}\}_{i=1}^2$. Since the metric tensor g_{ij} is constant over M , the Christoffel symbols (computed via (4.21)) are given by

$$\Gamma_{ij}^k = 0.$$

The geodesic equations then write

$$\begin{aligned} \ddot{\gamma}^k(t) &= 0, \\ \dot{\gamma}^k(t) &= c^k. \end{aligned}$$

The geodesics in a Riemannian manifold with constant metric tensor g_{ij} , such as in the Euclidean manifold, are thus straight lines.

In the 2D Euclidean case the straight curves and shortest curves (geodesics) coincide, and both are auto parallel curves with respect to the Levi-Civita connection. In our sub-Riemannian geometry on $SE(2)$ this is not the case! Here we deal with a curved geometry (in which case $\Gamma_{ij}^k \neq 0$) and the "straight curves" and shortest curves no longer coincide. As we will see in the next Subsection, the straight curves (the exponential curves) are instead the auto parallel curves with respect to the Cartan connection ∇ .

4.5.3 The Left Cartan Connection on $SE(2)$

Consider the Riemannian manifold $M = (SE(2), \mathcal{G}_\epsilon^\xi)$. Recall that our left-invariant vector fields (2.42) are obtained from the basis $\{\partial_x|_e, \partial_y|_e, \partial_\theta|_e\}$ in $T_e(SE(2))$ by the

4.5 Short \neq Straight: the Left Cartan Connection

push-forward $(L_g)_*$ of the left-multiplication L_g . Conversely, we can use the so-called Maurer-Cartan form $(L_g^{-1})_*$ to map all $T_g(SE(2))$ back to $T_e(SE(2))$. This allows us to ‘connect’ all tangent spaces in a principle fiber bundle structure Spivak (1999). When using the adjoint representation for the associated vector bundle (Duits & Franken, 2010b, App.B) one obtains the left Cartan connection on the tangent bundle. Here we just provide the resulting Cartan connection ∇ on the tangent bundle (and provide some intuitive explanations):

$$\nabla_{\dot{\gamma}} Y := \sum_{k=1}^3 \left(\dot{y}^k + d\omega^k \Big|_{\gamma(t)} (\dot{\gamma}(t), Y) \right) \mathcal{A}_k, \quad (4.24)$$

with $d\omega^k \Big|_{\gamma(t)} (\dot{\gamma}(t), Y) \in \mathbb{R}$, recall (4.18), and with

$$\dot{y}^k(t) := \frac{d}{dt} y^k(t) := \frac{d}{dt} \omega^k \Big|_{\gamma(t)} (Y|_{\gamma(t)}),$$

which produces a vector field $\nabla_{\dot{\gamma}} Y$ that indicates the covariant derivative of vector field Y along the flow-field of γ .

The intuition is that this covariant derivative (4.24) takes into account that, when taking the covariant derivative of vector field Y , one differentiates its components

$$y^k(t) := \omega^k \Big|_{\gamma(t)} (Y|_{\gamma(t)}),$$

and simultaneously accounts for the movement of the (dual) left-invariant frame (recall Cartan’s structural formula (4.18)).

Expressed in components of the left-invariant frame and coframe this becomes (via Cartan’s structural formula (4.18)):

$$\nabla_{\dot{\gamma}} Y := \sum_{k=1}^3 \left(\dot{y}^k - \sum_{i,j=1}^3 c_{ij}^k \dot{\gamma}^i y^j \right) \mathcal{A}_k. \quad (4.25)$$

So now instead of the Christoffels in (4.21) we have Christoffel symbols that are minus the structure constants $\Gamma_{ij}^k = -c_{ij}^k$. Since $c_{ij}^k = -c_{ji}^k$ we have that $\sum_{i,j=1}^3 c_{ij}^k \dot{\gamma}^i y^j = 0$ and see that the auto parallel curves are the exponential curves as defined in Eq. (2.29) on page 44:

$$\nabla_{\dot{\gamma}} \dot{\gamma} = 0 \iff \begin{cases} \ddot{\gamma}^k(t) = 0, \\ \dot{\gamma}^k(t) = c^k. \end{cases}.$$

By duality, connection ∇ on the tangent bundle induces also a connection ∇^* on the cotangent bundle:

$$\nabla_{\dot{\gamma}}^* \lambda = \sum_{i=1}^3 \left(\dot{\lambda}_i + \sum_{j,k=1}^3 c_{ij}^k \lambda_k \dot{\gamma}^j \right) \omega^i, \quad (4.26)$$

4. SUB-RIEMANNIAN GEOMETRY IN ORIENTATION SCORES

with a sign change before the Christoffels, and with $\dot{\lambda}_i(t) = \frac{d}{dt} \langle \lambda|_{\gamma(t)}, \mathcal{A}_i|_{\gamma(t)} \rangle$. The formula (4.26), follows by $c_{ij}^k = -c_{ji}^k$, (4.24), and

$$0 = \frac{d}{dt} \delta_j^i = \frac{d}{dt} \langle \omega^i|_{\gamma(t)}, \mathcal{A}_j|_{\gamma(t)} \rangle = \langle \nabla_{\gamma(t)}^* \omega^i|_{\gamma(t)}, \mathcal{A}_j|_{\gamma(t)} \rangle + \langle \omega^i|_{\gamma(t)}, \nabla_{\gamma(t)} \mathcal{A}_j|_{\gamma(t)} \rangle$$

where brackets denote functional evaluation (not inner-products).

For the sub-Riemannian case one has a direct hard constraint $Y \in \Delta$ on the tangent bundle (but not on the co-tangent bundle) and one has to rely on a partial connection $\bar{\nabla}$ instead:

$$\begin{aligned} \bar{\nabla}_{\dot{\gamma}} Y &:= \sum_{k \in \{1,3\}} \left(\dot{y}^k - \sum_{i,j \in \{1,3\}} c_{ij}^k \dot{\gamma}^i y^j \right) \mathcal{A}_k, \\ \bar{\nabla}_{\dot{\gamma}}^* \lambda &:= \sum_{i=1}^3 \left(\dot{\lambda}_i + \sum_{j \in \{1,3\}} \sum_{k=1}^3 c_{ij}^k \lambda_k \dot{\gamma}^j \right) \omega^i. \end{aligned} \quad (4.27)$$

4.5.4 Why Do We Use the Left Cartan Connection?

Now that we introduced the Cartan connection let us see why it is a useful connection for our purposes. Here we list its nice properties:

- ‘Straight curves’, i.e. solutions to $\nabla_{\dot{\gamma}} \dot{\gamma} = 0$, are the exponential curves as we considered in Subsec. 2.2.3. Left-invariant PDE’s on $SE(2)$ that we shall consider in this thesis (hypo-elliptic diffusions in Ch. 5 and wavefront propagation in Ch. 8) can be expressed in covariant derivatives and left-invariant flow; transport takes place along these curves.
- ‘Shortest curves’, i.e., minimizers to (4.1) have instead parallel momentum $\nabla_{\dot{\gamma}}^* \lambda = 0$. This can be observed by the nested sub-Riemannian spheres, where we note that covectors may be geometrically represented by local parallel planes, see for example Fig. 4.2. The property of parallel momentum follows from the definition of the Cartan connection ∇^* and Pontryagin’s maximum principle (see e.g. (Duits *et al.*, 2014, Thm. 5.2)), which we use in Ch. 8 in the computation of sub-Riemannian geodesics in $SE(2)$.
- When considering second order best exponential curve fits for determining locally adaptive frames Duits & Janssen *et al.* (2016), which we employ for both vessel enhancement (Chapter 6) and vessel curvature measurements (Chapter 11), curve fitting boils down to eigenvector analysis of Hessians induced by this very connection (Duits & Janssen *et al.*, 2016, App. 4).

4.5 Short \neq Straight: the Left Cartan Connection

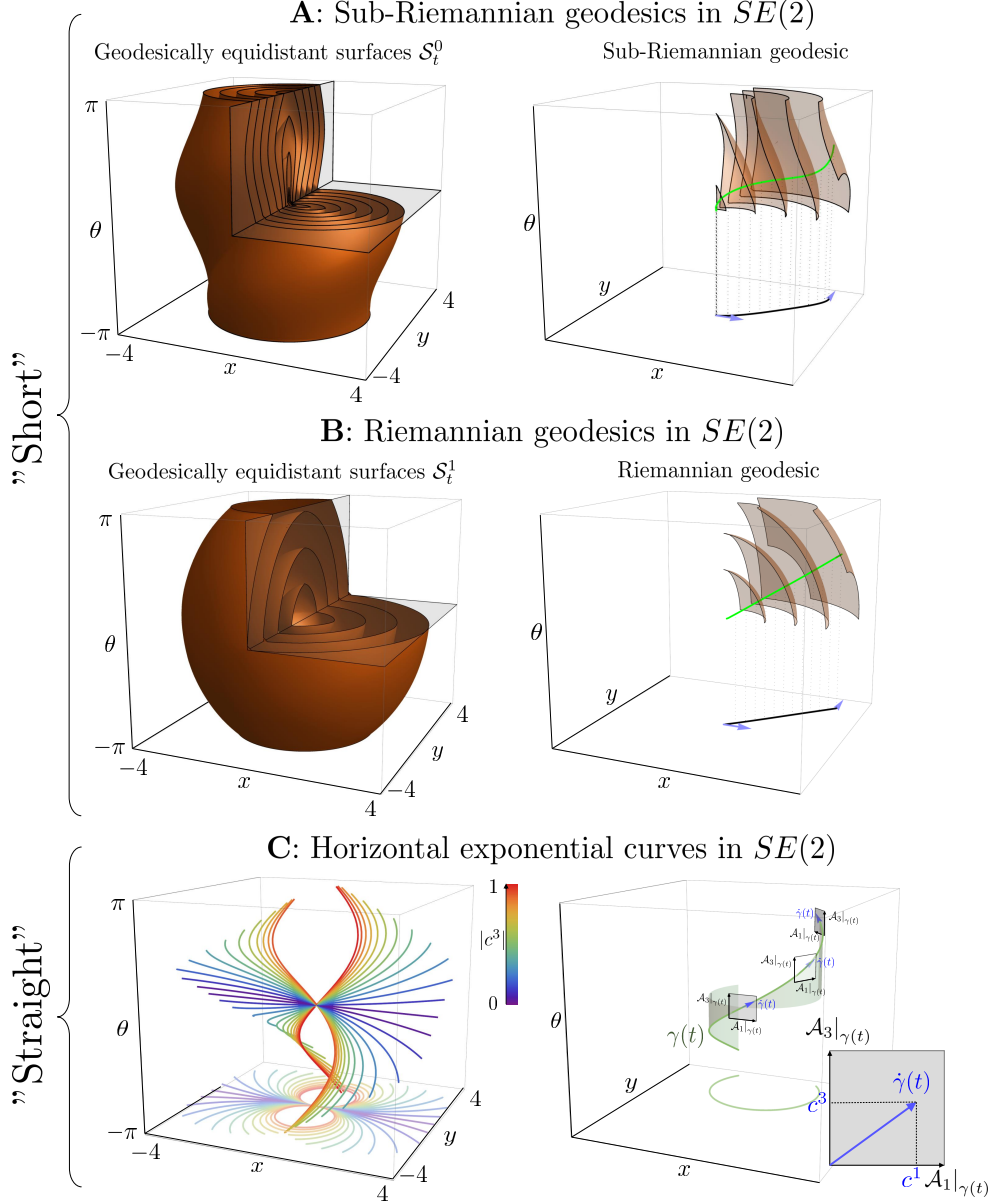


Figure 4.2: **A:** Geodesically equidistant surfaces $S_t^\epsilon = \{g \in SE(2) | d_\epsilon(0, g) = t\}$ and geodesic (in green) for the sub-Riemannian case: $\epsilon = 0$ and $\mathcal{C} = 1$. **B:** Geodesically equidistant surfaces S_t^ϵ and geodesic for the isotropic Riemannian case: $\epsilon = 1$ and $\mathcal{C} = 1$. Now the geodesics are straight lines. **C:** A set of horizontal exponential curves for which $\dot{\gamma}(t) = c^1 \mathcal{A}_1|_{\gamma(t)} + c^3 \mathcal{A}_3|_{\gamma(t)} \in \Delta$, with constant tangent vector components c^1 and c^3 .

4. SUB-RIEMANNIAN GEOMETRY IN ORIENTATION SCORES

- It correctly accounts for the motion of the moving frame of reference when taking derivatives of vector fields and covector fields.

In summary we have the following equivalences.

Theorem 1. *In a Riemannian manifold $(SE(2), T(SE(2)), \mathcal{G}_\epsilon^\xi)$, with the tangent bundle $T(SE(2))$ defined in (4.3), with the metric tensor \mathcal{G}_ϵ^ξ defined in (4.8), the metric d_ϵ defined in (4.10), and the Cartan connection defined in (4.24), we have the following relations for "straight" curves:*

$$\gamma \text{ is a } \nabla\text{-straight curve} \Leftrightarrow \gamma \text{ is an exponential curve} \Leftrightarrow \nabla_{\dot{\gamma}} \dot{\gamma} = 0 \Leftrightarrow \gamma \text{ has } \nabla\text{-auto parallel velocity ,}$$

and the following for "shortest" curves:

$$\gamma_\epsilon \text{ is a shortest curve} \Leftrightarrow \gamma_\epsilon \text{ is a minimizing curve in } d_\epsilon \Leftrightarrow \begin{cases} \nabla_{\dot{\gamma}_\epsilon}^* \lambda_\epsilon = 0 \\ \mathcal{G}_\epsilon^{\xi^{-1}} \dot{\gamma}_\epsilon = \lambda_\epsilon \end{cases} \Leftrightarrow \gamma_\epsilon \text{ has } \nabla^*\text{-parallel momentum .}$$

In a sub-Riemannian manifold $(SE(2), \Delta, \mathcal{G}_0^\xi)$ with tangent bundle Δ defined in (4.5), the sub-Riemannian metric tensor \mathcal{G}_0^ξ defined in (4.7), and the partial Cartan connection defined in (4.27) we have the following relations for "straight" curves

$$\gamma \text{ is a } \bar{\nabla}\text{-straight curve} \Leftrightarrow \gamma \text{ is a horizontal exponential curve} \Leftrightarrow \bar{\nabla}_{\dot{\gamma}} \dot{\gamma} = 0 \Leftrightarrow \gamma \text{ has } \bar{\nabla}\text{-auto parallel velocity ,}$$

and the following for "shortest" curves

$$\gamma_0 \text{ is a shortest curve} \Leftrightarrow \gamma_0 \text{ is a minimizing curve in } d_0 \Leftrightarrow \begin{cases} \bar{\nabla}_{\dot{\gamma}_0}^* \lambda_0 = 0 \\ \mathcal{G}_0^{\xi^{-1}} \dot{\gamma}_0 = \mathbb{P}_\Delta^* \lambda_0 \end{cases} \Leftrightarrow \gamma_0 \text{ has } \bar{\nabla}^*\text{-parallel momentum ,}$$

in which $\mathbb{P}_\Delta^*(\lambda_1 \omega^1 + \lambda_2 \omega^2 + \lambda_3 \omega^3) = \lambda_1 \omega^1 + \lambda^3 \omega^3$.

Part III

Applications

Chapter 5

Retinal Landmark Detection

This chapter is based on:

Bekkers, E.J., Loog, M., ter Haar Romeny, B.M., Duits, R.: Template matching via densities on the roto-translation group. *arXiv* preprint arXiv:1603.03304 (2016)

Bekkers, E., Duits, R., Loog, M.: Training of templates for object recognition in invertible orientation scores: Application to optic nerve head detection in retinal images. In Tai, X.C., Bae, E., Chan, T., Lysaker, M., eds.: Energy Minimization Methods in Computer Vision and Pattern Recognition (*EMMCVPR*). Volume 8932 of Lecture Notes in Computer Science. Springer International Publishing (2015) 464477

Bekkers, E., Duits, R., ter Haar Romeny, B.: Optic nerve head detection via group correlations in multi-orientation transforms. In Campilho, A., Kamel, M., eds.: Image Analysis and Recognition (*ICIAIR*). Volume 8815 of Lecture Notes in Computer Science. Springer International Publishing (2014) 293-302

5. RETINAL LANDMARK DETECTION

5.1 Introduction

In this chapter we describe a new cross-correlation based template matching scheme for the detection of objects characterized by orientation patterns. Our main application of interest is that of optic nerve head and fovea detection in retinal images. However, as we will show with an additional application to pupil detection in webcam images, the method is more generally applicable to the detection of objects that are characterized by curvilinear structures.

As one of the most basic forms of template matching, cross-correlation is intuitive, easy to implement, and due to the existence of optimization schemes for real-time processing a popular method to consider in computer vision tasks Yoo & Han (2009). However, as intensity values alone provide little context, cross-correlation for the detection of objects has its limitations. More advanced data representations may be used, e.g. via wavelet transforms or via feature descriptors Azzopardi & Petkov (2013); Bay *et al.* (2006); Dalal & Triggs (2005); Felsberg (2013); Lowe (1999); Viola & Jones (2001). However, then standard cross-correlation can usually no longer be used and one typically resorts to classifiers, which take the new representations as input feature vectors. While in these approaches the detection performance often increases with the choice of a more complex representation, so does the computation time. In contrast, in this chapter we stay in the framework of template matching via cross-correlation while working with a contextual representation of the image. To this end, we lift an image $f : \mathbb{R}^2 \rightarrow \mathbb{R}$ to an invertible orientation score $U_f : \mathbb{R}^2 \rtimes S^1 \rightarrow \mathbb{C}$ via a wavelet-type transform using anisotropic filters (Sec. 2.1). Cross-correlation based template matching is then defined via \mathbb{L}_2 inner-products of a template $T \in \mathbb{L}_2(SE(2))$ and an orientation score $U_f \in \mathbb{L}_2(SE(2))$. In this chapter we learn templates T by means of generalized linear regression.

In the \mathbb{R}^2 -case (which we later extend to orientation scores, the $SE(2)$ -case), we define templates $t \in \mathbb{L}_2(\mathbb{R}^2)$ via the optimization of energy functionals of the form

$$t^* = \underset{t \in \mathbb{L}_2(\mathbb{R}^2)}{\operatorname{argmin}} \{E(t) := S(t) + R(t)\}, \quad (5.1)$$

where the energy functional $E(t)$ consists of a data term $S(t)$, and a regularization term $R(t)$. Since the templates optimized in this form are used in a linear cross-correlation based framework, we will use inner products in S , in which case (5.1) can be regarded as a generalized linear regression problem with a regularization term. For example, (5.1) becomes a regression problem generally known under the name *ridge regression*

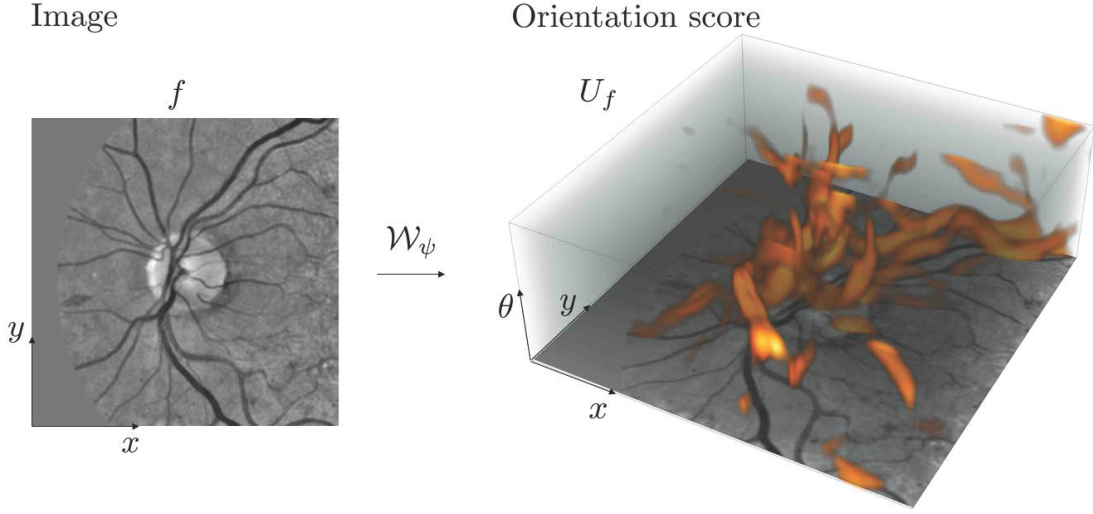


Figure 5.1: A retinal image f of the optic nerve head and a volume rendering of the orientation score U_f (obtained via a wavelet transform \mathcal{W}_ψ).

Hoerl & Kennard (1970), when taking

$$S(t) = \sum_{i=1}^N ((t, f_i)_{\mathbb{L}_2(\mathbb{R}^2)} - y_i)^2, \text{ and } R(t) = \mu \|t\|_{\mathbb{L}_2(\mathbb{R}^2)}^2,$$

where f_i is one of N image patches, $y_i \in \{0, 1\}$ is the corresponding desired filter response, and where μ is a parameter weighting the regularization term. The regression is then from an input image patch f_i to a desired response y_i , and the template t can be regarded as the ‘‘set of weights’’ that are optimized in the regression problem. In this chapter we consider both quadratic (linear regression) and logistic (logistic regression) losses in S . In order to include regularization we consider terms of the form

$$R(t) = \lambda \int_{\mathbb{R}^2} \|\nabla t(\mathbf{x})\|^2 d\mathbf{x} + \mu \|t\|_{\mathbb{L}_2(\mathbb{R}^2)}^2,$$

and thus combine the classical ridge regression with a smoothing term (weighted by parameters $\lambda > 0$ and $\mu > 0$ which we will set automatically by a generalized cross validation method in Subsec. 5.5.1.3).

In our extension of smoothed regression to orientation scores we employ similar techniques. However, here we must however take care of the curved geometry (Subsec. 2.1.6) on the domain $SE(2)$. Accordingly, we must work with a rotating derivative frame (instead of axis aligned derivatives) that is aligned with the group elements $(\mathbf{x}, \theta) \in SE(2)$, see e.g. the $\{\mathcal{A}_1, \mathcal{A}_2, \mathcal{A}_3\}$ -frames in Fig. 5.2. This left-invariant frame

5. RETINAL LANDMARK DETECTION

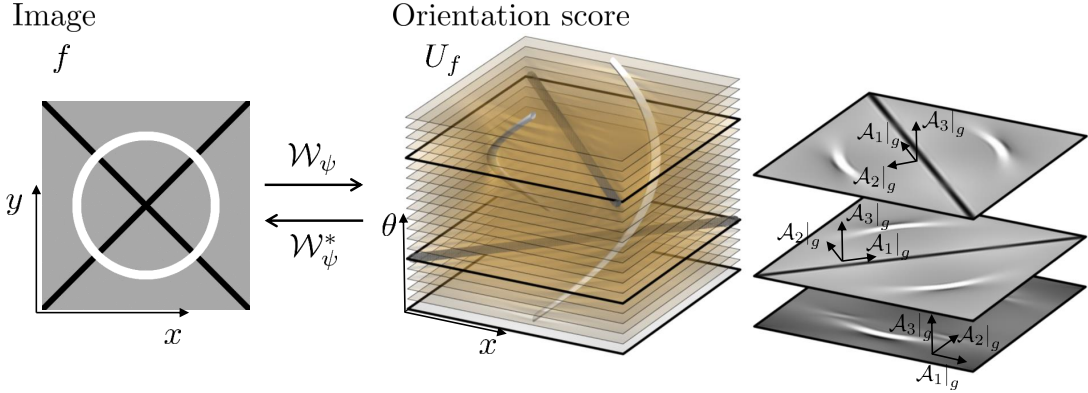


Figure 5.2: In orientation scores U_f , constructed from an image f via the orientation score transform \mathcal{W}_ψ , we make use of a left-invariant derivative frame $\{\mathcal{A}_1|_g, \mathcal{A}_2|_g, \mathcal{A}_3|_g\}$ attached to each $g = (x, y, \theta) \in SE(2)$. Three slices and the corresponding left-invariant frames are shown separately (at $\theta \in \{0, \frac{\pi}{4}, \frac{3\pi}{4}\}$).

(defined in Eq. 2.42) allows for (anisotropic) smoothing along oriented structures. As we will show in this chapter (and in more detail in App. 5.4), the proposed smoothing scheme has the probabilistic interpretation of time integrated Brownian motion on $SE(2)$ Duits & Franken (2010a); Zhang *et al.* (2016b).

Regression and Group Theory Regularization in (generalized) linear regression generally leads to more robust classifiers/regressions, especially when a low number of training samples are available. Different types of regularizations in regression problems have been intensively studied in e.g. Cuingnet *et al.* (2013); Hastie *et al.* (2009); Hebiri & van de Geer (2011); Qazi *et al.* (2010); Xu *et al.* (2009), and the choice for regularization-type depends on the problem: E.g. \mathbb{L}_1 -type regularization is often used to sparsify the regression weights, whereas \mathbb{L}_2 -type regularization is more generally used to prevent over-fitting by penalizing outliers (e.g. in ridge regression Hoerl & Kennard (1970)). Smoothing of regression coefficients by penalizing the \mathbb{L}_2 -norm of the derivative along the coefficients is less common, but it can have a significant effect on performance Cuingnet *et al.* (2013); Li & Li (2008).

We solve problem (5.1) in the context of smoothing splines: We discretize the problem by expanding the templates in a finite B-spline basis, and optimize over the spline coefficients. For d-dimensional Euclidean spaces, smoothing splines have been well studied De Boor (1978); Green & Silverman (1993); Unser (1999); Unser *et al.* (1993). In this chapter, we extend the concept to the curved space $SE(2)$ and provide

5.1 Introduction

explicit forms of the discrete regularization matrices. Furthermore, we show that the extended framework can be used for time integrated Brownian motions on $SE(2)$, and show near to perfect comparisons to the exact solutions found in Duits & Franken (2010a); Zhang *et al.* (2016b).

In general, statistics and regression on Riemannian manifolds are powerful tools in medical imaging and computer vision Miolane & Pennec (2015); Pennec (2006); Thomas Fletcher (2013); Vidal *et al.* (2005). More specifically, in pattern matching and registration problems, Lie groups are often used to describe deformations. E.g. in Tuzel *et al.* (2008) the authors learn a regression function $\mathbb{R}^m \rightarrow A(2)$ from a discrete m -dimensional feature vector to a deformation in the affine group $A(2)$. Their purpose is object tracking in video sequences. This work is however not concerned with deformation analysis, we instead learn a regression function $\mathbb{L}_2(SE(2)) \rightarrow \mathbb{R}$ from continuous densities on the Lie group $SE(2)$ (obtained via an invertible orientation score transform) to a desired filter response. Our purpose is object detection in 2D images. In our regression we impose smoothed regression with a time-integrated hypo-elliptic Brownian motion prior and thereby extend least squares regression to smoothed regression on $SE(2)$ involving first order variation in Sobolev-type of norms.

Application Area of the Proposed Method The strength of our approach is demonstrated with the application to anatomical landmark detection in medical retinal images and pupil localization in regular camera images. In the retinal application we consider the problem of detecting the optic nerve head (ONH) and the fovea. Many image analysis applications require the robust, accurate and fast detection of these structures, see e.g. Gegundez-Arias *et al.* (2013); Hansen & Ji (2010); Patton *et al.* (2006); Ramakanth & Babu (2014). In all three detection problems the objects of interest are characterized by (surrounding) curvilinear structures (blood vessels in the retina; eyebrow, eyelid, pupil and other contours for pupil detection), which are conveniently represented in *invertible* orientation scores. The invertibility condition implies that all image data is contained in the orientation score Duits *et al.* (2007a)Bekkers *et al.* (2014a). With the proposed method we achieve state-of-the-art results both in terms of detection performance and speed: high detection performance is achieved by learning templates that make optimal use of the line patterns in orientation scores; speed is achieved by a simple, yet effective, cross-correlation template matching approach.

Contribution of This Work. This work builds upon two published conference papers Bekkers *et al.* (2014b, 2015a). In the first we demonstrated that high detection performance could be achieved by considering cross-correlation based template

5. RETINAL LANDMARK DETECTION

matching in $SE(2)$, using only handcrafted templates and with the application of ONH detection in retinal images Bekkers *et al.* (2014b). In the second we then showed on the same application that better performance could be achieved by training templates using the optimization of energy functionals of the form of (5.1), where then only a (left-invariant) smoothing regularizer was considered Bekkers *et al.* (2015a). In this chapter we provide a complete framework for training of templates and matching on $SE(2)$ and contribute to literature by:

1. Extending the linear regression $SE(2)$ framework Bekkers *et al.* (2015a) to logistic regression.
2. Studying different types of regression priors, now introducing also a ridge regression prior.
3. Establishing a link of the $SE(2)$ smoothing prior with hypo-elliptic diffusion equations on $SE(2)$.
4. Showing state-of-the-art performance on two new benchmark applications: fovea and pupil detection.
5. Improving previous results on ONH detection.
6. Making the developed code publicly available at <http://erikbekkers.bitbucket.io/TMSE2.html>.

Chapter Outline The remainder of this chapter is organized as follows. In Sec. 5.2 we provide the theory for template matching and template construction in the \mathbb{R}^2 -case. The theory is then extended to the $SE(2)$ -case in Sec. 5.3. Additionally, in Sec. 5.4 we provide a probabilistic interpretation of the proposed $SE(2)$ prior, and relate it to Brownian motions on $SE(2)$. In Sec. 5.5 we apply the method to retinal images for ONH (Subsec. 5.5.2) and fovea detection (Subsec. 5.5.3), and to regular camera images for pupil detection (Subsec. 5.5.4). Finally, we conclude the chapter in Sec. 5.6.

5.2 Template Matching & Regression on \mathbb{R}^2

5.2.1 Object Detection via Cross-Correlation

We are considering the problem of finding the location of objects (with specific orientation patterns) in an image. While in principle an image may contain multiple objects

5.2 Template Matching & Regression on \mathbb{R}^2

of interest, the applications discussed in this chapter only require the detection of one object per image. We search for the most likely location

$$\mathbf{x}^* = \operatorname{argmax}_{\mathbf{x} \in \mathbb{R}^2} P(\mathbf{x}), \quad (5.2)$$

with $P(\mathbf{x}) \in \mathbb{R}$ denoting the objective functional for finding the object of interest at location \mathbf{x} . We define P based on inner products in a *linear regression* and *logistic regression* context, where we respectively define P by

$$P(\mathbf{x}) = P_{lin}^{\mathbb{R}^2}(\mathbf{x}) := (\mathcal{T}_{\mathbf{x}} t, f)_{\mathbb{L}_2(\mathbb{R}^2)}, \quad (5.3)$$

or

$$P(\mathbf{x}) = P_{log}^{\mathbb{R}^2}(\mathbf{x}) := \sigma((\mathcal{T}_{\mathbf{x}} t, f)_{\mathbb{L}_2(\mathbb{R}^2)}), \quad (5.4)$$

with $\sigma(x) = e^x / (1 + e^x)$,

where $\mathcal{T}_{\mathbf{x}}$ denotes translation by \mathbf{x} via

$$(\mathcal{T}_{\mathbf{x}} t)(\tilde{\mathbf{x}}) = t(\tilde{\mathbf{x}} - \mathbf{x}),$$

and where the $\mathbb{L}_2(\mathbb{R}^2)$ inner product is given by

$$(t, f)_{\mathbb{L}_2(\mathbb{R}^2)} := \int_{\mathbb{R}^2} \overline{t(\tilde{\mathbf{x}})} f(\tilde{\mathbf{x}}) d\tilde{\mathbf{x}}, \quad (5.5)$$

with associated norm $\|\cdot\|_{\mathbb{L}_2(\mathbb{R}^2)} = \sqrt{(\cdot, \cdot)_{\mathbb{L}_2(\mathbb{R}^2)}}$. For a generalization of cross-correlation based template matching to *normalized* cross correlation (not used in this chapter), we refer the reader to App. A.2.

5.2.2 Optimizing t Using Linear Regression

Our aim is to construct templates t that are “aligned” with image patches that contain the object of interest, and which are orthogonal to non-object patches. Hence, template t is found via the minimization of the following energy

$$E_{lin}(t) = \sum_{i=1}^N ((t, f_i)_{\mathbb{L}_2(\mathbb{R}^2)} - y_i)^2 + \lambda \int_{\mathbb{R}^2} \|\nabla t(\tilde{\mathbf{x}})\|^2 d\tilde{\mathbf{x}} + \mu \|t\|_{\mathbb{L}_2(\mathbb{R}^2)}^2, \quad (5.6)$$

with f_i one of the N training patches extracted from an image f , and y_i the corresponding label ($y_i = 1$ for *objects* and $y_i = 0$ for *non-objects*). In (5.6), the data-term (first term) aims for alignment of template t with object patches, in which case the inner product $(t, f_i)_{\mathbb{L}_2(\mathbb{R}^2)}$ is ideally one, and indeed aims orthogonality to non-object patches (in which case the inner product is zero). The second term enforces spatial smoothness of the template by penalizing its gradient, controlled by λ . The third (ridge) term improves stability by suppressing the \mathbb{L}_2 -norm of t , controlled by μ .

5. RETINAL LANDMARK DETECTION

5.2.3 Optimizing t Using Logistic Regression

In object detection we are essentially considering a two-class classification problem: the object is either present or not. In this respect, the quadratic loss term in (5.6) might not be the best choice as it penalizes any deviation from the desired response y_i , regardless of whether or not the response $(t, f_i)_{\mathbb{L}_2(\mathbb{R}^2)}$ is on the correct side of a decision boundary. In other words, the aim is not necessarily to construct a template that best maps an image patch f_i to a response $y_i \in \{0, 1\}$, but rather the aim is to construct a template that best makes the separation between *object* and *non-object* patches. With this in mind we resort to the logistic regression model, in which case we interpret the non-linear objective functional given in (5.4) as a probability, and define

$$\begin{aligned} p_1(f_i ; t) &= p(f_i ; t), \\ p_0(f_i ; t) &= 1 - p(f_i ; t), \\ \text{with } p(f_i ; t) &= \sigma((t, f_i)_{\mathbb{L}_2(\mathbb{R}^2)}), \end{aligned} \quad (5.7)$$

with $p_1(f_i; t)$ and $p_0(f_i; t)$ denoting respectively the probabilities of a patch f_i being an *object* or *non-object* patch, and σ given by (5.4). Our aim is now to maximize the likelihood (of each patch f_i having maximum probability $p_{y_i}(f_i; t)$ for correct label y_i):

$$\ell(t) = \prod_{i=1}^N p_{y_i}(f_i; t) = \prod_{i=1}^N p(f_i; t)^{y_i} (1 - p(f_i; t))^{1-y_i}. \quad (5.8)$$

We maximize the log-likelihood instead, which is given by

$$\begin{aligned} \ell_{log}(t) &:= \log(\ell(t)) \\ &= \sum_{i=1}^N \log(p(f_i; t)^{y_i} (1 - p(f_i; t))^{1-y_i}) \\ &= \sum_{i=1}^N y_i(t, f_i)_{\mathbb{L}_2(\mathbb{R}^2)} - \log\left(1 + e^{(t, f_i)_{\mathbb{L}_2(\mathbb{R}^2)}}\right). \end{aligned} \quad (5.9)$$

Maximizing (5.9) is known as the problem of logistic regression. Similar to the linear regression case, we impose additional regularization and define the following regularized logistic regression energy, which we aim to *maximize*:

$$E_{log}^\ell(t) = \ell_{log}(t) - \lambda \int_{\mathbb{R}^2} \|\nabla t(\tilde{\mathbf{x}})\|^2 d\tilde{\mathbf{x}} - \mu \|t\|_{\mathbb{L}_2(\mathbb{R}^2)}^2. \quad (5.10)$$

5.2.4 Template Optimization in a B-Spline Basis

5.2.4.1 Templates in a B-Spline Basis

In order to solve the optimizations (5.6) and (5.10), the template is described in a basis of direct products of n -th order B-splines B^n :

$$t(x, y) = \sum_{k=1}^{N_k} \sum_{l=1}^{N_l} c_{k,l} B^n\left(\frac{x}{s_k} - k\right) B^n\left(\frac{y}{s_l} - l\right), \quad (5.11)$$

with $B^n(x) = \left(1_{[-\frac{1}{2}, \frac{1}{2}]} *^{(n)} 1_{[-\frac{1}{2}, \frac{1}{2}]}\right)(x)$ a n -th order B-spline obtained by n -fold convolution of the indicator function $1_{[-\frac{1}{2}, \frac{1}{2}]}$, and $c_{k,l}$ the coefficients belonging to the shifted B-splines. Here s_k and s_l scale the B-splines and typically depend on the number N_k and N_l of B-splines to sample the domain.

5.2.4.2 Linear Regression

By substitution of (5.11) into (5.6), the energy functional can be expressed in matrix-vector form (see App. A.1):

$$E_{lin}^B(\mathbf{c}) = \|\mathbf{Sc} - \mathbf{y}\|^2 + \lambda \mathbf{c}^\dagger \mathbf{R} \mathbf{c} + \mu \mathbf{c}^\dagger \mathbf{I} \mathbf{c}. \quad (5.12)$$

Regarding our notations we note that for spatial template t given by (5.11) we have $E_{lin}(t) = E_{lin}^B(\mathbf{c})$, and label ‘B’ indicates finite expansion in the B-spline basis. The minimizer of (5.12) is given by

$$(\mathbf{S}^\dagger \mathbf{S} + \lambda \mathbf{R} + \mu \mathbf{I}) \mathbf{c} = \mathbf{S}^\dagger \mathbf{y}, \quad (5.13)$$

with \dagger denoting the conjugate transpose, and \mathbf{I} denoting the identity matrix. Here \mathbf{S} is a $[N \times N_k N_l]$ matrix given by

$$\begin{aligned} \mathbf{S} &= \{(s_{1,1}^i, \dots, s_{1,N_l}^i, s_{2,1}^i, \dots, s_{2,N_l}^i, \dots, \dots, s_{N_k,N_l}^i)\}_{i=1}^N, \\ s_{k,l} &= (B_{s_k s_l}^n * f_i)(k, l), \end{aligned} \quad (5.14)$$

with $B_{s_k s_l}^n(x, y) = B^n\left(\frac{x}{s_k}\right) B^n\left(\frac{y}{s_l}\right)$, for all (x, y) on the discrete spatial grid on which the input image $f_D : \{1, N_x\} \times \{1, N_y\} \rightarrow \mathbb{R}$ is defined. Here N_k and N_l denote the number of splines in resp. x and y direction, and $s_k = \frac{N_x}{N_k}$ and $s_l = \frac{N_y}{N_l}$ are the corresponding resolution parameters. The $[N_k N_l \times 1]$ column vector \mathbf{c} contains the B-spline coefficients, and the $[N \times 1]$ column vector \mathbf{y} contains the labels, stored in the following form

$$\begin{aligned} \mathbf{c} &= (c_{1,1}, \dots, c_{1,N_l}, c_{2,1}, \dots, c_{2,N_l}, \dots, \dots, c_{N_k,N_l})^T \\ \mathbf{y} &= (y_1, y_2, \dots, y_N)^T. \end{aligned} \quad (5.15)$$

5. RETINAL LANDMARK DETECTION

The $[N_k N_l \times N_k N_l]$ regularization matrix \mathbf{R} is given by

$$\mathbf{R} = \mathbf{R}_x^{s_k} \otimes \mathbf{R}_x^{s_l} + \mathbf{R}_y^{s_k} \otimes \mathbf{R}_y^{s_l}, \quad (5.16)$$

where \otimes denotes the matrix Kronecker product, and with

$$\begin{aligned} \mathbf{R}_x^{s_k}(k, k') &:= -\frac{1}{s_k} \frac{\partial^2 B^{2n+1}}{\partial x^2}(k' - k), \\ \mathbf{R}_x^{s_l}(l, l') &:= s_l B^{2n+1}(l' - l), \\ \mathbf{R}_y^{s_k}(k, k') &:= s_k B^{2n+1}(k' - k), \\ \mathbf{R}_y^{s_l}(l, l') &:= -\frac{1}{s_l} \frac{\partial^2 B^{2n+1}}{\partial y^2}(l' - l), \end{aligned} \quad (5.17)$$

with $k, k' = 1, 2, \dots, N_k$ and $l, l' = 1, 2, \dots, N_l$. The coefficients \mathbf{c} can then be computed by solving (5.13) directly, or via linear system solvers such as conjugate gradient descent. For a derivation of the regularization matrix \mathbf{R} we refer to App. A.1.

5.2.4.3 Logistic Regression

The logistic regression log-likelihood functional (5.10) can be expressed in matrix-vector notations as follows:

$$E_{log}^{\ell, B}(\mathbf{c}) = \left[\mathbf{y}^\dagger \mathbf{S} \mathbf{c} - \mathbf{1}_N^\dagger \log(\mathbf{1}_N + \exp(\mathbf{S} \mathbf{c})) \right] - \lambda \mathbf{c}^\dagger \mathbf{R} \mathbf{c} - \mu \mathbf{c}^\dagger \mathbf{I} \mathbf{c}, \quad (5.18)$$

where $\mathbf{1}_N = \{1, 1, \dots, 1\}^T \in \mathbb{R}^{N \times 1}$, and where the exponential and logarithm are evaluated element-wise. We follow a standard approach for the optimization of (5.18), see e.g. Hastie *et al.* (2009), and find the minimizer by setting the derivative to \mathbf{c} to zero

$$\nabla_{\mathbf{c}} E_{log}^{\ell, B}(\mathbf{c}) = \mathbf{S}^\dagger (\mathbf{y} - \mathbf{p}) - \lambda \mathbf{R} \mathbf{c} - \mu \mathbf{I} \mathbf{c} = \mathbf{0}, \quad (5.19)$$

with $\mathbf{p} = (p_1, \dots, p_N)^T \in \mathbb{R}^{N \times 1}$, with $p_i = \sigma((S\mathbf{c})_i)$. To solve (5.19), we use a Newton-Raphson optimization scheme. This requires computation of the Hessian matrix, given by

$$\mathcal{H}(E_{log}^{\ell, B}) = -(\mathbf{S}^\dagger \mathbf{W} \mathbf{S} + \lambda \mathbf{R} + \mu \mathbf{I}), \quad (5.20)$$

with diagonal matrix $\mathbf{W} = \text{diag}_{i \in \{1, \dots, N\}} \{p_i(1 - p_i)\}$. The Newton-Raphson update rule is then given by

$$\begin{aligned} \mathbf{c}^{new} &= \mathbf{c}^{old} - \mathcal{H}(E_{log}^{\ell, D})^{-1} (\nabla_{\mathbf{c}} E_{log}^{\ell, D}(\mathbf{c})) \\ &= (\mathbf{S}^\dagger \mathbf{W} \mathbf{S} + \lambda \mathbf{R} + \mu \mathbf{I})^{-1} \mathbf{S}^\dagger \mathbf{W} \mathbf{z}, \end{aligned} \quad (5.21)$$

with $\mathbf{z} = \mathbf{S} \mathbf{c}^{old} + \mathbf{W}^{-1}(\mathbf{y} - \mathbf{p})$, see e.g. (Hastie *et al.*, 2009, ch. 4.4). We denote the optimal coefficients found at convergence of the algorithm by \mathbf{c}^* .

Summarizing, we obtain the solution of (5.2) by substituting the optimized B-spline coefficients \mathbf{c}^* into (5.11), and the resulting template t enters (5.3) for the linear case, or (5.4) for the logistic case. After this, the most likely object location \mathbf{x}^* is found by (5.2).

5.3 Template Matching & Regression on $SE(2)$

This section starts with details on the representation of image data in the form of orientation scores (Subsec. 5.3.1). Then, we repeat the sections from Sec. 5.2 in Subsections 5.3.2 to 5.3.5, but now in the context of the extended domain $SE(2)$.

5.3.1 Orientation Scores on $SE(2)$

Transformation. An orientation score, constructed from image $f : \mathbb{R}^2 \rightarrow \mathbb{R}$, is defined as a function $U_f : \mathbb{R}^2 \times S^1 \rightarrow \mathbb{C}$ and depends on two variables (\mathbf{x}, θ) , where $\mathbf{x} = (x, y) \in \mathbb{R}^2$ denotes position and $\theta \in [0, 2\pi)$ denotes the orientation variable. An orientation score U_f of image f is constructed via the orientation score transform defined in Eq. (2.1) in Subsec. 2.1.4.

In this work we choose to use cake wavelets (defined in Eq. (2.7) in Subsec. 2.1.5) in the orientation score transform. While in general any kind of anisotropic wavelet could be used to lift the image to $SE(2)$, cake wavelets ensure that no data-evidence is lost (!) during the transformation before template matching is performed Duits & Franken (2010a); Duits *et al.* (2007b).

Left-Invariant Derivatives We will rely on the left-invariant derivative frame $\{\mathcal{A}_1, \mathcal{A}_2, \mathcal{A}_3\}$ defined in Eq. (2.42) in Subsec. 2.3.3. Using this derivative frame we will construct in Subsec. 5.3.3 a regularization term in which we can control the amount of (anisotropic) smoothness along line structures.

5.3.2 Object Detection via Cross-Correlation

As in Section 5.2, we search for the most likely *object* location \mathbf{x}^* via (5.2), with

$$P^{SE(2)}(\mathbf{x}) := \max_{\alpha \in [0, 2\pi)} \tilde{P}^{SE(2)}(\mathbf{x}, \alpha). \quad (5.22)$$

However, now matching is based on $\mathbb{L}_2(SE(2))$ inner products, and we define the corresponding functionals

$$\tilde{P}_{lin}^{SE(2)}(\mathbf{x}, \alpha) := (\mathcal{L}_g T, U_f)_{\mathbb{L}_2(SE(2))}, \quad (5.23)$$

$$\tilde{P}_{log}^{SE(2)}(\mathbf{x}, \alpha) := \sigma((\mathcal{L}_g T, U_f)_{\mathbb{L}_2(SE(2))}), \quad (5.24)$$

with $g = (\mathbf{x}, \alpha)$, and with shift-twist operator \mathcal{L}_g (shift by \mathbf{x} , rotation by α) defined by

$$(\mathcal{L}_g T)(\tilde{\mathbf{x}}, \tilde{\theta}) = T(\mathbf{R}_\alpha^{-1}(\tilde{\mathbf{x}} - \mathbf{x}), \tilde{\theta} - \alpha). \quad (5.25)$$

5. RETINAL LANDMARK DETECTION

The $\mathbb{L}_2(SE(2))$ -inner product is defined by

$$(T, U_f)_{\mathbb{L}_2(SE(2))} := \int_{\mathbb{R}^2} \int_0^{2\pi} \overline{T(\tilde{\mathbf{x}}, \tilde{\theta})} U_f(\tilde{\mathbf{x}}, \tilde{\theta}) d\tilde{\mathbf{x}} d\tilde{\theta}, \quad (5.26)$$

with norm $\|\cdot\|_{\mathbb{L}_2(SE(2))} = \sqrt{(\cdot, \cdot)_{\mathbb{L}_2(SE(2))}}$.

5.3.3 Optimizing T Using Linear Regression

Following the same reasoning as in Section 5.2.2 we search for the template that minimizes

$$\begin{aligned} \mathcal{E}_{lin}(T) = & \sum_{i=1}^N ((T, U_{f_i})_{\mathbb{L}_2(SE(2))} - y_i)^2 \\ & + \lambda \int_{\mathbb{R}^2} \int_0^{2\pi} \|\nabla T(\tilde{\mathbf{x}}, \tilde{\theta})\|_D^2 d\tilde{\mathbf{x}} d\tilde{\theta} + \mu \|T\|_{\mathbb{L}_2(SE(2))}^2, \end{aligned} \quad (5.27)$$

with smoothing term:

$$\|\nabla_{(\tilde{\mathbf{x}}, \tilde{\theta})} T(g)\|_D^2 = D_{11} |(\mathcal{A}_1 T)(g)|^2 + D_{22} |(\mathcal{A}_2 T)(g)|^2 + D_{33} |(\mathcal{A}_3 T)(g)|^2. \quad (5.28)$$

Here, $\nabla_g T(g) = (\mathcal{A}_1 T)(g), (\mathcal{A}_2 T)(g), (\mathcal{A}_3 T)(g))^T$ denotes a left-invariant gradient at $g \in SE(2)$, recall (4.16) where we set $\mathcal{C} = \xi_i = 1$. Recall also Fig. 5.2 and Eq. (2.15). The parameters D_{11} , D_{22} and $D_{33} \geq 0$ are used to balance the regularization in the three directions. Similar to this problem, first order Tikhonov-regularization on $SE(2)$ is related, via temporal Laplace transforms, to left-invariant diffusions on the group $SE(2)$ (Sec. 5.4), in which case D_{11} , D_{22} and D_{33} denote the diffusion constants in \mathcal{A}_1 , \mathcal{A}_2 and \mathcal{A}_3 direction. Here we set $D_{11} = 1$, $D_{22} = 0$, and thereby we get Laplace transforms of hypo-elliptic diffusion processes Citti & Sarti (2006); Duits & Franken (2010a). Parameter D_{33} can be used to tune between isotropic (large D_{33}) and anisotropic (low D_{33}) diffusion (see e.g. (Bekkers *et al.*, 2015a, Fig. 3)). Note that anisotropic diffusion, via a low D_{33} , is preferred as we want to maintain line structures in orientation scores.

5.3.4 Optimizing T Using Logistic Regression

Similarly to what is done in Subsec. 5.2.3 we can change the quadratic loss of (5.27) to a logistic loss, yielding the following energy functional

$$\mathcal{E}_{log}(T) = \mathcal{L}_{log}(T) - \lambda \int_{\mathbb{R}^2} \int_0^{2\pi} \|\nabla T(\tilde{\mathbf{x}}, \tilde{\theta})\|_D^2 d\tilde{\mathbf{x}} d\tilde{\theta} - \mu \|T\|_{\mathbb{L}_2(SE(2))}^2, \quad (5.29)$$

5.3 Template Matching & Regression on $SE(2)$

with log-likelihood (akin to (5.9) for the \mathbb{R}^2 case)

$$\mathcal{L}_{log}(T) = \sum_{i=1}^N y_i(T, U_{f_i})_{\mathbb{L}_2(SE(2))} - \log \left(1 + e^{(T, U_{f_i})_{\mathbb{L}_2(SE(2))}} \right). \quad (5.30)$$

The optimization of (5.27) and (5.29) follows quite closely the procedure as described in Sec. 5.2 for the 2D case. In fact, when T is expanded in a B-spline basis, the exact same matrix-vector formulation can be used.

5.3.5 Template Optimization in a B-Spline Basis

5.3.5.1 Templates in a B-Spline Basis

The template T is expanded in a B-spline basis as follows

$$T(x, y, \theta) = \sum_{k=1}^{N_k} \sum_{l=1}^{N_l} \sum_{m=1}^{N_m} c_{k,l,m} B^n \left(\frac{x}{s_k} - k \right) B^n \left(\frac{y}{s_l} - l \right) B^n \left(\frac{\theta \bmod 2\pi}{s_m} - m \right), \quad (5.31)$$

with N_k , N_l and N_m the number of B-splines in respectively the x , y and θ direction, $c_{k,l,m}$ the corresponding basis coefficients, and with angular resolution parameter $s_m = 2\pi/N_m$.

5.3.5.2 Linear Regression

The shape of the minimizer of energy functional $\mathcal{E}_{lin}(T)$ in the $SE(2)$ case is the same as for $E_{lin}(t)$ in the \mathbb{R}^2 case, and is again of the form given in (5.12). However, now the definitions of \mathbf{S} , \mathbf{R} and \mathbf{c} are different. Now, \mathbf{S} is a $[N \times N_k N_l N_m]$ matrix given by

$$\begin{aligned} \mathbf{S} &= \{(s_{1,1,1}^i, \dots, s_{1,1,N_m}^i, \dots, s_{1,N_l,N_m}^i, \dots, s_{N_k,N_l,N_m}^i)\}_{i=1}^N, \\ s_{k,l,m} &= (B_{s_k s_l s_m}^n * U_{f_i})(k, l, m), \end{aligned} \quad (5.32)$$

with $B_{s_k s_l s_m}^n(x, y, \theta) = B^n \left(\frac{x}{s_k} \right) B^n \left(\frac{y}{s_l} \right) B^n \left(\frac{\theta \bmod 2\pi}{s_m} \right)$. Vector \mathbf{c} is a $[N_k N_l N_m \times 1]$ column vector containing the B-spline coefficients and is stored as follows:

$$\mathbf{c} = (c_{1,1,1}, \dots, c_{1,1,N_m}, \dots, c_{1,N_l,N_m}, \dots, c_{N_k,N_l,N_m})^T. \quad (5.33)$$

The explicit expression and the derivation of $[N_k N_l N_m \times N_k N_l N_m]$ matrix \mathbf{R} , which encodes the left invariant derivatives, can be found in App. A.1.

5. RETINAL LANDMARK DETECTION

5.3.5.3 Logistic Regression

Also for the logistic regression case we optimize energy functional (5.29) in the same form as (5.10) in the \mathbb{R}^2 case, by using the corresponding expressions for \mathbf{S} , \mathbf{R} , and \mathbf{c} in Eq. (5.18). These expressions can be inserted in the functional (5.18) and again the same techniques (as presented in Subsection 5.2.4.3) can be used to minimize this cost on $SE(2)$.

5.4 Probabilistic Interpretation of the Smoothing Prior in $SE(2)$

In this section we relate the $SE(2)$ smoothing prior to time resolvent hypo-elliptic¹ diffusion processes on $SE(2)$. First we aim to familiarize the reader with the concept of resolvent diffusions on \mathbb{R}^2 in Subsec. 5.4.1. Then we pose in Subsec. 5.4.2 a new problem (the single patch problem), which is a special case of our $SE(2)$ linear regression problem, that we use to link the left-invariant regularizer to the resolvents of hypo-elliptic diffusions on $SE(2)$.

5.4.1 Resolvent Diffusion Processes

A classic approach to noise suppression in images is via diffusion regularizations with PDE's of the form Duits & Burgeth (2007)

$$\begin{cases} \frac{\partial}{\partial \tau} u &= \Delta u, \\ u|_{\tau=0} &= u_0, \end{cases} \quad (5.34)$$

where Δ denotes the Laplace operator. Solving (5.34) for any diffusion time $\tau > 0$ gives a smoothed version of the input u_0 . The time-resolvent process of the PDE is defined by the Laplace transform with respect to τ ; time τ is integrated out using a memoryless negative exponential distribution $P(\mathcal{T} = \tau) = \alpha e^{-\alpha \tau}$. Then, the time integrated solutions

$$t(\mathbf{x}) = \alpha \int_0^\infty u(\mathbf{x}, \tau) e^{-\alpha \tau} d\tau,$$

¹This diffusion process on $SE(2)$ is called *hypo-elliptic* as its generator equals $(\mathcal{A}_1)^2 + D_{33}(\mathcal{A}_3)^2$ and diffuses only in 2 directions in a 3D space. This boils down to a sub-Riemannian manifold structure Citti & Sarti (2006); Zhang *et al.* (2016b). Smoothing in the missing (\mathcal{A}_2) direction is achieved via the commutator: $[\partial_\theta, \cos \theta \partial_x + \sin \theta \partial_y] = -\sin \theta \partial_x + \cos \theta \partial_y$.

5.4 Probabilistic Interpretation of the Smoothing Prior in $SE(2)$

with decay parameter α , are in fact the solutions

$$t = \operatorname{argmin}_{t \in \mathbb{L}_2(\mathbb{R}^2)} \left[\|t - t_0\|_{\mathbb{L}_2(\mathbb{R}^2)}^2 + \lambda \int_{\mathbb{R}^2} \|\nabla t(\tilde{\mathbf{x}})\|^2 d\tilde{\mathbf{x}} \right], \quad (5.35)$$

with $\lambda = \alpha^{-1}$, and corresponding Euler-Lagrange equation

$$(I - \lambda \Delta)t = t_0 \iff t = \lambda^{-1} \left(\frac{1}{\lambda} - \Delta \right)^{-1} t_0, \quad (5.36)$$

to which we refer as the “resolvent” equation Yosida (1995), as it involves operator $(\alpha I - \Delta)^{-1}$, $\alpha = \lambda^{-1}$. In the next subsections, we follow a similar procedure with $SE(2)$ instead of \mathbb{R}^2 , and show how the smoothing regularizer in Eq. (5.27) and (5.29) relates to Laplace transforms of hypo-elliptic diffusions on the group $SE(2)$ Duits & Franken (2010a); Zhang *et al.* (2016b).

5.4.2 The Fundamental Single Patch Problem

In order to grasp what the (anisotropic regularization term) in Eq. (5.27) and (5.29) actually means in terms of stochastic interpretation/probabilistic line propagation, let us consider the following single patch problem and optimize

$$\begin{aligned} \mathcal{E}_{sp}(T) = & |(G_s *_{\mathbb{R}^2} T(\cdot, \cdot, \theta_0))(\mathbf{x}_0) - 1|^2 \\ & + \lambda \int_{\mathbb{R}^2} \int_0^{2\pi} \|\nabla T(\tilde{\mathbf{x}}, \tilde{\theta})\|_D^2 d\tilde{\mathbf{x}} d\tilde{\theta} + \mu \|T\|_{\mathbb{L}_2(SE(2))}^2, \end{aligned} \quad (5.37)$$

with $(\mathbf{x}_0, \theta_0) = g_0 := (x_0, y_0, \theta_0) \in SE(2)$ the fixed center of the template, and with spatial Gaussian kernel

$$G_s(\mathbf{x}) = \frac{1}{4\pi s} e^{-\frac{\|\mathbf{x}\|^2}{4s}}.$$

Regarding this problem, we note the following:

- In the original problem (5.27) we take $N = 1$, with

$$U_{f_1}(x, y, \theta) = G_s(x - x_0, y - y_0) \delta_{\theta_0}(\theta) \quad (5.38)$$

representing a local spatially smoothed spike in $SE(2)$, and set $y_1 = 1$. The general single patch case (for arbitrary U_{f_1}) can be deduced by superposition of such impulse responses.

- We use $\mu > 0$ to suppress the output elsewhere.

5. RETINAL LANDMARK DETECTION

- We use $0 < s \ll 1$. This minimum scale due to sampling removes the singularity at $(\mathbf{0}, 0)$ from the kernel that solves (5.37), as proven in Zhang *et al.* (2016b).

Theorem 1. *The solution to the single patch problem (5.37) coincides up to scalar multiplication with the time integrated hypo-elliptic Brownian motion kernel on $SE(2)$ (depicted in Fig. 5.3).*

Proof. We optimize $\mathcal{E}_{sp}(T)$ over the set $\mathcal{S}(SE(2))$ of all functions $T : SE(2) \rightarrow \mathbb{R}$ that are bounded and on $SE(2)$, infinitely differentiable on $SE(2) \setminus \{g_0\}$, and rapidly decreasing in spatial direction, and 2π periodic in θ . We omit topological details on function spaces and Hörmanders condition Hörmander (1967). Instead, we directly proceed with applying the Euler-Lagrange technique to the single patch problem:

$$\forall_{\delta \in \mathcal{S}(SE(2))} : \lim_{\epsilon \downarrow 0} \left\{ \frac{\mathcal{E}_{sp}(T + \epsilon\delta) - \mathcal{E}_{sp}(T)}{\epsilon} \right\} = 0 \Leftrightarrow (S_s^* S_s + \lambda R + \mu I)T = S_s^* y_1 = S_s^* 1, \quad (5.39)$$

with linear functional (distribution) \mathcal{S}_s given by

$$(S_s T) = (G_s *_{\mathbb{R}^2} T(\cdot, \theta_0))(\mathbf{x}_0),$$

and with regularization operator R given by

$$R = -\Delta_{SE(2)} := -(D_{11}\mathcal{A}_1^2 + D_{22}\mathcal{A}_2^2 + D_{33}\mathcal{A}_3^2) \geq 0.$$

Note that $\lim_{s \rightarrow 0} S_s = \delta_{(\mathbf{x}_0, \theta_0)}$ in distributional sense, and that the constraint $s > 0$ is crucial for solutions T to be bounded at (\mathbf{x}_0, θ_0) . By definition the adjoint operator S_s^* is given by

$$\begin{aligned} (S_s^* y, T)_{\mathbb{L}_2(SE(2))} &= (y, S_s T) = y \int_{\mathbb{R}^2} G_s(\mathbf{x} - \mathbf{x}_0) T(\mathbf{x}, \theta_0) d\mathbf{x} \\ &= y \int_0^{2\pi} \int_{\mathbb{R}^2} G_s(\mathbf{x} - \mathbf{x}_0) \delta_{\theta_0}(\theta) T(\mathbf{x}, \theta) d\mathbf{x} d\theta, \\ &= (y G_s(\cdot - \mathbf{x}_0) \delta_{\theta_0}(\cdot), T)_{\mathbb{L}_2(SE(2))} \end{aligned}$$

and thereby we deduce that

$$\begin{aligned} (S_s^* y)(\mathbf{x}, \theta) &= y G_s(\mathbf{x} - \mathbf{x}_0) \delta_{\theta_0}(\theta), \\ S_s^*(S_s T) &= T_0^s G_s(\mathbf{x} - \mathbf{x}_0) \delta_{\theta_0}(\theta), \end{aligned}$$

with $\infty > T_0^s := (G_s *_{\mathbb{R}^2} T(\cdot, \theta_0))(\mathbf{x}_0) > 1$ for $0 < s \ll 1$. The Euler-Lagrange equation (5.39) becomes

$$(-\lambda \Delta_{SE(2)} + \mu I)T = (1 - T_0^s) G_s(\mathbf{x} - \mathbf{x}_0) \delta_{\theta_0}(\theta).$$

5.4 Probabilistic Interpretation of the Smoothing Prior in $SE(2)$

Now, when setting $T_{new} = \frac{T}{1-T_0^s}$ we arrive at the hypo-elliptic resolvent equation on $SE(2)$:

$$\begin{aligned} (-\lambda\Delta_{SE(2)} + \mu I)T_{new} &= (G_s *_{\mathbb{R}^2} \delta_{\mathbf{x}_0})\delta_{\theta_0} \quad \Leftrightarrow \\ T_{new} &= (-\lambda\Delta_{SE(2)} + \mu I)^{-1} e^{s\Delta_{\mathbb{R}^2}} \delta_{g_0} \\ &= e^{s\Delta_{\mathbb{R}^2}} (-\lambda\Delta_{SE(2)} + \mu I)^{-1} \delta_{g_0} \end{aligned} \quad (5.40)$$

where we write $e^{s\Delta_{\mathbb{R}^2}} f = G_s *_{\mathbb{R}^2} f$ for the diffusion operator, to stress the vanishing commutators

$$[e^{s\Delta_{\mathbb{R}^2}}, \Delta_{SE(2)}] = e^{s\Delta_{\mathbb{R}^2}} \Delta_{SE(2)} - \Delta_{SE(2)} e^{s\Delta_{\mathbb{R}^2}} = 0,$$

which directly follows from $[\Delta_{\mathbb{R}^2}, \Delta_{SE(2)}] = 0$. In fact, from these vanishing commutators one can deduce that, thanks to the isotropy of Gaussian kernel, blurring with inner-scale $s > 0$ can be done either before applying the resolvent operator or after (as seen in (5.40)).

The solutions T_{new} are precisely the probabilistic kernels $R_{\alpha,s} : SE(2) \rightarrow \mathbb{R}$ for time integrated contour enhancements studied in Duits & Franken (2010a); Zhang *et al.* (2016b). In fact we see that

$$T_{new}(g) = \mu^{-1} R_{\alpha,s}(g_0^{-1} g),$$

where $R_{\alpha,s} = (I - \alpha^{-1}\Delta_{SE(2)})^{-1} e^{s\Delta_{\mathbb{R}^2}} \delta_{(\mathbf{0},0)}$ (i.e., the impuls response of the resolvent operator) denotes the time-integration of the hypo-elliptic diffusion kernel $K_{\tau,s} = e^{\tau\Delta_{SE(2)}} e^{s\Delta_{\mathbb{R}^2}} \delta_{(\mathbf{0},0)}$:

$$R_{\alpha,s}(g) = \alpha \int_0^\infty K_{\tau,s}(g) e^{-\alpha\tau} d\tau,$$

for which 3 different exact analytic formulas are derived in Duits & Franken (2010a). The kernel $R_{\alpha,s}(\mathbf{x}, \theta)$ denotes the probability density of finding a random brush stroke (regardless its traveling time) at location \mathbf{x} with orientation θ given that a ‘drunkman’s pencil’ starts at $g = (\mathbf{0}, 0)$ at time zero. Here the traveling time τ of the random pencil is assumed to be negatively exponentially distributed with expectation α^{-1} . \square

5.4.3 Expansion in B-splines

Now we consider the B-spline expansions (Eq. (5.31)) and apply our optimization algorithm to the single patch problem (5.37), with $(\mathbf{x}_0, \theta_0) = (\mathbf{0}, 0)$. Here we no longer need a smoothing with a continuous Gaussian G_s , as expansion in the B-spline basis already includes regularization. Now we set for the smooth spike $U_{f_1}(x, y, \theta) = B^n\left(\frac{x}{s_k}\right) B^n\left(\frac{y}{s_l}\right) B^n\left(\frac{\theta \bmod 2\pi}{s_m}\right)$, and we thus approximate spikes by the same B-spline

5. RETINAL LANDMARK DETECTION

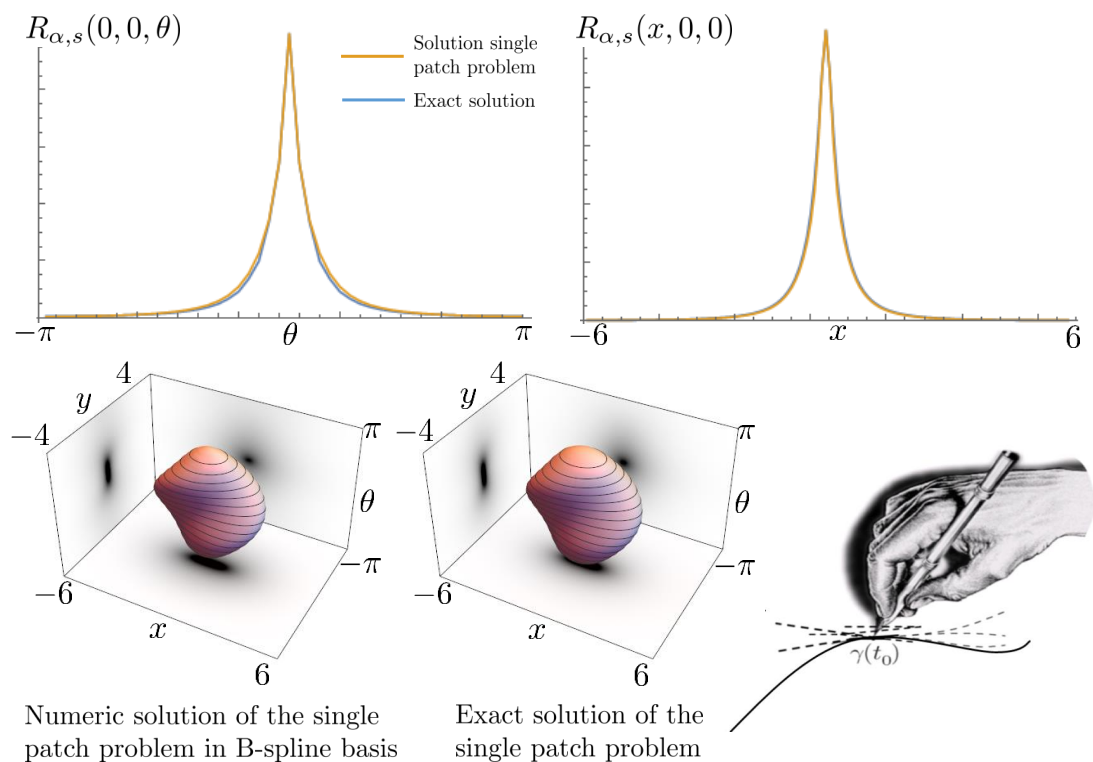


Figure 5.3: Top row: Comparison of kernel $R_{\alpha,s}(x, y, \theta)$ along respectively the θ and x axis. Bottom row: Isosurface of the kernel computed by solving the fundamental single patch problem (5.37), the exact solution, and an illustration of the drunkman's pencil in the xy -plane.

5.4 Probabilistic Interpretation of the Smoothing Prior in $SE(2)$

basis in which we expressed our templates. We accept extra regularization (like we did with the Gaussian in the previous section) and choose to represent a spike by a normal B-spline. After all, via the central limit theorem B-splines converge to Gaussians when increasing n . We also considered to instead use the fundamental B-Spline (Unser *et al.*, 1993, Fig. 2), which is sharper but suffers from oscillations, yielding less favorable results.

In our normal B-spline setting, this choice of smooth spike representation leads to the following equations

$$(\mathbf{S}^\dagger \mathbf{S} + \lambda \mathbf{R} + \mu \mathbf{I}) \mathbf{c} = \mathbf{S}^\dagger \mathbf{1},$$

with \mathbf{S} the $[1 \times N_k N_l N_m]$ -matrix with components $B_{s_k s_l s_m}(k, l, m)$. Akin to the previous derivations (5.40) this matrix-equation can be rewritten as

$$(\lambda \mathbf{R} + \mu \mathbf{I}) \mathbf{c}_{new} = \mathbf{S}^\dagger \mathbf{1}.$$

In particular our B -spline basis algorithm is a new algorithm that can be used for the resolvent (hypo-)elliptic diffusion process on $SE(2)$. The benefit over Fourier based algorithms is the local support of the basis functions, which allows for sparse representations.

In Fig. 5.3 we compare the impulse response for Tikhonov regularization via our B-spline expansion algorithm with the Brownian motion prior on $SE(2)$ (using a fine B-spline basis) to the exact solutions derived in Duits & Franken (2010a); Zhang *et al.* (2016b). The strong accuracy of our algorithm shows that even in the discrete B-spline setting the probabilistic interpretation (Thm. 1) of our prior in $SE(2)$ -template matching holds.

5.4.4 The Drunkman's Pencil

Similar to the diffusions on \mathbb{R}^2 , given by (5.34), the hypo-elliptic diffusion process on $SE(2)$ is described by the following PDE:

$$\begin{cases} \frac{\partial}{\partial \tau} W &= (D_{11}\mathcal{A}_1^2 + D_{33}\mathcal{A}_3^2)W, \\ W|_{\tau=0} &= W_0, \end{cases} \quad (5.41)$$

initialized with $W_0 \in \mathbb{L}_2(\mathbb{R}^2)$ at time $\tau = 0$. The PDE can be used to obtain the solutions of our single patch problem by initializing W_0 with a smooth spike such as we did in Subsec. 5.4.3, e.g., by setting $W_0(x, y, \theta) = U_{f_1}(x, y, \theta) = B^n\left(\frac{x}{s_k}\right) B^n\left(\frac{y}{s_l}\right) B^n\left(\frac{\theta \bmod 2\pi}{s_m}\right)$.

5. RETINAL LANDMARK DETECTION

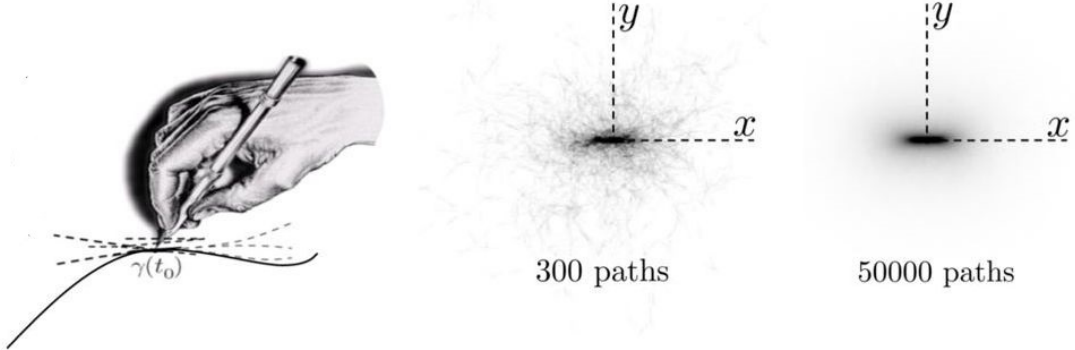


Figure 5.4: Stochastic random process for contour enhancement.

The PDE in (5.41) is the forward Kolmogorov equation Hsu (2002) of the following stochastic process Zhang *et al.* (2016b):

$$\begin{cases} \mathbf{x}(\tau) = \mathbf{x}(0) + \sqrt{2D_{11}} \epsilon_\xi \int_0^\tau (\cos \theta(\tau) \mathbf{e}_x + \sin \theta(\tau) \mathbf{e}_y) \frac{1}{2\sqrt{\tau}} d\tau \\ \theta(\tau) = \theta(0) + \sqrt{\tau} \sqrt{2D_{33}} \epsilon_\theta, \quad \epsilon_\xi, \epsilon_\theta \sim \mathcal{N}(0, 1), \end{cases} \quad (5.42)$$

where ϵ_ξ and ϵ_θ are sampled from a normal distribution with expectation 0 and unit standard deviation. The stochastic process in (5.42) can be interpreted as the motion of a drunkman's pencil: it randomly moves forward and backwards, and randomly changes its orientation along the way. The resolvent hypo-elliptic diffusion kernels $R_{\alpha,s}(g)$ (solutions to the fundamental single patch problem, up to scalar multiplication) can then also be obtained via Monte Carlo simulations, where the stochastic process is sampled many times with a negatively exponentially distributed traveling time ($P(\mathcal{T} = \tau) = \alpha e^{-\alpha\tau}$) in order to be able to estimate the probability density kernel $R_{\alpha,s}(g)$. This process is illustrated in Fig. 5.4.

5.5 Applications

Our applications of interest are in retinal image analysis. In this section we establish and validate an algorithm pipeline for the detection of the optic nerve head (Subsec. 5.5.2), the fovea (Subsec. 5.5.3), and the pupil (Subsec. 5.5.4). Before we proceed to the application sections, we first describe the experimental set-up (Subsec. 5.5.1). All experiments discussed in this section are reproducible; the data (with annotations) as well as the full code (Wolfram *Mathematica* notebooks) used in the experiments are made available at: <http://erikbekkers.bitbucket.io/TMSE2.html>.

5.5.1 The Experimental Set-Up

5.5.1.1 Templates

In our experiments we compare the performance of different template types, which we label as follows:

- A: Templates obtained by taking the average of all positive patches ($y_i = 1$) in the training set, then normalized to zero mean and unit standard deviation.
- B: Templates optimized without any regularization.
- C: Templates optimized with an optimal μ , and with $\lambda = 0$.
- D: Templates optimized with an optimal λ and with $\mu = 0$.
- E: Templates optimized with optimal μ and λ .

The trained templates (*B-E*) are obtained either via linear regression or logistic regression in the \mathbb{R}^2 setting (see Subsec. 5.2.4.2 and Subsec. 5.2.4.3), or in the $SE(2)$ setting (see Subsec. 5.3.5.2 and Subsec. 5.3.5.3). In both the \mathbb{R}^2 and $SE(2)$ case, linear regression based templates are indicated with subscript lin , and logistic regression based templates with log . Optimality of parameter values is defined using generalized cross validation (GCV), which we soon explain in Subsec. 5.5.1.3. We generally found that (via optimization using GCV) the optimal settings for template *E* were $\mu \approx 0.5\mu^*$, and $\lambda \approx 0.5\lambda^*$, with μ^* and λ^* respectively the optimal parameters for template *C* and *D*.

5.5.1.2 Matching with Multiple Templates

When performing template matching, we use Eq. (5.3) and Eq. (5.23) for respectively the \mathbb{R}^2 and $SE(2)$ case for templates obtained via linear regression and for template *A*. For templates obtained via logistic regression we use respectively Eq. (5.4) and Eq. (5.24). When we combine multiple templates we simply add the objective functionals. E.g, when combining template $C_{lin:\mathbb{R}^2}$ and $D_{log:SE(2)}$ we solve the problem

$$\mathbf{x}^* = \underset{\mathbf{x} \in \mathbb{R}^2}{\operatorname{argmax}} \ P_{C_{lin}}^{\mathbb{R}^2}(\mathbf{x}) + P_{D_{log}}^{SE(2)}(\mathbf{x}),$$

where $P_{C_{lin}}^{\mathbb{R}^2}(\mathbf{x})$ is the objective functional (see Eq. (5.3)) obtained with template $C_{lin:\mathbb{R}^2}$, and $P_{D_{log}}^{SE(2)}(\mathbf{x})$ (see Eq. (5.24)) is obtained with template $D_{log:SE(2)}$.

5. RETINAL LANDMARK DETECTION

5.5.1.3 Automatic Parameter Selection via Generalized Cross Validation

An ideal template generalizes well to new data samples, meaning that it has low prediction error on independent data samples. One method to predict how well the system generalizes to new data is via generalized cross validation (GCV), which is essentially an approximation of leave-one-out cross validation Craven & Wahba (1978). The vector containing all predictions is given by $\tilde{\mathbf{y}} = \mathbf{Sc}_{\mu,\lambda}$, in which we can substitute the solution for $\mathbf{c}_{\mu,\lambda}$ (from Eq. (5.13)) to obtain

$$\begin{aligned}\tilde{\mathbf{y}} &= \mathbf{A}_{\mu,\lambda} \mathbf{y}, && \text{with} \\ \mathbf{A}_{\mu,\lambda} &= \mathbf{S}(\mathbf{S}^\dagger \mathbf{S} + \lambda \mathbf{R} + \mu \mathbf{I})^{-1} \mathbf{S}^\dagger,\end{aligned}\tag{5.43}$$

where $\mathbf{A}_{\mu,\lambda}$ is the so-called *smoother matrix*. Then the generalized cross validation value Craven & Wahba (1978) is defined as

$$GCV(\mu, \lambda) \equiv \frac{\frac{1}{N} \|\Omega(\mathbf{I} - \mathbf{A}_{\mu,\lambda}) \mathbf{y}\|^2}{(1 - \text{trace}(\mathbf{A}_{\mu,\lambda})/N)^2}.\tag{5.44}$$

In the retinal imaging applications we set $\Omega = \mathbf{I}$. In the pupil detection application we set $\Omega = \underset{i \in \{1, \dots, N\}}{\text{diag}} \{y_i\}$. As such we do not penalize errors on negative samples, as in this application the diversity of negative patches is too large for parameter optimization via GCV. Parameter settings are considered optimal when they minimize the GCV value.

In literature various extensions of GCV are proposed for generalized linear models Gu (1992); O'sullivan *et al.* (1986); Xiang & Wahba (1996). For logistic regression we use the approach by O'Sullivan *et al.* O'sullivan *et al.* (1986): we iterate the Newton-Raphson algorithm until convergence, then, at the final iteration we compute the GCV value on the quadratic approximation (Eq. (5.21)).

5.5.1.4 Success Rates

Performance of the templates is evaluated using success rates. The success rate of a template is the percentage of images in which the target object was successfully localized. In both optic nerve head (Subsec. 5.5.2) and fovea (Subsec. 5.5.3) detection experiments, a successful detection is defined as such if the detected location \mathbf{x}^* (Eq. (5.2)) lies within one optic disk radius distance to the actual location. For pupil detection both the left and right eye need to be detected and we therefore use the following normalized error metric

$$e = \frac{\max(d_{left}, d_{right})}{w},\tag{5.45}$$

in which w is the (ground truth) distance between the left and right eye, and d_{left} and d_{right} are respectively the distances of detection locations to the ground truth positions of the left and right eye.

5.5.1.5 k-Fold Cross Validation

For correct unbiased evaluation, none of the test images are used for training of the templates, nor are they used for parameter optimization. We perform k -fold cross validation: The complete dataset is randomly partitioned into k subsets. Training (patch extraction, parameter optimization and template construction) is done using the data from $k - 1$ subsets. Template matching is then performed on the remaining subset. This is done for all k configurations with $k - 1$ training subsets and one test subset, allowing us to compute the average performance (success rate) and standard deviation. We set $k = 5$.

5.5.1.6 Training Samples

In all three applications training samples were used to compute the templates. Positive training samples were centered around the object of interest. Negative training samples were centered around random locations in the image, but not within a certain distances to the true positive object location. In the retinal applications this distance was one optic disk radius, in the pupil detection application this was a normalized distance of 0.1. An selection of the 2D image pathes that were used in the experiments are shown in Fig. 5.5.

5.5.2 Optic Nerve Head Detection in Retinal Images

Our first application to retinal images is optic nerve head detection. The ONH is one of the key anatomical landmarks in the retina, and its location is often used as a reference point to define regions of interest for the analysis of the retina. The detection hereof is therefore an essential step in many automated retinal image analysis pipelines.

The ONH has two main characteristics: 1) it often appears as a bright disk-like structure on color fundus (CF) images (dark on SLO images), and 2) it is the place from which blood vessels and nerve fibres leave (and enter) the retina. Traditionally, methods have mainly focused on the first characteristic Aquino *et al.* (2012); Dashtbozorg *et al.* (2015); Lu & Lim (2011). However, in case of bad contrast of the optic disk, or in the presence of pathology (especially bright lesions, see e.g. Fig. 5.6), these methods typically fail. Most of the recent ONH detection methods therefore also include the

5. RETINAL LANDMARK DETECTION



Figure 5.5: A selection of positive and negative image patches f_i used in the training of templates.

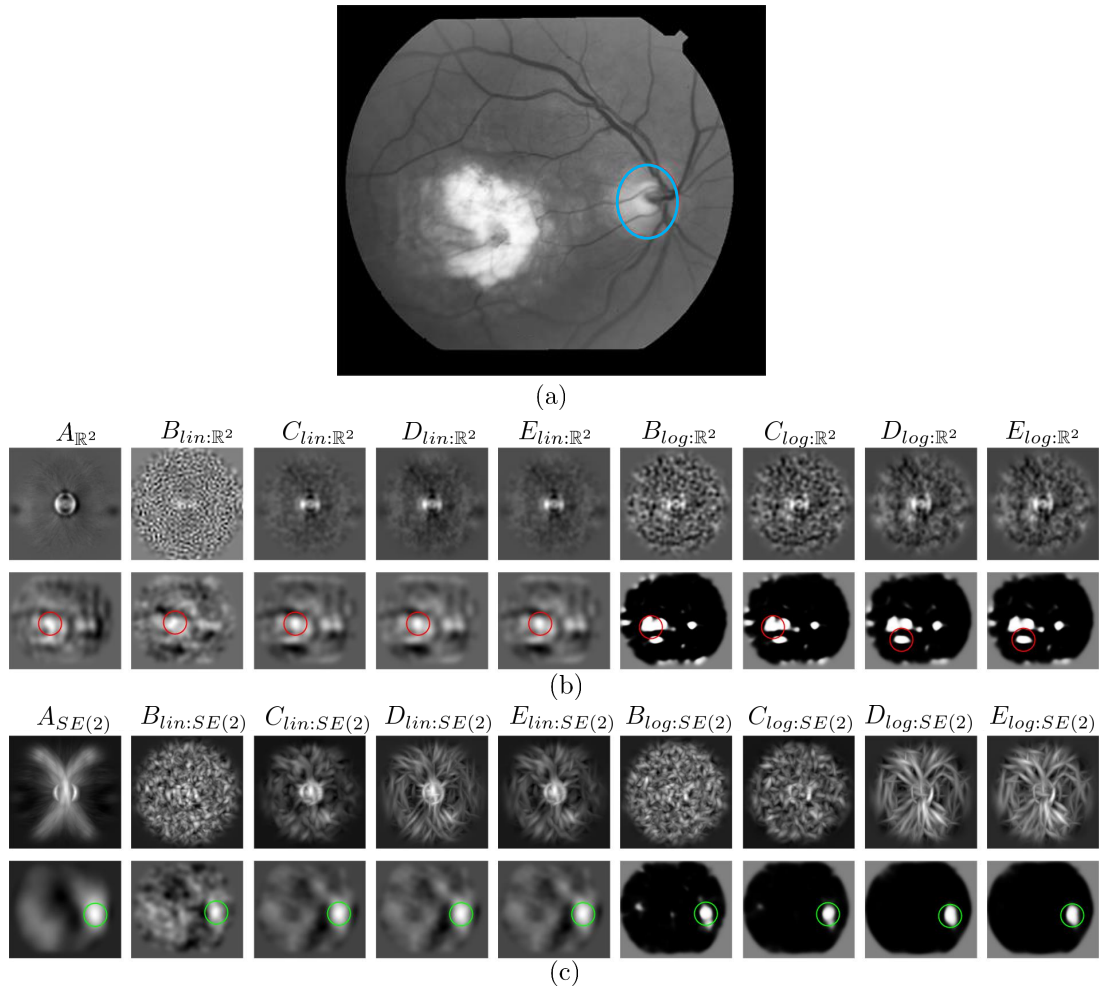


Figure 5.6: Overview of trained templates for ONH detection, and their responses to a challenging retinal image. (a) The example input image with true ONH location in blue. (b) The \mathbb{R}^2 -type templates (top row) and their responses to the input image (bottom row). (c) The maximum intensity projections (over θ) of the $SE(2)$ -type templates (top row) and their responses to the input image (bottom row). Detected ONH locations are indicated with colored circles (green = correct, red = incorrect).

5. RETINAL LANDMARK DETECTION

Table 5.1: Average template matching results (\pm standard deviation) for optic nerve head detection in 5-fold cross validation, number of failed detections in parentheses.

Template ID	ES (SLO)	TC 208	MESSIDOR 1200	DRIVE 40	STARE 81	All Images 1737
	\mathbb{R}^2 templates					
$A_{\mathbb{R}^2}$	96.20% \pm 2.63% (8)	99.60% \pm 0.89% (1)	98.75% \pm 0.29% (15)	95.56% \pm 6.09% (2)	73.23% \pm 10.13% (21)	97.30% \pm 0.32% (47)
$B_{lin:\mathbb{R}^2}$	82.57% \pm 5.54% (36)	61.66% \pm 8.00% (81)	42.93% \pm 2.16% (685)	40.22% \pm 24.65% (22)	16.43% \pm 9.38% (66)	48.76% \pm 2.99% (890)
$C_{lin:\mathbb{R}^2}$	88.95% \pm 3.66% (23)	100.0% \pm 0.00% (0)	98.51% \pm 0.68% (18)	97.78% \pm 4.97% (1)	68.87% \pm 11.18% (23)	96.26% \pm 1.10% (65)
$D_{lin:\mathbb{R}^2}$	88.91% \pm 2.31% (23)	100.0% \pm 0.00% (0)	98.17% \pm 0.55% (22)	97.78% \pm 4.97% (1)	68.87% \pm 11.18% (23)	96.03% \pm 0.97% (69)
$E_{lin:\mathbb{R}^2}$	88.95% \pm 2.73% (23)	100.0% \pm 0.00% (0)	98.34% \pm 0.56% (20)	97.78% \pm 4.97% (1)	70.04% \pm 10.94% (22)	96.20% \pm 0.89% (66)
$B_{log:\mathbb{R}^2}$	10.01% \pm 5.49% (187)	80.27% \pm 4.66% (42)	80.75% \pm 2.02% (231)	85.78% \pm 10.75% (5)	49.04% \pm 13.87% (39)	70.98% \pm 1.62% (504)
$C_{log:\mathbb{R}^2}$	31.73% \pm 5.18% (142)	87.81% \pm 7.17% (27)	89.26% \pm 1.63% (129)	86.06% \pm 10.03% (5)	52.70% \pm 14.65% (37)	80.43% \pm 1.97% (340)
$D_{log:\mathbb{R}^2}$	34.69% \pm 5.22% (136)	96.93% \pm 3.37% (7)	94.76% \pm 1.47% (63)	93.33% \pm 9.94% (3)	52.93% \pm 11.66% (37)	85.84% \pm 2.01% (246)
$E_{log:\mathbb{R}^2}$	25.03% \pm 5.19% (156)	96.48% \pm 3.75% (8)	94.18% \pm 1.09% (70)	93.33% \pm 9.94% (3)	50.21% \pm 11.37% (39)	84.11% \pm 1.75% (276)
<i>SE(2) templates</i>						
$A_{SE(2)}$	100.0% \pm 0.00% (0)	98.99% \pm 1.39% (2)	99.75% \pm 0.37% (3)	97.78% \pm 4.97% (1)	90.93% \pm 7.43% (6)	99.31% \pm 0.38% (12)
$B_{lin:SE(2)}$	95.67% \pm 3.17% (9)	94.65% \pm 3.37% (11)	93.35% \pm 1.95% (80)	95.28% \pm 6.48% (2)	73.82% \pm 7.96% (21)	92.92% \pm 1.67% (123)
$C_{lin:SE(2)}$	98.54% \pm 2.18% (3)	99.60% \pm 0.89% (1)	99.75% \pm 0.37% (3)	97.78% \pm 4.97% (1)	91.28% \pm 7.65% (6)	99.19% \pm 0.56% (14)
$D_{lin:SE(2)}$	94.67% \pm 5.31% (11)	99.60% \pm 0.89% (1)	99.42% \pm 0.63% (7)	97.78% \pm 4.97% (1)	90.10% \pm 6.31% (7)	98.44% \pm 0.83% (27)
$E_{lin:SE(2)}$	97.11% \pm 2.05% (6)	99.60% \pm 0.89% (1)	99.59% \pm 0.59% (5)	97.78% \pm 4.97% (1)	91.28% \pm 7.65% (6)	98.90% \pm 0.51% (19)
$B_{log:SE(2)}$	88.52% \pm 6.78% (24)	84.28% \pm 6.05% (33)	90.10% \pm 1.55% (19)	88.28% \pm 8.91% (4)	77.00% \pm 8.66% (18)	88.60% \pm 1.33% (198)
$C_{log:SE(2)}$	91.28% \pm 4.50% (18)	97.77% \pm 3.23% (9)	97.76% \pm 1.61% (27)	97.78% \pm 4.97% (1)	85.38% \pm 7.50% (11)	96.20% \pm 1.01% (66)
$D_{log:SE(2)}$	84.98% \pm 8.63% (31)	99.15% \pm 1.17% (2)	98.43% \pm 1.53% (19)	93.33% \pm 9.94% (3)	93.76% \pm 7.25% (5)	96.55% \pm 1.10% (60)
$E_{log:SE(2)}$	87.87% \pm 5.82% (25)	99.15% \pm 1.17% (2)	98.51% \pm 1.88% (18)	95.56% \pm 9.94% (2)	92.58% \pm 7.64% (6)	96.95% \pm 0.86% (53)
<i>Template combinations (sorted on performance)</i>						
$A_{\mathbb{R}^2}$ + $E_{log:SE(2)}$	100.0% \pm 0.00% (0)	100.0% \pm 0.00% (0)	99.84% \pm 0.22% (2)	97.78% \pm 4.97% (1)	98.82% \pm 2.63% (1)	99.83% \pm 0.26% (3)
$A_{\mathbb{R}^2}$ + $D_{log:SE(2)}$	100.0% \pm 0.00% (0)	100.0% \pm 0.00% (0)	99.84% \pm 0.22% (2)	97.78% \pm 4.97% (1)	98.82% \pm 2.63% (1)	99.83% \pm 0.26% (3)
$E_{lin:\mathbb{R}^2}$ + $E_{log:SE(2)}$	100.0% \pm 0.00% (0)	100.0% \pm 0.00% (0)	99.83% \pm 0.25% (2)	100.0% \pm 0.00% (0)	94.57% \pm 6.29% (4)	99.66% \pm 0.31% (6)
$D_{lin:\mathbb{R}^2}$ + $E_{log:SE(2)}$	100.0% \pm 0.00% (0)	100.0% \pm 0.00% (0)	99.83% \pm 0.23% (2)	100.0% \pm 0.00% (0)	94.57% \pm 6.29% (4)	99.66% \pm 0.31% (6)
$D_{lin:\mathbb{R}^2}$ + $D_{log:SE(2)}$	100.0% \pm 0.00% (0)	100.0% \pm 0.00% (0)	99.83% \pm 0.23% (2)	100.0% \pm 0.00% (0)	94.57% \pm 6.29% (4)	99.66% \pm 0.31% (6)
$C_{lin:\mathbb{R}^2}$ + $E_{log:SE(2)}$	100.0% \pm 0.00% (0)	99.83% \pm 0.23% (2)	100.0% \pm 0.00% (0)	94.57% \pm 6.29% (4)	99.66% \pm 0.31% (6)	99.66% \pm 0.31% (6)
$C_{lin:\mathbb{R}^2}$ + $D_{log:SE(2)}$	100.0% \pm 0.00% (0)	99.83% \pm 0.23% (2)	100.0% \pm 0.00% (0)	94.57% \pm 6.29% (4)	99.66% \pm 0.31% (6)	99.66% \pm 0.31% (6)
$A_{\mathbb{R}^2}$ + $C_{log:SE(2)}$	100.0% \pm 0.00% (0)	100.0% \pm 0.00% (0)	99.83% \pm 0.23% (2)	100.0% \pm 0.00% (0)	94.57% \pm 6.29% (4)	99.66% \pm 0.31% (6)
$A_{\mathbb{R}^2}$ + $E_{log:SE(2)}$	100.0% \pm 0.00% (0)	100.0% \pm 0.00% (0)	99.75% \pm 0.23% (3)	100.0% \pm 0.00% (0)	94.82% \pm 8.67% (3)	99.65% \pm 0.13% (6)

vessel patterns in the analysis; either via explicit vessel segmentation Marin *et al.* (2015); Sekhar *et al.* (2011), vessel density measures Giachetti *et al.* (2013); Yu *et al.* (2012), or via additional orientation pattern matching steps Youssif *et al.* (2008). In our method, both the appearance and vessel characteristics are addressed in an efficient integrated template matching approach, resulting in state-of-the-art performance both in terms of success rates and computation time. We target the first characteristic with template matching on \mathbb{R}^2 . The second is targeted with template matching on $SE(2)$.

5.5.2.1 Processing Pipeline

First, the images are rescaled to a working resolution of $40 \mu\text{m}/\text{pix}$. In our experiments the average resolution per dataset was determined using the average optic disk diameter (which is on average 1.84mm). The images are normalized for contrast and illumination variations using the method from Foracchia *et al.* (2005). Finally, in order to put more emphasis on contextual/shape information, rather than pixel intensities, we apply a soft binarization to the normalized image f via the mapping $\text{erf}(8f)$.

For the orientation score transform we use $N_\theta = 12$ uniformly sampled orientations from 0 to π and lift the image using cake wavelets Bekkers *et al.* (2014a); Duits *et al.* (2007b). For phase-invariant, nonlinear, left-invariant Duits & Franken (2010a), and contractive Bruna & Mallat (2013) processing on $SE(2)$, we work with the modulus of the complex valued orientation scores rather than with the complex-valued scores themselves (taking the modulus of quadrature filter responses is an effective technique for line detection, see e.g. Freeman *et al.* Freeman & Adelson (1991)).

Due to quite large differences in image characteristics, training and matching is done separately for the SLO and the color fundus images. For SLO images we use the near infrared channel, for RGB fundus images we use the green channel.

Positive training samples f_i are defined as $N_x \times N_y$ patches, with $N_x = N_y = 251$, centered around the true ONH location in each image. For every image, a negative sample is defined as an image patch centered around a random location in the image that does not lie within one optic disk radius distance to the true ONH location. An exemplary ONH patch is given in Fig. 5.1. For the B-spline expansion of the templates we set $N_k = N_l = 51$ and $N_m = 12$.

5.5.2.2 Data

In our experiments we made use of both publicly available data, and a private database. The private database consists of 208 SLO images taken with an EasyScan fundus camera

5. RETINAL LANDMARK DETECTION

(EasyScan B.V., the Netherlands) and 208 color fundus images taken with a Topcon NW200 (Topcon Corp., Japan). Both cameras were used to image both eyes of the same patient, taking an ONH centered image, and a fovea centered image per eye. The two sets of images are labeled as "ES" and "TC" respectively. The following (widely used) public databases are also used: MESSIDOR (<http://messidor.crihan.fr/index-en.php>), DRIVE (<http://www.isi.uu.nl/Research/Databases/DRIVE>) and STARE (<http://www.ces.clemson.edu/~ahoover/stare>), consisting of 1200, 40 and 81 color fundus images respectively. For each image, the circumference of the ONH was annotated manually, and parameterized by an ellipse. The annotations for the MESSIDOR dataset were kindly made available by the authors of Aquino *et al.* (2010) (<http://www.uhu.es/retinopathy>). The ONH contour in the remaining images were manually outlined by ourselves. The annotations are made available on our website (<http://erikbekkers.bitbucket.io/TMSE2.html>). The images in the databases contain a mix of good quality healthy images, and challenging diabetic retinopathy cases. Especially the MESSIDOR and STARE database contain challenging images.

5.5.2.3 Results and Discussion

The Templates The different templates for ONH detection are visualized in Fig. 5.6. The $SE(2)$ templates are visualized using maximum intensity projections over θ . In this figure we have also shown template responses to an example image. Visually one can clearly recognize the typical disk shape in the \mathbb{R}^2 templates, whereas the $SE(2)$ templates also seem to capture the typical pattern of outward radiating blood vessels (compare e.g. $A_{\mathbb{R}^2}$ with $A_{SE(2)}$). Indeed, when applied to a retinal image, where we took an example with an optic disk-like pathology, we see that the \mathbb{R}^2 templates respond well to the disk shape, but also (more strongly) to the pathology. In contrast, the $SE(2)$ templates respond mainly to vessel pattern and ignore the pathology. We also see, as expected, a smoothing effect of gradient based regularization (D and E) in comparison to standard \mathbb{L}_2 -norm regularization (C) and no regularization (B). Finally, in comparison to linear regression templates, the logistic regression templates have a more binary response due to the logistic sigmoid mapping.

Detection Results Table 5.1 gives a breakdown of the quantitative results for the different databases used in the experiments. The templates are grouped in \mathbb{R}^2 templates, $SE(2)$ templates, and combination of templates. Within these groups, they are further divided in average, linear regression, and logistic regression templates. The best overall performance within each group is highlighted in gray.

Overall, we see that the $SE(2)$ templates out-perform their \mathbb{R}^2 equivalents, and that

5.5 Applications

Table 5.2: Comparison to state of the art: Optic nerve head detection success rates, the number of fails (in parentheses), and computation times.

Method	MESSIDOR	DRIVE	STARE	Time (s)
Lu Lu (2011)	99.8% (3)		98.8% (1)	5.0
Lu et al. Lu & Lim (2011)		97.5% (1)	96.3% (3)	40.0
Yu et al. Yu et al. (2012)	99.1% (11)			4.7
Aquino et al. Aquino et al. (2012)	99.8% (14)			1.7
Giachetti et al. Giachetti et al. (2013)	99.7% (4)			5.0
Ramakanth et al. Ramakanth & Babu (2014)	99.4% (7)	100% (0)	93.83% (5)	0.2
Marin et al. Marin et al. (2015)	99.8% (3)			5.4 [†]
Dashtbozorg et al. Dashtbozorg et al. (2015)	99.8% (3)			10.6 [†]
Proposed	99.8% (2)	97.8% (1)	98.8% (1)	0.5

[†]Timings include simultaneous disk segmentation.

combinations of the two types of templates give best results. The two types are nicely complementary to each other due to the disk-like sensitivity of the \mathbb{R}^2 templates and the vessel pattern sensitivity of the $SE(2)$ templates. If one of the two ONH characteristics is less obvious (as is e.g. for the disk-shape in Fig. 5.6), the other can still be detected. Also, the failures of \mathbb{R}^2 templates are mainly due to either distracting pathologies in the retina, or poor contrast of the optic disk. As reflected by the increased performance of $SE(2)$ templates over \mathbb{R}^2 templates, a more stable pattern seems to be the (contextual) vessel pattern.

From Table 5.1 we also deduce that the individual performances of the linear regression templates outperform the logistic regression templates. Moreover, the average templates give best individual performance, which indicates that with our effective template matching framework good performance can already be achieved with basic templates . However, we also see that low performing individual templates can prove useful when combining templates. In fact, we see that combinations with all linear \mathbb{R}^2 templates are highly ranked, and for the $SE(2)$ templates it is mainly the logistic regression templates. This can be explained by the binary nature of the logistic templates: even when the maximum response of the templates is at an incorrect location, the difference with the correct location is often small. The \mathbb{R}^2 template then adds to the sensitivity and precision, as these response are often more fine and detailed. Finally, we observe that in the combination of templates smooth templates (D and E) are preferred.

5. RETINAL LANDMARK DETECTION

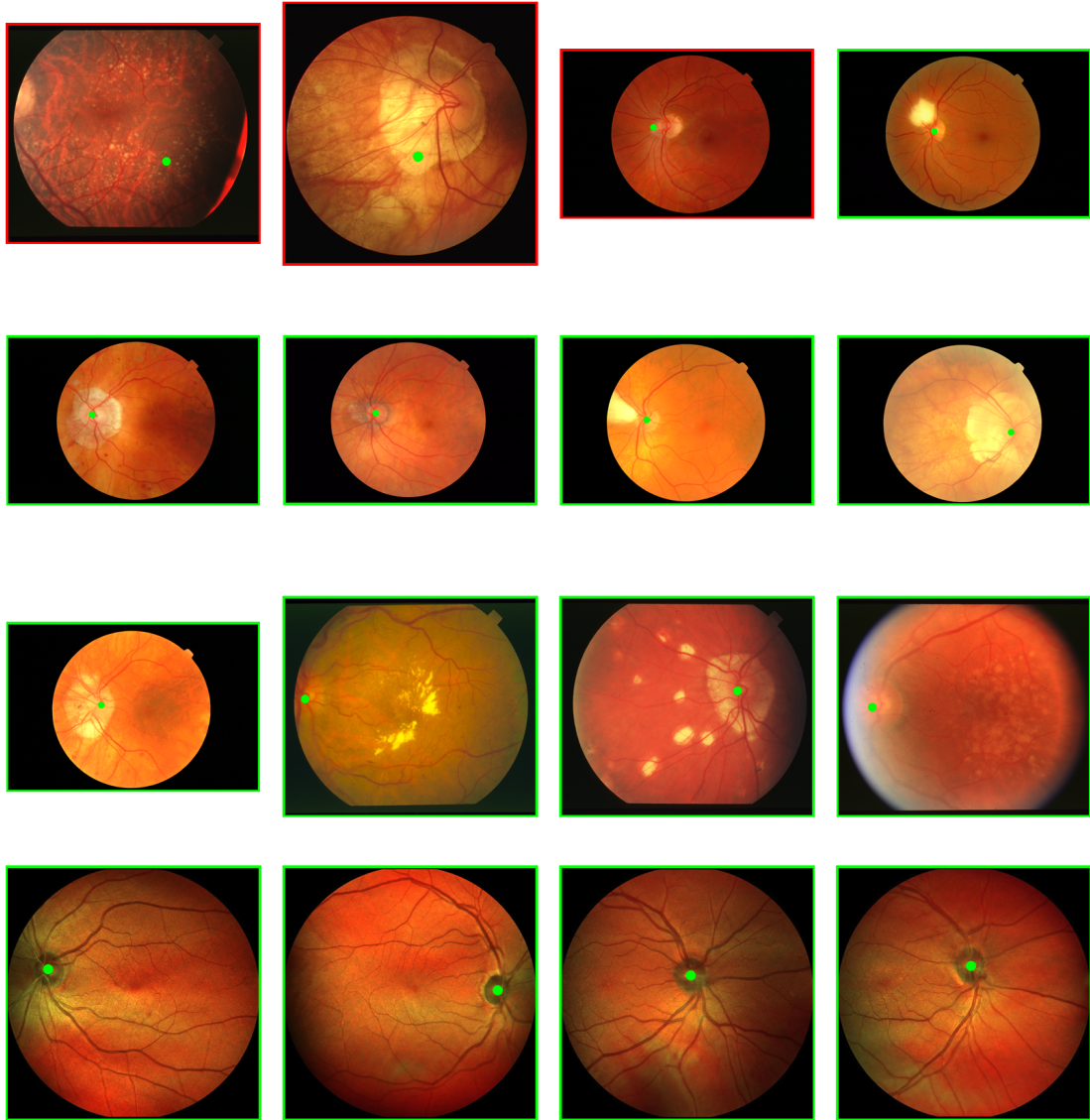


Figure 5.7: Detection results of our best method for optic nerve head detection in retinal images. Successful detections are indicated with a green frame around the image, failed detections are indicated with a red frame. In the ONH detection application there were only 3 failures in a set of 1737 images.

In Fig. 5.7 we show the 3 failed cases for ONH detection, and a selection of correct ONH localizations in difficult images.

State of the Art In Table 5.2 we compare our results on the publicly available benchmark databases MESSIDOR, DRIVE and STARE, with the most recent methods for ONH detection (sorted from oldest to newest from top to bottom). In this comparison, our best performing method ($A_{\mathbb{R}^2} + E_{log:SE(2)}$) performs better than or equally well as the best methods from literature. We have also listed the computation times, and see that our method is also ranked as one of the fastest methods for ONH detection. The average computation time, using our experimental implementation in Wolfram *Mathematica* 10.4, was 0.5 seconds per image on a computer with an Intel Core i703612QM CPU and 8GB memory. Here we note that in the retinal image datasets the maximum template response always occurs at rotation $\alpha = 0$, so for the sake of reduced computation time we have set $P^{SE(2)}(\mathbf{x}) := \tilde{P}^{SE(2)}(\mathbf{x}, 0)$ instead of (5.22). A detailed breakdown of timings of the full processing pipeline is given in App. A.3.1.

5.5.3 Fovea Detection in Retinal Images

Our second application to retinal images is for the detection of the fovea (recall Fig. 1.1). Since the foveal area is responsible for detailed vision, this area is weighted most heavily in grading schemes that describe the severity of a disease. Therefore, correct localization of the fovea is essential in automatic grading systems Abramoff & Niemeijer (2015); Agurto *et al.* (2011); van Grinsven *et al.* (2013).

Methods for the detection of the fovea heavily rely on contextual features in the retina Aquino (2014); Gegundez-Arias *et al.* (2013); Giachetti *et al.* (2013); Niemeijer *et al.* (2009); Yu *et al.* (2011), and take into account the prior knowledge that 1) the fovea is located approximately 2.5 optic disk diameters lateral to the ONH center, that 2) it lies within an avascular zone, and that 3) it is surrounded by the main vessel arcades. All of these methods restrict their search region for the fovea location to a region relative to the (automatically detected) ONH location. To the best of our knowledge, the proposed detection pipeline is the first that is completely independent of vessel segmentations and ONH detection. This is made possible due to the fact that anatomical reference patterns, in particular the vessel structures, are generically incorporated in the learned templates via data representations in orientation scores.

5.5.3.1 Processing Pipeline

The proposed fovea detection pipeline is the same as for ONH detection, however, now the positive training samples f_i are centered around the fovea.

5. RETINAL LANDMARK DETECTION

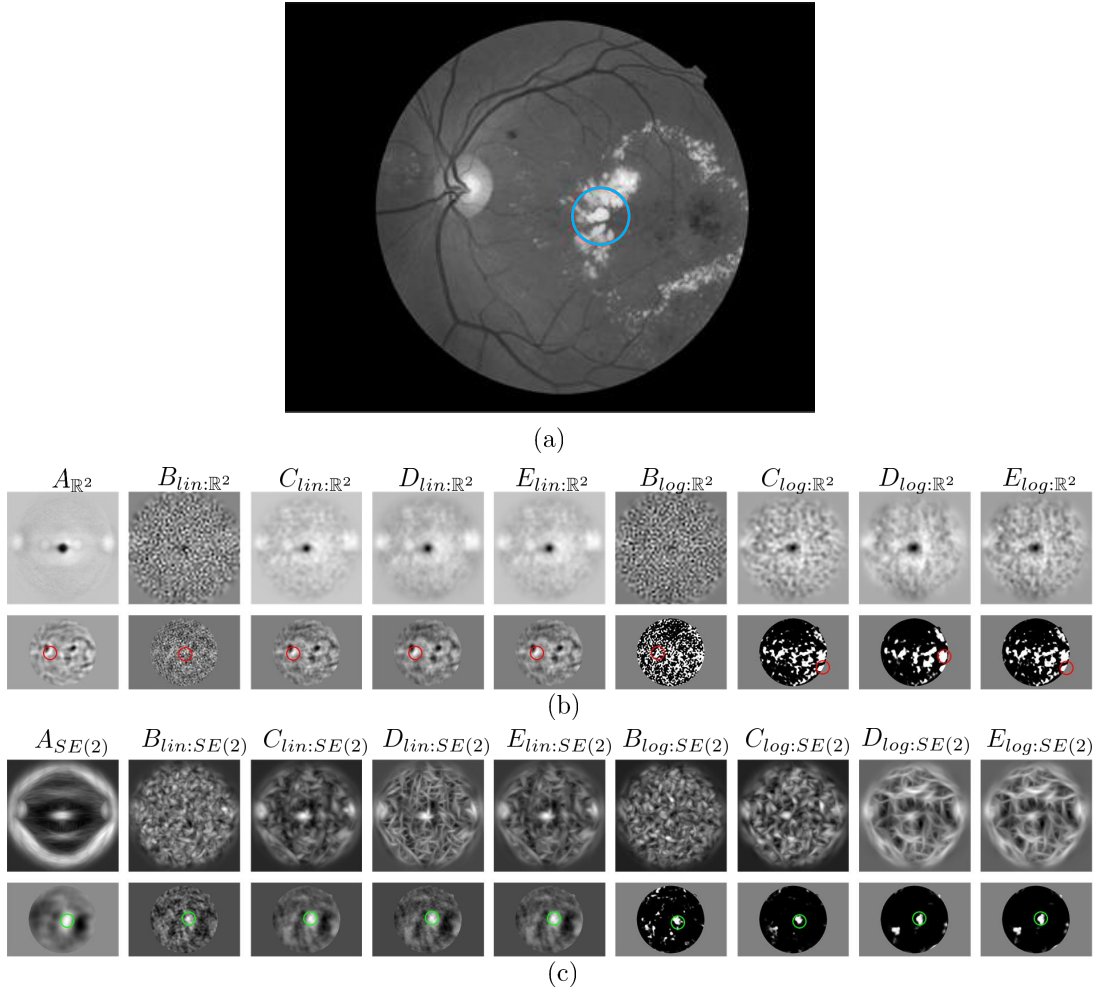


Figure 5.8: Overview of trained templates for fovea detection, and their responses to a challenging retinal image. (a) The example input image with true fovea location in blue. (b) The \mathbb{R}^2 -type templates (top row) and their responses to the input image (bottom row). (c) The maximum intensity projections (over θ) of the $SE(2)$ -type templates (top row) and their responses to the input image (bottom row). Detected fovea locations are indicated with colored circles (green = correct, red = incorrect).

5.5.3.2 Data

The proposed fovea detection method is validated on our (annotated) databases “ES” and “TC”, each consisting of 208 SLO and 208 color fundus images respectively (cf. Subsec.5.5.2.2). We further test our method on the popular publicly available benchmark dataset MESSIDOR (1200 images). Success rates were computed based on the fovea annotations kindly made available by the authors of Gegundez-Arias *et al.* (2013).

5.5.3.3 Results and Discussion

The Templates Akin to Fig. 5.6, in Fig. 5.8 the trained fovea templates and their responses to an input image are visualized. The \mathbb{R}^2 templates seem to be more tuned towards the dark (isotropic) blob like appearance of the fovea, whereas in the $SE(2)$ templates one can also recognize the pattern of vessels surrounding the fovea (compare $A_{\mathbb{R}^2}$ with $A_{SE(2)}$). To illustrate the difference between these type of templates, we selected an image in which the fovea location is occluded by bright lesions. In this case the method has to rely on contextual information (e.g. the blood vessels). Indeed, we see that the \mathbb{R}^2 templates fail due to the absence of a clear foveal blob shape, and that the $SE(2)$ templates correctly identify the fovea location. The effect of regularization is also clearly visible; no regularization (B) results in noisy templates, standard L_2 regularization (C) results in more stable templates, and smoothed regularization (D and E) results in smooth templates. In templates $D_{SE(2)}$ and $E_{SE(2)}$ we see that more emphasis is put on line structures.

Detection Results. A Table of detection performance for each type of template is provided in Tab. 5.3. Again there is an improvement using $SE(2)$ templates over \mathbb{R}^2 templates, although the difference is smaller than in the ONH application. Apparently both the dark blob-like appearance (\mathbb{R}^2 templates) and vessel patterns ($SE(2)$ templates) are equally reliable features of the fovea. A combination of templates leads to improved results and we conclude that the templates are again complementary to each other. Furthermore, again linear regression performs better than logistic regression. In fovea detection we do observe a large improvement of template training over basic averaging: 1529 (of 1616) successful detections with $C_{lin:SE(2)}$ versus 1488 with $A_{SE(2)}$. The best performing \mathbb{R}^2 template was $A_{\mathbb{R}^2}$, the best $SE(2)$ template was $C_{lin:SE(2)}$, and the best combination was $C_{lin:\mathbb{R}^2} + C_{log:SE(2)}$.

As can also be read from Tab. 5.3, we found that fovea detection in SLO images was significantly more difficult than fovea detection in CF images. The reason for this is that on SLO images the clear dark blob-like shape is not always present on these

Table 5.3: Average template matching results (\pm standard deviation) for fovea detection in 5-fold cross validation, number of failed detections in parentheses.

Template ID	ES (SLO)	TC	MESSIDOR	All Images
	208	208	1200	1616
\mathbb{R}^2 templates				
$A_{\mathbb{R}^2}$	76.36% \pm 6.79% (49)	98.24% \pm 2.74% (3)	98.41% \pm 0.22% (19)	95.60% \pm 0.98% (71)
$B_{lin:\mathbb{R}^2}$	23.50% \pm 3.81% (159)	31.66% \pm 9.03% (142)	51.19% \pm 5.97% (587)	45.07% \pm 3.33% (888)
$C_{lin:\mathbb{R}^2}$	45.65% \pm 8.61% (113)	98.24% \pm 2.74% (3)	98.59% \pm 0.36% (17)	91.77% \pm 1.26% (133)
$D_{lin:\mathbb{R}^2}$	44.21% \pm 4.62% (116)	98.49% \pm 1.14% (1)	98.84% \pm 0.31% (14)	91.90% \pm 0.59% (131)
$E_{lin:\mathbb{R}^2}$	46.10% \pm 8.11% (112)	98.86% \pm 1.57% (2)	98.67% \pm 0.34% (16)	91.95% \pm 1.18% (130)
$B_{log:\mathbb{R}^2}$	1.43% \pm 1.31% (205)	10.27% \pm 5.09% (185)	20.07% \pm 3.00% (959)	16.53% \pm 2.52% (1349)
$C_{log:\mathbb{R}^2}$	9.59% \pm 3.74% (188)	70.30% \pm 8.57% (61)	77.61% \pm 4.64% (267)	68.06% \pm 3.53% (516)
$D_{log:\mathbb{R}^2}$	11.48% \pm 4.70% (184)	83.47% \pm 7.80% (32)	88.22% \pm 2.81% (141)	77.90% \pm 2.00% (357)
$E_{log:\mathbb{R}^2}$	2.86% \pm 2.62% (202)	79.68% \pm 7.92% (40)	84.79% \pm 5.16% (181)	73.82% \pm 2.62% (423)
$SE(2)$ templates				
$A_{SE(2)}$	67.81% \pm 4.69% (67)	79.13% \pm 9.11% (40)	98.25% \pm 0.68% (21)	92.08% \pm 0.84% (128)
$B_{lin:SE(2)}$	83.19% \pm 2.76% (35)	71.53% \pm 7.36% (58)	91.31% \pm 0.68% (104)	87.81% \pm 1.25% (197)
$C_{lin:SE(2)}$	83.65% \pm 3.18% (34)	84.13% \pm 6.25% (32)	98.23% \pm 1.04% (21)	94.62% \pm 0.36% (87)
$D_{lin:SE(2)}$	73.57% \pm 4.71% (55)	83.69% \pm 6.83% (33)	97.88% \pm 1.17% (25)	93.01% \pm 1.09% (113)
$E_{lin:SE(2)}$	77.83% \pm 4.29% (46)	84.88% \pm 6.69% (30)	98.22% \pm 1.23% (21)	94.00% \pm 0.93% (97)
$B_{log:SE(2)}$	75.49% \pm 5.73% (51)	60.80% \pm 5.68% (80)	92.79% \pm 1.98% (86)	86.56% \pm 2.20% (217)
$C_{log:SE(2)}$	79.33% \pm 6.57% (43)	70.87% \pm 10.28% (59)	96.90% \pm 0.71% (37)	91.39% \pm 1.36% (139)
$D_{log:SE(2)}$	62.09% \pm 6.66% (79)	72.57% \pm 8.59% (54)	96.64% \pm 0.05% (40)	89.30% \pm 0.63% (173)
$E_{log:SE(2)}$	68.34% \pm 8.59% (66)	72.20% \pm 8.53% (55)	96.57% \pm 0.96% (41)	89.98% \pm 1.25% (162)
Template combinations (sorted on performance)				
$C_{lin:\mathbb{R}^2} + C_{log:SE(2)}$	97.17% \pm 3.01% (6)	99.17% \pm 1.13% (2)	99.74% \pm 0.38% (3)	99.32% \pm 0.26% (11)
$A_{\mathbb{R}^2} + C_{lin:SE(2)}$	98.08% \pm 2.03% (4)	98.07% \pm 1.95% (4)	99.68% \pm 0.33% (4)	99.26% \pm 0.47% (12)
$E_{lin:\mathbb{R}^2} + C_{log:SE(2)}$	96.20% \pm 3.15% (8)	99.17% \pm 1.13% (2)	99.75% \pm 0.23% (3)	99.20% \pm 0.35% (13)
$E_{lin:\mathbb{R}^2} + C_{lin:SE(2)}$	96.65% \pm 2.13% (7)	99.17% \pm 1.13% (2)	99.66% \pm 0.36% (4)	99.19% \pm 0.42% (13)
$C_{lin:\mathbb{R}^2} + C_{lin:SE(2)}$	97.14% \pm 1.97% (6)	98.78% \pm 1.78% (3)	99.58% \pm 0.31% (5)	99.13% \pm 0.40% (14)
$A_{\mathbb{R}^2} + E_{lin:SE(2)}$	97.55% \pm 1.73% (5)	98.07% \pm 1.95% (4)	99.59% \pm 0.28% (5)	99.13% \pm 0.25% (14)
$E_{lin:\mathbb{R}^2} + E_{lin:SE(2)}$	96.16% \pm 2.76% (8)	99.17% \pm 1.13% (2)	99.58% \pm 0.31% (5)	99.07% \pm 0.38% (15)
$E_{lin:\mathbb{R}^2} + D_{lin:SE(2)}$	95.71% \pm 3.07% (9)	99.17% \pm 1.13% (2)	99.58% \pm 0.31% (5)	99.01% \pm 0.40% (16)
$C_{lin:\mathbb{R}^2} + E_{lin:SE(2)}$	96.16% \pm 2.76% (8)	98.78% \pm 1.78% (3)	99.58% \pm 0.31% (5)	99.01% \pm 0.51% (16)
$A_{\mathbb{R}^2} + C_{log:SE(2)}$	96.65% \pm 2.13% (7)	98.07% \pm 1.95% (4)	99.58% \pm 0.42% (5)	99.01% \pm 0.26% (16)

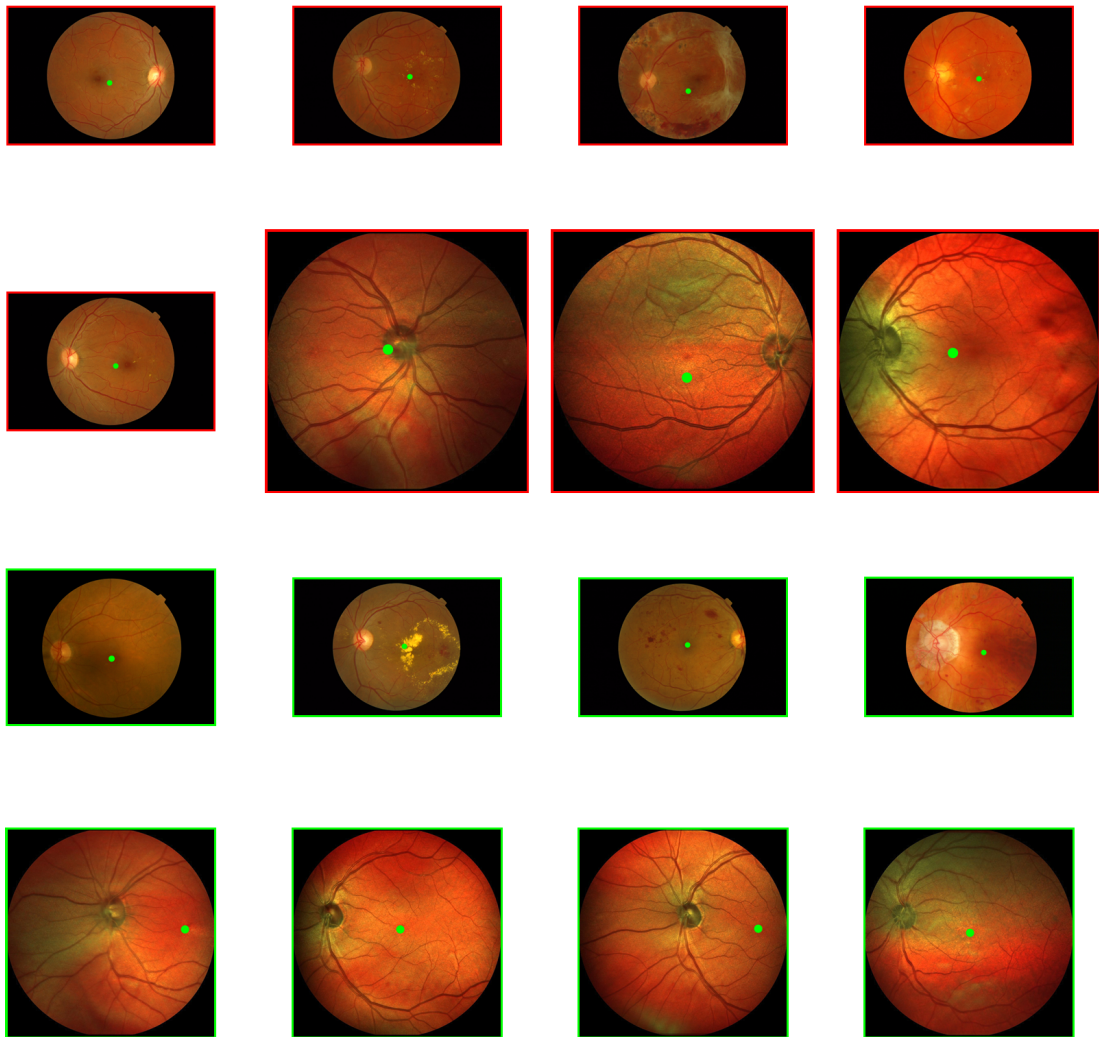


Figure 5.9: Detection results of our best method for fovea detection in retinal images. Successful detections are indicated with a green frame around the image, failed detections are indicated with a red frame. In the fovea detection application there were only 5 fails in a set of 1408 conventional color fundus (CF) camera images. Out of the 208 scanning laser ophthalmoscopy (SLO) images there were 6 failures, 3 of them are shown in this figure.

5. RETINAL LANDMARK DETECTION

Table 5.4: Comparison to state of the art: Fovea detection success rates, the number of fails (in parentheses), and computation times.

Method	MESSIDOR		Time (s)
Niemeijer et al. Gegundez-Arias et al. (2013); Niemeijer et al. (2009)	97.9%	(25)	7.6 [†]
Yu et al. Yu et al. (2011)	95.0%*	(60)	3.9 [†]
Gegundez-Arias et al. Gegundez-Arias et al. (2013)	96.9%	(37)	0.9
Giachetti et al. Giachetti et al. (2013)	99.1%	(11)	5.0 [†]
Aquino Aquino (2014)	98.2%	(21)	10.9 [†]
Proposed	99.7%	(3)	0.5

* Success-criterion based on half optic radius.

[†] Timing includes ONH detection.

images. Compare for example the positive fovea patches from Fig. 5.5 (where one generally sees a dark blob at the center) with the fovea locations in the bottom row of images in Figs. 5.7 and 5.9.

Additionally, the ES (SLO) and CF databases are also more difficult than the MESSIDOR database for fovea detection, as these two databases contain a mix of both fovea centered and ONH centered images. The MESSIDOR database contains only fovea centered images, in which case the fovea is always located around the center of the image. Therefore, even though MESSIDOR is one of the most used databases, it might not be the most representative database for fovea detection benchmarking.

In Fig. 5.9 we show next to a selection of successful detections the only 5 failed cases on images from conventional color fundus (CF) cameras (TC, MESSIDOR, DRIVE, STARE), and 3 of the failed detections in images coming from a scanning laser ophthalmoscopy (SLO) camera.

State of the Art In Table 5.4 we compared our results on the publicly available benchmark database MESSIDOR with the most recent methods for fovea detection (sorted from oldest to newest from top to bottom). In this comparison, our best performing method ($C_{lin:\mathbb{R}^2} + C_{log:SE(2)}$) quite significantly outperforms the best methods from literature. Furthermore, our detection pipeline is also the most efficient one; the computation time for fovea detection is the same as for ONH detection, which is 0.5 seconds.

5.5.4 Pupil Detection

Our third application is that of pupil localization in regular camera images, which is relevant in many applications as they provide important visual cues for face detection,

face recognition, and understanding of facial expressions. In particular in gaze estimation the accurate localization of the pupil is essential. Eye detection and tracking is however challenging due to, amongst others: occlusion by the eyelids and variability in size, shape, reflectivity, or head pose.

Many pupil localization algorithms are designed to work on periocular images, these are close-up views of the eyes. Such images can be acquired by dedicated eye imaging devices, or by means of cropping a full facial image (see Fig. 5.11(a)). We will consider both the problem of detection pupils in periocular images and the more difficult problem of detection in full images.

We compare our method against the seven most recent pupil detection methods from literature, for a full overview see Leo *et al.* (2014) and Markuš *et al.* (2014). A method similar to our \mathbb{R}^2 approach (in the sense that it is also based on 2D linear filtering) is the method by Kroon *et al.* Kroon *et al.* (2008). In their paper templates are obtained via linear discriminant analysis of pupil images. Asteriadis *et al.* Asteriadis *et al.* (2009) detect the pupil by matching templates using features that are based on distances to the nearest strong (facial) edges in the image. Campadelli *et al.* Campadelli *et al.* (2009) use a supervised approach with a SVM classifier and Haar wavelet features. The method by Timm *et al.* Timm & Barth (2011) is based on searching for gradient fields with a circular symmetry. Valenti *et al.* Valenti & Gevers (2012) use a similar approach but additionally include information of isophote curvature, with supervised refinement. Markus *et al.* Markuš *et al.* (2014) employ a supervised approach using an ensemble of randomized regression trees. Leo *et al.* Leo *et al.* (2014) employ a completely unsupervised approach similar to those in Timm & Barth (2011); Valenti & Gevers (2012), but additionally include analysis of self-similarity.

A relevant remark is that all of the above mentioned methods rely on prior face detection, and restrict their search region to periocular images. Our method works completely stand alone, and can be used on full images.

5.5.4.1 Processing Pipeline

Interestingly, we could again employ the same processing pipeline (including local normalization via Foracchia *et al.* (2005)) which was used for ONH and fovea detection. In our experiments we train templates for the left and right eye separately.

5. RETINAL LANDMARK DETECTION



Figure 5.10: Detection results of our best method for pupil detection. Successful detection are indicated with a green frame around the image, failed detections are indicated with a red frame.

5.5.4.2 Data

We validated our pupil detection approach on the publicly available BioID database (<http://www.bioid.com>), which is generally considered as one of the most challenging and realistic databases for pupil detection in facial images. The database consists of 1521 frontal face grayscale images with significant variation in illumination, scale and pose.

5.5.4.3 Results and Discussion

The Templates Fig. 5.11(b) and (c) show respectively the trained \mathbb{R}^2 and $SE(2)$ templates for pupil detection of the right eye, and their filtering response to the input image in Fig. 5.11(a). Here the trained \mathbb{R}^2 templates seemed to capture the pupil as a

5.5 Applications

Table 5.5: Average template matching results (\pm standard deviation) for pupil detection in 5-fold cross validation, number of failed detections in parentheses. A successful detection has a normalized error $e \leq 0.1$.

Template ID	BioID (Full image) 1521	BioID (Periocular image) 1521
\mathbb{R}^2 templates		
$A_{\mathbb{R}^2}$	41.03% \pm 1.45% (897)	59.70% \pm 1.52% (613)
$B_{lin:\mathbb{R}^2}$	0.00% \pm 0.00% (1521)	3.62% \pm 1.09% (1466)
$C_{lin:\mathbb{R}^2}$	12.95% \pm 2.22% (1324)	67.26% \pm 2.55% (498)
$D_{lin:\mathbb{R}^2}$	8.28% \pm 1.80% (1395)	75.68% \pm 2.33% (370)
$E_{lin:\mathbb{R}^2}$	11.51% \pm 2.25% (1346)	71.47% \pm 2.76% (434)
$B_{log:\mathbb{R}^2}$	0.00% \pm 0.00% (1521)	0.00% \pm 0.00% (1521)
$C_{log:\mathbb{R}^2}$	12.89% \pm 2.06% (1325)	39.91% \pm 3.37% (914)
$D_{log:\mathbb{R}^2}$	1.84% \pm 0.95% (1493)	22.09% \pm 2.37% (1185)
$E_{log:\mathbb{R}^2}$	10.39% \pm 2.26% (1363)	37.21% \pm 4.37% (955)
$SE(2)$ templates		
$A_{SE(2)}$	57.72% \pm 1.68% (643)	75.34% \pm 1.31% (375)
$B_{lin:SE(2)}$	8.74% \pm 2.00% (1388)	41.81% \pm 5.04% (885)
$C_{lin:SE(2)}$	84.61% \pm 4.19% (234)	86.78% \pm 3.68% (201)
$D_{lin:SE(2)}$	85.53% \pm 3.44% (220)	87.18% \pm 3.71% (195)
$E_{lin:SE(2)}$	85.47% \pm 3.82% (221)	87.11% \pm 3.87% (196)
$B_{log:SE(2)}$	0.00% \pm 0.00% (1521)	0.13% \pm 0.29% (1519)
$C_{log:SE(2)}$	86.52% \pm 0.77% (205)	93.95% \pm 1.33% (92)
$D_{log:SE(2)}$	75.21% \pm 2.18% (377)	89.48% \pm 2.27% (160)
$E_{log:SE(2)}$	83.30% \pm 1.68% (254)	92.77% \pm 1.02% (110)
Template combinations (sorted on performance full image)		
$C_{lin:\mathbb{R}^2} + E_{lin:SE(2)}$	93.49% \pm 1.49% (99)	95.60% \pm 1.46% (67)
$C_{lin:\mathbb{R}^2} + D_{lin:SE(2)}$	93.16% \pm 1.54% (104)	95.00% \pm 1.15% (76)
$E_{lin:\mathbb{R}^2} + E_{lin:SE(2)}$	93.10% \pm 1.04% (105)	95.59% \pm 0.89% (67)
$E_{lin:\mathbb{R}^2} + D_{lin:SE(2)}$	92.97% \pm 1.62% (107)	95.27% \pm 1.31% (72)
$C_{lin:\mathbb{R}^2} + C_{lin:SE(2)}$	92.70% \pm 1.41% (111)	95.33% \pm 0.97% (71)
$E_{lin:\mathbb{R}^2} + C_{lin:SE(2)}$	92.64% \pm 0.94% (112)	95.33% \pm 0.94% (71)
$D_{lin:\mathbb{R}^2} + D_{lin:SE(2)}$	92.51% \pm 0.96% (114)	95.79% \pm 0.82% (64)
$D_{lin:\mathbb{R}^2} + E_{lin:SE(2)}$	92.24% \pm 1.23% (118)	95.86% \pm 0.89% (63)
$E_{log:\mathbb{R}^2} + D_{lin:SE(2)}$	92.11% \pm 2.26% (120)	93.23% \pm 1.93% (103)
$D_{lin:\mathbb{R}^2} + C_{log:SE(2)}$	92.05% \pm 1.52% (121)	95.14% \pm 0.78% (74)
Template combinations (sorted on performance periorcular image)		
$D_{lin:\mathbb{R}^2} + E_{lin:SE(2)}$	92.24% \pm 1.23% (118)	95.86% \pm 0.89% (63)
$D_{lin:\mathbb{R}^2} + D_{lin:SE(2)}$	92.51% \pm 0.96% (114)	95.79% \pm 0.82% (64)
$D_{lin:\mathbb{R}^2} + C_{lin:SE(2)}$	91.52% \pm 1.25% (129)	95.73% \pm 0.77% (65)
$E_{lin:\mathbb{R}^2} + E_{lin:SE(2)}$	93.10% \pm 1.04% (105)	95.59% \pm 0.89% (67)
$C_{lin:\mathbb{R}^2} + E_{lin:SE(2)}$	93.49% \pm 1.49% (99)	95.60% \pm 1.46% (67)
$E_{lin:\mathbb{R}^2} + C_{lin:SE(2)}$	92.64% \pm 0.94% (112)	95.33% \pm 0.94% (71)
$C_{lin:\mathbb{R}^2} + C_{lin:SE(2)}$	92.70% \pm 1.41% (111)	95.33% \pm 0.97% (71)
$E_{lin:\mathbb{R}^2} + D_{lin:SE(2)}$	92.97% \pm 1.62% (107)	95.27% \pm 1.31% (72)
$D_{lin:\mathbb{R}^2} + E_{log:SE(2)}$	91.72% \pm 1.23% (126)	95.27% \pm 0.79% (72)
$D_{lin:\mathbb{R}^2} + C_{log:SE(2)}$	92.05% \pm 1.52% (121)	95.14% \pm 0.78% (74)

5. RETINAL LANDMARK DETECTION

small blob in the center of the template, but apart from that no real structure can be observed. In the average template we do however clearly see structure in the form of an “average face”. The $SE(2)$ templates reveal structures that resemble the eyelids in nearly all templates. The linear regression templates look sharper and seem to contain more detail than the average template, and the logistic regression templates seem to take a good compromise between coarse features and details.

Detection Results A Table of detection performance for each type of template is provided in Tab. 5.5. In terms of success rates we see a similar pattern as with the ONH and fovea application, however, here we see that the learned templates (C , D and E) significantly outperform the average templates, and that logistic regression leads to better templates than using linear regression. Overall, the $SE(2)$ templates outperform the \mathbb{R}^2 templates, linear regression templates outperform the average template, and (regularized) logistic regression templates outperform linear regression templates. The best \mathbb{R}^2 template was $D_{lin:\mathbb{R}^2}$, the best $SE(2)$ template was $C_{log:SE(2)}$. The best combination of templates was $D_{lin:\mathbb{R}^2}$ with $E_{lin:SE(2)}$. Success rates (under condition $e \leq 0.1$, recall (5.45)) using these templates are given in Fig. 5.12(a) and (b). The processing time for detection both pupils simultaneously was on average 0.7 seconds per image.

In Fig. 5.10 we show a selection of failed and successful detections. By inspection of the failed cases we found that a main source of failed detections was due to rotations of the head. As discussed in the section A.3.1 of the appendix, we did not employ a rotation invariant detection scheme. Doing so might improve the results. Other failed detections could be attributed to closed eyes, reflection of glasses, distracting background objects and different scales (object distance to camera).

State of the Art In Fig. 5.12(a) we compared our approach to the two most recent pupil detection methods from literature for several normalized error thresholds. Here we see that with allowed errors of 0.1 (blue circles Fig. 5.11(a)) and higher our method competes very well with the state of the art, despite the fact that our generic method is not adapted to the application. Further application specific tuning and preprocessing could be applied to improve precision (for $e \ll 0.1$), but this is beyond the scope of this chapter. Moreover, we see that our method can be used on full images instead of the periocular images without much loss in performance. The fact that our method is still very accurate on full image processing, considering standard accuracy requirements ($e \leq 0.1$, see also Fig. 5.11(a)), shows that it can be used as a preprocessing step for other applications.

If Fig. 5.12(b) we compared our approach to the seven most recent methods from

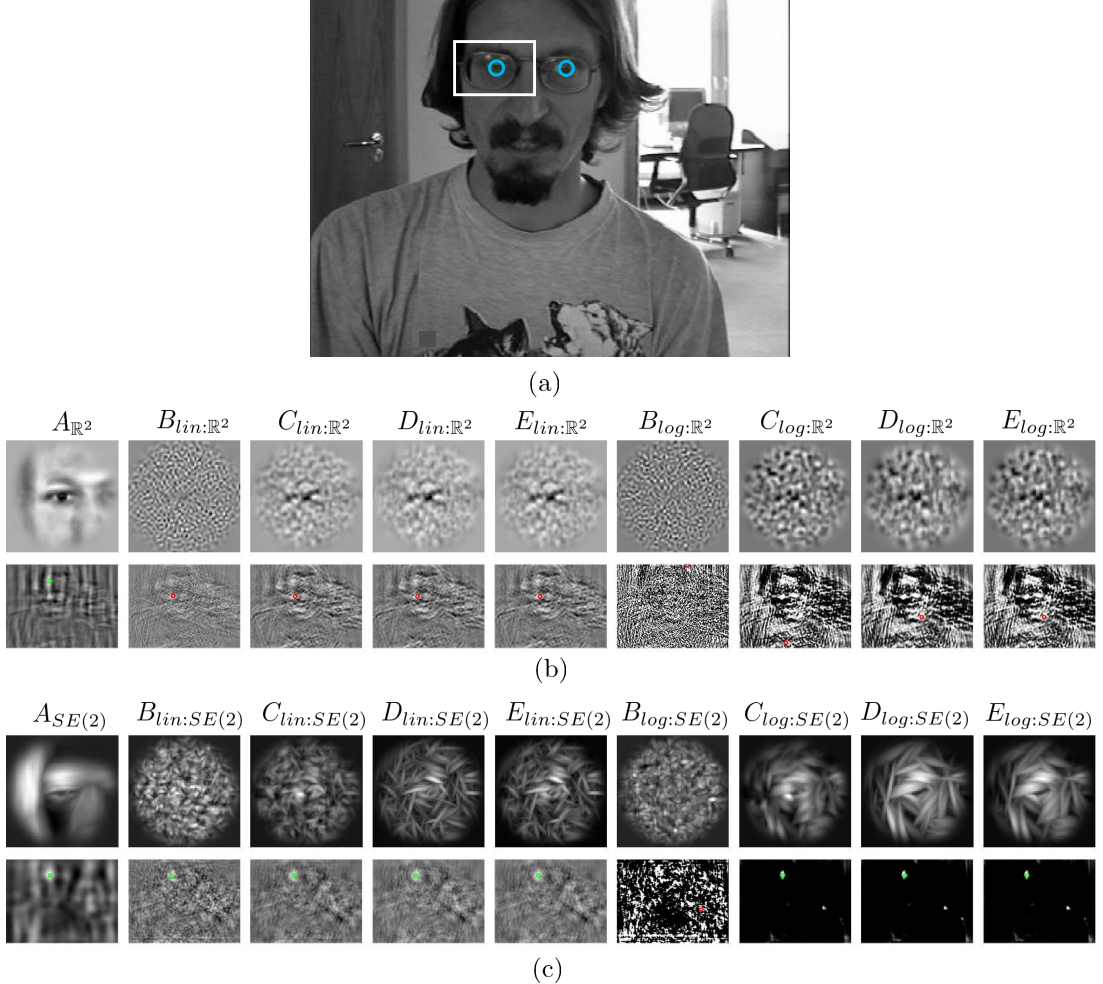


Figure 5.11: Overview of trained templates for right-eye pupil detection, and their responses to a challenging image from the BioID database. **(a)** The example input image with true pupil locations (blue circle with a radius that corresponds to a normalized error threshold of 0.1, see Eq. (5.45)). The white square indicates the periocular image region for the right eye. **(b)** The \mathbb{R}^2 -type templates (top row) and their responses to the input image (bottom row). **(c)** The maximum intensity projections (over θ) of the $SE(2)$ -type templates (top row) and their responses to the input image (bottom row). Detected pupil locations are indicated with colored circles (green = correct, red = incorrect, based on a normalized error threshold of 0.1).

5. RETINAL LANDMARK DETECTION

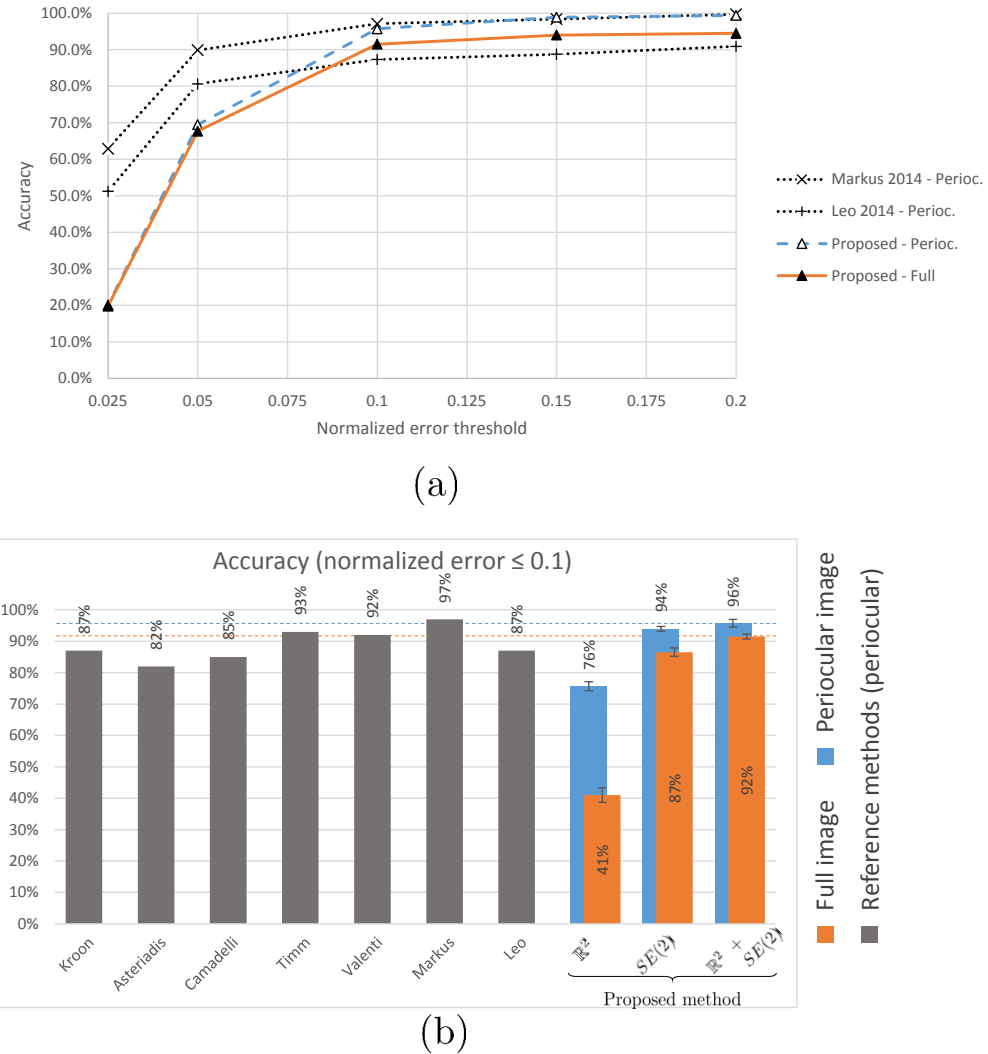


Figure 5.12: (a) Accuracy curves generated by varying thresholds on the normalized error, in comparison with the two most recent methods from literature. (b) Accuracy (at a normalized error threshold of 0.1) comparison with pupil detection methods from literature.

literature (sorted from old to new). Here we see that the only method outperforming our method, at standard accuracy requirements ($\epsilon \leq 0.1$), is the method by Markus et al. Markuš *et al.* (2014). Even when considering processing of the full images the only other method that outperforms ours is the method by Timm et al. Timm & Barth (2011), whose performance is measured using periocular images.

5.5.5 General Observations

The application of our method to the three problems (ONH, fovea and pupil detection) showed the following:

1. Cross correlation based template matching via data representations on $SE(2)$ improves results over standard \mathbb{R}^2 filtering.
2. Trained templates, obtained using energy functionals of the form (5.1), often perform better than basic average templates.
3. Our newly introduced logistic regression approach leads to improved results. In particular in the combination of the templates the soft-binariization due to the logistic sigmoid leads to more robust filtering. In particular in the pupil detection application logistic regression produced better results.
4. Regularization in both linear and logistic regression is important. Here both ridge and smoothing regularization priors have complementary benefits.
5. Our method does not rely on any other detection systems (such as ONH detection in the fovea application, or face detection in the pupil detection), and still performs well compared to methods that do.
6. Our method is fast and parallelizable as it is based on inner products, as such it could be efficiently implemented using convolutions.

5.6 Conclusion

In this chapter we have presented an efficient cross-correlation based template matching scheme for the detection of combined orientation and blob patterns. Furthermore, we have provided a generalized regression framework for the construction of templates. The method relies on data representations in orientation scores, which are functions on the Lie group $SE(2)$, and we have provided the tools for proper smoothing priors

5. RETINAL LANDMARK DETECTION

via resolvent hypo-elliptic diffusion processes on $SE(2)$ (solving time-integrated hypo-elliptic Brownian motions on $SE(2)$). The strength of the method was demonstrated with two applications in retinal image analysis (the detection of the optic nerve head (ONH), and the detection of the fovea) and additional experiments for pupil detection in regular camera images. In the retinal applications we achieved state-of-the-art results with an average detection rate of 99.83% on 1737 images for ONH detection, and 99.32% on 1616 images for fovea detection. Also on pupil detection we obtained state-of-the-art performance with a 95.86% success rate on 1521 images. We showed that the success of the method is due to the inclusion of both intensity and orientation features in template matching. The method is also computationally efficient as it is entirely based on a sequence of convolutions (which can be efficiently done using fast Fourier transforms). These convolutions are parallelizable, which can further speed up our already fast experimental *Mathematica* implementations that are publicly available at <http://erikbekkers.bitbucket.io/TMSE2.html>. In future work we plan to investigate further applicability of smoothing on $SE(2)$ in other variational problems such as (sparse) line enhancement and segmentation problems.

Chapter 6

Vessel Enhancement

This chapter is based on:

Hannink, J., Duits, R., Bekkers, E.: Crossing-preserving multi-scale vesselness. In Golland, P., Hata, N., Barillot, C., Hornegger, J., Howe, R., eds.: Medical Image Computing and Computer-Assisted Intervention (*MICCAI*). Volume 8674 of Lecture Notes in Computer Science. Springer International Publishing (2014) 603-610

6. VESSEL ENHANCEMENT

This chapter is based on joint work with Julius Hannink and Remco Duits is published in Hannink *et al.* (2014). Julius Hannink is gratefully acknowledged for his leading role in the development and implementation of an $SE(2)$ vessel enhancement method inspired by the Frangi vesselness filter Frangi *et al.* (1998).

6.1 Introduction

To automatically assess the state of the retinal vascular tree, vessel segmentations and/or models have to be created and analyzed. Because retinal images usually suffer from low contrast at small scales, the vasculature needs to be enhanced prior to model creation/segmentation. One well-established approach is the Frangi vesselness filter Frangi *et al.* (1998), which is frequently used in robust retinal vessel segmentation methods Budai *et al.* (2013); Lupascu *et al.* (2010). However, the Frangi filter has a known drawback. It cannot properly enhance vessels throughout crossings or bifurcations that make up large parts of the retinal vascular network. To generically deal with this issue, we apply the principle of image processing via invertible orientation scores (Fig. 6.1) and derive a multi-scale crossing-preserving vesselness filter.

In this chapter we will develop vesselness filters on the extended Lie-group domains of the rotation translation group $SE(2)$ and the rotation, translation and scaling group $SIM(2)$. In the $SIM(2)$ case we arrive at continuous wavelet transforms on $SIM(2)$ Jacques & Antoine (2007). In the $SE(2)$ case our approach is closely related (see (Bekkers *et al.*, 2014a, ch. 2.3)) to the work by Krause et al. Krause *et al.* (2013) who rely on a local Radon transform.

The general idea is as follows. Frangi's vesselness relies on a Hessian in the image domain and it only copes with one orientation per location. Since complex structures in retinal images exhibit multiple orientations per position, invertible (multiple scale) orientation scores provide a generic disentanglement of all orientations and scales without tampering of the data evidence, see Sec. 2.1. We employ differential frames in the score, providing us specific Hessians, and subsequent vesselness filters that cope generically with (multiple-scale) crossings/bifurcations without having to classify them.

In the end, we show the performance of this new type of vesselness filters by comparison to the multi-scale Frangi vesselness Frangi *et al.* (1998), both qualitatively and quantitatively on the High Resolution Fundus (HRF) image dataset available at <http://www5.cs.fau.de/research/data/fundus-images/>.

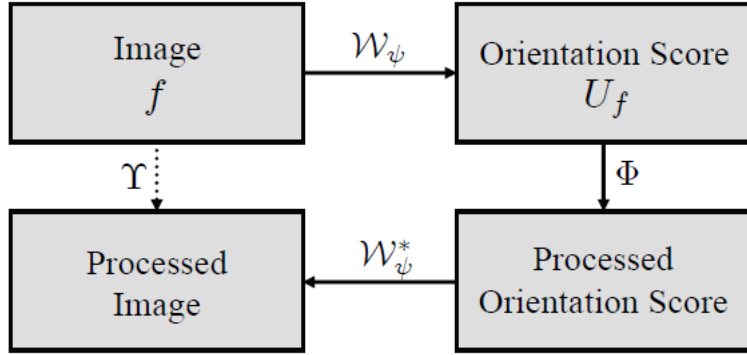


Figure 6.1: *Image processing via invertible orientation scores.*

6.2 Methods

6.2.1 Orientation Scores

As described in Ch. 2, an orientation score $U_f : SE(2) \rightarrow \mathbb{C}$ is obtained by correlating an input image f with a rotating set of anisotropic wavelets ψ . In this chapter we use for ψ the cake wavelets that are described in Subsec. 2.7 on page 27. The orientation score transformation is given in Eq. (2.1) on page 25. Stable and exact image reconstruction (cf. Subsec. 2.1.4) is achieved by Eq. (2.3). In Subsec. 6.2.4 we describe an extension to multi-scale cake wavelets. These wavelets allow for a scale and orientation decomposition of the image data, and they also allow for a stable reconstruction from the scale-orientation score back to the image.

6.2.2 Gaussian Derivatives in Orientation Scores

The orientation score domain is essentially the 2D special Euclidean motion group $SE(2)$ (cf. Ch. 2). Because of this, all operations Φ on this domain (see Fig. 6.1) have to be left-invariant to produce a Euclidean invariant net operator Υ on the image Duits (2005), recall Subsec. 2.3.2. This is desirable since the result should be independent of rotation and translation of the input. So we must rely on the left-invariant derivatives $\{\mathcal{A}_1, \mathcal{A}_2, \mathcal{A}_3\}$, defined in (2.42), when constructing vesselness filters on $SE(2)$. In the next Subsec. 6.2.3 we will adapt this frame locally to the score, following the theory of best exponential curve fits presented in (Franken, 2008, ch.6); Duits & Janssen *et al.* (2016). This will compensate for the fact that our wavelet kernel is not always perfectly

6. VESSEL ENHANCEMENT

aligned with all local orientations present in the image.

In order to extract local features in $SE(2)$ with well-posed, left-invariant derivative operators, regularization is needed. The only left-invariant diffusion regularization in $SE(2)$ that preserves the non-commutative group structure via the commutators is elliptic diffusion (see also App. 5.4), which is isotropic w.r.t. the (sub-)Riemannian metric \mathcal{G}_e^ξ defined (4.8). Then regularization is achieved via a spatially isotropic Gaussian with scale $\frac{1}{2}\sigma_s^2$ and a 1D-Gaussian in θ with scale $\frac{1}{2}(\xi\sigma_s)^2$ (Franken, 2008, ch.5). Recall from Subsec. 4.3.1 that ξ is a parameter with dimensions 1/length that balances spatial and angular motion. The regularized derivative operators are convolutions with differentiated ξ -isotropic Gaussians and generalize the concept of Gaussian derivatives used in the Frangi vesselness filter Frangi *et al.* (1998) to $SE(2)$. In our subsequent extension to $SIM(2)$, where we include scaling $a > 0$, we will choose $\xi = 0.05/a$ as we must take into account both physical dimensions, and typical tortuosities of retinal vessels.

6.2.3 Gauge Derivatives and Exponential Curve Fits in $SE(2)$

Another possible coordinate system is the locally adaptive gauge frame $\{\mathcal{B}_i\}_{i=1}^3$, which we illustrate in Fig. 6.2. There we see that the $\{\mathcal{A}_i\}_{i=1}^3$ frames are aligned with the discrete orientations of the anisotropic kernel used to construct the orientation score. Each orientation layer (corresponding to some θ) thus has its own derivative frame. However, the data in the score is not always perfectly aligned with the kernels used to do the lifting, especially when a low number of orientations is used. The gauge frame $\{\mathcal{B}_i\}_{i=1}^3$ is constructed in such a way that it is better aligned with the data in the score, as can be seen in Fig. 6.2. In order to construct the new gauge frames $\{\mathcal{B}_i\}_{i=1}^3$ we first fit an exponential curve $\gamma_g^{\mathbf{c}^*}$ (cf. Subsec. 2.2.3) at each g in the orientation score U . The tangent vector components \mathbf{c}^* of the best exponential curve fit is then used to re-align the left-invariant frame to the data.

In the exponential curve fitting we minimize the norm of the first-order derivative of the gradient along the exponential curve:

$$\begin{aligned} \mathbf{c}^*(g) = \underset{\mathbf{c} \in \mathbb{R}^3, \|\mathbf{c}\|_\xi = 1}{\operatorname{argmin}} \left\{ \mathcal{G}_1^\xi \left(\frac{d}{dt} \nabla U(\gamma_g^{\mathbf{c}}(t)) \Big|_{t=0}, \frac{d}{dt} \nabla U(\gamma_g^{\mathbf{c}}(t)) \Big|_{t=0} \right) \right\}, \end{aligned} \quad (6.1)$$

with the exponential curves $\gamma_g^{\mathbf{c}} : \mathbb{R} \rightarrow SE(2)$ defined in Eq. (2.28) on page 44, the

6.2 Methods

(ξ -isotropic) Riemannian metric tensor \mathcal{G}_1^ξ on $SE(2)$ defined in Eq. (4.8) on page 82, and the left-invariant gradient ∇U given in Eq. (4.16) on page 85. The ξ -norm is given by $\|\mathbf{c}\|_\xi = \sqrt{\mathcal{G}_1^\xi(\mathbf{c}, \mathbf{c})} = \|\mathbf{M}_\xi \mathbf{c}\|$, with diagonal matrix $\mathbf{M}_\xi = \text{diag}\{\xi, \xi, 1\}$.

As shown in (Duits & Janssen *et al.*, 2016, Thm. 3), the minimizing $\mathbf{c}^*(g)$ at each g in (6.1) can be obtained from the eigenvector $\mathbf{M}_\xi \mathbf{c}^*(g)$ with smallest eigenvalue of the (dimensionless) rescaled and symmetrized Hessian matrix

$$\mathbf{H}_\xi(g) = \mathbf{M}_{\xi^{-1}} (\mathbf{H}(g))^T \mathbf{M}_{\xi^{-2}} \mathbf{H}(g) \mathbf{M}_{\xi^{-1}}, \quad (6.2)$$

with the left-invariant Hessian matrix $\mathbf{H}(g)$ at g , defined using the left-Cartan (dual) connection ∇^* (see Eq. (4.26) in Subsec. 4.5.3), given by

$$\mathbf{H}(g) := [(\nabla_{\mathcal{A}_i}^* dU)(\mathcal{A}_j)] = [\mathcal{A}_j(\mathcal{A}_i U)], \quad (6.3)$$

in which i denotes the row index and j denotes the column index¹. I.e., the (dimensionless) eigenvector $\tilde{\mathbf{c}}$ with smallest eigenvalue λ is obtained by solving the following eigensystem

$$\mathbf{H}_\xi(g) \tilde{\mathbf{c}}(g) = \lambda \tilde{\mathbf{c}}(g), \quad (6.4)$$

and is then rescaled to obtain $\mathbf{c}^*(g) = \mathbf{M}_\xi^{-1} \tilde{\mathbf{c}}(g)$.

Once the tangent vector $\mathbf{c}^*(g) = \sum_{i=1}^3 c^i(g) \mathcal{A}_i|_g$ is found, the gauge frame is constructed in the following way (see also Fig. 6.2):

$$\underline{\mathcal{B}} := (\mathbf{R}^{\mathbf{c}^*})^T \mathbf{M}_\xi^{-1} \underline{\mathcal{A}}, \quad (6.5)$$

with $\underline{\mathcal{A}} := (\mathcal{A}_1, \mathcal{A}_2, \mathcal{A}_3)^T$, $\underline{\mathcal{B}} := (\mathcal{B}_1, \mathcal{B}_2, \mathcal{B}_3)^T$, and with rotation matrix

$$\begin{aligned} \mathbf{R}^{\mathbf{c}^*} &= \mathbf{R}_2 \mathbf{R}_1 \in SO(3), \text{ with} \\ \mathbf{R}_1 &= \begin{pmatrix} \cos \nu & 0 & \sin \nu \\ 0 & 1 & 0 \\ -\sin \nu & 0 & \cos \nu \end{pmatrix}, \quad \mathbf{R}_2 = \begin{pmatrix} \cos \chi & -\sin \chi & 0 \\ \sin \chi & \cos \chi & 0 \\ 0 & 0 & 1 \end{pmatrix}, \end{aligned} \quad (6.6)$$

where the rotation angles are the deviation from horizontality angle

$$\chi = \arctan \left(\frac{c^2}{c^1} \right), \quad (6.7)$$

¹Note the following two: 1) The left-invariant Hessian $\mathbf{H}(g)$ is not symmetric due to the non-commutative derivatives, i.e., $\mathcal{A}_1(\mathcal{A}_3 U) \neq \mathcal{A}_3(\mathcal{A}_1 U)$. 2) The switched row and column indices i and j in Eq. (6.3) might seem odd, but this follows from the Cartan connection on the co-tangent bundle (Duits & Janssen *et al.*, 2016, App. 4).

6. VESSEL ENHANCEMENT

and the spherical angle

$$\nu = \arcsin \left(\frac{c^3}{\|\mathbf{c}\|_\xi} \right). \quad (6.8)$$

As explained in Subsec. 2.1.6 the exponential curves have constant tangent vector components in the moving frame of reference $\{\mathcal{A}_i\}_{i=1}^3$ and they are circular spirals (and their projections to the plane are circles). The spherical angle χ is directly related to the (signed) norm of the curvature of an exponential curve that is projected to the plane:

$$\nu = \arctan(\kappa),$$

in which κ is the signed curvature magnitude given by

$$\kappa = \frac{c^3 \operatorname{sign}(c^1)}{\sqrt{(c^1)^2 + (c^2)^2}}. \quad (6.9)$$

Although here we do not explicitly use the curvature values κ , it is good to realize that the gauge frame takes into account both deviation from horizontality and curvature. As such, the vesselness filter defined in the gauge frame better deals with highly curved blood vessels (the curvature aspect) and still performs well even when a low number of orientations is used in the orientation score transform (the deviation from horizontality aspect).

6.2.4 Scale–Orientation Scores

To make the cake kernels described in Subsec. 2.1.5 scale-selective, the pieces of cake have to be further divided. By cutting out pieces in the log–radial direction, they are made sensitive to a specific frequency range that can be identified with a scale a in the spatial domain (see Fig. 6.3). To construct scale-selective cake kernels (anisotropic wavelets), Sharma & Duits (2015) uses a radial envelope function

$$B^{\text{MS}}(\rho) = \sum_{l=0}^{N_\rho-1} B_l^k(\rho) := \sum_{l=0}^{N_\rho-1} B^k \left(\frac{\log(\rho a_l)}{s_\rho} \right), \text{ with } a_l = a_0 e^{ls_\rho}, \quad (6.10)$$

where $B^k(x)$ is the k -th order B-spline function (cf. Eq. (2.9) on page 28), ρ is the radial parameter in polar coordinates (cf. Eq. (2.8)), N_ρ is the total number of scales to sample in the Fourier domain and $s_\rho > 0$ denotes the stepsize in log-scale. The multiplicative character in $a_l = a_0 e^{ls_\rho}$ reflects the typical scale transitions at bifurcations in bloodvessels. Because of the B-spline approach, the scale-selective envelopes $B_l^k(\rho)$ sum to 1 and the $M_\psi \approx 1$ requirement is met (Fig. 6.3). Scale layers outside a spatially

6.2 Methods

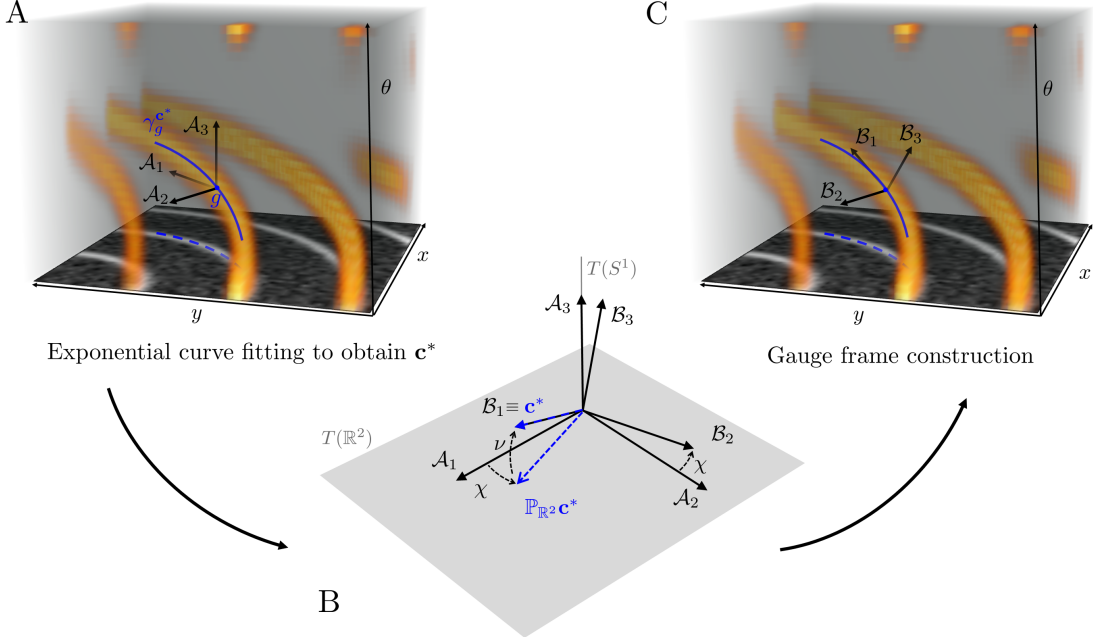


Figure 6.2: **A:** A gauge frame $\{\mathcal{B}_i\}_{i=1}^3$ is constructed by first fitting an exponential curve $\gamma_g^{c^*}$ to the data. **B:** Then the gauge frame is constructed by a normalization and two subsequent rotations (over angles χ and ν , see Eqs. (6.5–6.8)) of the left-invariant frame $\{\mathcal{A}_i\}_{i=1}^3$. **C:** The new gauge frame is now aligned with the best fit exponential curve.

defined range of interest are merged to reduce the computational load (Fig. 6.3). We propose the following multi-scale cake kernel

$$\psi^{\text{MS}}(\mathbf{x}) = \left(\mathcal{F}^{-1} \left[\boldsymbol{\omega} \mapsto M^{-1}(\boldsymbol{\omega}) \mathcal{F} \left[\tilde{\psi}^{\text{MS}} \right] (\boldsymbol{\omega}) \right] \right) (\mathbf{x}) \quad (6.11)$$

where $\tilde{\psi}^{\text{MS}}(\mathbf{x})$ denotes the wavelet

$$\tilde{\psi}^{\text{MS}}(\mathbf{x}) = \left(\mathcal{F}^{-1} \left[\boldsymbol{\omega} \mapsto A(\varphi) B_0^k(\rho) \right] \right) (\mathbf{x}) G_{s_x, s_y}(\mathbf{x}) \quad (6.12)$$

at the finest scale a_0 , with $\boldsymbol{\omega} = (\rho \cos \varphi, \rho \sin \varphi)$. The function $A(\varphi)$ is given by $B^k(s_\theta^{-1}[(\varphi \bmod 2\pi) - \pi/2])$ for $\rho > 0$ and $1/N_\theta$ for $\rho = 0$ with the angular stepsize $s_\theta = 2\pi/N_\theta$. The anisotropic Gaussian window $G_{s_x, s_y}(\mathbf{x})$ reduces long tails along the orientation of the wavelet and suppresses oscillations perpendicular to it induced by narrow sampling bandwidths in $B^{\text{MS}}(\rho)$. Changes in the Fourier domain are resolved via normalization with $M(\boldsymbol{\omega}) = N_\rho^{-1} N_\theta^{-1} \sum_{l=0}^{N_\rho-1} \sum_{j=1}^{N_\theta} a_l^{-1} |\mathcal{F}[\tilde{\psi}^{\text{MS}}](a_l R_{\theta_j}^{-1} \vec{\omega})|$. Thereby, approximative reconstruction is done by summation over scales and angles. The contin-

6. VESSEL ENHANCEMENT

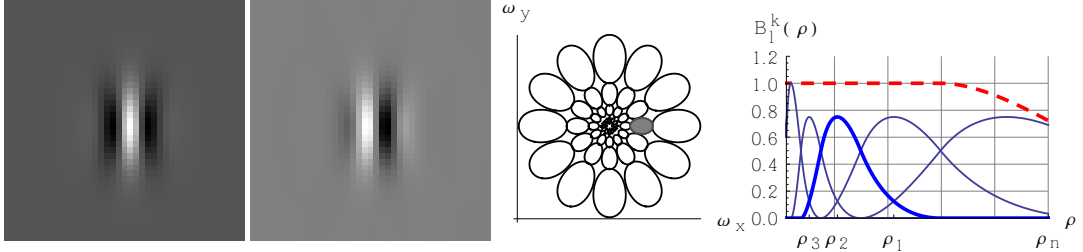


Figure 6.3: Real and imaginary part of the multi-scale cake kernel at a_2 (left), Fourier contours of all wavelets (at 70% of the maximum) and $B^{MS}(\rho)$ (red, dashed) with components $B_l^k(\rho)$ (blue).

uous wavelet transform $(\mathcal{W}_\psi f)(\mathbf{x}, \theta, a) = (\overline{\psi_\theta^a} \star f)(\mathbf{x})$ with $\psi_\theta^a(\mathbf{x}) = a^{-1}\psi^{\text{MS}}(a^{-1}R_\theta^{-1}\mathbf{x})$ is now set and processing can begin.

6.2.5 Vesselness Filtering on Scale–Orientation Scores

The single-scale Frangi vesselness filter $\mathcal{V}_0^{\text{Fr}}$ makes use of an anisotropy measure \mathcal{R} and a structure measure \mathcal{S} based on second order derivatives in a coordinate system aligned with the local elongated structures Frangi *et al.* (1998), recall Sec. 3.2 (page 56). This approach is now generalized to (scale–)orientation scores for crossing–preserving vesselness filtering. Given a convexity criterion $\mathcal{Q} > 0$ on transversal vessel profiles and the measures \mathcal{R} resp. \mathcal{S} , the setup for the $SE(2)$ vesselness expression $\mathcal{V}_0^{SE(2)}(\mathcal{U}_f^a) : SE(2) \rightarrow \mathbb{R}^+$ is identical to the one proposed by Frangi *et al.* (1998):

$$\mathcal{V}_0^{SE(2)}(\mathcal{U}_f^a) = \begin{cases} 0 & \text{if } \mathcal{Q} \leq 0 \\ \exp\left(-\frac{\mathcal{R}^2}{2\sigma_1^2}\right) \left[1 - \exp\left(-\frac{\mathcal{S}}{2\sigma_2}\right)\right] & \text{if } \mathcal{Q} > 0 \end{cases} \quad (6.13)$$

where $\mathcal{U}_f^a(\mathbf{x}, \theta) = (\mathcal{W}_\psi f)(\mathbf{x}, \theta, a)$, $a > 0$ fixed, is a single scale layer of the multi-scale wavelet transform. We always set $\sigma_1 = 0.5$, and following the recommendations given in Frangi *et al.* (1998) we let σ_2 depend on the maximum structureness value: $\sigma_2 = 0.2 \|\mathcal{S}\|_\infty$.

There are two natural generalizations of $\mathcal{V}_0^{\text{Fr}}$ to $SE(2)$ that differ in the choice of coordinate system used to define \mathcal{R}, \mathcal{S} and \mathcal{Q} . One option is to work in the moving

6.2 Methods

frame of reference $\{\mathcal{A}_1, \mathcal{A}_2, \mathcal{A}_3\}$, recall Eq. (2.42) on page 48, in which case we set

$$\begin{aligned}\mathcal{R} &= \frac{(\mathcal{A}_1^2 \mathcal{U}_f^a)^{s,\xi}}{(\mathcal{A}_2^2 \mathcal{U}_f^a)^{s,\xi} + (\mathcal{A}_3^2 \mathcal{U}_f^a)^{s,\xi}}, \\ \mathcal{S} &= \left[(\mathcal{A}_1^2 \mathcal{U}_f^a)^{s,\xi} \right]^2 + \left[(\mathcal{A}_2^2 \mathcal{U}_f^a)^{s,\xi} + (\mathcal{A}_3^2 \mathcal{U}_f^a)^{s,\xi} \right]^2, \\ \mathcal{Q} &= (\mathcal{A}_2^2 \mathcal{U}_f^a)^{s,\xi} + (\mathcal{A}_3^2 \mathcal{U}_f^a)^{s,\xi}.\end{aligned}\quad (6.14)$$

where the superscripts s,ξ indicate Gaussian derivatives at spatial scale $s = \frac{1}{2}\sigma_s^2$ and angular scale $\frac{1}{2}(\xi\sigma_s)^2$. The generalization of the filter in the $\{\mathcal{A}_1, \mathcal{A}_2, \mathcal{A}_3\}$ frame is referred to as $\mathcal{V}_0^{\mathcal{A}_i}$ at single scales and as $\mathcal{V}^{\mathcal{A}_i}$ in the multiple scale recombination, similar to the notation in Frangi *et al.* (1998). The other possible coordinate system is the Gauge frame $\{\mathcal{B}_1, \mathcal{B}_2, \mathcal{B}_3\}$ determined by the eigendirections of the left-invariant Hessian. As the filter is no longer confined to fixed θ -slices, and the Gauge frame is fully aligned with the 3D-line structures in the score, the analogies to Frangi *et al.* (1998) are even stronger in this frame. Note that the vesselness filter with respect to the gauge frame arises by replacing $\mathcal{A}_i \rightarrow \mathcal{B}_i$ in (6.14) which yields

$$\begin{aligned}\mathcal{R} &= \frac{(\mathcal{B}_1^2 \mathcal{U}_f^a)^{s,\xi}}{(\mathcal{B}_2^2 \mathcal{U}_f^a)^{s,\xi} + (\mathcal{B}_3^2 \mathcal{U}_f^a)^{s,\xi}}, \\ \mathcal{S} &= \left[(\mathcal{B}_1^2 \mathcal{U}_f^a)^{s,\xi} \right]^2 + \left[(\mathcal{B}_2^2 \mathcal{U}_f^a)^{s,\xi} + (\mathcal{B}_3^2 \mathcal{U}_f^a)^{s,\xi} \right]^2, \\ \mathcal{Q} &= (\mathcal{B}_2^2 \mathcal{U}_f^a)^{s,\xi} + (\mathcal{B}_3^2 \mathcal{U}_f^a)^{s,\xi}\end{aligned}\quad (6.15)$$

The $SE(2)$ -generalization of the vesselness filter in this frame is referred to as $\mathcal{V}_0^{\mathcal{B}_i}$, whereas the multi-scale $SIM(2)$ -generalization is written as $\mathcal{V}^{\mathcal{B}_i}$. In the $SIM(2)$ -generalizations of the vesselness filters (regardless the choice of reference frame) the final image reconstruction from vesselness filtered scale–orientation scores are obtained via

$$(\mathcal{V}^{SIM(2)}(f))(\mathbf{x}) = \mu_{\infty}^{-1} \sum_{l=1}^{N_s} \mu_{l,\infty}^{-1} \sum_{j=1}^{N_{\theta}} (\mathcal{V}_0^{SE(2)}(U_f^{a_l}))(\mathbf{x}, \theta_j) \quad (6.16)$$

where μ_{∞} and $\mu_{l,\infty}$ are the maximum values, i.e. $\|\cdot\|_{\infty}$ norms, taken over the subsequent sums. For comparison, the multi-scale Frangi vesselness filter is also computed via summation over single scale results and max-normalized.

Fig. 6.4 shows multi-scale vesselness filtering results for a retinal image f obtained with the Frangi filter and our two methods for five scales $\{1.5, 2.4, 3.8, 6.0, 9.5\}$ px,

6. VESSEL ENHANCEMENT

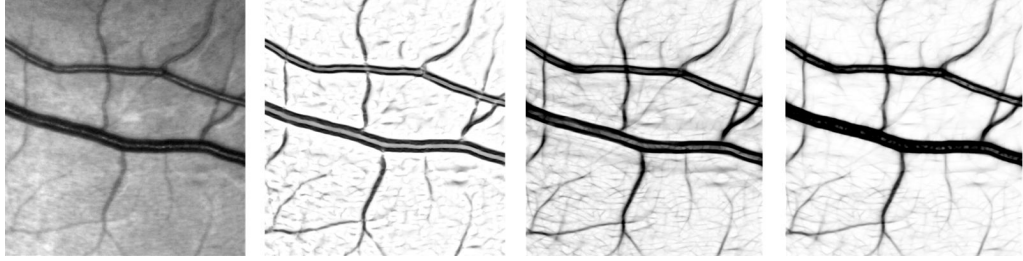


Figure 6.4: Retinal image f and multi-scale vesselness filtering results for the Frangi filter $\mathcal{V}^{\text{Fr}}(f)$ and our two methods $\mathcal{V}^{\mathcal{A}_i}(f)$ resp. $\mathcal{V}^{\mathcal{B}_i}(f)$ (left to right).

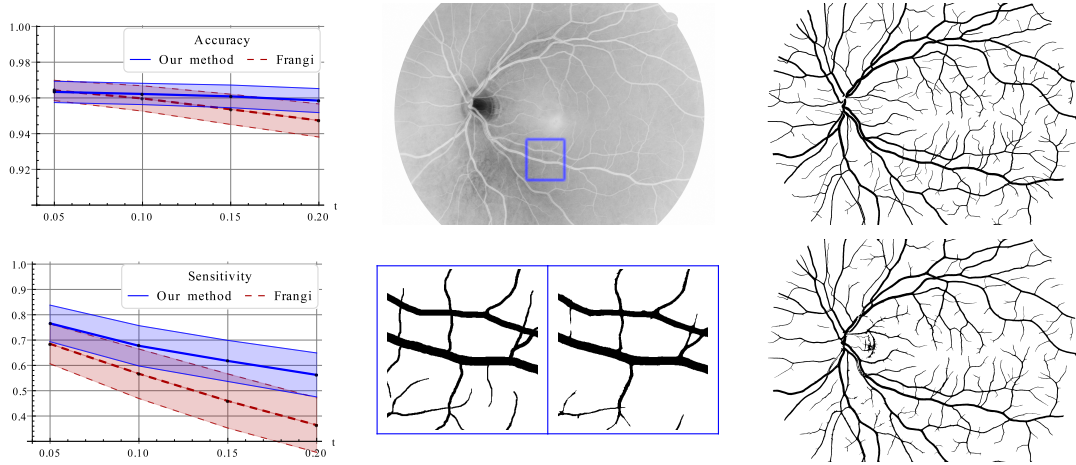


Figure 6.5: Mean accuracy and sensitivity on the HRF dataset over threshold values t . Shading shows $\pm 1\sigma$ (left). Retinal image and patch ground truth/segmentation at $t = 0.05$ (center). Full ground truth and segmentation (right).

$\xi = 0.05/a$ and 12 orientations. Both our methods clearly outperform the Frangi filter at crossings and bifurcations. The Gauge-frame method $\mathcal{V}^{\mathcal{B}_i}$ gives best results as it aligns with 3D-elongated structures in the score.

6.3 Experiments

To show the benefit of crossing-preservation in multiple scale vesselness filtering, we devised a simple segmentation algorithm to turn a vesselness filtered image $\mathcal{V}(f)$ into a binary vessel map. First, a local thresholding is applied so that we obtain the binary image $f_B = \Theta([\mathcal{V}(f) - G_\gamma * \mathcal{V}(f)] - t)$ where Θ is the Heaviside step function and G_γ is a Gaussian with standard deviation $\gamma \gg 1$. In a second step, the connected

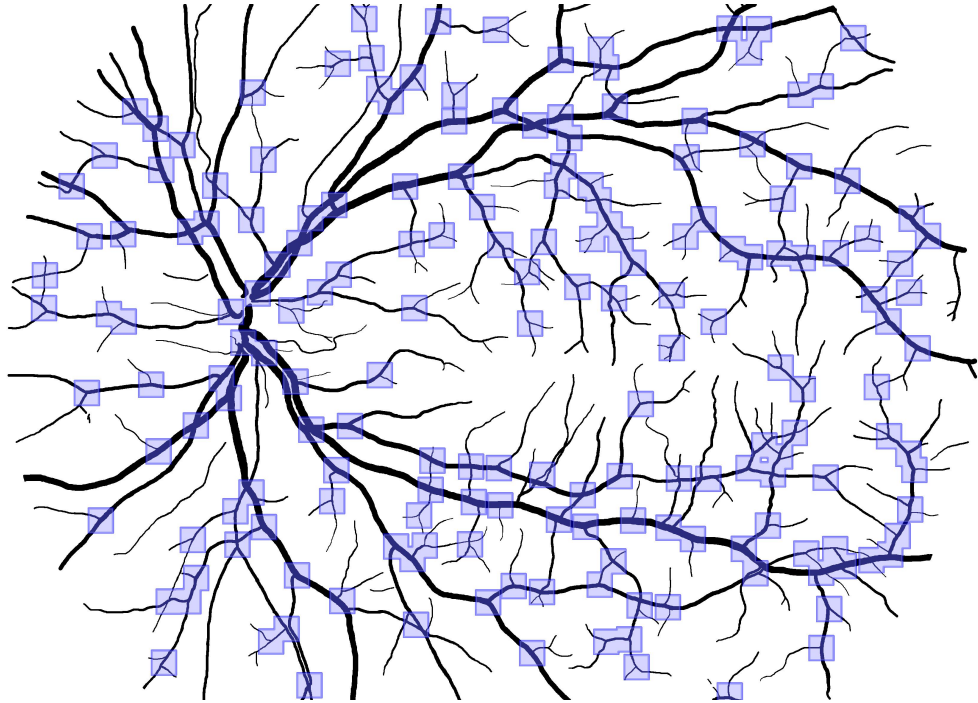


Figure 6.6: Shaded regions specify areas containing junction points. Junction points are found by thinning and pruning the binary ground truth.

Table 6.1: Results for bifurcation and crossing areas (junctions) compared to the complement of this set (non-junctions). See Fig.6.6 for sample areas.

Method	Junctions		Non-junctions	
	Sens.	Acc.	Sens.	Acc.
Our method				
All	0.84	0.92	0.76	0.97
Healthy	0.82	0.94	0.75	0.97
Glaucoma	0.84	0.93	0.74	0.97
Diabetic	0.85	0.90	0.78	0.96
Frangi <i>et al.</i> (1998)				
All	0.71	0.92	0.67	0.97
Healthy	0.71	0.93	0.67	0.97
Glaucoma	0.75	0.93	0.68	0.97
Diabetic	0.69	0.91	0.65	0.97

6. VESSEL ENHANCEMENT

morphological components in f_B counting less than τ pixels or showing elongations below a threshold ν are removed. The parameters γ, τ and ν are fixed at 100 px, 500 px and 0.85 respectively. $\mathcal{V}(f)$ is either obtained with \mathcal{V}^{Fr} or via the $SIM(2)$ method $\mathcal{V}^{\mathcal{B}_i}$ using the settings mentioned earlier.

This segmentation algorithm is evaluated on the HRF dataset consisting of fundus images for a healthy, diabetic retinopathy and glaucoma group (15 images each, ground truths provided). Average sensitivity and accuracy on the whole dataset are shown in Fig. 6.5 over threshold values t . Our methods via invertible scale–orientation scores, and in particular the $\mathcal{V}^{\mathcal{B}_i}$ method, perform considerably better than the method based on the multi–scale Frangi filter. The segmentation results obtained with $\mathcal{V}^{\mathcal{B}_i}$ are more stable w.r.t. variations in the threshold t and the performance on the small vasculature has improved as measured via the sensitivity. Average sensitivity, specificity and accuracy at a threshold $t = 0.05$ resp. given by 0.786, 0.988, 0.969 (healthy), 0.811, 0.963, 0.953 (diabetic retinopathy) and 0.797, 0.976, 0.964 (glaucoma) compare well with other algorithms evaluated on the HRF dataset (see (Budai *et al.*, 2013, Tab. 5)). On the diabetic retinopathy group, our method even outperforms existing segmentation methods. Fig. 6.5 shows a full segmentation computed with the proposed method and an in–detail patch. In Table 6.1 and Fig. 6.6 we see that our method improves sensitivity both at non-crossing line structures (due to line propagation of anisotropic wavelets) and at crossing/bifurcating structures. As expected, we observe a larger improvement at crossings.

We also compared the results of $SIM(2)$ vesselness filtering based on the left-invariant frames $\{\mathcal{A}_i\}_{i=1}^3$ with the results based on the gauge frame $\{\mathcal{B}_i\}_{i=1}^3$. Here we see that the gauge frame produces a visually much more appealing soft-segmentation of the blood vessels than $SIM(2)$ -vesselness filtering via the non-adaptive frame, see for example Fig. 6.7. It therefore also produces a more accurate segmentation as can be deducted from the comparison presented in Fig. 3.3 on page 58. Generally, we conclude from the experiments that the gauge frame approach better reduces background noise, showing much less false positives in the final segmentation results, especially at crossings.

6.4 A Fast Alternative $SE(2)$ Gauge Frame Method

A fast and simplified alternative to the orientation score based vesselness filters developed in this chapter is presented in Zhang *et al.* (2016a). There, an approach is developed that merely relies on the second order spatial derivative of perpendicular

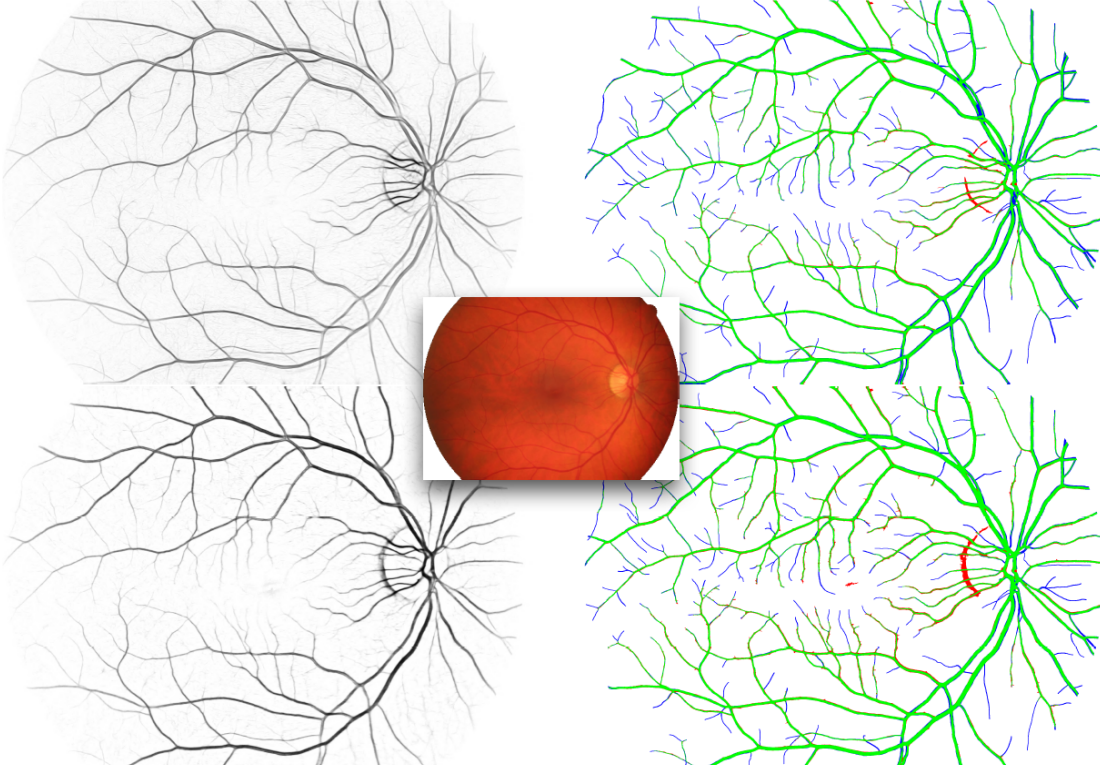


Figure 6.7: Center original image from HRF dataset (healthy subject nr. 5). Rows show the soft-segmentation (left) and the corresponding performance maps (right), based on the hard segmentation. In green true positives, in blue true negatives, in red false positives, compared to manual segmentation by an expert. First row $SIM(2)$ -vesselness based on non-adaptive frame $\{\mathcal{A}_i\}_{i=1}^3$. Second row $SIM(2)$ -vesselness based on the gauge frame $\{\mathcal{B}_i\}_{i=1}^3$. Figure from Duits & Janssen et al. (2016).

vessel cross-sections, which are directly computed via Gaussian derivatives with the gauge frame \mathcal{B}_i . This results in an effective vessel enhancement via

$$\mathcal{V}^{Zhang}(U_f)(\mathbf{x}, \theta) = (\mathcal{B}_2^2(G_{\sigma_s, \sigma_o} * U_f))(\mathbf{x}, \theta). \quad (6.17)$$

Here, one takes the advantage that in the generic gauge frame spatial generators stay spatial.

6.5 Conclusion

We developed (multi-scale) crossing-preserving vesselness filters as generalizations of Frangi *et al.* (1998) to the Lie-group domains $SE(2)$ resp. $SIM(2)$. The new filters

6. VESSEL ENHANCEMENT

were evaluated qualitatively and quantitatively on a public dataset and outperformed the Frangi filter and existing segmentation methods. This shows the method's potential for application in other areas of vascular imaging.

Chapter 7

Vessel Tracking Part I: Iterative Tracking via Local Optimization

This chapter is based on:

Bekkers, E., Duits, R., Berendschot, T., ter Haar Romeny, B.: A multi-orientation analysis approach to retinal vessel tracking. *Journal of Mathematical Imaging and Vision (JMIV)* 49(3) (2014) 583-610

7.1 Introduction

As motivated in Chapter 1, a large variety of diseases affect the vascular system in a way that may cause geometrical and functional changes (Sec. 1.3). Such changes can be observed and quantified in retinal images. The quantification of geometrical properties of the retinal vasculature requires tools such as retinal vessel tracking and segmentation. In this chapter we propose a fully automated tracking method for the construction of complete models of the retinal vasculature.

Retinal Vessel Tracking Typically there are two types of methods for vessel extraction: pixel classification methods Budai *et al.* (2009); Krause *et al.* (2013); Odstrcilik *et al.* (2009); Philipsen (2012) and vessel tracking methods Al-Diri *et al.* (2009); Can *et al.* (1999); Chutatape *et al.* (1998); Espona *et al.* (2007); Grisan *et al.* (2004); Poletti *et al.* (2011); Yin *et al.* (2012). The first type of method classifies pixels as either being part of a vessel or background, resulting in a pixel map in which white pixels represent blood vessels. Of the pixel classification methods, the approach by Krause *et al.* Krause *et al.* (2013) is most similar to our method presented in this chapter, as both methods rely on a transformation to a higher dimensional domain. In their work they applied vessel detection based on the local Radon transform, of which we will show later in this chapter that this is a special case of an orientation score transform based on cake wavelets.

The other type of method, vessel tracking, is based on recursively expanding a model of the vasculature from a set of seed points. One advantage of vessel tracking over pixel classification is that it guarantees connectedness of vessel segments, whereas in pixel classification methods this is not necessarily the case. For further quantitative analysis of the vasculature, tracking algorithms are preferred because they intrinsically provide geometrical and topological information. For example, vessel widths, curvatures, segment lengths, bifurcation density and other features can relatively easily be extracted from the generated vessel models.

Several different approaches to vessel tracking can be found in literature. There are methods based on active contours Al-Diri *et al.* (2009); Espona *et al.* (2007), matched filters Can *et al.* (1999); Chutatape *et al.* (1998); Grisan *et al.* (2004), and probabilistic models Yin *et al.* (2012) among others Poletti *et al.* (2011); Yin *et al.* (2012). The majority of papers on vessel tracking report limitations regarding tracking blood vessels through crossings, bifurcations and/or more complex situations. In this chapter we aim at effectively solving these problems by means of orientation analysis via orientation scores. We propose two new tracking algorithms that act directly on the domain of an

7.2 Tools From Orientation Score Theory

orientation score, and we show that these methods are highly capable of dealing with the aforementioned problems. Afterwards, we will extend one of the orientation score based algorithms to a vasculature tracking algorithm, which is capable of constructing models of the complete retinal vasculature.

Chapter Outline The chapter is structured as follows: First, in Section 7.2, we summarize the tools from orientation score theory that are required in this application. In Section 7.3, two vessel tracking approaches based on orientation scores are then described:

- the ETOS-algorithm: an all-scale approach based on a new class of wavelets, the so-called *cake wavelets*
- the CTOS-algorithm: a multi-scale approach based on the classical Gabor wavelets

Both tracking methods rely on a novel generic geometrical principle for curve optimization within $SE(2)$, which is explained and mathematically underpinned in Appendix B.1. We will show that ETOS generally works with different types of orientation scores, however with best performance on invertible orientation scores based on cake wavelets (in comparison to non-invertible orientation scores based on Gabor wavelets). The second approach requires a multi-scale and multi-orientation decomposition. The two approaches are described in Section 7.3.1, and evaluated in Section 7.3.2. It will turn out that ETOS based on cake wavelets has several advantages over CTOS based on Gabor wavelets. We have validated ETOS more extensively by comparing it to the state of the art in retinal vessel tracking Al-Diri *et al.* (2009); Bankhead *et al.* (2012); Xu *et al.* (2011) using the publicly available REVIEW database Al-Diri *et al.* (2009). In Section 7.4.1 we describe our vasculature tracking algorithm, composed of proper initialization, junction detection and junction resolver algorithms. In Section 7.4.2 the correctness of the topology of the models is evaluated using images of the HRFI-database Budai (2011). General conclusions can be found in Section 7.5.

7.2 Tools From Orientation Score Theory

The vessel tracking method described in this chapter relies on the construction and analysis of orientation scores, for which the theory is provided in Sec. 2.1. More specifically, we construct orientation scores U_f via Eq. (2.1) (page 25) using the (cake and Gabor) wavelets ψ defined in Subsec. 2.1.5. Whenever it is relevant to make this distinction, an orientation score constructed using cake wavelets will be denoted by U_f^{cake}

7. VES. TRACK. I: TRACKING VIA LOCAL OPTIMIZATION

and using Gabor wavelets at scale a with $U_{f,a}^{Gabor}$. Typical responses of the wavelets are shown in Fig. 7.1. Additionally, we propose in this chapter a decomposition of the wavelets in a forward- and backward-oriented part, which makes the wavelets better suited for tracking in orientation scores. This will be the topic of Subsec. 7.2.1.

We shall also rely on the left-invariant vector fields defined in (2.42). Recall from Remark 5 (page 43) that tangent vectors can be algebraically considered as local differential operators or geometrically as tangent vectors (to equivalence classes) of curves. In this chapter we need both viewpoints. For the algebraic viewpoint we write $\{\mathcal{A}_1|_{(x,y,\theta)}, \mathcal{A}_2|_{(x,y,\theta)}, \mathcal{A}_3|_{(x,y,\theta)}\}$ for the left-invariant basis at $(x, y, \theta) \in SE(2)$. For the geometric viewpoint we use the notation¹.

$$\begin{aligned}\mathbf{e}_\xi(x, y, \theta) &= \cos \theta \mathbf{e}_x(x, y, \theta) + \sin \theta \mathbf{e}_y(x, y, \theta), \\ \mathbf{e}_\eta(x, y, \theta) &= -\sin \theta \mathbf{e}_x(x, y, \theta) + \cos \theta \mathbf{e}_y(x, y, \theta), \\ \mathbf{e}_\theta(x, y, \theta) &= (0, 0, 1),\end{aligned}\tag{7.1}$$

with $\mathbf{e}_x(x, y, \theta) = (1, 0, 0)$ and $\mathbf{e}_y(x, y, \theta) = (0, 1, 0)$. The moving frame of reference is defined for each coordinate (x, y, θ) . For notational convenience, however, we omit the coordinate dependency of the moving frame of reference in the remainder of this chapter, and simply write $\{\mathbf{e}_\xi, \mathbf{e}_\eta, \mathbf{e}_\theta\}$.

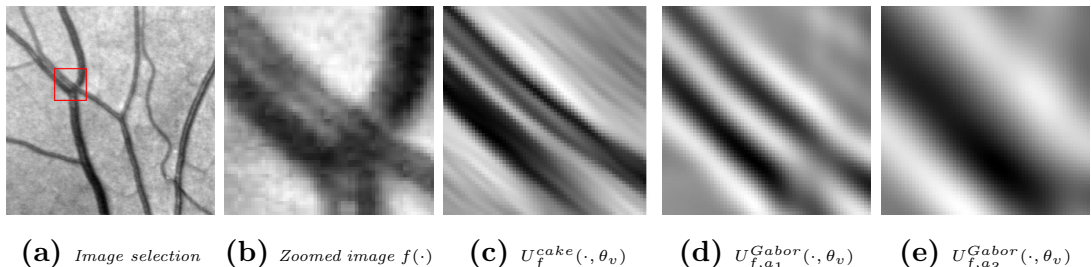


Figure 7.1: Parallel blood vessels and orientation scores. (a) A selection of a fundus image and (b) a close-up view. (c-d) Slices of orientation scores constructed from (b) using cake wavelets and Gabor wavelets at scale $a_1 = 3 * 10/(2\pi)$ and $a_3 = 3 * 30/(2\pi)$ respectively. The slices correspond to the orientation θ_v of two parallel blood vessels.

¹We stress that this gives a non-holonomic coordinate basis for the coordinates (ξ, η, θ) . As such, \mathbf{e}_ξ for example does not relate to a local coordinate derivative $\frac{\partial}{\partial \xi}$, i.e., $\mathbf{e}_\xi \neq \frac{\partial}{\partial \xi}$. This observation is in line with Remark 8.

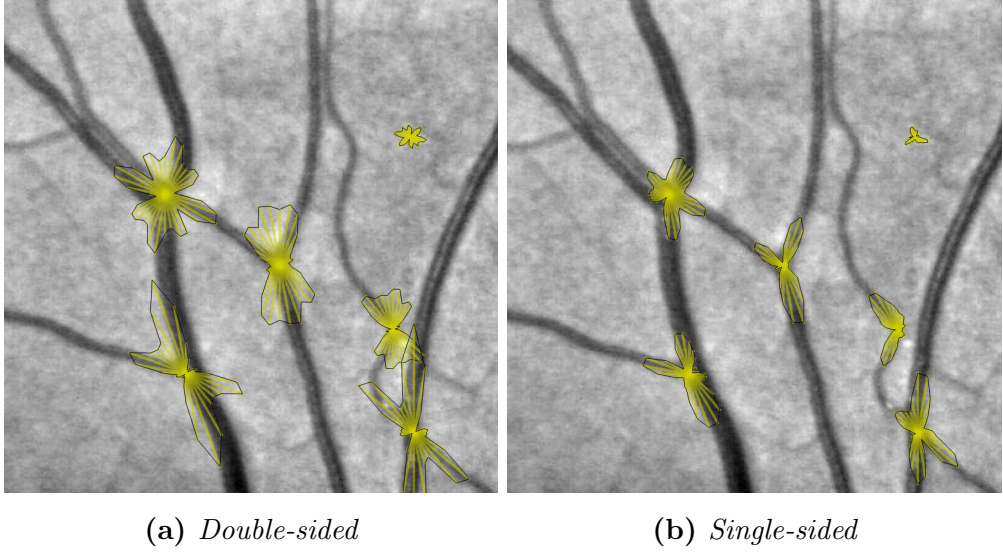


Figure 7.2: Comparison between double- and single-sided cake wavelets by visualisation of the orientation column $U_f(\mathbf{x}, \cdot)$ at several points in a fundus image. The orientation column at a certain point \mathbf{x} is visualized by drawing 36 lines, at evenly distributed angles $0 \leq \theta < 2\pi$, and of which the length in direction θ is given by the absolute value of the score $|U_f(\mathbf{x}, \theta)|$.

7.2.1 Double-Sided vs Single-Sided Wavelets, Orientation vs Direction

The cake and Gabor wavelets are double-sided wavelets which do not distinguish between a forward or backward direction (they are symmetric with respect to the y-axis). In order to distinguish between π symmetries and 2π symmetries (see Fig. 7.2), and to be able to handle bifurcations, we decompose the orientation scores into a forward and backward direction¹, denoted by a + and - symbol respectively:

$$U_f(x, y, \theta) = U_f^+(x, y, \theta) + U_f^-(x, y, \theta), \quad (7.2)$$

where

$$\begin{aligned} U_f^+(\mathbf{x}, \theta) &= \int_{\mathbb{R}^2} \overline{\psi^+(\mathbf{R}_\theta^{-1}(\mathbf{y} - \mathbf{x}))} f(\mathbf{y}) d\mathbf{y}, \\ U_f^-(\mathbf{x}, \theta) &= \int_{\mathbb{R}^2} \overline{\psi^-(\mathbf{R}_\theta^{-1}(\mathbf{y} - \mathbf{x}))} f(\mathbf{y}) d\mathbf{y}, \end{aligned} \quad (7.3)$$

¹I.e. we extend the domain $SE(2) = \mathbb{R}^2 \rtimes SO(2)$ of our orientation scores to the group $E(2) = \mathbb{R}^2 \rtimes O(2)$, where $O(2) = \{M \in \mathbb{R}^{2 \times 2} | M^T = M^{-1}\}$ also includes, besides rotations (with $\det M = +1$), reflections (with $\det M = -1$).

7. VES. TRACK. I: TRACKING VIA LOCAL OPTIMIZATION

and where

$$\begin{aligned}\psi^+(x, y) &= w(x)\psi(x, y), \\ \psi^-(x, y) &= w(-x)\psi(x, y) = (1 - w(x))\psi(x, y)\end{aligned}\quad (7.4)$$

with

$$w(x) = \frac{1}{2} + \frac{1}{2}\text{erf}(x) = \frac{1}{2} + \frac{1}{2\pi} \int_0^x e^{-y^2} dy. \quad (7.5)$$

Note that by using the error function, we have $\psi = \psi^- + \psi^+$ and $U_f^-(x, y, \theta) = \overline{U_f^+(x, y, \theta + \pi)}$, so that $U_f(x, y, \theta) = U_f^+(x, y, \theta) + \overline{U_f^+(x, y, \theta + \pi)}$. It is thus possible to choose one of the single-sided wavelets to construct a *directional* orientation score, while still being able to access the original (double-sided) orientation score. Fig. 7.2 demonstrates the advantage of using single-sided wavelets over double-sided wavelets in the case of direction estimation based on the orientation column of a score $U_f(x, y, \cdot)$.

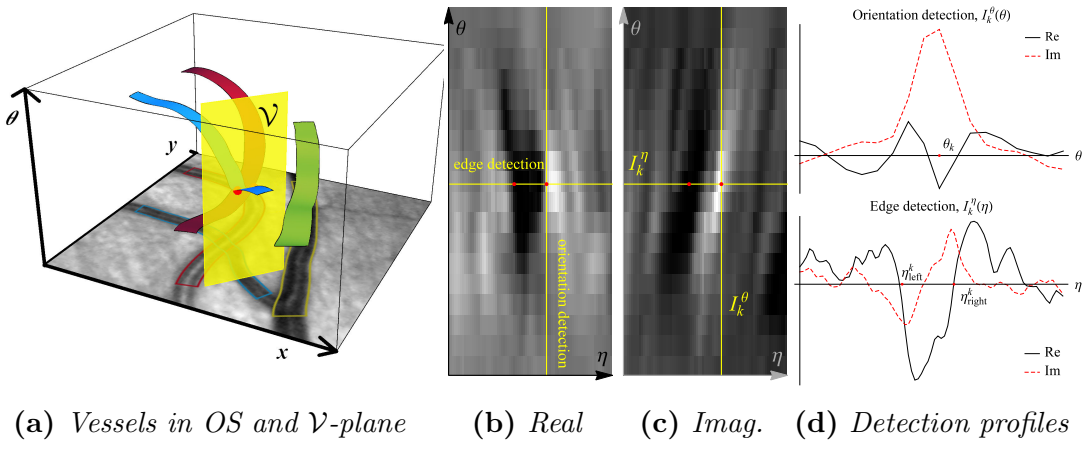


Figure 7.3: Edge tracking in a π -periodic orientation score constructed from double-sided wavelets. (a) Graphical representation of blood vessels in the orientation score. The real and imaginary part of the orientation score on the yellow plane V (perpendicular to the blood vessel) are represented in (b) and (c) respectively. In (c) the left and right edge of the blood vessel are expressed as black and white blobs respectively. The edge and orientation detection profiles are demonstrated in (d).

7.3 Vessel Tracking in Orientation Scores via Optimization in Transversal Tangent Planes \mathcal{V}

In orientation scores, information from the original image is both maintained and neatly organized in different orientations, leading to the disentanglement of crossing structures. Moreover, because of the quadrature property of the wavelets used in the construction of orientation scores, important edge information is well represented in the imaginary part of the score. We therefore propose tracking algorithms that directly act on the orientation score:

1. The ETOS algorithm: Edge Tracking based on Orientation Scores (Section 7.3.1.1).
2. The CTOS algorithm: Centerline Tracking based on multi-scale Orientation Scores (Section 7.3.1.2).

In both tracking algorithms we rely on a fundamental geometric principle to extract the most probable paths in orientation scores. Consider to this end Fig. 7.3a, where a track $t \mapsto g(t) = (\mathbf{x}(t), \theta(t))$ is considered locally optimal if it is locally optimized in each¹ transversal 2D-tangent plane

$$\mathcal{V}|_g = \text{span}\{\mathcal{A}_2|_g, \mathcal{A}_3|_g\} \subset T_g(SE(2)), \quad (7.6)$$

spanned by \mathcal{A}_2 , and \mathcal{A}_3 defined in Eq. (2.42), within the full tangent space $T_g(SE(2))$ defined in Eq. (2.19). For more details on this optimization principle we refer to Appendix B.1.

7.3.1 Methods

7.3.1.1 ETOS: Edge Tracking in Orientation Scores

The ETOS algorithm tracks both vessel edges simultaneously through an orientation score. The method iteratively expands a blood vessel model by detecting, at each forward step k , the optimal edge locations $(\mathbf{u}_k, \theta_k), (\mathbf{v}_k, \theta_k) \in SE(2)$ from the orientation score. Here \mathbf{u}_k and \mathbf{v}_k denote the 2D left and right edge position respectively, θ_k denotes the orientation of the blood vessel. At each iteration the vessel center point \mathbf{c}_k

¹That is locally optimal in $\mathcal{V}|_g$ for each $g = g(t)$, $t \in \text{Dom}(g)$.

7. VES. TRACK. I: TRACKING VIA LOCAL OPTIMIZATION

and the vessel width w_k are defined as follows:

$$\mathbf{c}_k = \frac{\mathbf{u}_k + \mathbf{v}_k}{2}, \quad (7.7)$$

$$w_k = \|\mathbf{u}_k - \mathbf{v}_k\|. \quad (7.8)$$

To describe our method we will rely on a moving frame of reference with basis vectors \mathbf{e}_{η_k} , \mathbf{e}_{ξ_k} and \mathbf{e}_{θ_k} , which are described by the orientation parameter θ_k and Eq. (7.1).

In our method the edge positions g_{u_k} and g_{v_k} are detected in the orientation score from the tangent plane \mathcal{V} (yellow plane in Fig. 7.3a). An edge can be detected as a local optimum from the imaginary part of this plane; a local minimum and maximum for the left and right edge respectively (as indicated by the two red dots in Fig. 7.3c). A schematic overview of the tracking process, including the symbols used in this section, is presented in Fig. 7.4.

For the sake of speed and simplicity, we follow a 2-step approach where the process of detecting the optimal edge positions is separated into two 1D optimization tasks which simply involve the detection of local minima (left edges) and maxima (right edge); in step 1 the edge locations \mathbf{u}_k and \mathbf{v}_k are optimized in the \mathbf{e}_η direction (η -optimization), in step 2 the corresponding orientation is optimized in the \mathbf{e}_θ direction (θ -optimization), see Fig. 7.3b-d. By considering the continuous properties of the blood vessels (e.g. continuous vessel widths), we use a paired edge tracking approach where the left and right edges are detected simultaneously. This approach has the advantage that even if one of the edges is less apparent in the image (e.g. at crossing points, parallel vessels and bifurcations), both edges and their orientation can still be tracked. A possible disadvantage of this approach is however that abrupt changes in vessel width (e.g. at stenoses and aneurysms) may become unnoticed or detected with less detail.

Step 1: Based on a-priori knowledge about the previous vessel orientation, edges and center point, stored in

$$\{(\theta_l, \mathbf{u}_l, \mathbf{v}_l, \mathbf{c}_l) | k - M \leq l \leq k - 1\},$$

where we set $M = 10$, a new vessel center point $\tilde{\mathbf{c}}_k$ is calculated as

$$\tilde{\mathbf{c}}_k = \mathbf{c}_{k-1} + \lambda \mathbf{e}_{\xi_{k-1}}, \quad (7.9)$$

where λ (typically in the order of 2 pixels) is the tracking step-size. New edge points are selected from a set of points $\mathbf{p}_k(\eta)$ on a line L_k going through the estimated center point $\tilde{\mathbf{c}}_k$ and perpendicular to the vessel orientation θ_{k-1} :

$$L_k = \{\mathbf{p}_k(\eta) \mid \eta \in [-\eta_{max}, \eta_{max}]\}, \quad (7.10)$$

7.3 Vessel Tracking in Orientation Scores via Optimization in Transversal Tangent Planes \mathcal{V}

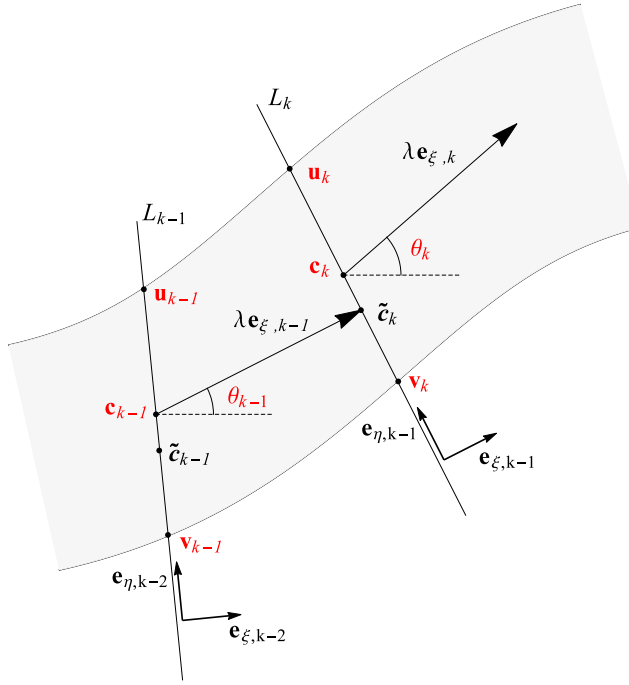


Figure 7.4: Schematic overview image of ETOS. Using the detected vessel center point \mathbf{c}_{k-1} and the orientation θ_{k-1} detected at the vessel edges \mathbf{u}_{k-1} and \mathbf{v}_{k-1} at iteration $k - 1$, a rough estimation of the next center point $\tilde{\mathbf{c}}_k$ found by stepping forward in the vessel direction $\mathbf{e}_{\xi,k-1}$ with step size λ . Through the estimated center point a line L_k is defined on which the new vessel edges \mathbf{u}_k and \mathbf{v}_k are detected. At these edges the vessel orientation θ_k is detected and the final precise vessel center point \mathbf{c}_k is calculated as the mean of the two edges.

with

$$\mathbf{p}_k(\eta) = \tilde{\mathbf{c}}_k + \eta \mathbf{e}_{\eta_{k-1}}, \quad (7.11)$$

where η is a parameter describing the distance to the estimated vessel center point and $\eta_{max} > \|\mathbf{u}_k - \mathbf{v}_k\|$ denotes the maximum distance to the estimated vessel center point. Note that orientation θ_{k-1} of the previous iteration is used as the new orientation is yet to be detected.

An intensity profile $I_k^\eta(\eta)$ can then be obtained from the orientation scores according to

$$I_k^\eta(\eta) = U_f(\mathbf{p}_k(\eta), \theta_{k-1}), \quad (7.12)$$

see Fig. 7.3d. New edge points can now easily be found by detecting the local optima on the imaginary part of this profile. However, the detection of vessel edges is made

7. VES. TRACK. I: TRACKING VIA LOCAL OPTIMIZATION

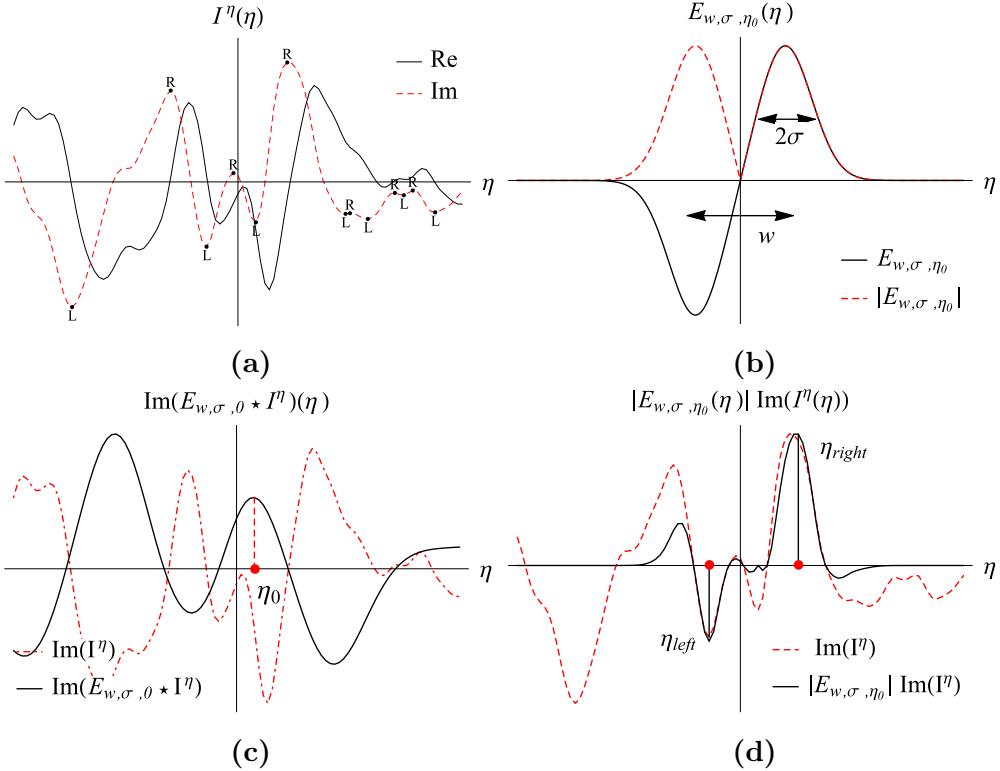


Figure 7.5: Edge detection using the edge probability envelope. (a) Cross-sectional intensity profile taken from Fig. 7.1c, showing many potential candidate left (L) and right (R) edge positions. (b) The edge probability profile. (c) Centering of the edge probability profile on the vessel of interest by means of correlation. (d) Enveloping the intensity profile results in clearly detectable left and right edge points.

more robust by taking into account that the vessel wall is a continuous structure, and that the width of a blood vessel gradually changes, rather than abruptly. Therefore, we introduce the (adaptive) edge probability envelope. The edge probability envelope is used to indicate the most likely position of the vessel edges and it consists of two Gaussian distributions, one around the expected left vessel edge position and one around the right vessel edge position. The envelope function is given by:

$$E_{\bar{w}_k, \sigma, \eta_0}(\eta) = -G_\sigma(\eta + \frac{\bar{w}_k}{2} - \eta_0) + G_\sigma(\eta - \frac{\bar{w}_k}{2} - \eta_0),$$

$$G_\sigma(x) = \frac{1}{\sigma\sqrt{2\pi}} e^{-\frac{x^2}{2\sigma^2}}, \quad (7.13)$$

where η_0 is the estimated location of the vessel center on L_k , \bar{w}_k is the mean vessel

7.3 Vessel Tracking in Orientation Scores via Optimization in Transversal Tangent Planes \mathcal{V}

width calculated over the last M iterations:

$$\bar{w}_k = \frac{1}{M} \sum_{m=1}^M w_{k-m} = \frac{1}{M} \sum_{m=1}^M \|\mathbf{u}_{k-m} - \mathbf{v}_{k-m}\|, \quad (7.14)$$

the standard deviation of the Gaussian distributions is denoted with σ , and η_0 is used to align the envelope with the actual vessel profile. A robust value for η_0 is found by optimizing the cross-correlation of the envelope with the imaginary part of the actual profile:

$$\eta_0 = \operatorname{argmax}_{\eta^* \in [-0.5\bar{w}_k, 0.5\bar{w}_k]} \int_{-\eta_{max}}^{-\eta_{max}} \operatorname{Im}(I_k^\eta(\eta)) E_{\bar{w}_k, \sigma, \eta^*}(\eta) d\eta, \quad (7.15)$$

see Fig. 7.5c. The left and right edges are finally detected as the arguments corre-

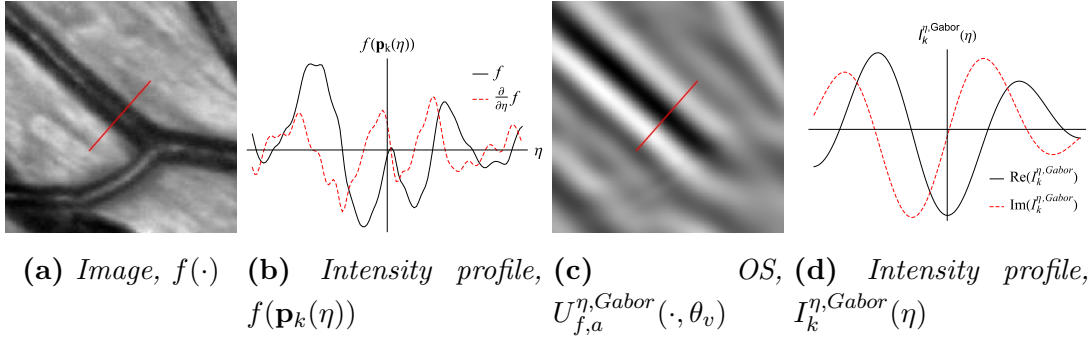


Figure 7.6: Scale selective orientation scores can filter out a vessels' central light reflex. (a) A small sub-image showing a vessel with central light reflex and (b) the corresponding intensity profile. (c) A slice, corresponding to the vessel orientation θ_v , of the orientation score constructed from (a) and (d) the corresponding intensity profile taken hereof. Note that from (d) the vessels center point can be roughly detected as a local minimum.

sponding to the minimum and maximum points, η_{left}^k and η_{right}^k respectively, of the product of the envelope and the intensity profile:

$$\begin{aligned} \eta_{left}^k &= \operatorname{argmin}_{\eta \in [-\eta_{max}, \eta_0]} \{\operatorname{Im} I_k^\eta(\eta) |E_{\bar{w}_k, \sigma, \eta_0}(\eta)|\}, \\ \eta_{right}^k &= \operatorname{argmax}_{\eta \in [\eta_0, \eta_{max}]} \{\operatorname{Im} I_k^\eta(\eta) |E_{\bar{w}_k, \sigma, \eta_0}(\eta)|\}, \end{aligned} \quad (7.16)$$

see Fig. 7.5d for an example. The new edge points can then be assigned by

$$\begin{aligned} \mathbf{u}_k &= \mathbf{p}_k(\eta_{left}^k), \\ \mathbf{v}_k &= \mathbf{p}_k(\eta_{right}^k). \end{aligned} \quad (7.17)$$

7. VES. TRACK. I: TRACKING VIA LOCAL OPTIMIZATION

Step 2: Orientation θ_k can be estimated by selecting the orientation that provides the highest orientation score response at both vessel edges. The orientation score response is a combination of the orientation columns at the left and right edges ($U_f(\mathbf{u}_k, \cdot)$ and $U_f(\mathbf{v}_k, \cdot)$ resp.), and the optimal orientation is calculated as:

$$\theta_k = \underset{\theta \in [0, 2\pi]}{\operatorname{argmax}} \operatorname{Im}(-U_f(\mathbf{u}_k, \theta) + U_f(\mathbf{v}_k, \theta)). \quad (7.18)$$

Finally the new center point \mathbf{c}_k , which may not be equal to $\tilde{\mathbf{c}}_k$, is calculated as the point between the two edges, according to Eq. (7.7).

7.3.1.2 CTOS: Multi-Scale Vessel Center-Line Tracking in Orientation Scores

In this section the scale-selective property of the Gabor wavelets is exploited in the design of a fast orientation score based method called CTOS. The potential presence of a central light reflex in a blood vessel makes the design of a simple and fast centerline tracking algorithm based on local minima tracking in the image nearly impossible. However, by using Gabor wavelets and appropriate scale selection, central light reflexes can be filtered out such that vessel center points can easily be detected as local minima on detection profiles (see Fig. 7.6).

The CTOS algorithm follows the same geometric principle as the ETOS algorithm, for a mathematical underpinning see Appendix B.1, however CTOS is done on the real part of orientation scores in order to find the vessel center line, rather than the vessel edges. In this algorithm each iteration k consists of 3-steps: In step 1 the center point \mathbf{c}_k is detected (η -optimization), in step 2 the orientation θ_k is detected (θ -optimization) and in step 3 the vessel scale a_k is detected (a -optimization).

Step 1: Using the vessel center point \mathbf{c}_{k-1} , orientation θ_{k-1} and scale a_{k-1} , which were detected during iteration $k-1$, phase 1 at iteration k is started by estimating the new center point $\tilde{\mathbf{c}}_k$ as given by Eq. (7.9). The new center point \mathbf{c}_k is selected from a set of candidate points $\mathbf{p}_k(\eta)$ as given by Eq. (7.11). From the candidate points $\mathbf{p}_k(\eta)$ a center point detection profile $I_k^{\eta, Gabor}(\eta)$ is obtained by:

$$I_k^{\eta, Gabor}(\eta) = U_{f, a_{k-1}}^{Gabor}(\mathbf{p}_k(\eta), \theta_{k-1}) \quad (7.19)$$

with $U_{f, a_{k-1}}^{Gabor}$ the orientation score generated by the Gabor wavelets at scale a_{k-1} . The new center point is detected as the coordinate belonging to the local minimum on the

7.3 Vessel Tracking in Orientation Scores via Optimization in Transversal Tangent Planes \mathcal{V}

intensity profile nearest to $\tilde{\mathbf{c}}_k$:

$$\begin{aligned} \mathbf{c}_k &= \mathbf{p}_k(\eta_0), \\ \eta_0 &= \underset{\eta \in [-\eta_{max}, +\eta_{max}]}{\operatorname{argmin}} \left\{ \operatorname{Re} I_k^{\eta, Gabor}(\eta) \right\}. \end{aligned} \quad (7.20)$$

Step 2: The new vessel orientation is detected as the local maximum of the negative orientation response, nearest to the previous vessel orientation θ_{k-1} :

$$\theta_k = \underset{\theta \in [0, 2\pi]}{\operatorname{argmax}} \operatorname{Re}(-U_{f, a_{k-1}}^{Gabor}(\mathbf{c}_k, \theta)). \quad (7.21)$$

Step 3: At the new center point \mathbf{c}_k and orientation θ_k , scale a_k is detected as the scale that gives the largest negative response:

$$a_k = \underset{a > 0}{\operatorname{argmax}} \operatorname{Re}(-U_{f, a}^{Gabor}(\mathbf{c}_k, \theta_k)). \quad (7.22)$$

Compared to the ETOS algorithm, this algorithm is very fast since it only requires three basic (deterministic) detection steps. However the combination of scale and orientation detection makes the algorithm slightly less stable: orientation detection depends on the correct detection of scale and vice versa.

7.3.2 Validation

The algorithms were tested on the green channel of color fundus images. For each image the luminosity is normalized by disposing low frequency luminosity drifts. The low frequency drifts are detected by large scale Gaussian blurring of the image (typically $\sigma = 32$), and are subtracted from the original image.

7.3.2.1 Algorithm Behavior at Complex Vessel Junctions

A qualitative validation is done using a challenging set of 4 sub-images (see Fig. 7.7), which were taken from the high-resolution fundus images of the HRFI database Budai (2011). This set of sub-images contains crossings, overlapping bifurcations with crossings, small vessels crossing large vessels, small vessels, curved vessels, parallel vessels, etc. In each sub-image we manually placed seed points at the start of each blood vessel and at each bifurcation. In total 27 seed points were marked. Each seed point contains initial vessel center position, left edge position, right edge position and orientation, denoted by \mathbf{c}_0 , \mathbf{u}_0 , \mathbf{v}_0 and θ_0 . The initial scale for the CTOS algorithm is detected as the scale that provides the largest scale response at \mathbf{c}_0 and θ_0 (see Eq. (7.22)).

7. VES. TRACK. I: TRACKING VIA LOCAL OPTIMIZATION

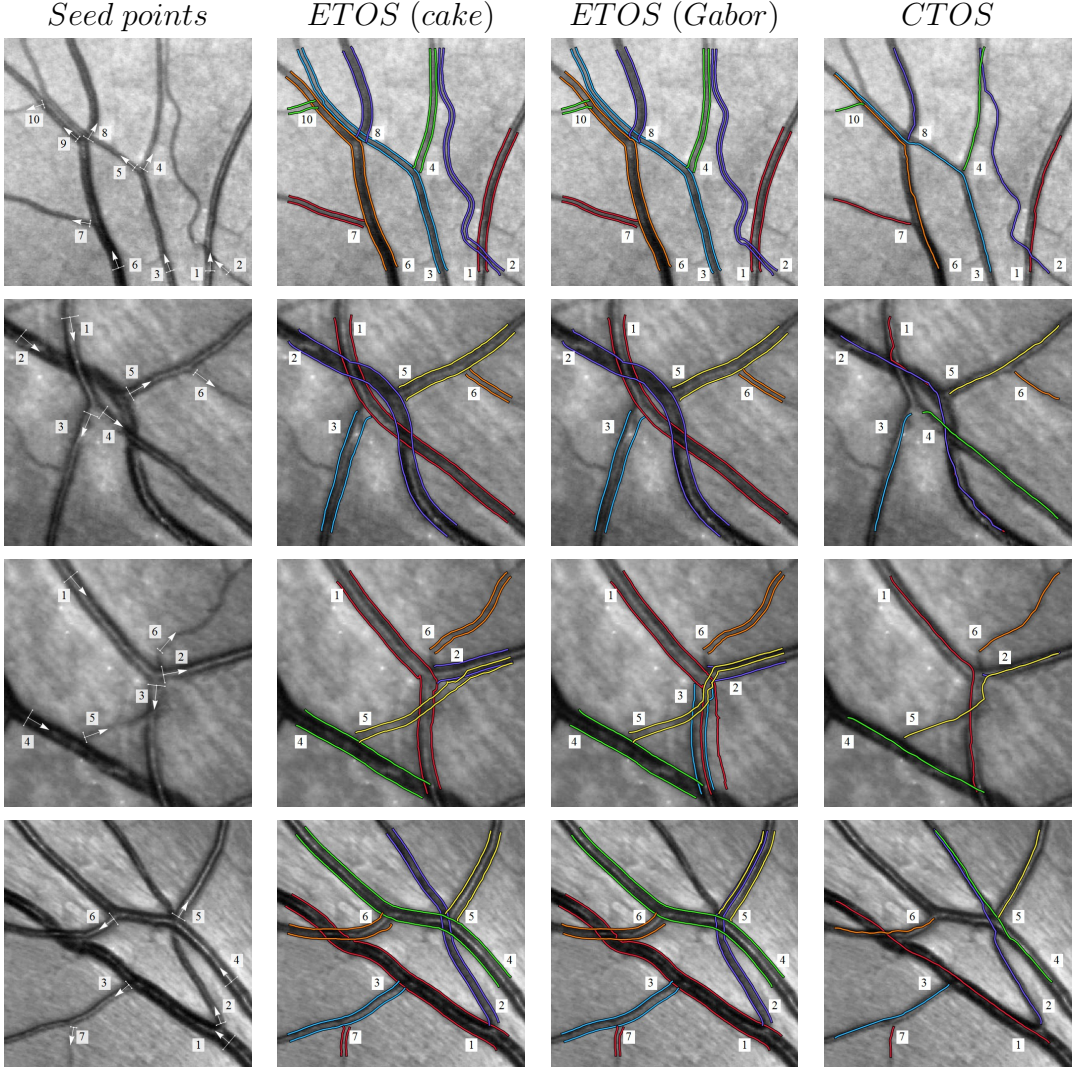


Figure 7.7: Results of vessel tracking on the test image set. From left to right: seed points, tracking results using the ETOS algorithm using invertible orientation scores (cake wavelets), tracking results of the ETOS algorithm using non-invertible orientation scores (Gabor wavelets at scale $\tau = 10$) and tracking results of the CTOS algorithm using orientation scores constructed at scales $\tau = 5, 10, 15, 20, 25$ and 30 . Note that the results of the CTOS algorithm are only represented as centerlines since vessel width is not measured. From top to bottom: results on test image 1, 2, 3 and 4.

The tracking experiments are conducted using the following set of tracking parameters:

7.3 Vessel Tracking in Orientation Scores via Optimization in Transversal Tangent Planes \mathcal{V}

Table 7.1: REVIEW database comparison of successful measurement percentages (%), mean vessel widths (Mean) and standard deviations of the measurement errors (σ_χ).

	KPIS			CLRIS			VDIS			HRIS		
	%	Mean	σ_χ	%	Mean	σ_χ	%	Mean	σ_χ	%	Mean	σ_χ
Standard	100.0	7.51	0.00	100.0	13.79	0.00	100.0	8.83	0.00	100.0	4.35	0.00
O1	100.0	7.00	0.23	100.0	13.19	0.57	100.0	8.50	0.54	100.0	4.12	0.27
O2	100.0	7.60	0.21	100.0	13.69	0.70	100.0	8.91	0.62	100.0	4.35	0.28
O3	100.0	7.97	0.23	100.0	14.52	0.57	100.0	9.15	0.67	100.0	4.58	0.30
Gregson	100.0	7.29	0.60	100.0	12.80	2.84	100.0	10.07	1.49	100.0	7.64	1.48
HHFW	96.3	6.47	0.39	0.0			78.4	7.94	0.88	88.3	4.97	0.93
1DG	100.0	4.95	0.40	98.6	6.30	4.14	99.9	5.78	2.11	99.6	3.81	0.90
2DG	100.0	5.87	0.34	26.7	7.00	6.02	77.2	6.59	1.33	98.9	4.18	0.70
ESP	100.0	6.56	0.33	93.0	15.70	1.47	99.6	8.80	0.77	99.7	4.63	0.42
Graph	99.4	6.38	0.67	94.1	14.05	1.78	96.0	8.35	1.43	100.0	4.56	0.57
ARIA	100.0	6.30	0.29	100.0	14.27	0.95	99.0	8.07	0.95	99.5	4.66	0.32
ETOS	100.0	6.14	0.36	100.0	14.03	0.53	99.87	8.36	0.80	99.83	4.95	0.45

Measurement method abbreviations: (Standard) - Ground truth measurements based on three human observer measurements, (O1-O3) - Human Observers 1-3, (Gregson) - Gregson rectangle fitting Gregson et al. (1995), (HHFW) - Half Height Full Width Brinchmann-Hansen & Heier (1986), (1DG) - 1D Gaussian model fitting Zhou et al. (1994), (2DG) - 2D Gaussian model fitting Lowell et al. (2004), (ESP) - Extraction of Segment Profiles Al-Diri et al. (2009), (Graph) - Graph based method Xu et al. (2011), (ARIA) - Autmated Retinal Image Analyzer Bankhead et al. (2012) and (ETOS) - Edge Tracking on Orientation Scores. **Dataset abbreviations:** (KPIS) - the Kick Point Image Set, (CLRIS) - Central Light Reflex Image Set, (VDIS) - Vascular Disease Image Set and (HRIS) - the downsampled High Resolution Image Set (HRIS). See Section 7.3.2.2 for more details.

ters: The step size is set to $\lambda = 2$ pixels; The width of the scan line is set to $2\eta_{max} = 40$ pixels; The number of orientations used to construct the orientation scores is set to $N_o = 36$ and the standard deviation of the Gaussian distributions used in the edge probability envelope is set to $\sigma = 3$.

The ETOS algorithm was tested on both invertible orientation scores, which were constructed by cake wavelets, and non-invertible orientation scores, which were constructed by Gabor wavelets. The scale of the Gabor wavelets was chosen in such a way

7. VES. TRACK. I: TRACKING VIA LOCAL OPTIMIZATION

that the relevant vessel features were presented as well as possible in the orientation scores (e.g. a scale too large would only represent the very large blood vessels correctly, and a scale too low only the small vessels). We found that $a = \frac{3}{2\pi}10$ gave best results. For the CTOS algorithm we used a set of orientation scores constructed by Gabor wavelets at scales $a = \frac{3\tau}{2\pi}$ with $\tau = 5, 10, 15, 20, 25$ and 30 .

Results of the tracking experiments are shown in Fig. 7.7. From this figure we see that, at complex situations, the ETOS method (column 2 and 3) outperforms the CTOS method (column 4). Best results are obtained when ETOS is used with invertible orientation scores (column 2). The ETOS algorithm acting on the invertible orientation scores generated by the cake kernels only fails to correctly track blood vessel nr 5 from image 3. The algorithm gives excellent results for all other vessels and manages to track the blood vessels through all complex situations, even when the contrast of the vessel edges is very low.

The performance of the ETOS algorithm is slightly decreased when applied to non-invertible orientation scores based on Gabor filters. It now fails to track 3 vessels correctly. The scale selective property of the Gabor wavelets, resulting in non-invertible orientation scores, causes the ETOS algorithm to perform less accurately compared to the application to invertible orientation scores.

The CTOS algorithm, which relies on a multi-scale orientation score approach, has the lowest performance. It fails to correctly track 5 blood vessels. In some cases, incorrect scale selection causes small parallel blood vessel to be detected as one large blood vessel (vessel 2 with 4, and 3 with 6 in the first image). Other tracks failed as a result of incorrect orientation detection.

In conclusion we can state that ETOS outperforms CTOS and that it gives best results when applied on *invertible* orientation scores.

7.3.2.2 Validation of Width Measurements

In the previous section we showed that the ETOS algorithm is very well capable of tracking blood vessels through complex situations. In this section we quantitatively validate the reliability of the measured *vessel widths* that are provided by the ETOS algorithm. This is done by comparing the measured widths to ground truth width measurements provided by the REVIEW database Al-Diri *et al.* (2009). The REVIEW database consists of 16 color fundus images, which can be divided into 4 subsets: 1) Kick point image set (KPIS), 2) Central light reflex image set (CLRIS), 3) Vascular disease image set (VDIS) and 4) the high resolution image set (HRIS). Each image set

7.3 Vessel Tracking in Orientation Scores via Optimization in Transversal Tangent Planes \mathcal{V}

represents images of different quality and resolution, and all are provided with manual width measurements that are performed by three individual observers. A ground truth of the vessel widths is constructed by averaging the measurements of the observers. The HRIS set contains high resolution images (3584x2438) and were down-sampled by a factor of four before submission to the ETOS algorithm. For more information on the dataset we would like to refer to Al-Diri *et al.* (2009).

When testing our algorithm, we tracked each segment by initializing the algorithm using the first pair of manually marked edge points. The same parameters that are described in Section 7.3.2.1 were used. Fig. 7.9 shows a selection of the tracking results in comparison to ground truth vessel edge labeling.

In total 5066 vessel width measurements are available. The error between automated measurements and the ground truth measurements is defined as

$$\chi_i = w_i - w_i^{GT} = \|\mathbf{u}_i - \mathbf{v}_i\| - w_i^{GT} \quad (7.23)$$

where w_i is the estimated width as measured by the ETOS algorithm (recall Eq. (7.8)), and w_i^{GT} is the ground truth width of the i th profile. To be able to compare our method with others we follow the same validation procedure as described in Al-Diri *et al.* (2009); Bankhead *et al.* (2012); Xu *et al.* (2011), where the main focus is on the standard deviation of the errors. This is motivated by the idea that different implicit definitions of vessel widths may lead to consistent errors. If this bias however is consistent enough, the error could easily be accounted for by subtraction of a bias constant. A low standard deviation of the errors indicates that the error is consistent.

Table 7.1 shows the validation results of our ETOS algorithm, in comparison with methods by other authors that published their results using the same database Al-Diri *et al.* (2009); Bankhead *et al.* (2012); Xu *et al.* (2011). The first four rows of the table show the results of the manual annotations (observer 1, 2 and 3) and the golden standard. The next four rows show results of four classic approaches to vessel width measurements:

- Gregson: a rectangle is fitted to a vessel intensity profile, and the width is set such that the area under the rectangle and profile Gregson *et al.* (1995) are equal.
- Half Height Full Width (HHFW): the standard half-height method, which uses thresholds set half-way between the maximum and minimum intensities at either side of an estimated center point Brinchmann-Hansen & Heier (1986).
- 1D Gaussian (1DG): a 1D Gaussian model is fit to the vessel intensity profile Zhou *et al.* (1994).

7. VES. TRACK. I: TRACKING VIA LOCAL OPTIMIZATION

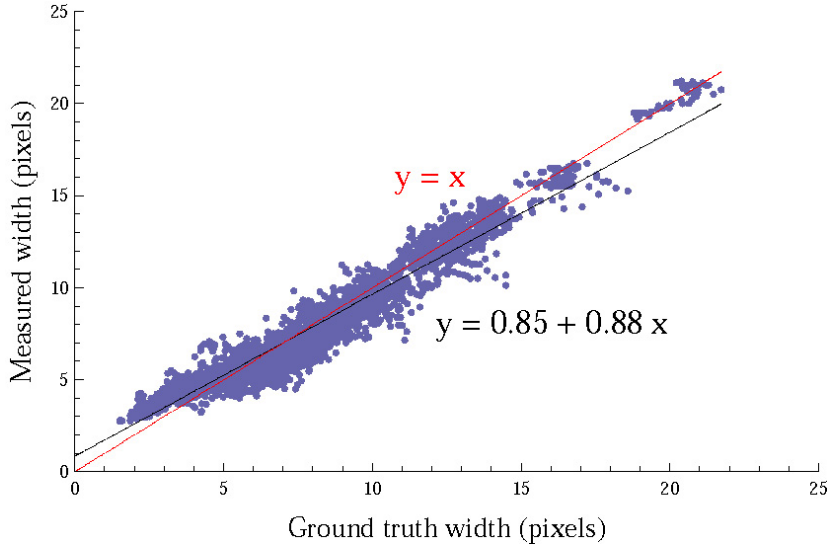


Figure 7.8: A scatter plot, plotting 5059 ground truth widths against the widths measured by our ETOS algorithm. The linear regression model $y = 0.85 + 0.88x$ indicates an offset of less than a pixel, suggesting that ETOS slightly over-estimates the vessel widths. The slope of 0.88 indicates a strong positive relation between the ground truth and measured widths.

- 2D Gaussian: a 2D Gaussian model is fit to the vessel intensity profile Lowell *et al.* (2004).

The next three rows give results of the most recent, state of the art methods that published their results:

- The Extraction of Segment Profiles (ESP) is an active contour algorithm by Al-Diri *et al.* Al-Diri *et al.* (2009).
- The Graph method is a graph based edge segmentation technique developed by Xu *et al.* Xu *et al.* (2011).
- The Automated Retinal Image Analyzer (ARIA) is an algorithm developed by Bankhead *et al.* Bankhead *et al.* (2012), they used a wavelet approach to vessel segmentation after which the edge locations are refined.

The last row shows the results we achieved using our ETOS algorithm.

The column labeled with % shows the success rate, it indicates how many width measurements could successfully be validated (for more detail see Al-Diri *et al.* (2009)).

7.3 Vessel Tracking in Orientation Scores via Optimization in Transversal Tangent Planes \mathcal{V}

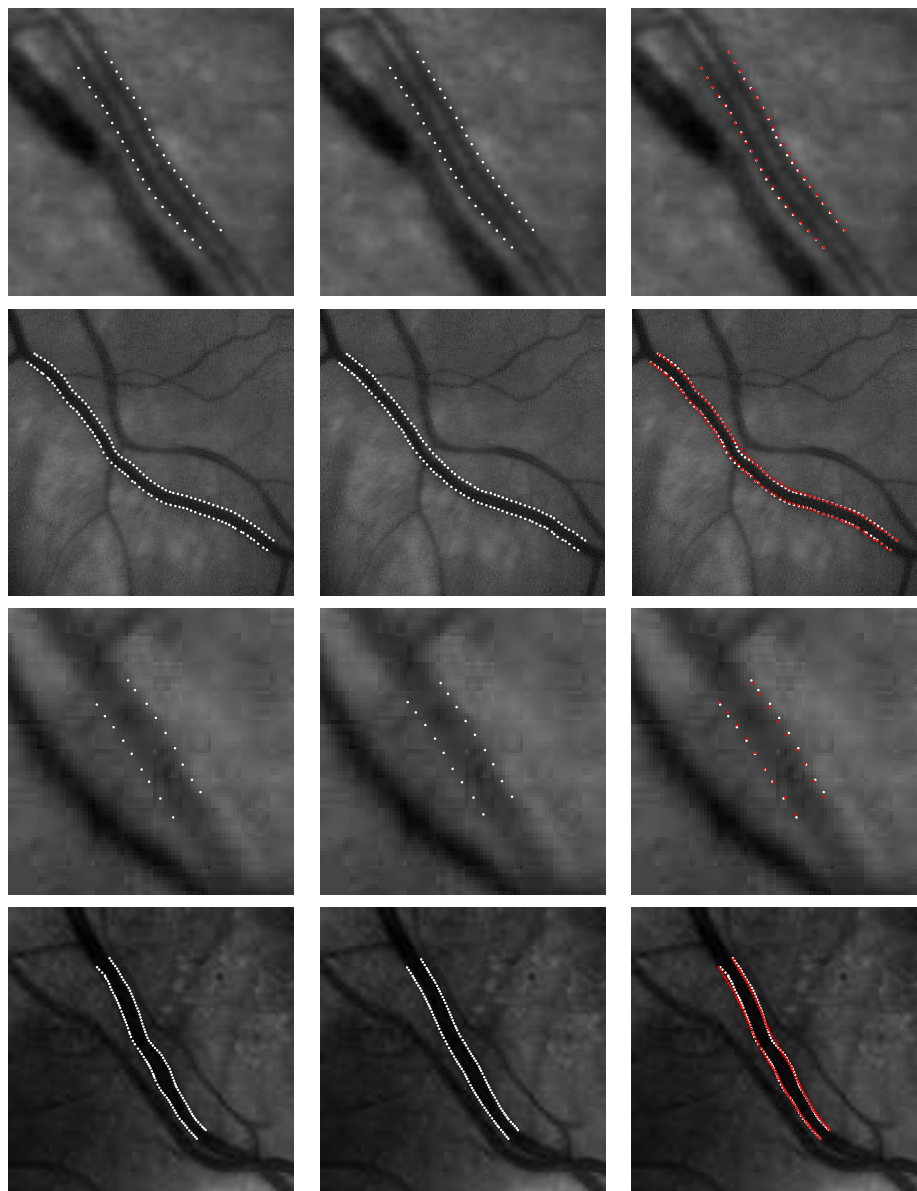


Figure 7.9: Several tracked vessel segments by ETOS in comparison with manual width measurements. Left column shows the ground truth vessel edge labeling as provided by the REVIEW database. The middle column shows results obtained by the ETOS algorithm and the right column shows both the ground truth (in white) and our results (in red).

7. VES. TRACK. I: TRACKING VIA LOCAL OPTIMIZATION

The success percentage is smaller than 100% whenever measurements failed to converge, e.g. when the distance between the ground truth and measured edge pair was too large. The column labeled with *Mean* indicates the mean vessel width of all the measured vessel profiles. The column labeled with σ_χ indicates the standard deviation of the error (Eq. (7.23)), a lower σ_χ is favorable since it indicates that the error is consistent.

From Table 7.1 it can be observed that ESP, Graph, ARIA and our ETOS algorithm all outperform the classic width measurement techniques. Also compared to the state of the art methods our algorithm scores very well. The ETOS algorithm performs remarkably well on the CLRIS dataset, which contains a large number of vessels with the central light reflex. For these images, the standard deviation of the errors is even lower than those of the observers. For other datasets, our method's performance is comparable to the state of the art.

Fig. 7.8 shows a scatter plot of the ground truth widths against the widths measured by our ETOS algorithm, together with a linear regression model that was fit through these points. The points are very much centered around the line $y = x$, indicating a strong positive correlation. This is confirmed by the slope of the linear regression model $y = 0.85 + 0.88x$, which is near to 1. The low number of outliers in the scatter plot confirms the low standard deviation in errors, as demonstrated by Table 7.1. The offset of 0.85, together with slope 0.88, indicate that the ETOS algorithm has the tendency to slightly overestimate for vessels of size up to 7 pixels and underestimates for larger vessel sizes.

We conclude that our ETOS algorithm, which is highly capable of tracking blood vessels through all sorts of complex situations, also provides reliable width measurements.

7.4 Vasculature Tracking

In this section we describe additions to the ETOS algorithm, so as to be able to construct models of the complete retinal vasculature. Our vasculature tracking algorithm consists of:

1. Optic disk detection.
2. Seed point detection in the optic disk region.
3. Correct initialization of the ETOS algorithm by robust initial edge detection.
4. Automatic termination based on a set of stopping criteria.

5. Junction detection, classification and numbering.
6. Junction resolving.

Each of these items is described in Sections 7.4.1.1 to 7.4.1.5 and the complete algorithm is validated in Section 7.4.2. We omit details on the basic optic disk detection algorithm that we used in the experiments as it is inferior to the method of Sec. 5.5.2. For details on this method (which relies on a combination of variance filtering Sinthanayothin *et al.* (1999), edge focussing Bergholm (1987) and the Hough transform Hough (1962)) see (Bekkers *et al.*, 2014a, Sec. 4.1.1)).

7.4.1 Methods

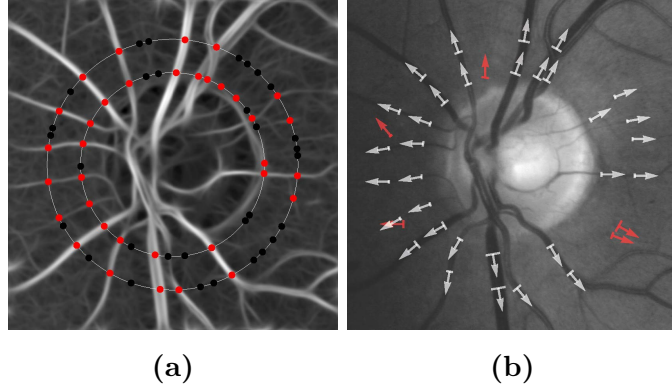


Figure 7.10: Initial seed point detection from vessel likelihood maps. (a) A vessel likelihood map of the optic disk region, with two circular profiles on which initial seed points are detected. Detected seed points are shown as red dots, discarded as black dots. (b) Edge initialization and true positive seed point selection. White arrows show the detected seed points, red arrows are seed points classified as false positives.

7.4.1.1 Vessel Likelihood Map and Seed Point Detection

For the detection of the initial seed points, a vessel likelihood map $V : \mathbb{R}^2 \mapsto \mathbb{R}$ of the optic disk region is constructed using invertible orientation scores. For simplicity this is done via (see (Bekkers *et al.*, 2014a, Sec. 4.1.2) for a motivation)

$$V(\mathbf{x}) = \max_{\theta \in [0, 2\pi]} \operatorname{Re}(-U_f(\mathbf{x}, \theta)). \quad (7.24)$$

7. VES. TRACK. I: TRACKING VIA LOCAL OPTIMIZATION

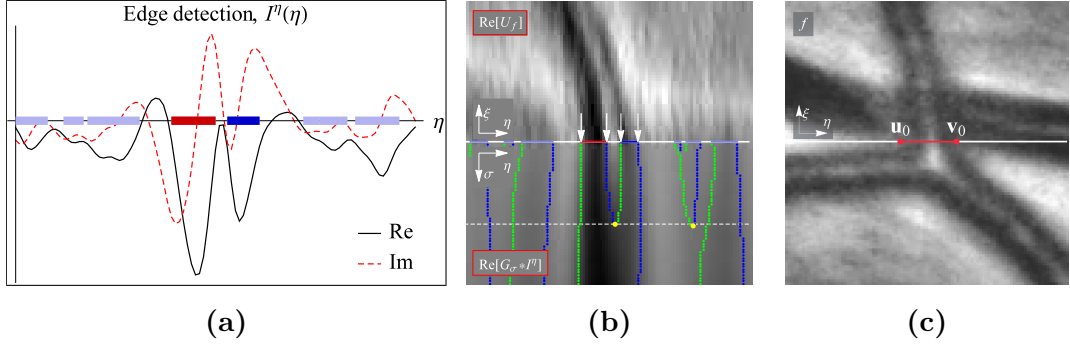


Figure 7.11: Initial edge detection. (a) Based on local optima in the imaginary part of I^η , potential vessel patches are formed (shown as horizontal blocks). The main patch of interest is denoted in red and neighbouring patches of interest in non-transparent blue. (b) The edges of the patches of interest are tracked in scale (lower part of this figure) up to the scale σ of the corresponding top points (yellow points) Florack & Kuijper (2000); Johansen (1994). (c) The strongest edges at this scale are initialized to be the vessel edges u_0 and v_0 .

Seed points are detected as local maxima on circular intensity profiles centered around the optic disk (Fig. 7.10a) with radii $R = \{R_{OD}, 1.5R_{OD}\}$, where R_{OD} is the detected optic disk radius (Bekkers *et al.*, 2014a, Sec. 4.1.1)). A seed point is discarded whenever its value in the vessel likelihood map V is smaller than the average value of all points on the circle. For each remaining seed point c_0 , the initial orientation θ_0 is detected as the orientation that provides the highest modulus of the orientation scores: $\theta_0 = \underset{\theta \in [0, 2\pi]}{\operatorname{argmax}} |U_f(c_0, \theta)|$. An additional filtering step, in which the seed points are classified as either true or false positive, is described in Section 7.4.1.2.

7.4.1.2 Initial Edge Detection

The ETOS algorithm is initialized with a starting vessel center point c_0 , orientation θ_0 and edges u_0 and v_0 . Starting with an already detected initial center point c_0 and orientation θ_0 , intensity profile I^η can be obtained from the orientation scores using Eq. (7.12). Candidate edges are detected as local optima on the imaginary part of I^η . Beside the main vessel edges that we are interested in, it is very likely that multiple other candidate edges are detected as well (as a result of noise or a central light reflex). Therefore, we use an edge focussing approach to detect the dominant edges. Each combination of neighboring left and right edges will form potential vessel patches (see Fig. 7.11a). Note that a blood vessel with a central light reflex consists of

two neighboring vessel patches. We start initial edge detection by detecting the main vessel patch of interest by scoring each edge pair (\mathbf{u}, \mathbf{v}) , based on the initial center point estimate \mathbf{c}_0 and initial orientation θ_0 , as follows:

$$s_{\mathbf{c}_0, \theta_0}(\mathbf{u}, \mathbf{v}) = \nu_{\theta_0}(\mathbf{u}, \mathbf{v}) e^{-\frac{1}{2} \frac{\|(\mathbf{u} + \mathbf{v})/2 - \mathbf{c}_0\|^2}{(0.5\langle w \rangle_{av})^2}}, \quad (7.25)$$

with

$$\nu_{\theta}(\mathbf{u}, \mathbf{v}) = \frac{1}{\|\mathbf{u} - \mathbf{v}\|} \int_0^1 |U_f(\mathbf{u} + t(\mathbf{v} - \mathbf{u}), \theta)| dt, \quad (7.26)$$

and with

$$\langle w \rangle_{av} \approx \langle w \rangle_{av}^{ref} \cdot res = (200\mu m) \cdot res \quad (7.27)$$

an estimated of the average vessel width in pixels, obtained from a reference vessel width $\langle w \rangle_{av}^{ref} = 200\mu m$ and an estimate of the image resolution res (in $pix/\mu m$). This estimated vessel width $\langle w \rangle_{av}$ will be used in other steps as well in order to scale parameters which are sensitive to the image resolution. The function $\nu_{\theta}(\mathbf{u}, \mathbf{v})$ provides the so called *vessel value* and basically is the average value of the modulus of the orientation score at orientation θ , calculated from the left to the right edge. This value is high for elongated/vessel structures, and low for background structures in the score. The exponential in Eq. (7.25) penalizes the distance of the edge pair to the initialized center point. The edge pair with the highest score will be our main pair of interest.

Neighboring pairs are considered only if the distance between the nearest edges of the main and neighboring pair is smaller than the width of the main patch, Fig. 7.11a shows typical results. All edges from the main patch and its neighbors are now traced (in scale) in the Gaussian scale space of profile I^n . The edges are traced up to the scale of the first appearing topoint. The strongest edges at this scale are chosen as the true vessel edge points \mathbf{u}_0 and \mathbf{v}_0 (Fig. 7.11c).

An initialized seed point whose vessel value is lower than a threshold T_{ν} is regarded as a false positive (Fig. 7.10b). The threshold T_{ν} is defined as:

$$T_{\nu} = 0.5\langle \nu \rangle_{av}, \\ \langle \nu \rangle_{av} = \frac{1}{N_{sp}} \sum_{i=1}^{N_{sp}} \nu_{\theta_0^i}(\mathbf{u}_0^i, \mathbf{v}_0^i), \quad (7.28)$$

where using all N_{sp} initialized seed points, each with initial edge points $(\mathbf{u}_0^i, \mathbf{v}_0^i)$ and orientation (θ_0^i) , an average vessel value $\langle \nu \rangle_{av}$ is calculated. All true positive seed points are submitted to the ETOS algorithm to start expanding a model of the retinal vasculature.

7. VES. TRACK. I: TRACKING VIA LOCAL OPTIMIZATION

7.4.1.3 Stopping Criteria

For ETOS to stop tracking a single vessel, three stopping-criteria are defined:

1. Tracking stops whenever a vessel being tracked leaves a prescribed region of interest. For this purpose a mask image is generated that covers the (typically circular) field of view in the fundus image.
2. Tracking stops whenever a blood vessel is already tracked. Each tracked segment is used to construct a pixel map, in which each pixel within the vessel edge contours is set to 1 and outside to 0. Whenever a point within the vessel being tracked lies within the pixel map for $\lceil 4\langle w \rangle_{av}/\lambda \rceil$ iterations in a row, the ETOS algorithm terminates. Recall $\langle w \rangle_{av}$ defined in Eq. (7.27) and λ being the step size (Fig. 7.4).
3. Tracking stops whenever the vessel value ν_θ (Eq. (7.26)) drops below threshold value T_ν . Here we assumed that T_ν , which is based on the average vessel value $\langle \nu \rangle_{av}$ calculated in the optic disk region, is a good indicator of the vessel values of the vessels elsewhere in the retina.

7.4.1.4 Junction Detection, Classification and Numbering

In order to model the complete vasculature, starting by expanding a model from a set of initial seed points, the vasculature tracking algorithm should also be able to automatically detect junctions. Junction points are points where blood vessels bifurcate/branch or where two blood vessels cross. Either way, at a junction point multiple orientations may be observed.

During vessel tracking, the orientation columns at the left and right edge are scanned for the presence of a junction point, and the location and orientation are stored (top image Fig. 7.12). The detected junction points are clustered on position by grouping all points whose distance to one another is smaller than $\langle w \rangle_{av}$. Within each cluster, the candidate junction points are clustered on orientation to prevent merging two proximate junction points. Clustering on orientation is done according to the number of local maxima in the histogram of orientations. Finally, clusters are merged to a single junction point by averaging the positions and by taking the most common orientation within the cluster. The found center points and orientations are then subjected to the edge initialization method described in Section 7.4.1.2, and are discarded whenever their vessel value is lower than T_ν .

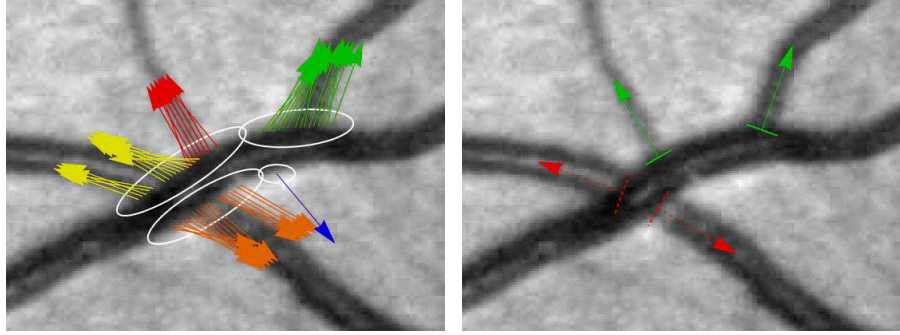


Figure 7.12: Junction detection. *Left:* Candidate junction points (colored arrows) are clustered on position (indicated by white ellipsoids) after which they are clustered on orientation (indicated by different colors). *Right:* Each cluster is merged to a single junction point and based on proximity to other junction points, orientation and width, junction points are classified as bifurcation (green arrows) or crossing (red dashed arrows).

To classify between junctions and bifurcations we check for alignment of local orientations in $\text{SE}(2)$ via the sub-Riemannian metric tensor of Eq. (4.7) for $\mathcal{C} = 1$ (see also Ch. 8 for more details).

Each detected seed point is assigned two ID numbers, a number that is unique for each vessel segment and the ID number of the vessel from which it originates. This way the relation between each vessel segment remains known, and the vessel segments can be organized in a hierarchical fashion. Vasculature tracking terminates whenever all detected bifurcations and crossings are evaluated.

7.4.1.5 Junction Resolving

As mentioned in Section 7.4.1.3 vessel tracking is terminated whenever the algorithm is tracking a vessel that is already tracked. This criterion can be met at several situations, where for each situation appropriate actions need to be taken in order to maintain correct topological models of the vasculature. A detected point that suggests inappropriate modeling of the vasculature will be called an *unresolved junction point*. The detection of an unresolved junction point, together with the corresponding actions that are necessary to solve it will be called *junction resolving*. The appropriate actions necessary for junction resolving are based on the position of the junction point on the already established track, whether or not the two overlapping segments have the same

7. VES. TRACK. I: TRACKING VIA LOCAL OPTIMIZATION

with and in the case the

The junction resolving steps are described using the following labeling: S_{old} is the tracked segment of the established track before the junction point (Source), T_{old} is the tracked segment of the same track after the junction point (Target), S_{new} is the segment of the new track before the junction point, and T_{new} is the segment of the new track after the junction point. The appropriate actions necessary for junction resolving are based on

1. the position of the junction point on the established track (S_{new} - T_{new}),
2. whether or not the 2 overlapping segments (T_{new} , T_{old}) have the same width,
3. and the similarity between the source and target tracks.

The detailed junction resolving scheme can be found in Bekkers (2012).

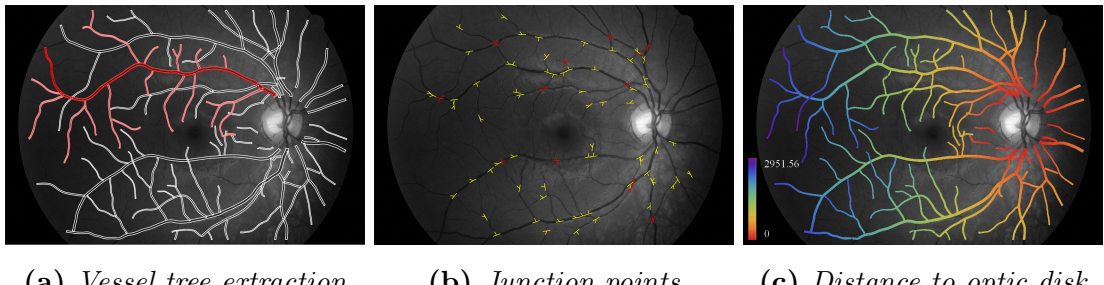


Figure 7.13: (a):The hierarchical structure of the generated vasculature models allow the segmentation and analysis of complete branches. (b) The automatic extraction of branching (yellow) and crossing points (red). (c) The distance to the optic disk; a feature that can easily be extracted because of the guaranteed connectedness of vessel segments in the generated vasculature models.

7.4.2 Validation

In Section 7.3.2.2 we demonstrated the reliability of the width measurements provided by the ETOS algorithm. In the following section we validate the topological correctness of the complete vasculature models that are generated by our algorithm. The correctness of the models is validated by analyzing the junction points. The results discussed in this section are generated with the same parameters for the ETOS algorithm that are described in Section 7.3.2.1. A typical model generated by the vasculature tracking algorithm with these parameters is shown in Fig. 7.13.

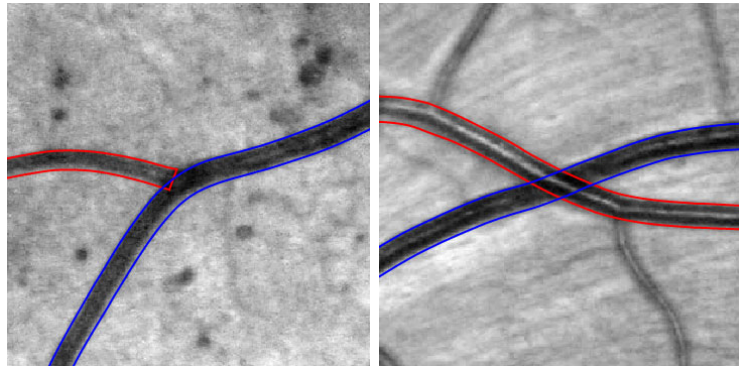


Figure 7.14: A typical bifurcation (left) and crossing (right), detected from a model generated by our vasculature tracking algorithm.

7.4.2.1 Validation of Topological Correctness

For each vessel it is known from which parent vessel it originates and bifurcations can thus be directly extracted from the model. Crossings can easily be extracted by detecting overlapping vessel segments. Fig. 7.13b provides an overview of detected junction points for one image of the HRFI-database, Fig. 7.14 shows detailed views of a bifurcation and a crossing. We evaluated the junction points of the first three images from each of the three HRFI-datasets (healthy, diabetes and glaucoma). The 9 generated vasculature models provided 495 junction points, of which 381 were bifurcation points and 114 were crossing points. The following types of errors for bifurcations were identified: the bifurcation was actually part of a crossing (E1), the vessel originating from the bifurcation did not represent a blood vessel according to the ground truth pixel map provided by the HRFI-database (E2). E2 errors indicate the presence of incorrect single vessel models, non-vessel elongated structures such as the optic disk border or pathological features such as aneurysms. Crossings are extracted by searching the vasculature model for overlapping vessel segments. A false positive crossing can thus only occur if false positive vessel segments exists within the models. The results are summarized in Table 7.2.

In total 290 out of 381 bifurcations and 109 out of 114 crossings were correctly detected, corresponding to precision rates of 76.54% and 96.03% respectively. Most of the incorrectly identified bifurcations were correct in the sense that they represent a true blood vessel, however they were actually part of a crossing. Only 5.25% of the bifurcations were incorrect in the sense that they did not represent a blood vessel. While the first kind of false positive bifurcations only affects the topological correctness

7. VES. TRACK. I: TRACKING VIA LOCAL OPTIMIZATION

Table 7.2: Validation of detected bifurcations for three different image groups: healthy (H), diabetes (D) and glaucoma (G).

Group	Bifurcations				Crossings		
	Correct	Crossing (E1)	False Vessel (E2)	Total	Correct	Incorrect	Total
H	90 (81.82%)	16 (14.55%)	4 (3.64%)	110	41 (100.0%)	0 (0.00%)	41
D	111 (73.03%)	25 (16.45%)	16 (10.53%)	152	37 (88.10%)	5 (11.90%)	42
G	89 (74.79%)	30 (25.21%)	0 (0.00%)	119	31 (100.0%)	0 (0.00%)	31
All	290 (76.12%)	71 (18.64%)	20 (5.25%)	381	109 (95.61%)	5 (4.39%)	114

of the model, the latter also pollutes the model with false positive vessel segments. The low percentage of E2 errors indicates that the generated vasculature models are very clean in the sense that almost all vessel segments actually represent true blood vessels.

7.5 Conclusion

In this chapter we demonstrated that by representing image information in an invertible orientation score, one can exploit the disentanglement of crossing structures to track blood vessels through crossing points. We introduced a new algorithm that tracks vessel edges through the orientation score of an image (ETOS). The ETOS algorithm can generally be used with both invertible and non-invertible orientation scores, which were in this chapter constructed with cake wavelets and Gabor wavelets respectively. We demonstrated that best results were obtained using invertible orientation scores. We also introduced a fast alternative method based on vessel centerline tracking through a multi-scale set of non-invertible orientation scores (CTOS). While the CTOS algorithm is very fast, the multi-scale approach makes the algorithm less stable at critical vessel points (crossings and parallel vessels) compared to ETOS.

The ETOS algorithm was used as a basis for our vasculature tracking algorithm, which we used to construct detailed hierarchical models of the retinal vasculature. Within this chapter we validated the reliability of the width measurements provided by the models using ground truth data, and showed that our method performs excellently in comparison to other state of the art algorithms. Validation of the topology of the models showed that our method constructs clean topological models of the vasculare tree, i.e. they contain very few false positive vessels.

Tracking within orientation scores relies on a novel and basic geometrical principle (\mathcal{V} -plane optimization) within a sub-Riemannian manifold within $SE(2)$. In Ap-

7.5 Conclusion

pendix B.1 we relate probabilistic approaches to find optimal curves in $\text{SE}(2)$ to this geometric principle. Here we include supporting examples of analytic and numeric computations on completion fields on $\text{SE}(2)$. Such completion fields are obtained from collision probabilities on $\text{SE}(2)$, while the orientation score provides a whole distribution of these particles. The next step is to apply tracking by geometric control Duits *et al.* (2013a) in (enhanced) orientation scores. This will allow for tracking along curves that are minimizers of a global curve optimization problem instead of local optimization by \mathcal{V} -plane optimization. This will be the topic of the next Chapter 8.

Chapter 8

Vessel Tracking Part II: Sub-Riemannian Geodesics in $\text{SE}(2)$

This chapter is based on:

Bekkers, E.J., Duits, R., Mashtakov, A., Sanguinetti, G.R.: A PDE approach to data-driven sub-Riemannian geodesics in $\text{SE}(2)$. *SIAM Journal on Imaging Sciences (SIIMS)* 8(4) (2015) 27402770

Bekkers, E., Duits, R., Mashtakov, A., Sanguinetti, G.: Data-driven sub-Riemannian geodesics in $\text{SE}(2)$. In Aujol, J.F., Nikolova, M., Papakadis, N., eds.: *Scale Space and Variational Methods in Computer Vision (SSVM)*. Volume 9087 of *Lecture Notes in Computer Science*. Springer International Publishing (2015) 613-625

Sanguinetti, G., Duits, R., Bekkers, E., Janssen, M., Mashtakov, A., Mirebeau, J.: Sub-Riemannian fast marching in $\text{SE}(2)$. In Kittler, J., Pardo, A., eds.: *Proceedings of the Iberoamerican Conference on Pattern Recognition (ICIP)*, Montevideo, Uruguay, November 9-12, 2015. *Lecture Notes in Computer Science* (2015) 366-374

8.1 Introduction

In computer vision, it is common to extract salient curves in images via minimal paths or geodesics minimizing a length functional Citti & Sarti (2006). The minimizing geodesic is defined as the curve that minimizes the length functional, which is typically weighted by a cost function with low values on image locations with high curve saliency. Two classical approaches to computing data-adaptive geodesics are 1) via level set approaches for geometric/geodesic active contours (see e.g., Caselles *et al.* (1997); Sethian (1999); Osher & Fedkiw (2006); Kimmel & Bruckstein (2003)), such methods provide locally optimal geodesics, or 2) via a Hamilton-Jacobi-Bellman approach in which globally optimal geodesics are found via backtracking on geodesic distance maps that are obtained as solutions to the eikonal equation (see e.g. Cohen & Kimmel (1997); Sethian (1999); Peyré *et al.* (2010)). In this chapter we use the latter approach.

Another set of geodesic methods, partially inspired by the psychology of vision was developed in Citti & Sarti (2006); Petitot (2003). In particular, in Citti & Sarti (2006) the roto-translation group $SE(2) = \mathbb{R}^2 \rtimes S^1$ endowed with a sub-Riemannian (SR) metric models the functional architecture of the primary visual cortex and geodesics (stratifying a minimal surface) are used for completion of occluded contours. A stable wavelet-like approach to lift 2D-images to functions on $SE(2)$ was proposed in Duits *et al.* (2007b). Within the $SE(2)$ framework, images and curves are lifted to the 3D space $\mathbb{R}^2 \rtimes S^1$ of coupled positions and orientations in which intersecting curves are disentangled. The SR-structure applies a restriction to so-called horizontal curves which are the curves naturally lifted from the plane (see Fig. 8.1A). For a general introduction to sub-Riemannian geometry see Montgomery (2006). For explicit formulas of SR-geodesics and optimal synthesis in $SE(2)$ see Sachkov (2011). SR-geodesics in $SE(2)$ were also studied in Ben-Yosef & Ben-Shahar (2012); Boscain *et al.* (2014); Duits *et al.* (2013a); Hladky & Pauls (2009); Mashtakov *et al.* (2013); Moiseev & Sachkov (2010).

Here, we propose a new wavefront propagation-based method for finding SR-geodesics within $SE(2)$ with a metric tensor depending on a smooth external cost $\mathcal{C} : SE(2) \rightarrow [\delta, 1]$, $\delta > 0$ fixed. Our solution is based on a Hamilton-Jacobi-Bellman (HJB) equation in $SE(2)$ with a SR metric that includes the cost. This method adapts a classical PDE approach for finding geodesics used in computer vision Cohen & Kimmel (1997); Sethian (1999); Peyré *et al.* (2010) to the SR-geometry case. It is of interest to interpret the viscosity solution of the corresponding HJB equation as a sub-Riemannian distance map Trélat (2006). Using Pontryagin's Maximum Principle (PMP), we derive the HJB-system with an eikonal equation providing the propagation of geodesically equidistant surfaces departing from the origin. We prove this in Thm. 2, and we show that SR-

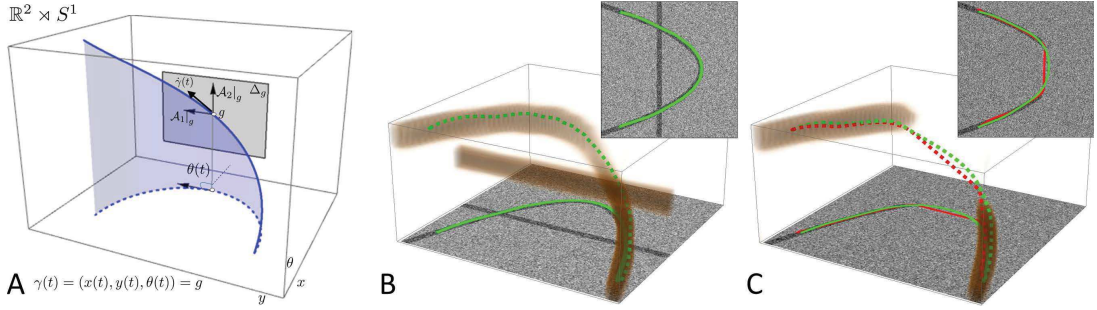


Figure 8.1: **A:** Every point in the planar curve $\gamma_{2D}(t) = (x(t), y(t))$ is lifted to a point $g = \gamma(t) = (x(t), y(t), \theta(t)) \in SE(2)$ on a horizontal curve (solid line) by considering the direction of the tangent vector $\dot{\gamma}_{2D}(t)$ of the planar curve as the third coordinate. Then, tangent vectors $\dot{\gamma}(t) \in \text{span}\{\mathcal{A}_1|_{\gamma(t)}, \mathcal{A}_3|_{\gamma(t)}\} = \Delta|_{\gamma(t)}$. **B:** In the lifted domain $SE(2)$ crossing structures are disentangled. **C:** The SR-geodesic (green) better follows the curvilinear structure along the gap than the Riemannian geodesic (red).

geodesics are computed by backtracking via PMP. In Thm. 3, we consider the uniform cost case (i.e. $\mathcal{C} = 1$) and we show that the surfaces coincide with the SR-spheres, i.e. the surfaces from which every tracked curve is globally optimal. This uniform cost case has been deeply studied in Sachkov (2011) relying on explicit ODE-integration in PMP. In this chapter, we will rely on a PDE-approach, allowing us to extend the SR geodesic problem to the general case where \mathcal{C} is a smooth cost uniformly bounded from below and above. We will often use the results in Sachkov (2011) as a golden standard to verify optimality properties of the viscosity solutions and accuracy of the involved numerics of our PDE-approach. We find a remarkable accuracy and convergence towards exact solutions, 1st Maxwell sets (i.e. the location where for the first time two distinct geodesics with equal length meet), and to the cusp surface Boscain *et al.* (2014); Duits *et al.* (2013a).

Potential towards applications of the method with non-uniform cost is demonstrated by performing vessel tracking in retinal images. Here the cost function is computed by lifting the images via oriented wavelets, as is explained in Section 8.5. Similar ideas of computing geodesics via wavefront propagation in the extended image domain of positions and orientations, and/or scales, have been proposed in Benmansour & Cohen (2011); Li & Yezzi (2007); Péchaud *et al.* (2009b). In addition to these interesting works we propose to rely on a SR geometry. Let us illustrate some key features of our method. In Fig. 8.1B one can see how disentanglement of intersecting structures, due to their difference in orientations, allows to automatically deal with crossings (a similar result

8. VES. TRACK. II: SUB-RIEMANNIAN GEODESICS IN SE(2)

can be obtained with the algorithm in Péchaud *et al.* (2009b)). The additional benefit of using a SR geometry is shown in Fig. 8.1C where the SR-geodesic better follows the curvilinear structure along the gap. Further benefits follow in the experimental section where the inclusion of the SR constraint helps to resolve complex configurations containing crossings, low contrast image regions and/or near parallel vessels. More supporting tracking experiments are provided in the supplementary material of Bekkers *et al.* (2015c), which are available at <http://pubs.siam.org/doi/suppl/10.1137/15M1018460>.

8.1.1 Structure of the Chapter

First, in Section 8.2, we give the mathematical formulation of the curve optimization problem that we aim to solve in this chapter. In Section 8.3 we describe our PDE approach that provides the SR distance map as the viscosity solution of a boundary value problem (BVP) involving a sub-Riemannian eikonal equation. Furthermore, in Theorem 2, we show that sub-Riemannian geodesics are obtained from this distance map by back-tracking (imposed by the PMP computations presented in Appendix C.1). In Theorem 3 we show that for the uniform cost case (i.e. $\mathcal{C} = 1$) such back-tracking will never pass Maxwell-points nor conjugate points, and thereby our approach provides only the globally optimal solutions.

In Section 8.4 we describe an iterative procedure on how to solve the BVP by solving a sequence of initial value problems (IVP) for the corresponding HJB-equation. Before involvement of numerics, we express the *exact solutions* in concatenated morphological convolutions (erosions) and time-shifts in Appendix C.5. Here we rely on morphological scale space PDE's Akian *et al.* (1994); Burgeth & Weickert (2005); Duits *et al.* (2013c); Schmidt & Weickert (2016), and we show that solutions of the iterative procedure converge towards the sub-Riemannian distance map. Then in Section 8.5 we construct the external cost \mathcal{C} , based on a lifting of the original image to an orientation score Duits *et al.* (2007b). In Section 8.6, we describe a numerical PDE-implementation of our method by using left-invariant finite differences Franken & Duits (2009) in combination with an upwind-scheme Rouy & Tourin (1992).

In Section 8.7 we present numerical experiments and results. In Subsection 8.7.1 we verify the proposed method with comparisons to exact solutions for the uniform cost case. We also provide simple numerical approaches (extendable to the non-uniform cost case) to compute 1st Maxwell points and cusp points Duits *et al.* (2013a), which we verify for the uniform cost case with results in Sachkov (2011). Finally, in Subsec-

tion 8.7.2, we show application of the method to vessel tracking in optical images of the retina. We discuss the two main parameters that are involved: the balance between external and internal cost, and the balance between spatial and angular motion. First feasibility studies are presented on patches, and we discuss on how to proceed towards automated retinal vessel tree segmentation.

This chapter is an extension of an SSVM conference article Bekkers *et al.* (2015b). In addition to Bekkers *et al.* (2015b) we include the following theoretical results: the proofs of our main theorems (Theorem 2 and Theorem 3); the underlying differential geometrical tools in Appendices C.1, C.2, C.3 and embedding into geometric control theory in Appendix C.6; proof of our limiting procedure expressing exact solutions of the sub-Riemannian HJB-system in terms of concatenated morphological convolutions (with offsets) in Appendix C.5. Regarding experiments and applications, we now include: new experiments supporting the accuracy of our method; evaluation of the practical potential for vessel tree tracking; simple practical computation of specific surfaces of geometric interest (cusp surface and 1st Maxwell set); analysis of the cost function and evaluation of the parameters involved; and the road map towards a fast marching implementation.

8.2 Problem Formulation

In this chapter we consider the sub-Riemannian manifold $(SE(2), \Delta, \mathcal{G}_0^{\xi, \mathcal{C}})$, with the Lie group $SE(2)$ as base manifold (cf. Sec. 2.3), with the sub-tangent bundle Δ (cf. Sec. 4.2 and Eq. 4.5 on page 81), and with *data-adaptive* sub-Riemannian metric tensor $\mathcal{G}_0^{\xi, \mathcal{C}} : SE(2) \times \Delta \times \Delta \rightarrow \mathbb{R}$ given by Eq. 4.7.

Remark 9. Define $\mathcal{L}_g\phi(h) = \phi(g^{-1}h)$ then we have:

$$\mathcal{G}_0^{\xi, \mathcal{C}}|_{\gamma}(\dot{\gamma}, \dot{\gamma}) = \mathcal{G}_0^{\xi, \mathcal{L}_g\mathcal{C}}\Big|_{g\gamma}((L_g)_*\dot{\gamma}, (L_g)_*\dot{\gamma}).$$

Thus, $\mathcal{G}_0^{\xi, \mathcal{C}}$ is not left-invariant, but if shifting the cost as well, we can, for the computation of SR-geodesics, restrict ourselves to $\gamma(0) = e$.

We study the problem of finding SR minimizers, i.e. for given boundary conditions $\gamma(0) = e, \gamma(T) = g$, we aim to find the horizontal curve $\gamma(t)$ that minimizes the total SR length

$$l = \int_0^T \sqrt{\mathcal{G}_0^{\xi, \mathcal{C}}\Big|_{\gamma(t)}(\dot{\gamma}(t), \dot{\gamma}(t))} dt. \quad (8.1)$$

8. VES. TRACK. II: SUB-RIEMANNIAN GEODESICS IN SE(2)

If t is the sub-Riemannian arclength parameter, which is our default parameter, then $\sqrt{g_0^{\xi, \mathcal{C}}|_{\gamma(t)}}(\dot{\gamma}(t), \dot{\gamma}(t)) = 1$ and $l = T$. Then, SR minimizers γ are solutions to the optimal control problem (with free $T > 0$):

$$\mathbf{P}_{\text{mec}}^{\mathcal{C}}(SE(2)) : \left\{ \begin{array}{l} \dot{\gamma} = u^1 \mathcal{A}_1|_{\gamma} + u^3 \mathcal{A}_3|_{\gamma}, \\ \gamma(0) = e, \quad \gamma(T) = g, \\ l(\gamma(\cdot)) = \int_0^T \mathcal{C}(\gamma(t)) \sqrt{\xi^2 |u^1(t)|^2 + |u^3(t)|^2} dt \rightarrow \min, \\ \gamma(t) \in SE(2), \quad (u^1(t), u^3(t)) \in \mathbb{R}^2, \quad \xi > 0. \end{array} \right. \quad (8.2)$$

In the naming¹ of this geometric control problem we adhere to terminology in previous work Boscain *et al.* (2014); Duits *et al.* (2013a). Stationary curves of the problem (8.2) are found via PMP Agrachev & Sachkov (2013). Existence of minimizers follows from Chow-Rashevsky and Filippov's theorem Agrachev & Sachkov (2013), and because of the absence of abnormal trajectories (due to the 2-bracket generating distribution Δ) they are smooth.

Remark 10. *The Cauchy-Schwarz inequality implies that the minimization problem for the SR length functional l with free T is equivalent (see e.g. Montgomery (2006)) to the minimization problem for the action functional with fixed T :*

$$J(\gamma) = \frac{1}{2} \int_0^T \mathcal{C}^2(\gamma(t)) (\xi^2 |u^1(t)|^2 + |u^3(t)|^2) dt. \quad (8.3)$$

8.3 Solutions via Data-driven Wavefront Propagation

The following theorem summarizes our method for the computation of data-driven sub-Riemannian geodesics in $SE(2)$. It is an extension of classical methods in the Euclidean setting Osher & Fedkiw (2006); Peyré *et al.* (2010); Sethian (1999) to the sub-Riemannian manifold $(SE(2), \Delta, g_0^{\xi, \mathcal{C}})$. The idea is illustrated in Fig. 8.2.

Theorem 2. *Let $W(g)$ be a solution of the following boundary value problem (BVP) with eikonal-equation*

$$\left\{ \begin{array}{l} \sqrt{(\mathcal{C}(g))^{-2} (\xi^{-2} |\mathcal{A}_1 W(g)|^2 + |\mathcal{A}_3 W(g)|^2)} - 1 = 0, \text{ for } g \neq e, \\ W(e) = 0. \end{array} \right. \quad (8.4)$$

¹The label "mec" comes from the *mechanical* problem in geometric control, where a so-called Reeds-Shepp car (Remark 7) can proceed forward and backward in the path-optimization. See also App. C.6.

8.3 Solutions via Data-driven Wavefront Propagation

Then the isosurfaces

$$\mathcal{S}_t = \{g \in SE(2) \mid W(g) = t\} \quad (8.5)$$

are geodesically equidistant with unit speed $\mathcal{C}(\gamma(t))\sqrt{\xi^2|u^1(t)|^2 + |u^3(t)|^2} = 1$ and they provide a specific part of the SR-wavefronts departing from $e = (0, 0, 0)$. A SR-geodesic ending at $g \in SE(2)$ is found by backward integration

$$\dot{\gamma}_b(t) = -\frac{\mathcal{A}_1 W|_{\gamma_b(t)}}{(\xi \mathcal{C}(\gamma_b(t)))^2} \mathcal{A}_1|_{\gamma_b(t)} - \frac{\mathcal{A}_3 W|_{\gamma_b(t)}}{(\mathcal{C}(\gamma_b(t)))^2} \mathcal{A}_3|_{\gamma_b(t)}, \quad \gamma_b(0) = g. \quad (8.6)$$

Proof The definition of geodesically equidistant surfaces is given in Definition 4 in Appendix C.2. Furthermore, in Appendix C.2 we provide two lemmas needed for the proof. In Lemma 1, we connect the Fenchel transform on Δ , to the Fenchel transform on \mathbb{R}^2 to obtain the result on geodesically equidistant surfaces in $(SE(2), \Delta, \mathcal{G}_0^{\xi, \mathcal{C}})$. Then, in Lemma 2 in Appendix C.2, we derive the HJB-equation for the homogeneous Lagrangian as a limit from the HJB-equation for the squared Lagrangian. The back-tracking result follows from application of PMP to the equivalent action functional formulation (8.3), as done in Appendix C.1. Akin to the \mathbb{R}^d -case Bressan (2010), characteristics are found by integrating the ODE's of the PMP where according to the proof of Lemma 1 we must set $p = d^{SR}W$, see Remark 11 below. \square

The next theorem provides our main theoretical result. Recall that Maxwell points are $SE(2)$ points where two distinct geodesics with the same length meet. The 1st Maxwell set corresponds to the set of Maxwell-points where the distinct geodesics meet for the first time. In the subsequent theorem we will consider a specific solution to (8.4), namely the viscosity solution as defined in Definition 7 in Appendix C.3.

Theorem 3. Let $\mathcal{C} = 1$. Let $W(g)$ be the viscosity solution of the BVP (8.4). Then \mathcal{S}_t , Eq. (8.5), equals the SR-sphere of radius t . Backward integration via (8.6) provides globally optimal geodesics reaching e at $t = W(g) = d(g, e) :=$

$$\min_{\begin{array}{l} \gamma \in C^\infty(\mathbb{R}^+, SE(2)), \\ \dot{\gamma} \in \Delta, \gamma(0) = e, \gamma(T) = g \end{array}} \int_0^T \sqrt{|\dot{\theta}(\tau)|^2 + \xi^2|\dot{x}(\tau) \cos \theta(\tau) + \dot{y}(\tau) \sin \theta(\tau)|^2} d\tau, \quad (8.7)$$

and $\gamma_b(t) = \gamma^{\min}(d(g, e) - t)$. The SR-spheres $\mathcal{S}_t = \{g \in SE(2) \mid d(g, e) = t\}$ are non-smooth at the 1st Maxwell set \mathcal{M} , cf. Sachkov (2011), contained in

$$\mathcal{M} \subset \{(x, y, \theta) \in SE(2) \mid x \cos \frac{\theta}{2} + y \sin \frac{\theta}{2} = 0 \vee |\theta| = \pi\}, \quad (8.8)$$

and the back-tracking (8.6) does not pass the 1st Maxwell set.

8. VES. TRACK. II: SUB-RIEMANNIAN GEODESICS IN SE(2)

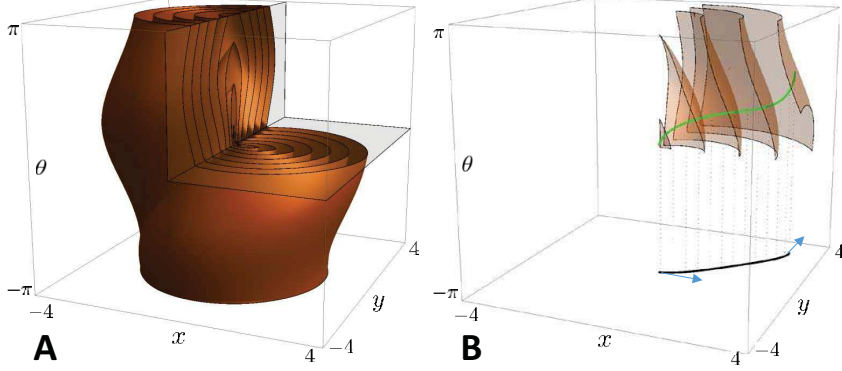


Figure 8.2: **A-B:** Our method provides both geodesically equidistant surfaces S_t (8.5) (depicted in A) and SR-geodesics. As depicted in B: geodesic equidistance holds with unit speed for all SR-geodesics passing through the surface, see Thm 2. Via Thm. 3 we have that $W(g) = d(g, e)$ and $\{S_t\}_{t \geq 0}$ is the family of SR-spheres with radius t depicted in this figure for the uniform cost case.

Proof of Thm. 3 can be found in Appendix C.4. The global optimality and non-passing of the 1st Maxwell set can be observed in Fig. 8.3. For the geometrical idea of the proof see Fig. 8.4.

Remark 11. The Hamiltonian H^{fixed} for the equivalent fixed time problem (8.3) equals

$$H^{fixed}(g, p) = \frac{1}{2} \frac{1}{(\mathcal{C}(g))^2} (\xi^{-2} h_1^2 + h_3^2) = \frac{1}{2}, \quad (8.9)$$

with momentum covector $p = h_1 \omega^1 + h_2 \omega^2 + h_3 \omega^3$ expressed in dual basis $\{\omega^i\}_{i=1}^3$ given by (cf. Sec. 4.4 on page 84)

$$\langle \omega^i, \mathcal{A}_j \rangle = \delta_j^i \Leftrightarrow \omega^1 = \cos \theta dx + \sin \theta dy, \quad \omega^2 = -\sin \theta dx + \cos \theta dy, \quad \omega^3 = d\theta. \quad (8.10)$$

The Hamiltonian H^{free} for the free time problem (8.2) minimizing l equals

$$H^{free}(g, p) = \sqrt{2H^{fixed}(g, p)} - 1 = 0. \quad (8.11)$$

For details see Appendix C.1 and C.2. These two Hamiltonians play a central role in the remainder of this chapter. For example, the SR-eikonal equation, Eq. (8.4), can be

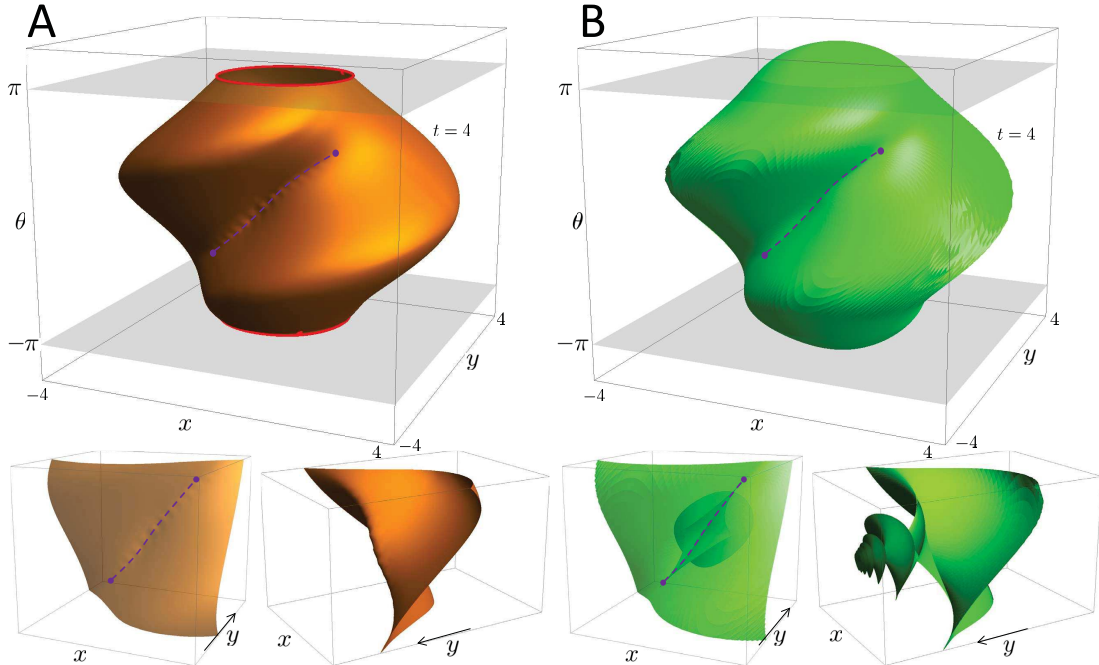


Figure 8.3: **A:** SR-sphere \mathcal{S}_t for $t = 4$ obtained by the method in Thm. 2 using $C = 1$ and δ_e^M as initial condition via viscosity solutions of the HJB-equation (8.12) implemented according to Section 8.6. **B:** The full SR-wavefront departing from e via the method of characteristics and formulae in Moiseev & Sachkov (2010) giving rise to interior folds (corresponding to multiple valued non-viscosity solutions of the HJB-equation). The Maxwell set \mathcal{M} consists precisely of the dashed line on $x \cos \frac{\theta}{2} + y \sin \frac{\theta}{2} = 0$ and the red circles at $|\theta| = \pi$. The dots are 2 (of the 4) conjugate points on \mathcal{S}_t which are limits of 1st Maxwell points (but not Maxwell points themselves). In **B** we see the astroidal structure of the conjugate locus El-Alaoui et al. (1996); Sachkov (2010). In **A** we see that the unique viscosity solutions stop at the 1st Maxwell set. Comparison of **A** and **B** shows the global optimality and accuracy of our method at **A**.

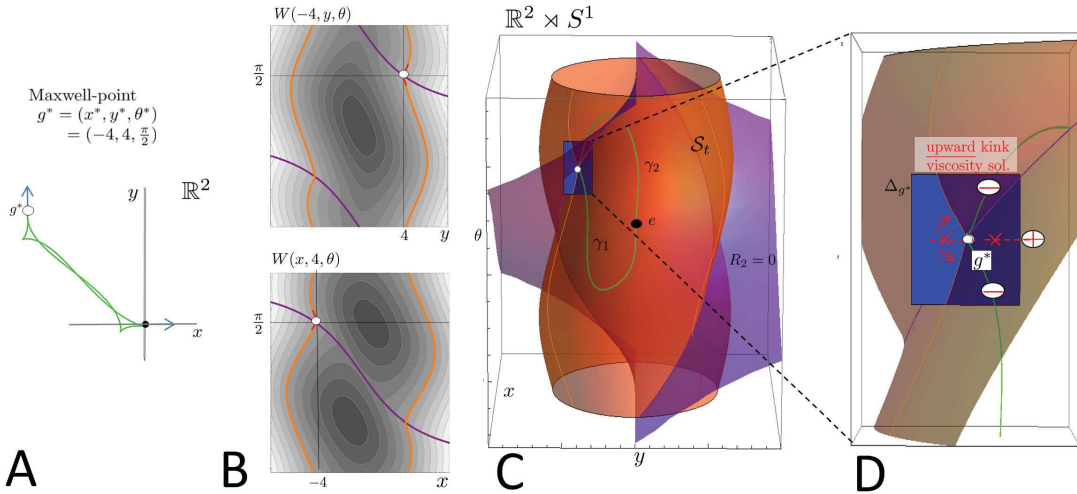


Figure 8.4: Maxwell point $g^* = (-4, 4, \pi/2)$ (in white) on SR-sphere S_t (in orange) for $C = 1$. At g^* two SR-geodesics $\gamma_1 \neq \gamma_2$ with equal SR-length t meet ($\gamma_1(t) = \gamma_2(t)$). From left to right: **A:** projection of γ_1 and γ_2 on the plane (x, y) , **B:** 2D-slices ($x = x^*$, $y = y^*$) of level sets of $W(g)$ with distinguished value $W(g) = t$ (again in orange). On top we plotted the Maxwell point, the intersection of surface $x \cos \frac{\theta}{2} + y \sin \frac{\theta}{2} = 0$ (in purple, this set contains a part of the 1st Maxwell set) with the 2D-slices. **C:** The SR-sphere S_t in $SE(2)$, **D:** section around g^* revealing the upward kink due to the viscosity solution. From this kink we see that the tracking (8.6) does not cross a 1st Maxwell point as indicated in red, yielding global optimality in Thm. 3.

8.4 An Iterative IVP-procedure to Solve the SR-Eikonal BVP

written as $H^{free}(g, p) = 0$ with momentum¹

$$p = d^{SR}W := \sum_{i \in \{1, 3\}} (\mathcal{A}_i W) \omega^i.$$

Remark 12. *SR geodesics loose their optimality either at a Maxwell point or at a conjugate point (where the integrator of the canonical ODE's, mapping initial momentum p_0 and time $t > 0$ to end-point $\gamma(t)$, is degenerate Agrachev & Sachkov (2013)). Some conjugate points are limits of Maxwell points, see Fig. 8.3, where the 1st astroidal shaped conjugate locus coincides with the void regions (cf. (Bayen & Tomlin, 2001, fig.1)) after 1st Maxwell set \mathcal{M} . When setting a Maxwell point as initial condition, the initial derivative $d^{SR}W|_{\gamma_b(0)}$ is not defined. Here there are 2 horizontal directions with minimal slope, taking these directions our algorithm produces the results in Fig. 8.4A and Fig. C.1.*

8.4 An Iterative IVP-procedure to Solve the SR-Eikonal BVP

To obtain an iterative implementation to obtain the viscosity solution of the SR-eikonal BVP given by (8.4), we rely on viscosity solutions of initial value problems (IVP). In this approach we put a connection between morphological scale spaces Akian *et al.* (1994); Burgeth & Weickert (2005), and morphological convolutions with morphological kernels, on the SR manifold $(SE(2), \Delta, \mathcal{G}_0^{\xi, \mathcal{C}})$ and the SR eikonal BVP.

In order to solve the sub-Riemannian eikonal BVP (8.4) we resort to subsequent auxiliary IVP's on $SE(2)$ for each $r \in [r_n, r_{n+1}]$, with $r_n = n\varepsilon$ at step $n \in \mathbb{N} \cup \{0\}$, $\varepsilon > 0$ fixed:

$$\begin{cases} \frac{\partial W_{n+1}^\varepsilon}{\partial r}(g, r) = 1 - \sqrt{(\mathcal{C}(g))^{-2} (\xi^{-2} |\mathcal{A}_1 W_{n+1}^\varepsilon(g, r)|^2 + |\mathcal{A}_3 W_{n+1}^\varepsilon(g, r)|^2)}, \\ W_{n+1}^\varepsilon(g, r_n) = W_n^\varepsilon(g, r_n) \text{ for } g \neq e, \\ W_{n+1}^\varepsilon(e, r_n) = 0 \end{cases} \quad (8.12)$$

for $n = 1, 2, \dots$, and

$$\begin{cases} \frac{\partial W_1^\varepsilon}{\partial r}(g, r) = 1 - \sqrt{(\mathcal{C}(g))^{-2} (\xi^{-2} |\mathcal{A}_1 W_1^\varepsilon(g, r)|^2 + |\mathcal{A}_3 W_1^\varepsilon(g, r)|^2)}, \\ W_1^\varepsilon(g, 0) = \delta_e^M(g), \end{cases} \quad (8.13)$$

¹Recall Example 4 on page 84, and note that the sub-Riemannian gradient $\nabla^{SR}W = (\mathcal{G}_0^{\xi, \mathcal{C}})^{-1} dW = \mathcal{C}^{-2} \sum_{i \in \{1, 3\}} \xi_i^{-2} \mathcal{A}_i W \mathcal{A}_i$, with $\xi_1 = \xi$, $\xi_3 = 1$, by definition is the Riesz-representative (being a vector) of this SR-derivative (being a covector).

8. VES. TRACK. II: SUB-RIEMANNIAN GEODESICS IN SE(2)

for $n = 0$, where δ_e^M is the morphological delta (i.e. the analogue of the Dirac delta in morphological scale space methods Akian *et al.* (1994); Burgeth & Weickert (2005)) given by

$$\delta_e^M(g) = \begin{cases} 0 & \text{if } g = e, \\ +\infty & \text{else.} \end{cases} \quad (8.14)$$

Let W_{n+1}^ε denote the viscosity solution of (8.12) carrying the following support

$$\text{supp}(W_{n+1}^\varepsilon) = SE(2) \times [r_n, r_{n+1}], \text{ with } r_n = n\varepsilon,$$

so in (8.12) at the n -th iteration ($n \geq 1$) we use, for $g \neq e$, the end condition $W_n^\varepsilon(g, r_n)$ of the n -th evolution as an initial condition $W_{n+1}^\varepsilon(g, r_n)$ of the $(n+1)$ -th evolution. Only for $g = e$ we set initial condition $W_{n+1}^\varepsilon(e, r_n) = 0$. Then we define the pointwise limit

$$W^\infty(g) := \lim_{\varepsilon \rightarrow 0} \left(\lim_{n \rightarrow \infty} W_{n+1}^\varepsilon(g, (n+1)\varepsilon) \right). \quad (8.15)$$

Finally, regarding the application of our optimality results, it is important that each IVP-solution $W_{n+1}^\varepsilon(g, r)$ is the unique *viscosity* solution of (8.12), as then via (8.15) the viscosity property for the viscosity solutions of the HJB-IVP problem naturally carries over to the viscosity property of the viscosity solutions of system (8.4). Thus we obtain $W = W^\infty$ as the unique viscosity solution of the SR-eikonal BVP.

Details on the limit (8.15), which takes place in the continuous setting before numeric discretization is applied, can be found in Appendix C.5. In Appendix C.5 we provide solutions of (8.12) by a time shift in combination with a morphological convolution¹ with the corresponding morphological kernel, and show why the double limit is necessary. A quick intuitive explanation is given in Figure 8.5, where we see that for $\varepsilon > 0$ we obtain stair-casing (due to a discrete rounding of the distance/value function) and where in the limit $\varepsilon \downarrow 0$ the solution $W^\infty(g) = W(g) = d(g, e)$ is obtained.

Remark 13. *The choice of our initial condition in Eq. (8.13) comes from the relation between linear and morphological scale spaces Akian et al. (1994); Burgeth & Weickert (2005), recently refined by Schmidt & Weickert (2016) using the Cramer-Fourier transform. Here, for linear $SE(2)$ -convolutions over the $(\cdot, +)$ -algebra one has $\delta_e *_{SE(2)} U = U$. For morphological $SE(2)$ -convolutions (erosions) over the $(\min, +)$ -algebra Duits et al. (2013a) one has a similar property:*

$$(\delta_e^M \ominus U)(g) := \inf_{q \in SE(2)} \{\delta_e^M(q^{-1}g) + U(q)\} = U(g), \quad (8.16)$$

¹In fact, an ‘erosion’ according to the terminology in morphological scale space theory, see e.g. Burgeth & Weickert (2005).

8.4 An Iterative IVP-procedure to Solve the SR-Eikonal BVP

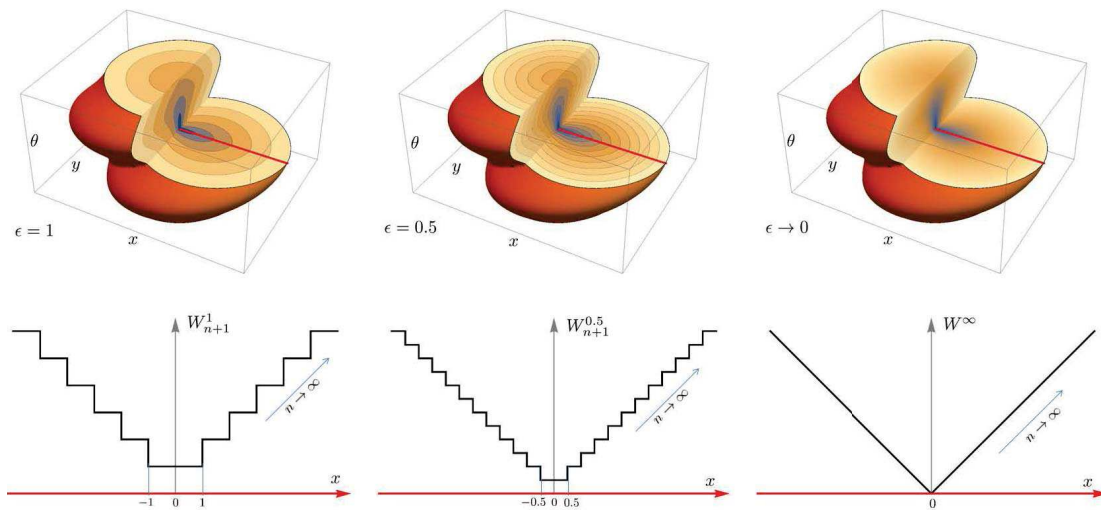


Figure 8.5: Illustration of the pointwise limits in Eq. (8.15). Top: plot of $g \mapsto \lim_{n \rightarrow \infty} W_{n+1}^\varepsilon(g, r_{n+1})$ (from left to right, resp. for $\varepsilon = 1$, $\varepsilon = 0.5$ and $\varepsilon \downarrow 0$) which is piecewise step-function, see Corollary 2 in Appendix C.5. Along the red axis $\{(x, 0, 0) \mid x \in \mathbb{R}\}$ we have $x = d(g, e)$. Bottom: the corresponding graph of $x \mapsto W_{n+1}^\varepsilon((x, 0, 0), r_{n+1})$. As n grows the staircase grows, as $\varepsilon \rightarrow 0$ the size of the steps in the staircase vanishes and we see $W^\infty(g) = d(g, e)$ in the most right column.

8. VES. TRACK. II: SUB-RIEMANNIAN GEODESICS IN SE(2)

where we recall (8.14). This is important for representing viscosity solutions of left-invariant HJB-equations on SE(2) by Lax-Oleinik Evans (1997) type of formulas (akin to the SE(3)-case Duits et al. (2013c)). This is for example employed in Appendix C.5.

Remark 14. The stair-casing limit depicted in Figure 8.5 is similar to the basic eikonal BVP on \mathbb{R} with solution $d(x, 0) = |x|$. On \mathbb{R} the approach (8.12), (8.13) and (8.15) provides the pointwise limit: $|x| = \lim_{\varepsilon \rightarrow 0} \sum_{m=0}^{\infty} r_{m+1} 1_{[r_m, r_m + \varepsilon]}(|x|) = \lim_{\varepsilon \rightarrow 0} \sum_{m=0}^{\lceil \frac{|x|}{\varepsilon} \rceil} r_{m+1} 1_{[r_m, r_m + \varepsilon]}(|x|)$, with $r_m = m\varepsilon$.

Remark 15. By general semigroup theory Akian et al. (1994), one cannot impose both the initial condition and a boundary condition $W^\varepsilon(e, r) = 0$ at the same time, which forced us to update the initial condition (at $g = e$) in our iteration scheme (8.12). The separate updating with value 0 for $g = e$ in Eq. (8.12) is crucial for the convergence in Eq. (8.15).

8.5 Construction of the Non-Uniform Cost

The cost should have low values on locations with high curve saliency, and high values otherwise. Based on image f we define the cost-function $\delta \leq \mathcal{C} \leq 1$ via

$$\mathcal{C}(x, y, \theta) = \frac{1}{1 + \lambda \left| \frac{(\mathcal{A}_2^2 U_f)_+(x, y, \theta)}{\|(\mathcal{A}_2^2 U_f)_+\|_\infty} \right|^p}, \quad (8.17)$$

where $\lambda \geq 0$, $p \in \mathbb{N}$; $U_f : SE(2) \rightarrow \mathbb{R}$ is a lift of the image, with $\|\cdot\|_\infty$ the sup-norm, and

$$(\mathcal{A}_2^2 U_f)_+(x, y, \theta) = \max\{0, (-\sin \theta \partial_x + \cos \theta \partial_y)^2 U_f(x, y, \theta)\}$$

is a ridge-detector Lindeberg (1998) where we use spatially isotropic Gaussian derivatives Franken & Duits (2009). Our ridge-detector, which is similar to the vessel enhancement method by Zhang et al. (2016a) discussed in Ch. 6, is based on a 2nd order derivative in the \mathcal{A}_2 -direction and gives responses only if there are convex variations orthogonal to the elongated-structures of interest in $U_f(x, y, \theta)$. Note that by (8.17) we have $\delta = \frac{1}{1+\lambda} \leq \mathcal{C} \leq 1$.

The lifting is done using real-valued anisotropic wavelets ψ via the orientation score transform (cf. Eq. (2.1) on page 25). To do the lifting we used the real part of cake wavelets (cf. Subsec. 2.1.5). Other type of 2D wavelets could be used as well. In related work by Péchaud et al. Péchaud et al. (2009b) the cost \mathcal{C} was obtained via normalized cross correlation with a set of templates.

In Eq. (8.17) two parameters, λ and p , are introduced. Parameter λ can be used to increase the contrast in the cost function. E.g., by choosing $\lambda = 0$ one creates a uniform cost function and by choosing $\lambda > 0$ data-adaptivity is included. Parameter $p > 1$ controls the steepness of the cost function, and in our experiments it is always set to $p = 3$.

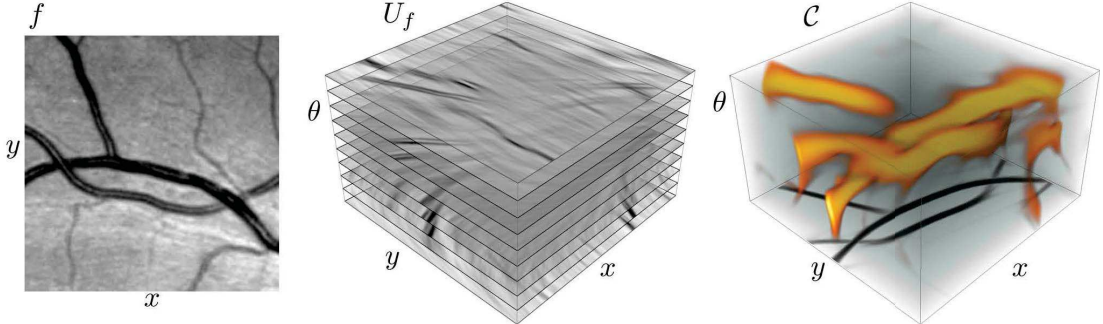


Figure 8.6: Illustration of the cost function C . **Left:** retinal image patch f . **Middle:** corresponding function U_f ('invertible orientation score') using the real part of a cake-wavelet ψ Duits et al. (2007b). **Right:** the cost function C computed via Eq. (8.17) visualized via volume rendering. The orange corresponds to locations where C has a low value.

8.6 Implementation

To compute the SR geodesics with given boundary conditions we first construct the value function W in Eq. (8.4), implementing the iterations at Eq. (8.12), after which we obtain our geodesic γ via a gradient descent on W from g back to e , recall Thm. 2 (and Thm. 3). Throughout this section, we keep using the continuous notation $g \in SE(2)$ although within all numerical procedures g is sampled on the following $(2N + 1) \times (2N + 1) \times (2N_\theta)$ equidistant grid:

$$\{(x_i, y_j, \theta_k) | x_i = s_{xy}i, y_j = s_{xy}j, \theta_k = s_\theta k, \text{ with } i, j = -N, \dots, N, k = -N_\theta + 1, \dots, N_\theta\}, \quad (8.18)$$

with step-sizes $s_\theta = \frac{\pi}{N_\theta}$, $s_{xy} = \frac{x_{max}}{N}$, with $N, N_\theta \in \mathbb{N}$. As a default we set $N = 70$, $x_{max} = 7$, $N_\theta = 64$. The time-discretization grid is also chosen to be equidistant with time steps $\Delta r = \varepsilon$.

On this grid we compute an iterative upwind scheme to obtain the viscosity solution W^ε at iteration Eq. (8.12). Here we initialize $W^\varepsilon(\cdot, 0) = \delta_e^{MD}(\cdot)$, with the discrete

8. VES. TRACK. II: SUB-RIEMANNIAN GEODESICS IN SE(2)

morphological delta, given by $\delta_e^{MD}(g) = 0$ if $g = e$ and 1 if $g \neq e$, and iterate

$$\begin{cases} W^\varepsilon(g, r + \Delta r) &= W^\varepsilon(g, r) - \Delta r H_D^{free}(g, dW^\varepsilon(g, r)) \quad \text{for } g \neq e \\ W^\varepsilon(e, r + \Delta r) &= 0, \end{cases} \quad (8.19)$$

with free-time Hamiltonian (see Appendix C.1, Eq. (C.4)) given by

$$H_D^{free}(g, dW^\varepsilon(g, r)) = \left(\frac{1}{\mathcal{C}(g)} \sqrt{\xi^{-2}(\mathcal{A}_1 W^\varepsilon(g, r))^2 + (\mathcal{A}_3 W^\varepsilon(g, r))^2} - 1 \right),$$

until convergence. We set $\Delta r = \varepsilon$ in Eq. (8.12). In the numerical upwind scheme, the left-invariant derivatives are calculated via

$$\mathcal{A}_i W^\varepsilon(g, r) = \max \{ \mathcal{A}_i^- W^\varepsilon(g, r), -\mathcal{A}_i^+ W^\varepsilon(g, r), 0 \},$$

where \mathcal{A}_i^+ and \mathcal{A}_i^- denote respectively the forward and backward finite difference approximations of \mathcal{A}_i . Note that W^ε in (8.19) is a first order finite difference approximation of W_{n+1}^ε in (8.12) at time interval $r \in [n\varepsilon, (n+1)\varepsilon]$ and we iterate until the subsequent \mathbb{L}_∞ -norms differ less than 10^{-6} . This upwind scheme is a straightforward extension of the scheme proposed in Rouy & Tourin (1992) for HJB-systems on \mathbb{R}^n . It produces sharp ridges at the 1st Maxwell set (cf. Fig. 8.3) as it is consistent at local maxima. For numerical accuracy and left-invariance we applied finite differences in the moving frame of left-invariant vector fields, using B -spline interpolation. This is favorable over finite differences in the fixed coordinate grid $\{x, y, \theta\}$. For details on these kind of left-invariant finite differences, and comparisons to other finite difference implementations (e.g. in fixed coordinate grid) see Franken & Duits (2009).

In our implementation the origin e is treated separately as our initial condition is not differentiable. We apply the update $W^\varepsilon(e, r) = 0$ for all $r \geq 0$. We set step size $\varepsilon = 0.1 \min(s_{xy}\xi, s_\theta)$ with s_{xy} and s_θ step sizes in respectively the x - y -directions and θ -direction.

8.7 Experiments and Results

8.7.1 Verification for the Uniform Cost Case

Throughout this chapter we have illustrated the theory with figures obtained via our new wavefront propagation technique. As the problem (8.2) for $\mathcal{C} = 1$ was solved Sachkov (2011);Duits *et al.* (2013a) using different parameterizations, we use this as a golden standard for comparison. In this subsection we present experiments that support the accuracy of our method.

8.7.1.1 Comparison of BVP Solutions and the Cuspsurface

Let us consider Fig. 8.7A. Here an arbitrary SR-geodesic between the $SE(2)$ points $\gamma(0) = e$ and $\gamma(T) = (6, 3, \pi/3)$ is found via the IVP in Sachkov (2011) with end-time $T = 7.11$ and initial momentum

$$p_0 = h_1(0)dx + h_3(0)dy + h_2(0)d\theta,$$

with $h_1(0) = \sqrt{1 - |h_3(0)|^2}$, $h_3(0) = 0.430$ and $h_2(0) = -0.428$, is used for reference (in black in Fig. 8.7A). Using the semi-analytic approach for solving the BVP in Duits *et al.* (2013a) an almost identical result is obtained. The curves computed with our method with $s_{xy} = 0.1$, and with angular step-sizes of $s_\theta = 2\pi/12$ and $s_\theta = 2\pi/64$ are shown in Fig. 8.7A in red and green respectively. Already at low resolution we observe accurate results. In Fig. 8.3 we compare one SR-sphere for $T = 4$ (Fig. 8.3A) found via our method with the exact SR-wavefront departing from e (Fig. 8.3B) computed by the method of characteristics Moiseev & Sachkov (2010). We observe that our solution is non-smooth at the 1st Maxwell set \mathcal{M} (8.8) and that the unique viscosity solution stops precisely there, confirming Theorem 3. Finally, the blue surface in Fig. 8.7B represents the cusp surface, i.e. the surface consisting of all cusp points. Cusps are points that can occur on geodesics when they are projected into the image plane (see Fig. 8.7B). This happens at points g where the geodesic is tangent to $\partial_\theta|_g = \mathcal{A}_3|_g$. Then, the cusp surface \mathfrak{S}_{cusp} is easily computed as a zero-crossing:

$$\mathfrak{S}_{cusp} := \{g \in SE(2) \mid \mathcal{A}_1 W(g) = 0\}. \quad (8.20)$$

It is in agreement with the exact cusp surface analytically computed in (Duits *et al.*, 2013a, Fig. 11).

The geometric idea behind (8.20) is that we have a cusp at time t if $u^1(t) = \frac{1}{C^2(\gamma(t))} h_1(t) = \frac{1}{C^2(\gamma(t))} \mathcal{A}_1 W(\gamma(t)) = 0$ which directly follows from Appendix C.1. For further details on the set of end-conditions reachable without cusps, see Appendix C.6.

8.7.1.2 Comparison and Computation of SR-spheres

In order to validate the solutions obtained with our PDE method we compare them with the exact SR-distance map. This exact SR-distance map was computed by explicit formulas for SR-geodesics (given on p.386 in Moiseev & Sachkov (2010)) in combination with explicit formulas for the cut time, which coincides with the 1st Maxwell time, given by (5.18)–(5.19) in Moiseev & Sachkov (2010). The experiments were done in the following way:

8. VES. TRACK. II: SUB-RIEMANNIAN GEODESICS IN SE(2)

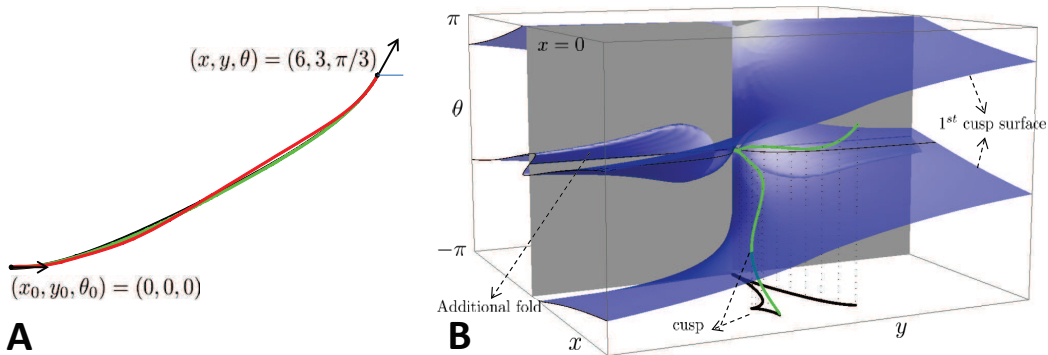


Figure 8.7: **A:** SR-geodesic example for the uniform cost case shows our PDE-discretizations (with 12 and 64 sampled orientations in red and green respectively) are accurate in comparison to analytic solutions in Duits et al. (2013a); Sachkov (2011) (in black). **B:** The blue surface represents the cusp surface numerically computed via the proposed HJB-system (with $C = 1$) and subsequent calculation of the zero-crossings of $\mathcal{A}_1 W(x, y, \theta)$. Indeed if a SR-geodesic (in green) passes this surface, it passes in θ -direction (with infinite curvature Boscain et al. (2014); Duits et al. (2013a)), yielding a cusp on the spatial ground plane. The same blue surface is computed in (Duits et al., 2013a, Fig. 11). We even see the additional fold (top left passing the grey-plane) as some globally optimal SR-geodesics even exhibit 2 cusps.

1. Compute a set of end points:

$$EP(T) = \{(x_i, y_i, \theta_i) = \text{Exp}(p_i, T) \mid p_i \in C, T \leq t_1^{\text{MAX}}(p_i), i = 1, \dots, i_{\max}\}$$

lying on the SR-sphere of fixed radius T using analytic formulas for the exponential map (cf. Remark 16 below) and 1st Maxwell time t_1^{MAX} Moiseev & Sachkov (2010). The number of end points was chosen as $i_{\max} = 72 T^2$ and C is the cylinder in momentum space given by

$$C = \{p \in T_e^*(SE(2)) \mid H^{\text{fixed}}(e, p) = 1/2\},$$

where we recall (8.9). The sampling points p_i are taken by a uniform grid on the rectifying coordinates (φ, k) of the mathematical pendulum (the ODE that arises in the PMP procedure, cf. (Moiseev & Sachkov, 2010, ch:3.2)), both for the rotating pendulum case ($p_i \in C_2$, yielding S -curves) and the oscillating pendulum case ($p_i \in C_1$, yielding U -curves), where we note that $C = \overline{C_1 \cup C_2}$.

8.7 Experiments and Results

2. Evaluate the distance function $W(g_i) = W(x_i, y_i, \theta_i)$ obtained by our numerical PDE-approach in section 8.6 for every point of the set $EP(T)$. We use 3rd order Hermite interpolation for $W(x_i, y_i, \theta_i)$ at $g = g_i \in EP(T)$ in between the grid (8.18).
3. Compute the maximum absolute error $\max_{g_i \in EP(T)} |W(g_i) - T|$ and the maximum relative error $\max_{g_i \in EP(T)} (|W(g_i) - T|/T)$.

Remark 16. *The exponential map $Exp : C \times \mathbb{R}^+ \rightarrow SE(2)$ provides the end-point $(x(t), y(t), \theta(t)) = \gamma(t) = Exp(p_0, t)$ of the SR-geodesic γ , given SR-arclength t and initial momentum $p_0 \in T_e^*(SE(2))$. This exponential map integrates the PMP ODE's in Appendix C.1, and should not be confused with exponential map from the Lie algebra to the Lie group.*

The absolute and relative errors of the SR-distance computations for each of the end points located on SR-spheres of radii T are presented in Figure 8.9. The red graph corresponds to a sampling of $(N, N_\theta) = (50, 64)$, recall Eq. (8.18), used in the SR-distance computation by our numerical PDE approach, and the blue graph corresponds to the finer sampling $(N, N_\theta) = (140, 128)$. We see that the maximum absolute error does not grow, and that the relative error decreases when increasing the radius of the SR-sphere. Increase of sampling rate improves the result. For the finer sampling case, neither absolute nor relative errors exceed 0.1.

8.7.1.3 Comparison and Computation of 1st Maxwell Set

We can compute the 1st Maxwell set (recall eq. (8.8), see also Appendix C.4) as the set of points where forward and backward left-invariant derivatives acting on the SR-distance map have different signs:

$$\mathcal{M}_{num} = \bigcup_{i \in \{1,3\}} \{(x, y, \theta) \in SE(2) \mid \mathcal{A}_i^+ W(x, y, \theta) > 0, \mathcal{A}_i^- W(x, y, \theta) < 0\}. \quad (8.21)$$

Here $i = 1$ corresponds to the *local* component of the 1st Maxwell set, and $i = 2$ corresponds to the *global* component of the 1st Maxwell set. The local component consists of two connected components lying on the surface given by $x \cos \frac{\theta}{2} + y \sin \frac{\theta}{2} = 0$ (i.e. the purple surface in Figure 8.4), and the global component is the plane given by equation $\theta = \pi$ (for details, see Sachkov (2011)). In Figure 8.10 we compare the local component of \mathcal{M}_{num} computed by our PDE approach with its exact counterpart \mathcal{M} , presented in (Sachkov, 2011, thm 3.5). It shows that \mathcal{M}_{num} is close to the exact

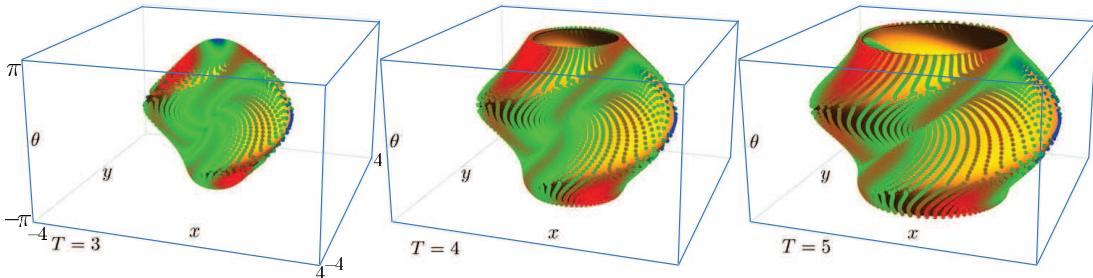


Figure 8.8: Comparison of SR-spheres obtained by our numerical PDE-approach and the set of points $EP(T)$ lying on exact SR-spheres obtained by analytic formulas. From left to right: the SR-sphere with radius $t = T = 3$, $T = 4$ and $T = 5$. The color indicates the difference between the exact and the numerical values of the SR-distance (blue for smallest, green for middle, and red for highest differences). Thus, we see our algorithm is accurate, in particular along the fixed coordinate grid directions along x and θ -axis.

\mathcal{M} . Although not shown here a similar picture was obtained for the global component, where \mathcal{M}_{num} indeed covers the plane $\theta = \pi$. Summarizing, this experiment verifies the correctness of the proposed method, but it also shows that the method allows to observe the behavior of the 1st Maxwell set. Eq. (8.21) allows us to numerically compute the Maxwell set for the data-driven cases $\mathcal{C} \neq 1$ where exact solutions are out of reach.

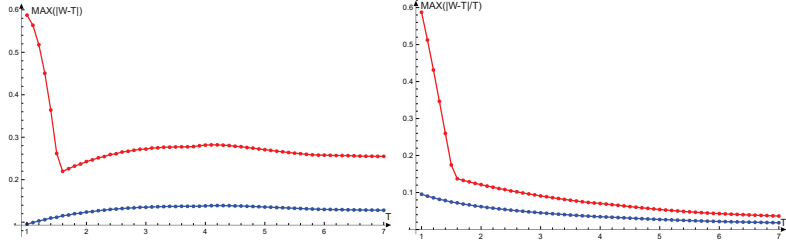
8.7.2 Feasibility Study for Application in Retinal Imaging

As a feasibility study for the application of our method in retinal images we tested the method on numerous image patches exhibiting both crossings, bifurcations, and low contrast, (Fig. 8.11, Fig. 8.12). For each seed point g_0 the value function $g \mapsto W(g_0^{-1}g)$ was calculated according to the implementation details in Section 8.6, after which multiple end-points were traced back to the seed point. The image dimensions of the patches is 180×140 .

For the construction of the cost function (see e.g. Fig. 8.6) we set $p = 3$, and the lifting was done using cake wavelets with angular resolution $\pi/16$. More precisely we used a cake-wavelet with standard parameters ($N = 8$, $N_\theta = 32$, $s_\theta = \frac{\pi}{8}$, $\sigma_s = 20px$, $\gamma = 0.8$), for details see (Bekkers *et al.*, 2014a, ch:2). The precise choice of anisotropic wavelet is not decisive for the algorithm (so other type of anisotropic wavelets and cost constructions could have been applied as well).

In all experiments we run with 4 settings for the two parameters (ξ, λ) determining

8.7 Experiments and Results



A: Maximum absolute error B: Maximum relative error

Figure 8.9: Maximum error in computing of SR-distance for end points located on SR-spheres of different radii $t = T$ (from 1 to 7 with step 0.1), with number of end points $i_{\max} = 72T^2$. In red: errors are computed on a coarser grid $(N, N_\theta) = (50, 64)$ and in blue: errors on a finer grid $(N, N_\theta) = (140, 128)$, with step sizes $s_\theta = \frac{2\pi}{N_\theta}$ and $s_{xy} = \frac{7}{N}$.

the sub-Riemannian geodesics, we set $\xi_{small} = 0.05$, $\xi_{large} = 0.1$, $\lambda_{small} = 10$, $\lambda_{large} = 100$. The idea of these settings is to see the effect of the parameters, where we recall ξ controls global stiffness of the curves, and λ controls the influence of the external cost. We also include comparisons to a Riemannian wavefront propagation method on \mathbb{R}^2 , and a Riemannian wavefront propagation method on $SE(2)$. These comparisons clearly show the advantage of including the sub-Riemannian geometry in the problem. For results on two representative patches, see Figure 8.11. For results on 25 other patches see the supplementary materials of Bekkers *et al.* (2015c), available at <http://pubs.siam.org/doi/suppl/10.1137/15M1018460>. Here, for fair and basic comparison of the geometries, we rely on the same cost function \mathcal{C} . That is, we compare to

- Riemannian geodesics $\gamma(t) = (x(t), y(t), \theta(t))$ in $(SE(2), \mathcal{G}_1^{\xi, \mathcal{C}})$ with
$$\mathcal{G}_1^{\xi, \mathcal{C}} \Big|_{\gamma(t)} (\dot{\gamma}(t), \dot{\gamma}(t)) = (\mathcal{C}(\gamma(t)))^2 (|\dot{\theta}(t)|^2 + \xi^2 |\dot{x}(t)|^2 + \xi^2 |\dot{y}(t)|^2)$$
- Riemannian geodesics $\mathbf{x}(s) = (x(s), y(s))$ in $(\mathbb{R}^2, \mathcal{G}_{\mathbb{R}^2}^{\mathcal{C}})$ with metric tensor
$$\mathcal{G}_{\mathbb{R}^2}^{\mathcal{C}} \Big|_{\mathbf{x}(s)} (\dot{\mathbf{x}}(s), \dot{\mathbf{x}}(s)) = (c(\mathbf{x}(s)))^2 (|\dot{x}(s)|^2 + |\dot{y}(s)|^2),$$

with $c(x(s), y(s)) = \min_{\theta \in [0, 2\pi]} \mathcal{C}(x(s), y(s), \theta)$.

Typically, the wavefront propagation tracking methods on $(\mathbb{R}^2, \mathcal{G}_{\mathbb{R}^2}^{\mathcal{C}})$ produce incorrect short-cuts at crossings and very non-smooth curves. The Riemannian wavefront propagation tracking method (with spatial isotropy) $(SE(2), \mathcal{G}_1^{\xi, \mathcal{C}})$ often deals correctly with crossings, but typically suffers from incorrect jumps towards nearly parallel neighboring

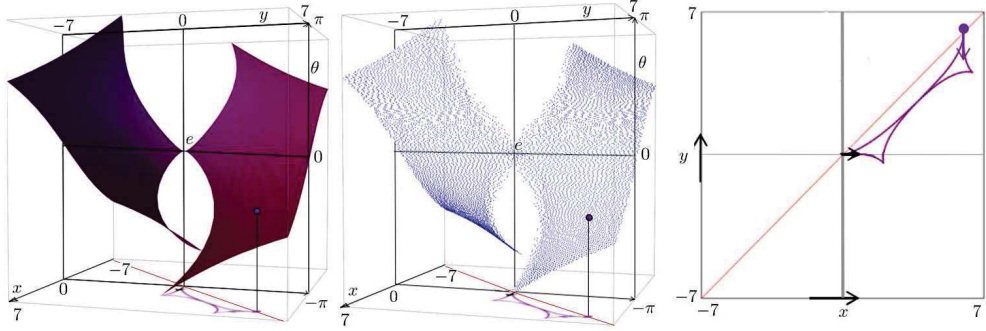


Figure 8.10: Comparison of the 1st Maxwell set obtained by our numerical PDE-approach with the exact 1st Maxwell set Sachkov (2011). Note that the local components of the 1st Maxwell set are part of the purple surface in Figure 8.4. **Left:** Local component of the exact Maxwell set \mathcal{M} obtained by (Sachkov, 2011, thm 3.5) (where we recall that the cut locus coincides with the closure $\overline{\mathcal{M}}$ of the first Maxwell set (Sachkov, 2010, th:3.3)). **Middle:** Local components of the Maxwell set \mathcal{M}_{num} computed numerically by eq. (8.21). **Right:** Single case of a Maxwell point on the local part of the Maxwell set.

vessels. Also it yields non-smooth curves. This can be corrected for when including extreme anisotropy, see Sec. 4.3.2. The sub-Riemannian wavefront propagation method produces smooth curves that appropriately deal with crossings. For high contrast images with reliable cost function \mathcal{C} best results are obtained with low ξ and large λ . However, in low contrast images and/or patient data with severe abnormalities, low λ is preferable, as in these cases the cost function is less reliable. This can be observed in Figure 8.12.

The experiments indicate that $\xi = 0.01$ (small) in combination with $\lambda = 100$ (large) are preferable on our patches. This typically holds for good quality retinal images of healthy volunteers. In lower quality retinal images of diabetic patients, however, the cost function is less reliable and here $\lambda = 10$ (small) can be preferable, see Figure 8.12. However, it might not be optimal to set the ξ parameter globally, as we did in these experiments, as smaller vessels are often more tortuous and therefore require more flexibility, see e.g. (Bekkers *et al.*, 2015b, fig.7). Furthermore, we do not include precise centerline extraction, which could e.g. be achieved by considering the vessel width as an extra feature (as in Benmansour & Cohen (2011); Li & Yezzi (2007); Péchaud *et al.* (2009b)).

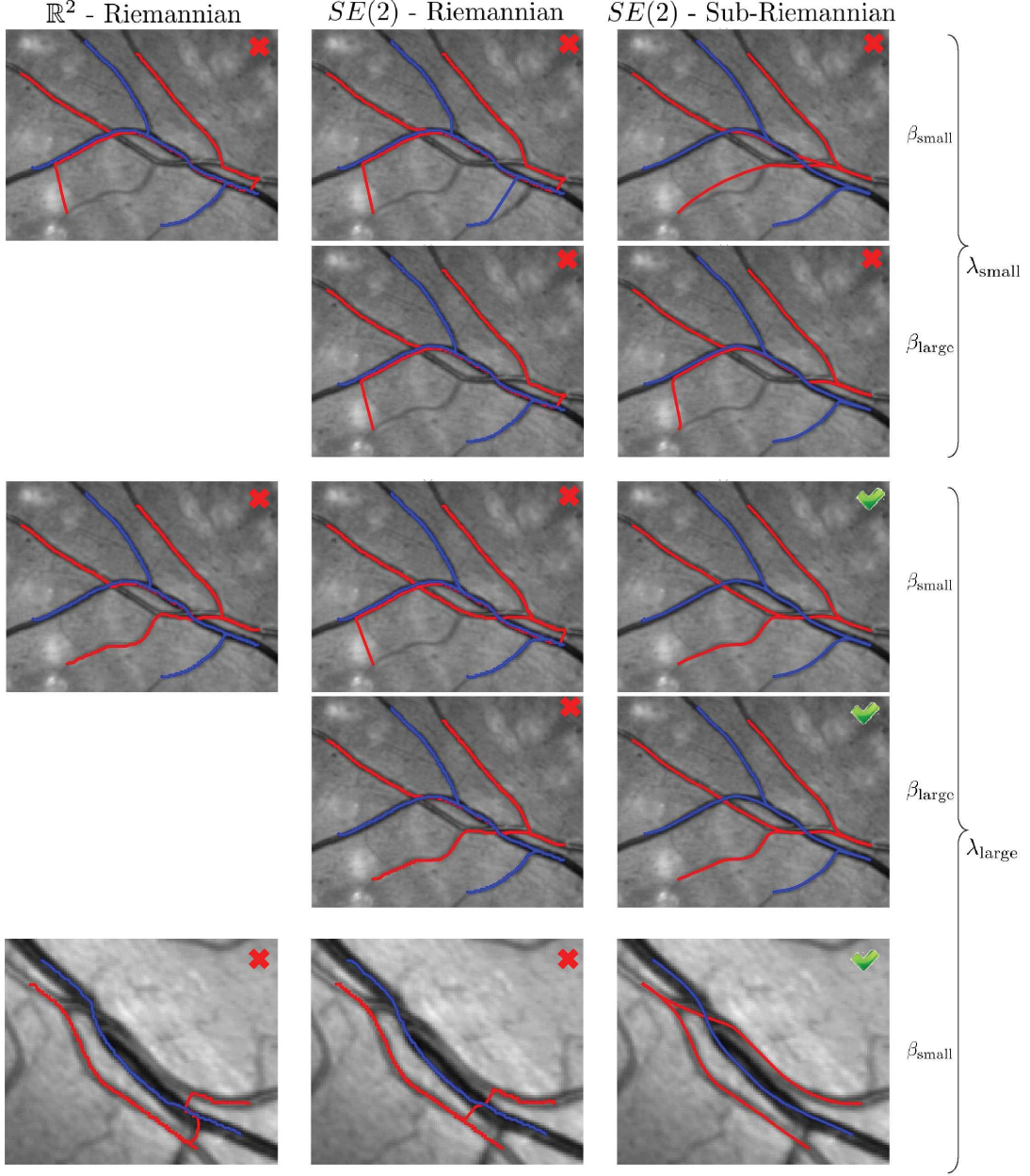


Figure 8.11: Data-adaptive sub-Riemannian geodesics obtained via our proposed tracking method (Thm. 2), with external cost (8.17), with $p = 3$, ξ equals $\xi_{\text{small}} = 0.01$, $\xi_{\text{large}} = 0.1$ and λ equals $\lambda_{\text{small}} = 10$, $\lambda_{\text{large}} = 100$. We applied tracking from 2 seed-points each with several end-points (to test the crossings/bifurcations). To distinguish between tracks from the two seed-points we plotted tracts in different lighting-intensity. We indicated the valid cases only if all trajectories are correctly dealt with.

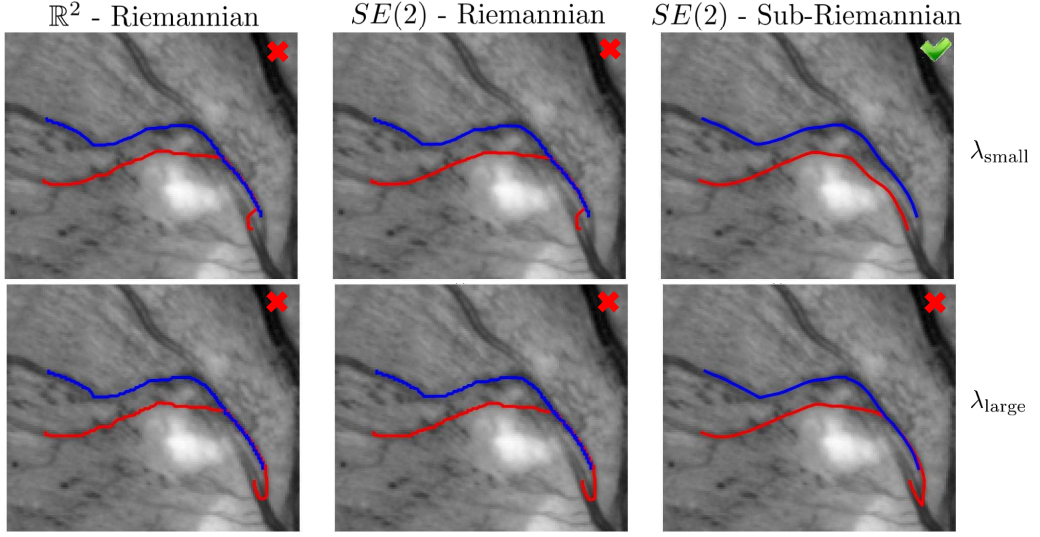


Figure 8.12: Tractography (again for $\lambda = \lambda_{small} = 10$, $\lambda = \lambda_{large} = 100$ and $\xi = 0.01$, $p = 3$) in a patch of a challenging low-contrast retinal image of a diabetic patient. In case of low-contrast (and less reliable cost) it is better to keep λ small, in contrast to high contrast cases depicted in Figure 8.11. To distinguish between tracks from the two seed-points we plotted tracts in different lighting-intensity.

8.7.3 Sub-Riemannian Fast Marching

It is possible to construct a family of anisotropic Riemannian metric tensors, recall (8.10): $\mathcal{G}_\epsilon^{\xi,C} = C^2 (\xi^2 \omega^1 \otimes \omega^1 + \xi^2 \epsilon^{-2} \omega^2 \otimes \omega^2) + \omega^3 \otimes \omega^3$, which bridges the SR-metric $\mathcal{G}_0^{\xi,C}$ of our method (obtained by $\epsilon \rightarrow 0$) to the full Riemannian metric tensor $\mathcal{G}_1^{\xi,C}$ (obtained by $\epsilon \rightarrow 1$). For the values of ξ considered here, Riemannian geodesics and smooth Riemannian spheres for highly anisotropic cases $\epsilon \leq 0.1$ approximate SR-geodesics and non-smooth SR-spheres. In fact, with such extreme anisotropy in the Riemannian setting, the non-smooth ridges \mathcal{M} in the SR spheres (see e.g. the 1st Maxwell sets in Figure 8.3) are only little smoothed, and also the cusp-surface hardly changes. This observation allows to use the anisotropic fast marching (FM) Mirebeau (2014) as an alternative fast method for computing the solution of (8.4), instead of the iterative upwind finite difference approach in Section 8.4. The numerical advantages of such a fast marching approach are discussed next.

In Sanguinetti *et al.* (2015) we have studied the computational advantages of using an anisotropic fast marching method for computing sub-Riemannian geodesics using the approximate metric tensor (Subsec. 4.3.2). Full details can be found in Sanguinetti *et al.* (2015), here we will only summarize the findings.

In our experiment the sub-Riemannian distance volumes W are computed using the PDE approach presented in this chapter, and the fast marching approach presented in Sanguinetti *et al.* (2015). The fast marching method relies on the lattice basis reduction (FM-LBR) proposed in Mirebeau (2014). The generated volumes W were compared against the solutions via the approach described in Subsec. 8.7.1.2. The volumes W are sampled on an increasingly finer grid, where the spatial directions are sampled with $2n + 1$ samples, and the angular direction with $2n$ samples from 0 to $2\pi - \pi/n$. The grid is thus of size $(2n + 1)(2n + 1)(2n - 1)$.

The graph in Fig. 8.13(left) shows the comparison of the accuracy achieved in the computation of the SR-sphere of radius $t = 4$ when n increases. The behaviour for SR-spheres of different radii is similar. The CPU time is compared in Fig. 8.13(center). The 3rd plot illustrates the method for computing the accuracy. The orange surface is the SR-sphere of radius $t = 4$ computed with the FM-LBR method on a grid corresponding to $n = 101$. The points are the geodesic endpoints, their color is proportional to the error of the FM-LBR (blue-low, green-medium, red-high error). The first observation is that even though the iterative method is more accurate, both methods seem to have the same order of convergence (the slope in the log-log graphs) when the grid resolution increases. This seems reasonable as both methods use first order approximations of the derivatives. Also, we hypothesize that the offset in favour of the iterative method is due to the Riemannian approximation of the SR-metric (i.e. selecting $\epsilon = 0.1$), but this needs further investigation. The second key observation is that the CPU time increases dramatically with n for the iterative method. Therefore, it is clear that we can achieve the same accuracy using the FM-LBR but with much less computational effort, which is of vital importance in real world applications such as vessel tracking.

8.8 Conclusion

In this chapter we proposed a novel, flexible and accurate numerical method for computing solutions to the optimal control problem (8.2), i.e. finding SR-geodesics in $SE(2)$ with non-uniform cost. The method generalizes the classical approach Osher & Fedkiw (2006); Peyré *et al.* (2010); Sethian (1999) for finding cost adaptive geodesics in Euclidean settings to the SR-case. It consists of a wavefront propagation of geodesically equidistant surfaces computed via the viscosity solution of a HJB-system in $(SE(2), \Delta, \mathcal{G}_0^{\xi, \mathcal{C}})$, and subsequent backwards integration, which gives the optimal tracks. We used PMP to derive both the HJB-equation and the backtracking. We have shown global optimality for the uniform cost case ($\mathcal{C} = 1$) and that our method generates

8. VES. TRACK. II: SUB-RIEMANNIAN GEODESICS IN SE(2)

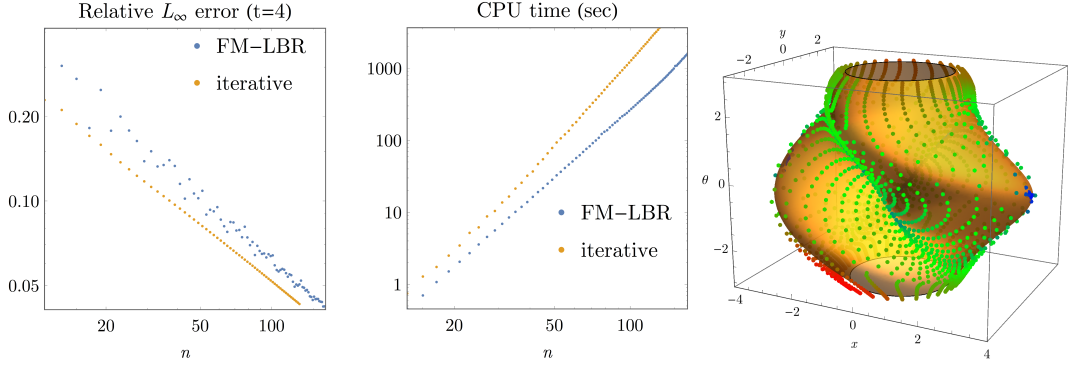


Figure 8.13: Validation via comparison in the uniform cost case. The experiment (illustrated on the left, see the text) shows that even though the iterative method in Subsec. 8.6 is more accurate we can still achieve with the FM-LBR method better results and with less CPU effort, just by increasing the grid sampling.

SR-spheres. Compared to previous works regarding SR-geodesics in $(SE(2), \Delta, g_0^{\xi,1})$ Duits *et al.* (2013a); Mashtakov *et al.* (2013); Sachkov (2011), we solve the boundary value problem without shooting techniques, using a computational method that always provides the optimal solution. Compared with wavefront propagation methods on the extended domain of positions and orientations in image analysis Péchaud *et al.* (2009a,b), we consider a SR-metric instead of a Riemannian metric. Results in retinal vessel tracking are promising, and by our data-adaptive approach, it now follows that sub-Riemannian geometry can make a considerable difference in real medical imaging applications.

Chapter 9

Vessel Tracking Part III: Sub-Riemannian Geodesics in $\text{SO}(3)$

This chapter is based on:

Mashtakov, A., Duits, R., Sachkov, Y., Bekkers, E. & Beschastnyi, I. (2016). Tracking of lines in spherical images via sub-riemannian geodesics on $\text{SO}(3)$. *arXiv* preprint arXiv:1604.03800

9. VES. TRACK. III: SUB-RIEMANNIAN GEODESICS IN $SO(3)$

This chapter is based on joint work with Alexey Mashtakov, Remco Duits, Yuri Sachkov and Ivan Beschatsnyi and is published in Mashtakov *et al.* (2016). They are gratefully acknowledged for the theoretical development of data-adaptive sub-Riemannian geodesics in $SO(3)$. The publication Mashtakov *et al.* (2016) has a strong focus on the theoretical analysis of sub-Riemannian geodesics in $SO(3)$, including exact solutions of sub-Riemannian geodesics and an extensive analysis of wavefronts, optimality, Maxwell sets, and conjugate points. In this chapter we describe the adaptation of the method of Ch. 8 for data-adaptive sub-Riemannian geodesics in $SE(2)$ to the Lie group $SO(3)$, and primarily focus on practical aspects. For full theoretical details we refer to Mashtakov *et al.* (2016). Additionally, we propose in Sec. 9.4 an alternative derivation of the analytic solutions for sub-Riemannian geodesics, which is based on the left-Cartan connection (Ch. 4).

9.1 Introduction

In the previous Ch. 8 we described methods for computing data-adaptive sub-Riemannian geodesics in the Lie group $SE(2)$. The objective there was to track lines in flat images (i.e., on \mathbb{R}^2). The retina, however, is a spherical object and it is in this respect more natural to model the data by spherical images and to include the spherical object geometry in the tracking. As such, in this chapter we extend the line tracking framework described in Ch. 8 to tracking of lines in *spherical* images (e.g. the images of the retina, see Fig. 9.1). This adaptation requires a sub-Riemannian manifold structure in a different Lie group, namely the group $SO(3)$ (consisting of 3D rotations) acting transitively on the 2-sphere S^2 . In this chapter we describe the necessary adaptations of Ch. 8 for tracking in spherical images, and compare the difference between the two geometrical models ($SE(2)$ vs $SO(3)$).

Here we study the problem $\mathbf{P}_{\text{curve}}(S^2)$ of finding a smooth curve $\mathbf{n}(\cdot)$ on a unit sphere S^2 that satisfies given boundary conditions (both positions and velocities)

$$\mathbf{n}(0) = \mathbf{n}_0, \quad \mathbf{n}(l) = \mathbf{n}_1, \quad \mathbf{n}'(0) = \mathbf{n}'_0, \quad \mathbf{n}'(l) = \mathbf{n}'_1$$

and minimizes the functional

$$\int_0^l \mathfrak{C}(\mathbf{n}(s)) \sqrt{\xi^2 + k_g^2(s)} \, ds,$$

where $k_g(\cdot)$ denotes the geodesic curvature of $\mathbf{n}(\cdot)$, s denotes the spherical arclength, and total length l is free, see Fig. 9.2. In the optimization functional we also include an

external cost factor $\mathfrak{C} : S^2 \rightarrow \mathbb{R}^+$ adding for adaptation to given spherical image data. We state this problem, to which we refer as $\mathbf{P}_{\text{curve}}(S^2)$, more explicitly in Section 9.3.1.

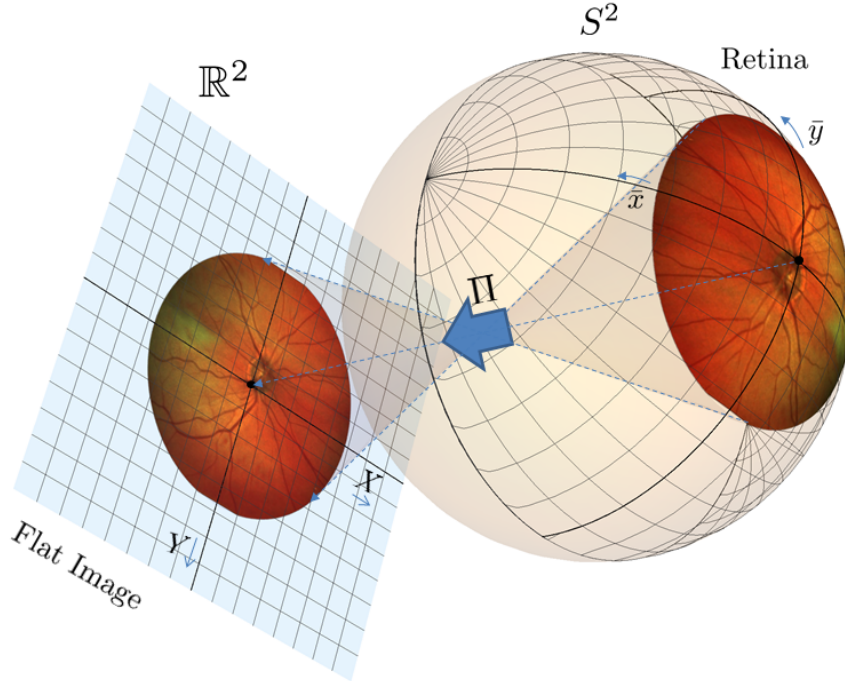


Figure 9.1: Photography of the retina. A part of the retina is projected onto the image plane. The camera coordinates are denoted by (X, Y) , and object coordinates are denoted by (\bar{x}, \bar{y}) .

The problem $\mathbf{P}_{\text{curve}}(S^2)$ is a spherical analogue of a well-known problem $\mathbf{P}_{\text{curve}}(\mathbb{R}^2)$ (see e.g. Fig. 9.2, App. C.6, and Boscain *et al.* (2014); Duits *et al.* (2013a)) of finding a smooth curve $\mathbf{x}(\cdot)$ on a plane \mathbb{R}^2 that satisfies given boundary conditions

$$\begin{aligned}\mathbf{x}(0) = \mathbf{x}_0 &= (X_0, Y_0), & \mathbf{x}'(0) = \mathbf{x}'_0 &= (\cos \Theta_0, \sin \Theta_0), \\ \mathbf{x}(l) = \mathbf{x}_1 &= (X_1, Y_1), & \mathbf{x}'(l) = \mathbf{x}'_1 &= (\cos \Theta_1, \sin \Theta_1),\end{aligned}$$

and minimizes the functional

$$\int_0^l \mathfrak{c}(\mathbf{x}(s)) \sqrt{\xi^2 + k^2(s)} \, ds,$$

where $k(s)$ denotes the curvature and l denotes the total length. The smooth external cost factor $\mathfrak{c} : \mathbb{R}^2 \rightarrow \mathbb{R}^+$ is added for adaptation to given flat image data (see e.g. Subsec. 8.7.2), and is bounded away from 0.

9. VES. TRACK. III: SUB-RIEMANNIAN GEODESICS IN $SO(3)$

While our main and first motivation to study sub-Riemannian geodesics in $SO(3)$ comes from the application in (spherical) retinal image analysis, there are two additional relevant motivations. The second motivation comes from models of the visual system of mammals. As mentioned by U. Boscain and F. Rossi Boscain & Rossi (2008), the problem $\mathbf{P}_{\text{curve}}(S^2)$ can be considered as a spherical extension of a (flat) cortical based model $\mathbf{P}_{\text{curve}}(\mathbb{R}^2)$ for perceptual completion, proposed by G. Citti, A. Sarti Citti & Sarti (2006), and J. Petitot Petitot (2003). Such a spherical extension is again motivated by the fact that the retina is not flat. By the same argument, cuspless sub-Riemannian geodesics on $SO(3)$ could provide a model of association fields in the psychology of vision (see Duits *et al.* (2013a)). Here, we will not focus on the neurophysiological aspect, but instead refer the interested reader to (Mashtakov *et al.*, 2016, App. F) for more details.

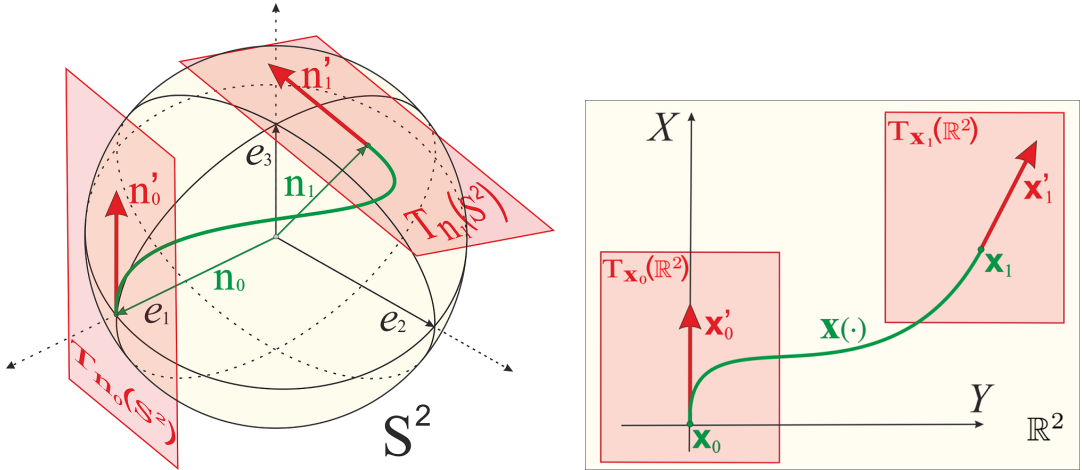


Figure 9.2: *Left:* Problem $\mathbf{P}_{\text{curve}}(S^2)$: for given boundary conditions on a 2D sphere (both positions and velocities), we aim to find a curve minimizing the functional compromising length and geodesic curvature. In the optimization functional we also include an external cost induced by spherical image data. *Right:* Problem $\mathbf{P}_{\text{curve}}(\mathbb{R}^2)$ Boscain et al. (2014); Duits et al. (2013a): for given boundary conditions on a 2D plane, to find a curve minimizing the compromise between length and curvature. The external cost factor is added for adaptation to flat image data (see Bekkers et al. (2015c)).

The third motivation for this study is that in geometric control theory optimal synthesis for the sub-Riemannian problem on $SO(3)$ has not been achieved in the general case (not even for the case of uniform cost $C = 1$), despite many strong efforts in this direction Berestovskii (2016, 1994); Beschastnyi & Sachkov (2014); Bonnard & Chyba (2014); Bonnard *et al.* (2014); Boscain & Rossi (2008); Calin *et al.* (2008);

Chang *et al.* (2009). In this chapter we will not provide optimal synthesis analytically, but instead we do provide a Hamilton-Jacobi-Bellman theory for computing globally optimal (data-driven) geodesics. In the previous chapter we achieved this for sub-Riemannian geodesics on $SE(2)$, which were used for tracking of blood vessels in flat 2D images.

In view of these three motivations, and to derive explicit and numeric solutions, we lift the problem $\mathbf{P}_{\text{curve}}$ on the set S^2 to a sub-Riemannian problem \mathbf{P}_{mec} on the group $SO(3)$. This allows us to describe the end points of $SO(3)$ reachable by geodesics with a cuspless spherical projection. Furthermore we present a Hamilton-Jacobi-Bellman PDE theory, that allows us to numerically compute the sub-Riemannian distance map, from which a steepest descent backtracking (via the Pontryagin maximum principle) provides only the *globally optimal* geodesics for general external cost and general $\xi > 0$. We verify our numerical solution, by comparison with exact geodesics in the case $C = 1$. Finally we use these results in a vessel tracking algorithm in spherical images of the retina, without central projection distortion.

9.1.1 Chapter Outline

In Sec. 9.2 we will first go through the required prerequisites which detail the coordinate system and mapping from (flat) camera coordinates to the spherical object coordinates (Subsec. 9.2.1) and the group structure of the Lie group $SO(3)$ (Subsec. 9.2.2). Then in Sec. 9.3 we formally state the problem which we are solving in this chapter. Here we make a distinction between the related problems $\mathbf{P}_{\text{curve}}$ (Subsec. 9.3.1: the curve optimization problem on the sphere) and \mathbf{P}_{mec} (Subsec. 9.3.2: the curve optimization on the group $SO(3)$). Then, based on the notion of parallel momentum of geodesics with respect to the left Cartan connection (recall Subsec. 4.5.4), we derive analytic solutions for non-data-adaptive sub-Riemannian geodesics on $SO(3)$ in Sec. 9.4. These solutions will provide the benchmark reference to which we compare the sub-Riemannian geodesics and distance volumes, which are computed via our numerical approach which we describe in Sec. 9.5. In Sec. 9.6 we compare results of our numerical method for computing sub-Riemannian geodesics in $SO(3)$ with exact solutions and also compare to the results of the $SE(2)$ model which is described in Ch. 8. This chapter is concluded with Sec. 9.7.

9.2 Prerequisites

9.2.1 Spherical Images

In this subsection we discuss the relevance of considering spherical images of the retina rather than flat images, which are commonly used in the medical application (see Fig. 9.1). We show that distortion appears inevitably on flat images, with a significant relative error (up to 7%) in length measures. Even larger relative errors (over 20%) appear in the application of differential operators (used for vessel detection).

We base our computations on the reduced schematic eye model (see Fig. 9.3), which is commonly used in clinical ophthalmology (see e.g. American Academy of Ophthalmology (2015)). Let R be the radius of an eyeball, a be the distance from the nodal point N to the center C , and ψ be the angle between visual axis and a light ray passing through N . Here we consider a simplified model, where the optical axis (the best approximation of a line passing through the optical center of the cornea, lens, and fovea) coincides with the visual axis (the line connecting fixation point and the fovea)¹. The average radius of a human eye is $R \approx 10.5\text{mm}$, and the maximum distance between nodal point N and the central point C is $a_{\max} = 17\text{mm} - 10.5\text{mm} = 6.5\text{mm}$.

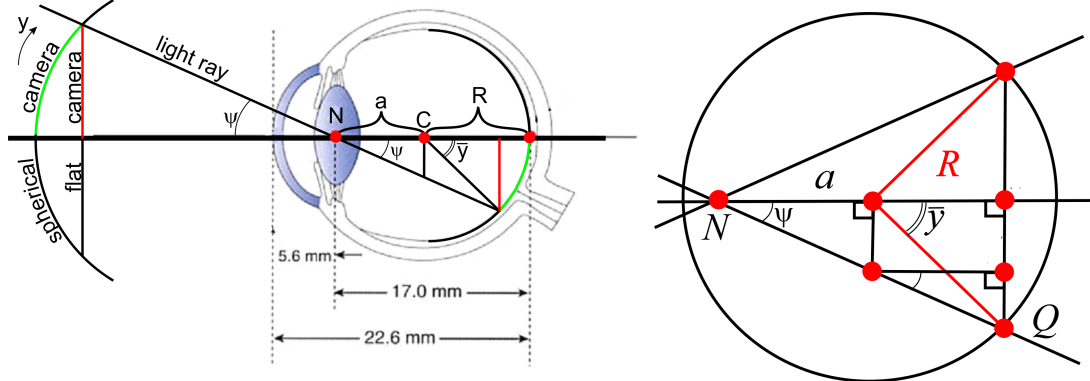


Figure 9.3: *Left:* Schematic eye (original illustration by C.H. Wooley American Academy of Ophthalmology (2015)) and central projection of images onto the retina. Here $R \approx 10.5\text{mm}$ is a radius of an eyeball, ψ is an angle between visual axis and light ray, and \bar{y} is an angle between visual axis and radius vector ending at the point where light ray hits the retina.

Right: Schematic eye, enlarged to support Eq. (9.1)

¹There is small difference between these two axes (c.f. Fig.33 American Academy of Ophthalmology (2015)) which we neglect in our basic model.

Now we switch to mathematical object coordinates of the retina where we use the eyeball radius to express lengths, i.e. we have $R = 1$ and $a_{max} = \frac{6.5mm}{10.5mm}R = \frac{13}{21}$ in dimensionless coordinates.

In order to compute the maximum absolute angle \bar{y}_{max} let us express the angle $|\bar{y}|$ with respect to center of the eyeball (see right Fig. 9.3). Expressing the squared distance of segment NQ yields

$$(a + R \cos |\bar{y}|)^2 \cos^{-2} \psi = (a + R \cos |\bar{y}|)^2 + R^2 \sin^2 |\bar{y}|.$$

Solving this equation with respect to $\cos |\bar{y}|$ we obtain unique nonnegative solution:

$$|\bar{y}(a, R, \psi)| = \arccos \left(\cos \psi \sqrt{1 - \frac{a^2 \sin^2 \psi}{R^2}} - \frac{a \sin^2 \psi}{R} \right). \quad (9.1)$$

A standard fundus camera used for producing of the retinal images has the angular range $\psi \in [-\frac{\pi}{8}, \frac{\pi}{8}]$. Thus, substitution $R = 1$, $a = \frac{13}{21}$ and $\psi = \frac{\pi}{8}$ in Eq. (9.1) gives the maximum angle

$$\bar{y}_{max} \approx 0.63 \text{rad} \approx 36^\circ. \quad (9.2)$$

We rely on the following parametrization of the image sphere S^2 and the retinal sphere \bar{S}^2 (see Fig. 9.4):

$$\begin{aligned} S^2 &\ni \mathbf{n}(x, y) = (\cos x \cos y, \cos x \sin y, \sin x)^T, \\ \bar{S}^2 &\ni (-2a, 0, 0)^T - (\cos \bar{x} \cos \bar{y}, \cos \bar{x} \sin \bar{y}, \sin \bar{x})^T, \end{aligned}$$

with $x, \bar{x} \in [-\frac{\pi}{2}, \frac{\pi}{2}]$ and $y, \bar{y} \in [-\pi, \pi]$.

Next we present the explicit relation between the object coordinates (\bar{x}, \bar{y}) — spherical coordinates on a unit sphere \bar{S}^2 representing the surface of the eyeball; flat photo coordinates (X, Y) — Cartesian coordinates on the image plane; and the spherical coordinates (x, y) on the image sphere. See Fig. 9.1 and Fig. 9.4.

To take into account the distance from the eyeball to the camera in our model we introduce a parameter $\eta > 0$. In Fig. 9.4, by setting $\eta = 1$ we fix the distance equal to $(a + c)$ radiiuses of the eyeball. This corresponds to the case when the image sphere S^2 is obtained by reflection of the physical retinal sphere \bar{S}^2 through the point $(-a, 0, 0)^T \in \mathbb{R}^3$. In this case we have

$$(x, y) = (\bar{x}, \bar{y}), \quad (9.3)$$

and we will always rely on this identification in the sequel. The general case $\eta > 0$ can be taken into account by congruency and scaling $X \mapsto \eta RX$, $Y \mapsto \eta RY$.

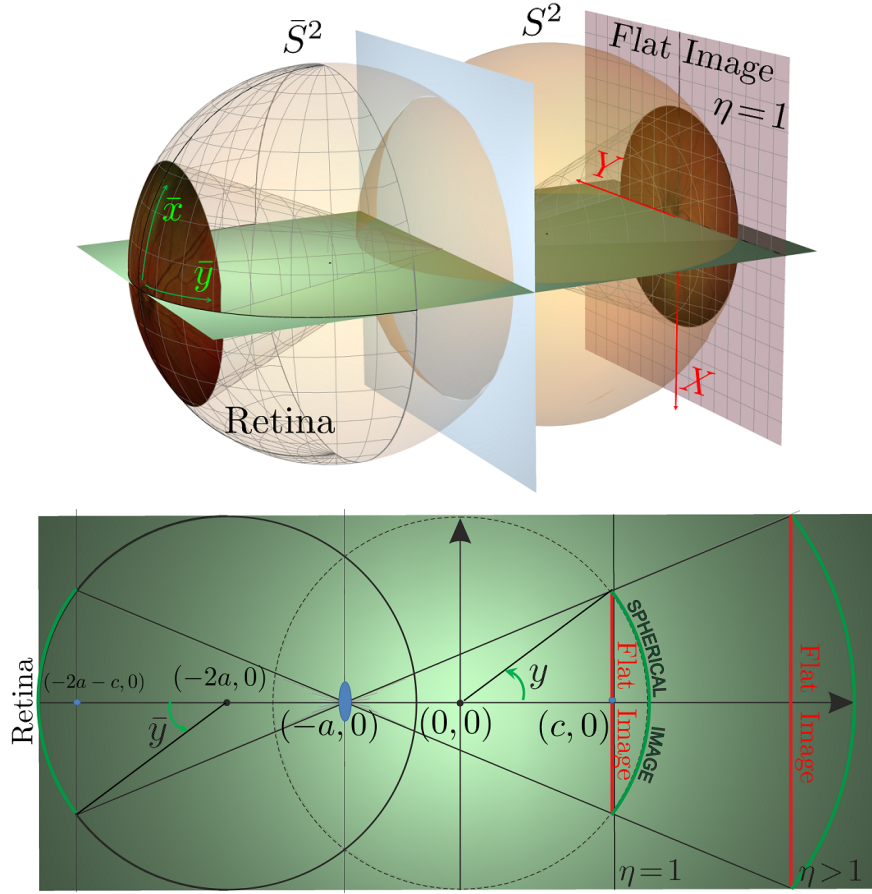


Figure 9.4: Spherical object coordinates (\bar{x}, \bar{y}) on a retina, Cartesian camera coordinates (X, Y) on a flat image of the retina, and spherical camera coordinates (x, y) on a spherical image of the retina.

The central projection Π (cf. Fig. 9.1) from (x, y) to (X, Y) including the scaling factor $\eta > 0$ (with physical dimension length in units of R) is given by

$$X = \frac{(a + c) \sin x}{a + \cos x \cos y} \eta, \quad Y = \frac{(a + c) \cos x \sin y}{a + \cos x \cos y} \eta. \quad (9.4)$$

Remark 17. In practice, the objective lens of a fundus cameras is typically at a distance of 0.5cm to 1.5cm away from the cornea, in which a reasonable range for η is $0.5 \leq \eta \leq 1.5$.

The inverse mapping Π^{-1} from (X, Y) to (x, y) for $\eta = 1$ is given by

$$\begin{aligned} x &= \arcsin(X \bar{p}(X, Y)), \\ y &= \arg(p_1(X, Y) + i Y \bar{p}(X, Y)), \end{aligned} \quad (9.5)$$

where

$$\bar{p}(X, Y) = \frac{a(a+c) + \Xi_{a,c}(X, Y)}{(X^2 + Y^2) + (a+c)^2},$$

$$p_1(X, Y) = \frac{(a+c)\Xi_{a,c}(X, Y) - a(X^2 + Y^2)}{(X^2 + Y^2) + (a+c)^2},$$

with $\Xi_{a,c}(X, Y) = \sqrt{(X^2 + Y^2)(1 - a^2) + (a+c)^2}$.

In these formulas we need to substitute $a = a_{max} = \frac{13}{21}$ and $c = \frac{4}{5} < R = 1$, depicted in Fig. 9.4, where we work in dimensionless coordinates.

Quantification of local and global deformation

The local deformation from spherical coordinates (x, y) to planar photo coordinates (X, Y) is now given by the Jacobian

$$J(x, y) = \det \begin{pmatrix} \frac{\partial X}{\partial x}(x, y) & \frac{\partial X}{\partial y}(x, y) \\ \frac{\partial Y}{\partial x}(x, y) & \frac{\partial Y}{\partial y}(x, y) \end{pmatrix}$$

$$= \frac{(a+c)^2 \cos x (1 + a \cos x \cos y)}{(a + \cos x \cos y)^3} \eta^2.$$

In mathematical analysis we can set $\eta = 1$, however in experiments η is to be taken into consideration. Note that for $\eta = 1$ we have

$$0.77 \approx J(0, 0) \leq J(x, y) \leq J(y_{max}, y_{max}) \approx 1.1,$$

showing that local deformation plays a role and varies considerably in (x, y) .

Next we consider the global distortion along the line $x = 0$. It is defined as $\mathcal{GD}(y) = \frac{|y - Y(0, y)|}{|y|}$, and it has a maximum when $y = y_{max}$. We have

$$0 \leq \mathcal{GD}(y) \leq \mathcal{GD}(y_{max}) \approx 0.07,$$

and we see the distortion up to 7% along the line $x = 0$. The same holds along the line $y = 0$.

We conclude that it makes a considerable difference to study $\mathbf{P}_{\text{curve}}(S^2)$ or $\mathbf{P}_{\text{curve}}(\mathbb{R}^2)$ in the retinal imaging application. In the sequel we will write $\mathbf{P}_{\text{curve}}$ instead of $\mathbf{P}_{\text{curve}}(S^2)$ as we will always be concerned with the case where the base manifold equals S^2 .

9. VES. TRACK. III: SUB-RIEMANNIAN GEODESICS IN $\text{SO}(3)$

9.2.2 The Lie Group $SO(3)$

The Lie group $SO(3)$ is the group of all rotations about the origin in \mathbb{R}^3 . We shall denote a counter-clockwise rotation around axis $\mathbf{a} \in S^2$ with angle ϕ via $R_{\mathbf{a},\phi}$. In particular for rotations around standard axes

$$\mathbf{e}_1 = (1, 0, 0)^T, \quad \mathbf{e}_2 = (0, 1, 0)^T, \quad \mathbf{e}_3 = (0, 0, 1)^T.$$

We use representation of $SO(3)$ by 3×3 matrices

$$R(x, y, \theta) = R_{\mathbf{e}_3, y} R_{\mathbf{e}_2, -x} R_{\mathbf{e}_1, \theta} =$$

$$\begin{pmatrix} cx \, cy & -sx \, cy \, s\theta - sy \, c\theta & sy \, s\theta - sx \, cy \, c\theta \\ cx \, sy & cy \, s\theta - sx \, sy \, s\theta & -cy \, s\theta - sx \, sy \, c\theta \\ sx & cx \, s\theta & cx \, c\theta \end{pmatrix}, \quad (9.6)$$

where we denote $cx = \cos x$, $cy = \cos y$, $c\theta = \cos \theta$, $sx = \sin x$, $sy = \sin y$, $s\theta = \sin \theta$, and where

$$(x, y, \theta) \in [-\frac{\pi}{2}, \frac{\pi}{2}] \times \mathbb{R}/\{2\pi\mathbb{Z}\} \times \mathbb{R}/\{2\pi\mathbb{Z}\}. \quad (9.7)$$

The Lie group $SO(3)$ defines an associated Lie algebra

$$so(3) = T_{\text{Id}}(SO(3)) = \text{span}(A_1, A_2, A_3),$$

$$A_1 = \begin{pmatrix} 0 & 0 & 0 \\ 0 & 0 & -1 \\ 0 & 1 & 0 \end{pmatrix}, \quad A_2 = \begin{pmatrix} 0 & 0 & 1 \\ 0 & 0 & 0 \\ -1 & 0 & 0 \end{pmatrix}, \quad A_3 = \begin{pmatrix} 0 & -1 & 0 \\ 1 & 0 & 0 \\ 0 & 0 & 0 \end{pmatrix},$$

where $T_{\text{Id}}(SO(3))$ denotes the tangent space at the unity element.

The nonzero Lie brackets are given by

$$[A_1, A_2] = A_3, \quad [A_1, A_3] = -A_2, \quad [A_2, A_3] = A_1. \quad (9.8)$$

There is a natural isomorphism between $so(3)$ and Lie algebra L of left-invariant vector fields on $SO(3)$, where commutators of vector fields in L correspond to the matrix commutators in $so(3)$

$$[RA, RB] = R[A, B], \quad A, B \in so(3), R \in SO(3). \quad (9.9)$$

We express L in matrix form as

$$L = \text{span}(X_1, X_2, X_3), \quad \begin{cases} X_1(x, y, \theta) = -R(x, y, \theta)A_2, \\ X_2(x, y, \theta) = R(x, y, \theta)A_1, \\ X_3(x, y, \theta) = R(x, y, \theta)A_3, \end{cases} \quad (9.10)$$

9.3 The Problems $\mathbf{P}_{\text{curve}}$ on S^2 and \mathbf{P}_{mec} on $SO(3)$

We also use the isomorphism between $so(3)$ and \mathbb{R}^3

$$A_i \sim \mathbf{e}_i, \quad RA_i R^{-1} \sim R\mathbf{e}_i, \quad (9.11)$$

where $A_i \in so(3)$, $R \in SO(3)$, $\mathbf{e}_i \in \mathbb{R}^3$, $i = 1, 2, 3$.

Finally, note that (9.6) is a product of matrix exponentials:

$$R(x, y, \theta) = \exp(yA_3) \exp(-xA_2) \exp(\theta A_1). \quad (9.12)$$

We choose to rely on this parametrization to keep the analogy with previous $SE(2)$ models, such as the one in Ch. 8 and Duits *et al.* (2013a); Sachkov (2011).

9.3 The Problems $\mathbf{P}_{\text{curve}}$ on S^2 and \mathbf{P}_{mec} on $SO(3)$

9.3.1 Statement of the Problem $\mathbf{P}_{\text{curve}}$

Let $S^2 = \{\mathbf{n} \in \mathbb{R}^3 \mid \|\mathbf{n}\| = 1\}$ be a sphere of unit radius. We consider the problem $\mathbf{P}_{\text{curve}}$ (see Fig. 9.2), which is for given boundary points $\mathbf{n}_0, \mathbf{n}_1 \in S^2$ and directions $\mathbf{n}'_0 \in T_{\mathbf{n}_0}(S^2)$, $\mathbf{n}'_1 \in T_{\mathbf{n}_1}(S^2)$, $\|\mathbf{n}'_0\| = \|\mathbf{n}'_1\| = 1$ to find a smooth curve $\mathbf{n}(\cdot) : [0, l] \rightarrow S^2$ that satisfies the boundary conditions

$$\mathbf{n}(0) = \mathbf{n}_0, \quad \mathbf{n}(l) = \mathbf{n}_1, \quad \mathbf{n}'(0) = \mathbf{n}'_0, \quad \mathbf{n}'(l) = \mathbf{n}'_1, \quad (9.13)$$

and for given $\xi > 0$ minimizes the functional

$$\mathcal{L}(\mathbf{n}(\cdot)) := \int_0^l \mathfrak{C}(\mathbf{n}(s)) \sqrt{\xi^2 + k_g^2(s)} \, ds, \quad (9.14)$$

where $k_g(s)$ denotes the geodesic curvature on S^2 of $\mathbf{n}(\cdot)$ evaluated in time s , and $\mathfrak{C} : S^2 \rightarrow [\delta, +\infty)$, $\delta > 0$, is an analytic function that we call "external cost".

Here the total length l is free and $s = \int_0^s 1 \, d\sigma = \int_0^s \|\mathbf{n}'(\sigma)\| \, d\sigma$ denotes the spherical arclength. Thus, we have $\|\mathbf{n}'(s)\| = 1$ and the Gauss-Bonnet formula

$$k_g(s) = \mathbf{n}''(s) \cdot (\mathbf{n}(s) \times \mathbf{n}'(s)). \quad (9.15)$$

9.3.2 Statement of the Problem \mathbf{P}_{mec} on $SO(3)$

We call \mathbf{P}_{mec} the following sub-Riemannian problem on $SO(3)$:

$$\dot{R} = -u_1 RA_2 + u_2 RA_1, \quad (9.16)$$

$$R(0) = \text{Id}, \quad R(T) = R_{fin}, \quad (9.17)$$

$$\mathcal{L}(R(\cdot)) := \int_0^T C(R(t)) \sqrt{\xi^2 u_1^2(t) + u_2^2(t)} \, dt \rightarrow \min, \quad (9.18)$$

$$R \in SO(3), \quad (u_1(t), u_2(t)) \in \mathbb{R}^2, \quad \xi > 0, \quad (9.19)$$

9. VES. TRACK. III: SUB-RIEMANNIAN GEODESICS IN $SO(3)$

with $T > 0$ free.

The external cost $C : SO(3) \rightarrow [\delta, +\infty)$, $\delta > 0$, is an analytic function that is typically obtained by lifting the external cost \mathfrak{C} from the sphere S^2 to the group $SO(3)$, i.e. $C(R) = \mathfrak{C}(R \mathbf{e}_1)$.

We study the problem \mathbf{P}_{mec} for $C = 1$ (case of uniform external cost) in Section 9.4, but let us first consider some preliminaries.

Remark 18. In problem \mathbf{P}_{mec} we only have 2 velocity controls u_1 and u_2 in a 3D tangent space $T_{R(t)}(SO(3))$.

Remark 19. Sub-Riemannian manifolds are commonly defined by a triplet $(\mathcal{M}, \Delta, \mathcal{G}_0^{\xi, C})$, with manifold \mathcal{M} , distribution $\Delta \subset T(\mathcal{M})$ and metric tensor $\mathcal{G}_0^{\xi, C}$. In our case

$$\begin{aligned} \mathcal{M} &= SO(3), \quad \Delta = \text{span}\{RA_1, RA_2\}, \\ \mathcal{G}_0^{\xi, C}(\dot{R}, \dot{R}) &= C^2(\cdot) (\xi^2 u_1^2 + u_2^2), \end{aligned} \tag{9.20}$$

where the controls u_1 and u_2 are components of the velocity vector w.r.t. the moving frame of reference, see (9.16).

Remark 20. In analogy with the sub-Riemannian problem \mathbf{P}_{mec} in $SE(2)$, cf. Boscain et al. (2014); Duits et al. (2013a), we sometimes call $X_1 = -RA_2$ the “spatial generator” and $X_2 = RA_1$ the “angular generator”, despite the fact that X_1 and X_2 are both angular generators on S^2 . The problem $\mathbf{P}_{\text{mec}}(SO(3))$ can be seen as a model of the Reeds-Shepp car on a sphere. The Reeds-Shepp car can move forward and backward and rotate on a place. The control u_1 controls the motion along X_1 , and the control u_2 controls the motion along X_2 . See Fig. 9.5.

9.3.3 Relation Between the Problems $\mathbf{P}_{\text{curve}}$ and \mathbf{P}_{mec}

We call a spherical projection the following projection map from $SO(3)$ onto S^2 (see Fig. 9.6)

$$SO(3) \ni R \mapsto R \mathbf{e}_1 \in S^2. \tag{9.21}$$

In coordinates (x, y, θ) defined by (9.6) we have

$$R(x, y, \theta) \mathbf{e}_1 = \begin{pmatrix} \cos x \cos y \\ \cos x \sin y \\ \sin x \end{pmatrix} = \mathbf{n}(x, y) \in S^2. \tag{9.22}$$

So we see, that (x, y) are spherical coordinates on S^2 .

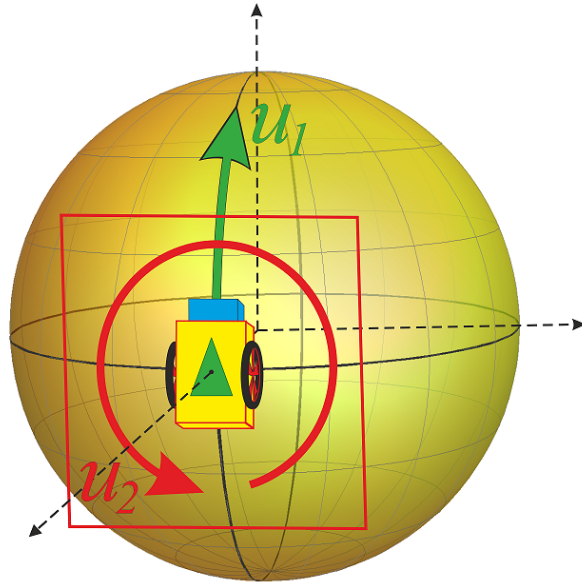


Figure 9.5: The controls u_1 and u_2 along the “spatial generator” X_1 and the “angular generator” X_2 (cf. Remark 20).

We can observe that in $\mathbf{P}_{\text{curve}}$ one is interested in a curve $\mathbf{n}(s) = R(t(s)) \mathbf{e}_1$, which satisfies (9.13) and minimizes (9.14). Here $R(t) = R(x(t), y(t), \theta(t))$, and

$$t(s) = \int_0^s \mathfrak{C}(\mathbf{n}(\sigma)) \sqrt{\xi^2 + k_g^2(\sigma)} d\sigma. \quad (9.23)$$

Next we show that the spherical projection (9.21) of certain minimizers of \mathbf{P}_{mec} provides the solution of problem $\mathbf{P}_{\text{curve}}$. More precisely this holds for the minimizers whose spherical projection does not have a cusp.

Definition 1. The spherical projection of a minimizer of \mathbf{P}_{mec} is said to have a cusp at $t = t_{\text{cusp}}^n$ if there exists $\epsilon > 0$, s.t. $u_1(a)u_1(b) < 0$ for all $a \in (t_{\text{cusp}}^n - \epsilon, t_{\text{cusp}}^n)$ and $b \in (t_{\text{cusp}}^n, t_{\text{cusp}}^n + \epsilon)$. I.e. if the control in front of the “spatial” generator X_1 switches sign locally. We are interested in the first cusp time $t_{\text{cusp}} = \min_{n \in \mathbb{N}} \{t_{\text{cusp}}^n > 0\}$, and we call s_{\max} the corresponding value of spherical arclength, s.t. $t_{\text{cusp}} = t(s_{\max})$ via (9.23).

Notice that if $u_1 \equiv 0$ then the trajectory of \mathbf{P}_{mec} is projected at a single point on S^2 which does not provide a solution to $\mathbf{P}_{\text{curve}}$. This allows us to define s_{\max} as

$$s_{\max} = \min\{s > 0 \mid u_1(t(s)) = 0\}, \quad (9.24)$$

so that $t_{\text{cusp}} = t(s_{\max})$.

9. VES. TRACK. III: SUB-RIEMANNIAN GEODESICS IN $\text{SO}(3)$

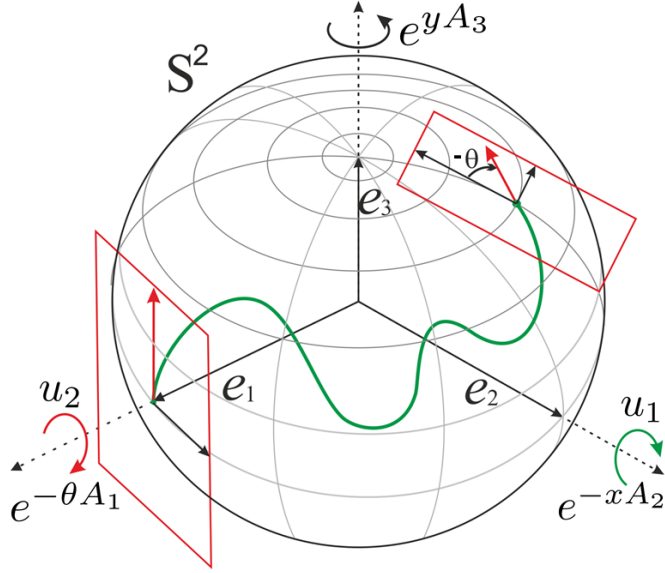


Figure 9.6: Illustration of the parametrizations used in \mathbf{P}_{mec} and $\mathbf{P}_{\text{curve}}$. The rotations are parameterized by (9.12), i.e. by angles x, y and θ of rotation about basis axes, see (9.7).

The following theorem states that minimizers $\mathbf{n}(s)$ of $\mathbf{P}_{\text{curve}}$ for $s \in [0, s_{\max}]$ are given by spherical projection of the minimizers $R(t)$ of \mathbf{P}_{mec} for $t \in [0, t_{\text{cusp}}]$.

Theorem 4. Let $R(t)$, $t \in [0, T]$ be a minimizer of \mathbf{P}_{mec} whose spherical projection does not exhibit a cusp (i.e. $T < t_{\text{cusp}}$). Set

$$\begin{cases} R(T) \mathbf{e}_1 = \mathbf{n}_1 = R_{\text{fin}} \mathbf{e}_1, \\ R(T) \mathbf{e}_3 = \mathbf{n}'_1 = R_{\text{fin}} \mathbf{e}_3, \\ \mathbf{n}_0 = \mathbf{e}_1, \quad \mathbf{n}'_0 = \mathbf{e}_3. \end{cases} \quad (9.25)$$

Then for such boundary conditions $\mathbf{P}_{\text{curve}}$ is well-posed and along such minimizers we have

$$\mathbf{n}(s) = R(t(s)) \mathbf{e}_1, \quad \begin{cases} u_1 = \frac{ds}{dt}, \\ u_2 = -k_g \frac{ds}{dt}, \end{cases} \quad (9.26)$$

with $t(s) = \int_0^s \mathfrak{C}(\mathbf{n}(\sigma)) \sqrt{\xi^2 + k_g^2(\sigma)} d\sigma$, for $0 \leq s \leq l < s_{\max}$, and $T = t(l)$. The limit $\lim_{s \uparrow s_{\max}} t(s) = t(s_{\max})$ is well-defined, despite the fact that $\lim_{s \uparrow s_{\max}} k_g(s) = \infty$.

Proof See (Mashtakov *et al.*, 2016, App. A). □

9.4 Analytic Formulas Obtained via the Left-Cartan Connection

Geodesics can be obtained as Hamiltonian flows ((Jost, 2011, Ch. 2.2)), in which the geodesics are integral curves of a Hamiltonian vector field defined on the cotangent bundle $T^*(SO(3))$. Such geodesics have a vertical part (the adjoint variables) and a horizontal part (the state variables). The sub-Riemannian geodesics are obtained as the horizontal part of the solutions to the Hamiltonian system of ordinary differential equations (ODEs). Such an approach is also used in the $SE(2)$ case in Ch. 8, App. C.1 and Agrachev & Sachkov (2013).

In Mashtakov *et al.* (2016), the Hamiltonian system is obtained via Pontryagin's maximum principle. In this section we follow an alternative route to obtain the Hamiltonian system in which we rely on the left Cartan connection on the cotangent bundle. Our starting point is that sub-Riemannian geodesics have parallel momentum with respect to the (dual) left Cartan connection (see Thm. 1 on page 92).

Once the Hamiltonian system is defined, the sub-Riemannian geodesics are obtained as its solutions. In Mashtakov *et al.* (2016) exact solutions are obtained for the $C = 1$ case (no data-adaptivity). These exact solutions are later used in Sec. 9.6 for the validation of our numerical method for computing data-adaptive sub-Riemannian geodesics (Sec. 9.5).

9.4.1 Cartan Connection

The sub-Riemannian left Cartan connection on $SO(3)$ has the same form as the left Cartan connection on $SE(2)$ (see Subsec. 4.5.3) and is in local coordinates defined as

$$\bar{\nabla}_{\dot{\gamma}}^{SO(3)} Y := \sum_{k=1}^2 \left(\dot{y}^k - \sum_{i,j=1}^2 c_{ij}^k \dot{\gamma}^i y^j \right) X_k, \quad (9.27)$$

with vector field $Y|_{\gamma} = \sum_{i=1}^3 y^i(\gamma) X_i|_{\gamma}$, with $\dot{y}^k|_{\gamma} = \frac{d}{dt} \omega^k|_{\gamma(t)} (Y|_{\gamma(t)})$ the derivative of each component y^k along the curve γ , with basis $\{\omega^i\}_{i=1}^3$ dual to $\{X_i\}_{i=1}^3$ defined by $\langle \omega^i, X_j \rangle = \delta_j^i$, and with the non-zero structure constants c_{ij}^k (see also commutators in (9.8)) given by

$$c_{1,2}^3 = -c_{2,1}^3 = 1, \quad c_{1,3}^2 = -c_{3,1}^2 = -1, \quad c_{2,3}^1 = -c_{3,2}^1 = 1. \quad (9.28)$$

9. VES. TRACK. III: SUB-RIEMANNIAN GEODESICS IN $SO(3)$

The connection on the cotangent bundle is given by

$$\bar{\nabla}_{\dot{\gamma}}^{*,SO(3)} \lambda = \sum_{i=1}^3 \left(\dot{\lambda}_i + \sum_{j=1}^2 \sum_{k=1}^3 c_{ij}^k \lambda_k \dot{\gamma}^j \right) \omega^i, \quad (9.29)$$

with $\dot{\lambda}_i(t) = \frac{d}{dt} \langle \lambda|_{\gamma(t)}, X_i|_{\gamma(t)} \rangle$.

9.4.2 Parallel Momentum

Now, (sub-Riemannian) geodesics have parallel momentum with respect to the left Cartan connection, and they satisfy the following set of equations

$$\bar{\nabla}_{\dot{\gamma}}^{*,SO(3)} \lambda = 0 \quad (9.30a)$$

$$\mathcal{G}_0^\xi \dot{\gamma} = \mathbb{P}_\Delta^* \lambda, \quad (9.30b)$$

with the sub-Riemannian metric tensor on $SO(3)$ for $C = 1$ given by

$$\mathcal{G}_0^\xi|_{\gamma(t)} (\dot{\gamma}(t), \dot{\gamma}(t)) = \sum_{i,j=1}^2 g_{ij} u^i u^j = \xi^2 |u^1(t)|^2 + |u^2(t)|^2, \quad (9.31)$$

with

$$\dot{\gamma}(t) = \begin{pmatrix} \dot{x}(t) \\ \dot{y}(t) \\ \dot{\theta}(t) \end{pmatrix} = u^1(t) X_1|_{\gamma(t)} + u^2 X_2|_{\gamma(t)}, \quad (9.32)$$

with

$$X_1|_{\gamma(t)} = \begin{pmatrix} \cos \theta \\ -\sec x \sin \theta \\ \tan x \sin \theta \end{pmatrix}, \quad X_2|_{\gamma(t)} = \begin{pmatrix} 0 \\ 0 \\ 1 \end{pmatrix}. \quad (9.33)$$

As we will see, (9.30a) provides us the vertical part and (9.30b) the horizontal part of the Hamiltonian system.

9.4.3 The Hamiltonian System in Sub-Riemannian Arc-Length Parameterization

From the set of equations in (9.30) we can derive the following Hamiltonian system of ODEs:

$$\begin{cases} \dot{\lambda}_1 = -\lambda_2 \lambda_3, \\ \dot{\lambda}_2 = \frac{1}{\xi^2} \lambda_1 \lambda_3, \\ \dot{\lambda}_3 = \left(1 - \frac{1}{\xi^2}\right) \lambda_1 \lambda_2 \end{cases} \quad \begin{cases} \dot{x} = \frac{\lambda_1}{\xi^2} \cos \theta, \\ \dot{y} = -\frac{\lambda_1}{\xi^2} \sec x \sin \theta, \\ \dot{\theta} = \frac{\lambda_1}{\xi^2} \sin \theta \tan x + \lambda_2 \end{cases} \quad \begin{matrix} \text{— vertical part,} \\ \text{— horizontal part,} \end{matrix} \quad (9.34)$$

9.4 Analytic Formulas Obtained via the Left-Cartan Connection

with the boundary conditions

$$\begin{aligned} \lambda_1(0) &= \lambda_1^0, & \lambda_2(0) &= \lambda_2^0, & \lambda_3(0) &= \lambda_3^0, \\ x(0) &= 0, & y(0) &= 0, & \theta(0) &= 0. \end{aligned} \quad (9.35)$$

The horizontal part of the Hamiltonian system (expressed in our coordinate chart (9.12)) follows directly by substituting

$$u^k = \xi_k^{-2} \lambda_k, \quad \text{with } \xi_1 = \xi, \quad \xi_2 = 1, \quad (9.36)$$

which we obtained from (9.30b), into (9.32). By substituting (9.36) into (9.29) we obtain the following:

$$\begin{aligned} \sum_{i=1}^3 \left(\dot{\lambda}_i + \sum_{j=1}^2 \sum_{k=1}^3 c_{ij}^k \lambda_k \xi_j^{-2} \lambda_j \right) \omega^i &= 0 \\ \Leftrightarrow \\ \dot{\lambda}_i &= - \sum_{j=1}^2 \sum_{k=1}^3 c_{ij}^k \xi_j^{-2} \lambda_k \lambda_j. \end{aligned} \quad (9.37)$$

This (together with the structure constants given in (9.28)) gives us then the vertical part of the Hamiltonian system.

9.4.4 Exact Solutions

The Hamiltonian system (9.34) in sub-Riemannian arclength parametrization (i.e., $\mathcal{G}_0^\xi(\dot{\gamma}, \dot{\gamma}) = 1$) is solved in Mashtakov *et al.* (2016). There exact solutions are provided, and these curves are the minimizers of $\mathbf{P}_{\text{mec}}(SO(3))$ (Subsec. 9.3.2). In Thm. 6 of Mashtakov *et al.* (2016) exact solutions are provided as well for sub-Riemannian geodesics in $SO(3)$ that do not contain cusps. We provide these solutions below. Such cuspless geodesics can be parametrized in spherical arc-length parametrization ($|u^1(t)|^2 = 1$), and their projections to S^2 are solutions to the problem $\mathbf{P}_{\text{curve}}(S^2)$ (Subsec. 9.3.1). In spherical arc-length parametrization the Hamiltonian system in (9.34) becomes

$$\begin{cases} \lambda_1(s) = \xi^2 \frac{ds}{dt} \geq 0, \\ \lambda'_2(s) = \lambda_3(s), \\ \lambda'_3(s) = (\xi^2 - 1)\lambda_2(s), \end{cases} \quad \begin{cases} x'(s) = \cos \theta(s), \\ y'(s) = -\sec x(s) \sin \theta(s), \\ \theta'(s) = \sin \theta(s) \tan x(s) + \xi \lambda_2(s) / \sqrt{1 - \lambda_2^2(s)}, \end{cases} \quad \begin{array}{l} \text{— vertical part,} \\ \text{— horizontal part,} \end{array} \quad (9.38)$$

9. VES. TRACK. III: SUB-RIEMANNIAN GEODESICS IN $\text{SO}(3)$

in which we write $\lambda_i(s) := \lambda_i(t(s))$ and $\lambda'_i(s) = \frac{d}{ds}\lambda_i$. Although still quite technical, the solution to the system (9.38) in s -parametrization is considerably simpler than the solution of (9.34) in t -parametrization (Mashtakov *et al.*, 2016, Thm. 2). Full details are provided in Mashtakov *et al.* (2016), here we only provide the main results in the following theorems.

Theorem 5. *A solution of the vertical part in (9.38) for all $\xi \neq 1$ reads as*

$$\begin{cases} \lambda_2(s) = \lambda_2^0 \cosh s\chi + \frac{\lambda_3^0}{\chi} \sinh s\chi, \\ \lambda_3(s) = \lambda_3^0 \cosh s\chi + \chi \lambda_2^0 \sinh s\chi, \\ \lambda_1(s) = \xi \sqrt{1 - \lambda_2^2(s)}, \end{cases} \quad (9.39)$$

with $\chi \in \mathbb{C}$ given by

$$\chi = \sqrt{\xi^2 - 1} = \begin{cases} \sqrt{1 - \xi^2} \cdot 1, & \text{for } 0 < \xi < 1, \\ \sqrt{\xi^2 - 1}, & \text{for } \xi \geq 1, \end{cases} \quad (9.40)$$

and for the case $\xi = 1$ we find straight lines parallel to the λ_2 axis in the (λ_2, λ_3) -phase portrait:

$$\begin{cases} \lambda_2(s) = \lambda_2^0 + \lambda_3^0 s, \\ \lambda_3(s) = \lambda_3^0, \\ \lambda_1(s) = \sqrt{1 - \lambda_2^2(s)}. \end{cases} \quad (9.41)$$

Theorem 6. *The unique solution of (9.38) is defined for $s \in [0, s_{\max}(\lambda(0))]$, where $s_{\max}(\lambda(0))$ is given by (9.43), defined in Thm. 7 below. The solution to the vertical part is given by Theorem 5 and the solution to the horizontal part is given by*

$$\begin{aligned} x(s) &= \arg(\sqrt{R_{11}^2(s) + R_{21}^2(s)} + iR_{31}(s)), \\ y(s) &= \arg(R_{11}(s) + iR_{21}(s)), \\ \theta(s) &= \arg(R_{33}(s) + iR_{32}(s)), \end{aligned} \quad (9.42)$$

where

$$\begin{aligned} R(s) &= \begin{pmatrix} R_{11}(s) & R_{12}(s) & R_{13}(s) \\ R_{21}(s) & R_{22}(s) & R_{23}(s) \\ R_{31}(s) & R_{32}(s) & R_{33}(s) \end{pmatrix} = D_0^T e^{\tilde{y}(s)A_3} e^{-\tilde{x}(s)A_2} e^{\tilde{\theta}(s)A_1}, \\ D_0 &= \frac{1}{M} \begin{pmatrix} \mu & \frac{\xi \lambda_2^0 \sqrt{1 - (\lambda_2^0)^2}}{\mu} & -\frac{\lambda_2^0 \lambda_3^0}{\mu} \\ 0 & \frac{M \lambda_3^0}{\mu} & \frac{\xi M \sqrt{1 - (\lambda_2^0)^2}}{\mu} \\ \lambda_2^0 & -\xi \sqrt{1 - (\lambda_2^0)^2} & \lambda_3^0 \end{pmatrix}, \quad \text{and} \end{aligned}$$

9.4 Analytic Formulas Obtained via the Left-Cartan Connection

$$\begin{aligned}\tilde{x}(s) &= \arg \left(\sqrt{M^2 - \lambda_2^2(s)} + i\lambda_2(s) \right), \\ \tilde{y}(s) &= \xi M^2 \left(\int_0^s \frac{\sqrt{1 - \lambda_2^2(\sigma)}}{M^2 - \lambda_2^2(\sigma)} d\sigma \right), \\ \tilde{\theta}(s) &= \arg \left(\lambda_3(s) - i\xi \sqrt{1 - \lambda_2^2(s)} \right),\end{aligned}$$

with $\mu = \sqrt{M^2 - (\lambda_2^0)^2}$, $M = \sqrt{\xi^2(1 - (\lambda_2^0)^2) + (\lambda_2^0)^2 + (\lambda_3^0)^2}$.

Theorem 7. When moving along a sub-Riemannian geodesic $t \mapsto \gamma(t)$ the first cusp time is computed as $t_{cusp}(\lambda(0)) = t(s_{max}(\lambda(0)))$, recall (9.23), where

$$s_{max}(\lambda(0)) = \begin{cases} \frac{\operatorname{sgn}(\lambda_3^0) - \lambda_2^0}{\lambda_3^0} & \text{for } \chi = 0, \lambda_3^0 \neq 0, \\ \frac{1}{\chi} \log \left(\frac{s_1(\sqrt{\kappa} + \chi)}{\lambda_2^0 \chi + \lambda_3^0} \right) & \text{for } \chi \neq 0, \kappa \geq 0, \lambda_2^0 \chi + \lambda_3^0 \neq 0, \\ +\infty & \text{otherwise,} \end{cases} \quad (9.43)$$

with $s_1 = \operatorname{sgn}(\Re(\lambda_2^0 \chi + \lambda_3^0))$

and $\kappa = (\lambda_3^0)^2 + (1 - (\lambda_2^0)^2) \chi^2 \in \mathbb{R}$.

As a result we see that (in contrast to the $SE(2)$ case, where cuspless sub-Riemannian geodesics are always optimal), in the sub-Riemannian manifold $(SO(3), \Delta, \mathcal{G}_0^\xi)$ there do exist nonoptimal cuspless geodesics.

9.4.5 Alternative Derivation of the Analytic Solution via the Left Cartan Connection

In Mashtakov *et al.* (2016) we derived the exact solutions via the Pontryagin Maximum principle. Here we provide a short derivation via our fundamental tool: the left-Cartan connection (recall Thm. 1). In matrix vector notation we can write (9.30a) as follows

$$\bar{\nabla}_\gamma^{*, SO(3)} \lambda = 0 \Rightarrow d\lambda - \underline{\lambda} \mathbf{R}(\gamma)^{-1} d\mathbf{R}(\gamma) = 0, \quad (9.44)$$

with row vector $\underline{\lambda} = (\lambda^1, \lambda^2, \lambda^3)$, with matrix representation $\mathbf{R}(\gamma(t))$ of the group elements $\gamma(t) \in SO(3)$, and with $\mathbf{R}(\gamma)^{-1} d\mathbf{R}(\gamma)$ the Cartan matrix. Consider now the following relation (obtained using the chain-rule and inverse matrix differentiation):

$$\begin{aligned}d(\lambda \mathbf{R}(\gamma)^{-1}) &= d\underline{\lambda} \mathbf{R}(\gamma)^{-1} - \underline{\lambda} \mathbf{R}(\gamma)^{-1} d\mathbf{R}(\gamma) \mathbf{R}(\gamma)^{-1} \\ d(\underline{\lambda} \mathbf{R}(\gamma)^{-1}) \mathbf{R}(\gamma) &= d\underline{\lambda} - \underline{\lambda} \mathbf{R}(\gamma)^{-1} d\mathbf{R}(\gamma),\end{aligned} \quad (9.45)$$

which allows us to rewrite (9.44) as follows

$$d(\underline{\lambda} \mathbf{R}(\gamma)^{-1}) = 0. \quad (9.46)$$

9. VES. TRACK. III: SUB-RIEMANNIAN GEODESICS IN $SO(3)$

This gives us the following relation

$$\underline{\lambda}(s)\mathbf{R}(\gamma(s))^{-1} = \underline{\lambda}(0)\mathbf{R}(\gamma(0)), \quad (\gamma(0) = e, \mathbf{R}(e) = \mathbf{I})$$

$$\underline{\lambda}(s)\mathbf{R}(\gamma(s))^{-1} = \underline{\lambda}(0), \quad (9.47)$$

$$\underline{\lambda}(s) = \underline{\lambda}(0)\mathbf{R}(\gamma(s)). \quad (9.48)$$

This relation allows us to compute (9.42) in Thm. 5 directly from (9.39), because it directly relates momentum curves (in phase space) to geodesics in the group.

9.5 PDE Approach for Data-Driven Sub-Riemannian Geodesics on $SO(3)$

In this section we adapt the PDE approach for data-driven sub-Riemannian geodesics in $SE(2)$ (cf. Ch. 8) to the $SO(3)$ group. Here we consider the basis left-invariant vector fields X_i as differential operators of the first order, and we write $X_i(\mathcal{W})$ for the derivative of a function $\mathcal{W} : SO(3) \rightarrow \mathbb{R}$ along X_i . We aim to solve the following geometric control problem

$$\begin{aligned} \dot{\gamma}(t) &= \sum_{i=1}^2 u_i X_i|_{\gamma(t)}, \text{ for } t \in [0, T], \\ \gamma(t) &\in SO(3), \quad \gamma(0) = e, \quad \gamma(T) = g_1, \quad (u_1, u_2) \in \mathbb{R}^2, \\ l(\gamma(\cdot)) &= \int_0^T C(\gamma(t)) \sqrt{\xi^2 u_1^2(t) + u_2^2(t)} dt \rightarrow \min, \end{aligned}$$

Here the terminal time T is free; and $C : SO(3) \rightarrow [\delta, 1]$, $\delta > 0$ is an analytic function that we call “external cost”.

The following theorem summarizes our approach for the computation of data-driven sub-Riemannian length minimizers on $SO(3)$.

Theorem 8. *Let $\mathcal{W}(g)$ be a viscosity solution of the following boundary value problem:*

$$\begin{cases} \sqrt{\frac{(X_1|_g(\mathcal{W}))^2}{\xi^2} + (X_2|_g(\mathcal{W}))^2} = C(g), & \text{for } g \neq e, \\ \mathcal{W}(e) = 0. \end{cases} \quad (9.49)$$

Then the isosurfaces $\mathcal{S}_t = \{g \in SO(3) \mid \mathcal{W}(g) = t\}$ are sub-Riemannian spheres of radius t centered at e .

A sub-Riemannian length minimizer $\gamma(t) = \gamma_b(\mathcal{W}(g_1) - t)$ ending at g_1 is found by backward integration for $t \in [0, \mathcal{W}(g_1)]$

$$\begin{cases} \dot{\gamma}_b(t) = -u_1(t) X_1|_{\gamma_b(t)} - u_2(t) X_2|_{\gamma_b(t)}, \\ \gamma_b(0) = g_1, \end{cases} \quad (9.50)$$

where $u_1(t) = \frac{X_1|_{\gamma_b(t)}(\mathcal{W})}{(\xi C(\gamma_b(t)))^2}$ and $u_2(t) = \frac{X_2|_{\gamma_b(t)}(\mathcal{W})}{(C(\gamma_b(t)))^2}$.

Proof See (Mashtakov *et al.*, 2016, App. D). □

9.5.1 Sub-Riemannian Fast Marching in $SO(3)$

Here we propose a method SR-FM (sub-Riemannian Fast Marching) for the computation of data driven sub-Riemannian length minimizers (not necessarily cuspless) on $SO(3)$ group, as a solution to the sub-Riemannian eikonal system (9.49). This method was successfully used in Ch. 8 for the computation of data-driven sub-Riemannian length minimizers on $SE(2)$ group. The method is based on a Riemannian approximation of sub-Riemannian manifold, and computing Riemannian geodesics in highly anisotropic space, which becomes the sub-Riemannian manifold in the limiting case as anisotropy tends to infinity.

Here we follow the explanation in Sec. 8.7.3, where we work now in new settings of the $SO(3)$ group and use the coordinate chart (x, y, θ) given by (9.6). Recall, that the basis left invariant vector fields X_i on $SO(3)$ are given by the following differential operators:

$$X_1 = \cos \theta \partial_x - \sec x \sin \theta \partial_y + \tan x \sin \theta \partial_\theta,$$

$$X_2 = \partial_\theta,$$

$$X_3 = \sin \theta \partial_x + \sec x \cos \theta \partial_y - \tan x \cos \theta \partial_\theta,$$

and corresponding basis left-invariant one forms ω^i , satisfying $\langle \omega^i, X_j \rangle = \delta_i^j$, are expressed as

$$\begin{aligned} \omega^1 &= \cos \theta dx - \cos x \sin \theta dy, \\ \omega^2 &= \sin x dy + d\theta, \\ \omega^3 &= \sin \theta dx + \cos x \cos \theta dy. \end{aligned} \tag{9.51}$$

The sub-Riemannian metric tensor

$$\mathcal{G}_0^{\xi, C} = C^2(\cdot) (\xi^2 \omega^1 \otimes \omega^1 + \omega^2 \otimes \omega^2)$$

is defined only on the distribution Δ , recall Remark 19, but can be seen as a limiting case (when ϵ tends to zero) of the Riemannian metric tensor

$$\mathcal{G}_\epsilon^{\xi, C} = C^2(\cdot) (\xi^2 \omega^1 \otimes \omega^1 + \omega^2 \otimes \omega^2 + \xi^2 \epsilon^{-2} \omega^3 \otimes \omega^3). \tag{9.52}$$

However we stress that this limit does not exist in (9.52), since the term $\xi^2 \epsilon^{-2} \omega^3 \otimes \omega^3$ tends to infinity. This corresponds to a penalty of infinite cost when moving in the

9. VES. TRACK. III: SUB-RIEMANNIAN GEODESICS IN $SO(3)$

direction X_3 orthogonal to the distribution Δ . Nevertheless, one can approximate the sub-Riemannian manifold by Riemannian by fixing some finite small $\epsilon > 0$. Moreover the sub-Riemannian eikonal equation (9.49) is well-defined and it can be derived as a limiting case of the eikonal equation on a Riemannian manifold via the *inverse* metric tensor $\mathcal{G}_0^{\xi, C^{-1}} = \lim_{\epsilon \rightarrow \infty} \mathcal{G}_\epsilon^{\xi, C^{-1}}$ (a well-defined limit).

From the above derivations we see that the fast-marching approach for computing sub-Riemannian geodesics on $SE(2)$ is easily generalized to the $SO(3)$ -case. To this end we replace the matrix-representation for $\mathcal{G}_\epsilon^{\xi, C}$ expressed in the fixed (x, y, θ) Cartesian coordinate frame. In the $SO(3)$ -case it equals

$$M_\epsilon = \Re \begin{pmatrix} C^2(\cdot) \xi^2 & 0 & 0 \\ 0 & C^2(\cdot) & 0 \\ 0 & 0 & C^2(\cdot) \xi^2 \epsilon^2 \end{pmatrix} \Re^T,$$

with

$$\Re = \begin{pmatrix} \cos \theta & 0 & \sin \theta \\ -\cos x \sin \theta & \sin x & \cos x \cos \theta \\ 0 & 1 & 0 \end{pmatrix}$$

Here the diagonal matrix in the middle encodes the anisotropy between the X_i directions while the matrix \Re is the basis transformation from the moving coframe $\{\omega^1, \omega^2, \omega^3\}$ to the fixed coframe $\{dx, dy, d\theta\}$, recall (9.51), in which the Fast Marching implementation via special anisotropic stencils Mirebeau (2014) is used.

In Section 9.6.1 we will show that the thereby obtained fast-marching approach already presents reasonable precision for $\epsilon = 0.1$. Experiments in Section 9.6.3 show the application of the method (with data-adaptive non-uniform cost) to tracking of blood vessels in retinal images.

9.6 Experiments

In Subsection 9.6.1 we verify the sub-Riemannian Fast Marching method (SR-FM) by comparison of sub-Riemannian length minimizers obtained via SR-FM with the exact sub-Riemannian geodesics (cf. Section 9.4) for the case of uniform external cost (i.e. $C = 1$). In Subsection 9.6.2 we compare sub-Riemannian geodesics in the groups $SE(2)$ and $SO(3)$ for the uniform external cost case. In Subsection 9.6.3 we provide experiments of vessel tracking by sub-Riemannian geodesics on $SO(3)$ when the external cost C is induced by spherical data, and compare them to the result of vessel tracking on the corresponding flat image by sub-Riemannian geodesics on $SE(2)$.

9.6.1 Verification of the Fast Marching Method in the Case of Uniform External Cost

In this subsection we perform the experiments to validate the sub-Riemannian Fast Marching method proposed in Subsection 9.5.1. The goal of the experiments is to check that the method produces an accurate approximate solution to the sub-Riemannian problem in $SO(3)$ group in the case of uniform external cost $C = 1$. In all the experiments we fixed the anisotropy parameter of the Riemannian approximation as $\epsilon = 0.1$.

In the first experiment we compare the geodesics $\gamma^{FM}(\cdot)$ obtained via SR-FM with the exact cuspless geodesics $\gamma(\cdot)$ computed via analytic formulas in Theorem 6. We perform the comparison as follows:

1. Fix $\xi > 0$ and the initial momenta $\lambda(0)$.
2. Compute the first cusp time $s_{max}(\lambda(0))$ corresponding to $\lambda(0)$, and set $s_{end} = \min\{s_{max}(\lambda(0)), \frac{\pi}{2}\}$.
3. Compute the geodesic $\gamma(s)$, $s \in [0, s_{end}]$ via Thm. 6.
4. Compute the distance function $\mathcal{W}(g)$ in the domain $g = (x, y, \theta) \in [-\frac{\pi}{2}, \frac{\pi}{2}] \times [-\pi, \pi] \times [-\pi, \pi]$ via SR-FM. Here we compute the distance function in the grid of $201 \times 401 \times 401$ points and then interpolate it using third order Hermite interpolation.
5. Compute the geodesic $\gamma^{FM}(t)$, $t \in [0, \mathcal{W}(g_{end})]$ via backtracking (9.50) from the endpoint $g_1 = \gamma(s_{end})$.
6. Plot the spherical projections of $\gamma(s)$ and $\gamma^{FM}(t)$ and compare them.

A typical result of the comparison is shown in Fig. 9.7, where we put $\xi = 1.5$, $\lambda_3(0) = 0$ for all the curves and varied initial momentum $\lambda_2(0) \in \{-0.99, -0.81, -0.63, -0.45, -0.27, -0.09, 0.09, 0.27, 0.45, 0.63, 0.81, 0.99\}$. As a result we see that the geodesics computed numerically via SR-FM accurately follow the exact geodesics.

We have performed a series of such experiments and always obtained similar results when the geodesics $\gamma^i(s)$ were optimal for $s \in [0, s_{end}^i]$. It was also remarkable that SR-FM resulted into different curves (length-minimizers) when the geodesic $\gamma^i(s)$ was not optimal for $s \in [0, s_{end}^i]$. Such an example is illustrated in Fig. 9.7 (right). The question of optimality of sub-Riemannian geodesics in $SO(3)$ in the general case $\xi > 0$ is still an open important problem. Here we provide a numeric SR-FM method for

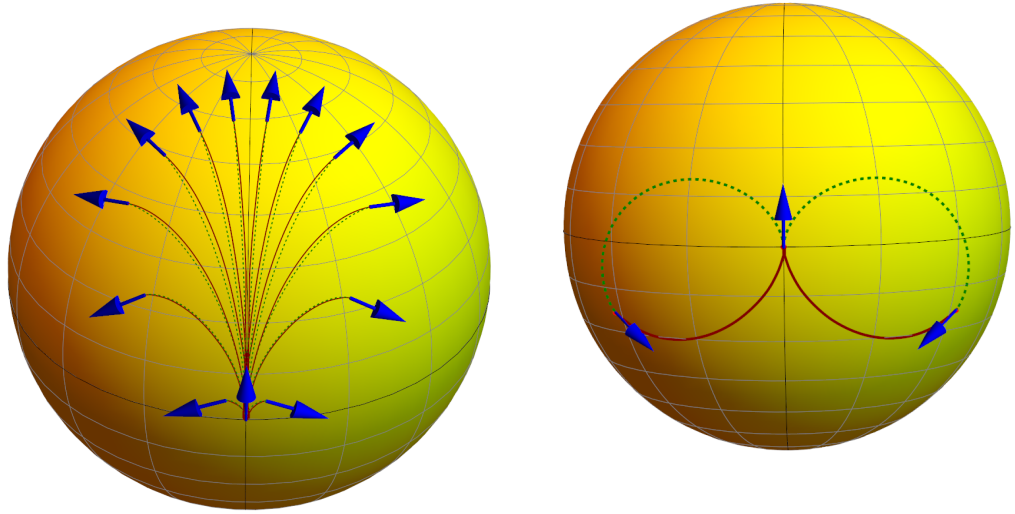


Figure 9.7: *Left:* Comparison of the exact cuspless sub-Riemannian geodesics on $SO(3)$ (green dashed lines) obtained via analytic formulas (Theorem 6) and the sub-Riemannian geodesics obtained via numerical Fast Marching method (red lines). Here the spherical projection of the geodesics is depicted together with the boundary conditions. *Right:* An example of a nonoptimal cuspless geodesics. It can be observed, that the exact geodesics and the optimal geodesics computed via SR-FM satisfy the same boundary conditions, but the red lines are shorter.

computing only the optimal geodesics. In analogy with how it was done in Ch. 8 it is possible to compute Maxwell sets numerically.

9.6.2 Comparison of Sub-Riemannian Geodesics in $SO(3)$ and $SE(2)$ for $C = 1$

In this subsection we again consider the case $C = 1$ and compare sub-Riemannian geodesics $\gamma^{SO(3)}(\cdot) = (x(\cdot), y(\cdot), \theta(\cdot))$ and $\gamma^{SE(2)}(\cdot) = (X(\cdot), Y(\cdot), \Theta(\cdot))$ in the image plane. The SR-FM method is used for computation of the geodesics parameterized by sub-Riemannian arclength. Here we prepare background for comparison of the geodesics in retinal images via the schematic eye model, recall Subsec. 9.2.1, where as a departure point we use an image (white for $C = 1$) on a plane O_{XY} , recall Fig. 9.4.

See Fig. 9.8, where we compare $SE(2)$ and $SO(3)$ sub-Riemannian geodesics projected on the plane and on the sphere (via mappings Π and Π^{-1}). For additional details see (Mashtakov *et al.*, 2016, App. E).

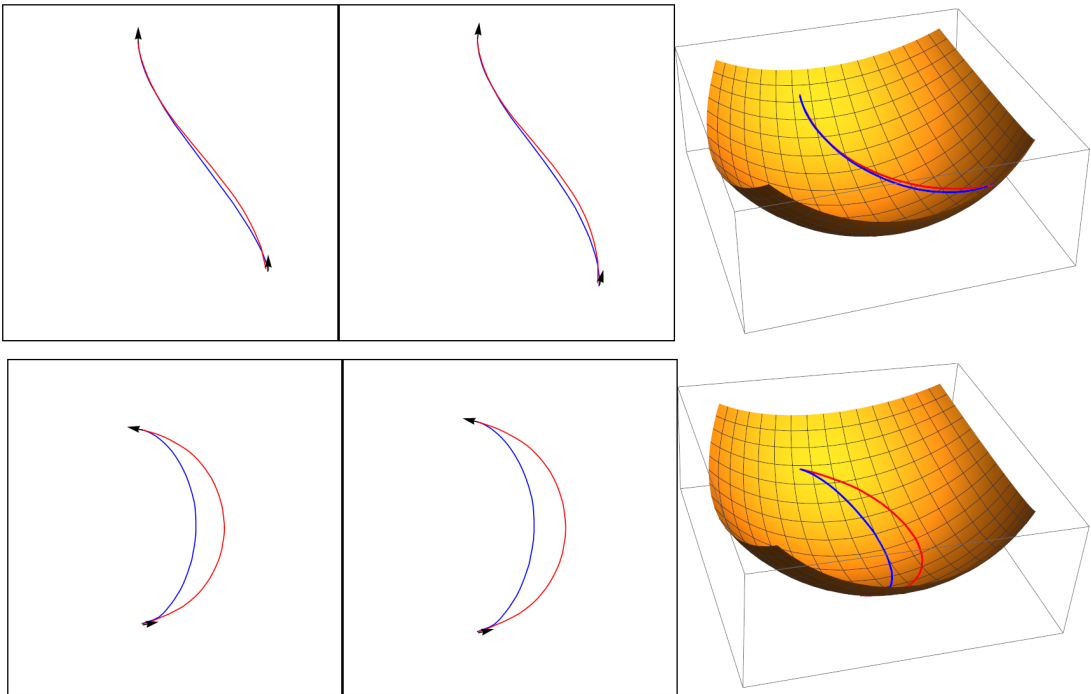


Figure 9.8: Comparison of an $SE(2)$ sub-Riemannian geodesic (blue) and an $SO(3)$ sub-Riemannian geodesic (red), from left to right in (x, y) spherical image coordinates, (X, Y) flat image coordinates, and plotted on the sphere S^2 .

9.6.3 Vessel Analysis via Sub-Riemannian Geometry on $SO(3)$ and $SE(2)$

As explained in the introduction we need to include the spherical geometry of the retina rather than the flat geometry of the flat image. This spherical geometry is encoded in our spherical image model, see Fig. 9.4. Next we will analyze the effect of including this geometry in the SR-FM vessel tracking method along data-driven sub-Riemannian geodesics in $SO(3)$.

More precisely we propose vessel tracking in object coordinates (or spherical image coordinates) via sub-Riemannian geometry in $SO(3)$ as an extension of vessel tracking in flat images Bekkers *et al.* (2015b,c) along sub-Riemannian geodesics in $SE(2)$. Therefore we want to investigate whether including the correct spherical geometry makes a difference in the vessel tracking in practice. Although a complete detailed comparison on large data sets is left for future work, we present preliminary experiments which indeed indicate considerable differences in both tractography and curvature measure-

9. VES. TRACK. III: SUB-RIEMANNIAN GEODESICS IN $SO(3)$

ments. These experiments are shown in Fig. 9.9, Fig. 9.10 which we explain next.

We apply the same scheme as in Subsection 9.6.2, but now we compute data-driven geodesics, where the external cost is induced by image data. For the sake of simple comparison we restrict ourselves to a cost depending on the spherical coordinates only, and we set

$$\mathfrak{C}(\mathbf{n}(x, y)) = \left(1 + \frac{\mathcal{V}^{Fr} F(\Pi(x, y))}{\lambda \|\mathcal{V}^{Fr} F\|_\infty^2}\right)^{-1}, \quad (9.53)$$

where we use the standard 2D multiscale vesselness filter \mathcal{V}^{Fr} Frangi *et al.* (1998), with $\sigma_1 = 0.3$, $\sigma_2 = 0.3\|\mathcal{S}\|_\infty$ and scales $s = \frac{1}{2}\sigma^2 \in \{2, 3, 4, 5\}$ in terms of pixel sizes, see Eq. (3.3) and Ch. 6.

In the experiment in Figure 9.9 we show that there is a considerable difference between $SE(2)$ sub-Riemannian geodesics and $SO(3)$ sub-Riemannian geodesics. We see that when internal geometry is dominant over the external cost (λ small) the sub-Riemannian geodesics in $SO(3)$ are more stiff than sub-Riemannian geodesics in $SE(2)$, and therefore in the boundary value problem they are less eager to take short cuts and better follow the vessel structure. In case λ is large (external cost is dominant over the internal geometry) we see only small differences in the overall locations of the $SE(2)$ -curves and $SO(3)$ -curves. The results are stable w.r.t. choice of $1 \leq \eta \leq 2$ (which controls the distance from the camera to the eye ball, relative to eye ball radius, recall Fig. 9.4).

In the next experiment we measure the curvature of the curves obtained by vessel tracking method via $SE(2)$ -geometry and via $SO(3)$ geometry. For this experiment we used the values $\xi = 3$, $\lambda = 50$ and $\eta = 2$. Although in this case the result of tractography is very similar for the $SE(2)$ and $SO(3)$ curves, we show that there is a considerable difference in their curvature.

Corollary 1. (from Theorem 4) *The geodesic curvature of a spherical projection of data-driven geodesic $\gamma^{SO(3)}(\cdot)$ satisfies*

$$\kappa_g^{SO(3)}(\cdot) = -\xi^2 \frac{X_2|_{\gamma^{SO(3)}(\cdot)}(\mathcal{W}^{SO(3)})}{X_1|_{\gamma^{SO(3)}(\cdot)}(\mathcal{W}^{SO(3)})}.$$

It can be checked (see Duits *et al.* (2013a) and Bekkers *et al.* (2015c)) that the planar curvature of spatial projection of a sub-Riemannian geodesic in $SE(2)$ satisfies

$$\kappa^{SE(2)}(\cdot) = -\xi^2 \frac{\mathcal{A}_2|_{\gamma^{SE(2)}(\cdot)}(\mathcal{W}^{SE(2)})}{\mathcal{A}_1|_{\gamma^{SE(2)}(\cdot)}(\mathcal{W}^{SE(2)})}.$$

Thus the curvature analysis can be simply done based on vessel tracking, and this shows the benefit of our algorithm. In Figure 9.10 we show an experiment of vessel

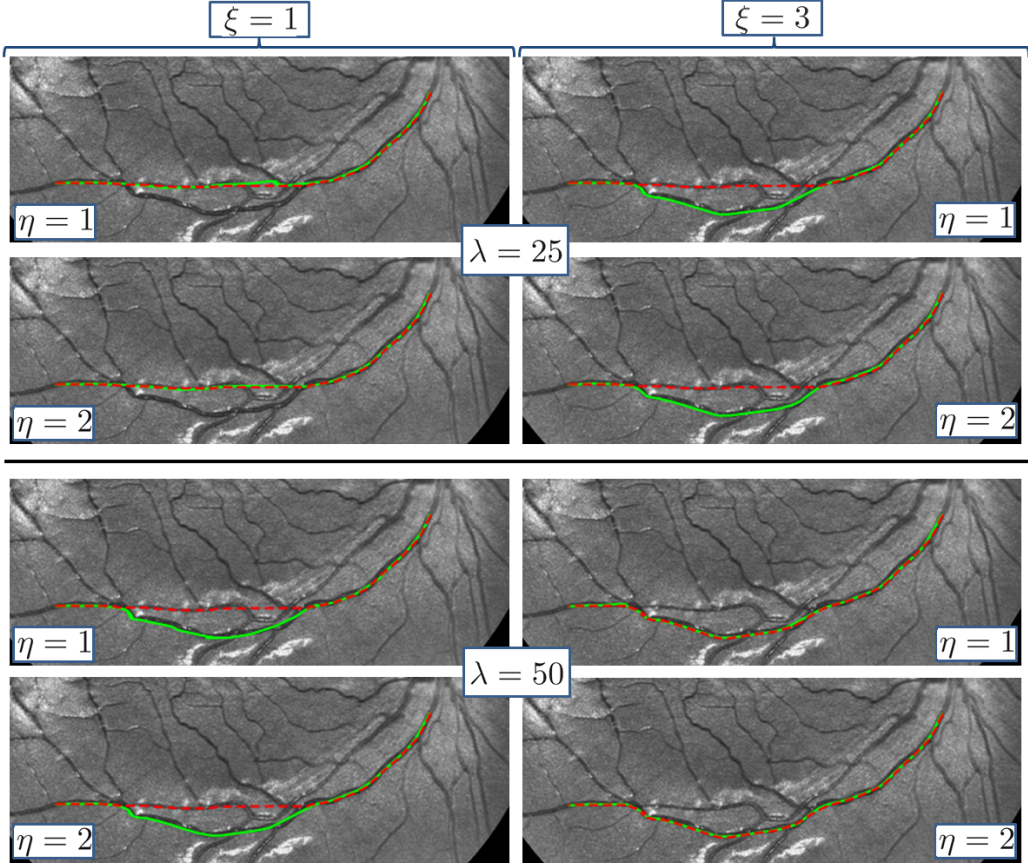


Figure 9.9: Comparison of vessel tracking via $\gamma^{SO(3)}$ sub-Riemannian geodesics on $SO(3)$ (green solid lines) and via $\gamma^{SE(2)}$ sub-Riemannian geodesics on $SE(2)$ (red dashed lines) in the planar camera coordinates. Here the planar projection $\Gamma^{SO(3)}$ of $\gamma^{SO(3)}$, and spatial projection $\Gamma^{SE(2)}$ of $\gamma^{SE(2)}$ are depicted in the same flat image. $SO(3)$ -geodesics are more stiff than $SE(2)$ -geodesics, and in the boundary value problem they are less eager to take short cuts. If λ is large we see only small differences in the overall locations of the $SE(2)$ -curves and $SO(3)$ -curves. The results are stable w.r.t. choice of $1 \leq \eta \leq 2$ (distance from the camera to the eye ball, relative to eye ball radius, cf. Fig. 9.4)

9. VES. TRACK. III: SUB-RIEMANNIAN GEODESICS IN $SO(3)$

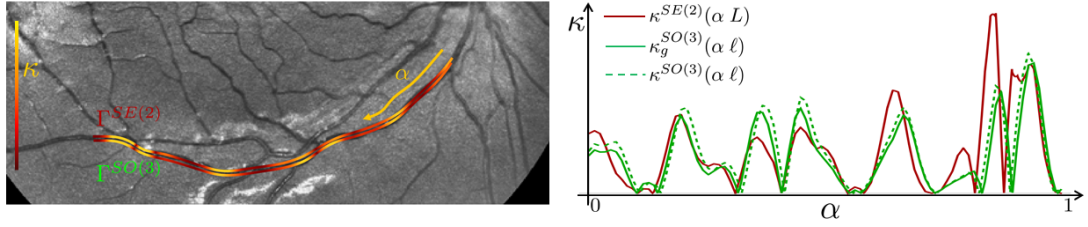


Figure 9.10: *Left:* Two curves from the experiment in Fig. 9.9 (right-bottom figure) are depicted with slight offset. The upper curve is a spatial projection $\Gamma^{SE(2)}$ of the data-driven sub-Riemannian geodesic $\gamma^{SE(2)}$ with depicted (in color) planar curvature $\kappa^{SE(2)}$ on top of the curve. The lower curve $\Gamma^{SO(3)}$ is the planar projection of the sub-Riemannian geodesic $\gamma^{SO(3)}$ with depicted geodesic curvature $\kappa_g^{SO(3)}$ on top of it. *Right:* Three graphs are shown in the same plot: planar curvature $\kappa^{SE(2)}$ of $\Gamma^{SE(2)}$; geodesic curvature $\kappa_g^{SO(3)}$ of spherical projection of $\gamma^{SO(3)}$; planar curvature $\kappa^{SO(3)}$ of $\Gamma^{SO(3)}$. The effect of considering geodesic curvature $\kappa_g^{SO(3)}$ in object coordinates on S^2 rather than planar curvature $\kappa^{SO(3)}$ in photo coordinates on projection on \mathbb{R}^2 is visible (compare the green solid and dashed graphs). A bigger difference comes from using $SO(3)$ sub-Riemannian geometry than $SE(2)$ sub-Riemannian geometry (compare red and green graphs).

curvature measurement based on tracking via $SO(3)$ -geometry and via $SE(2)$ -geometry. For completeness we added also a comparison with a planar curvature $\kappa^{SO(3)}(\cdot)$ of a planar projection $\Gamma^{SO(3)}(\cdot) := \Pi(x(\cdot), y(\cdot))$ of $\gamma^{SO(3)}(\cdot) = (x(\cdot), y(\cdot), \theta(\cdot))$.

We can see a considerable difference in curvature measurement via $SO(3)$ -geometry and $SE(2)$ -geometry. It is also seen that the difference between $\kappa^{SO(3)}$ and $\kappa_g^{SO(3)}$ is not very significant. Thus, both in terms of vessel tracking and curvature analysis there is a significant difference between using the $SE(2)$ and $SO(3)$ model. In terms of vessel tracking this difference decreases when the external cost dominates with respect to the internal geometry in the metric. In particular in the analysis of curvature it is important to realize that it makes a large difference whether geodesic curvature is computed on the sphere, or planar curvature is computed on the plane.

9.7 Conclusion

Data-driven sub-Riemannian geodesics on 3D Lie groups are a suitable tool for tractography of blood vessels in retinal imaging. In the previous Ch. 8 on the $SE(2)$ -case practical advantages have been shown in comparison to the (isotropic) Riemannian case,

and geodesic methods in the image domain. However, these models included a sub-Riemannian geometry on $SE(2)$ based on lifts of flat images, which does not match the actual object-geometry: the retina is spherical rather than planar, cf. Fig. 9.1, Fig. 9.3 and Fig. 9.4.

Therefore, for geometric tracking we propose a frame bundle above S^2 , cf. Fig. 9.6, instead of a frame bundle above \mathbb{R}^2 . Geometric tracking of geodesics is done along globally optimal data-driven sub-Riemannian geodesics in $SO(3)$ (and their spherical projections) by our new numerical wavefront propagation method. We have validated our method for the uniform cost case, cf. Fig. 9.7.

Furthermore, we used a specific parametrization of Lie group $SO(3)$ that allowed us to compare between sub-Riemannian geodesics in $SO(3)$ to sub-Riemannian geodesics in $SE(2)$. In our comparison we took into account a standard optical model for the mapping between object coordinates on the retina and camera-coordinates in the acquired planar retinal image. In our experiments, the differences between the $SO(3)$ case and the $SE(2)$ case are considerable, both for the case of uniform cost, cf. Fig. 9.8, and for the data-driven case in the retinal image analysis application, cf. Fig. 9.9. In general we see that for realistic parameter settings (in optics) the $SO(3)$ -geodesics have a slower variation in curvature, and are less eager to take short-cuts, see e.g. Fig. 9.9 and Fig. 9.10. Furthermore, there are visible differences between geodesic curvature of data-driven sub-Riemannian geodesics on the sphere and the curvature of their planar projections. As in retinal imaging applications curvature is considered as a relevant biomarker for detection of diabetic retinopathy and other systemic diseases (cf. Ch. 1), the data-driven sub-Riemannian geodesic model on $SO(3)$ is a relevant extension of our data-driven geodesic model on $SE(2)$. In this chapter, however, we restricted ourselves to feasibility studies. More extensive comparisons are left for future work.

Finally, we note that the computation time for data-driven sub-Riemannian geodesics on $SO(3)$ is exactly the same as for the $SE(2)$ -case. Our specific choice of coordinates of $SO(3)$ allowed us to modify the very efficient fast-marching approach Sanguinetti *et al.* (2015), with a simple replacement of the metric tensor matrix, as we have shown in Subsec. 9.5.1.

Chapter 10

Artery-Vein Classification

This chapter is based on:

Eppenhof, K., Bekkers, E., Berendschot, T.T., Pluim, J.P., ter Haar Romeny, B.M.: Retinal artery/vein classification via graph cut optimization. In Trucco, E., Chen, X., Garvin, M.K., Liu, J.J., Frank, X.Y., eds.: Proceedings of the Ophthalmic Medical Image Analysis Second International Workshop, OMIA 2015, Held in Conjunction with MICCAI 2015, Munchen, Germany, October 9, 2015. Iowa Research Online (2015) 121-128

10. ARTERY-VEIN CLASSIFICATION

This chapter is based on joint work with Koen Eppenhof, Tos Berendschot, Josien Pluim, and Bart ter Haar Romeny and is published in Eppenhof *et al.* (2015). Here, in particular Koen Eppenhof is gratefully acknowledged for his design and development of a graph-cut approach to artery-vein labeling of the vessels in the vasculature models constructed by the method of Ch. 7.

10.1 Introduction

The retinal vasculature can change function or geometry in a variety of ocular and systemic diseases, including glaucoma, macular degeneration, atherosclerosis, and hypertensive or diabetic retinopathy, see Ch. 1. One of the earliest signs of these diseases is generalized arteriolar narrowing, in which the calibers of arteries decrease relatively to the calibers of veins. This phenomenon can be quantified using the ratio of the arteriolar and venular diameters, which is summarized in a value called the arteriovenous ratio (AVR). The AVR is commonly computed from the six arteries and veins with highest caliber in a zone around the optic disc Knudtson *et al.* (2003). Automated methods that measure the AVR directly from a retinal image require localization of the vessels and classification of vessels into arteries and veins. Additionally, artery/vein classification of retinal vessels is necessary for other artery/vein specific vessel features, such as vessel tortuosity.

Most existing automated artery/vein classification methods have focused on classification of vessels via local intensity-based features Grisan & Ruggeri (2003); Li *et al.* (2003); Niemeijer *et al.* (2011). The difference in appearance of arteries and veins in white light retinal images is primarily determined by the oxygen-content of the blood, causing arteries to appear bright red, whereas veins look darker. An additional difference in intensity is sometimes present in the central light reflex on the vessels caused by the white flash of the camera. In arteries this reflection is often more pronounced, and can be used to distinguish them from veins Li *et al.* (2003); Niemeijer *et al.* (2011). Recent methods have also focused on contextual information present in bifurcations and crossings of vessels. These methods make use of the fact that vessels that join in a bifurcation must be of the same type, and two crossing vessels must be of opposite type Dashtbozorg *et al.* (2014); Joshi *et al.* (2014); Rothaus *et al.* (2009).

We propose a novel and generic graph-based method to combine local and contextual features of the retinal vasculature for artery/vein classification. In contrast to previous graph-based methods such as Dashtbozorg *et al.* (2014); Joshi *et al.* (2014); Rothaus *et al.* (2009), our classification is defined as an optimization problem, based on

a non-submodular energy function that is minimized exactly and efficiently using the Quadratic Pseudo-Boolean Optimization (QPBO) graph cut algorithm. Optimization of this energy generates a classification of all detected vessels based on local features, while the contextual features limit the number of possible configurations of vessel labels. This results in a flexible approach in which the influence of contextual and local information can be weighted based on their confidence levels.

10.2 Methods

Models of the retinal vasculature form the basis of our approach. Here, we rely on models of the vessels around the optic disc, made using the Edge Tracking in Orientation Scores (ETOS) algorithm presented in Ch. 7, but in principle any model that provides the edges of vessels and detects their crossings and bifurcations can be used, for example Al-Diri *et al.* (2010); Dashtbozorg *et al.* (2014); Perez *et al.* (2002). The models are used to define an energy function (Section 10.2.1) that uses features extracted from both the image and the model (Section 10.2.2). Optimization of the energy results in artery/vein labeling of the vessels in the model (Section 10.2.3).

10.2.1 Energy Function Definition

In our artery/vein classification approach we make use of a graph representation of the vascular network that consists of a set of vertices V and edges E . Each vertex $u \in V$ represents a single blood vessel, and our goal is to assign to each vertex a label $y_u \in \{0, 1\}$ that represents the type of the blood vessel: $y_u = 1$ for arteries and $y_u = 0$ for veins. The edges in the graph encode the relations and interactions between vessels, such as parent-child relations at bifurcations and crossings of vessels. An optimal labeling of the vascular network is then obtained by solving the following problem:

$$\mathbf{y}^* = \arg \min_{\mathbf{y}} U(\mathbf{y}), \quad (10.1)$$

in which $\mathbf{y} = \{y_u\}_{u \in V}$ and in which the energy function U has the form of a binary first-order Markov Random Field (MRF):

$$U(\mathbf{y}) = \underbrace{\sum_{u \in V} \theta_u(y_u, \mathbf{x}_u)}_{\text{unary term}} + \lambda \underbrace{\sum_{(u,v) \in E} \theta_{uv}(y_u, y_v)}_{\text{pairwise term}}. \quad (10.2)$$

In this formulation, the first term is a sum of unary potential functions θ_u , taking as input a binary label y_u and an evidence feature vector \mathbf{x}_u for this label. The second

10. ARTERY-VEIN CLASSIFICATION

term consists of pairwise potentials θ_{uv} , each a function of a pair of labels. The binary MRF variables is then described as a set of vertices V in an undirected graph $G = (V, E)$ in which the set of edges E contain the pairwise potentials. The λ parameter weights the pairwise term relative to the unary term.

The unary potentials optimize the labels based on local feature vectors \mathbf{x}_u that have been extracted for each vessel. We define the unary potential as

$$\theta_u(y_u, \mathbf{x}_u) := -\ln p(y_u | \mathbf{x}_u), \quad (10.3)$$

where $p(y_u | \mathbf{x}_u)$ is a posterior PDF (via Bayes rule):

$$p(y_u | \mathbf{x}_u) = \frac{p(\mathbf{x}_u | y_u)p(y_u)}{p(\mathbf{x}_u | y_u = 0)p(y_u = 0) + p(\mathbf{x}_u | y_u = 1)p(y_u = 1)}, \quad (10.4)$$

where $p(\mathbf{x}_u | y_u)$ is the likelihood of a feature vector \mathbf{x}_u for a given label y_u , and $p(y_u)$ is the prior PDF of the label y_u . We assume that the likelihood of the feature vectors \mathbf{x}_u follows a multivariate Gaussian distribution $p(\mathbf{x}_u | y_u) = \mathcal{N}(\boldsymbol{\mu}_{y_u} | \boldsymbol{\Sigma}_{y_u})$ for both classes $y_u \in \{0, 1\}$. This means a training step is required to obtain the mean vectors $\boldsymbol{\mu}_{y_u}$, covariance matrices $\boldsymbol{\Sigma}_{y_u}$, and prior probabilities $p(y_u)$ for $y_u \in \{0, 1\}$.

The pairwise potentials $\theta_{uv}(y_u, y_v)$ penalize crossings of vessels with the same label, or bifurcations of vessels with different labels. We define

$$\theta_{uv}(y_u, y_v) = \gamma_{uv}(1 - \delta(y_u, y_v)), \quad (10.5)$$

where $\gamma_{uv} := -1$ if vessels u and v cross, $\gamma_{uv} := 1$ if vessel u bifurcates from v or vice versa, and $\delta(y_u, y_v) := 1$ if $y_u = y_v$ and $\delta(y_u, y_v) := 0$ otherwise. This results in a utility of $-\lambda$ for correct crossings and a penalty of λ for incorrect bifurcations.

We arrive at the following problem-specific cost function

$$U(\mathbf{y}) = \underbrace{\sum_{u \in V} -\ln p(y_u | \mathbf{x}_u)}_{\text{local features}} + \lambda \underbrace{\sum_{(u,v) \in E} \gamma_{uv}(1 - \delta(y_u, y_v))}_{\text{contextual features}}. \quad (10.6)$$

10.2.2 Feature Extraction and Training

To find the unary and pairwise potential functions, two types of features are required. To determine the posterior PDF in the unary potentials, a feature vector \mathbf{x}_u , representative of the differences between arteries and veins, is needed. To determine the pairwise potentials, the method requires contextual information from the tracking models.

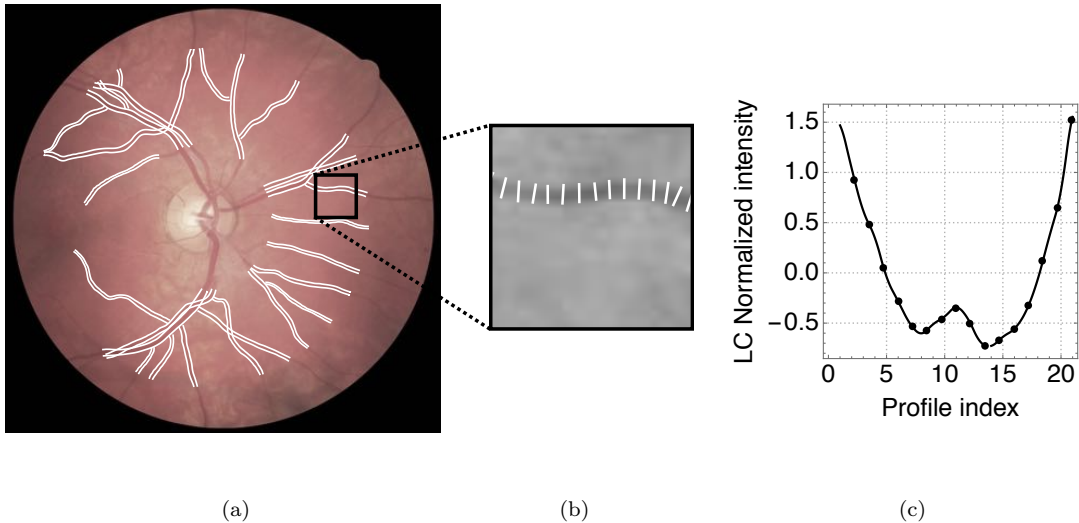


Figure 10.1: (a) Example of a retinal vasculature tracking model. (b) Detail of a tracked vessel and its profile measurement locations. (c) Average (transversal) vessel intensity profile sampled from edge to edge with 21 points.

10.2.2.1 Local Features

The differences in color and central light reflex of arteries and veins can be captured in transverse intensity profiles Grisan & Ruggeri (2003); Li *et al.* (2003); Vazquez *et al.* (2010). Like in previous work Dashtbozorg *et al.* (2014), we found that these differences are largest in the red color channel.

For each pair of edge points on the tracked vessels, the intensity values on 21 points on a line between the edge points were extracted via cubic Hermite spline interpolation of the red channel of the image. The number of points is constant, independent of vessel width or resolution. This resulted in a number of intensity profiles for each vessel the size of which depends on the length of the tracked vessel. Prior to this, the red channel had been normalized using a lightness and contrast (LC) normalization described in Foracchia *et al.* (2005). Additionally, each of the intensity profiles was normalized to zero mean and unit standard deviation. The intensity profiles of each vessel were averaged pointwise, resulting in one feature vector \mathbf{x}_u per vessel (Fig. 10.1). The intensity profiles of a training set were used to determine $p(y_u|\mathbf{x}_u)$ by calculating the mean vector $\boldsymbol{\mu}_{y_u}$, covariance matrix $\boldsymbol{\Sigma}_{y_u}$, and prior PDF $p(y_u)$ for arteries and veins separately.

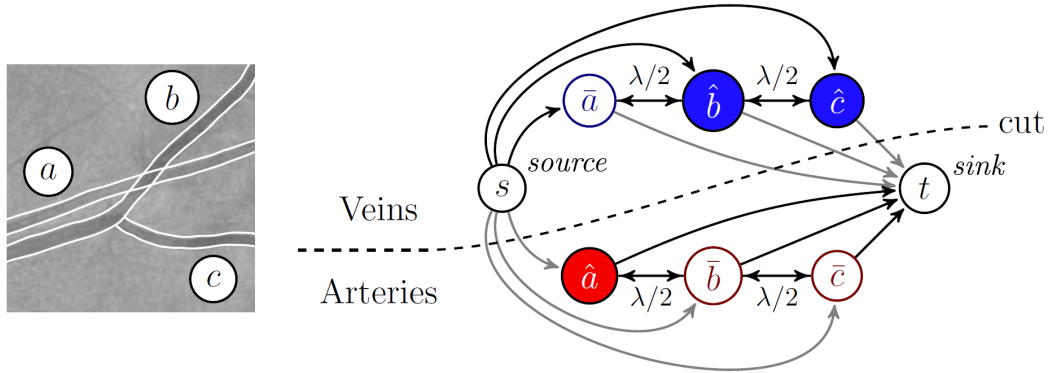


Figure 10.2: Example of a set of vessels and resulting QPBO graph. Vessels a and b cross and need to be labeled oppositely, whereas vessels b and c belong to the same branch and thus must receive the same label. Hence, in the QPBO graph, \hat{a} and \bar{a} are connected to \bar{b} and \hat{b} , while \hat{b} and \bar{b} are connected to \hat{c} and \bar{c} respectively. These edges all have weight $\lambda/2$. The edge weights of the edges to s and t correspond to the unary terms in equation (10.6). The graph cut shown is the result if the sum of weights of the black edges is higher than the sum of the weights of the gray edges, and results in a labeling where a is an artery and b and c are veins.

10.2.2.2 Contextual Features

The contextual features γ_{uv} can be directly extracted from the tracking models made with the ETOS algorithm (Ch. 7). The actual crossings were detected by determining intersections of the tracked center lines of the vessels. Bifurcations are detected during tracking itself (see Subsec. 7.4.1.4).

10.2.3 Energy Minimization

Energy functions of binary variables which have the form of (10.2) can be optimized exactly using graph cuts Greig *et al.* (1989) if they are graph representable Kolmogorov & Zabin (2004). Such an energy function is graph representable if it is *submodular*, which means that all pairwise terms must satisfy

$$\theta_{uv}(0,0) + \theta_{uv}(1,1) \leq \theta_{uv}(1,0) + \theta_{uv}(0,1). \quad (10.7)$$

Our energy function $U(\mathbf{y})$ defined in (10.6) is, however, not sub-modular due to the fact that submodularity (Eq. (10.7)) is not satisfied for the case of crossings, as there $\gamma_{uv} = -1 < 0$. This means that the energy function cannot be optimized using a

standard graph cut algorithm. Therefore, we use the Quadratic Pseudo-Boolean Optimization algorithm (QPBO) Kolmogorov & Rother (2007). This algorithm transforms supermodular problems into submodular problems which have partial solutions. The solutions are partial in the sense that in theory they may contain ‘unknown’ labels (as we explain below). I.e., now $y_u \in \{0, 1, \emptyset\}$ with \emptyset denoting the ‘unknown’ label. Before we explain the QPBO algorithm, let us first provide the basics of energy minimization via graph cuts.

10.2.3.1 Energy Minimization using Graph Cuts.

In graph cut methods all terms in the energy function are described in a graph by edges with positive weights. In order to describe the unary terms as edges, two additional vertices are added to the graph: a source s and a sink t . These two new vertices are then connected to all other vertices. The edges connecting to s get a weight of $\theta_u(1, \mathbf{x}_u)$, and the edges connecting to t get weights equal to $\theta_u(0, \mathbf{x}_u)$. A graph cut is then defined as the cut that partitions the full set of vertices into two subsets S and V (which respectively contain s and t), and the cut-set is defined as the set of all edges that connect a vertex in S to a vertex in T . The sum of all edge weights in the cut-set is called the cut weight, and the graph cut that results in a minimal total cut weight is called the minimal cut. All vertices in S are then labeled with $y_u = 1$ and the vertices in T with $y_u = 0$.

It can be shown that the problem of finding the minimal graph cut is equivalent to the minimization of submodular energy functions of the form (10.2) Kolmogorov & Zabin (2004). Due to the theorem of Ford & Fulkerson (1956), finding the minimal graph cut is equivalent to computing the maximum flow from the source to sink (in which edge weights are interpreted as capacity).

10.2.3.2 The QPBO Algorithm

For every vertex u in the original problem, the QPBO problem has two vertices \hat{u} and \bar{u} . Each of these vertices is connected to a source s and a sink t in a flow graph Ford & Fulkerson (1956), see Fig. 10.2. The \hat{u} vertices connect to s by an edge with weight $\theta_u(1, \mathbf{x}_u)$ and to t by an edge with weight $\theta_u(0, \mathbf{x}_u)$. These edge weights correspond to the unary terms in equation (10.6). The \bar{u} vertices connect to s by an edge with weight $\theta_u(0, \mathbf{x}_u)$ and to t by an edge with weight $\theta_u(1, \mathbf{x}_u)$. The pairwise terms are modeled as edges between vertices. For two crossing vessels u and v the weights are $\theta_{\hat{u}\bar{v}} = \lambda/2$ and $\theta_{\bar{v}\hat{u}} = \lambda/2$, for bifurcating vessels u and v the weights are also $\theta_{\bar{u}\bar{v}} = \lambda/2$ and $\theta_{\hat{u}\hat{v}} = \lambda/2$.

10. ARTERY-VEIN CLASSIFICATION

All other pairwise weights are 0.

To find the minimum cut in the QPBO-version of the flow graph, we used the Ford-Fulkerson method Ford & Fulkerson (1956). After computing a minimum $s - t$ cut (S, T) , the final labels of the vertices are determined as follows: if \hat{u} and \bar{u} are in opposite cut sets, the original vertex u receives the label of \hat{u} . If \hat{u} and \bar{u} are in the same cut set, an ‘unknown’ label $y_u = \emptyset$ is attached to u . In our experiments, however, we did not once encounter the ‘unknown’ label in the solutions. The method is illustrated in Fig. 10.2.

10.3 Experiments

10.3.1 Ground Truth Data

We validated the method on a ground truth data set of 150 images. All images were taken with a digital non-mydriatic white light fundus camera of the Nidek brand, model AFC-230, with a 45° field of view and a resolution of 3744×3744 . For each of the images, a model of the vasculature was generated using the ETOS algorithm (Ch. 7), and corrected manually when necessary. The vessels were labeled as arteries and veins through consensus of two graders. In total, the dataset contains 3186 vessels, divided in 1693 arteries and 1493 veins.

10.3.2 Method Parameterization and Validation

The energy function in Equation (10.6) contains one parameter λ which weights the influence of local and contextual features. To determine the dependence of our method on this parameter, the accuracies for classification for increasing values of λ was evaluated.

In our experiments we used a leave-one-out cross validation and computed 150 times a confusion matrix. Each time the data of 149 images were used for training of the unary potential functions and then the method was tested on the left-out image. By summing the confusion matrices for all images, we obtained a confusion matrix of the whole data set, and thus accuracy and sensitivity, for each of the λ values.

By setting λ to zero, no contextual information is included at all. This setting is used as a baseline, achieving a classification accuracy of 81.2% for all vessels, and 91.8% for the six arteries and veins with highest caliber (the ‘Big-6’ arteries and veins, see Table 10.1). Accuracy increased with increasing λ , to 94.0% for the ‘Big-6’ arteries and veins, and to 88.0% for all vessels. This compares well to accuracy levels acquired

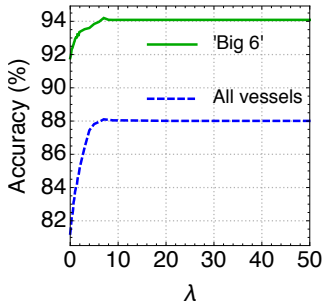


Figure 10.3: Classification accuracy against the value of λ for all vessels, and the six biggest arteries and veins found after classification for all images ('Big-6'). For $\lambda > 8$ accuracy remains constant.

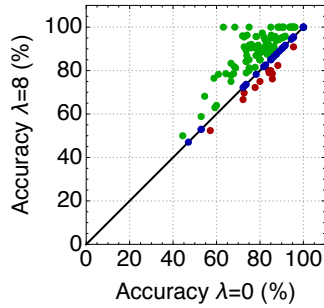


Figure 10.4: Accuracies for each image for $\lambda = 8$ against $\lambda = 0$. A majority of 105 images (green) show an increase in accuracy, 12 images show a decrease (red) and 33 images show no change (blue).

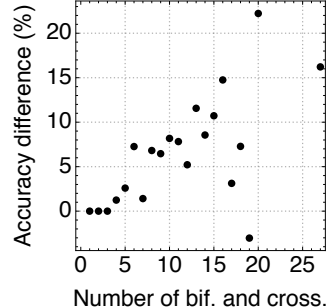


Figure 10.5: Accuracy difference between using $\lambda = 8$ and $\lambda = 0$ against total number of bifurcations and crossings. Each point shows the average for images with that number of bifurcations and crossings.

with methods in literature that were validated on different data sets (87.6% Grisan & Ruggeri (2003), 85.5% Li *et al.* (2003), 88.3% Dashtbozorg *et al.* (2014), 88.8% Vazquez *et al.* (2010)).

We evaluated the accuracy for values of λ up to 50, which is sufficient to let the pairwise terms dominate the unary terms completely. At $\lambda = 8$, accuracy stopped increasing, which is why this value is used in subsequent experiments (Fig. 10.3). We confirmed the significance of the improvement of using $\lambda = 8$ compared to using $\lambda = 0$ using McNemar's test ($\chi^2 = 150, p < 0.001$).

In 105 out of 150 images the accuracy was higher for $\lambda = 8$ than for $\lambda = 0$ (Fig. 10.4). In twelve images the accuracy did not improve. This is caused by incorrect high posterior probabilities of a vessel that bifurcates from (or has a crossing with) another vessel. As an example, consider the case of a crossing of an artery v_A and vein v_V for which the posteriors $p(\mathbf{x}_u|\text{Artery})$ are 0.6 and 0.7 respectively. Based on the posterior probabilities, both would be classified as arteries, but by the fact that they cross, they are classified as a vein and artery respectively, since the penalties for classifying v_V as a vein or classifying both as arteries is higher than classifying v_A as a vein.

Other errors are caused by incorrect local classifications. Table 10.1 shows that overall veins are classified more accurately than arteries, which was seen before by

10. ARTERY-VEIN CLASSIFICATION

Table 10.1: Comparison of accuracy and sensitivity for arteries and veins for $\lambda = 0$ and $\lambda = 8$ (maximal contextual information), for vessels of different calibers, all vessels, and the six biggest arteries and veins found in the classification. N is the number of vessels in the category. For the ‘Big 6’ category the number N reflects how many of the six required arteries and veins were found in the classification.

Caliber	N	Accuracy	$\lambda = 0$		$\lambda = 8$			
			Sensitivity				Sensitivity	
			Arteries	Veins			Arteries	Veins
0 - 20 pixels	960	65.7%	64.4%	74.5%	960	78.2%	75.3%	86.9%
20 - 25 pixels	985	83.2%	82.2%	86.1%	985	89.1%	88.6%	90.4%
25 - 30 pixels	664	90.1%	89.3%	90.9%	664	94.1%	93.5%	94.9%
≥ 30 pixels	577	93.4%	85.0%	96.6%	577	95.3%	88.7%	97.8%
All vessels	3186	81.2%	76.4%	90.1%	3186	88.0%	84.5%	93.2%
‘Big 6’	1704	91.8%	88.8%	95.1%	1797	94.0%	92.4%	95.8%

other authors Dashtbozorg *et al.* (2014); Li *et al.* (2003).

To investigate which vessels benefit most from the contextual information, we separated the vessels into groups based on caliber. We found that the accuracy improves most for the smallest vessels (0-25 pixels in caliber) and less for the larger vessels (above 25 pixels, see Table 10.1). Furthermore, we clearly see a positive correlation of the accuracy with the total number of crossings and bifurcations, which demonstrates the value of contextual features for classification (Fig. 10.5).

10.4 Conclusion

In this work we propose a graph-based method to combine local and contextual features in artery/vein classification of vessels in retinal images, which we validated on a clinical dataset of 150 retinal images. As local features of the vessels we use intensity profiles, and as contextual features we include restrictions imposed by bifurcations and crossings. The inclusion of contextual features significantly improves the classification accuracy compared with using local features alone. The classification accuracy of our method of 88.0% compares well with previous methods. For the six arteries and veins with highest caliber we obtain an accuracy of 94.0%. The classification of vessels with a lower caliber benefits most from the contextual information. Because local information is less reliable in these vessels, contextual information is essential.

Chapter 11

Vessel Geometry In Orientation Scores Part I: Pixel-wise Curvature Measurements and Curvature-Based Biomarkers

This chapter is based on¹:

Bekkers, E., Zhang, J., Duits, R., ter Haar Romeny, B.: Curvature based biomarkers for diabetic retinopathy via exponential curve fits in SE(2). In Trucco, E., Chen, X., Garvin, M.K., Liu, J.J., Frank, X.Y., eds.: Proceedings of the Ophthalmic Medical Image Analysis Second International Workshop, OMIA 2015, Held in Conjunction with MICCAI 2015, Munchen, Germany, October 9, 2015. Iowa Research Online (2015) 113-120

¹ Tos Berendschot (Maastricht University Eye Hospital) is gratefully acknowledged for his involvement in the clinical validation of the developed biomarkers using data of the Maastricht study (Subsec. 11.5.2). Robert Zivadinov (Buffalo Neuroimaging Analysis Center) is gratefully acknowledged for sharing with us data of the CEG-MS study (Subsec. 11.5.3).

11.1 Introduction

Systemic diseases, such as diabetes, may cause quantifiable changes to the geometry of the retinal microvasculature Ikram *et al.* (2013); Kalitzeos *et al.* (2013). One of the most relevant geometrical features of the microvasculature is vessel tortuosity Cheung *et al.* (2012); Hart *et al.* (1999); Kalitzeos *et al.* (2013); Sasongko *et al.* (2011). While for some geometrical features (such as vessel calibre) there is a general consensus Ikram *et al.* (2013) on how they are associated to several diseases. This is not the case for vessel tortuosity, which makes it still a very relevant topic of research. E.g., in Cheung *et al.* (2012) a positive, and in Sasongko *et al.* (2011) a negative association of vessel tortuosity with progression towards diabetic retinopathy (DR) is found. In this work, we present a novel robust and fully automated method for the extraction of tortuosity measures, and show strong positive associations of the measures with diabetes and progressive stages of DR.

Vessel tortuosity descriptors are typically computed via an extensive pipeline (including manual interventions) of image pre-processing, segmentation, thinning and splitting of the vascular network, after which tortuosity values are computed from the extracted vessel center lines Cheung *et al.* (2012); Hart *et al.* (1999); Kalitzeos *et al.* (2013); Wilson *et al.* (2008). In such pipelines, errors introduced in each processing step may accumulate, and information might get lost along the way. In particular the computation of curvature from segmentation is highly dependent on the accuracy of the segmentation. Alternatively, we propose in this chapter a reduced pipeline that does not rely on explicit segmentation of the blood vessels, but instead computes tortuosity features directly from retinal image data.

The proposed method is based on theory of best exponential curve fits in the roto-translation group $SE(2)$ (cf. Sec. 6.2.3), developed by Duits, Franken and Janssen Franken & Duits (2009); Duits & Franken (2010b); Duits & Janssen *et al.* (2016). To this end, we lift 2D images to three-dimensional orientation scores by including an orientation dimension. In the extended domain of positions and orientations we study exponential curves, whose curvatures are constant. By locally fitting exponential curves Duits & Janssen *et al.* (2016) to data in orientation scores, we are able to assign to each location a curvature and measurement-confidence value, which we use to define global tortuosity measures.

In this chapter we additionally improve the accuracy of best-exponential curve fits via a novel refinement procedure that results in more accurate curvature estimations. In the validation section we quantify this improvement (Subsec. 11.4.1), and in a stability analysis, where we use repeated measurements on a number of healthy subjects (Subsec. 11.4.2), we show that our novel method for the computation of tortuosity based biomarkers via exponential curve fits in $SE(2)$ is more repeatable than a conventional segmentation based pipeline. Finally, we demonstrate the potential use of the developed biomarker for use in clinical epidemiological studies with the application to clinical datasets. We analyse four different datasets and show a positive association of our tortuosity based biomarker with diabetes mellitus (Subsec. 11.5.2) and hypertension (Subsec. 11.5.3), which is in line with similarly reported findings in Cheung *et al.* (2011b); Han (2012); Hughes *et al.* (2006); Owen *et al.* (2011); Sasongko *et al.* (2011,

2015); Tam *et al.* (2011); Weiler *et al.* (2015). Before we describe our results let us start with the theory and methods in Sec. 11.2 and Sec. 11.3.

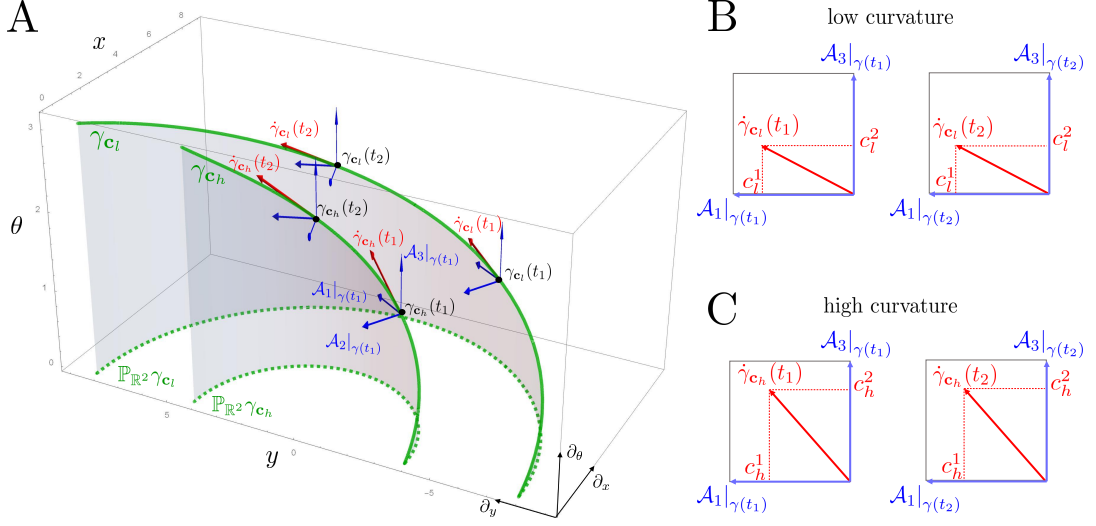


Figure 11.1: **A:** Two exponential curves $\gamma_{\mathbf{c}_h}$ and $\gamma_{\mathbf{c}_l}$ in $SE(2)$, with high and low curvature respectively. The coefficients $\mathbf{c} = (c^1, c^2, c^3)^T$ of tangent vectors $\dot{\gamma}_{\mathbf{c}}(t)$, expressed in the left invariant basis at location $\gamma_{\mathbf{c}}(t)$ are constant along the exponential curves $\gamma_{\mathbf{c}}$. This is emphasized in **B** and **C**, where one also observes a steeper slope in θ -direction of the tangent vector $\dot{\gamma}_{\mathbf{c}_h}(t)$ compared to $\dot{\gamma}_{\mathbf{c}_l}(t)$. In case of horizontal curves (for which $c^2 = 0$), the ratio $\kappa = \frac{c^3}{c^1}$ directly gives the curvature of curves $\mathbb{P}_{\mathbb{R}^2}\gamma_{\mathbf{c}}$ projected to the plane, which is indeed higher for the high curvature exponential curve $\gamma_{\mathbf{c}_h}$ compared to $\gamma_{\mathbf{c}_l}$.

11.2 Theory

11.2.1 Exponential Curves in $SE(2)$

Curves and Tangent Vectors in $SE(2)$ Recall from Subsec. 2.1.6 and Subsec. 4.2.3 that planar curves $\gamma_{2D}(t) = (x(t), y(t))^T$ can be naturally lifted to curves $\gamma_{SE(2)}(t) = (x(t), y(t), \theta(t))^T \in SE(2)$ in the space of positions and orientations by considering the direction of the tangent vector $\dot{\gamma}_{2D}(t)$ as the third coordinate ($\theta(t) = \arg(\dot{x}(t) + i \dot{y}(t))$). Tangent vectors of planar curves $\dot{\gamma}(t) = (\dot{x}(t), \dot{y}(t)) \in T(\mathbb{R}^2)$ are usually spanned by a global basis $\{\partial_x, \partial_y\}$, i.e., $T(\mathbb{R}^2) = \text{span}\{\partial_x, \partial_y\}$. In $SE(2)$ we must however work with a rotating frame of reference $\{\mathcal{A}_1|_g, \mathcal{A}_2|_g, \mathcal{A}_3|_g\} = \{\cos \theta \partial_x + \sin \theta \partial_y, -\sin \theta \partial_x + \cos \theta \partial_y, \partial_\theta\}$, aligned with the orientation at each $g \in SE(2)$, rather than with a global frame $\{\partial_x, \partial_y, \partial_\theta\}$. The tangent space at each g is spanned by the left-invariant frame $T_g(SE(2)) = \text{span}\{\mathcal{A}_1|_g, \mathcal{A}_2|_g, \mathcal{A}_3|_g\}$.

11. VESSEL GEOMETRY I: PIXEL-WISE CURVATURE

Exponential Curves in $SE(2)$ An exponential curve is a curve whose tangent vector components $\mathbf{c} = (c^1, c^2, c^3)^T$ expressed in the local left-invariant basis $\{\mathcal{A}_i|_{\gamma_c(t)}\}_{i=1}^3$ are constant, i.e., $\dot{\gamma}_c(t) = c^1 \mathcal{A}_1|_{\gamma_c(t)} + c^2 \mathcal{A}_2|_{\gamma_c(t)} + c^3 \mathcal{A}_3|_{\gamma_c(t)}$, for all $t \in \mathbb{R}$. Exponential curves in $SE(2)$ can be regarded as "straight lines" with respect to the curved geometry of $SE(2)$. The exponential curve through g with tangent \mathbf{c} is denoted by $\gamma_c^g(t) = g \cdot \exp(t(\sum_{i=1}^3 c^i A_i))$ with $\{A_1, A_2, A_3\}$ the basis for the Lie algebra (cf. Subsec. 2.3.3). By direct computation it follows that γ_c^g is a helix with constant curvature and torsion in $SE(2)$. For details see Sec. 2.2.3, Sec. 2.3.3, and Chirikjian (2000); Duits & Janssen *et al.* (2016). For intuition see Fig. 11.1. The explicit formulas for these exponential curves are well-known (see e.g. Sec. 2.3.3 and Duits & Janssen *et al.* (2016); Sanguinetti *et al.* (2010)). Here however, we do not need these formulas as we directly deduce curvature of spatially projected curves $\mathbb{P}_{\mathbb{R}^2}\gamma_c$ (cf. Fig. 11.1) from vector \mathbf{c} via

$$\kappa = \frac{c^3 \operatorname{sign}(c^1)}{\sqrt{|c^1|^2 + |c^2|^2}}. \quad (11.1)$$

See also Duits & Janssen *et al.* (2016) and (Franken & Duits, 2009, ch. 2.9) for more details.

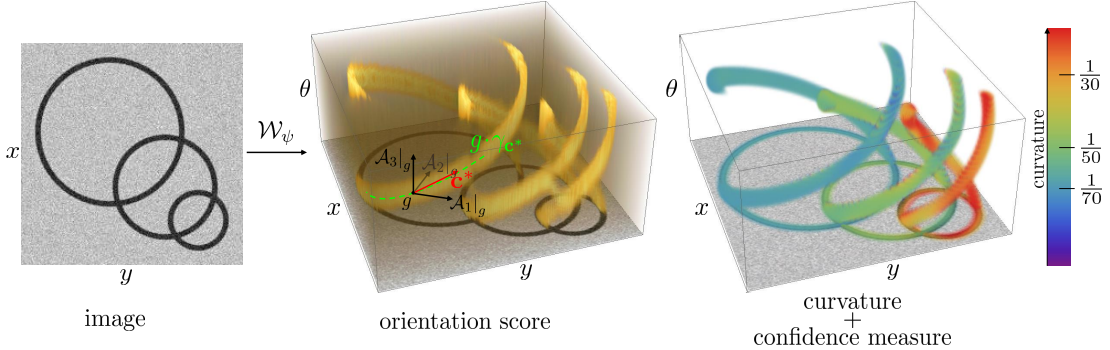


Figure 11.2: Construction of an orientation score (OS) (middle panel) from an image (left panel) via the OS-transform \mathcal{W}_ψ . In the score a derivative frame $\{\mathcal{A}_1|_g, \mathcal{A}_2|_g, \mathcal{A}_3|_g\}$, aligned with group elements $g = (x, y, \theta)$, is used for tangent vector (\mathbf{c}^*) estimation of exponential curves $\gamma_{\mathbf{c}^*}$. Using \mathbf{c}^* , curvature and measurement confidence values can be computed, which are encoded resp. in color and opacity in the right panel.

11.2.2 Exponential Curve Fits

Orientation Scores In this chapter we analyse image data in the form of real valued orientation scores $U : \mathbb{L}_2(SE(2)) \rightarrow \mathbb{R}$, which are functions on $SE(2)$, and which are constructed from an image f by means of correlation with some anisotropic wavelet ψ via the wavelet transform as defined in Eq. (2.1) on page 25. For more details on orientation scores see Sec. 2.1. In this chapter we again use cake wavelets (cf. Subsec. 2.1.5) for ψ in the transformation. The left

two panels of Fig. 11.2 show an image with different curvature circles and the corresponding orientation score.

Best Exponential Curve Fits We compute curvature values directly from tangent vectors (see Eq. (11.1)) of exponential curves that locally best fit the data. In medical image analysis applications the direction of minimal principal curvature, obtained via eigensystem analysis of the Hessian matrix, is often used in the computation of vectors tangent to oriented (tubular) structures. This concept is for example used in the well-known Frangi vesselness filter Frangi *et al.* (1998), see also Sec. 3.2. Here we exploit a similar approach, however, when considering the curved domain $\mathbb{R}^2 \times S^1$ we must pay attention to the following:

1. Rather than using a global $\{\partial_x, \partial_y, \partial_\theta\}$ derivative frame (we use short hand notation $\partial_i = \frac{\partial}{\partial i}$) we must take into consideration the curved geometry of the domain, and compute the Hessian matrix $\mathbf{H}(g)$ at each $g = (x, y, \theta)$ via left-invariant derivatives, where we rely on (6.3):

$$\mathbf{H}(g) = \begin{pmatrix} (\mathcal{A}_1^2 U)(g) & (\mathcal{A}_2(\mathcal{A}_1 U))(g) & (\mathcal{A}_3(\mathcal{A}_1 U))(g) \\ (\mathcal{A}_1(\mathcal{A}_2 U))(g) & (\mathcal{A}_2^2 U)(g) & (\mathcal{A}_3(\mathcal{A}_2 U))(g) \\ (\mathcal{A}_1(\mathcal{A}_3 U))(g) & (\mathcal{A}_2(\mathcal{A}_3 U))(g) & (\mathcal{A}_3^2 U)(g) \end{pmatrix}, \quad (11.2)$$

with the left-invariant vector fields \mathcal{A}_i defined in (2.42) on page 48. For more details on the left-invariant Hessian see Subsec. 6.2.3 and Duits & Janssen *et al.* (2016); Franken & Duits (2009).

2. Since left-invariant derivatives are non-commutative, e.g. $\mathcal{A}_3\mathcal{A}_1 U \neq \mathcal{A}_1\mathcal{A}_3 U$, the Hessian matrix $\mathbf{H}(g)$ is not symmetric. In order to obtain real-valued eigenvalues of a dimensionless matrix, we symmetrize the Hessian matrix via

$$\mathcal{H}_\xi(g) := \mathbf{M}_{\xi^{-1}} \mathbf{H}(g)^T \mathbf{M}_{\xi^{-2}} \mathbf{H}(g) \mathbf{M}_{\xi^{-1}},$$

and perform eigenanalysis on $\mathbf{H}_\xi(g)$. Here matrix $\mathbf{M}_\xi = \text{diag}\{\xi, \xi, 1\}$ and ξ is a parameter with unit $1/\text{length}$ that makes the new symmetrized Hessian dimensionless.

The exponential curve fitting used in this chapter follows the same procedure as described in Subsec. 6.2.3, and is as follows. Eigenvector $\mathbf{M}_\xi \mathbf{c}^*$ with lowest eigenvalue of the dimensionless (ξ -scaled) matrix $\mathbf{H}_\xi(g)$ does not give the minimal principal curvature direction, but rather provides the solution to the following optimization problem Duits & Janssen *et al.* (2016):

$$\mathbf{c}^*(g) = \underset{\mathbf{c} \in \mathbb{R}^3, \|\mathbf{c}\|_\mu=1}{\operatorname{argmin}} \left\{ \left\| \frac{d}{dt} (\nabla U(\gamma_{\mathbf{c}}^g(t))) \Big|_{t=0} \right\|_\mu^2 \right\}, \quad (11.3)$$

with left-invariant gradient $\nabla U = \mathbf{M}_{\xi^{-2}}(\mathcal{A}_1 U, \mathcal{A}_2 U, \mathcal{A}_3 U)^T$ and $\|\mathbf{c}\|_\xi^2 = \xi^2 |c^1|^2 + \xi^2 |c^2|^2 + |c^3|^2$. Intuitively speaking, \mathbf{c}^* gives the tangent vector components of the exponential curve $\gamma_{\mathbf{c}^*}^g(t)$, starting at position g at $t = 0$, along which the left-invariant gradient has fewest variations (Fig. 11.2). As an alternative approach, tangent vector estimation can be done based on the structure tensor as well, which is done in work by van Ginkel van Ginkel (2002). A full overview

11. VESSEL GEOMETRY I: PIXEL-WISE CURVATURE

of exponential curve fit models, with 3D extensions, can be found in Duits & Janssen *et al.* (2016).

Gaussian Derivatives In our implementation we use Gaussian derivatives to compute the Hessian matrix, i.e., in Eq. (11.2) we substitute $U \leftarrow (G_{\sigma_s, \sigma_o} * U)$, with $G_{\sigma_s, \sigma_o}(\mathbf{x}, \theta)$ a Gaussian kernel with spatial isotropic scale $\frac{1}{2}\sigma_s^2$, and orientation scale $\frac{1}{2}\sigma_o^2$. For the numerical implementation it is important to take into account the non-commutative structure of the group. In particular when computing the Hessian matrix in two steps it is important to put the orientation derivative \mathcal{A}_3 up front, and take the following two properties into account:

$$[\mathcal{A}_i^{\mathbf{s}}, \mathcal{A}_j^{\mathbf{s}}] = \sum_{k=1}^3 c_{ij}^k \mathcal{A}_k^{2\mathbf{s}}, \quad \text{and} \quad \mathcal{A}_i^{\mathbf{s}} \mathcal{A}_j^{\mathbf{s}} = \mathcal{A}_j^{\mathbf{s}} \mathcal{A}_i^{\mathbf{s}} + [\mathcal{A}_i^{\mathbf{s}}, \mathcal{A}_j^{\mathbf{s}}], \quad (11.4)$$

where a Gaussian derivative¹ at scale $\mathbf{s} = (\frac{1}{2}\sigma_s^2, \frac{1}{2}\sigma_o^2)$ is denoted with $\mathcal{A}_i^{\mathbf{s}}$, and the commutators and structure constants c_{ij}^k are respectively given in (2.44) and (2.45) on page 48. E.g., $\mathcal{A}_3^{\mathbf{s}} \mathcal{A}_1^{\mathbf{s}} = \mathcal{A}_1^{\mathbf{s}} \mathcal{A}_3^{\mathbf{s}} + \mathcal{A}_2^{2\mathbf{s}}$.

11.3 Global Tortuosity Measures From Pixel-Wise Curvature Voting

11.3.1 Global Tortuosity Measures

Based on the exponential curve fits in orientation scores we can assign to each location $g = (x, y, \theta)$ in the score a curvature value

$$\kappa(g) = \mathcal{K}(U)(g) = \frac{c^3(g) \operatorname{sign}(c^1(g))}{\sqrt{|c^1(g)|^2 + |c^2(g)|^2}}, \quad (11.5)$$

with \mathcal{K} denoting the operator that computes the curvature values, and with $\mathbf{c} = (c^1(g), c^2(g), c^3(g))$ the coefficients of the best exponential curve fit at g . It is also possible to compute for each g an confidence measure $s(g)$ that indicates the reliability of the measurement. This measure, called the *orientation confidence* is defined below in Eq. (11.9). See for example the right-most panel in Fig. 11.2.

As global tortuosity measures we then consider the weighted average² of absolute curvature

¹Recall that in the vessel enhancement chapter (Ch. 6) we used a different notation since we considered the special case $\mathbf{s} = (\frac{1}{2}\sigma_s^2, \frac{1}{2}(\xi\sigma_s)^2)$. Note that then the notations relate via $\mathcal{A}_i^{\mathbf{s}}U = (\mathcal{A}_iU)^{\mathbf{s}, \xi}$.

²Weighted by the orientation confidence $s(g)$.

11.3 Global Tortuosity Measures From Pixel-Wise Curvature Voting

values $\mu_{|\kappa|}^{SE(2)}$, and the weighted standard deviation of absolute curvature values $\sigma_{|\kappa|}^{SE(2)}$:

$$\mu_{|\kappa|}^{SE(2)} = \frac{1}{s_{total}} \int_{\mathbb{R}^2} \int_0^\pi |\kappa(\mathbf{x}, \theta)| s(\mathbf{x}, \theta) d\theta d\mathbf{x} \quad (11.6a)$$

$$\sigma_{|\kappa|}^{SE(2)} = \sqrt{\frac{1}{s_{total}} \int_{\mathbb{R}^2} \int_0^\pi (|\kappa(\mathbf{x}, \theta)| - \mu_{|\kappa|})^2 s(\mathbf{x}, \theta) d\theta d\mathbf{x}}, \quad (11.6b)$$

with $s_{total} = \int_{-\infty}^\infty \int_0^\pi s(\mathbf{x}, \theta) d\mathbf{x} d\theta$.

We want our new approach to global tortuosity measures to be compatible with other 2D "confidence" maps (such as e.g. the 2D Frangi vesselness filter Frangi *et al.* (1998)), and as such we also define 2D curvature and confidence maps as follows

$$\kappa(\mathbf{x}) := \kappa(\mathbf{x}, \theta^*(\mathbf{x})) \quad (11.7a)$$

$$s(\mathbf{x}) := s(\mathbf{x}, \theta^*(\mathbf{x})), \quad \text{with} \quad (11.7b)$$

$$\theta^*(\mathbf{x}) = \operatorname{argmax}_{\theta \in S^1} s(\mathbf{x}, \theta), \quad (11.7c)$$

and define the global tortuosity measures based on these (compactly supported) 2D maps as follows:

$$\mu_{|\kappa|} = \frac{1}{s_{total}} \int_{\mathbb{R}^2} |\kappa(\mathbf{x})| s(\mathbf{x}) d\mathbf{x} \quad (11.8a)$$

$$\sigma_{|\kappa|} = \sqrt{\frac{1}{s_{total}} \int_{\mathbb{R}^2} (|\kappa(\mathbf{x})| - \mu_{|\kappa|})^2 s(\mathbf{x}) d\mathbf{x}}, \quad (11.8b)$$

with $s_{total} = \int_{\mathbb{R}^2} s(\mathbf{x}) d\mathbf{x}$.

11.3.2 Orientation Confidence

Based on the Hessian matrix and the obtained principle directions it is possible to define a gauge frame \mathcal{B}_i as described in Subsec. 6.2.3, and compute a Laplacian in the plane orthogonal to the tangent direction $\mathbf{c}^*(g)$ which we use to define the orientation confidence measure $s(g)$:

$$s(g) = \mathcal{S}(U)(g) = (-\Delta_o U(g))_+ = (-((\mathcal{B}_2^2 U)(g) + (\mathcal{B}_3^2 U)(g)))_+ \quad (11.9)$$

in which S denotes the operator of computing the orientation confidence, Δ_o the Laplacian operator in the plane orthogonal to the tangent direction \mathbf{c}^* , where $(v)_+ = \max\{v, 0\}$, and where \mathcal{B}_i are the gauge derivatives defined in Eq. (6.5) on page 143. For computational efficiency it is useful to realize that the second order gauge derivatives \mathcal{B}_i^2 can be computed directly from the Hessian matrix $\mathbf{H}(g)$ and the eigenvectors $\mathbf{M}_\xi \mathbf{c}^i$ as follows

$$(\mathcal{B}_i^2 U)(g) = \mathbf{c}^i(g)^T \mathbf{H}(g) \mathbf{c}^i(g). \quad (11.10)$$

11.3.3 Iterative Stabilization of Orientation Confidence

Improved accuracy of the confidence and curvature measurements is achieved via the following stabilizing refinement scheme:

$$s_{n+1} = \frac{1}{\|\mathcal{S}(s_n)\|_\infty} \mathcal{S}(s_n), \text{ with } s_1 = \mathcal{S}(U), \quad \kappa_{n+1} = \mathcal{K}(s_n), \text{ with } \kappa_1 = \mathcal{K}(U), \quad (11.11)$$

where we denote the computation of the confidence map s from input volume U with $\mathcal{S}(U)$, and the computation of curvature κ with $\mathcal{K}(U)$. We experimentally observed that the above iterative scheme converges (see Fig. 11.3 for an example), and found $n = 3$ iterations to be a good balance between accuracy of curvature measurements and computation time. This number of iterations will be used in further experiments, unless indicated otherwise. A formal prove of convergence of the iterative refinement scheme is left for future work.

11.3.4 Extensions and a Conventional Processing Pipeline

In addition to the orientation confidence we consider the following variations of weighting functions for weighting the pixel-wise curvature measures:

- $\mu_{|\kappa|}^{conf}$: This is the weighted average curvature value as described in Eq. 11.8a. The weighting function is thus the orientation confidence.
- $\mu_{|\kappa|}^{vess}$: This is the weighted average curvature value in which a vesselness image (a soft segmentation) is used instead of $s(\mathbf{x})$. In this chapter we used the soft segmentation method described in Zhang *et al.* (2016a), which is a fast gauge-frame based orientation score method that approximates and improves the vesselness method described in Ch. 6.
- $\mu_{|\kappa|}^{segm}$: In this tortuosity measure the curvature values are weighted by a binary vessel segmentation. The hard-segmentation is constructed by thresholding the previously described soft-segmentation, followed by a false positive vessel removal pipeline Zhang *et al.* (2016a).
- $\mu_{|\kappa|}^{cent}$: Here the curvature values are only averaged at vessel center line locations, which are obtained by thinning the hard segmentation described in the previous item. This approach is most similar to conventional processing pipelines, however, here the curvature values are still computed from orientation scores and not from segmentations.

It is expected that $\mu_{|\kappa|}^{conf}$ and $\mu_{|\kappa|}^{vess}$ are the more stable measures due to their probabilistic nature; high confidence locations have a high contribution to the average, and low confidence regions are not completely ignored, but simply included with a lower weight. In theory, the segmentation and center line method $\mu_{|\kappa|}^{segm}$ and $\mu_{|\kappa|}^{cent}$ should give the best representation of the actual vessel geometry, provided that the segmentation is accurate and it does not contain false positives. It is however also expected that this method gets increasingly unstable with decreasing image quality due to binary weighting functions; false positive segmentations contribute equally strong to the final tortuosity measure. Finally, we compare our method with a conventional approach:

- $\mu_{|\kappa|}^{cent,conv}$: This method is similar to the $\mu_{|\kappa|}^{cent}$, however, now the curvature values are computed from B-spline functions which are fitted to each sequence of center line coordinates.

Such a conventional approach has the drawback that inaccurate vessel segmentations introduce errors both by (1) weighting false positive vessels as strongly as true positive vessels in the tortuosity measure, and (2) producing incorrect local vessel curvature measurements due to inaccurate vessel parameterizations. Finally, it should be remarked that the center line methods weight both large and small vessels equally heavily, while the other methods put more emphasis on larger blood vessels.

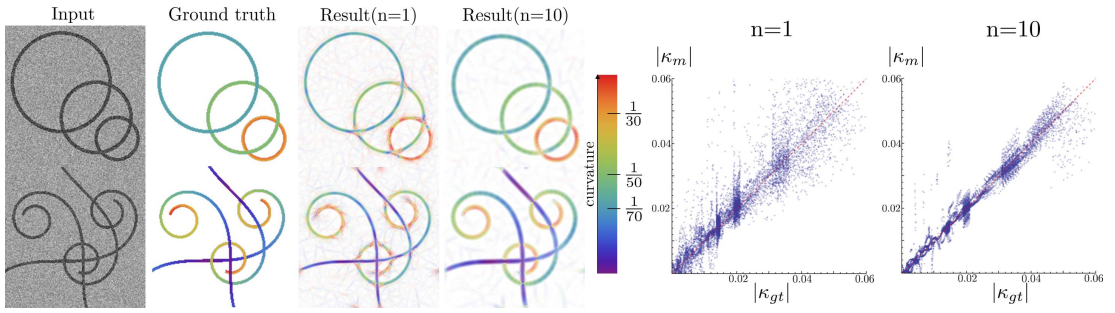


Figure 11.3: From left to right: input image ($SNR=1$), ground truth color-coded curvature map, measured curvature map with resp. $n = 1$ and $n = 10$ refinements, scatter plot of ground truth vs measured curvatures for resp. $n = 1$ and $n = 10$.

11.4 Validation

11.4.1 Validation on Local Curvature Measurements

In all experiments discussed in this chapter the scales $\sigma_s = 3$ and $\sigma_o = \frac{\pi}{18}$ are fixed, and are chosen as to best match the cross-sectional scales of vessels/lines in the orientation score (Sec. 2.1). We set $\mu = \frac{\sigma_o}{\sigma_s}$, and sample the orientation score with 18 orientations. Unless indicated otherwise, we used $n = 3$ refinement iterations in the computation of orientation confidence and curvature.

Our method is validated on two synthetic images (201px by 201px) with Gaussian white noise ($SNR=1$): One image composed of three circles with radii of 50px, 70px and 90px; One image composed of three crossing Euler spirals. The curvatures computed with our method (third and fourth image in Fig. 11.3), with $n = 1$ and $n = 10$ refinement iterations (Eq. (11.11)), were compared against the ground truth (second image Fig. 8.13). In the curvature maps, curvature is encoded with color and confidence with opacity (see e.g. also Fig. 11.2). Visual comparison shows a remarkable agreement between our method and the ground truth, and

11. VESSEL GEOMETRY I: PIXEL-WISE CURVATURE

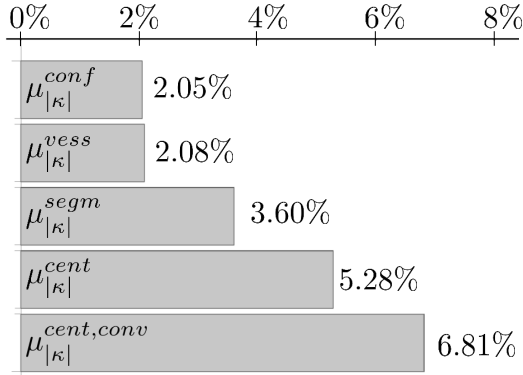


Figure 11.4: Mean normalized standard deviation for five different methods. A low mean normalized standard deviation indicates high repeatability. See Subsec. 11.3.4 for a description of the biomarkers $\mu_{|\kappa|}^{conf}$, $\mu_{|\kappa|}^{vess}$, $\mu_{|\kappa|}^{segm}$, $\mu_{|\kappa|}^{cent}$ and $\mu_{|\kappa|}^{cent,conv}$.

we observe improved precision of both the confidence and curvature measurements with an increasing number of refinement iterations n . This is also confirmed by the comparison of curvature measurements against the ground truth via scatter plots (the most right two figures in Fig. 8.13). The root mean squared error of $|\kappa|$ was reduced from 0.0138 for $n = 1$ to 0.0024 for $n = 10$.

11.4.2 Repeatability/Reproducibility

For the quantification of the stability of the proposed tortuosity based biomarker extraction methods we made repeated fundus photographs (Model AFC-230, Nidek) of 12 healthy subjects. The nasal view of each subject's right eye was photographed 5 times, with an interval of ± 2 minutes in between the acquisitions. Due to the relatively short intervals between the acquisitions the pupils start to narrow as a result of the camera flash. In our test dataset this resulted in realistic variations in image quality due to varying pupil sizes.

To quantify repeatability of the methods we computed the tortuosity biomarkers on each image, and computed for each patient a normalized standard deviation. A low normalized standard deviation indicates high repeatability. The final score for each biomarker extraction method evaluated in this section is then given as the mean (over all 12 subjects) normalized standard deviation. Results are depicted in Fig. 11.4.

As expected (see explanation of the methods in Subsec. 11.3.4) the methods with non-binary weighting functions, $\mu_{|\kappa|}^{conf}$ and $\mu_{|\kappa|}^{vess}$, have highest repeatability. These methods are less affected by imaging artifacts. The binary weighting method $\mu_{|\kappa|}^{segm}$ has medium performance in comparison to the other methods. The center line methods $\mu_{|\kappa|}^{cent}$ and $\mu_{|\kappa|}^{cent,conv}$ have low repeatability, with the conventional method $\mu_{|\kappa|}^{cent,conv}$ giving lowest repeatability.

11.5 Application to Clinical Data

11.5.1 Response to Diabetic Retinopathy Images

In this section we investigate the applicability of the pixel-wise curvature measurement method in combination with the iterative orientation confidence method introduced in Subsec. 11.3.3.

Tortuosity measures $\mu_{|\kappa|}^{conf}$ and $\sigma_{|\kappa|}^{conf}$ (cf. Eq. (11.8)) are computed on images of two publicly available database that include pathological images: 1) the high resolution fundus (HRF) database Odstrcilik *et al.* (2013), consisting of 15 images of healthy controls, and 15 images of diabetes patients; 2) the MESSIDOR database MESSIDOR (2008), consisting of 1200 images of diabetes patients which are graded for diabetic retinopathy: R0 (no retinopathy), R1, R2 and R3 (severe retinopathy). All images are made with 45 degree field of view (FOV) cameras, however with varying image resolutions. In order to have approximately the same physical pixel size in all images, they are cropped and resized such that the FOV area spans a width of 1024px. Curvature and confidence measures were computed with $n = 3$ refinement iterations.

Fig. 11.5 shows a selection of results. Fig. 11.6 and Tab. 11.1 show the distribution of feature values for different subgroups of the HRF and MESSIDOR database. Based on a Mann-Whitney U test (p-values reported in Tab. 11.1) we conclude that all subgroups show a significant increase in $\mu_{|\kappa|}$ and $\sigma_{|\kappa|}$ in comparison to the corresponding base groups (healthy for HRF, and R0 for MESSIDOR).

We also observe that our *method detects microbleeds and hemorrhages* as high curvature regions (Fig. 11.5). While this was not our intention, it is a very welcome property when using features $\mu_{|\kappa|}$ and $\sigma_{|\kappa|}$ as biomarkers for DR. However, for research dedicated to the retinal vasculature one only wants to analyse blood vessels. As such we consider in the subsequent Subsecs. 11.5.2 and 11.5.3 also a weighting of the curvature values with vesselness specific weighting functions.

11.5.2 Curvature Biomarker in Association with Diabetes Mellitus Type 2

In this and the following subsection we apply our method to large clinical datasets which we can use to study the association of our developed biomarkers with general health status parameters such as diabetes status, hypertension and age.

Dataset and Analysis The goal of our first study is to investigate the association of vessel tortuosity with the status of diabetes mellitus type 2. The dataset consists of people suffering from diabetes and healthy controls which have been imaged (with a Nidek AFC-230) in the Maastricht Study. The Maastricht study is an epidemiological study which studies the prevention, causes and treatment of diabetes mellitus and cardiovascular diseases.

The dataset and our analysis have the following characteristics:

- The dataset contains 810 healthy controls.

11. VESSEL GEOMETRY I: PIXEL-WISE CURVATURE

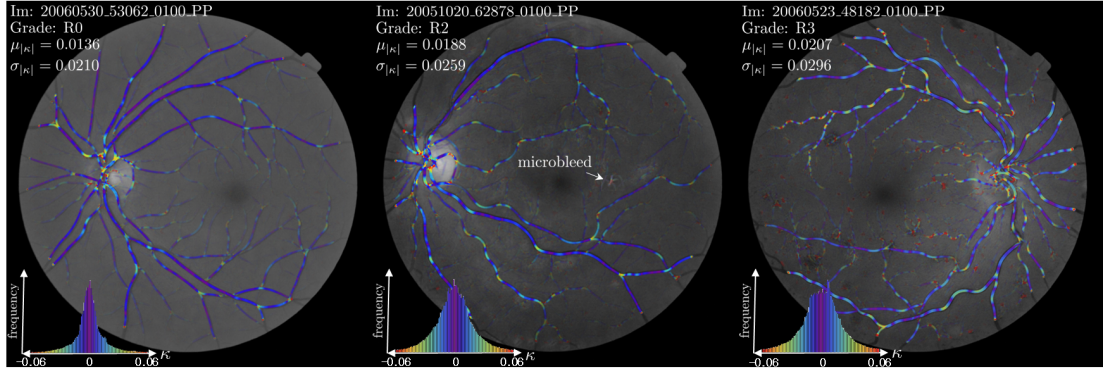


Figure 11.5: Results on three images of the MESSIDOR database. Measured absolute curvature $|\kappa|$ encoded in color, and confidence s encoded with opacity, overlain on the original image, together with the histogram of measured κ values.

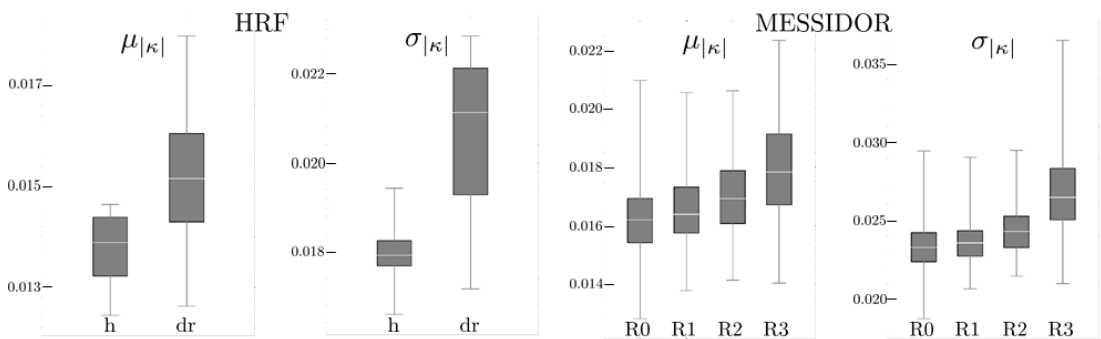


Figure 11.6: Box-and-whisker plots of tortuosity measures $\mu_{|\kappa|}$ and $\sigma_{|\kappa|}$ in subgroups of the HRF and MESSIDOR database.

11.5 Application to Clinical Data

Table 11.1: Tortuosity measures $\mu_{|\kappa|}$ and $\sigma_{|\kappa|}$ in the HRF and MESSIDOR database.

Subgroup	Mean \pm (STD)	
	$\mu_{ \kappa } (10^{-2})$	$\sigma_{ \kappa } (10^{-2})$
HRF		
Healthy	1.372 \pm (0.069)	1.796 \pm (0.072)
Diabetic	1.521 \pm (0.130)	2.073 \pm (0.185)
p-value ^a	< 0.001	< 0.001
MESSIDOR		
R0	1.624 \pm (0.120)	2.333 \pm (0.134)
R1	1.657 \pm (0.124)	2.365 \pm (0.131)
p-value ^b	0.007	0.020
R2	1.698 \pm (0.122)	2.436 \pm (0.144)
p-value ^b	< 0.001	< 0.001
R3	1.795 \pm (0.160)	2.674 \pm (0.235)
p-value ^b	< 0.001	< 0.001

^a Compared to Healthy.

^b Compared to R0.

- The dataset contains 53 patients with a fasting glucose impairment (IFG).
- The dataset contains 156 patients with a glucose tolerance impairment (IGT).
- The dataset contains 555 patients with diabetes mellitus type 2 (DM2).
- The average age was 58.08 (standard deviation 8.09).
- The gender ratio was 0.5.
- Of each subject an optic nerve head centered fundus image of the right eye was processed to compute the tortuosity biomarkers.
- In each image the optic nerve head was automatically detected using the method proposed in Ch. 5. The weighting functions were masked in order to standardize the measurement region to the region from 2 to 6 optic disk radii away from the optic nerve head center.
- The same camera was used on which we have tested the repeatability of our methods.

As is common in statistics in ophthalmic epidemiological studies (see e.g. Armstrong (2013) for guidelines), our analyses are based on linear regression tests. Here the dummy variables IFG, IGT and DM2 are binary and we additionally correct for age and gender. In this test each parameter is tested for a significant contribution (p-value) to the linear model that explains the curvature biomarkers. The linear model has a so-called β coefficient for each parameter. Here we only report the sign of the β coefficient: it represents either a positive or negative association.

11. VESSEL GEOMETRY I: PIXEL-WISE CURVATURE

Tab. 11.2 summarizes our results. The parameters that had a significant¹ influence on the regression are highlighted in boldface. Two images from this database with respectively low and high curvature are shown in Fig. 1.5 on page 11 with a curvature and segmentation overlay.

Associations With DM2 After correction for IFG, IGT, age and gender, the proposed segmentation and centerline based tortuosity measures $\mu_{|\kappa|}^{segm}$ and $\mu_{|\kappa|}^{cent}$ were significantly and positively associated with diabetes type 2. These results are in line with other results published in literature Sasongko *et al.* (2011, 2015); Tam *et al.* (2011); Weiler *et al.* (2015), however contradicts a publication by Cheung *et al.* (2012) in which a negative association of tortuosity was found with DM2 (see Subsec. 1.3.3 for a possible explanation).

In Subsec. 11.4.2 we saw that the confidence and vesselness based weighting functions resulted in the most repeatable measurements (resp. $\mu_{|\kappa|}^{conf}$ and $\mu_{|\kappa|}^{vess}$). These features however do not show a significant association with DM2, whereas the binary weight function methods (except for the conventional method) do. An explanation for this could be that the soft segmentation based weight functions include too much non-vessel curvature in the average, by which a distorted measurement could be obtained. These methods are thus stable due to their probabilistic nature, but as a consequence they are also less specific in the identification of the vessel measurement regions (also observed in Subsec. 11.5.1). Finally, we remark that the conventional centerline based method did not show a significant association with DM2. Since the only difference between $\mu_{|\kappa|}^{cent,conv}$ and $\mu_{|\kappa|}^{cent}$ is the way curvature is computed, we conclude that this difference is caused by the method for computing curvature.

Associations With Age The regression test also shows that after correction for IFG, IGT, DM2 and gender the features $\mu_{|\kappa|}^{conf}$ and $\mu_{|\kappa|}^{cent,conv}$ were significantly associated with age. Interestingly, $\mu_{|\kappa|}^{conf}$ shows a positive and $\mu_{|\kappa|}^{cent,conv}$ shows a negative association with age. An often occurring condition in elderly people is cataract, this affects the visibility of blood vessels in retinal images. It could be that this affects both methods in different ways. This possible aspect will be further investigated in future work.

11.5.3 Curvature Biomarker in Association with Hypertension

Dataset and Analysis The goal of our second study is to investigate the association of vessel tortuosity with hypertension. The dataset consists of SLO images (Model Spectralis, Heidelberg Engineering) which are obtained during the CEG-MS study. The goal of the CEG-MS study is to identify the role of cardiovascular, genetic and environmental risk factors and their interactions with respect to radiological and clinical progression in Clinically Isolated Syndrome (CIS) and Multiple Sclerosis (MS) subjects, as compared to controls and patients with other neurological disorders over 5 years. In the sub-study discussed in this section we focus on the aspect of hypertension and vessel tortuosity.

The dataset and our analysis have the following characteristics:

¹We consider a test to be significant if the resulting p-value is below 0.05.

Table 11.2: Regression analysis of retinal vascular curvature based biomarkers with different statuses of diabetes such as impaired fasting glucose (IFG), impaired glucose tolerance (IGT), diabetes mellitus type 2 (DM2), with corrections for gender and age in volunteers from the Maastricht study. A p-value below 0.05 is considered a significant association and is marked in boldface. The sign of the β -parameter indicates a positive (+) or negative (-) association.

Feature name	DM2		Age		Gender	
	sign(β)	p-value	sign(β)	p-value	sign(β)	p-value
$\mu_{ \kappa }^{conf}$	+	0.122	+	≤ 0.001	-	0.479
$\mu_{ \kappa }^{vess}$	+	0.154	+	0.127	+	0.682
$\mu_{ \kappa }^{segm}$	+	0.004	+	0.544	-	0.805
$\mu_{ \kappa }^{cent}$	+	0.045	+	0.194	-	0.770
$\mu_{ \kappa }^{cent,conv}$	+	0.103	-	0.022	+	0.537

- The dataset contains 291 non-hypertensive controls.
- The dataset contains 130 hypertension patients.
- The average age was 45.16 (standard deviation 13.76).
- The gender ratio was 0.3 (more females than males).
- Of each subject an optic nerve head centered fundus image of the right eye was processed to compute the tortuosity biomarkers.
- In each image the optic nerve head was automatically detected using the method proposed in Ch. 5. The weighting functions were masked in order to standardize the measurement region to the region from 2 to 5 optic disk radii away from the optic nerve head center.
- Automatically generated vessel center line pixel maps were manually checked: false positive vessels were removed and the remaining vessels were labeled as either artery or vein.

In contrast to the previously discussed diabetes study, with the current dataset we can additionally study differences between arteries and veins. Since the artery/vein labeling was only done on centerline pixels, all other pixels were labeled automatically via nearest neighbor interpolation. This allows us to define the weighted average curvature features for arteries and veins separately. The artery and vein separated features have respectively an additional superscript label A and V . Tab. 11.3 summarizes our results.

Associations With Hypertension After correction for age and gender, almost all developed tortuosity measures show a significant positive association with hypertension. Only the conventional tortuosity measures did not show a significant association. The significant

11. VESSEL GEOMETRY I: PIXEL-WISE CURVATURE

Table 11.3: Regression analysis of retinal vascular curvature based biomarkers with hypertension, gender and age in volunteers from the CEG-MS study. A p-value below 0.05 is considered a significant association and is marked in boldface. The sign of the β -parameter indicates a positive (+) or negative (-) association.

Feature	Hypertension		Age		Gender		
	approach	sign(β)	p-value	sign(β)	p-value	sign(β)	p-value
All Blood Vessels							
$\mu_{ \kappa }^{conf}$	full-autom.	+	0.003	+	0.334	-	0.581
$\mu_{ \kappa }^{vess}$	full-autom.	+	0.002	+	0.310	-	0.261
$\mu_{ \kappa }^{segm}$	full-autom.	+	0.028	-	0.261	-	0.291
$\mu_{ \kappa }^{cent}$	full-autom.	+	0.196	-	0.303	+	0.662
$\mu_{ \kappa }^{cent,conv}$	semi-autom. [†]	+	0.073	-	0.456	-	0.680
Arteries							
$\mu_{ \kappa }^{conf,A}$	semi-autom. [‡]	+	≤ 0.001	+	0.803	-	0.127
$\mu_{ \kappa }^{vess,A}$	semi-autom. [‡]	+	≤ 0.001	+	0.568	-	0.041
$\mu_{ \kappa }^{segm,A}$	semi-autom. [‡]	+	0.017	-	0.047	-	0.098
$\mu_{ \kappa }^{cent,A}$	semi-autom. [‡]	+	0.006	-	0.059	-	0.284
$\mu_{ \kappa }^{cent,conv,A}$	semi-autom. ^{†‡}	+	0.064	-	0.006	-	0.100
Veins							
$\mu_{ \kappa }^{conf,V}$	semi-autom. [‡]	+	0.027	+	0.225	+	0.244
$\mu_{ \kappa }^{vess,V}$	semi-autom. [‡]	+	0.046	+	0.351	+	0.619
$\mu_{ \kappa }^{segm,V}$	semi-autom. [‡]	+	0.159	-	0.774	+	0.715
$\mu_{ \kappa }^{cent,V}$	semi-autom. [‡]	-	0.685	-	0.755	+	0.055
$\mu_{ \kappa }^{cent,conv,V}$	semi-autom. ^{†‡}	+	0.163	-	0.646	+	0.061

[†]Includes manual removal of false positive centerlines.

[‡]Includes manual labeling of arteries and veins.

The labels *conf*, *vess*, *cent* indicate that a weighted average of the absolute curvature $|\kappa|$ is obtained by weighting respectively with the orientation confidence map, vesselness map or a vessel centerline map. The label *cent,conv* denotes computation of vessel curvature using a conventional approach, measuring only at the vessel centerline.

increase in overall retinal vascular tortuosity as observed with $\mu_{|\kappa|}^{conf}$, $\mu_{|\kappa|}^{vess}$ and $\mu_{|\kappa|}^{segm}$ is mainly explained by an increase in arteriolar tortuosity: a positive significant association was found for $\mu_{|\kappa|}^{conf,A}$, $\mu_{|\kappa|}^{vess,A}$, $\mu_{|\kappa|}^{segm,A}$ and $\mu_{|\kappa|}^{cent,A}$. When looking at the venular tortuosity features, only a significant association with $\mu_{|\kappa|}^{conf,V}$ and $\mu_{|\kappa|}^{vess,V}$ is observed.

The observed general increase in retinal vascular tortuosity with hypertension is in line with other results reported in literature Cheung *et al.* (2011b); Han (2012); Hughes *et al.* (2006); Owen *et al.* (2011). However, the observation that this is mainly caused by an increase in arteriolar tortuosity is only in line with Han (2012); Owen *et al.* (2011), but conflicts the findings of Cheung *et al.* (2011b); Hughes *et al.* (2006) in which it is the venular tortuosity that explains an overall increase in tortuosity.

Associations With Age and Gender Finally, we observe a significant negative association of age with the features $\mu_{|\kappa|}^{segm,A}$ and $\mu_{|\kappa|}^{cent,conv,A}$. This suggests a straightening of blood vessels with age. The regression tests also showed a significant decrease in tortuosity in males (coded with dummy parameter value 1) when compared to females (coded with dummy parameter value 0). This observed association is in line with Cheung *et al.* (2011b); Wu *et al.* (2013); Zhu *et al.* (2014). Note, however, that $\mu_{|\kappa|}^{vess,A}$ is the only significantly associated feature (out of 15 tested features).

11.6 Conclusion

We developed new vessel tortuosity descriptors based on curvature estimations from best exponential curve fits in orientation scores and proposed a novel refinement scheme for improved accuracy in curvature and confidence measures. Validation on synthetic images showed high accuracy of our curvature extraction approach.

Application to clinical retinal image datasets showed strong positive associations of the proposed tortuosity descriptors with different stages of diabetic retinopathy, diabetes mellitus type 2 and hypertension. Our findings are in line with reported research results of other studies (recall Sec. 1.3).

We also showed that our new approach to weighted average curvature biomarkers is more stable than conventional approaches. Moreover, our new approach is modular: it allows freedom in the choice of weighting function, and allows for the inclusion of artery/vein pixel maps for artery/vein specific measurements. In particular the aspect of artery/vein specific measurements could provide interesting insight in geometrical vascular components of diseases, such as we have shown with the found association of increased arteriolar tortuosity with hypertension in Subsec. 11.5.3.

Except for the artery/vein specific analysis done in Subsec. 11.5.3, the proposed method is fully automatic and highly repeatable. In order to also automate the artery/vein analyses we develop in the next Ch. 12 the automated construction of artery/vein pixel maps.

Chapter 12

Vessel Geometry In Orientation Scores Part II: A New Tubularity Measure

12.1 Introduction

This chapter aims to further explore the potential of analyzing and processing orientation scores for the analysis of geometrical vessel properties. In this chapter we propose a new tubularity measure which allows us to add several new pixel-wise feature computation methods such as pixel-wise vessel width measurement, and pixel-wise artery/vein classification. As such, in the later sections of this chapter proof of concepts are discussed with a strong focus on future work.

In Sec. 12.2 we develop two new tubularity measures $V^{add} : SE(2) \times \mathbb{R}^+ \rightarrow \mathbb{R}$ and $V^{prod} : SE(2) \times \mathbb{R}^+ \rightarrow \mathbb{R}^+$ based on orientation scores and the *right*-regular representation \mathcal{R} of $SE(2)$ (recall Subsec. 2.3.2). The two tubularity measures are respectively based on an additive (linear) and multiplicative (non-linear) combination of edge information encoded in orientation scores. As we will show in this chapter, the multiplicative model is preferred over the linear model. The proposed tubularity measures $V^{add}(\mathbf{x}, \theta, r)$ and $V^{prod}(\mathbf{x}, \theta, r)$ depend on 3 variables and provide a measure for the likelihood of finding a tubular structure at each location \mathbf{x} with orientation θ and with radius r , see for example Fig. 12.1.

Our tubularity measures have similarities with the popular optimally oriented flux (OOF) filter Law & Chung (2008) and with a recently proposed invertible orientation score based tubularity filter proposed by Chen & Cohen (2014) which we will briefly discuss below. The OOF filter extends the image gradient flux filter, which was proposed in Bouix *et al.* (2005) for centerline extraction of curvilinear structures. The image gradient flux is a scalar measure which quantifies the amount of image gradient flowing in or out a local spherical region (with certain radius r). The extension by Law & Chung (2008) includes orientation sensitivity and introduces a notion of oriented flux.

Similar to the OOF filter and the Chen-Cohen (CC) method, the tubularity measures proposed in this chapter have the property that their responses are based on highly localized edge responses. As such, in contrast to more classical Hessian based methods (cf. Sato *et al.* (1998)), the OOF, CC and the proposed tubularity measures have the advantage that they are robust against disturbance by closely parallel structures. Finally, the new measure V^{prod} has several additional advantages over the OOF filter, which are as follows:

1. It allows for the selection of concave/convex curvilinear structures. I.e., it allows for the specific detection of bright lines on a dark background, or dark lines on a bright background.
2. It provides sharper responses at the centerlines of curvilinear structures compared to the OOF filter, due to its non-linearity.
3. It can be computed at low computational cost. Once an orientation score is computed the tubularity measure follows from basic translation operations in each θ -plane of the score.

In Chen & Cohen (2014) a method is proposed for simultaneous tracking of centerlines, orientations and widths of blood vessels. Similar to our tracking methods proposed in Ch. 7, 8 and 9 tracking takes place in a higher dimensional domain. However, in addition to including

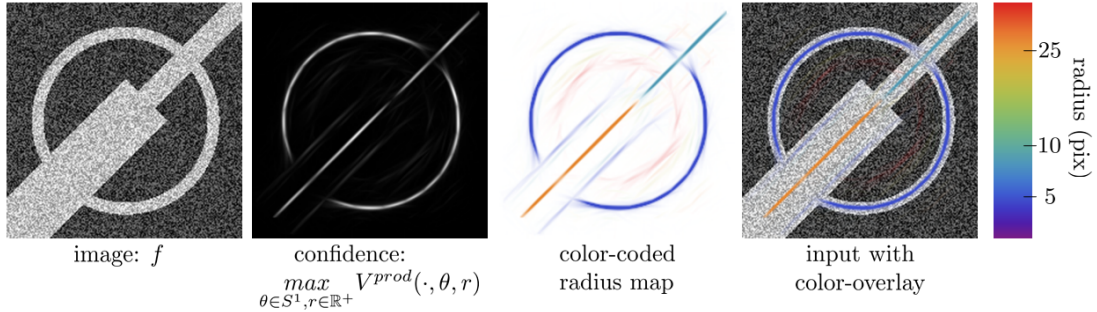


Figure 12.1: From left to right: a test image f ; a maximum intensity projection of the proposed tubularity measure over orientation and radius; a radius map showing in color (see scale on the right) the radius that gave the maximum response; and on the most right the color coded radius map on the input image.

orientation in the domain they also included radius. There, a fast marching method was used to track vessels in a 4D domain using a potential function that has clear similarities (discussed in Subsec. 12.2.1) with the linear measure V^{add} proposed in this chapter. In relation to their tubularity measure only the first two advantages of our method apply.

In Sec. 12.2 we describe the new tubularity measure (Subsec. 12.2.1), compare it to the OOF method (Subsec. 12.2.2), and list some properties of our new method (Subsec. 12.2.3). In Sec. 12.3 we then list some potential application areas, and show with an example that the new tubularity measure allows for pixel wise vessel width measurement and pixel-wise artery vein classification.

12.2 A Tubularity Measure Obtained From the Right-Regular Representation

12.2.1 A Tubularity Measure Obtained from the Right-Regular Representation

The Right-Regular Representation Let $g_\eta(r) \in SE(2)$ be the group element that denotes a translation over a distance r to the left:

$$g_\eta(r) := (0, r, 0). \quad (12.1)$$

Then any point at a distance r to the left of a certain group element $g = (x, y, \theta)$ is obtained by *right*-multiplication

$$R_{g_\eta(r)} g = g g_\eta(r) = (x, y, \theta) (0, r, 0) = (x - r \sin \theta, y + r \cos \theta, \theta),$$

12. VESSEL GEOMETRY II: PIXEL-WISE WIDTH AND A/V

where R_g denotes right-multiplication (cf. (2.39) on page 47). Similar to the left-regular representation (Eq. (2.38)), the right regular representation given by

$$(\mathcal{R}_{g_\eta(r)} U_f)(g) = U_f(R_{g_\eta(r)} g) = U_f(g g_\eta(r)),$$

translates each orientation layer in the orientation score to the *right*.

A Variation of the Edge Detector $\mathcal{A}_2^2 U_f$ The second order derivative can be obtained by a finite central difference limit:

$$(\mathcal{A}_2^2 U_f)(g) = (\mathcal{A}_2(\mathcal{A}_2 U))(g) = \lim_{h \rightarrow 0} \frac{(\mathcal{A}_2 U)(g g_\eta(h)) - (\mathcal{A}_2 U)(g g_\eta(-h))}{2h}, \quad (12.2)$$

with \mathcal{A}_2 the vector field that differentiates in orthogonal line directions (cf. Subsec. 2.3.3), and recall that this is a line/ridge detector. In this section however, we are interested in detecting lines with a certain thickness/radius r . Therefore, in the sequel we propose a variation of this line detector and we will not take this limit but instead consider $h = r > 0$ bounded and away from zero. We will later refer to this variation as the *additive* tubularity measure. On top of this, as vessel boundaries are symmetric around the center line, we need *both* edges to be present, and we shall rely on product filtering rather than difference filtering. This tubularity measure will be referred to as the *product* tubularity measure.

The definition of our tubularity measure is based on combinations of first order edge detections in orientation scores. In the subsequent sections it is therefore convenient to attach suffix e to orientation scores objects to label them as *edge encoding* orientation scores. E.g. an edge encoding orientation score U_f^e can be obtained via

$$U_f^e(g) := (\mathcal{A}_2(\text{Re}(U_f)))(g). \quad (12.3)$$

In Sec. 2.1 of Ch. 2 we saw that the imaginary part of orientation scores constructed with cake wavelets acts as an edge detector, and in Ch. 7 we saw that it can be directly used for tracking of vessel edges. Since the imaginary part of orientation scores has a similar behavior as $\mathcal{A}_2 U$ we can alternatively obtain an edge encoding orientation score via

$$U_f^e(g) = (\text{Im } U_f)(g). \quad (12.4)$$

In fact, this is the function on which the tubularity measure in Chen & Cohen (2014) is based.

A Linear Additive Tubularity Measure Tubular structures are characterized by opposing edges at certain orientations, and the directional derivatives perpendicular to the orientation of the tubular structure have opposite sign at each of the edges. Consider for example the top image in Fig. 12.2, which shows the edge encoding orientation score corresponding to the image of Fig. 12.1. The proposed tubularity measure is based on matching left and right edges by shifting them respectively to the right and left until they overlap, which occurs at the corresponding radius r . We then define our first tubularity measure $V^{add} : SE(2) \times \mathbb{R}^+ \rightarrow \mathbb{R}$ based on this alignment as follows

$$\begin{aligned} V^{add}(g, r) : &= -(\mathcal{R}_{g_\eta(r)} U_f^e)(g) + (\mathcal{R}_{g_\eta(-r)} U_f^e)(g) \\ &= -U_f^{e,r}(g) + U_f^{e,-r}(g), \end{aligned} \quad (12.5)$$

12.2 A Tubularity Measure Obtained From the Right-Regular Representation

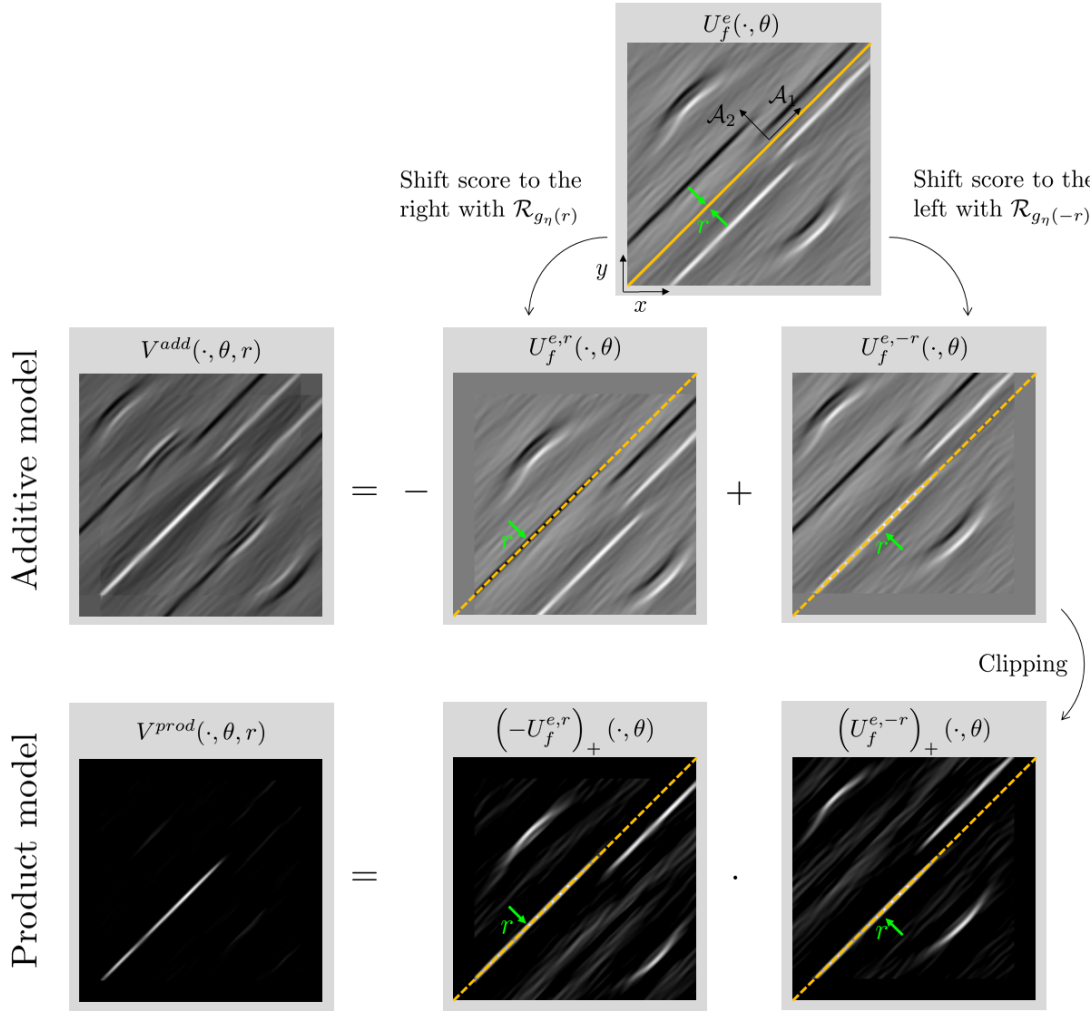


Figure 12.2: Illustration of the construction of tubularity measures $V^{add}(x, y, \theta, r)$ and $V^{prod}(x, y, \theta, r)$ from the input image f of Fig. 12.1 at $\theta = \pi/4$ and $r = 25$. The edge responses encoded in $U_f^e : SE(2) \rightarrow \mathbb{R}$ are shifted towards the center center of the tubular structure)via the right-regular representation \mathcal{R} of the Lie group $SE(2)$), and are combined using either the linear additive model or the non-linear product model.

12. VESSEL GEOMETRY II: PIXEL-WISE WIDTH AND A/V

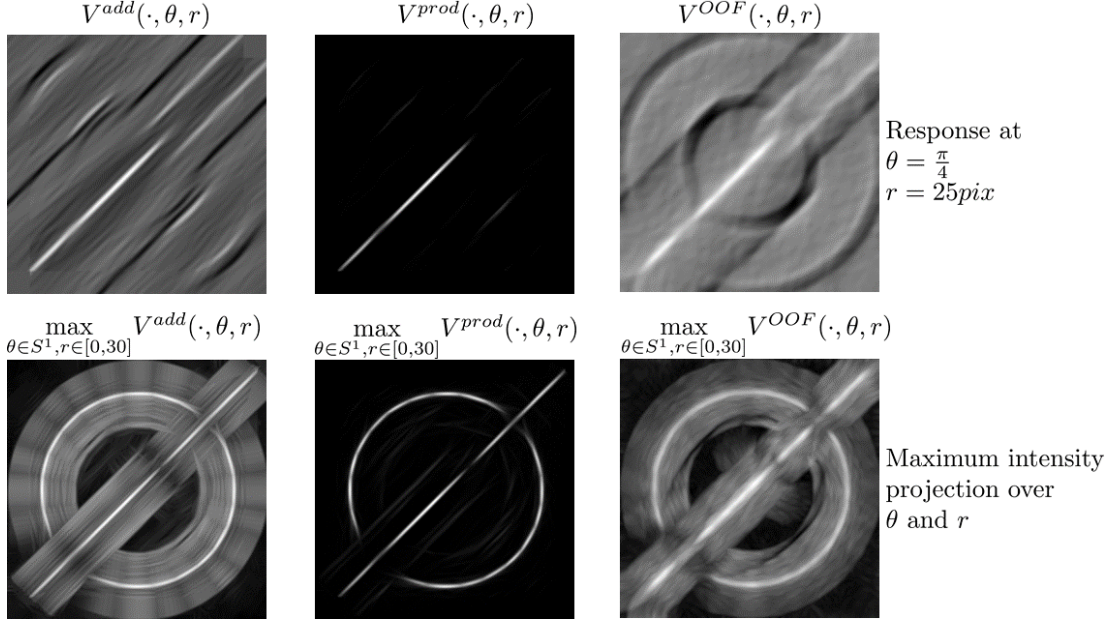


Figure 12.3: A comparison of tubularity measures. Top row from left to right a (x, y) -plane of the linear additive tubularity model V^{add} , the non-linear product tubularity model V^{prod} and the optimally oriented flux tubularity model V^{OOF} for $\theta = \pi/4$ and $r = 25$. Bottom row from left to right the corresponding maximum intensity projections over orientations θ and radii r .

in which we denote an orientation score shifted to the right by r using $U_f^{e,r}(g) := (\mathcal{R}_{g_\eta(r)} U_f^e)(g)$. A minus sign is placed in front of the left edge to account for the difference in sign of the two opposing edges. Thus, for an r that coincides with the actual radius of the tubular structure the measure $V^{add}(g, r)$ has maximum response. For an illustration of this method see the middle row of Fig. 12.2. Note that this model is (up to a scaling factor) equivalent to the finite central difference model given in Eq. (12.2), but then with stepsize $h = r$.

In Chen & Cohen (2014) additional steps are included to construct a tubularity measure which they used in a 4D fast marching algorithm for tubular structure segmentation. There, each orientation plane of the edge encoding orientation score is anisotropically blurred, and only the positive part of their equivalent of V^{add} is used to construct the potential function.

A Non-Linear Product Based Tubularity Measure In our second tubularity model we rely on a product rather than addition. In terms of logic, the product is often used as an *and* operator, and addition as the *or* operator. In such terminology the additive model V^{add} considers only the presence of either one of the edges, whereas the product model which we propose next strictly requires the presence of both edges.

In our next definition we assume that the tubular structures are bright lines on a dark background, due to which the right edges have a positive sign and the left edges have a negative

12.2 A Tubularity Measure Obtained From the Right-Regular Representation

sign (cf. Fig. 12.2). The data that represents the left and right edges are then respectively selected as follows:

$$\begin{aligned} \text{left edges} &\rightarrow \left(-U_f^e \right)_+, \\ \text{right edges} &\rightarrow \left(U_f^e \right)_+, \end{aligned}$$

in which $\left(U_f^e \right)_+(g) = \max\{U_f^e(g), 0\}$. For an illustration see the third image row in Fig. 12.2. The tubularity measure $V^{prod} : SE(2) \times \mathbb{R}^+ \rightarrow \mathbb{R}^+$ is then defined as the product of the two edges shifted towards the center by r :

$$V^{prod}(g, r) := \left(-\mathcal{R}_{g_\eta(r)} U_f^e \right)_+(g) \left(\mathcal{R}_{g_\eta(-r)} U_f^e \right)_+(g). \quad (12.6)$$

When r matches the radius of the tubular structure the edge responses coincide and $V^{prod}(g, r)$ takes a large value, this is illustrated in the last row of Fig. 12.2.

12.2.2 Relation to the Optimally Oriented Flux Filter and the Chen-Cohen Tubularity Measure

The Optimally Oriented Flux Filter In this section we only focus on the practical aspects of the optimally oriented flux filter, and omit theoretical details. For full background and theoretical details we refer to the original paper by Law & Chung (2008), and refer to Benmansour & Cohen (2011) for a theoretical and practical comparison with a Gaussian Hessian based tubularity measure.

Our newly designed tubularity measure has a close relation to the 2D optimally oriented flux filter, which can be defined as

$$\psi_{\theta,r}^{OOF} = (\partial_x^2 G_\sigma \star 1_r)(\mathbf{R}_\theta \mathbf{x}), \quad (12.7)$$

with G_σ a 2D Gaussian function with variance σ , in which \star denotes correlation, and with 1_r the indicator function of a disk of radius r . The OOF filter is thus essentially a rotated version of a second order horizontal Gaussian derivative of the indicator function 1_r of a disk of radius r , and is visualized in Fig. 12.4(a). An OOF based tubularity measure can then be obtained from an image f via

$$V^{OOF}(\mathbf{x}, \theta, r) = (\psi_{\theta,r}^{OOF} \star f)(\mathbf{x}). \quad (12.8)$$

The Filter Corresponding to the Orientation Score Based Additive Tubularity Measure The tubularity measure proposed in (12.6) can also be directly constructed by filtering the image with a family of filters, similar to the OOF based tubularity measure. Let ψ^e be the filter that is used to construct the edge encoding orientation score U_f^e , e.g., let $\psi^e = \text{Im}(\psi)$ be the imaginary part of a cake wavelet. Then the shifted orientation score can be obtained as follows

$$\begin{aligned} U_f^{e,r}(g) &= (\mathcal{R}_{g_\eta(r)} U_f^e)(g) = U_f^e(g g_\eta(r)) = (\mathcal{U}_g g_\eta(r) \psi^e, f)_{\mathbb{L}_2(\mathbb{R}^2)} \\ &= (\mathcal{U}_g \mathcal{U}_{g_\eta(r)} \psi^e, f)_{\mathbb{L}_2(\mathbb{R}^2)} = (\mathcal{U}_g \psi_r^e, f)_{\mathbb{L}_2(\mathbb{R}^2)} = (\psi_{\theta,r}^e \star f)(\mathbf{x}), \end{aligned} \quad (12.9)$$

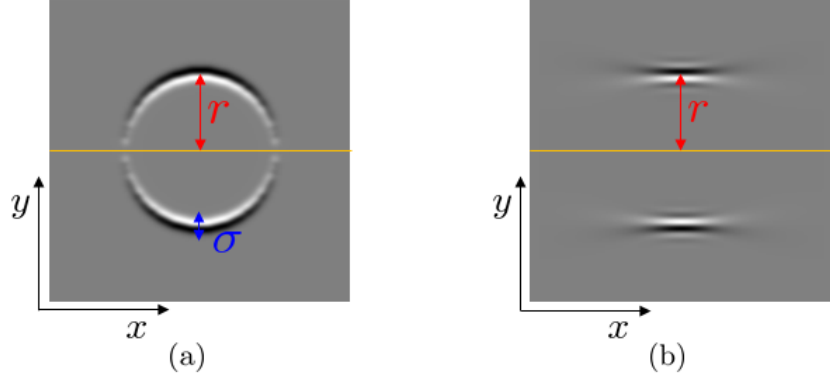


Figure 12.4: (a) The optimally oriented flux filter $\psi_{\theta,r}^{OOF}$ and (b) the cake wavelet based tubularity filter $\psi_{\theta,r}^{cake}$ at $r = 20 \text{ pix}$ and $\theta = 0$.

with \mathcal{U}_g the left-regular representation of $SE(2)$ on \mathbb{R}^2 defined in (2.38) on page 47, recall also that $U_f(\mathbf{x}, \theta) = (\mathcal{U}_{(\mathbf{x}, \theta)}\psi, f)_{\mathbb{L}_2(\mathbb{R}^2)}$. In Eq. (12.9) we define

$$\begin{aligned}\psi_r^e(x, y) &:= \psi^e(x, y - r), \quad \text{and} \\ \psi_{\theta,r}^e(x, y) &:= \psi^e(x - r \sin \theta, y - r \cos \theta).\end{aligned}\tag{12.10}$$

The shifted orientation score $U_f^{e,r}$ can thus be obtained by correlation of the image with the shifted wavelets $\psi_{\theta,r}$. Thus, similar to the OOF based tubularity model, the additive tubularity model V^{add} can also be obtained by linear filtering via

$$\begin{aligned}V^{add}(g, r) &= -(\mathcal{R}_{g_\eta(r)} U_f^e)(g) + (\mathcal{R}_{g_\eta(-r)} U_f^e)(g) = ((-\psi_{\theta,r}^e + \psi_{\theta,-r}^e) \star f)(\mathbf{x}) \\ &= (\psi_{\theta,r}^{cake} \star f)(\mathbf{x}),\end{aligned}\tag{12.11}$$

with $\psi_{\theta,r}^{cake}$ the corresponding linear cake wavelet based tubularity filter, visualized in Fig. 12.4(b), and given by

$$\psi_{\theta,r}^{cake} = -\psi_{\theta,r}^e + \psi_{\theta,-r}^e.\tag{12.12}$$

12.2.3 Some Properties of the New Tubularity Measure

Both $\psi_{\theta,r}^{OOF}$ and $\psi_{\theta,r}^{cake}$ depicted in Fig. 12.4 concentrate around edges at a certain distance r from the centerline. A main difference with our orientation score based approach is that the OOF filter includes curvature (with radius r) in the edge detection, with opposing curvature-sign at each edge. This is remarkable, as one would assume the edges of tubular structures to be more or less parallel, with approximately equal curvature on each side of the curvilinear structure. The cake wavelet based tubularity measure is based on the same parameters as used for construction of orientation scores, which makes the measure flexible and tuneable for different applications. For example, the angular sensitivity s_θ of the filter is controlled by the amount of angular spread of the "piece of cake" in the Fourier domain, see e.g. Fig. 2.4 on page 29, and its scale (or coarseness) can be controlled by the inflection point of the radial envelope

12.3 Applications of the Tubularity Measure

in the Fourier domain, see e.g. Fig. 2.3 on page 26. Note here that instead of blurring the orientation planes of the orientation scores, as is done in the Chen-Cohen method, we prefer to tune this scale parameter instead.

Two crucial differences should be observed when comparing the correlation based construction of V^{add} (Eq. (12.11)) and V^{OOOF} (Eq. (12.8)) with the construction of the non-linear measure V^{prod} (Eq. (12.6)):

1. Due to both phase selection via $(\cdot)_+$ and the multiplication of edge responses in the construction of V^{prod} via Eq. (12.6), the proposed method is highly non-linear. This has the advantage of sharp responses and high contrast at center line locations, see e.g., Fig. 12.3. Additionally, this means that the measure can not be constructed via correlations of the image with a family of filters, which is possible with V^{add} and V^{OOOF} . This is however not a disadvantage due to computational efficiency of the orientation score approach, as we discuss next.
2. The left and right edge encoding orientation scores $(-U_f^e)_+$ and $(U_f^e)_+$ only have to be computed once, and can then be used to obtain the filter response V^{prod} for any r by a basic translation of each orientation plane in the edge encoding scores. In contrast to a linear filtering approach, in which the filter size and thus the computational cost increases with r , the computational cost of the translations are independent of r .

12.3 Applications of the Tubularity Measure

12.3.1 New Biomarkers

In the previous chapter (Ch. 11) we saw that we can construct 2D- (and $SE(2)$ -) feature maps such as orientation confidence s and curvature κ via the analysis of orientation scores. These feature maps were then used to construct weighted histograms and new biomarker definitions based on the weighted average or standard deviation of the pixel-wise curvature measurements. For any arbitrary feature map $f : \mathbb{R}^2 \rightarrow \mathbb{R}$, and any confidence measure $s : \mathbb{R}^2 \rightarrow \mathbb{R}^+$, weighted averages and weighted standard deviations can be computed as follows:

$$\mu_f = \frac{\int_{-\infty}^{\infty} f(\mathbf{x})s(\mathbf{x})d\mathbf{x}}{\int_{-\infty}^{\infty} s(\mathbf{x})d\mathbf{x}}, \quad \sigma_f = \sqrt{\frac{\int_{-\infty}^{\infty} (f(\mathbf{x}) - \mu_f)^2 s(\mathbf{x})d\mathbf{x}}{\int_{-\infty}^{\infty} s(\mathbf{x})d\mathbf{x}}}. \quad (12.13)$$

In Ch. 11 we computed such biomarkers using the following two feature maps:

$$\begin{aligned} \text{Orientation Confidence: } & s^o(\mathbf{x}), \\ \text{Curvature: } & \kappa(\mathbf{x}), \end{aligned} \quad (12.14)$$

with s^o and κ defined in Eq. (11.7). There we also showed that such a weighted average approach to computing average feature values was more stable than binary weighting of feature values (Subsec. 11.4.2). We also showed there that our approach to the computation of curvature

12. VESSEL GEOMETRY II: PIXEL-WISE WIDTH AND A/V

values via the analysis of orientation scores was more stable when compared to a classical approach in which these were computed from segmentations.

Now, using any tubularity measure $V : SE(2) \times \mathbb{R}^+ \rightarrow \mathbb{R}$ we can expand our 2D feature map toolset, and add the following features:

$$\begin{aligned} \text{Tubularity Confidence: } s^t(\mathbf{x}) &= \max_{\theta \in S^1, r \in \mathbb{R}^+} V(\mathbf{x}, \theta, r), \\ \text{Orientation: } \theta^*(\mathbf{x}) &= \operatorname{argmax}_{\theta \in S^1} \max_{r \in \mathbb{R}^+} V(\mathbf{x}, \theta, r), \\ \text{Radius: } r^*(\mathbf{x}) &= \operatorname{argmax}_{r \in \mathbb{R}^+} \max_{\theta \in S^1} V(\mathbf{x}, \theta, r). \end{aligned} \quad (12.15)$$

Furthermore, to each vessel we can also assign a vessel confidence measure using the vessel enhancement techniques discussed in Ch. 6, yielding:

$$\text{Vessel Confidence: } s^v(\mathbf{x}). \quad (12.16)$$

Finally, as we will show in the next example it is possible to use the tubularity based feature maps to also assign to each pixel in the image a confidence measure for it belonging to an artery or a vein, resulting in the following feature maps:

$$\begin{aligned} \text{Artery Confidence: } s^{artery}(\mathbf{x}), \\ \text{Vein Confidence: } s^{vein}(\mathbf{x}). \end{aligned} \quad (12.17)$$

Example 6. Instead of using the edge tracking method developed in Ch. 7, which generated at each iteration k a left and right vessel edge point \mathbf{u}_k and \mathbf{v}_k (recall Fig. 7.4 on page 161), we can now directly compute for each location \mathbf{x} in the image the vessel edge points via

$$\begin{aligned} \mathbf{u}(\mathbf{x}) &= \mathbf{x} + (-r^*(\mathbf{x}) \sin \theta^*(\mathbf{x}), r^*(\mathbf{x}) \cos \theta^*(\mathbf{x})) \\ \mathbf{v}(\mathbf{x}) &= \mathbf{x} - (-r^*(\mathbf{x}) \sin \theta^*(\mathbf{x}), r^*(\mathbf{x}) \cos \theta^*(\mathbf{x})), \end{aligned} \quad (12.18)$$

with the radius map r^* and orientation map θ^* defined in Eq. (12.15). From these edge points it is then possible to construct cross-sectional intensity profiles (recall Fig. 10.1 on page 243). Subsequently, the same Bayesian approach as used in Ch. 10 can then be used to assign to each profile at each location \mathbf{x} a likelihood of it being part of an artery or a vein, for details see Ch. 10. Some results of this pixel-wise artery/vein probability assignment approach are depicted in Fig. 12.5.

The above described set of feature maps allows for a wide range of new biomarker definitions, and in future work we aim to explore such new biomarkers in the analysis of the retinal vasculature in association with disease progression. In Ch. 11 (in particular in Subsec. 11.5.3) we for example saw that it is very relevant to make a distinction between arteries and veins when analyzing geometrical features of the vasculature. In that analysis we for example defined

$$\mu_{|\kappa|}^{vess, artery} = \frac{\int_{-\infty}^{\infty} |\kappa(\mathbf{x})| s(\mathbf{x}) d\mathbf{x}}{\int_{-\infty}^{\infty} s(\mathbf{x}) d\mathbf{x}}, \quad \text{with } s(\mathbf{x}) = s^o(\mathbf{x}) s^{artery}(\mathbf{x}), \quad (12.19)$$

where in that analysis the artery confidence maps s^{artery} were constructed from *manual* labelings. With the tools described in this chapter we will now be able to compute such biomarkers

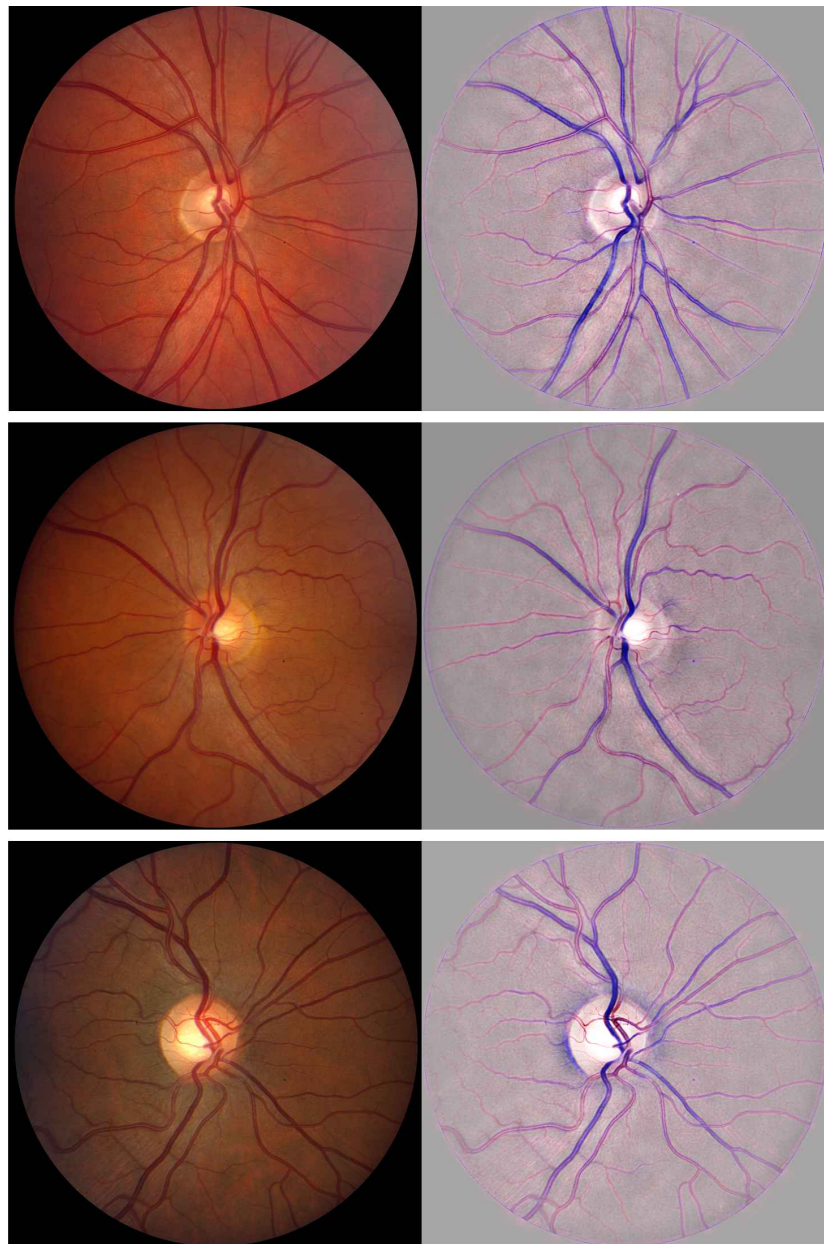


Figure 12.5: Pixel-wise artery/vein probabilities computed on three images of the publicly available INSPIRE-AVR dataset Niemeijer et al. (2011). Left column: the input images. Right column: the artery/vein probabilities as computed using the method described in Example 6. A color RGB image was constructed in which a red channel $s^o(\mathbf{x})s^{artery}(\mathbf{x})$ and a blue channel $s^o(\mathbf{x})s^{vein}(\mathbf{x})$ were added to the original green channel of the image.

12. VESSEL GEOMETRY II: PIXEL-WISE WIDTH AND A/V

fully automatically! This opens doors for (very) large scale clinical studies, using stable (probabilistic) biomarkers obtained via the analysis orientation scores.

12.3.2 Vessel Tracking and Connectivity Analysis

Vessel Tracking in Extended Domains In this thesis we considered the analysis and processing of images by extending the domain with an orientation dimension in an invertible orientation score. One of the main applications was robust vessel center line extraction via the extraction of sub-Riemannian geodesics in the extended domain of positions and orientations.

In other methods for tracking of curvilinear and tubular structures the domain was extended with a radius dimension and tracking was performed on the 3D space of positions and radii Li & Yezzi (2007); Benmansour & Cohen (2011); Chen *et al.* (2016). The idea of tracking tubular structures in a domain extended with a radius dimension was first proposed by Li & Yezzi (2007) and three different (application specific) isotropic metrics on this space were proposed. In Benmansour & Cohen (2011) this approach was later adapted for *anisotropic* metrics which were constructed using the optimally oriented flux filter Law & Chung (2008). In Chen & Cohen (2014); Péchaud *et al.* (2009b) tracking was performed on a domain extended with both an orientation and a radius dimension.

The type of tracking methods discussed above are now also possible with the tubularity measure developed in this chapter. It is worth mentioning, however, that in none of the above cases a sub-Riemannian geometry was employed. An interesting extension of the fast marching approach developed in Ch. 8 would therefore be to construct a 4D (position, orientation, radius) metric tensor which can be described by the following matrix:

$$\mathbf{M}_{\epsilon,tube}(\gamma_{tube}(t)) = \frac{1}{V^{prod}(\gamma_{tube}(t))^2} \begin{pmatrix} 0 & & & \\ \mathbf{M}_\epsilon(\mathbb{P}_{SE(2)}\gamma_{tube}(t)) & 0 & & \\ & 0 & & \\ 0 & 0 & 0 & \xi_4^2 \end{pmatrix}, \quad (12.20)$$

with $\gamma_{tube}(t) = (x(t), y(t), \theta(t), r(t)) \in SE(2) \times \mathbb{R}^1$ the curve in the extended four dimensional domain, with $\mathbb{P}_{SE(2)}\gamma_{tube}(t) = (x(t), y(t), \theta(t)) \in SE(2)$ its projection to $SE(2)$, with \mathbf{M}_ϵ the approximate sub-Riemannian metric tensor on $SE(2)$ defined in Ch. 4 in Eq. (4.11) on page 83, and in which the metric is scaled with the tubularity measure V^{prod} defined in Eq. (12.6). In this new metric the radius dimension is uncoupled from the $SE(2)$ part, and changes in this direction are scaled with ξ_4 . A fast marching approach that employs this metric would directly track data-adaptive horizontal curves (cf. Subsec. 4.2.3) in which change in radius is penalized, and in which curvature is penalized by the approximate sub-Riemannian metric.

Connectivity Analysis In vessel clustering and connectivity analysis in retinal imaging, features like vessel caliber, orientation and curvature are often used to match and disentangle blood vessels at crossings and bifurcations. In this thesis for example orientation and vessel radius information was used for junction resolving in full vasculature tracking (Subsec. 7.4.1.5 in Ch. 7), see (Bekkers, 2012, App. A) for more details. In Favali & Abbasi-Sureshjani *et al.*

(2016) both orientation and pixel intensity consistency were used in a spectral clustering method based on the Fokker-Plank equation (incorporating the sub-Riemannian geometry). In Abbasi-Sureshjani and Favali *et al.* (2016) this spectral clustering method was then extended to clustering of points in a space of positions, orientation, curvature and intensity. In Chen & Cohen (2015) optimal vessel paths were found using an anisotropic 2D Riemannian metric in which color consistency was incorporated to deal with the problem of crossing and nearby vessels of a different artery/vein type. In all of the above intensity consistency was used as a useful feature in connectivity analysis. However, along a vessel the pixel intensities might vary significantly, especially in the presence of vessel central light reflection. A more stable feature instead of pixel intensity could be the pixel-wise artery/vein classification, e.g., using the feature map $s^{artery}(\mathbf{x})$ instead of pixel intensity $f(\mathbf{x})$.

12.4 Conclusion

In the final chapter of this thesis we have proposed a new tubularity measure (Sec. 12.2) and have shown that it can be used to compute new-pixel wise vessel measurements such as vessel width and artery/vein labeling. In Sec. 12.3 we explored new types of retinal image analyses (and extensions of the methods developed in this thesis) that are made possible by considering the analysis of tubularity measures and the feature maps that can be computed from them. Both in vessel tracking and in connectivity analyses the tools presented in this chapter can be most helpful and will be pursued in future work. Motivated by the results of Ch. 11 in which the clinical analyses of biomarkers in population studies showed that it is relevant to consider artery or vein specific features, the main focus of future work will be on the computation and analysis of a wide range of new (artery/vein specific) biomarkers that can now be fully automatically computed.

Part IV

Appendices

Appendix A

Retinal Landmark Detection

A.1 The Smoothing Regularization Matrix \mathbf{R}

When expanding the templates t and T in a finite B-spline basis (Sec. 5.2 and 5.3 of Ch. 5), the energy functionals (5.6), (5.10), (5.27) and (5.29) of Ch. 5 can be expressed in matrix-vector form. The following theorems summarize how to compute the matrix \mathbf{R} , which encodes the smoothing prior, for respectively the \mathbb{R}^2 and $SE(2)$ case.

Lemma 1. *The discrete smoothing regularization-term of energy functional (5.6) can be expressed directly in the B-spline coefficients \mathbf{c} as follows*

$$\iint_{\mathbb{R}^2} \|\nabla t(x, y)\|^2 dx dy = \mathbf{c}^\dagger \mathbf{R} \mathbf{c}, \quad (\text{A.1})$$

with \mathbf{c} given by Eq. (5.15) of Ch. 5, and with

$$\mathbf{R} = \mathbf{R}_x^k \otimes \mathbf{R}_x^l + \mathbf{R}_y^k \otimes \mathbf{R}_y^l, \quad (\text{A.2})$$

a $[N_k N_l \times N_k N_l]$ matrix. The elements of the matrices in (A.2) are given by

$$\begin{aligned} \mathbf{R}_x^k(k, k') &= -\frac{1}{s_k} \frac{\partial^2 B^{2n+1}}{\partial x^2}(k' - k) \\ \mathbf{R}_x^l(l, l') &= s_l B^{2n+1}(l' - l), \\ \mathbf{R}_y^k(k, k') &= s_k B^{2n+1}(k' - k), \\ \mathbf{R}_y^l(l, l') &= -\frac{1}{s_l} \frac{\partial^2 B^{2n+1}}{\partial y^2}(l' - l). \end{aligned} \quad (\text{A.3})$$

Proof. For the sake of readability we divide the regularization-term in two parts:

$$\begin{aligned} \iint_{\mathbb{R}^2} \|\nabla t(x, y)\|^2 dx dy &= \iint_{\mathbb{R}^2} \left| \frac{\partial t}{\partial x}(x, y) \right|^2 + \left| \frac{\partial t}{\partial y}(x, y) \right|^2 dx dy \\ &= \mathcal{R}_x + \mathcal{R}_y, \end{aligned} \quad (\text{A.4})$$

where

$$\begin{aligned} \mathcal{R}_x &= \iint_{\mathbb{R}^2} \left| \frac{\partial t}{\partial x}(x, y) \right|^2 dx dy, \text{ and} \\ \mathcal{R}_y &= \iint_{\mathbb{R}^2} \left| \frac{\partial t}{\partial y}(x, y) \right|^2 dx dy. \end{aligned}$$

A. RETINAL LANDMARK DETECTION

We first derive the matrix-vector representation of \mathcal{R}_x as follows:

$$\begin{aligned}
\mathcal{R}_x &= \iint_{\mathbb{R}^2} \left| \frac{\partial t}{\partial x}(x, y) \right|^2 dx dy \\
&= \sum_{k, k'=1}^{N_k} \sum_{l, l'=1}^{N_l} \iint_{\mathbb{R}^2} \overline{c_{k,l}} \frac{\partial B^n}{\partial x} \left(\frac{x}{s_k} - k \right) B^n \left(\frac{y}{s_l} - l \right) \\
&\quad c_{k,l} \frac{\partial B^n}{\partial x} \left(\frac{x}{s_k} - k' \right) B^n \left(\frac{y}{s_l} - l' \right) dx dy \\
&= \sum_{k, k'=1}^{N_k} \sum_{l, l'=1}^{N_l} \overline{c_{k,l}} c_{k',l'} \\
&\quad \left[\int_{-\infty}^{\infty} \frac{\partial B^n}{\partial x} \left(\frac{x}{s_k} - k \right) \frac{\partial B^n}{\partial x} \left(\frac{x}{s_k} - k' \right) dx \right] \\
&\quad \left[\int_{-\infty}^{\infty} B^n \left(\frac{y}{s_l} - l \right) B^n \left(\frac{y}{s_l} - l' \right) dy \right] \\
&\stackrel{1}{=} \sum_{k, k'=1}^{N_k} \sum_{l, l'=1}^{N_l} \overline{c_{k,l}} c_{k',l'} \left[\frac{1}{s_k} \left(\frac{\partial B^n}{\partial x} * \frac{\partial B^n}{\partial x} \right) (k' - k) \right] \\
&\quad [s_l (B^n * B^n) (l' - l)] \\
&\stackrel{2}{=} \sum_{k, k'=1}^{M} \sum_{l, l'=1}^{N} \overline{c_{k,l}} c_{k',l'} \left[\frac{1}{s_k} \frac{\partial^2 B^{2n+1}}{\partial x^2} (k' - k) \right] \\
&\quad [s_l B^{2n+1} (l' - l)] \\
&= \mathbf{c}^\dagger (\mathbf{R}_x^k \otimes \mathbf{R}_x^l) \mathbf{c}.
\end{aligned} \tag{A.5}$$

Here the following properties are used:

1. The integrals of shifted B-splines can be expressed as convolutions:

$$\begin{aligned}
&\int_{-\infty}^{\infty} \frac{\partial B^n}{\partial x} \left(\frac{x}{s_k} - k \right) \frac{\partial B^n}{\partial x} \left(\frac{x}{s_k} - k' \right) dx \\
&= -\frac{1}{s_k} \int_{-\infty}^{\infty} \frac{\partial B^n}{\partial u} (u) \frac{\partial B^n}{\partial u} ((k' - k) - u) du = -\frac{1}{s_k} \left(\frac{\partial B^n}{\partial u} * \frac{\partial B^n}{\partial u} \right) (k' - k).
\end{aligned}$$

This is easily verified by substitution of integration variable ($u = -\frac{x}{s_k} + k$) and noting that $B^n(x) = B^n(-x)$ and $\frac{\partial B^n}{\partial x}(x) = -\frac{\partial B^n}{\partial x}(-x)$.

2. Convolution of two B-splines B^n of order n yields:

$$B^n * B^n = B^{2n+1}.$$

The elements of the matrices R_y^k and R_y^l are derived in a similar manner. \square

As a result of Lemma 1 we can state the following.

Corollary 1. Let $V = \text{span}\{B_{k,l}^n\}$, with $k = 1, \dots, N_k, l = 1, \dots, N_l$, and shifted B-splines $B_{k,l}^n$ of order n . Let the energy function $E_{lin}^B : \mathbb{R}^{N_k N_l} \rightarrow \mathbb{R}^+$ be given by Eq. (5.12) of Ch. 5. Then the optimal continuous template of the constrained optimization problem (cf. Eq. (5.6) of Ch. 5)

$$t^* = \underset{t \in V}{\operatorname{argmin}} E_{lin}(t)$$

A.1 The Smoothing Regularization Matrix \mathbf{R}

has coefficients \mathbf{c}^* w.r.t. the B-spline basis for V , that are the unique solution of

$$\nabla_{\mathbf{c}} E_{lin}^B(\mathbf{c}^*) = \mathbf{0},$$

which boils down to Eq. (5.13) of Ch. 5.

Lemma 2. *The discrete regularization-term of energy functional (5.27) of Ch. 5 can be expressed directly in the B-spline coefficients:*

$$\iiint_{SE(2)} \|\nabla T\|_D \, dx dy d\theta = \mathbf{c}^T (D_{11}\mathbf{R}_1 + D_{22}\mathbf{R}_2 + D_{33}\mathbf{R}_3)\mathbf{c}. \quad (\text{A.6})$$

Matrix \mathbf{R}_1 is given by

$$\begin{aligned} \mathbf{R}_1 = & \left(\mathbf{R}_1^{Ix} \otimes \mathbf{R}_1^{Iy} \otimes \mathbf{R}_1^{I\theta} \right) + \left(\mathbf{R}_1^{IIx} \otimes \mathbf{R}_1^{Ily} \otimes \mathbf{R}_1^{I\theta} \right) \\ & + \left(\mathbf{R}_1^{IIIx} \otimes \mathbf{R}_1^{IIly} \otimes \mathbf{R}_1^{I\theta} \right) + \left(\mathbf{R}_1^{IVx} \otimes \mathbf{R}_1^{IVy} \otimes \mathbf{R}_1^{IV\theta} \right) \end{aligned} \quad (\text{A.7})$$

with the elements of the matrices used in the Kronecker products given by

$$\begin{aligned} \mathbf{R}_1^{Ix}(k, k') &= -\frac{1}{s_k} \frac{\partial^2 B^{2n+1}}{\partial x^2}(k' - k), \\ \mathbf{R}_1^{Iy}(l, l') &= s_l B^{2n+1}(l' - l), \\ \mathbf{R}_1^{I\theta}(m, m') &= \int_0^\pi \cos^2(\theta) B^n\left(\frac{\theta}{s_m} - m\right) B^n\left(\frac{\theta}{s_m} - m'\right) d\theta, \end{aligned} \quad (\text{A.8})$$

$$\begin{aligned} \mathbf{R}_1^{IIx}(k, k') &= -\mathbf{R}_1^{IIIx}(k, k') = \frac{\partial B^{2n+1}}{\partial x}(k' - k), \\ \mathbf{R}_1^{Ily}(l, l') &= -\mathbf{R}_1^{IIly}(l, l') = -\frac{\partial B^{2n+1}}{\partial y}(l' - l), \\ \mathbf{R}_1^{I\theta}(m, m') &= \mathbf{R}_1^{III\theta}(m, m') = \int_0^\pi \cos(\theta) \sin(\theta) B^n\left(\frac{\theta}{s_m} - m\right) B^n\left(\frac{\theta}{s_m} - m'\right) d\theta, \end{aligned} \quad (\text{A.9})$$

$$\begin{aligned} \mathbf{R}_1^{IVx}(k, k') &= s_k B^{2n+1}(k' - k), \\ \mathbf{R}_1^{IVy}(l, l') &= -\frac{1}{s_l} \frac{\partial^2 B^{2n+1}}{\partial y^2}(l' - l), \\ \mathbf{R}_1^{IV\theta}(m, m') &= \int_0^\pi \sin^2(\theta) B^n\left(\frac{\theta}{s_m} - m\right) B^n\left(\frac{\theta}{s_m} - m'\right) d\theta. \end{aligned} \quad (\text{A.10})$$

Matrix \mathbf{R}_2 is given by

$$\begin{aligned} \mathbf{R}_2 = & \left(\mathbf{R}_1^{Ix} \otimes \mathbf{R}_1^{Iy} \otimes \mathbf{R}_1^{IV\theta} \right) - \left(\mathbf{R}_1^{Ix} \otimes \mathbf{R}_1^{Ily} \otimes \mathbf{R}_1^{I\theta} \right) \\ & - \left(\mathbf{R}_1^{IIIx} \otimes \mathbf{R}_1^{IIly} \otimes \mathbf{R}_1^{I\theta} \right) + \left(\mathbf{R}_1^{IVx} \otimes \mathbf{R}_1^{IVy} \otimes \mathbf{R}_1^{I\theta} \right). \end{aligned} \quad (\text{A.11})$$

Matrix \mathbf{R}_3 is given by

$$\mathbf{R}_3 = (\mathbf{R}_3^x \otimes \mathbf{R}_3^y \otimes \mathbf{R}_3^\theta), \quad (\text{A.12})$$

with the elements of the matrices given by

$$\begin{aligned} \mathbf{R}_3^x(k, k') &= s_k B^{2n+1}(k' - k), \\ \mathbf{R}_3^y(l, l') &= s_l B^{2n+1}(l' - l), \\ \mathbf{R}_3^\theta(m, m') &= -\frac{1}{s_m} \frac{\partial^2 B^{2n+1}}{\partial \theta^2}(m' - m). \end{aligned} \quad (\text{A.13})$$

A. RETINAL LANDMARK DETECTION

Proof. The proof of Lemma 2 follows the same steps as in the proof of Lemma 1, only here left-invariant derivatives are used. The four separate terms $I - IV$ of Eq. (A.7) arise from the left invariant derivative \mathcal{A}_1 : $|\mathcal{A}_1 T|^2 = \left| \cos(\theta) \frac{\partial T}{\partial x} + \sin(\theta) \frac{\partial T}{\partial y} \right|^2$. \square

Corollary 2. Let $V = \text{span}\{B_{k,l,m}^n\}$, with $k = 1, \dots, N_k, l = 1, \dots, N_l, m = 1, \dots, N_m$, and shifted B-splines $B_{k,l,m}^n$ of order n . Let the energy function $\mathcal{E}_{lin}^B : \mathbb{R}^{N_k N_l N_m} \rightarrow \mathbb{R}^+$ be given by

$$\mathcal{E}_{lin}^B(\mathbf{c}) = \frac{1}{N} \|\mathbf{Sc} - \mathbf{y}\|^2 + \mathbf{c}^\dagger (\lambda \mathbf{R} + \mu \mathbf{I}) \mathbf{c}$$

With \mathbf{S} and \mathbf{y} given by (5.32) of Ch. 5 and with $\mathbf{R} = D_{11}\mathbf{R}_1 + D_{22}\mathbf{R}_2 + D_{33}\mathbf{R}_3$ given in Lemma 2. Then the optimal continuous template of the constrained optimization problem (cf. Eq. (5.27) of Ch. 5)

$$T^* = \underset{T \in V}{\operatorname{argmin}} \mathcal{E}_{lin}(T)$$

has coefficients \mathbf{c}^* w.r.t. the B-spline basis for V that are the unique solution of

$$\nabla_{\mathbf{c}} \mathcal{E}_{lin}^B(\mathbf{c}^*) = \mathbf{0}.$$

This boils down to Eq. (5.13) of Ch. 5, but then on $\mathbb{R}^{N_k N_l N_m}$.

A.2 Normalized Cross Correlation

In most applications it is necessary to make the detection system invariant to local contrast and luminosity changes. In our template matching framework this can either be achieved via certain pre-processing steps that filter out these variations, or by means of normalized cross-correlation. In normalized cross-correlation, both the template as well as the image are (locally) normalized to zero mean and unit standard deviation (with respect to the inner product used in the cross-correlations). In this section, we explain the necessary adaptations to extend the standard cross-correlation based framework to normalized cross-correlations.

A.2.1 Normalized Cross-Correlation in \mathbb{R}^2

In the usual cross-correlation based template matching approach, as described in Sec. 5.2 of Ch. 5, we rely on the standard $\mathbb{L}_2(\mathbb{R}^2)$ inner product. In normalized cross-correlation it is however convenient to extend this inner product to include a windowing function m which indicates the relevant region (support) of the template. As such, the inner product with respect to windowing function m is given by

$$(t, f)_{\mathbb{L}_2(\mathbb{R}^2, md\tilde{x})} := \int_{\mathbb{R}^2} \overline{t(\tilde{x})} f(\tilde{x}) m(\tilde{x}) d\tilde{x}, \quad (\text{A.14})$$

with associated norm $\|\cdot\|_{\mathbb{L}_2(\mathbb{R}^2, md\tilde{x})} = \sqrt{(\cdot, \cdot)_{\mathbb{L}_2(\mathbb{R}^2, md\tilde{x})}}$. The windowing function has to be a smooth function $m : \mathbb{R}^2 \rightarrow \mathbb{R}^+$ with $\int_{\mathbb{R}^2} m(\tilde{x}) d\tilde{x} = 1$. In this work, the use of a window m

A.2 Normalized Cross Correlation

is also convenient to deal with boundary conditions in the optimization problems for template construction. We define

$$m(\mathbf{x}) := \varsigma e^{-\frac{\|\mathbf{x}\|^2}{s}} \sum_{i=0}^n \frac{(\|\mathbf{x}\|^2/s)^i}{i!}, \quad (\text{A.15})$$

which smoothly approximates the indicator function $1_{[0,r]}(\|\mathbf{x}\|)$, covering a disk with radius r , when setting $s = \frac{2r^2}{1+2n}$, see e.g. (Bekkers *et al.*, 2014a, Fig. 2). The constant ς normalizes the function such that $\int_{\mathbb{R}^2} m(\tilde{\mathbf{x}}) d\tilde{\mathbf{x}} = 1$.

In normalized cross-correlation the image is locally normalized (at position \mathbf{x}) to zero mean and unit standard deviation, which is done as follows

$$\hat{f}_{\mathbf{x}}(\tilde{\mathbf{x}}) := \frac{f(\tilde{\mathbf{x}}) - \langle f \rangle_{\mathcal{T}_{\mathbf{x}} m}}{\|f(\tilde{\mathbf{x}}) - \langle f \rangle_{\mathcal{T}_{\mathbf{x}} m}\|_{L_2(\mathbb{R}^2, \mathcal{T}_{\mathbf{x}} m d\tilde{\mathbf{x}})}}, \quad (\text{A.16})$$

with local mean $\langle f \rangle_m = (1, f)_{L_2(\mathbb{R}^2, m d\tilde{\mathbf{x}})}$. Template \hat{t} can be obtained via normalization of a given template t via

$$\hat{t}(\tilde{\mathbf{x}}) := \frac{t(\tilde{\mathbf{x}}) - \langle t \rangle_m}{\|t(\tilde{\mathbf{x}}) - \langle t \rangle_m\|_{L_2(\mathbb{R}^2, m d\tilde{\mathbf{x}})}}. \quad (\text{A.17})$$

Template matching is then done in the usual way (via (5.3) of Ch. 5), however now \hat{t} and $\hat{f}_{\mathbf{x}}$ are used instead of t and f . In fact, the entire \mathbb{R}^2 cross-correlation template matching and template optimization framework is extended to normalized cross-correlation by substituting all instances of t with \hat{t} , f with $\hat{f}_{\mathbf{x}}$, and $(\cdot, \cdot)_{L_2(\mathbb{R}^2)}$ with $(\cdot, \cdot)_{L_2(\mathbb{R}^2, m d\tilde{\mathbf{x}})}$. However, since templates \hat{t} are directly constructed via the minimization of energy functionals, we will not explicitly normalize the templates, unless they are obtained by other methods. E.g., Eq. (A.17) is used in the main chapter to construct basic templates obtained by averaging positive object patches.

A.2.2 Normalized Cross-Correlation in $SE(2)$

Similar to the \mathbb{R}^2 case, templates and orientation scores are locally normalized to zero mean and unit standard deviation, however, now with respect to the $L_2(SE(2), M d\tilde{g})$ inner product, which is given by

$$(T, U_f)_{L_2(SE(2), M d\tilde{g})} := \int_{\mathbb{R}^2} \int_0^{2\pi} \overline{T(\tilde{\mathbf{x}}, \tilde{\theta})} U_f(\tilde{\mathbf{x}}, \tilde{\theta}) M(\tilde{\mathbf{x}}, \tilde{\theta}) d\tilde{\mathbf{x}} d\tilde{\theta}, \quad (\text{A.18})$$

with norm $\|\cdot\|_{L_2(SE(2), M d\tilde{g})} = \sqrt{(\cdot, \cdot)_{L_2(SE(2), M d\tilde{g})}}$. Also here windowing function M indicates the support of the template, and has the property $\int_{\mathbb{R}^2} \int_0^{2\pi} M(\tilde{\mathbf{x}}, \tilde{\theta}) d\tilde{\mathbf{x}} d\tilde{\theta} = 1$. We define

$$M(\mathbf{x}, \theta) := \frac{1}{2\pi} m(\mathbf{x}), \quad (\text{A.19})$$

independent of θ , with $m(\mathbf{x})$ given by (A.15), and with front factor $\frac{1}{2\pi}$ such that it integrates to 1.

A. RETINAL LANDMARK DETECTION

The (locally at g) normalized orientation score and template T are then given by

$$\hat{U}_{f,g}(\tilde{\mathbf{x}}, \tilde{\theta}) := \frac{U_f(\tilde{\mathbf{x}}, \tilde{\theta}) - \langle U_f \rangle_{\mathcal{L}_g M}}{\|U_f(\tilde{\mathbf{x}}, \tilde{\theta}) - \langle U_f \rangle_{\mathcal{L}_g M}\|_{\mathbb{L}_2(SE(2), \mathcal{L}_g M d\tilde{g})}}, \quad (\text{A.20})$$

$$\hat{T}(\tilde{\mathbf{x}}, \tilde{\theta}) := \frac{T(\tilde{\mathbf{x}}, \tilde{\theta}) - \langle T \rangle_M}{\|T(\tilde{\mathbf{x}}, \tilde{\theta}) - \langle T \rangle_M\|_{\mathbb{L}_2(SE(2), M d\tilde{g})}}, \quad (\text{A.21})$$

with mean $\langle U_f \rangle_M = (1, U_f)_{\mathbb{L}_2(SE(2), M d\tilde{g})}$.

A.2.3 Efficient Local Normalization of $\hat{f}_{\mathbf{x}}$ and $\hat{U}_{f,g}$.

Since the normalized image $\hat{f}_{\mathbf{x}}$ depends on the location \mathbf{x} it needs to be calculated for every translation of the template, which makes normalized cross-correlation computationally expensive. Therefore, (A.16) can be approximated by assuming that the local average is approximately constant in the area covered by m . That is, assuming $\langle f \rangle_{\mathcal{T}_{\mathbf{x}} m}(\tilde{\mathbf{x}}) \approx \langle f \rangle_{\mathcal{T}_{\tilde{\mathbf{x}}} m}(\tilde{\mathbf{x}}) = (m \star f)(\tilde{\mathbf{x}})$ for $\|\tilde{\mathbf{x}} - \mathbf{x}\| < r$, with r the radius that determines the extent of m , (A.16) is approximated as follows:

$$\hat{f}_{\mathbf{x}}(\tilde{\mathbf{x}}) \approx \frac{f(\tilde{\mathbf{x}}) - (m \star f)(\tilde{\mathbf{x}})}{\sqrt{(m \star (f - (m \star f))^2)(\tilde{\mathbf{x}})}}. \quad (\text{A.22})$$

Similarly, in the $SE(2)$ -case (A.20) can be approximated via

$$\hat{U}_{f,g}(\tilde{\mathbf{x}}, \tilde{\theta}) \approx \frac{U_f(\tilde{\mathbf{x}}, \tilde{\theta}) - (M \star_{SE(2)} U_f)(\mathbf{x}, \tilde{\theta})}{\sqrt{(M \star_{SE(2)} (U_f - (M \star_{SE(2)} U_f))^2)(\mathbf{x}, \tilde{\theta})}}. \quad (\text{A.23})$$

A.2.4 Including a Region of Interest Mask

Depending on the application, large portions of the image might be masked out. This for example is the case in retinal images (see circular masks in Fig. 5.7). To deal with this, template matching is only performed inside the region of interest defined by a mask image $m^{roi} : \mathbb{R}^2 \rightarrow \{0, 1\}$. Including such a mask is important in normalized template matching, and can be done by replacing the standard inner products by

$$(t, f)_{\mathbb{L}_2(\mathbb{R}^2, m, d\tilde{\mathbf{x}})}^{roi} := \frac{(t, f m^{roi})_{\mathbb{L}_2(\mathbb{R}^2, m, d\tilde{\mathbf{x}})}}{(1, m^{roi})_{\mathbb{L}_2(\mathbb{R}^2, m, d\tilde{\mathbf{x}})}}, \quad (\text{A.24})$$

$$(T, U_f)_{\mathbb{L}_2(SE(2), M, d\tilde{g})}^{roi} := \frac{(T, U_f M^{roi})_{\mathbb{L}_2(SE(2), M, d\tilde{g})}}{(1, M^{roi})_{\mathbb{L}_2(SE(2), M, d\tilde{g})}}, \quad (\text{A.25})$$

with $M^{roi}(\mathbf{x}, \theta) = m^{roi}(\mathbf{x})$.

A.3 Additional Details on the Detection Problems

Table A.1: Average processing times. For optic nerve head detection (ONH) the average is taken over 1529 images of the TC, MESSIDOR, DRIVE and STARE database. For fovea detection the average is taken over 1408 images of the TC and MESSIDOR database. For pupil detection the average is taken over 1521 images of the BioID database.

	ONH		Fovea		Pupil (left & right)	
	\mathbb{R}^2	$SE(2)$	\mathbb{R}^2	$SE(2)$	\mathbb{R}^2	$SE(2)$
Timings (ms)						
1. Rescaling	106	106	111	111	0	0
2. \mathbb{R}^2 -Processing	66	66	64	64	71	71
3. OS Transform	0	108	0	108	0	121
4. $SE(2)$ -Processing	0	5	0	5	0	6
5. Template Matching	20	195	19	190	26	116
Total	192	479	195	477	97	313
Combined Total Timings (ms) - \mathbb{R}^2 and $SE(2)$						
	497		501		420	
Combined Total Timings (ms) - Fovea and ONH						
	730					

A.3 Additional Details on the Detection Problems

In this section we describe additional details about the implementation and results of the three detection problems discussed in Ch. 5.

A.3.1 Processing Pipeline, Settings and Timings

A.3.1.1 Processing Pipeline

In all three applications the same processing pipeline was used. The pipeline can be divided into the following 5 steps:

1. *Resizing.* Each input image is resized to a certain operating resolution and cropped to remove large regions with value 0 (outside the field of view mask in retinal images, see e.g. Fig. 5.7). The retinal images are resized such that the pixel size was approximately $40\mu m/pix$. In the pupil detection application no rescaling or cropping was done.

A. RETINAL LANDMARK DETECTION

2. \mathbb{R}^2 -*Processing.* In all three applications we applied a local intensity and contrast normalization step using an adaptation of Foracchia *et al.* (2005) which we explain below. The locally normalized image \hat{f} is then mapped through an error function via $\text{erf}(8\hat{f})$ to suppress outliers.
3. *Orientation score transform.* The processed image is then taken as input for an orientation score transform. For the oriented wavelets we used cake wavelets Bekkers *et al.* (2014a); Duits *et al.* (2007b) of size $[51 \times 51]$ and with angular resolution $s_\theta = \pi/12$, and with sampling θ from 0 to π .
4. *SE(2)-Processing.* For phase-invariant, nonlinear, left-invariant Duits & Franken (2010a), and contractive Bruna & Mallat (2013) processing on $\text{SE}(2)$, we work with the modulus of the complex valued orientation scores rather than with the complex-valued scores themselves (taking the modulus of quadrature filter responses is an effective technique for line detection, see e.g. Freeman *et al.* Freeman & Adelson (1991)).
5. *Template Matching.* Finally we perform template matching using respectively Eqs. (5.2),(5.3) and (5.4) for the \mathbb{R}^2 case and Eqs. (5.2),(5.23) and (5.24) of Ch. 5 for the $\text{SE}(2)$ case.

Regarding the image resolutions (step 1) we note that the average image size after rescaling was $[300 \times 300]$. The average image resolutions in each database were as follows:

- *ES (SLO)* contained images of average resolution $13.9\mu\text{m}/\text{pix}$.
- *TC* contained images of average resolution $9.4\mu\text{m}/\text{pix}$.
- *MESSIDOR* contained images of 3 cameras with average resolutions $13.6\mu\text{m}/\text{pix}$, $9.1\mu\text{m}/\text{pix}$ and $8.6\mu\text{m}/\text{pix}$.
- *DRIVE* contained images of average resolution $21.9\mu\text{m}/\text{pix}$.
- *STARE* contained images of average resolution $17.6\mu\text{m}/\text{pix}$.

Regarding local image normalization (step 2) we note the following. Local image normalization was done using an adaptation of Foracchia *et al.* (2005). The method first computes a local average and standard deviation of pixel intensities, and the image is locally normalized to zero mean and unit standard deviation. This is done via Eq. (A.22). Then a background mask is constructed by setting pixels with a larger distance than 1 standard deviation to the average (Mahalanobis distance) to 0, and other pixels to 1. This mask is then used to ignore outliers in a second computation of the local average and standard deviation. The final normalized image is again computed via Eq. (A.22) but now with the inclusion of the background mask, see Eq. (A.24).

A.3.1.2 Template Settings

In the retinal applications we used \mathbb{R}^2 templates of size $[N_x \times N_y] = [251 \times 251]$ which were covered by a grid of B-spline basis functions of size $[N_k \times N_l] = [51 \times 51]$, the $\text{SE}(2)$ templates

A.3 Additional Details on the Detection Problems

were of size $[N_x \times N_y \times N_\theta] = [251 \times 251 \times 12]$ and were covered by a grid of B-spline basis functions of size $[N_k \times N_l \times N_m] = [51 \times 51 \times 12]$.

In the pupil detection application we used \mathbb{R}^2 templates of size $[N_x \times N_y] = [101 \times 101]$ which were also covered by a grid of B-spline basis functions of size $[N_k \times N_l] = [51 \times 51]$, the $SE(2)$ templates were of size $[N_x \times N_y \times N_\theta] = [101 \times 101 \times 12]$ and were also covered by a grid of B-spline basis functions of size $[N_k \times N_l \times N_m] = [51 \times 51 \times 12]$.

A.3.1.3 Timings

We computed the average time for detecting one (or two) object(s) in an image and tabulated the results in Tab. A.1. Here we sub-divided the timings into the 5 processing steps explained in Subsec. A.3.1.1. The average (full) processing time on the retinal images was in both applications approximately 500ms. When both the ONH and fovea are detected by the same processing pipeline the processing took 730ms. For pupil detection the average time to detect *both* the left and right pupil on the *full* images was 420ms.

The retinal images were on average of size $[1230 \times 1792]$, and $[300 \times 300]$ after cropping and resizing. The images in the pupil detection application were not resized or cropped and were of size $[286 \times 384]$.

All experiments were performed using Wolfram *Mathematica* 10.4, on a computer with an Intel Core i703612QM CPU and 8GB memory. Here we note that in the retinal image datasets the maximum template response always occurs at rotation $\alpha = 0$, so for the sake of reduced computation time we have set $P^{SE(2)}(\mathbf{x}) := \hat{P}^{SE(2)}(\mathbf{x}, 0)$ instead of Eq. (5.22) of Ch. 5. In the pupil detection application we also make this assumption, however, we remark that detection performance could slightly be improved with the inclusion of a certain search range for α . (see also Subsec. 5.5.4.3).

Appendix B

Vessel Tracking Part I: Iterative Tracking via Local Optimization

This appendix is based on joint work with Remco Duits, Tos Berendschot, and Bart ter Haar Romeny, cf. Bekkers *et al.* (2014a), and provides a mathematical underpinning of our method for vessel tracking via local optimization in transversal tangent planes in $SE(2)$, as described in Ch. 7. Here, in particular Remco Duits is gratefully acknowledged for his theoretical contributions.

B.1 A Mathematical Underpinning of Optimization in the Tangent Planes \mathcal{V}

B.1.1 Geometrical Principle Behind the ETOS-algorithm

The ETOS-algorithm presented in Section 7.3.1.1 heavily relies on local optimization in each transversal 2D-tangent plane $\mathcal{V} = \text{span}\{\mathcal{A}_2, \mathcal{A}_3\}$ spanned by $\mathcal{A}_2 = -\sin \theta \partial_x + \cos \theta \partial_y$ and $\mathcal{A}_3 = \partial_\theta$ in tangent-bundle $T(SE(2))$.

To this end we recall Fig. 7.3 where one can observe that each tangent vector to the lifted curve $s \mapsto (x(s), y(s), \theta(s))$ with $\theta(s) = \arg(\dot{x}(s) + i\dot{y}(s))$ (e.g. the curve following the right edge of a blood vessel) in $SE(2)$ is pointing orthogonal to a plane \mathcal{V} (plotted in yellow). Within \mathcal{V} we see that the maximum values of the absolute value of the imaginary part of the score is located at the origin of the yellow plane in the tangent space.

Definition 2. *A smooth curve $s \mapsto \gamma(s) = (x(s), y(s), \theta(s))$ in $SE(2)$ is called the lifted curve of a smooth planar curve iff for all $s \in [0, \ell]$ we have $\theta(s) = \arg(\dot{x}(s) + i\dot{y}(s))$.*

Definition 3. *If a curve γ is equal to the lift of its spatial projection (i.e. if its satisfies Eq. (B.1)) it is called horizontal.*

B. VESSEL TRACKING PART I: ITERATIVE TRACKING VIA LOCAL OPTIMIZATION

Tangent vectors to horizontal curves always lay in the tangent plane $\Delta = \text{span}\{\mathcal{A}_1, \mathcal{A}_3\}$, spanned by \mathcal{A}_1 and \mathcal{A}_3 , since one has

$$\theta(s) = \arg(\dot{x}(s) + i\dot{y}(s)) \Leftrightarrow \dot{\gamma}(s) \in \text{span}\{\mathcal{A}_1|_{\gamma(s)}, \mathcal{A}_3|_{\gamma(t)}\} = \Delta|_{\gamma(t)}. \quad (\text{B.1})$$

In this appendix we will underpin and discuss our fundamental venture point: The most salient curves in the smooth imaginary part/real part/absolute value $C : SE(2) \rightarrow \mathbb{R}$ of the smooth orientation score $U : SE(2) \rightarrow \mathbb{C}$ are given by

$$\gamma \text{ is horizontal such that } (\mathcal{A}_3|_{\gamma} C)(\gamma) = 0 \text{ and } (\mathcal{A}_2|_{\gamma} C)(\gamma) = 0.$$

The intuitive idea behind this is as follows. Let $C : SE(2) \mapsto \mathbb{R}^+$ denote an a priori given cost. Now, if a horizontal curve $s \mapsto \gamma(s) := (\mathbf{x}(s), \theta(s))$ satisfies

$$\begin{aligned} (\mathcal{A}_2 C)(\mathbf{x}(s), \theta(s)) &= (-\sin \theta(s) \partial_x C + \cos \theta \partial_y C)(\mathbf{x}(s), \theta(s)) \\ &= (\mathcal{A}_3 C)(\mathbf{x}(s), \theta(s)) = 0 \end{aligned} \quad (\text{B.2})$$

with $\mathcal{A}_2^2 C(\mathbf{x}(s), \theta(s)) < 0$ and $\mathcal{A}_3^2 C(\mathbf{x}(s), \theta(s)) < 0$, then there is no gain in moving¹ the curve $s \mapsto \gamma(s) = (\mathbf{x}(s), \theta(s))$ in directions orthogonal to the spatial propagation vector $\mathcal{A}_1|_{\gamma(s)} = \cos \theta(s) \partial_x + \sin \theta(s) \partial_y$.

In fact, we expect the curve $\gamma(s) = (\mathbf{x}(s), \theta(s))$ satisfying (B.2) to be optimal in some sense within the sub-Riemannian manifold

$$M = (SE(2), \Delta, \mathcal{G}_0^{\xi, \mathcal{C}=1})$$

with metric tensor $\mathcal{G}_0^{\xi, \mathcal{C}=1} : SE(2) \times \Delta \times \Delta \rightarrow \mathbb{R}$ given by

$$\mathcal{G}_0^{\xi, \mathcal{C}=1}|_{(x,y,\theta)} = d\theta \otimes d\theta + \xi^2 (\cos \theta dx + \sin \theta dy) \otimes (\cos \theta dx + \sin \theta dy), \quad (\text{B.3})$$

where \otimes denotes the tensor product. Note that this metric tensor is the same as the sub-Riemannian metric tensor $\mathcal{G}_0^{\xi, \mathcal{C}}$ defined in (4.7), but without an external cost, i.e., $\mathcal{C} = 1$ (not to be confused with C). Note also that

$$\begin{aligned} (\cos \theta dx + \sin \theta dy)(\dot{\gamma}(s)) &= \dot{x}(s) \cos \theta(s) + \dot{y}(s) \sin \theta(s) \\ &\Rightarrow \\ \mathcal{G}_0^{\xi, \mathcal{C}=1}(\dot{\gamma}(s), \dot{\gamma}(s)) &= \xi^2 |\cos \theta(s) \dot{x}(s) + \sin \theta(s) \dot{y}(s)|^2 + |\dot{\theta}(s)|^2. \end{aligned}$$

If s equals arclength (i.e. we have $\|\dot{\mathbf{x}}(s)\|^2 = 1$) of the spatial part $s \mapsto \mathbf{x}(s) = (x(s), y(s))$ of the horizontal curve $s \mapsto \gamma(s) = (\mathbf{x}(s), \theta(s))$ we have $\kappa^2(s) = |\dot{\theta}(s)|^2$, so that

$$\|\dot{\gamma}(s)\| = \sqrt{\mathcal{G}_0^{\xi, \mathcal{C}=1}(\dot{\gamma}(s), \dot{\gamma}(s))} = \sqrt{\kappa^2(s) + \xi^2}. \quad (\text{B.4})$$

Intuitively, such a sub-Riemannian manifold M equals the group $SE(2)$ where one restricts oneself to horizontal curves with a constant relative penalty for bending and stretching determined by $\xi > 0$ which has physical dimension one over length.

For special cases of C we can show that our geometrical principle for local optimality indeed produces optimal curves in $SE(2)$, as we will show in the subsequent section.

¹In such a way that the perturbed curve is again horizontal.

B.1.2 Application of the Geometrical Principle to Completion Fields

In general the real part, imaginary part, or absolute value of an orientation score is a complicated function on $SE(2)$. Therefore we will consider the case where $C : SE(2) \rightarrow \mathbb{R}^+$ is a so-called “completion field” August (2001); August & Zucker (2003); Thornber & Williams (1996, 2000); Zweck & Williams (2004). This corresponds to collision probability densities of a source particle $g_1 \in SE(2)$ and a sink particle $g_2 \in SE(2)$.

There exist remarkable relations Duits & Franken (2010b); Duits & Van Almsick (2008) between optimal curves (i.e. curves minimizing an optimal control problem on $SE(2)$) and solutions of Eq. (B.2) for special cases where C denotes a so-called completion distribution (or “completion field”). Given two sources at the origin $g_1 = (0, 0, 0)$ and at $g_2 = (x_1, y_1, \theta_1)$, such completion fields are defined as products of resolvent Green’s functions of stochastic processes for contour completion Mumford (1994) and contour enhancement Citti & Sarti (2006); Duits & Franken (2010a) in $SE(2)$:

$$C(g) := \lambda^2 \cdot R_\lambda(g_1^{-1}g)R_{\lambda,*}(g_2^{-1}g), \quad (\text{B.5})$$

where $R_\lambda(g)$ denotes the probability density of finding a random walker g in the underlying stochastic process Duits & Franken (2010a); Mumford (1994) given that it started at $g = (x, y, \theta) = (0, 0, 0)$ regardless its memoryless traveling time T which is negatively exponentially distributed with expectation $E(T) = \lambda^{-1}$. Furthermore, $g \mapsto R_{\lambda,*}(g)$ denotes the adjoint resolvent kernel (i.e. the resolvent that arises by taking the adjoint of the generator (Duits & Van Almsick, 2008, ch:4.4).

Exact formulas for the resolvent Green’s function R_λ for contour enhancement can be found in Duits & Franken (2010a), whereas exact formulae for resolvent kernels R_λ for contour completion (direction process) can be found in Duits & Van Almsick (2008). In both cases there are representations involving 4 Mathieu functions. For a visual impression of exact Green’s functions see Fig. 5.3 on page 112 and Fig. B.1 (where in dashed lines we have depicted level sets of the corresponding Heisenberg approximations that we will discuss and employ in the next subsection).

These completion fields relate to the well-known Brownian bridges (in probability theory) where the traveling time is integrated out. This relation is relevant, since it is known that such Brownian bridges concentrate on geodesics Wittich (2005).

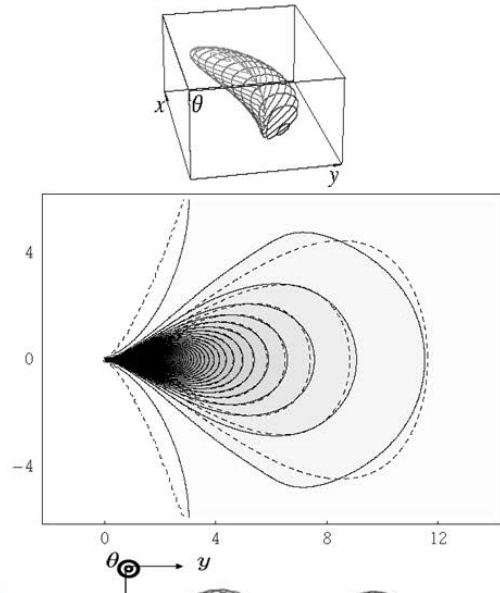
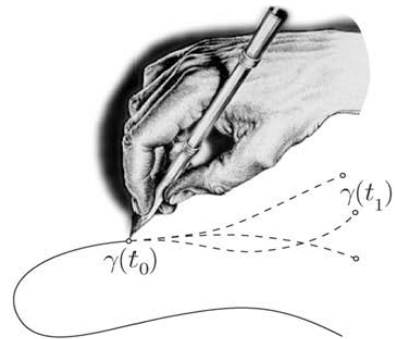
If $G_t : SE(2) \rightarrow \mathbb{R}^+$ denotes the time dependent Green’s function of the Fokker-Planck equation of the underlying time dependent stochastic process Duits & Franken (2009, 2010a); Mumford (1994) at time $t > 0$ we have

$$C(g) = \lambda^2 \int_0^\infty \int_0^t G_{t-s}(g_1^{-1}g)e^{-\lambda(t-s)}G_s(g_2^{-1}g)e^{-\lambda s} ds dt.$$

This identity follows from two facts. Firstly, the resolvent Green’s function follows from the

B. VESSEL TRACKING PART I: ITERATIVE TRACKING VIA LOCAL OPTIMIZATION

Contour completion



Contour enhancement

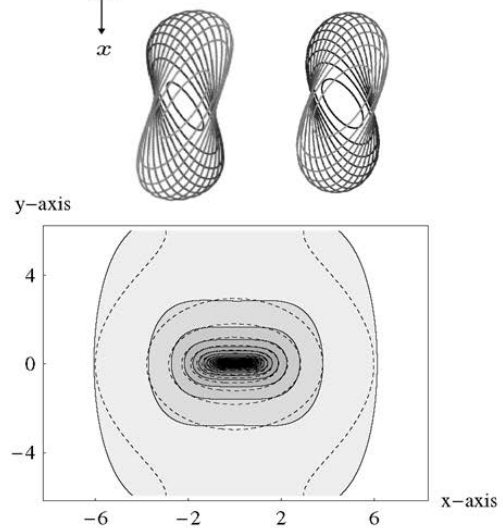
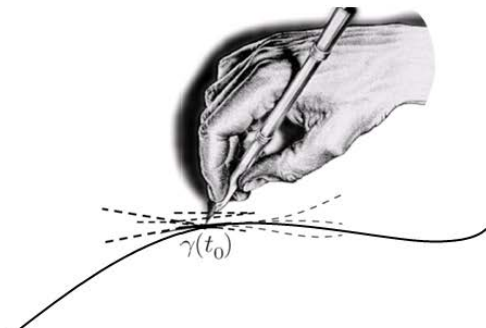


Figure B.1: Top: A contour completion process and the corresponding Green's function (in $SE(2)$) and its planar θ -integrated version. Bottom: A contour enhancement process and the corresponding Green's function (in $SE(2)$) and its planar θ -integrated version. In the completion process one has randomness in θ with variance $2D_{11} > 0$ and non-random advection in spatial e_ξ -direction (Eq. (7.1)). In the enhancement process one has randomness both in θ -direction (with variance $2D_{11} > 0$) and in e_ξ -direction (with variance $2D_{22} > 0$).

time dependent Green's function via the Laplace transform:

$$R_\lambda(g) = \lambda \mathcal{L}(t \mapsto G_t(g))(\lambda) = \lambda \int_0^\infty G_t(g) e^{-\lambda t} dt.$$

Secondly, a temporal convolution relates to a product in the Laplace domain. As Brownian bridge measures concentrate on geodesics when $\lambda \rightarrow 0$, cf. Wittich (2005), (Duits & Franken, 2007, App.B), the completion field for contour enhancement concentrates on sub-Riemannian geodesics within M , which we studied in Ch. 8.

On the other hand, in his paper Mumford (1994) Mumford showed that the modes of the direction process (also known as the contour completion process) coincide with elastica curves which are the solutions to the following optimal control problem

$$\begin{aligned} \inf_{\mathbf{x} \in C^1[0, \ell], \ell > 0} \quad & \int_0^\ell \kappa^2(s) + \xi^2 ds \\ (\mathbf{x}(0), \dot{\mathbf{x}}(0)) &= g_0, \\ (\mathbf{x}(\ell), \dot{\mathbf{x}}(\ell)) &= g_1 \end{aligned} \tag{B.6}$$

Similar to the Onsager-Machlup approach to optimal paths Takahashi & Watanabe (1980) he obtains these modes by looking at the most probable/likely realization of discretized versions of the direction process.

As this cannot be (efficiently) realized in practice, one needs a more tangible description of the mode. To this end, we will call solution curves of (B.2) the “modes”. In case of the direction process and in case one uses the completion distribution (Eq. (B.5)) for the function $C(g)$, the solution curves of (B.2) indeed seem to numerically coincide with the elastica curves. Remarkably, this holds exactly for the corresponding Heisenberg approximations as we will explain next.

B.1.3 In the Heisenberg Approximation of Completion Fields our Approach Produces B-splines

The Heisenberg group approximation (obtained by contraction Duits & Franken (2010a)) of the Green's functions and induced completion field arises by replacing the moving frame of left-invariant vector fields

$$\{\cos \theta \partial_x + \sin \theta \partial_y, -\sin \theta \partial_x + \cos \theta \partial_y, \partial_\theta\}$$

on $SE(2)$ by the moving frame of reference of left-invariant vector fields on the Heisenberg group

$$\{\partial_x + \theta \partial_y, \partial_y, \partial_\theta\}$$

and by replacing spatial arc-length parametrization via s by spatial coordinate x . Intuitively, such replacement boils down to replacing the space of positions and orientations by the space of positions and velocities.

B. VESSEL TRACKING PART I: ITERATIVE TRACKING VIA LOCAL OPTIMIZATION

When contracting (for details on this contraction see (Duits & Franken, 2010a, Ch.5.4)) our fundamental equation (B.2) with cost C given by Eq. (B.5) towards the Heisenberg group H_3 we obtain

$$\frac{d}{dy} \tilde{C}(x, y, \theta) = \frac{d}{d\theta} \tilde{C}(x, y, \theta) = 0, \quad (\text{B.7})$$

where again in the Heisenberg group each tangent plane $\{\partial_\theta, \partial_y\}$ is orthogonal to the propagation direction $\partial_x + \theta \partial_y$ and where the completion field is the product of two resolvent Green's functions

$$\tilde{C}(x, y, \theta) = R_\lambda(x, y, \theta)R_\lambda(-x + x_1, y - y_1 - \theta_1(x - x_1), -\theta)$$

which can be derived in exact form as

$$R_\lambda(x, y, \theta) = \frac{\lambda\sqrt{3}}{2D_{11}\pi x^2} e^{-\lambda x} e^{-\frac{3(x\theta-2y)^2+x^2\theta^2}{4x^3D_{11}}} u(x),$$

where $D_{11} > 0$ stands for the amount of diffusion in θ -direction and u for the unit step function, for details¹ see (cf. (Duits & Van Almsick, 2008, Thm 4.6)).

Interestingly, the solution of (B.7) is a third order polynomial $y(x)$ naturally lifted to (the corresponding sub-Riemannian manifold within) $H(3)$ by setting $\theta(x) = y'(x)$. The solutions of Eq. (B.7) are therefore cubic B -splines which are the solutions of the Euler-Lagrange equation

$$y^{(4)}(x) = \theta^{(3)}(x) = 0$$

of a curve optimization problem which arises by contracting (B.6) towards the Heisenberg group. This gives the following “Heisenberg group equivalent” of control problem (B.6):

$$\begin{aligned} \min_{\gamma(\cdot) = (\cdot, y(\cdot), \theta(\cdot)) \in C^1(H_3), \quad \int_0^{x_2} \xi^2 + |\theta'(x)|^2 dx} \quad &= \quad \xi^2 x_2 + \frac{4(3y_2^2 + 3x_2 y_2 \theta_2 + x_2^2 \theta_2^2)}{x_2^3}, \\ \gamma(0) &= (0, 0, 0), \\ \gamma(x_2) &= (x_2, y_2, \theta_2), \\ \theta(x) &= y'(x), \end{aligned}$$

which takes the minimum along a lifted cubic-B spline $(x, y(x), y'(x))$ (with $y(x)$ a third order polynomial matching the boundary conditions). For details see (Duits & Van Almsick, 2008, Eq. (4.6.2)), (Duits & Franken, 2007, ch:9.1.1), and van Almsick (2007). See Fig. B.2.

B.1.4 Concluding Remarks

By the results of the previous section the conjecture rises whether elastica curves coincide with Eq. (B.5) as such a relation holds for their counterparts in the Heisenberg group. Numeric computations seem to provide a confirmation of this conjecture, see Fig. B.3.

On the one hand, we expect with respect to the contour enhancement process that our approach produces the sub-Riemannian geodesics (based on the results in Duits & Franken

¹Set $\kappa_0 = \kappa_1 = 0$ in Duits & Van Almsick (2008).

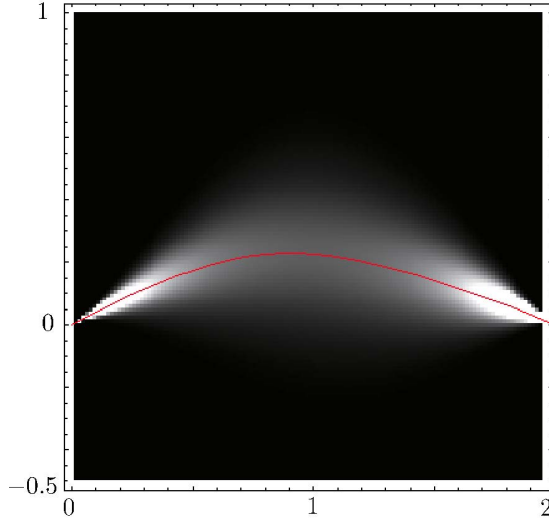


Figure B.2: The intersection of the planes $\{(x, y, \theta) \in \mathbb{R}^3 \mid \partial_\theta \tilde{C}(x, y, \theta) = 0\}$ and $\{(x, y, \theta) \in \mathbb{R}^3 \mid \partial_y \tilde{C}(x, y, \theta) = 0\}$ of the Heisenberg approximation $\tilde{C}(g)$ of the completion field $C(g)$ given by Eq. (B.5), produces a cubic B-spline lifted in $H(3)$, i.e. $(x, y(x), \theta(x) = y'(x))$ with $y^{(4)}(x) = 0$. Boundary conditions have been set to $x_1 = y_1 = 0$, $\theta_1 = 0.4$, $x_2 = 2$, $y_2 = 0$, $\theta_2 = -0.4$, $D_{11} = 1/8$.

(2007, 2010b); Wittich (2005)), but this is a point for future investigation. On the other hand, the conjecture together with the result in Mumford (1994) (and the result that B-splines solve Eq. (B.7)) would underpin our alternative *applicable definition* of modes as solution curves of Eq. (B.2).

In fact this means that optimization in each (η, θ) -plane \mathcal{V} , as is done in our ETOS algorithm, produces the most probable curves (in the sense of Mumford (1994); Takahashi & Watanabe (1980)) in direction processes.

B. VESSEL TRACKING PART I: ITERATIVE TRACKING VIA LOCAL OPTIMIZATION

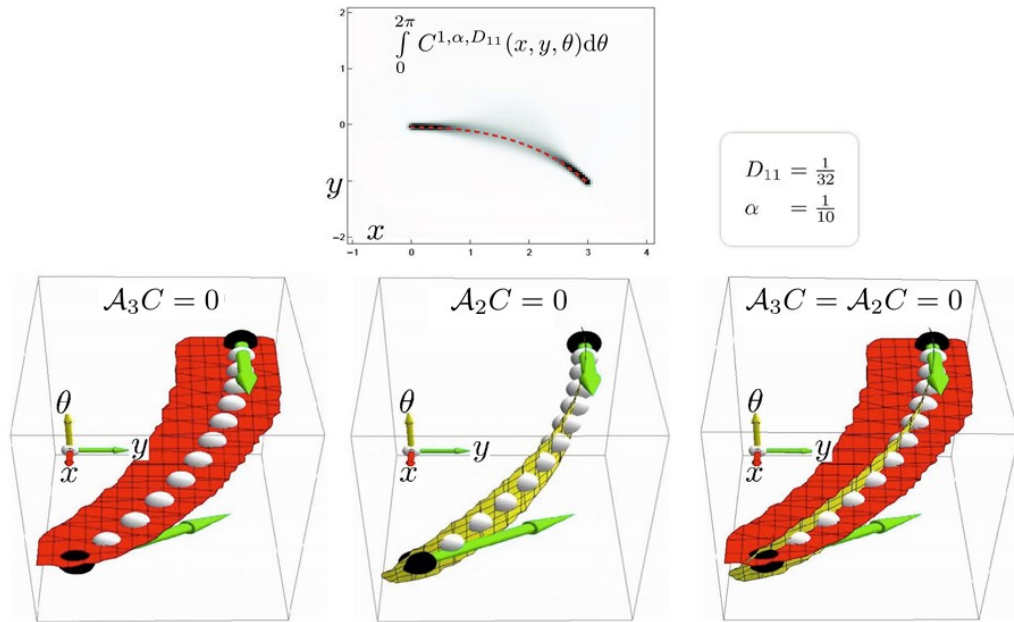


Figure B.3: The intersection of the planes $\{g \in SE(2) \mid \mathcal{A}_3 C(g) = 0\}$ (depicted in red) and $\{g \in SE(2) \mid \mathcal{A}_2 C(g) = 0\}$ (depicted in yellow) of the exact completion field $g = (x, y, \theta) \mapsto C(g)$ given by Eq. (B.5), with $x_1 = y_1 = \theta_1 = 0$ and $x_2 = 3$, $y_2 = -1$, $\theta_2 = 7/4\pi$, $\lambda = 0.1$, $D_{11} = 1/32$. The intersection of these planes seems to coincides with an elastica (with $\xi^2 = 4\lambda D_{11}$), which we plotted in dashed red in the top figure and by white balls in the bottom figures.

Appendix C

Vessel Tracking Part II: Sub-Riemannian Geodesics in $\mathbf{SE}(2)$

This appendix is based on joint work with Remco Duits, Alexey Mashtakov and Gonzalo Sanginetti, cf. Bekkers *et al.* (2015c), and provides: (1) additional theoretical details on our method for computing data-adaptive sub-Riemannian geodesics as described in Ch. 8; and (2) formal proofs of the main theorems Thm. 2 and Thm. 3. These theoretical results are in particular due to the efforts of Remco Duits and Alexey Mashtakov, for which they are gratefully acknowledged.

C.1 Application of Pontryagin's Maximum Principle

Here we study the optimal control problem (8.2), recall also Remark 10, and we apply Pontryagin's Maximum Principle (PMP) to the action functional J of Eq. (8.3) with fixed total time $T > 0$. Since $[\mathcal{A}_i, \mathcal{A}_j] = \sum_{k=1}^3 c_{ij}^k \mathcal{A}_k$, with non-zero coefficients $c_{13}^2 = -c_{31}^2 = -1$, $c_{23}^1 = -c_{32}^1 = -1$, we have $[\Delta, \Delta] = T(\mathbf{SE}(2))$ and we only need to consider normal trajectories. Then the control dependent Hamiltonian of PMP expressed via left-invariant Hamiltonians $h_i(p, g) = \langle p, \mathcal{A}_i(g) \rangle$, $i = 1, 2, 3$, with momentum $p \in T_g^*(\mathbf{SE}(2))$, and $g = (x, y, \theta) \in \mathbb{R}^2 \rtimes S^1$ reads as

$$H_u(p, g) = u^1 h_1(p, g) + u^3 h_3(p, g) - \frac{1}{2} \mathcal{C}^2(g) (\beta^2 |u^1|^2 + |u^3|^2).$$

Optimization over all controls produces the (maximized) Hamiltonian

$$H^{fixed}(g, p) = \frac{1}{2 \mathcal{C}^2(g)} \left(\frac{h_1^2}{\beta^2} + h_3^2 \right),$$

C. VESSEL TRACKING PART II: SUB-RIEMANNIAN GEODESICS IN SE(2)

and gives the expression for extremal controls $u^1(t) = \frac{h_1(t)}{\mathcal{C}^2(\gamma(t))\beta^2}$, $u^3(t) = \frac{h_3(t)}{\mathcal{C}^2(\gamma(t))}$. Using SR-arclength parametrization $\mathcal{G}_0^{\xi, \mathcal{C}} \Big|_{\gamma(t)} (\dot{\gamma}(t), \dot{\gamma}(t)) = 1$ implies $H^{fixed} = \frac{1}{2}$ along extremal trajectories. We have the Poisson brackets

$$\{H, h_1\} = \frac{\mathcal{A}_1 \mathcal{C}}{\mathcal{C}} + \frac{h_3 h_2}{\mathcal{C}^2}, \quad \{H, h_2\} = \frac{\mathcal{A}_2 \mathcal{C}}{\mathcal{C}} - \frac{h_3 h_1}{\mathcal{C}^2}, \quad \{H, h_3\} = \frac{\mathcal{A}_3 \mathcal{C}}{\mathcal{C}} - \frac{h_1 h_2}{\beta^2 \mathcal{C}^2}, \quad (\text{C.1})$$

where $H = H^{fixed}$ and with $\{F, G\} = \sum_{i=1}^3 \frac{\partial F}{\partial h_i} \mathcal{A}_i G - \frac{\partial G}{\partial h_i} \mathcal{A}_i F$. By Eq. (C.1), by $\{h_i, h_j\} = \mathcal{A}_i h_j - \mathcal{A}_j h_i = \sum_{k=1}^3 c_{ij}^k h_k$, and by $\dot{h}_i = \{H, h_i\}$, PMP gives us:

$$p(\cdot) = \sum_{i=1}^3 h_i(\cdot) \omega^i \Big|_{\gamma(\cdot)} \text{ and } \begin{cases} \dot{h}_1 = \frac{1}{\mathcal{C}(\gamma(\cdot))} \mathcal{A}_1 \Big|_{\gamma(\cdot)} \mathcal{C} + \frac{h_3 h_2}{\mathcal{C}^2(\gamma(\cdot))}, \\ \dot{h}_2 = \frac{1}{\mathcal{C}(\gamma(\cdot))} \mathcal{A}_2 \Big|_{\gamma(\cdot)} \mathcal{C} - \frac{h_3 h_1}{\mathcal{C}^2(\gamma(\cdot))}, \\ \dot{h}_3 = \frac{1}{\mathcal{C}(\gamma(\cdot))} \mathcal{A}_3 \Big|_{\gamma(\cdot)} \mathcal{C} - \frac{h_1 h_2}{\beta^2 \mathcal{C}^2(\gamma(\cdot))}, \end{cases} \quad (\text{C.2})$$

— vertical part (for adjoint variables),

$$\dot{\gamma}(\cdot) = \sum_{i \in \{1, 3\}} u^i(\cdot) \mathcal{A}_i \Big|_{\gamma(\cdot)} \text{ and } \begin{cases} \dot{x} = \frac{h_1}{\mathcal{C}^2(\gamma(\cdot)) \beta^2} \cos \theta, \\ \dot{y} = \frac{h_1}{\mathcal{C}^2(\gamma(\cdot)) \beta^2} \sin \theta, \\ \dot{\theta} = \frac{h_3}{\mathcal{C}^2(\gamma(\cdot))}, \end{cases} \quad (\text{C.3})$$

— horizontal part (for state variables).

with dual basis $\{\omega^i\}$ for $T^*(SE(2))$ defined by $\langle \omega^i, \mathcal{A}_j \rangle = \delta_j^i$.

For a consistency check, we also apply the PMP-technique directly to Problem (8.2) with free terminal time T , where typically (cf. Agrachev & Sachkov (2013)) the Hamiltonian vanishes. Then, using SR arclength parameter t , the control dependent Hamiltonian of PMP equals

$$H_u(g, p) = u^1 h_1(p, g) + u^3 h_3(p, g) - \mathcal{C}(g) \sqrt{\beta^2 |u^1|^2 + |u^3|^2}.$$

Optimization over all controls under SR arclength parametrization constraint $\mathcal{C} \sqrt{\beta^2 |u^1|^2 + |u^3|^2} = 1$ produces via Euler-Lagrange optimization w.r.t. (u^1, u^3) (via unit Lagrange multiplier) the (maximized) Hamiltonian:

$$H^{free}(g, p) = \frac{1}{\mathcal{C}(g)} \sqrt{\frac{|h_1|^2}{\beta^2} + |h_3|^2} - 1 = 0 \text{ with } p = \sum_{i=1}^3 h_i \omega^i, \quad (\text{C.4})$$

and by straightforward computations one can verify that both the horizontal part and the vertical part of PMP (but now applied to H^{free}) is exactly the same as (C.3) and (C.2).

Remark 21. *The two approaches produce the same curves and equations, but their Hamiltonians are different. Nevertheless, we have $H^{free} = 0 \Leftrightarrow H^{fixed} = \frac{1}{2}$.*

C.2 Lemmas Applied in the Proof of Theorem 2

In this section we consider preliminaries and lemmas needed for Thm. 2. Before we can make statements on SR-spheres we need to explain the notion of geodesically equidistant surfaces,

C.2 Lemmas Applied in the Proof of Theorem 2

and their connection to HJB-equations. In fact, propagation of geodesically equidistant surfaces in $(SE(2), \Delta, \mathcal{G}_0^{\xi, \mathcal{C}})$ is described by a HJB-system on this SR-manifold.

Recall Remark 10. Also recall, that in Appendix C.1 we have applied PMP to this problem yielding constant Hamiltonian $H^{fixed} = \frac{1}{2c^2}(\beta^{-2}h_1^2 + h_3^2) = \frac{1}{2}$ relating to $H^{free} = \frac{1}{c}\sqrt{\beta^{-2}h_1^2 + h_3^2} - 1 = 0$ via $H^{free} = \sqrt{2H^{fixed}} - 1$.

In our analysis of geodesically equidistant surface propagation we first resort to the non-homogenous viewpoint on the Lagrangian and Hamiltonian (with fixed time), and then obtain the results on the actual homogeneous problem (with free time) via a limiting procedure.

Definition 4. Given $V : SE(2) \times \mathbb{R}^+ \rightarrow \mathbb{R}$ continuous. Given a Lagrangian $L(\gamma(r), \dot{\gamma}(r))$ on the SR manifold $(SE(2), \Delta, \mathcal{G}_0^{\xi, \mathcal{C}})$, with $L(\gamma, \cdot) : \Delta \rightarrow \mathbb{R}^+$ convex. Then the family of surfaces

$$\mathcal{S}_r := \{g \in SE(2) \mid V(g, r) = W_0(r)\}, \text{ with} \quad (\text{C.5})$$

$W_0 : \mathbb{R} \rightarrow \mathbb{R}$ monotonic, smooth, is geodesically equidistant if $L(\gamma(r), \dot{\gamma}(r)) = W'_0(r)$ for a SR geodesic γ in $(SE(2), \Delta, \mathcal{G}_0^{\xi, \mathcal{C}})$.

Remark 22. The motivation for this definition is

$$\frac{d}{dR} \int_0^R L(\gamma(r), \dot{\gamma}(r)) dr = L(\gamma(R), \dot{\gamma}(R)) = \frac{dW_0}{dr}(R).$$

Lemma 1. Let L be non-homogeneous and $\lim_{|v| \rightarrow \infty} \frac{L(\cdot, v)}{|v|} = \infty$. Then the family of surfaces $\{\mathcal{S}_r\}_{r \in \mathbb{R}}$ is geodesically equidistant if and only if V satisfies the HJB-equation (where r may be monotonically re-parameterized):

$$\frac{\partial V}{\partial r}(g, r) = -H(g, d^{SR}V(g, r)), \text{ with } d^{SR}V(g, r) = \mathbb{P}_\Delta^* dV(g, r) = \sum_{i \in \{1, 3\}} \mathcal{A}_i V(g, r) \omega^i|_g. \quad (\text{C.6})$$

Here $\mathbb{P}_\Delta^*(p) = \sum_{i \in \{1, 3\}} h_i \omega^i$, for all $p = \sum_{i=1}^3 h_i \omega^i$, is a dual projection expressed in dual basis ω^i given by $\langle \omega^i, \mathcal{A}_j \rangle = \delta_j^i$, and Hamiltonian $H(g, p) = \max_{v \in T_g(SE(2))} \{\langle p, v \rangle - L(g, v)\}$.

Proof Substitute an arbitrary transversal minimizer $\gamma(r)$ into $V(\cdot, r)$ and take the total derivative w.r.t. r :

$$\frac{d}{dr} V(\gamma(r), r) = \frac{\partial}{\partial r} V(\gamma(r), r) + \langle dV|_{\gamma(r)}, \dot{\gamma}(r) \rangle.$$

Now $\gamma(r)$ on S_r , with tangent $\dot{\gamma}(r) = \sum_{i \in \{1, 3\}} u^i(r) \mathcal{A}_i|_{\gamma(r)}$, and thereby

$$\frac{d}{dr} V(\gamma(r), r) = L(\gamma(r), \dot{\gamma}(r)) = \frac{\partial}{\partial r} V(\gamma(r), r) + \sum_{i=1}^2 u^i(r) \mathcal{A}_i|_{\gamma(r)} V(\gamma(r), r).$$

C. VESSEL TRACKING PART II: SUB-RIEMANNIAN GEODESICS IN SE(2)

As a result we have

$$\begin{aligned} -L(\gamma(r), \dot{\gamma}(r)) + \sum_{i \in \{1,3\}} u^i(r) \mathcal{A}_i|_{\gamma(r)} V(\gamma(r), r) &= -\frac{\partial V}{\partial r}(\gamma(r), r) \stackrel{(1)}{\Leftrightarrow} \\ \sup_{(u^1(r), u^3(r)) \in \mathbb{R}^2} \sum_{i \in \{1,3\}} u^i(r) h_i(r) - L(\gamma(r), \dot{\gamma}(r)) &= -\frac{\partial V}{\partial r}(\gamma(r), r) \stackrel{(2)}{\Leftrightarrow} \\ H(\gamma(r), \mathbb{P}_{\Delta}^* dV(\gamma(r), r)) &= -\frac{\partial V}{\partial r}(\gamma(r), r), \end{aligned} \quad (\text{C.7})$$

with components $h_i(r) = \mathcal{A}_i|_{\gamma(r)} V(\gamma(r), r)$ of projected momentum covector

$$\mathbb{P}_{\Delta}^* p(r) = \sum_{i \in \{1,3\}} h_i(r) \omega^i|_{\gamma(r)} = \mathbb{P}_{\Delta}^* dV(\gamma(r), r).$$

Now every point $g \in S_r$ is part of a transversal minimizing curve $\gamma(r)$ and the result follows. So the “ \Rightarrow ” is proven. Conversely, if the HJB-equation is satisfied it follows by the same computations (in reverse order) that $L(\gamma(r), \dot{\gamma}(r)) = \frac{d}{dr} V(\gamma(r), r)$, which equals $W'_0(r)$. \square

Remark 23. In PMP Agrachev & Sachkov (2013) (see also Appendix C.1) the controls are optimized to obtain the Hamiltonian H from the control dependent Hamiltonian H_u . The first equivalence in (C.7) is due to the maximum condition of PMP. The second equivalence in (C.7), is by definition of the Hamiltonian, where by the convexity assumption of the Lagrangian the supremum is actually a maximum (Evans, 1997, ch:8).

Next we apply the limiting procedure to obtain HJB-equations for geodesically equidistant surfaces in the actual homogeneous case of interest. The actual *homogeneous* Lagrangian case with T -free can be obtained as a limit ($1 \leq \eta \rightarrow \infty$) from non-homogeneous Lagrangian cases:

$$L_{\eta}(\gamma(t), \dot{\gamma}(t)) = \frac{2\eta-1}{2\eta} \left(\mathcal{G}_0^{\xi, \mathcal{C}}|_{\gamma(t)} (\dot{\gamma}(t), \dot{\gamma}(t)) \right)^{\frac{\eta}{2\eta-1}}, \quad (\text{C.8})$$

and corresponding Hamiltonian (see Remark 25 below) equals

$$H_{\eta}(\gamma(t), p(t)) = \frac{1}{2\eta} (\beta^{-2} h_1^2 + h_3^2)^{\eta} |\mathcal{C}(\gamma(t))|^{-2\eta}, \quad (\text{C.9})$$

and setting $r = t = W_0(t)$. Thus $\frac{\partial V}{\partial r}(\gamma(r), r) = \frac{\partial V}{\partial t}(\gamma(t), t) = W'_0(t) = L(\gamma(t), \dot{\gamma}(t)) = \sqrt{\mathcal{G}_0^{\xi, \mathcal{C}}|_{\gamma(t)} (\dot{\gamma}(t), \dot{\gamma}(t))} = 1$ in Eq. (C.7). Next we replace V by W to distinguish between the homogeneous and the non-homogeneous case).

Lemma 2. The family of surfaces given by Eq. (C.5) is geodesically equidistant w.r.t. the homogeneous Lagrangian $L_{\infty}(\gamma, \dot{\gamma}) = \sqrt{\mathcal{G}_0^{\xi, \mathcal{C}}|_{\gamma} (\dot{\gamma}, \dot{\gamma})}$, with $r = t = W_0(t)$, iff W satisfies the HJB-equation

$$\frac{1}{C} \sqrt{\beta^{-2} |\mathcal{A}_1 W|^2 + |\mathcal{A}_3 W|^2} = 1 \Leftrightarrow H = 0 \quad (\text{C.10})$$

where $H = \lim_{\eta \rightarrow \infty} H_{\eta} = H^{free}$ the vanishing free-time Hamiltonian in Appendix C.1. Defining Hamiltonian \tilde{H} by

$$\tilde{H}(g, p) := \mathcal{C}^{-1}(g) \sqrt{\beta^{-2} h_1^2 + h_3^2} \quad (\text{C.11})$$

puts Eq. (C.10) in eikonal form $\tilde{H}(g, d^{SR}W(g, t)) = 1$.

C.3 Viscosity Solutions for HJB-systems in SE(2)

Proof Tangential to the proof of Lemma 1. For $1 \leq \eta < \infty$ we can apply Lemma 1 to Lagrangian L_η given by (C.8) whose associated Hamilton H_η is given by (C.9) due to PMP (or just the Fenchel transform on \mathbb{R}^2). In the limiting case $\eta \rightarrow \infty$, where the Lagrangian is homogeneous and the Hamiltonian vanishes. Finally we note that now we have

$$\frac{\partial W}{\partial r}(\gamma(r), r) = \frac{\partial W}{\partial t}(\gamma(t), t) = W'_0(t) = L(\gamma(t), \dot{\gamma}(t)) = 1,$$

from which the result follows. \square

Remark 24. *The relation between the various Hamiltonians is*

$$H_{\eta \rightarrow \infty} = H^{free} = \sqrt{2H^{fixed}} - 1 = \sqrt{2H_{\eta=1}} - 1 = \tilde{H} - 1 = 0.$$

Remark 25. *The relation between the Lagrangian L_η given by (C.8) and the Hamiltonian (C.9) is the (left-invariant, SR) Fenchel transform on $SE(2)$. Due to left-invariance this Fenchel-transform actually boils down to an ordinary Fenchel-transform on \mathbb{R}^2 when expressing velocity and momentum in the left-invariant frame. Indeed we have*

$$H_\eta(\gamma, p) = [\mathfrak{F}_{\mathcal{L}(SE(2)) \cap \Delta}(L_\eta(\gamma, \cdot))](p) := \sup_{(u^1, u^3) \in \mathbb{R}^2} \left\{ -\frac{2\eta - 1}{2\eta} (\mathcal{C}(\gamma))^{\frac{2\eta}{2\eta-1}} (\beta^2 |u^1|^2 + |u^3|^2)^{\frac{\eta}{2\eta-1}} + h_1 u^1 + h_3 u^3 \right\} \quad (C.12)$$

with horizontal velocity $v = u^1 \mathcal{A}_1 + u^3 \mathcal{A}_3$, and momentum $p = \sum_{i=1}^3 h_i \omega^i$.

C.3 Viscosity Solutions for HJB-systems in SE(2)

Definition 5. *The (Cauchy problem) for a HJB-equation (akin to (Evans, 1997, ch:10.1)) on $SE(2)$ is given by*

$$\begin{cases} \frac{\partial W}{\partial t} = -H(g, d^{SR}W) \text{ in } SE(2) \times (0, T), \\ W(g, 0) = W_0, \end{cases} \quad (C.13)$$

whereas a boundary value problem for HJB-equation is given as

$$H(g, d^{SR}W) = 0 \text{ on } SE(2) \setminus \{e\}, \quad W(e) = 0; \quad (C.14)$$

where $T > 0$ is prescribed, W_0 is a given function (or a cost measure Akian et al. (1994)), $H(g, p) = H^{free}(g, p)$ is the free-time Hamiltonian given by (8.11), and $d^{SR}W = \sum_{i \in \{1, 3\}} \mathcal{A}_i W(g, t) \omega^i|_g$.

Remark 26. *Combined Cauchy-Dirichlet problems exist Trélat (2006), but they are defined on (analytic) open and bounded domains. Thereby they cannot be applied to our set of interest $SE(2) \setminus \{e\}$ as this would violate semigroup theory Akian et al. (1994); Burgeth & Weickert (2005); Evans (1997); Yosida (1995). This is also clear in view of the Cramer transform Akian et al. (1994), putting an isomorphism between HJB- and diffusion systems.*

C. VESSEL TRACKING PART II: SUB-RIEMANNIAN GEODESICS IN SE(2)

Remark 27. In Eq. (C.14) it is crucial that the free time Hamiltonian is used. In the definition of viscosity solutions of the Cauchy problem, Eq. (C.13), one can set both $H = H^{\text{free}}$ (as done in Ch. 8) or $H = H^{\text{fixed}}$ as done in Appendix C.2.

HJB-systems in general do not have unique solutions. To avoid multiple (non-desirable) solutions, one must impose the viscosity condition Evans (1997); Lions (1982) commonly applied in wavefront methods acting directly in the image domain \mathbb{R}^2 Osher & Fedkiw (2006); Sethian (1999). The viscosity solution is obtained by the vanishing viscosity method Lions (1982). The idea of this method is to add to the HJB-equation a term $\varepsilon\Delta$ and to pass to the limit, when ε goes to 0. Here Δ denotes the Laplacian, that in our case (for $\mathcal{C} = 1$) equals $\Delta^{SR} = \sum_{i \in \{1,3\}} \mathcal{A}_i(\beta_i)^{-2} \mathcal{A}_i$, with $\beta_1 = \beta, \beta_3 = 1$. Here the name “viscosity solutions” comes from fluid dynamics, where typically the term $\varepsilon\Delta$ represents a physical viscosity. For an intuitive illustration of the geometric property of such solutions see (Bressan, 2010, fig.30). The viscosity solution of the initial value problem can be defined alternatively as follows.

Definition 6. Let $H(g, \cdot)$ be a convex Hamiltonian for all $g \in SE(2)$ s.t. $H(g, p) \rightarrow \infty$ if $p \rightarrow \infty$. The function $W : SE(2) \times \mathbb{R} \rightarrow \mathbb{R}$ is viscosity solution of $\frac{\partial W}{\partial t} = -H(g, d^{SR}W)$ if it is a weak solution¹ such that for all functions $V \in C^1(SE(2) \times \mathbb{R}, \mathbb{R})$ one has

- $W - V$ attains a local maximum at $(g_0, t_0) \Rightarrow (\frac{\partial V}{\partial t} + H(g, d^{SR}V))|_{(g_0, t_0)} \leq 0$,
- $W - V$ attains a local minimum at $(g_0, t_0) \Rightarrow (\frac{\partial V}{\partial t} + H(g, d^{SR}V))|_{(g_0, t_0)} \geq 0$.

Similarly, the viscosity solution of the boundary value problem (that is equivalent to the eikonal equation, when t is SR-arclength) can be defined as follows:

Definition 7. A solution $W : SE(2) \rightarrow \mathbb{R}$ of Eq. (C.14) is called a viscosity solution if for all functions $V \in C^1(SE(2), \mathbb{R})$ one has

- $W - V$ attains a local maximum at $g_0 \Rightarrow H^{\text{free}}(g_0, d^{SR}V) \leq 0$,
- $W - V$ attains a local minimum at $g_0 \Rightarrow H^{\text{free}}(g_0, d^{SR}V) \geq 0$.

C.4 Proof of Theorem 3

The back-tracking (8.6) is a direct result of Lemma 2 in Appendix C.2 and PMP in Appendix C.1. According to these results one must set

$$u^1(t) = \frac{h_1(t)}{(C(\gamma(t)))^2 \beta^2} = \frac{\mathcal{A}_1 W|_{\gamma(t)}}{(C(\gamma(t)))^2 \beta^2} \text{ and } u^3(t) = \frac{h_3(t)}{(C(\gamma(t)))^2} = \frac{\mathcal{A}_3 W|_{\gamma(t)}}{(C(\gamma(t)))^2}$$

¹By weak solution we mean a not necessarily differentiable Lipschitz function, satisfying the equation almost everywhere (for further details see Evans (1997)).

C.4 Proof of Theorem 3

from which the result follows. Then we recall from Thm. 2 that \mathcal{S}_t given by (8.5) are geodesically equidistant surfaces propagating with unit speed from the origin. So \mathcal{S}_t are candidates for sub-Riemannian spheres, but it remains to be shown that the back-tracking (8.6) will neither pass a Maxwell point nor a conjugate point, i.e. $t \leq t_{cut}$. Here t_{cut} denotes cut time, where a geodesic loses its optimality.

At Maxwell points g^* induced by the 8 reflectional symmetries Moiseev & Sachkov (2010) two distinct SR-geodesics meet with the same SR distance. As SR-geodesics in $(SE(2), \Delta, G^1)$ are analytic Moiseev & Sachkov (2010), these two SR-geodesics do not coincide on an open set around end-condition g^* , and the SR spheres are non-smooth at g^* . Regarding the set \mathcal{M} , we note that the Maxwell sets related to the i -th reflectional symmetry ϵ_i are defined by

$$\begin{aligned} \text{MAX}^i &= \{(p_0, t) \in T_e^*(SE(2)) \times \mathbb{R}^+ \mid H(p_0) = \frac{1}{2} \text{ and } \text{Exp}(p_0, t) = \text{Exp}(\epsilon_i p_0, t)\}, \\ \max^i &= \text{Exp}(\text{MAX}^i), i = 1, \dots, 8, \end{aligned}$$

where we may discard the indices $i = 3, 4, 6$ as they are contained in $\{\max^1, \max^2, \max^5, \max^7\}$. Now with $\widetilde{\max}^i$ we denote the Maxwell set with *minimal* positive Maxwell times over all symmetries (i.e. we include the constraint $t \leq \min\{t_{max}^i\}$ where the minimum is taken over all positive Maxwell times along each trajectory), then we find \mathcal{M} to be contained within the union of the following sets¹:

$$\begin{aligned} \widetilde{\max}^2 &\subset \{(x, y, \theta) \in SE(2) \mid y \sin \theta/2 + x \cos \theta/2 = 0\}, \\ \widetilde{\max}^5 &= \{(x, y, \theta) \in SE(2) \mid \theta = \pi\}, \end{aligned}$$

where (Moiseev & Sachkov, 2010, th:5.2) shows we must discard the first reflectional symmetry ϵ_1 as it does not produce Maxwell points. Now for generic geodesics (not passing the special conjugate points that are limit points of Maxwell points and not Maxwell points themselves) $t_{cut} = t_{MAX}^1$, as proven in (Sachkov, 2010, th:3.3), where $t_{MAX}^1 > 0$ denotes the first Maxwell time associated to the 8 discrete reflectional symmetries.

During the back-tracking the set \mathcal{M} is never reached at internal times (only when starting at them, recall Remark 12), since they are “uphill” from all possible directions during dual steepest descent tracking (8.6), as we will show next. As a result we have $t \leq t_{cut} = t_{MAX}^1$. Consider Fig. 8.4. At Maxwell points $g^* \in \mathcal{M}$ due to the reflectional symmetries there exist two distinct directions in the 2D-horizontal part Δ_{g^*} of the tangent space $T_{g^*}(SE(2))$ where the directional derivative is positive. If there would be a direction in the tangent space where the directional derivative is negative then there would be a direction in Δ_{g^*} with zero directional derivative of $W(\cdot)$ at g^* towards the interior of the sphere yielding contradiction. Here we note that due to the viscosity property of the HJB-solution, kinks at the Maxwell points are pointing

¹In (Sachkov, 2011, Eq.3.13) it is shown that $\widetilde{\max}^2 = \{(x, y, \theta) \in SE(2) \mid y \sin \theta/2 + x \cos \theta/2 = 0 \text{ and } | -x \sin(\theta/2) + y \cos(\theta/2) | > |R_1^1(\theta)|\}$ with R_1^1 defined in (Sachkov, 2011, Lemma 2.5). We also observed such a loss of the Maxwell point property in our numerical algorithm, as kinks in $W(g) = t$ can disappear when moving on the set $y \sin \theta/2 + x \cos \theta/2 = 0$. See Figure 8.10.

C. VESSEL TRACKING PART II: SUB-RIEMANNIAN GEODESICS IN $\text{SE}(2)$

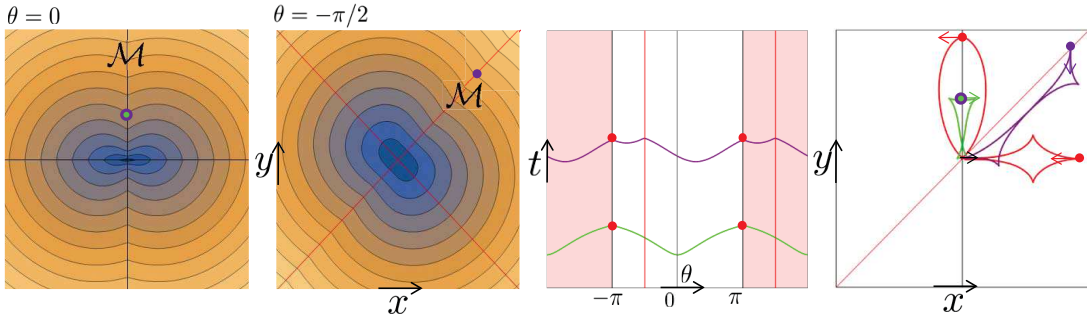


Figure C.1: Overview of Maxwell points. Two Maxwell points on the purple surface $x \cos \frac{\theta}{2} + y \sin \frac{\theta}{2} = 0$ and two red Maxwell points on the surface $|\theta| = \pi$ (recall Figure 8.4). In all cases we see that local kinks in the viscosity solutions are upward, and the backtracking algorithm can not pass these points.

upward (see Fig. 8.4 and Fig. C.1) in the backward minimization tracking process (Bressan, 2010, fig.30). Furthermore, we note that SR spheres \mathcal{S}_t are continuous Sachkov (2011) and compact, as they are the preimage $\mathcal{S}_t = d(\cdot, e)^{\leftarrow}(\{t\})$ of compact set $\{t\}$ under continuous mapping $d(\cdot, e)$. Continuity of $d(\cdot, e)$ implies the spheres are equal to the 2D-boundaries of the SR balls (w.r.t. the normal product topology on $\mathbb{R}^2 \times S^1$).

The algorithm also cannot pass conjugate points that are limits of 1st Maxwell points, but not Maxwell points themselves. See Fig. 8.3. Such points exist on the surface $R_2 = 0$ and are by definition within $\overline{\mathcal{M}} \setminus \mathcal{M}$. Suppose the algorithm would pass such a point at a time $t > 0$ (e.g. there exist 4 such points on the sphere with radius 4, see Fig. 8.4) then due to the astroidal shape of the wavefront at such a point, cf. (Sachkov, 2010, Fig.11), there is a close neighboring tract that would pass a 1st Maxwell point which was already shown to be impossible (due to the upward kink-property of viscosity solutions). \square

Remark 28. The sub-Riemannian spheres are non-smooth only at the 1st Maxwell set \mathcal{M} . They are smooth at the conjugate points in $\overline{\mathcal{M}} \setminus \mathcal{M}$ (where the reflectional symmetry no longer produce two curves/fronts). In the other points on $\mathcal{S}_t \setminus \overline{\mathcal{M}}$ the SR-spheres are locally smooth (by the Cauchy-Kovalevskaya theorem and the semigroup property of the HJB-equations).

C.5 The Limiting Procedure (8.15) for the Sub-Riemannian Eikonal Equation

In this section we study the limit procedure (8.15), illustrated in Figure 8.5. To this end we first provide a formal representation of the viscosity solutions of system (8.12), where we rely on viscosity solutions of morphological scale spaces obtained by super-position over the $(\min, +)$ algebra, i.e. obtained by morphological convolution (erosions) with the morphological impulse

C.5 The Limiting Procedure (8.15) for the Sub-Riemannian Eikonal Equation

response, cf. Burgeth & Weickert (2005). Now as the HJB-equations of such morphological scale spaces do not involve a global offset by 1 in the right-hand side of the PDE we need to combine such erosions with a time shift in order to take into account the global offset. It turns out that the combination of these techniques provide staircases with steps of size ϵ , so that we obtain the appropriate limit by taking the limit $\epsilon \rightarrow 0$ afterwards as is done in (8.15).

Morphological convolutions over the $SE(2)$ group are obtained by replacing in linear left-invariant convolutions, the usual $(+, \cdot)$ -algebra by the $(\min, +)$ -algebra. Such erosions on $SE(2)$ are given by

$$(k \ominus f)(g) := \inf_{h \in SE(2)} \{k(h^{-1}g) + f(h)\}. \quad (\text{C.15})$$

Furthermore, to include the updating of the initial condition in (8.12) we define

$$\tilde{W}(g) := \begin{cases} W(g) & \text{if } g \neq e \\ 0 & \text{if } g = e. \end{cases} \quad (\text{C.16})$$

Lemma 3. *Let $\epsilon > 0$, $n \in \mathbb{N}$. The viscosity solution of (8.12) is given by*

$$W_{n+1}^\epsilon(g, r) = (k_{r-n\epsilon} \ominus \tilde{W}_n^\epsilon)(g) + (r - n\epsilon), \quad (\text{C.17})$$

for $r \in [r_n, r_{n+1}] = [n\epsilon, (n+1)\epsilon]$ and morphological kernel $k_v(g)$, $v \geq 0$, given by

$$k_v(g) = \begin{cases} 0 & \text{if } d(g, e) \leq v, \\ \infty & \text{else,} \end{cases}$$

where $d(g, e)$ denotes the Carnot-Caratheodory distance (8.7) between $g \in SE(2)$ and $e = (0, 0, 0)$. For $n = 0$ we have that the viscosity solution of (8.13) is given by $W_1^\epsilon(g, r) = k_r(g) + r$.

Proof In order to care of the constant off-set in the HJB-equations of (8.12) and (8.13), we set $r = r_{new} + r_n$ and we define for $n = 0, 1, 2, \dots$ the functions $V_{n+1}^\epsilon : SE(2) \times [0, \epsilon] \rightarrow \mathbb{R}$ by

$$V_{n+1}^\epsilon(g, r_{new}) := W_{n+1}^\epsilon(g, r_{new} + r_n) - r_{new},$$

with $r_{new} \in [0, \epsilon]$ and V_{n+1}^ϵ the viscosity solution of

$$\left\{ \begin{array}{l} \frac{\partial V_{n+1}^\epsilon}{\partial r_{new}}(g, r_{new}) = -1 + 1 - \tilde{H}(g, d^{SR}V_{n+1}^\epsilon(g, r_{new})) = -\tilde{H}(g, d^{SR}V_{n+1}^\epsilon(g, r_{new})), \\ \text{for } g \neq e \text{ we have } V_{n+1}^\epsilon(g, 0) = \begin{cases} \infty & \text{if } n = 0, \\ W_n^\epsilon(g, r_n) & \text{if } n \in \mathbb{N} \end{cases} \\ \text{for } g = e \text{ we have } V_{n+1}^\epsilon(g, 0) = V_{n+1}^\epsilon(e, 0) = 0. \end{array} \right.$$

where we use short notation for the sub-Riemannian derivative $d^{SR}V := \sum_{i=1}^2 \mathcal{A}_i V \omega^i$, recall (8.10) in Remark 11, and where Hamiltonian \tilde{H} is given by (C.11).

Now let us first consider the case $n = 0$. By the results in Appendix C.2 the Hamiltonian system (8.13) provides geodesically equidistant wavefront propagation traveling with unit speed and departing directly from the unity element. As a result, we find

$$V_1^\epsilon(g, r_{new}) = k_{r_{new}}(g) = \begin{cases} 0 & \text{if } d(g, e) \leq r_{new} \\ \infty & \text{else.} \end{cases}$$

C. VESSEL TRACKING PART II: SUB-RIEMANNIAN GEODESICS IN SE(2)

and by left-invariant ‘superposition’ over the $(\min, +)$ -algebra we find for $n = 1, 2, \dots$ that $V_{n+1}^\epsilon(g, r_{new}) = (k_{r_{new}} \ominus \tilde{W}_n^\epsilon(\cdot, r_n))(g)$, where we recall (C.16). Finally, we have

$$W_{n+1}^\epsilon(g, r) = V_{n+1}^\epsilon(g, r - n\epsilon) + r - n\epsilon = (k_{r-n\epsilon} \ominus \tilde{W}_n^\epsilon(\cdot, r_n))(g) + r - n\epsilon.$$

Corollary 2. *Let $n \in \mathbb{N}$. Let $\epsilon > 0$. The following identity holds*

$$\begin{aligned} W_{n+1}^\epsilon(g, r_{n+1}) &= (k_\epsilon \ominus \tilde{W}_n^\epsilon(\cdot, r_n))(g) + \epsilon \\ &= \begin{cases} \sum_{m=0}^n (m+1)\epsilon 1_{[r_m, r_{m+1}]}(d(g, e)) & \text{if } d(g, e) \leq r_{n+1} = (n+1)\epsilon \\ \infty & \text{if } d(g, e) > r_{n+1}, \end{cases} \end{aligned} \quad (\text{C.18})$$

where $1_{[r_m, r_{m+1}]}$ denotes the indicator function on set $[r_m, r_{m+1}]$.

Proof The first part follows by Lemma 3 for $r = r_{n+1}$ (i.e. $r_{new} = \epsilon$). The second part follows by induction. Recall from Lemma 3 that $W_1^\epsilon(g, r) = k_r(g) + r$. Now application of (C.17) for $n = 1$ yields

$$\begin{aligned} W_2^\epsilon(g, r_2) &= (k_\epsilon \ominus \tilde{W}_1^\epsilon(\cdot, r_1))(g) + \epsilon = \epsilon + \inf_{h \in \overline{B}_{g,\epsilon}} \begin{cases} k_\epsilon(h) + \epsilon & \text{if } h \neq e \\ 0 & \text{if } h = e, \end{cases} = \\ \epsilon + \begin{cases} 0 & \text{if } d(g, e) \leq \epsilon \\ \epsilon & \text{if } \epsilon < d(g, e) \leq 2\epsilon \\ \infty & \text{else} \end{cases} &= \begin{cases} \sum_{m=0}^1 (m+1)\epsilon 1_{[r_m, r_{m+1}]}(d(g, e)) & \text{if } d(g, e) \leq r_2 \\ \infty & \text{else,} \end{cases} \end{aligned} \quad (\text{C.19})$$

with $\overline{B}_{g,\epsilon} = \{h \in SE(2) \mid d(g, h) \leq \epsilon\}$. This can intuitively be seen from the geometric meaning of an erosion $\tilde{W}_1^\epsilon \mapsto k_\epsilon \ominus \tilde{W}_1^\epsilon$ where one drops cylinders from below on the graph of $\tilde{W}_1^\epsilon(\cdot, r_n)$ and considering the new hull where cylinders get stuck. Eq. (C.19) can also be seen directly from the definition of k_ϵ . Let us verify each case separately:

- If $d(g, e) > 2\epsilon$ we have that the value must be infinite, since suppose it were finite then by the definition of the morphological kernel k_ϵ we would need to have that $d(g, e) \leq d(g, h) + d(h, e) \leq 2\epsilon$ yielding contradiction.
- If $d(g, e) \leq \epsilon$, then in the erosion-minimization we can take $h = e$ and we obtain $\epsilon + 0$.
- If $\epsilon < d(g, e) \leq 2\epsilon$, then in the erosion-minimization we cannot take $h = e$, but for allowed choices we obtain $k_\epsilon(e) = 0$ and $\epsilon + \epsilon$ as output.

Similarly we have by inserting induction hypothesis for n and recursion (C.17) we have

$$\begin{aligned} W_{n+2}^\epsilon(g, r_{n+2}) &= (k_\epsilon \ominus \tilde{W}_{n+1}^\epsilon(\cdot, r_{n+1}))(g) + \epsilon = \epsilon + \sum_{m=0}^{n+1} (m+1)\epsilon 1_{[r_{m+1}, r_{m+2}]}(d(g, e)) \\ &= \epsilon + \sum_{m'=1}^{n+2} m'\epsilon 1_{[r_{m'}, r_{m'+1}]}(d(g, e)) = \sum_{m'=0}^{n+1} (m'+1)\epsilon 1_{[r_{m'}, r_{m'+1}]}(d(g, e)), \end{aligned}$$

for $d(g, e) \leq r_{n+2}$. Here we applied $m' = m + 1$ so that the result follows for $n + 1$. \square

C.6 Embedding into Geometric Control Theory

Theorem 9. Let $g \in SE(2)$ be given. We have the following limit

$$\lim_{\epsilon \rightarrow 0} \lim_{n \rightarrow \infty} W_{n+1}^\epsilon(g, (n+1)\epsilon) = d(g, e).$$

Proof Application of Corollary 2 gives

$$\begin{aligned} \lim_{n \rightarrow \infty} W_{n+1}^\epsilon(g, (n+1)\epsilon) &= \sum_{k=0}^{\infty} (k+1)\epsilon \mathbf{1}_{[r_k, r_{k+1}]}(d(g, e)) \\ &= \sum_{k=0}^{N^*(g, \epsilon)} (k+1)\epsilon \mathbf{1}_{[r_k, r_{k+1}]}(d(g, e)), \end{aligned}$$

with $N^*(g, \epsilon) = \lceil \frac{d(g, e)}{\epsilon} \rceil$, i.e. the smallest integer $\geq \frac{d(g, e)}{\epsilon} \in \mathbb{R}^+$. As a result we have

$$\begin{aligned} \lim_{\epsilon \downarrow 0} \lim_{n \rightarrow \infty} W_{n+1}^\epsilon(g, r_{n+1}) &= \lim_{\epsilon \downarrow 0} W_{N^*(g, \epsilon)+1}^\epsilon(g, (n+1)\epsilon) \\ &= \lim_{\epsilon \downarrow 0} \sum_{k=0}^{N^*(g, \epsilon)} (k+1)\epsilon \mathbf{1}_{[r_k, r_{k+1}]}(d(g, e)) = d(g, e) \end{aligned}$$

where the size of the steps in the staircase towards $d(g, e)$ vanishes as $\epsilon \rightarrow 0$. Recall Figure 8.5.

C.6 Embedding into Geometric Control Theory

As mentioned in Remark 7 the problem $\mathbf{P}_{\text{mec}}^C(SE(2))$ given by (8.2) actually comes from a mechanical problem in geometric control, where a so-called Reeds-Shepp car Reeds & Shepp (1990) can proceed both forward and backward in the path-optimization. As pointed out in Boscain *et al.* (2010) such a problem, for certain end conditions, cannot be considered as a curve optimization problem on the plane. The underlying difficulty is that for certain boundary conditions, the smooth minimizers of problem $\mathbf{P}_{\text{mec}}^C(SE(2))$ have the property that their spatial projections exhibit a cusp and cannot be parameterized by spatial arc-length, since the control variable u^1 switches sign at the cusp. See Figure C.2.

In 2D image analysis applications solutions without cusps may be required. In this appendix, we propose problem $\mathbf{P}_{\text{contour}}^C(SE(2))$ as a modification of problem $\mathbf{P}_{\text{mec}}^C(SE(2))$, which considers only the end conditions such that cusps do not occur.

Let us denote $\mathbf{x} = (x, y) \in \mathbb{R}^2$, then for $g = (\mathbf{x}, \theta) \in \mathfrak{R} \subset SE(2)$ and $C = 1$ the following problem on the spatial plane is well-posed:

$$\mathbf{P}_{\text{curve}}^C(\mathbb{R}^2) : \left\{ \begin{array}{l} \gamma(0) = \mathbf{0}, \gamma(L) = \mathbf{x}, \\ \dot{\gamma}(0) = (1, 0)^T, \dot{\gamma}(L) = (\cos \theta, \sin \theta)^T, \\ l(\gamma(\cdot)) = \int_0^L \mathcal{C}(\gamma(s)) \sqrt{\beta^2 + \kappa^2(s)} ds \rightarrow \min, \\ \gamma : [0, L] \rightarrow \mathbb{R}^2, \beta > 0, \end{array} \right. \quad (\text{C.20})$$

where L denotes spatial length and κ curvature of the curve $\gamma \in C^\infty([0, L], \mathbb{R}^2)$, and where $\mathfrak{R} \subset SE(2)$ denotes the set of allowable end-conditions. In Duits *et al.* (2013c) this set is

C. VESSEL TRACKING PART II: SUB-RIEMANNIAN GEODESICS IN SE(2)

explicitly determined, and partially depicted in Figure C.2C. In Ch. 8 we studied $\mathbf{P}_{\text{mec}}^{\mathcal{C}}(SE(2))$ (and not (C.20)), and we look both forward and backward. Then, to avoid cusps we must consider the problem:

$$\mathbf{P}_{\text{contour}}^{\mathcal{C}}(SE(2)) : \begin{cases} \dot{\gamma}(t) = u^1(t) \mathcal{A}_1|_{\gamma(t)} + u^3(t) \mathcal{A}_3|_{\gamma(t)}, \text{ for } t \in [0, T] \\ \gamma(0) = e, \quad \gamma(T) = g = (\mathbf{x}, \theta) \in \mathfrak{R}^{\mathcal{C}}, \\ l(\gamma(\cdot)) = \int_0^T \mathcal{C}(\gamma(t)) \sqrt{\beta^2 |u^1(t)|^2 + |u^3(t)|^2} dt \rightarrow \min, \\ \text{with curve } \gamma : [0, T] \rightarrow SE(2), \text{ with controls:} \\ (u^1(t), u^3(t)) \in \mathbb{R}^2, \text{ and } u^1(t) \text{ does not change sign,} \end{cases} \quad (\text{C.21})$$

where $\mathfrak{R}^{\mathcal{C}}$ is the set of all $g \in SE(2)$ such that the minimizing SR-geodesic(s) $\gamma(\cdot) = (\mathbf{x}(\cdot), \theta(\cdot))$ do not exhibit a cusp in their spatial projections $\mathbf{x}(\cdot)$. We distinguish between 3 cases for the end-condition g (see Figure C.2):

- If g is chosen such that the optimal control $u^1 \geq 0$ then the lift of problem $\mathbf{P}_{\text{curve}}^{\mathcal{C}}(\mathbb{R}^2)$ coincides with $\mathbf{P}_{\text{mec}}^{\mathcal{C}}(SE(2))$ and also with $\mathbf{P}_{\text{contour}}^{\mathcal{C}}(SE(2))$.
- If g is chosen such that the optimal control $u^1 \leq 0$ then problem $\mathbf{P}_{\text{mec}}^{\mathcal{C}}(SE(2))$ and problem $\mathbf{P}_{\text{contour}}^{\mathcal{C}}(SE(2))$ coincide.
- If g is chosen such that the optimal control $u^1(t)$ switches sign at some internal time $t \in (0, T)$, then $g \in SE(2) \setminus \mathfrak{R}^{\mathcal{C}}$ and the spatial projection of the corresponding minimizing SR-geodesic(s) has an internal cusp, which we consider not desirable in our applications of interest.

Remark 29. Geodesics in $\mathbf{P}_{\text{contour}}^{\mathcal{C}}(SE(2))$ can depart forward or backward from the origin. Then, for $\mathcal{C} = 1$, the set $\mathfrak{R}^{\mathcal{C}=1}$ of allowable end-conditions can be obtained from the set $\mathfrak{R} \subset \{(x, y, \theta) \in SE(2) \mid x \geq 0\}$ by a reflectional symmetry:

$$\mathfrak{R}^{\mathcal{C}=1} = \mathfrak{R} \cup \mathfrak{Q} \text{ with } \mathfrak{Q} = \{(x, y, \theta) \in SE(2) \mid (-x, y, -\theta) \in \mathfrak{R}\}. \quad (\text{C.22})$$

Remark 30. In Section 8.7.1 we provided a very simple numerical tool to compute the surface in $SE(2)$ where cusps appear also for $\mathcal{C} \neq 1$, recall Eq. (8.21). This surface is a boundary of a volume in $SE(2)$ that contains the set $\mathfrak{R}^{\mathcal{C}}$.

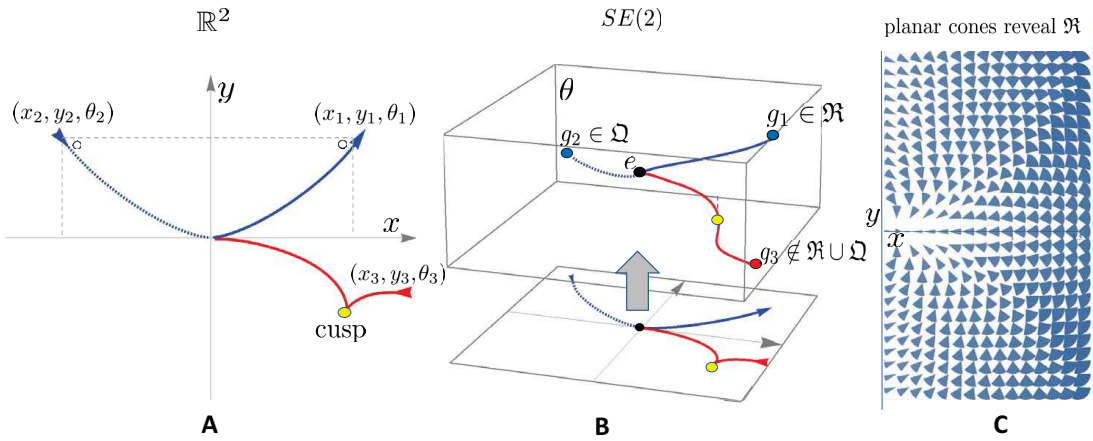


Figure C.2: 3 Sub-Riemannian geodesics for uniform cost $C = 1$ to reveal the differences of the 3 geometric control problems (8.2), (C.20) and (C.21), for $\beta = 1$. **A:** plots of spatial projections of sub-Riemannian geodesics in \mathbb{R}^2 , **B:** SR-geodesics in $SE(2)$, **C:** A part of \mathfrak{R} (the set of end-conditions for which $P_{\text{curve}}(\mathbb{R}^2)$ is well-defined Duits et al. (2013c)) depicted as reachable cones around the origin. End condition $g_1 = (x_1, y_1, \theta_1) \in \mathfrak{R}$ yields the minimizing curve of P_{contour} , P_{mec} and P_{curve} . End condition $g_2 = (-x_1, y_1, -\theta_1)$ yields the minimizing curve in P_{contour} , P_{mec} , and it is invalid for P_{curve} . End condition g_3 is invalid for both P_{curve} and P_{contour} , as it induces an internal cusp. For $C = 1$ the set of allowable end conditions for P_{contour} equals $\mathfrak{R}^{C=1} = \mathfrak{R} \cup \mathfrak{Q}$, recall (C.22). For $C \neq 1$ this set \mathfrak{R}^C differs, and can be computed, cf. Remark 30.

References

- ABBASI-SURESHJANI AND FAVALI, CITTI, G., SARTI, A. & TER HAAR ROMENY, B.M. (2016). Cortically-inspired spectral clustering for connectivity analysis in retinal images: Curvature integration. *arXiv preprint arXiv:1608.08049*. 279
- ABRAMOFF, M. & NIEMEIJER, M. (2015). Mass screening of diabetic retinopathy using automated methods. In G. Michelson, ed., *Teleophthalmology in Preventive Medicine*, 41–50, Springer. 125
- AGRACHEV, A.A. & SACHKOV, Y. (2013). *Control theory from the geometric viewpoint*, vol. 87. Springer Science & Business Media. 188, 193, 223, 302, 304
- AGURTO, C., BARRIGA, E.S., MURRAY, V., NEMETH, S., CRAMMER, R., BAUMAN, W., ZAMORA, G., PATTICHIS, M.S. & SOLIZ, P. (2011). Automatic detection of diabetic retinopathy and age-related macular degeneration in digital fundus images. *Investigative Ophthalmology & Visual Science*, **52**, 5862. 125
- AKIAN, M., QUADRAT, J.P. & VIOT, M. (1994). Bellman processes. In *11th International Conference on Analysis and Optimization of Systems Discrete Event Systems*, 302–311, Springer. 186, 193, 194, 196, 305
- AKMAN, A., KADAYIFILAR, S. & AYDIN, P. (1998). Effects of hypertension on the retinal vein width at the retinal arterio-venous crossings. *European Journal of Ophthalmology*, **8**, 71–75, cited By 3. 68
- AL-DIRI, B., HUNTER, A. & STEEL, D. (2009). An active contour model for segmenting and measuring retinal vessels. *IEEE TMI*, **28**, 1488–1497. 154, 155, 167, 168, 169, 170
- AL-DIRI, B., HUNTER, A., STEEL, D. & HABIB, M. (2010). Automated analysis of retinal vascular network connectivity. *Computerized medical imaging and graphics : the official journal of the Computerized Medical Imaging Society*, **34**, 462–70. 241
- ALIAHMAD, B., KUMAR, D.K., SAROSSY, M.G. & JAIN, R. (2014). Relationship between diabetes and grayscale fractal dimensions of retinal vasculature in the indian population. *BMC ophthalmology*, **14**, 1. 10

REFERENCES

- ALLEN, J. (1977). Short-term spectral analysis, and modification by discrete Fourier transform. *IEEE Transactions on Acoustics Speech and Signal Processing*, **25**, 235–238. 24
- AMERICAN ACADEMY OF OPHTHALMOLOGY (2015). *2015-2016 Basic and Clinical Science Course (BCSC), Section 3: Clinical Optics*. American Academy of Ophthalmology. 214
- AQUINO, A. (2014). "establishing the macular grading grid by means of fovea centre detection using anatomical-based and visual-based features ". *Comp. in Biology and Medicine*, **55**, 61 – 73. 57, 125, 130
- AQUINO, A., GEGUNDEZ-ARIAS, M.E. & MARIN, D. (2010). Detecting the optic disc boundary in digital fundus images using morphological, edge detection, and feature extraction techniques. *IEEE TMI*, **29**, 1860–9. 122
- AQUINO, A., GEG, M.E. & MAR, D. (2012). Automated optic disk detection in retinal images of patients with diabetic retinopathy and risk of macular edema. *IJBLS*, **8**, 87–92. 56, 117, 123
- ARMSTRONG, R.A. (2013). Statistical guidelines for the analysis of data obtained from one or both eyes. *Ophthalmic and Physiological Optics*, **33**, 7–14. 261
- ASTERIADIS, S., NIKOLAIDIS, N. & PITAS, I. (2009). Facial feature detection using distance vector fields. *Pattern Recognition*, **42**, 1388–1398. 131
- AUGUST, J. (2001). *The Curve Indicator Random Field*. Ph.D. thesis, Yale University. 295
- AUGUST, J. & ZUCKER, S. (2003). The curve indicator random field and Markov processes. *IEEE-PAMI, Pattern Recognition and Machine Intelligence*, **25**, number 4. 295
- AZZOPARDI, G. & PETKOV, N. (2013). Trainable cosfire filters for keypoint detection and pattern recognition. *IEEE Transactions on PAMI*, **35**, 490–503. 96
- BANKHEAD, P., SCHOLFIELD, C.N., McGEOWN, J.G. & CURTIS, T.M. (2012). Fast retinal vessel detection and measurement using wavelets and edge location refinement. *PLoS ONE*, **7**, e32435. 155, 167, 169, 170
- BAY, H., TUYTELAARS, T. & VAN GOOL, L. (2006). Surf: Speeded up robust features. In A. Leonardis, H. Bischof & A. Pinz, eds., *ECCV 2006*, vol. 3951 of *Lecture Notes in Computer Science*, 404–417, Springer Berlin Heidelberg. 96
- BAYEN, A.M. & TOMLIN, C.J. (2001). A construction procedure using characteristics for viscosity solutions of the Hamilton-Jacobi equation. In *Decision and Control, 2001. Proceedings of the 40th IEEE Conference on*, vol. 2, 1657–1662, IEEE. 193
- BEKKERS, E. (2012). *A New Retinal Vessel Tracking Method Based on Orientaiton Scores*. Master's thesis, Eindhoven University of Technology, Department of Biomedical Engineering, the Netherlands. 178, 278

REFERENCES

- BEKKERS, E., DUTS, R., BERENDSCHOT, T. & TER HAAR ROMENY, B. (2014a). A multi-orientation analysis approach to retinal vessel tracking. *JMIV*, 1–28. 26, 53, 60, 99, 121, 140, 173, 174, 202, 287, 290, 293
- BEKKERS, E., DUTS, R. & TER HAAR ROMENY, B. (2014b). Optic nerve head detection via group correlations in multi-orientation transforms. In A. Campilho & M. Kamel, eds., *Image Analysis and Recognition*, LNCS, 293–302, Springer. 99, 100
- BEKKERS, E., DUTS, R. & LOOG, M. (2015a). Training of templates for object recognition in invertible orientation scores: Application to optic nerve head detection in retinal images. In *EMMCVPR*, 464–477, Springer. 99, 100, 106
- BEKKERS, E., DUTS, R., MASHTAKOV, A. & SANGUINETTI, G. (2015b). Data-driven sub-Riemannian geodesics in $SE(2)$. In J.F. Aujol, M. Nikolova & N. Papadakis, eds., *Scale Space and Variational Methods in Computer Vision*, vol. 9087 of *Lecture Notes in Computer Science*, 613–625, Springer International Publishing. 187, 204, 233
- BEKKERS, E.J., DUTS, R., MASHTAKOV, A. & SANGUINETTI, G.R. (2015c). A PDE approach to data-driven sub-Riemannian geodesics in $SE(2)$. *SIAM Journal on Imaging Sciences*, 8, 2740–2770. 186, 203, 212, 233, 234, 301
- BEN-YOSEF, G. & BEN-SHAHAR, O. (2012). A tangent bundle theory for visual curve completion. *IEEE Transactions on Pattern Analysis and Machine Intelligence*, 34, 1263–1280. 65, 184
- BENMANSOUR, F. & COHEN, L.D. (2011). Tubular structure segmentation based on minimal path method and anisotropic enhancement. *International Journal of Computer Vision*, 92, 192–210. 185, 204, 273, 278
- BERESTOVSKII, V. (2016). (Locally) shortest arcs of a special sub-Riemannian metric on the Lie group $SO(2, 1)$. *St. Petersburg Mathematical Journal*, 27, 1–14. 65, 212
- BERESTOVSKII, V.N. (1994). Geodesics of a left-invariant nonholonomic Riemannian metric on the group of motions of the Euclidean plane. *Siberian Mathematical Journal*, 35, 1083–1088. 65, 212
- BERGHLOM, F. (1987). Edge focusing. *Pattern Analysis and Machine Intelligence, IEEE Transactions on*, 9, 726 –741. 173
- BESCHASTNYI, I.Y. & SACHKOV, Y.L. (2014). Sub-Riemannian and almost-Riemannian geodesics on $SO(3)$ and S^2 . *arXiv preprint arXiv:1409.1559*. 65, 212
- BOJKE, L., CLAXTON, K., SCULPHER, M.J. & PALMER, S. (2008). Identifying research priorities: the value of information associated with repeat screening for age-related macular degeneration. *Medical Decision Making*, 28, 33–43. 9

REFERENCES

- BONHOEFFER, T., GRINVALD, A. *et al.* (1991). Iso-orientation domains in cat visual cortex are arranged in pinwheel-like patterns. *Nature*, **353**, 429–431. 22
- BONNARD, B. & CHYBA, M. (2014). Two applications of geometric optimal control to the dynamics of spin particles. In *The Impact of Applications on Mathematics*, 67–83, Springer. 65, 212
- BONNARD, B., COTS, O., POMET, J.B. & SHCHERBAKOVA, N. (2014). Riemannian metrics on 2D-manifolds related to the Euler-Poinsot rigid body motion. *ESAIM: Control, Optimisation and Calculus of Variations*, **20**, 864–893. 65, 212
- BOOTHBY, W. (2003). *An Introduction to Differentiable Manifolds and Riemannian Geometry*. Pure and Applied Mathematics Series, Academic Press. 38
- BOSCAIN, U. & ROSSI, F. (2008). Invariant Carnot-Caratheodory metrics on S^3 , $SO(3)$, $SL(2)$, and lens spaces. *SIAM Journal on Control and Optimization*, **47**, 1851–1878. 65, 212
- BOSCAIN, U., CHARLOT, G. & ROSSI, F. (2010). Existence of planar curves minimizing length and curvature. *Differential equations and dynamical systems, Collected papers, Tr. Mat. Inst. Steklova*, **270**, 49–61. 311
- BOSCAIN, U., DUTS, R., ROSSI, F. & SACHKOV, Y. (2014). Curve cuspless reconstruction via sub-Riemannian geometry. *ESAIM: Control, Optimisation and Calculus of Variations*, **20**, 748–770. 22, 65, 66, 184, 185, 188, 200, 211, 212, 220
- BOSKING, W.H., ZHANG, Y., SCHOFIELD, B. & FITZPATRICK, D. (1997). Orientation selectivity and the arrangement of horizontal connections in tree shrew striate cortex. *The Journal of Neuroscience*, **17**, 2112–2127. 22
- BOUIX, S., SIDDIQI, K. & TANNENBAUM, A. (2005). Flux driven automatic centerline extraction. *Medical Image Analysis*, **9**, 209–221. 268
- BRESSAN, A. (2010). Viscosity solutions of Hamilton-Jacobi equations and optimal control problems. *Lecture notes*. 189, 306, 308
- BRINCHMANN-HANSEN, O. & HEIER, H. (1986). Theoretical relations between light streak characteristics and optical properties of retinal vessels. *Acta Ophthalmologica*, **64**, 33–37. 167, 169
- BROE, R., RASMUSSEN, M.L., FRYDKJAER-OLSEN, U., OLSEN, B.S., MORTENSEN, H.B., PETO, T. & GRAUSLUND, J. (2014). Retinal vascular fractals predict long-term microvascular complications in type 1 diabetes mellitus: the danish cohort of pediatric diabetes 1987 (dcpd1987). *Diabetologia*, **57**, 2215–2221. 10

REFERENCES

- BRUNA, J. & MALLAT, S. (2013). Invariant scattering convolution networks. *IEEE transactions on pattern analysis and machine intelligence*, **35**, 1872–1886. 121, 290
- BUDAI, A. (2011). Gold standard database for evaluation of fundus image segmentation algorithms. www5.informatik.uni-erlangen.de/en/research/data/fundus-images/. 155, 165
- BUDAI, A., HORNEGGER, J. & MICHELSON, G. (2009). Multiscale approach for blood vessel segmentation on retinal fundus images. *Invest. Ophth. & Vis. Sc.*, **50**, 325. 154
- BUDAI, A., BOCK, R., MAIER, A., HORNEGGER, J. & MICHELSON, G. (2013). Robust Vessel Segmentation in Fundus Images. *IJBI*, **2013**. 140, 150
- BURGETH, B. & WEICKERT, J. (2005). An explanation for the logarithmic connection between linear and morphological system theory. *International Journal of Computer Vision*, **64**, 157–169. 186, 193, 194, 305, 309
- CALIN, O., CHANG, D.C. & MARKINA, I. (2008). Sub-Riemannian geometry on the sphere S^3 . *arXiv preprint arXiv:0809.4571*. 65, 212
- CAMPADELLI, P., LANZAROTTI, R. & LIPORI, G. (2009). Precise eye and mouth localization. *International Journal of Pattern Recognition and Artificial Intelligence*, **23**, 359–377. 131
- CAN, A., SHEN, H., TURNER, J.N., TANENBAUM, H.L. & ROYSAM, B. (1999). Rapid automated tracing and feature extraction from retinal fundus images using direct exploratory algorithms. *IEEE Trans. Inform. Technol. Biomed.*, **3**, 125–138. 154
- CASELLES, V., KIMMEL, R. & SAPIRO, G. (1997). Geodesic active contours. *International journal of computer vision*, **22**, 61–79. 184
- CHANG, D.C., MARKINA, I. & VASILEV, A. (2009). Sub-Riemannian geodesics on the 3-D sphere. *Complex analysis and operator theory*, **3**, 361–377. 65, 213
- CHEN, D. (2016). *New Minimal Path Models for Tubular Structure Extraction and Image Segmentation*. Ph.D. thesis, Universite Paris Dauphine, PSL Research University. 83
- CHEN, D. & COHEN, L.D. (2014). Automatic vessel tree structure extraction by growing minimal paths and a mask. In *2014 IEEE 11th International Symposium on Biomedical Imaging (ISBI)*, 802–805. 268, 270, 272, 278
- CHEN, D. & COHEN, L.D. (2015). Interactive retinal vessel centrelne extraction and boundary delineation using anisotropic fast marching and intensities consistency. In *2015 37th Annual Int. Conference of the IEEE Eng. in Med. and Bio. Society (EMBC)*, 4347–4350. 279
- CHEN, D., MIREBEAU, J.M. & COHEN, L.D. (2016). Vessel tree extraction using radius-lifted keypoints searching scheme and anisotropic fast marching method. *Journal of Algorithms & Computational Technology*. 278

REFERENCES

- CHEUNG, C., LAMOUREUX, E., IKRAM, M. *et al.* (2012). Retinal vascular geometry in Asian persons with diabetes and retinopathy. *J Diab. Sci. Techn.*, **6**, 595–605. 8, 13, 70, 250, 262
- CHEUNG, C., IKRAM, M., KLEIN, R. & WONG, T. (2015). The clinical implications of recent studies on the structure and function of the retinal microvasculature in diabetes. *Diabetologia*, 1–15. 9
- CHEUNG, C.Y., TAY, W.T., MITCHELL, P., WANG, J.J., HSU, W., LEE, M.L., LAU, Q.P., ZHU, A.L., KLEIN, R. *et al.* (2011a). Quantitative and qualitative retinal microvascular characteristics and blood pressure. *Journal of hypertension*, **29**, 1380–1391. 10
- CHEUNG, C.Y.L., ZHENG, Y., HSU, W., LEE, M.L., LAU, Q.P., MITCHELL, P., WANG, J.J., KLEIN, R. & WONG, T.Y. (2011b). Retinal vascular tortuosity, blood pressure, and cardiovascular risk factors. *Ophthalmology*, **118**, 812–818. 10, 12, 250, 265
- CHIRIKJIAN, G.S. (2000). *Engineering Applications of Noncommutative Harmonic Analysis: With Emphasis on Rotation and Motion Groups*. CRC Press, Abingdon. 252
- CHUTATAPE, O., ZHENG, L. & KRISHNAN, S. (1998). Retinal blood vessel detection and tracking by matched Gaussian and kalman filters. In *Engineering in Medicine and Biology Society, 1998. Proceedings of the 20th Annual International Conference of the IEEE*, vol. 6, 3144 –3149 vol.6. 154
- CITTI, G. & SARTI, A. (2006). A cortical based model of perceptual completion in the roto-translation space. *JMIV*, **24**, 307–326. 22, 65, 106, 108, 184, 212, 295
- COHEN, L.D. & KIMMEL, R. (1997). Global minimum for active contour models: A minimal path approach. *International journal of computer vision*, **24**, 57–78. 184
- CRAVEN, P. & WAHBA, G. (1978). Smoothing noisy data with spline functions. *Numerische Mathematik*, **31**, 377–403. 116
- CUINGNET, R., GLAUNES, J., CHUPIN, M., BENALI, H. & COLLIOT, O. (2013). Spatial and anatomical regularization of SVM: A general framework for neuroimaging data. *Pattern Analysis and Machine Intelligence, IEEE Transactions on*, **35**, 682–696. 98
- DALAL, N. & TRIGGS, B. (2005). Histograms of oriented gradients for human detection. In *CVPR 2005. IEEE Computer Society Conference on*, vol. 1, 886–893. 96
- DASHTBOZORG, B., MENDONÇA, A.M. & CAMPILHO, A. (2014). An automatic graph-based approach for artery/vein classification in retinal images. *IEEE TIP*, **23**, 1073–83. 69, 240, 241, 243, 247, 248
- DASHTBOZORG, B., MENDONA, A.M. & CAMPILHO, A. (2015). Optic disc segmentation using the sliding band filter. *Computers in Biology and Medicine*, **56**, 1 – 12. 56, 117, 123

REFERENCES

- DE BOOR, C. (1978). A practical guide to splines. *Mathematics of Computation*. 98
- DUITS & JANSSEN, HANNINK, J. & SANGUINETTI, G. (2016). Locally adaptive frames in the roto-translation group and their applications in medical imaging. *Journal of Mathematical Imaging and Vision*, 1–36. 59, 90, 141, 143, 151, 250, 252, 253, 254
- DUITS, R. (2005). *Perceptual Organization in Image Analysis*. Ph.D. thesis, Eindhoven University of Technology, Department of Biomedical Engineering, the Netherlands. 20, 25, 26, 28, 48, 141
- DUITS, R. & BURGETH, B. (2007). Scale spaces on lie groups. In F. Sgallari, A. Murli & N. Paragios, eds., *Scale Space and Variational Methods in Computer Vision*, vol. 4485 of *Lecture Notes in Computer Science*, 300–312, Springer Berlin Heidelberg. 108
- DUITS, R. & FRANKEN, E. (2007). Left-invariant stochastic evolution equations on $SE(2)$ and its applications to contour enhancement and contour completion via invertible orientation scores. CASA-report and arxiv, arXiv: 0711.0951v4 , see <http://arxiv.org/abs/0711.0951> and <http://www.win.tue.nl/casa/research/casareports/2007.html>. 297, 298
- DUITS, R. & FRANKEN, E. (2009). Line enhancement and completion via linear left-invariant scale spaces on $SE(2)$. In X.C.e.a. Tai, ed., *Scale Space and Variational Methods in Computer Vision*, 795–807. 295
- DUITS, R. & FRANKEN, E. (2010a). Left-invariant parabolic evolutions on $SE(2)$ and contour enhancement via invertible orientation scores part I: Linear left-invariant diffusion equations on $SE(2)$. *Quarterly of Applied Mathematics*, **68**, 255–292. 98, 99, 105, 106, 109, 111, 113, 121, 290, 295, 297, 298
- DUITS, R. & FRANKEN, E. (2010b). Left-invariant parabolic evolutions on $SE(2)$ and contour enhancement via invertible orientation scores. part II: Non-linear left-invariant diffusions on invertible orientation score. *Q APPL MATH*, **68**, 293–331. 89, 250, 295, 299
- DUITS, R. & VAN ALMSICK, M. (2008). The explicit solutions of linear left-invariant second order stochastic evolution equations on the 2D Euclidean motion group. *Quarterly of Applied Mathematics*, 27–67. 60, 295, 298
- DUITS, R., DUIT, M., ALMSICK, M. & HAAR ROMENY, B. (2007a). Invertible orientation scores as an application of generalized wavelet theory. *PRIA*, **17**, 42–75. 20, 99
- DUITS, R., FELSBERG, M., GRANLUND, G.H. & TER HAAR ROMENY, B.M. (2007b). Image analysis and reconstruction using a wavelet transform constructed from a reducible representation of the Euclidean motion group. *IJCV*, **72**, 79–102. 20, 105, 121, 184, 186, 197, 290

REFERENCES

- DUITS, R., BOSCAIN, U., ROSSI, F. & SACHKOV, Y. (2013a). Association fields via cuspless sub-Riemannian geodesics in $SE(2)$. *Journal of Mathematical Imaging and Vision*, **49**, 384–417. 22, 65, 66, 181, 184, 185, 186, 188, 194, 198, 199, 200, 208, 211, 212, 219, 220, 234
- DUITS, R., FHR, H., JANSSEN, B., BRUURMIJN, M., FLORACK, L. & VAN ASSEN, H. (2013b). Evolution equations on Gabor transforms and their applications. *Applied and Computational Harmonic Analysis*, **35**, 483 – 526. 24
- DUITS, R., HAIJE, T.D., CREUSEN, E. & GHOSH, A. (2013c). Morphological and linear scale spaces for fiber enhancement in dw-mri. *Journal of Mathematical Imaging and Vision*, **46**, 326–368. 186, 196, 311, 313
- DUITS, R., GHOSH, A., HAIJE, T.D. & SACHKOV, Y. (2014). *Cuspless Sub-Riemannian Geodesics within the Euclidean Motion Group $SE(d)$* , 173–215. Springer. 90
- EL-ALAOUI, E.H.C., GAUTHIER, J.P. & KUPKA, I. (1996). Small sub-Riemannian balls on \mathbb{R}^3 . *Journal of dynamical and Control Systems*, **2**, 359–421. 191
- EPPENHOF, K., BEKKERS, E., BERENDSCHOT, T.T., PLUIM, J.P. & TER HAAR ROMENY, B.M. (2015). Retinal artery/vein classification via graph cut optimization. In E. Trucco, X. Chen, M.K. Garvin, J.J. Liu & X.Y. Frank, eds., *Proceedings of the Ophthalmic Medical Image Analysis Second International Workshop, OMIA 2015, Held in Conjunction with MICCAI 2015, Munchen, Germany, October 9, 2015*, 121–128. Iowa Research Online. 240
- ESPONA, L., CARREIRA, M.J., ORTEGA, M. & PENEZO, M.G. (2007). A snake for retinal vessel segmentation. In *Proceedings of the 3rd Iberian conference on Pattern Recognition and Image Analysis, Part II*, IbPRIA '07, 178–185, Springer-Verlag, Berlin, Heidelberg. 154
- EVANS, L.C. (1997). Partial differential equations and Monge-Kantorovich mass transfer. *Current developments in mathematics*, 65–126. 196, 304, 305, 306
- FAVALI & ABBASI-SURESHJANI, TER HAAR ROMENY, B.M. & SARTI, A. (2016). Analysis of vessel connectivities in retinal images by cortically inspired spectral clustering. *Journal of Mathematical Imaging and Vision*, **56**, 158–172. 278
- FELSBERG, M. (2013). Enhanced distribution field tracking using channel representations. In *Proceedings of the IEEE ICCV Workshops*, 121–128. 96
- FLEMING, A.D., PHILIP, S., GOATMAN, K.A., OLSON, J.A. & SHARP, P.F. (2006). Automated assessment of diabetic retinal image quality based on clarity and field definition. *Investigative Ophthalmology & Visual Science*, **47**, 1120. 53
- FLEMING, A.D., GOATMAN, K.A., PHILIP, S., OLSON, J.A. & SHARP, P.F. (2007). Automatic detection of retinal anatomy to assist diabetic retinopathy screening. *Physics in medicine and biology*, **52**, 331. 9

REFERENCES

- FLORACK, L. & KUIJPER, A. (2000). The topological structure of scale-space images. *Journal of Mathematical Imaging and Vision*, **79**, 65–79. 174
- FORACCHIA, M. et al. (2005). Luminosity and contrast normalization in retinal images. *MEDIA*, **9**, 179–90. 121, 131, 243, 290
- FORD, L.R. & FULKERSON, D.R. (1956). Maximal flow through a network. *Canadian Journal of Mathematics*, **8**, 399–404. 245, 246
- FRANGI, A., NIESSEN, W., VINCKEN, K. & VIERGEVER, M. (1998). Multiscale vessel enhancement filtering. In W. Wells, A. Colchester & S. Delp, eds., *MICCAI98*, vol. 1496 of *LNCS*, 130–137, Springer Berlin Heidelberg. 20, 57, 140, 142, 146, 147, 149, 151, 234, 253, 255
- FRANKEN, E. (2008). *Enhancement of Crossing Elongated Structures in Images*. Ph.D. thesis, Eindhoven University of Technology, Department of Biomedical Engineering, the Netherlands. 39, 141, 142
- FRANKEN, E. & DUTTS, R. (2009). Crossing-preserving coherence-enhancing diffusion on invertible orientation scores. *IJCV*, **85**, 253–278. 20, 186, 196, 198, 250, 252, 253
- FREEMAN, W. & ADELSON, E. (1991). The design and use of steerable filters. *IEEE TPAMI*, **13**, 891–906. 121, 290
- FREGNAC, Y. & SHULZ, D.E. (1999). Activity-dependent regulation of receptive field properties of cat area 17 by supervised Hebbian learning. *Journal of Neuroscience*, **41**, 68–82. 22
- GABOR, D. (1946). Theory of communication. part 1: The analysis of information. *Electrical Engineers-Part III: Radio and Communication Engineering, Journal of the Institution of*, **93**, 429–441. 24
- GEGUNDEZ-ARIAS, M.E., MARIN, D. et al. (2013). Locating the fovea center position in digital fundus images using thresholding and feature extraction techniques. *Computerized Medical Imaging and Graphics*, **37**, 386 – 393, retinal Image Analysis. 57, 99, 125, 127, 130
- GIACHETTI, A., BALLERINI, L., TRUCCO, E. & WILSON, P. (2013). The use of radial symmetry to localize retinal landmarks. *Computerized Medical Imaging and Graphics*, **37**, 369 – 376, retinal Image Analysis. 56, 57, 121, 123, 125, 130
- GRAUSLUND, J., GREEN, A., KAWASAKI, R., HODGSON, L., SJØLIE, A.K. & WONG, T.Y. (2010). Retinal vascular fractals and microvascular and macrovascular complications in type 1 diabetes. *Ophthalmology*, **117**, 1400–1405. 10

REFERENCES

- GREEN, P.J. & SILVERMAN, B.W. (1993). *Nonparametric regression and generalized linear models: a roughness penalty approach*. CRC Press. 98
- GREGSON, P.H., SHEN, Z., SCOTT, R.C. & KOZOUSEK, V. (1995). Automated grading of venous beading. *Comput. Biomed. Res.*, **28**, 291–304. 167, 169
- GREIG, D.M., PORTEOUS, B.T. & SEHEULT, A.H. (1989). Exact maximum a posteriori estimation for binary images. *Journal of the Royal Statistical Society. Series B (Methodological)*, 271–279. 244
- GRISAN, E. & RUGGERI, A. (2003). A divide et impera strategy for automatic classification of retinal vessels into arteries and veins. In *IEEE EMBS*, 890–893. 69, 240, 243, 247
- GRISAN, E., PESCE, A., GIANI, A., FORACCHIA, M. & RUGGERI, A. (2004). A new tracking system for the robust extraction of retinal vessel structure. *Conf Proc IEEE Eng Med Biol Soc*, **3**, 1620–1623. 154
- GRÖCHENIG, K. (2001). *Foundations of Time-Frequency Analysis*, chap. The Heisenberg Group: A Different Point of View, 175–201. Birkhäuser Boston, Boston, MA. 24
- GROUP, E.T.D.R.S.R. *et al.* (1991). Grading diabetic retinopathy from stereoscopic color fundus photographsan extension of the modified airlie house classification: Etdrs report number 10. *Ophthalmology*, **98**, 786–806. 53
- GU, C. (1992). Cross-validating non-Gaussian data. *Journal of Computational and Graphical Statistics*, **1**, 169–179. 116
- HAN, H.C. (2012). Twisted blood vessels: symptoms, etiology and biomechanical mechanisms. *Journal of vascular research*, **49**, 185–197. 10, 12, 250, 265
- HANNINK, J., DUIT, R. & BEKKERS, E. (2014). Crossing-preserving multi-scale vesselness. In P. Golland, N. Hata, C. Barillot, J. Hornegger & R. Howe, eds., *MICCAI 2014*, vol. 8674 of *LNCS*, 603–610, Springer International Publishing. 140
- HANSEN, D.W. & JI, Q. (2010). In the eye of the beholder: A survey of models for eyes and gaze. *Pattern Analysis and Machine Intelligence, IEEE Transactions on*, **32**, 478–500. 99
- HART, W.E., GOLDBAUM, M., KUBE, P. & NELSON, M.R. (1999). Measurement and classification of retinal vascular tortuosity. *IJMI*, **53**, 239–252. 70, 250
- HASTIE, T.J., TIBSHIRANI, R.J. & FRIEDMAN, J.H. (2009). *The elements of statistical learning : data mining, inference, and prediction*. Springer series in statistics, Springer, New York, autres impressions : 2011 (corr.), 2013 (7e corr.). 98, 104
- HEBIRI, M. & VAN DE GEER, S. (2011). The smooth-lasso and other $\ell_1 + \ell_2$ -penalized methods. *Electronic Journal of Statistics*, **5**, 1184–1226. 98

REFERENCES

- HELSTROM, C. (1966). An expansion of a signal in Gaussian elementary signals (corresp.). *IEEE Transactions on Information Theory*, **12**, 81–82. 24
- HLADKY, R.K. & PAULS, S.D. (2009). Minimal surfaces in the roto-translation group with applications to a neuro-biological image completion model. *Journal of Mathematical Imaging and Vision*, **36**, 1–27. 65, 184
- HOERL, A.E. & KENNARD, R.W. (1970). Ridge regression: Biased estimation for nonorthogonal problems. *Technometrics*, **12**, 55–67. 97, 98
- HÖRMANDER, L. (1967). Hypoelliptic second order differential equations. *Acta Mathematica*, **119**, 147–171. 110
- HOUGH, P. (1962). Method and Means for Recognizing Complex Patterns. U.S. Patent 3.069.654. 173
- HSU, E.P. (2002). *Stochastic analysis on manifolds*, vol. 38. American Mathematical Soc. 114
- HUANG, F., ZHANG, J., BEKKERS, E., DASHTBOZORG, B. & TER HAAR ROMENY, B.M. (2015). Stability analysis of fractal dimension in retinal vasculature. In E. Trucco, X. Chen, M.K. Garvin, J.J. Liu & X.Y. Frank, eds., *Proceedings of the Ophthalmic Medical Image Analysis Second International Workshop, OMIA 2015, Held in Conjunction with MICCAI 2015, Munchen, Germany, October 9, 2015*, 1–8, Iowa Research Online. 10
- HUBBARD, L.D., BROTHERS, R.J., KING, W.N., CLEGG, L.X., KLEIN, R., COOPER, L.S., SHARRETT, A.R., DAVIS, M.D. & CAI, J. (1999). Methods for evaluation of retinal microvascular abnormalities associated with hypertension/sclerosis in the Atherosclerosis Risk in Communities Study. *Ophthalmology*, **106**, 2269–80. 9
- HUBEL, D.H. & WIESEL, T.N. (1959). Receptive fields of single neurones in the cat's striate cortex. *The Journal of Physiology*, **148**, 574–591. 22
- HUGHES, A.D., MARTINEZ-PEREZ, E., JABBAR, A.S., HASSAN, A., WITT, N.W., MISTRY, P.D., CHAPMAN, N., STANTON, A.V., BEEVERS, G., PEDRINELLI, R. et al. (2006). Quantification of topological changes in retinal vascular architecture in essential and malignant hypertension. *Journal of hypertension*, **24**, 889–894. 10, 12, 250, 265
- IKRAM, M.K., JANSSEN, J.A., ROOS, A.M., RIETVELD, I., WITTEMAN, J.C., BRETELIER, M.M., HOFMAN, A., VAN DUIJN, C.M. & DE JONG, P.T. (2006a). Retinal vessel diameters and risk of impaired fasting glucose or diabetes the rotterdam study. *Diabetes*, **55**, 506–510. 13
- IKRAM, M.K., WITTEMAN, J.C., VINGERLING, J.R., BRETELIER, M.M., HOFMAN, A. & DE JONG, P.T. (2006b). Retinal vessel diameters and risk of hypertension the rotterdam study. *hypertension*, **47**, 189–194. 8, 9

REFERENCES

- IKRAM, M.K., ONG, Y.T., CHEUNG, C.Y. & WONG, T.Y. (2013). Retinal vascular caliber measurements: Clinical significance, current knowledge and future perspectives. *Ophthalmologica*, **229**, 125–136. 250
- INTERNATIONAL COUNCIL OF OPHTHALMOLOGY (2014). Ico guidelines for diabetic eye care. International Council of Ophthalmology, <http://www.icoph.org/taskforce-documents/diabetic-retinopathy-guidelines.html>, accessed: 2016-07-19. 17
- JACQUES, L. & ANTOINE, J.P. (2007). Multiselective pyramidal decomposition of images: wavelets with adaptive angular selectivity. *International Journal of Wavelets, Multiresolution and Information Processing* 5, **05**, 785–814. 140
- JBABDI, S., BELLEC, P., TORO, R., DAUNIZEAU, J., PÉLÉGRINI-ISSAC, M. & BENALI, H. (2008). Accurate anisotropic fast marching for diffusion-based geodesic tractography. *Journal of Biomedical Imaging*, **2008**, 2. 65
- JIANG, Y., BAINBRIDGE-SMITH, A., & MORRIS, A.B. (2007). Blood vessel tracking in retinal images. In *Proceedings of Image and Vision Computing*, 126 –131. 53
- JOHANSEN, P. (1994). On the classification of top points in scale space. *Journal of Mathematical Imaging and Vision*, **4**, 57–67. 174
- JOSHI, V.S., REINHARDT, J.M., GARVIN, M.K. & ABRAMOFF, M.D. (2014). Automated method for identification and artery-venous classification of vessel trees in retinal vessel networks. *PLoS ONE*, **9**, e88061. 240
- JOST, J. (2011). *Riemannian Geometry and Geometric Analysis, Sixth Edition*. Universitext, Springer Berlin Heidelberg. 88, 223
- KALITZEOS, A.A., LIP, G.Y. & HEITMAR, R. (2013). Retinal vessel tortuosity measures and their applications. *Experimental Eye Research*, **106**, 40 – 46. 70, 250
- KALITZIN, S.N., ROMENY, B.M.T.H. & VIERGEVER, M.A. (1999). Invertible apertured orientation filters in image analysis. *International Journal of Computer Vision*, **31**, 145–158. 20
- KANIZSA, G. (1955). Margini quasi percettivi in campi con stimolazione omogenea. *Rivista di Psicologia*, **49**, 7–30. 33
- KIMMEL, R. & BRUCKSTEIN, A.M. (2003). Regularized laplacian zero crossings as optimal edge integrators. *International Journal of Computer Vision*, **53**, 225–243. 184
- KLEIN, R., DAVIS, M.D., MAGLI, Y.L., SEGAL, P., KLEIN, B.E. & HUBBARD, L. (1991). The wisconsin age-related maculopathy grading system. *Ophthalmology*, **98**, 1128–1134. 17, 53

REFERENCES

- KLEIN, R., KLEIN, B.E., MOSS, S.E., WONG, T.Y., HUBBARD, L., CRUICKSHANKS, K.J. & PALTA, M. (2003). Retinal vascular abnormalities in persons with type 1 diabetes: the wisconsin epidemiologic study of diabetic retinopathy: Xviii. *Ophthalmology*, **110**, 2118–2125. 13
- KNUDTSON, M.D., LEE, K.E., HUBBARD, L.D., WONG, T.Y., KLEIN, R. & KLEIN, B.E.K. (2003). Revised formulas for summarizing retinal vessel diameters. *Current eye research*, **27**, 143–9. 240
- KOFFKA, K. (1935). *Principles of Gestalt Psychology*. Routledge, New York. 32, 33
- KOLMOGOROV, V. & ROTHER, C. (2007). Minimizing nonsubmodular functions with graph cuts - a review. *IEEE PAMI*, **29**, 1274–9. 245
- KOLMOGOROV, V. & ZABIN, R. (2004). What energy functions can be minimized via graph cuts? *IEEE transactions on pattern analysis and machine intelligence*, **26**, 147–159. 244, 245
- KRAUSE, M., ALLES, R., BURGETH, B. & WEICKERT, J. (2013). Fast retinal vessel analysis. *Journal of Real-Time Image Processing*, 1–10. 30, 140, 154
- KROON, B., HANJALIC, A. & MAAS, S.M. (2008). Eye localization for face matching: is it always useful and under what conditions? In *Proceedings of the 2008 international conference on Content-based image and video retrieval*, 379–388, ACM. 131
- LAW, M.W. & CHUNG, A.C. (2008). Three dimensional curvilinear structure detection using optimally oriented flux. In *European conference on computer vision*, 368–382, Springer. 268, 273, 278
- LEO, M., CAZZATO, D., DE MARCO, T. & DISTANTE, C. (2014). Unsupervised eye pupil localization through differential geometry and local self-similarity matching. *PloS one*, **9**, e102829. 131
- LEUNG, H., WANG, J.J., ROCHTCHINA, E., TAN, A.G., WONG, T.Y., KLEIN, R., HUBBARD, L.D. & MITCHELL, P. (2003). Relationships between age, blood pressure, and retinal vessel diameters in an older population. *Investigative Ophthalmology & Visual Science*, **44**, 2900–2904. 9
- LI, C. & LI, H. (2008). Network-constrained regularization and variable selection for analysis of genomic data. *Bioinformatics*, **24**, 1175–1182. 98
- LI, H. & YEZZI, A. (2007). Vessels as 4-d curves: Global minimal 4-D paths to extract 3-D tubular surfaces and centerlines. *IEEE Transactions on Medical Imaging*, **26**, 1213–1223. 185, 204, 278

REFERENCES

- LI, H., HSU, W., LEE, M. & WANG, H. (2003). A piecewise Gaussian model for profiling and differentiating retinal vessels. In *IEEE ICIP*, I–1069–72. 69, 240, 243, 247, 248
- LI, Q., YOU, J., ZHANG, L. & BHATTACHARYA, P. (2006). A multiscale approach to retinal vessel segmentation using Gabor filters and scale multiplication. In *Systems, Man and Cybernetics, 2006. SMC '06. IEEE International Conference on*, vol. 4, 3521 –3527. 30
- LIN, Q. (2003). Enhancement, extraction, and visualization of 3D volume data. 65
- LINDEBERG, T. (1998). Edge detection and ridge detection with automatic scale selection. *International Journal of Computer Vision*, **30**, 117–156. 196
- LIONS, P.L. (1982). *Generalized solutions of Hamilton-Jacobi equations*, vol. 69. Pitman Publishing. 306
- LOWE, D. (1999). Object recognition from local scale-invariant features. In *Computer Vision, 1999. The Proceedings of the Seventh IEEE International Conference on*, vol. 2, 1150–1157 vol.2. 96
- LOWELL, J., HUNTER, A., STEEL, D., BASU, A., RYDER, R., FLETCHER, E. & KENNEDY, L. (2004). Optic nerve head segmentation. *IEEE TMI*, **23**, 256–64. 167, 170
- LU, S. (2011). Accurate and efficient optic disc detection and segmentation by a circular transformation. *IEEE TMI*, **30**, 2126–2133. 56, 123
- LU, S. & LIM, J. (2011). Automatic optic disc detection from retinal images by a line operator. *Biomedical Engineering, IEEE TBME*, **58**, 88–94. 56, 117, 123
- LUPASCU, C.A., TEGOLO, D. & TRUCCO, E. (2010). FABC: Retinal Vessel Segmentation Using AdaBoost. *IEEE T-ITB*, **14**, 1267–1274. 140
- MALLAT, S. (1999). *A wavelet tour of signal processing*. Academic press. 31
- MANN, C. (2003). Observational research methods. research design ii: cohort, cross sectional, and case-control studies. *Emergency Medicine Journal*, **20**, 54–60. 9
- MARIN, D., GEGUNDEZ-ARIAS, M.E. et al. (2015). Obtaining optic disc center and pixel region by automatic thresholding methods on morphologically processed fundus images. *Computer Methods and Programs in Biomedicine*, **118**, 173 – 185. 56, 121, 123
- MARKUŠ, N., FRLJAK, M., PANDŽIĆ, I.S., AHLBERG, J. & FORCHHEIMER, R. (2014). Eye pupil localization with an ensemble of randomized trees. *Pattern recognition*, **47**, 578–587. 131, 137

REFERENCES

- MASHTAKOV, A., DUTS, R., SACHKOV, Y., BEKKERS, E. & BESCHASTNYI, I. (2016). Tracking of lines in spherical images via sub-Riemannian geodesics on $\text{SO}(3)$. *arXiv preprint arXiv:1604.03800*. 210, 212, 222, 223, 225, 226, 227, 229, 232
- MASHTAKOV, A.P., ARDENTOV, A.A. & SACHKOV, Y.L. (2013). Parallel algorithm and software for image inpainting via sub-Riemannian minimizers on the group of rototranslations. *Numerical Mathematics: Theory, Methods and Applications*, **6**, 95–115. 65, 184, 208
- MESSIDOR (2008). Methods to evaluate segmentation and indexing techniques in the field of retinal ophthalmology. <http://messidor.crihan.fr/download-en.php>. 259
- MIOLANE, N. & PENNÉC, X. (2015). A survey of mathematical structures for extending 2D neurogeometry to 3D image processing. In *MICCAI-MVC*, Munich, Germany. 99
- MIREBEAU, J.M. (2014). Anisotropic fast-marching on cartesian grids using lattice basis reduction. *SIAM Journal on Numerical Analysis*, **52**, 1573–1599. 65, 66, 206, 207, 230
- MITCHELL, P., CHEUNG, N., DE HASETH, K., TAYLOR, B., ROCHTCHINA, E., ISLAM, F.A., WANG, J.J., SAW, S.M. & WONG, T.Y. (2007). Blood pressure and retinal arteriolar narrowing in children. *Hypertension*, **49**, 1156–1162. 9
- MOISEEV, I. & SACHKOV, Y.L. (2010). Maxwell strata in sub-Riemannian problem on the group of motions of a plane. *ESAIM: Control, Optimisation and Calculus of Variations*, **16**, 380–399. 65, 184, 191, 199, 200, 307
- MONTGOMERY, R. (2006). *A tour of sub-Riemannian geometries, their geodesics and applications*. 91, American Mathematical Soc. 82, 184, 188
- MUMFORD, D. (1994). Elastica and computer vision. *Algebraic Geometry and Its Applications*. Springer-Verlag, 491–506. 295, 297, 299
- NGUYEN, T.T., WANG, J.J. & WONG, T.Y. (2007). Retinal vascular changes in pre-diabetes and prehypertension new findings and their research and clinical implications. *Diabetes care*, **30**, 2708–2715. 9
- NIEMEIJER, M., ABRÀMOFF, M.D. & VAN GINNEKEN, B. (2009). Fast detection of the optic disc and fovea in color fundus photographs. *MEDIA*, **13**, 859–70. 57, 125, 130
- NIEMEIJER, M., XU, X., DUMITRESCU, A.V., GUPTA, P., VAN GINNEKEN, B., FOLK, J.C. & ABRAMOFF, M.D. (2011). Automated measurement of the arteriolar-to-venular width ratio in digital color fundus photographs. *IEEE TMI*, **30**, 1941–50. 240, 277
- NIH-NATIONAL EYE INSTITUTE (2015). Facts about diabetic eye disease. National Institute of Health, <https://nei.nih.gov/health/diabetic/retinopathy>, accessed: 2016-06-07. 8

REFERENCES

- ODSTRCILIK, J., J.JAN, KOLAR, R. & GAZAREK, J. (2009). Improvement of vessel segmentation by matched filtering in colour retinal iamges. *IFMBE Proceeding of World Congress on Medical Physics and Biomedical Engineering*, 327–330. 154
- ODSTRCILIK, J. *et al.* (2013). Retinal vessel segmentation by improved matched filtering: evaluation on a new high-resolution fundus image database. *IEEE TIP*, **7**, 373–383(10). 59, 259
- OHKI, K., CHUNG, S., KARA, P., HÜBENER, M., BONHOEFFER, T. & REID, R.C. (2006). Highly ordered arrangement of single neurons in orientation pinwheels. *Nature*, **442**, 925–928. 22
- OLSON, J., STRACHAN, F., HIPWELL, J., GOATMAN, K., MC HARDY, K., FORRESTER, J. & SHARP, P. (2003). A comparative evaluation of digital imaging, retinal photography and optometrist examination in screening for diabetic retinopathy. *Diabetic medicine*, **20**, 528–534. 9
- O'REILLY, R.C., MUNAKATA, Y., FRANK, M.J., HAZY, T.E. & CONTRIBUTORS (2012). *Computational Cognitive Neuroscience*. Wiki Book, 1st Edition, URL: <http://ccnbook.colorado.edu>. 23
- OSHER, S. & FEDKIW, R. (2006). *Level set methods and dynamic implicit surfaces*, vol. 153. Springer Science & Business Media. 184, 188, 207, 306
- O'SULLIVAN, F., YANDELL, B.S. & RAYNOR JR, W.J. (1986). Automatic smoothing of regression functions in generalized linear models. *JASA*, **81**, 96–103. 116
- OWEN, C.G., NEWSOM, R.S., RUDNICKA, A.R., BARMAN, S.A., WOODWARD, E.G. & ELLIS, T.J. (2008). Diabetes and the tortuosity of vessels of the bulbar conjunctiva. *Ophthalmology*, **115**, e27–e32. 10, 12
- OWEN, C.G., RUDNICKA, A.R., NIGHTINGALE, C.M., MULLEN, R., BARMAN, S.A., SAT-TAR, N., COOK, D.G. & WHINCUP, P.H. (2011). Retinal arteriolar tortuosity and cardiovascular risk factors in a multi-ethnic population study of 10-year-old children; the child heart and health study in england (chase). *Arteriosclerosis, thrombosis, and vascular biology*, **31**, 1933–1938. 250, 265
- PATTON, N., ASLAM, T.M., MACGILLIVRAY, T., DEARY, I.J., DHILLON, B., EIJKELBOOM, R.H., YOGESAN, K. & CONSTABLE, I.J. (2006). Retinal image analysis: concepts, applications and potential. *Progress in retinal and eye research*, **25**, 99–127. 99
- PÉCHAUD, M., DESCOTEAUX, M. & KERIVEN, R. (2009a). Brain connectivity using geodesics in HARDI. In *Medical Image Computing and Computer-Assisted Intervention–MICCAI 2009*, 482–489, Springer. 65, 208

REFERENCES

- PÉCHAUD, M., KERIVEN, R. & PEYRÉ, G. (2009b). Extraction of tubular structures over an orientation domain. In *Computer Vision and Pattern Recognition, 2009. CVPR 2009. IEEE Conference on*, 336–342, IEEE. 185, 186, 196, 204, 208, 278
- PENNEC, X. (2006). Intrinsic statistics on Riemannian manifolds: Basic tools for geometric measurements. *Journal of Mathematical Imaging and Vision*, **25**, 127–154. 99
- PEREZ, M., HIGHES, A., STANTON, A., THORN, S., CHAPMAN, N., BHARATH, A. & PARKER, K. (2002). Retinal vascular tree morphology: a semi-automatic quantification. *IEEE TBME*, **49**, 912–917. 241
- PERONA, P. & MALIK, J. (1990). Scale-space and edge detection using anisotropic diffusion. *IEEE Transactions on Pattern Analysis and Machine Intelligence*, **12**, 629–639. 20
- PETITOT, J. (1999). *Naturalizing Phenomenology: Issues in Contemporary Phenomenology and Cognitive Science*. Writing science, Stanford University Press. 33
- PETITOT, J. (2003). The neurogeometry of pinwheels as a sub-Riemannian contact structure. *Journal of Physiology-Paris*, **97**, 265 – 309, neurogeometry and visual perception. 22, 65, 184, 212
- PEYRÉ, G., PÉCHAUD, M., KERIVEN, R. & COHEN, L.D. (2010). Geodesic methods in computer vision and graphics. *Foundations and Trends® in Computer Graphics and Vision*, **5**, 197–397. 65, 184, 188, 207
- PHILIPSEN, R. (2012). *Retinal Vascular Tree Segmentation and Classification by Means of Multiscale Vessel Filtering and Fractal Analysis*. Master's thesis, Eindhoven University of Technology, Department of Biomedical Engineering, the Netherlands. 154
- POLETTI, E., FIORIN, D., GRISAN, E. & RUGGERI, A. (2011). Automatic vessel segmentation in wide-field retina images of infants with retinopathy of prematurity. *Conf Proc IEEE Eng Med Biol Soc*, **2011**, 3954–3957. 154
- QAZI, A.A., JRGENSEN, D.R., LILLHOLM, M., LOOG, M., NIELSEN, M. & DAM, E.B. (2010). A framework for optimizing measurement weight maps to minimize the required sample size. *Medical Image Analysis*, **14**, 255 – 264. 98
- QUELLEC, G., LAMARD, M., ERGINAY, A., CHABOIS, A., MASSIN, P., COCHENER, B. & CAZUGUEL, G. (2016). Automatic detection of referral patients due to retinal pathologies through data mining. *Medical Image Analysis*, **29**, 47 – 64. 53
- RAMAKANTH, S.A. & BABU, R.V. (2014). Approximate nearest neighbour field based optic disk detection. *Computerized Medical Imaging and Graphics*, **38**, 49 – 56. 56, 99, 123

REFERENCES

- REEDS, J. & SHEPP, L. (1990). Optimal paths for a car that goes both forwards and backwards. *Pacific journal of mathematics*, **145**, 367–393. 311
- ROTHAUS, K., JIANG, X. & RHIEM, P. (2009). Separation of the retinal vascular graph in arteries and veins based upon structural knowledge. *Image and Vision Computing*, **27**, 864–875. 240
- ROUY, E. & TOURIN, A. (1992). A viscosity solutions approach to shape-from-shading. *SIAM Journal on Numerical Analysis*, **29**, 867–884. 186, 198
- RUDIN, W. (1973). *Functional analysis*. McGraw-Hill Book Co., New York, mcGraw-Hill Series in Higher Mathematics. 26
- SABANAYAGAM, C., LYE, W.K., KLEIN, R., KLEIN, B.E.K., COTCH, M.F., WANG, J.J., MITCHELL, P., SHAW, J.E., SELVIN, E., SHARRETT, A.R. & WONG, T.Y. (2015). Retinal microvascular calibre and risk of diabetes mellitus: a systematic review and participant-level meta-analysis. *Diabetologia*, **58**, 2476–2485. 9
- SACHKOV, Y.L. (2010). Conjugate and cut time in the sub-Riemannian problem on the group of motions of a plane. *ESAIM: Control, Optimisation and Calculus of Variations*, **16**, 1018–1039. 22, 191, 204, 307, 308
- SACHKOV, Y.L. (2011). Cut locus and optimal synthesis in the sub-Riemannian problem on the group of motions of a plane. *ESAIM: Control, Optimisation and Calculus of Variations*, **17**, 293–321. 82, 184, 185, 186, 189, 198, 199, 200, 201, 204, 208, 219, 307, 308
- SANGUINETTI, G., CITTI, G. & SARTI, A. (2010). A model of natural image edge co-occurrence in the rototranslation group. *Journal of Vision*, **10**. 252
- SANGUINETTI, G., BEKKERS, E., DUTTS, R., JANSSEN, M., MASHTAKOV, A. & MIREBEAU, J.M. (2015). Sub-Riemannian fast marching in SE(2). In A. Pardo & J. Kittler, eds., *Progress in Pattern Recognition, Image Analysis, Computer Vision, and Applications*, vol. 9423 of *Lecture Notes in Computer Science*, 366–374, Springer International Publishing. 206, 207, 237
- SASONGKO, M., WONG, T., NGUYEN, T. et al. (2011). Retinal vascular tortuosity in persons with diabetes and diabetic retinopathy. *Diabetologia*, **54**, 2409–2416. 250, 262
- SASONGKO, M.B., WONG, T.Y., NGUYEN, T.T., CHEUNG, C.Y., SHAW, J.E., KAWASAKI, R., LAMOUREUX, E.L. & WANG, J.J. (2015). Retinal vessel tortuosity and its relation to traditional and novel vascular risk markers in persons with diabetes. *Current eye research*, 1–7. 10, 13, 251, 262

REFERENCES

- SATO, Y., NAKAJIMA, S., SHIRAGA, N., ATSUMI, H., YOSHIDA, S., KOLLER, T., GERIG, G. & KIKINIS, R. (1998). Three-dimensional multi-scale line filter for segmentation and visualization of curvilinear structures in medical images. *MEDIA*, **2**, 143–168. 268
- SCHARR, H. (2006). Diffusion-like reconstruction schemes from linear data models. In *Joint Pattern Recognition Symposium*, 51–60, Springer Berlin Heidelberg. 20
- SCHEIE, H.G. (1953). Evaluation of ophthalmoscopic changes of hypertension and arteriolar sclerosis. *AMA archives of ophthalmology*, **49**, 117–138. 68
- SCHMIDT, M. & WEICKERT, J. (2016). Morphological counterparts of linear shift-invariant scale-spaces. *Journal of Mathematical Imaging and Vision*, **56**, 352–366. 186, 194
- SEKHAR, S., ABD EL-SAMIE, F.E., YU, P., AL-NUAIMY, W. & NANDI, A.K. (2011). Automated localization of retinal features. *Applied Optics*, **50**, 3064–75. 121
- SETHIAN, J. (1999). *Level Set Methods and Fast Marching Methods: Evolving Interfaces in Computational Geometry, Fluid Mechanics, Computer Vision, and Materials Science*. Cambridge Monographs on Applied and Computational Mathematics, Cambridge University Press. 65, 66, 184, 188, 207, 306
- SHARMA, U. & DUTTS, R. (2015). Left-invariant evolutions of wavelet transforms on the similitude group. *Applied and Computational Harmonic Analysis*, **39**, 110–137. 144
- SINTHANAYOTHIN, C., BOYCE, J.F., COOK, H.L. & WILLIAMSON, T.H. (1999). Automated localisation of the optic disc, fovea, and retinal blood vessels from digital colour fundus images. *The British Journal of Ophthalmology*, **83**, 902–10. 173
- SOARES, J.V., LEANDRO, J.J., CESAR JUNIOR, R.M., JELINEK, H.F. & CREE, M.J. (2006). Retinal vessel segmentation using the 2-D Gabor wavelet and supervised classification. *IEEE Trans Med Imaging*, **25**, 1214–1222. 30
- SOCHEN, N., KIMMEL, R. & MALLADI, R. (1998). A general framework for low level vision. *IEEE transactions on image processing*, **7**, 310–318. 20
- SPIVAK, M.D. (1999). *A Comprehensible Introduction to Differential Geometry*, Vol. 2, chap. Connections in Principal Bundles, 305–349. Publish or Perish, 3rd edition. 89
- STEWART, M.W. (2010). Pathophysiology of diabetic retinopathy. In *Diabetic Retinopathy*, 1–30, Springer. 8
- SUN, C., WANG, J.J., MACKEY, D.A. & WONG, T.Y. (2009). Retinal vascular caliber: systemic, environmental, and genetic associations. *Survey of ophth.*, **54**, 74–95. 9, 12, 13

REFERENCES

- TAARNHØJ, N.C., LARSEN, M., SANDER, B., KYVIK, K.O., KESSEL, L., HOUGAARD, J.L. & SØRENSEN, T.I. (2006). Heritability of retinal vessel diameters and blood pressure: a twin study. *Investigative ophthalmology & visual science*, **47**, 3539–3544. 9
- TAKAHASHI, Y. & WATANABE, S. (1980). The probability functionals (Onsager-Machlup functions) of diffusion processes. *Springer Lectures in Mathematics*, **851**, 432–463. 297, 299
- TAM, J., DHAMDHERE, K.P., TIRUVEEDHULA, P., MANZANERA, S., BAREZ, S., BEARSE, M.A., ADAMS, A.J. & ROORDA, A. (2011). Disruption of the retinal parafoveal capillary network in type 2 diabetes before the onset of diabetic retinopathy. *Investigative ophthalmology & visual science*, **52**, 9257–9266. 13, 251, 262
- TER HAAR ROMENY, B.M., BEKKERS, E.J., ZHANG, J., ABBASI-SURESHJANI, S., HUANG, F., DUITIS, R., DASHTBOZORG, B., BERENDSCHOT, T.T., SMIT-OCKELOEN, I., EPPENHOF, K.A. *et al.* (2016). Brain-inspired algorithms for retinal image analysis. *Machine Vision and Applications*, 1–19. 14
- THOMAS FLETCHER, P. (2013). Geodesic regression and the theory of least squares on Riemannian manifolds. *International Journal of Computer Vision*, **105**, 171–185. 99
- THORNBER, K. & WILLIAMS, L. (1996). Analytic solution of stochastic completion fields. *Biological Cybernetics*, **75**, 141–151. 295
- THORNBER, K. & WILLIAMS, L. (2000). Characterizing the distribution of completion shapes with corners using a mixture of random processes. *Pattern Recognition*, **33**, 543–553. 295
- TIMM, F. & BARTH, E. (2011). Accurate eye centre localisation by means of gradients. In *VISAPP*, 125–130, SciTePress. 131, 137
- TRÉLAT, E. (2006). Global subanalytic solutions of Hamilton–Jacobi type equations. In *Annales de l'IHP Analyse non linéaire*, vol. 23, 363–387. 184, 305
- TSITSIKLIS, J.N. (1995). Efficient algorithms for globally optimal trajectories. *Automatic Control, IEEE Transactions on*, **40**, 1528–1538. 65
- TUOMILEHTO, J., LINDSTRM, J., ERIKSSON, J.G., VALLE, T.T., HMLINEN, H., ILANNE-PARIKKA, P., KEINNEN-KIUKAANNIEMI, S., LAAKSO, M., LOUHERANTA, A., RASTAS, M., SALMINEN, V., AUNOLA, S., CEPAITIS, Z., MOLTCHANOV, V., HAKUMKI, M., MANNELIN, M., MARTIKKALA, V., SUNDVALL, J. & UUSITUPA, M. (2001). Prevention of type 2 diabetes mellitus by changes in lifestyle among subjects with impaired glucose tolerance. *New England Journal of Medicine*, **344**, 1343–1350, pMID: 11333990. 8
- TUZEL, O., PORIKLI, F. & MEER, P. (2008). Learning on Lie groups for invariant detection and tracking. In *CVPR*, 1–8, IEEE. 99

REFERENCES

- UNSER, M. (1999). Splines: A perfect fit for signal and image processing. *Signal Processing Magazine*, **16**, 22–38. 98
- UNSER, M., ALDROUBI, A., EDEN, M. & FELLOW, L. (1993). B-spline signal processing: Part I-theory. *IEEE Trans. Signal Processing*, **41**, 821–833. 98, 113
- VALENTI, R. & GEVERS, T. (2012). Accurate eye center location through invariant isocentric patterns. *Pattern Analysis and Machine Intelligence, IEEE Transactions on*, **34**, 1785–1798. 131
- VAN ALMSICK, M.A. (2007). *Context models of lines and contours*. Ph.D. thesis, Eindhoven University of Technology, Department of Biomedical Engineering, the Netherlands. 298
- VAN GINKEL, M. (2002). *Image Analysis using Orientation Space based on Steerable Filters*. Ph.D. thesis, Technical University Delft. 253
- VAN GRINSVEN, M.J.J.P., LECHANTEUR, Y.T.E., VAN DE VEN, J.P.H., VAN GINNEKEN, B., HOYNG, C.B., THEELEN, T. & SNchez, C.I. (2013). Automatic drusen quantification and risk assessment of age-related macular degeneration on color fundus imagesautomatic drusen quantification on color fundus images. *Investigative Ophthalmology & Visual Science*, **54**, 3019. 125
- VAZQUEZ, S.G., CANCELA, B., BARREIRA, N., PENEDO, M.G. & SAEZ, M. (2010). On the automatic computation of the arterio-venous ratio in retinal images: Using minimal paths for the artery/vein classification. In *IEEE DICTA*, 599–604. 69, 243, 247
- VIDAL, R., MA, Y. & SASTRY, S. (2005). Generalized principal component analysis (GPCA). *Pattern Analysis and Machine Intelligence, IEEE Transactions on*, **27**, 1945–1959. 99
- VIOLA, P. & JONES, M. (2001). Rapid object detection using a boosted cascade of simple features. In *CVPR 2001. Proceedings of the 2001 IEEE Computer Society Conference on*, vol. 1, I-511–I-518. 96
- SCOTLAND, G.S., MCNAMEE, P., PHILIP, S., FLEMING, A.D., GOATMAN, K.A., PRESCOTT, G.J., FONSECA, S., SHARP, P.F. & OLSON, J. (2007). cost-effectiveness of implementing automated grading within the national screening programme for diabetic retinopathy in scotland. *British Journal of Ophthalmology*, **91**, 1518–1523. 9
- WANG, J.J. & WONG, T.Y. (2006). Genetic determinants of retinal vascular caliber additional insights into hypertension pathogenesis. *Hypertension*, **47**, 644–645. 9
- WEICKERT, J. (1999). Coherence-enhancing diffusion of colour images. *Image and Vision Computing*, **17**, 201 – 212. 20
- WEILER, D.L., ENGELKE, C.B., MOORE, A.L. & HARRISON, W.W. (2015). Arteriole tortuosity associated with diabetic retinopathy and cholesterol. *Optometry & Vision Science*, **92**, 384–391. 13, 251, 262

REFERENCES

- WILKINSON, C., III, F.L.F., KLEIN, R.E., LEE, P.P., AGARDH, C.D., DAVIS, M., DILLS, D., KAMPIK, A., PARARAJASEGARAM, R. & VERDAGUER, J.T. (2003). Proposed international clinical diabetic retinopathy and diabetic macular edema disease severity scales. *Ophthalmology*, **110**, 1677 – 1682. 17, 53
- WILLIAMS, M.A., MCGOWAN, A.J., CARDWELL, C.R., CHEUNG, C.Y., CRAIG, D., PASSMORE, P., SILVESTRI, G., MAXWELL, A.P. & MCKAY, G.J. (2015). Retinal microvascular network attenuation in alzheimer's disease. *Alzheimer's & Dementia: Diagnosis, Assessment & Disease Monitoring*, **1**, 229–235. 8
- WILSON, C.M., COCKER, K.D., MOSELEY, M.J., PATERSON, C., CLAY, S.T., SCHULENBURG, W.E., MILLS, M.D., ELLS, A.L., PARKER, K.H., QUINN, G.E. et al. (2008). Computerized analysis of retinal vessel width and tortuosity in premature infants. *Investigative ophthalmology & visual science*, **49**, 3577–3585. 70, 250
- WITTICH, O. (2005). An explicit local uniform large deviation bound for brownian bridges. *Statistics and Probability Letters*, **73**, 51–56. 295, 297, 299
- WONG, T.Y., KLEIN, R., COUPER, D.J., COOPER, L.S., SHAHAR, E., HUBBARD, L.D., WOFFORD, M.R. & SHARRETT, A.R. (2001). Retinal microvascular abnormalities and incident stroke: the atherosclerosis risk in communities study. *The Lancet*, **358**, 1134–1140. 8
- WONG, T.Y., KLEIN, R., SHARRETT, A.R., SCHMIDT, M.I., PANKOW, J.S., COUPER, D.J., KLEIN, B.E., HUBBARD, L.D., DUNCAN, B.B., INVESTIGATORS, A. et al. (2002). Retinal arteriolar narrowing and risk of diabetes mellitus in middle-aged persons. *Jama*, **287**, 2528–2533. 9
- WONG, T.Y., KLEIN, R., KLEIN, B.E., MEUER, S.M. & HUBBARD, L.D. (2003). Retinal vessel diameters and their associations with age and blood pressure. *Investigative ophthalmology & visual science*, **44**, 4644–4650. 9
- WONG, T.Y., DUNCAN, B.B., GOLDEN, S.H., KLEIN, R., COUPER, D.J., KLEIN, B.E., HUBBARD, L.D., SHARRETT, A.R. & SCHMIDT, M.I. (2004). Associations between the metabolic syndrome and retinal microvascular signs: the atherosclerosis risk in communities study. *Investigative ophthalmology & visual science*, **45**, 2949–2954. 13
- WONG, T.Y., SHANKAR, A., KLEIN, R., KLEIN, B.E. & HUBBARD, L.D. (2005). Retinal arteriolar narrowing, hypertension, and subsequent risk of diabetes mellitus. *Archives of internal medicine*, **165**, 1060–1065. 9
- WONG, T.Y., ISLAM, F.A., KLEIN, R., KLEIN, B.E., COTCH, M.F., CASTRO, C., SHARRETT, A.R. & SHAHAR, E. (2006). Retinal vascular caliber, cardiovascular risk factors, and inflammation: the multi-ethnic study of atherosclerosis (MESA). *Investigative ophthalmology & visual science*, **47**, 2341–2350. 13

REFERENCES

- WU, R., CHEUNG, C.Y.L., SAW, S.M., MITCHELL, P., AUNG, T. & WONG, T.Y. (2013). Retinal vascular geometry and glaucoma: the singapore malay eye study. *Ophthalmology*, **120**, 77–83. 10, 12, 265
- XIANG, D. & WAHBA, G. (1996). A generalized approximate cross validation for smoothing splines with non-Gaussian data. *Statistica Sinica*, **6**, 675–692. 116
- XU, H., CARAMANIS, C. & MANNOR, S. (2009). Robustness and regularization of support vector machines. *The Journal of Machine Learning Research*, **10**, 1485–1510. 98
- XU, X., NIEMEIJER, M., SONG, Q., SONKA, M., GARVIN, M.K., REINHARDT, J.M. & ABRAMOFF, M.D. (2011). Vessel boundary delineation on fundus images using graph-based approach. *IEEE Trans Med Imaging*, **30**, 1184–1191. 155, 167, 169, 170
- YAU, J., KAWASAKI, R., ISLAM, F., SHAW, J., ZIMMET, P., WANG, J. & WONG, T. (2010). Retinal fractal dimension is increased in persons with diabetes but not impaired glucose metabolism: the australian diabetes, obesity and lifestyle (AusDiab) study. *Diabetologia*, **53**, 2042–2045. 10
- YIN, Y., ADEL, M. & BOURENNANE, S. (2012). Retinal vessel segmentation using a probabilistic tracking method. *Pattern Recognition*, **45**, 1235 – 1244. 154
- YOO, J.C. & HAN, T. (2009). Fast normalized cross-correlation. *CSSP*, **28**, 819–843. 96
- YOSIDA, K. (1995). Resolvent and spectrum. In *Functional Analysis*, vol. 123 of *Classics in Mathematics*, 209–231, Springer Berlin Heidelberg. 109, 305
- YOUSSIF, A. *et al.* (2008). Optic disc detection from normalized digital fundus images by means of a vessels' direction matched filter. *IEEE TMI*, **27**, 11–8. 121
- YU, H., BARRIGA, S., AGURTO, C., ECHEGARAY, S. *et al.* (2011). Fast localization of optic disc and fovea in retinal images for eye disease screening. 57, 125, 130
- YU, H. *et al.* (2012). Fast localization and segmentation of optic disk in retinal images using directional matched filtering and level sets. *IEEE TITB*, **16**, 644–57. 56, 121, 123
- ZAMPERINI, A., GIACCHETTI, A., TRUCCO, E. & CHIN, K.S. (2012). Effective features for artery-vein classification in digital fundus images. In *Computer-Based Medical Systems (CBMS), 2012 25th International Symposium on*, 1–6, IEEE. 53
- ZHANG, J., LI, H., NIE, Q. & CHENG, L. (2014). A retinal vessel boundary tracking method based on Bayesian theory and multi-scale line detection. *Computerized Medical Imaging and Graphics*, **38**, 517–525. 53

REFERENCES

- ZHANG, J., DASHTBOZORG, B., BEKKERS, E., PLUIM, J., DUIT, R. & TER HAAR ROMENY, B. (2016a). Robust retinal vessel segmentation via locally adaptive derivative frames in orientation scores. *IEEE Transactions on Medical Imaging*, **PP**, 2631–2644. 150, 196, 256
- ZHANG, J., DUIT, R., SANGUINETTI, G. & TER HAAR ROMENY, B.M. (2016b). Numerical approaches for linear left-invariant diffusions on $SE(2)$, their comparison to exact solutions, and their applications in retinal imaging. *Numerical Mathematics: Theory, Methods and Applications*, **9**, 1–50. 98, 99, 108, 109, 110, 111, 113, 114
- ZHOU, L., RZESZOTARSKI, M.S., SINGERMAN, L.J. & CHOKREFF, J.M. (1994). The detection and quantification of retinopathy using digital angiograms. *IEEE Trans Med Imaging*, **13**, 619–626. 167, 169
- ZHU, P., HUANG, F., LIN, F., LI, Q., YUAN, Y., GAO, Z. & CHEN, F. (2014). The relationship of retinal vessel diameters and fractal dimensions with blood pressure and cardiovascular risk factors. *PloS one*, **9**, e106551. 10, 12, 265
- ZWECK, J. & WILLIAMS, L.R. (2004). Euclidean group invariant computation of stochastic completion fields using shiftable-twistable functions. *Journal of Mathematical Imaging and Vision*, **21**, 135–154. 295

Summary

Retinal Image Analysis using Sub-Riemannian Geometry in $\text{SE}(2)$

Fundus photography is the process of acquiring images of the inside of the eye (the fundus) via optical means, and allows for the non-invasive and direct imaging of the living tissue of the retina. On retinal images, both the retina itself, and the retinal microvasculature can be studied. As such, retinal image analysis is not limited to the study of eye diseases alone, but more generally to any (systemic) disease with a vascular component.

Due to the low cost and non-invasive nature of fundus cameras, retinal imaging is often used in large scale screening programs and clinical studies. Large scale screening programs typically focus on the prevention of blindness via the detection of sight threatening retinal pathologies. Large scale clinical studies on the other hand, do not focus on detection of diseases per se, but rather focus on learning how vessel parameters are associated with (progression towards) certain diseases. In both scenarios (screening and clinical studies) there is a demand for automatic, reliable, robust and scalable image analysis tools as to be able to deal with large numbers of images, and to be able to quantify observations on the retina and its vasculature. This thesis is concerned with the development of such retinal image analysis tools.

The developed retinal image analysis tools rely on the processing of so-called invertible orientation scores. These are 3D functions on the coupled space of positions and orientations, and are obtained as lifts of 2D images using a continuous wavelet-like transform with anisotropic wavelets. Due to the neat organization of image data on positions and orientations, orientation scores are highly suited for the analysis of curvilinear structures (which are characterized by local orientations). In the retinal image analysis applications, these line structures are the blood vessels. As shown in this thesis, it is then beneficial to resort to processing of orientation scores considering that the blood vessels play an important role in any retinal image analysis application, whether they are considered as the main structure of interest (e.g., in clinical vessel parameter studies), used as a reference structure in retinal tissue analysis (e.g., in pathology detection), or as a structure whose specific pattern characterizes the location of key anatomical landmarks like the fovea and the optic nerve head.

In order to design effective algorithms for processing of orientation scores, one should however not treat the domain of positions and orientations as a flat Euclidean domain, but instead

recognize a curved geometry on the domain. To deal with this curved geometry the domain is identified with Lie group $SE(2)$, the group of planar roto-translations. Moreover, as orientation scores are obtained as lifts of 2D images, the curves analyzed in orientation scores are also to be considered as (natural) lifts of the lower dimensional planar curves. Such naturally lifted curves have their tangent vectors restricted to a sub-space of the full tangent space at each position and orientation. This gives rise to the notion of a sub-Riemannian geometry on $SE(2)$, where sub refers to the restriction of tangent vectors, and where the metric includes a relative cost for spatial and angular motions. Thus, in the processing of orientation scores differential geometrical tools from Lie group theory are used to deal with the curved geometry, and a sub-Riemannian geometrical approach is necessary to deal with structures that naturally appear in orientation scores. This approach enabled the development of the following applications, each of which show state-of-the-art performance in extensive benchmark comparisons:

1. Anatomical landmark detection via template matching, and template optimization in $SE(2)$.
2. Crossing preserving vessel enhancement via left-invariant processing of orientation scores.
3. Vessel tracking and segmentation via local curve optimization.
4. Vessel tracking via globally optimal sub-Riemannian geodesic extraction in $SE(2)$, where we show clear benefits of our sub-Riemannian framework compared to the Riemannian counterparts in the image/orientation scores.
5. Vessel geometry analysis and biomarker extraction by direct analysis of orientation scores.

The main theoretical results include:

1. A new framework for the computation of globally optimal data-adaptive sub-Riemannian geodesics in $SE(2)$ via a PDE and Fast-Marching approach, including extensions to the group $SO(3)$ for spherical images, including validation to exact formulas for the uniform cost case (no data-adaptivity), and including numerical techniques for the computation of the Maxwell and cusp surface.
2. A new framework for template matching in $SE(2)$, including a regularized regression framework for the construction of templates using smoothing splines in the orientation score domain. Here, also a relation is established between the regularization prior and hypo-elliptic Brownian motions $SE(2)$.

About the Author

Erik Bekkers was born on the 5th of June, 1987, in Woerden, The Netherlands. He finished his pre-university education (VWO) at Zwijsen College Veghel in 2005. In 2006 he obtained his propaedeutics degree in Mechanical Engineering at Eindhoven University of Technology (TU/e) and began his study at Biomedical Engineering at that same university. He obtained his bachelor's degree in 2009 and obtained his master's degree in 2012 in the biomedical image analysis group (BMIA). In his master studies he specialized in medical image analysis and performed internships at Philips Research Eindhoven (on simulating magnetic resonance volumes) and at Osaka University, Japan (on 3D deformation analysis of CT data of a collapsing lung). His master's thesis project was a collaboration with TU/e and Maastricht University Eye Hospital and focussed on the automated extraction of the retinal vascular tree. His thesis received industrial interest, which allowed him to continue his research in a PhD project that was a collaboration between i-Optics B.V. and Eindhoven University of Technology. From 2013 he worked as a PhD candidate on the topic of retinal image analysis using sub-Riemannian geometry. The results of this research are presented in this thesis.

List of Publications

Journal Papers

- [1] **Bekkers, E.J.**, Loog, M., ter Haar Romeny, B.M., Duits, R.: Template matching via densities on the roto-translation group. *IEEE Transactions on Pattern Analysis and Machine Intelligence* (2016) [In review, arXiv preprint arXiv:1603.03304]
- [2] **Bekkers, E.J.**, Duits, R., Mashtakov, A., Sanguinetti, G.R.: A PDE approach to data-driven sub-Riemannian geodesics in SE(2). *SIAM Journal on Imaging Sciences* 8(4) (2015) 2740-2770
- [3] **Bekkers, E.J.**, Duits, R., Berendschot, T., ter Haar Romeny, B.: A multi-orientation analysis approach to retinal vessel tracking. *Journal of Mathematical Imaging and Vision* 49(3) (2014) 583-610
- [4] Zhang, J., Dashtbozorg, B., **Bekkers, E.J.**, Pluim, J., Duits, R., ter Haar Romeny, B.: Robust retinal vessel segmentation via locally adaptive derivative frames in orientation scores. *IEEE Transactions on Medical Imaging* PP(99) (2016) 2631-2644
- [5] Mashtakov, A., Duits, R., Sachkov, Y., **Bekkers, E.J.**, Beschastnyi, I.: Tracking of lines in spherical images via sub-Riemannian geodesics on SO(3). *Journal of Mathematical Imaging and Vision* (2016) [In review, arXiv preprint arXiv:1604.03800]
- [6] Huang, F., Dashtbozorg, B., Zhang, J., **Bekkers, E.J.**, Abbasi-Sureshjani, S., Berendschot, T.T., ter Haar Romeny, B.M.: Reliability of using retinal vascular fractal dimension as a biomarker in the diabetic retinopathy detection. *Journal of Ophthalmology* 2016 (2016)
- [7] ter Haar Romeny, B.M., **Bekkers, E.J.**, Zhang, J., Abbasi-Sureshjani, S., Huang, F., Duits, R., Dashtbozorg, B., Berendschot, T.T., Smit-Ockeloen, I., Eppenhof, K.A., et al.: Brain-inspired algorithms for retinal image analysis. *Machine Vision and Applications* (2016) 1-19

Conference Papers

- [8] **Bekkers, E.J.**, Duits, R., Loog, M.: Training of templates for object recognition in invertible orientation scores: Application to optic nerve head detection in retinal images. In Tai, X.C., Bae, E., Chan, T., Lysaker, M., eds.: Energy Minimization Methods in Computer Vision and Pattern Recognition. Volume 8932 of Lecture Notes in Computer Science. Springer International Publishing (2015) 464-477
- [9] **Bekkers, E.J.**, Duits, R., Mashtakov, A., Sanguinetti, G.: Data-driven sub-Riemannian geodesics. In Aujol, J.F., Nikolova, M., Papakadis, N., eds.: Scale Space and Variational Methods in Computer Vision. Lecture Notes in Computer Science. Springer (2015) 613-625
- [10] **Bekkers, E.J.**, Zhang, J., Duits, R., ter Haar Romeny, B.: Curvature based biomarkers for diabetic retinopathy via exponential curve fits in SE(2). In Trucco, E., Chen, X., Garvin, M.K., Liu, J.J., Frank, X.Y., eds.: Proceedings of the Ophthalmic Medical Image Analysis Second International Workshop, OMIA 2015, Held in Conjunction with MICCAI 2015, Munchen, Germany, October 9, 2015. Iowa Research Online (2015) 113-120
- [11] **Bekkers, E.J.**, Duits, R., ter Haar Romeny, B.: Optic nerve head detection via group correlations in multi-orientation transforms. In Campilho, A., Kamel, M., eds.: Image Analysis and Recognition. Lecture Notes in Compute Science. Springer (2014) 293302
- [12] Sanguinetti, G., **Bekkers, E.J.**, Duits, R., Janssen, M.H., Mashtakov, A., Mirebeau, J.M.: Sub-Riemannian fast marching in SE(2). In: Progress in Pattern Recognition, Image Analysis, Computer Vision, and Applications. Springer International Publishing (2015) 366-374
- [13] Hannink, J., Duits, R., **Bekkers, E.J.**: Crossing-preserving multi-scale vesselness. In Golland, P., Hata, N., Barillot, C., Hornegger, J., Howe, R., eds.: Medical Image Computing and Computer-Assisted Intervention MICCAI 2014. Volume 8674 of Lecture Notes in Computer Science. Springer International Publishing (2014) 603-610
- [14] Zhang, J., **Bekkers, E.J.**, Abbasi, S., Dashtbozorg, B., ter Haar Romeny, B.M.: Robust and fast vessel segmentation via gaussian derivatives in orientation scores. In Murino, V., Puppo, E., Vernazza, G., eds.: International Conference on Image Analysis and Processing 2015. Lecture Notes in Computer Science. (2015) 537-547
- [15] Dashtbozorg, B., Abbasi-Sureshjani, S., Zhang, J., Huang, F., **Bekkers, E.J.**, ter Haar Romeny, B.M.: Infrastructure for retinal image analysis. In Trucco, E., Chen, X., Garvin, M.K., Liu, J.J., Frank, X.Y., eds.: Proceedings of the Ophthalmic Medical Image Analysis Third International Workshop, OMIA 2016, Held in Conjunction with MICCAI 2016, Athens, Greece, October 21, 2015. Iowa Research Online (2016) 1-8
- [16] Abbasi-Sureshjani, S., Smit-Ockeloen, I., **Bekkers, E.J.**, Dashtbozorg, B., ter Haar

List of Publications

Romeny, B.: Automatic detection of vascular bifurcations and crossings in retinal images using orientation scores. In: Biomedical Imaging(ISBI), 2016 IEEE 13th International Symposium on, IEEE (2016) 189-192

- [17] Eppenhof, K., **Bekkers, E.J.**, Berendschot, T.T., Pluim, J.P., ter Haar Romeny, B.M.: Retinal artery/vein classification via graph cut optimization. In Trucco, E., Chen, X., Garvin, M.K., Liu, J.J., Frank, X.Y., eds.: Proceedings of the Ophthalmic Medical Image Analysis Second International Workshop, OMIA 2015, Held in Conjunction with MICCAI 2015, Munchen, Germany, October 9, 2015. Iowa Research Online (2015) 121-128
- [18] Huang, F., Zhang, J., **Bekkers, E.J.**, Dashtbozorg, B., ter Haar Romeny, B.M.: Stability analysis of fractal dimension in retinal vasculature. In Trucco, E., Chen, X., Garvin, M.K., Liu, J.J., Frank, X.Y., eds.: Proceedings of the Ophthalmic Medical Image Analysis Second International Workshop, OMIA 2015, Held in Conjunction with MICCAI 2015, Munchen, Germany, October 9, 2015. Iowa Research Online (2015) 1-8